ADVANCES IN CHEMICAL PHYSICS VOLUME 128

STUART A. RICE

ADVANCES IN CHEMICAL PHYSICS

ADVANCES IN CHEMICAL PHYSICS

VOLUME 128

Advances in CHEMICAL PHYSICS

Edited by

STUART A. RICE

Department of Chemistry
and
The James Franck Institute
The University of Chicago
Chicago, Illinois

VOLUME 128

AN INTERSCIENCE PUBLICATION
JOHN WILEY & SONS, INC.

Published by John Wiley & Sons, Inc., Hoboken, New Jersey.
Published simultaneously in Canada.

Library of Congress Catalog Number: 58:9935

ISBN 0-471-44528-2

Printed in the United States of America

10 9 8 7 6 5 4 3 2 1

ILYA PRIGOGINE

January 25, 1917–May 28, 2003

Ilya Prigogine, the founding editor of *Advances in Chemical Physics*, died May 25, 2003. He was born in Moscow, fled Russia with his family in 1921, and, after brief periods in Lithuania and Germany, settled in Belgium, which was his home for 80 years. His many profound contributions to the theory of irreversible processes included extensions of both macroscopic thermodynamic analysis and statistical mechanical analysis of time-dependent processes and the approach to equilibrium. While sometimes controversial, these contributions were uniformly of outstanding intellectual merit and always addressed to the most fundamental issues; they earned him international repute and the Nobel Prize in Chemistry in 1977. Arguably equally important was his creation of a school of theoretical chemical physics centered at the University of Brussels, as well as the mentoring of numerous creative and productive scientists.

I met Ilya in 1955 while I was still a graduate student. He became a good friend, helpful and loyal, critical and encouraging, and above all personally warm. His extraordinarily broad interests in all intellectual matters, ranging from prehistoric art to philosophy, affected me deeply. I will miss him, as will the entire scientific community. The greatest tribute to his memory will be the continuation of the *Advances in Chemical Physics* series as a leading carrier of state-of-the-art science.

CONTRIBUTORS TO VOLUME 128

GABRIEL G. BALINT-KURTI, School of Chemistry, The University of Bristol, Bristol, BS8 1TS, United Kingdom

PETRA E. JÖNSSON, Department of Materials Science, Uppsala University, Box 534, SE-75121, Uppsala, Sweden

DAVID C. MORSE, Department of Chemical Engineering and Materials Science, University of Minnesota, 421 Washington Ave. S.E., Minneapolis, MN

M. MUTHUKUMAR, Polymer Science and Engineering Department, Materials Research Science and Engineering Center, University of Massachussetts, Amherst, MA

AJIT J. THAKKAR, Department of Chemistry, University of New Brunswick, Frederiction, New Brunswick E3B 6E2, Canada

INTRODUCTION

Few of us can any longer keep up with the flood of scientific literature, even in specialized subfields. Any attempt to do more and be broadly educated with respect to a large domain of science has the appearance of tilting at windmills. Yet the synthesis of ideas drawn from different subjects into new, powerful, general concepts is as valuable as ever, and the desire to remain educated persists in all scientists. This series, *Advances in Chemical Physics*, is devoted to helping the reader obtain general information about a wide variety of topics in chemical physics, a field that we interpret very broadly. Our intent is to have experts present comprehensive analyses of subjects of interest and to encourage the expression of individual points of view. We hope that this approach to the presentation of an overview of a subject will both stimulate new research and serve as a personalized learning text for beginners in a field.

STUART A. RICE

CONTENTS

NUCLEATION IN POLYMER CRYSTALLIZATION

M. MUTHUKUMAR

Polymer Science and Engineering Department, Materials Research Science and Engineering Center, University of Massachusetts, Amherst, MA 01003

CONTENTS

Advances in Chemical Physics, Volume 128, edited by Stuart A. Rice
ISBN 0-471-44528-2

I. INTRODUCTION

When a metastable liquid of small molecules undergoes a phase transition into a crystal, the mechanism of this ordering process [1] is recognized to be nucleation and growth. As sketched in Figure 1.1(*a*), nuclei of crystalline phase with linear dimension larger than a critical value r_c are formed by thermal fluctuations that then offer surfaces for further growth into full-fledged crystalline phase. The rate of nucleation of viable nuclei and the system-dependent value of r_c are determined by the extent of metastability [1].

Now, what happens to the nucleation and growth process if the small molecules are tethered together to form polymer chains, as sketched in Figure 1.1(*b*)? Clearly the ability of different portions of a long polymer chain to participate in different initial nuclei inevitably prohibits a polymer melt from forming a perfect polymer crystal. This results in a semicrystalline state. Starting from the original declaration [2] by Storks in 1938 that chains must fold back and forth in the formation of crystals, there has been a cultivation of rich phenomenology [3–9].

The modern availability of sensitive experimental techniques using synchrotron radiation and atomic force microscopy, and fast computers for molecular modeling, has spurred recent intense interest in following the mechanism of polymer crystallization. In spite of the heroic efforts by the

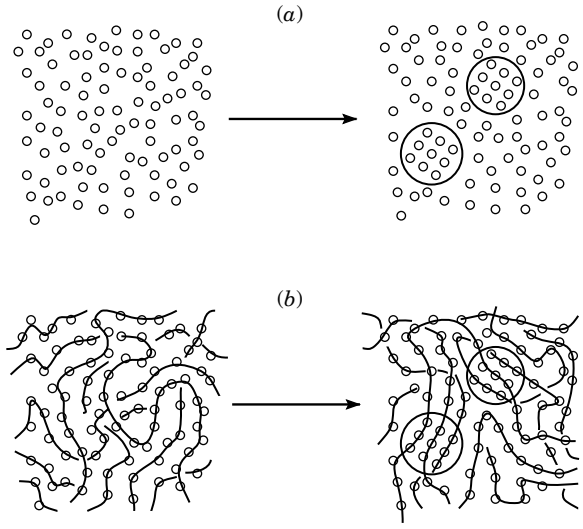

Figure 1.1. Effect of chain connectivity on nucleation.

polymer community since the early 1940s, the fundamental mechanism of polymer crystallization is still not understood. From a conceptual point of view, polymer crystallization requires an understanding of the free-energy landscape with many metastable states frustrated by entropic barriers separating them.

Among the numerous challenges faced in understanding polymer crystallization, the present review focuses only on the following issues, which are directly pertinent to the phenomenon of nucleation in polymer crystals.

A. Spontaneous Selection of Lamellar Thickness

Independent of crystallization conditions, whether from solutions or melt, the polymer molecules crystallize into thin lamellae. The lamellar thickness is about 10 nm, about two orders of magnitude smaller than values allowed by existing equilibrium considerations. This is in contrast to the case of crystallized short alkanes, where the lamellar thickness is proportional to the length of the molecules. Clearly the chains in the case of polymers should fold back and forth in the lamellae to support the experimentally observed lamellar thickness. It is believed in the literature [3–9] that the lamellar thickness is kinetically selected and that if enough time is permissible, the lamella would thicken to extended chain crystal dimension. What determines the spontaneous selection of lamellar thickness?

B. Nucleation in the Very Early Stage

There is considerable experimental evidence [9–15] for density fluctuations at very early times of crystallization before the full crystallographic features can be detected. What are the molecular origins of structural development in the primordial stage of polymer crystallization?

C. Kinetics at Growth Front

The problem of how a sufficiently large lamella grows further has attracted most of the theoretical effort [16–22] in the past and a vast amount of experimental data is available. In the analytically tractable model [4,8,16] of Lauritzen and Hoffman (LH) and further generalizations [17,19], the growth occurs via crossing another nucleation barrier associated with the formation of one stem of the polymer (of contour length comparable to lamellar thickness) followed by an essentially downhill process of lateral spreading by other stems. What are the molecular details of the barrier for the attachment of a stem at the growth front and what constitutes the stems?

D. Flow Effects

When polymers are crystallized under flow (stirring, extensional, etc.), the ubiquitous morphology [23] is the ''shish-kebab'' structure, consisting of central core (shish) surrounded by lamellae (kebabs) attached along the shish. What is the underlying mechanism behind the formation of ''shish-kebab'' structure?

Before addressing these fundamental questions, we present a brief review on phenomenology, classical thermodynamics, and kinetic models of polymer crystallization. Advances made recently (as of 2003) using molecular modeling are reviewed next.

II. PHENOMENOLOGY

Polymer crystals exhibit a myriad of morphologies with rich hierarchies of molecular organization, in distinct contrast to nonpolymeric systems. The chain connectivity plays a dramatic role in controlling the ordering process and the resulting semicrystalline morphologies, and has historically led to the emergence of the polymer age. Heroic efforts by the polymer community with exquisite structural elucidations since the early 1940s have resulted in rich phenomenology. Here we present only the very basic facts which are pertinent to the concept of nucleation.

A. Lamellae

When polyethylene is crystallized from its solutions in *p*-xylene at suitable temperatures (around 70°C), single crystals of polyethylene are formed as

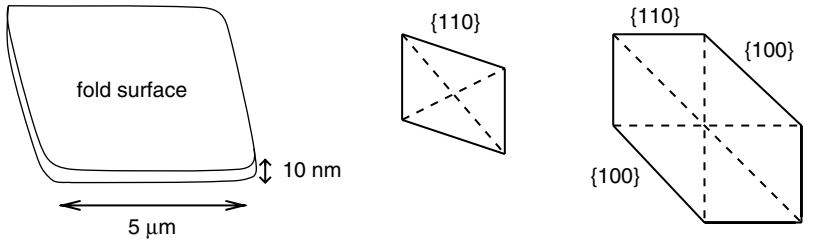

Figure 1.2. Sketch of a lamella and growth sectors.

lamellae. These are roughly 10-nm-thick platelets with regular facets, as sketched in Figure 1.2. As more molecules accumulate at the growth front, the lateral dimensions increase, by keeping the lamellar thickness (L) at 10–20 nm. Further, the small spontaneously selected lamellar thickness is essentially independent of molecular weight, for medium and high molecular weights.

The small ratio of lamellar thickness to the contour length of a polymer molecule clearly implies that chains must fold back and forth into stems with chain direction essentially perpendicular to the lamellar surface, as originally declared by Storks. The large surfaces of the lamellae containing the chain folds are called *fold surfaces*, and the thin surfaces are called *lateral surfaces*.

Crystallographic investigations showed that the polyethylene lamellae have growth sectors with orthorhombic crystal symmetry. For example, in the case of lamellae crystallized from 0.01% polyethylene in *p*-xylene at 70°C, there are four growth sectors, each with $\{110\}$ planes [Fig. 1.2(*b*)]. If crystallization is carried out at higher temperatures, new growth sectors with $\{100\}$ planes form. Different growth sectors have different thermal stability and growth rates. Further careful examination revealed that, for polyethylene lamellae, the chain axis is tilted at about 30° with respect to layer normal. This chain tilt results in a pyramid shape for the single-crystal lamella.

If crystallization is carried out from concentrated solutions, multilamellar aggregates are formed. In particular, melt crystallization of polyethylene gives bunched-up lamellae with an overall spherical symmetry. The space between the lamellae contains uncrystallized amorphous polymer. These objects are called *spherulites*, and their radii grow linearly with time, in spite of their intricate morphological features [9]. Another remarkable feature of spherulites formed by linear polyethylene is that they are gigantically chiral, although the molecules are achiral.

B. Lamellar Thickness

The initial lamellar thickness (L) depends on the degree of supercooling ΔT ($= T_m^0 - T_c$, where T_m^0 is the equilibrium melting temperature and T_c is the

crystallization temperature) according to [24]

$$L = \frac{C_1}{\Delta T} + C_2 \tag{1.1}$$

where C_1 and C_2 are system-dependent constants.

When the lamellae are annealed at a given temperature, they thicken with time. The thickening is usually continuous and L increases logarithmically with time. However, there are several examples, where the lamellar thickness increases in a stepwise manner. For example, the initial lamella may contain chains each with four folds (five stems). As thickening process continues, the lamellar thickness jumps discontinuously to three folds, and so on. This phenomenon is referred to as *quantized thickening* [25].

C. Crystallization Kinetics

As an example, we consider crystallization of polyethylene from a melt. As mentioned above, crystallization proceeds with the initial formation of isolated spherulites, which then grow until their mutual impingement with further slow crystallization. Time (t)-dependent measurements [26] of the density of the crystallizing melt at different temperatures are given in Figure 1.3 as a plot of degree of crystallinity versus logarithm of time.

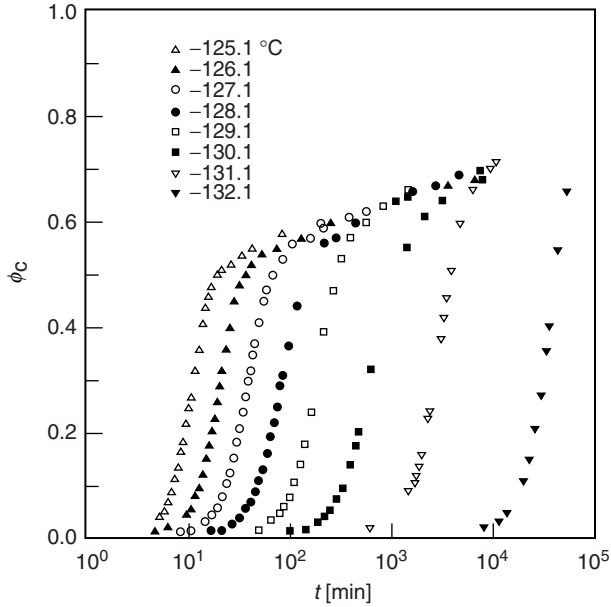

Figure 1.3. Degree of crystallinity ϕ_c versus time for linear polyethylene (molecular weight = 284,000) [26].

A decrease in the crystallization temperature results in a rapid increase in crystallization rate. All curves have similar sigmoidal shape. There is an initial induction time required for the formation of spherulitic nuclei, followed by a period of accelerated crystallization during which spherulites grow in radius. When the spherulites begin to touch each other, crystallization rates slow down again. Eventually, same degree of crystallinity is achieved, essentially independent of crystallization temperature. Complete crystallinity is almost never achieved, and the final degree of crystallinity is molecular-weight-dependent.

During the growth stage of spherulites, radial growth rate is a constant. This growth rate constant depends on temperature nonmonotonically, as illustrated in Figure 1.4 for spherulites of isotactic polystyrene [27]. As the supercooling is increased, growth rate increases first and then decreases after reaching a

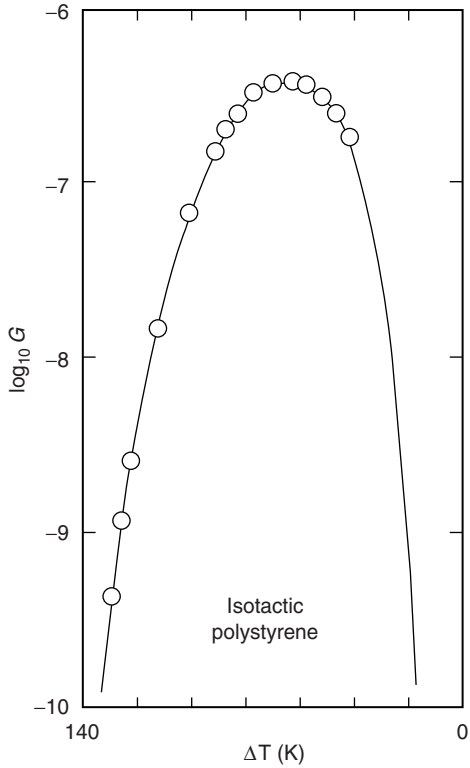

Figure 1.4. Dependence of spherulitic growth rate (cm/s) on supercooling (ΔT) for isotactic polystyrene [27].

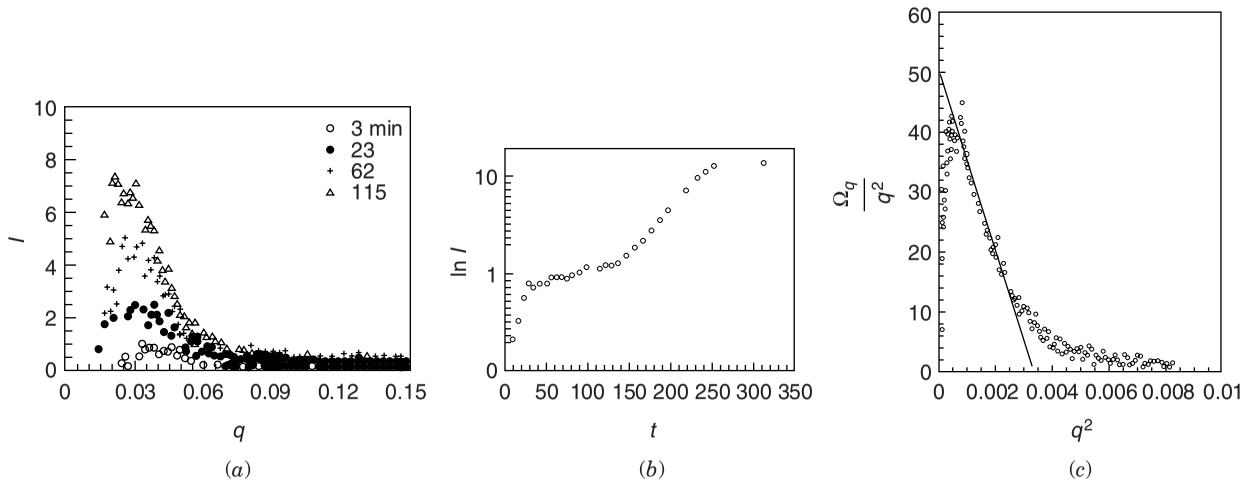

Figure 1.5. (*a*) Wavevector dependence of scattering intensity [10] at different times; (*b*) time dependence of integrated intensity [10]; (*c*) wavevector dependence of Ω_q/q^2 [14].

maximum value. As we will see below, the increase in rate with supercooling is due to nucleation processes and the decrease in rate with supercooling (i.e., decrease in temperature) is due to slowing down of diffusion of polymer chains.

At very early times of crystallization, there is considerable experimental evidence [9–15] for density fluctuations before the full crystallographic features can be detected. The major evidence is the appearance of a peak (at $q_{\max}$) in intensity, $I(q,t)$, of the small-angle X-ray scattering versus scattering wavevector $\mathbf{q}$ at an early time t, before any signal in the wide-angle X-ray scattering, for a wide variety of polymers. In the early stage, the integrated intensity grows exponentially with time, and $q_{\max}$ is proportional to $(\Delta T)^{1/2}$ (where ΔT is the supercooling). The rate (Ω_q) of growth of $I(q,t)$ divided by q^2 decreases linearly with q^2 for intermediate values of q, as shown in Figure 1.5.

These observations are analogous to those of phase-separating mixtures by spinodal decomposition mechanism, leading several researchers to invoke the idea that the early stage of polymer crystallization is spinodal decomposition.

D. Effect of Flow

In general, if the chains are oriented by external forces, the melting temperature is increased [28]. Further, it has been known for a long time that complex, ''row-nucleated'' structures occur if polymer solutions or melts are crystallized in the presence of flow [29,30]. These so-called shish-kebabs (sketched in Fig. 1.6), consist of a central fiber core, *shish*, surrounded by lamellar crystalline structures, *kebabs*, periodically attached along the shish.

The fiberlike crystalline structures (shish) are highly stable to the point that they can be superheated [31]. Therefore, it is believed that the core of the shish is formed by crystallization of completely stretched polymer chains. The kebabs are believed to be folded-chain lamellar structures. The direction of growth of the kebabs is normal to the shish. The chain alignment in the kebabs is believed to be parallel to the shish. Similar structures are obtained by crystallization in polymer melt films exposed to orientational deformation [32,33]. These ''two-dimensional'' shish-kebabs also consist of a central fiber, shish, and periodically attached ''linear'' kebabs, with growth direction normal to the shish.

III. THERMODYNAMICS

A. Melting Temperature and Supercooling

Consider a polymeric liquid where each polymer chain contains N repeat units. The chemical potential per repeat unit μ_u^0 in the liquid phase is

$$\mu_u^0 = h^l - Ts^l \tag{1.2}$$

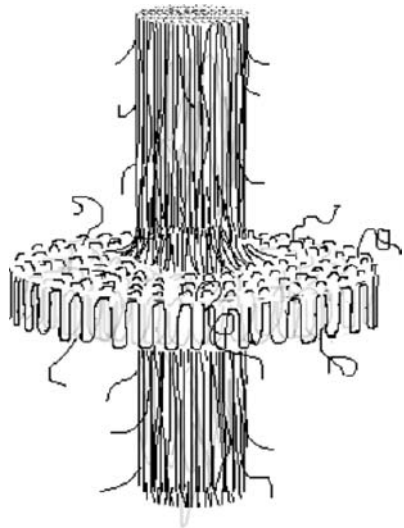

Figure 1.6. Sketch of shish-kebab morphology.

where h^l and s^l respectively are the corresponding enthalpy and entropy per repeat unit at the temperature T. Analogously, the chemical potential per repeat unit in the crystalline phase is

$$\mu_u^c = h^c - Ts^c \tag{1.3}$$

In writing these equations, effects of chain ends are not explicitly taken into account. At the equilibrium melting temperature T_m^0, we obtain

$$\mu_u^c = \mu_u^0 \tag{1.4}$$

which results in

$$T_m^0 = \frac{\Delta h}{\Delta s} \tag{1.5}$$

Here, $\Delta h(\equiv h^l - h^c)$ is the latent heat of fusion and $\Delta s(\equiv s^l - s^c)$ is the entropy of fusion, both per repeat unit.

This simple result for the equilibrium melting temperature offers a guidance in the chemical design of elastomers (low T_m^0) and engineering plastics (high T_m^0). For example, if the chain backbone is more flexible, then the change in

entropy associated with the transformation of more flexible conformations to rigid chain conformations in the crystal is large and consequently leads to lower values of T_m^0. Another example is polymer crystallization under elongational flows. In the presence of such flows, the polymer chains are already stretched (with lower conformational entropy) so that Δs accompanying crystallization is small. This is directly responsible for higher T_m^0. Consequently, the crystallization temperature of a polymeric liquid in elongational flows is higher than that in the quiescent state. For temperatures greater than T_m^0, μ_u^0 is lower than μ_u^c and the liquid phase is the stable phase. For $T < T_m^0$, the crystalline phase is more stable and the thermodynamic force for its formation is $\mu_u^0 - \mu_u^c$, given by

$$\mu_u^c - \mu_u^0 = -(\Delta h - T\Delta s) \tag{1.6}$$

Substituting Δs from Eq. (1.5), we obtain

$$\begin{aligned} \mu_u^c - \mu_u^0 &= -\Delta h\left(1 - \frac{T}{T_m^0}\right) \\ &= -\Delta h \frac{\Delta T}{T_m^0} \end{aligned} \tag{1.7}$$

where $\Delta T(\equiv T_m^0 - T)$, is the supercooling. Therefore, the free energy of the crystalline phase is increasingly lowered as the supercooling increases (i.e., as T decreases). We define the "gain in free energy" associated with the formation of the crystalline phase as

$$\begin{aligned} \mu_u^c - \mu_u^0 &= -\Delta\mu \\ \Delta\mu &= \Delta h \frac{\Delta T}{T_m^0} \end{aligned} \tag{1.8}$$

B. Depression of Melting Point

When a polymeric liquid contains a noncrystallizable component such as another polymer or impurity, the equilibrium melting temperature T_m is substantially different from T_m^0 and can be readily expected from thermodynamic arguments. As a specific example, consider a blend of n_1 chains of N_1 segments and n_2 chains of N_2 segments. According to the classical Flory–Huggins theory [34], the free energy of mixing is given by

$$\frac{\Delta G}{RT} = n_1 \ln \phi_1 + n_2 \ln \phi_2 + \chi n_1 N_1 \phi_2 \tag{1.9}$$

where χ is the chemical mismatch parameter, R is the gas constant, and

$$\begin{aligned}\phi_1 &= \frac{n_1 N_1}{n_1 N_1 + n_2 N_2} \\ \phi_2 &= \frac{n_2 N_2}{n_1 N_1 + n_2 N_2}\end{aligned} \tag{1.10}$$

For simplicity, we have taken the volume of each segment to be the same for both types of polymers, so that ϕ_1 and ϕ_2 are volume fractions. The case of polymer solutions is the special case of $N_1 = 1$. It follows from Eq. (1.9) that the chemical potential of the second component (assumed to be crystallizable) is given by

$$\frac{\mu_2 - \mu_2^0}{RT} = \left(\frac{\partial(\Delta G/RT)}{\partial n_2}\right)_{n_1,T} = \ln\phi_2 + \left(1 - \frac{N_2}{N_1}\right)(1 - \phi_2) + \chi N_2 (1 - \phi_2)^2 \tag{1.11}$$

where μ_2^0 is the chemical potential per chain in the pure liquid state. The chemical potential per mole of repeat units of the crystallizable polymer in the liquid phase of the blend is

$$\mu_u^l - \mu_u^0 = \frac{\mu_2}{N_2(v_1/v_u)} = RT\left(\frac{v_u}{v_1}\right)\left[\frac{\ln\phi_2}{N_2} + \left(\frac{1}{N_2} - \frac{1}{N_1}\right)(1 - \phi_2) + \chi(1 - \phi_2)^2\right] \tag{1.12}$$

Here, v_u and v_1 are the molar volumes of the repeating unit and a segment of the noncrystallizable first component, respectively. At the melting temperature T_m of the second polymer component in the blend

$$\mu_u^c = \mu_u^l \tag{1.13}$$

Note that at T_m^0, $\mu_u^c = \mu_u^0$. Subtracting μ_u^0 from both sides of this equation and substituting the results of Eqs. (1.8) and (1.12) at T_m, we get

$$\frac{1}{T_m} - \frac{1}{T_m^0} = -\frac{R}{\Delta h}\frac{v_u}{v_1}\left[\frac{1}{N_2}\ln\phi_2 + \left(\frac{1}{N_2} - \frac{1}{N_1}\right)(1 - \phi_2) + \chi(1 - \phi_2)^2\right] \tag{1.14}$$

In the case of polymer solutions, $N_1 = 1$ and $N_2 \gg 1$, we obtain

$$\frac{1}{T_m} - \frac{1}{T_m^0} = \frac{R}{\Delta h}\frac{v_u}{v_1}(\phi_1 - \chi\phi_1^2) \tag{1.15}$$

For ideal solutions ($\chi = 0$), the melting temperature of the crystallizable polymer from solutions follows as

$$\frac{1}{T_m} - \frac{1}{T_m^0} = \frac{R}{\Delta h}\frac{v_u}{v_1}\phi_1 \tag{1.16}$$

where ϕ_1 is the volume fraction of the solvent. Therefore the melting temperature is depressed by the presence of the diluent. Equation (1.15) has been used in earlier studies to determine the χ parameter and the equilibrium melting temperature T_m^0.

In the case of blends, $N_1 \gg 1$ and $N_2 \gg 1$, Eq. (1.14) gives

$$\frac{1}{T_m} - \frac{1}{T_m^0} = -\frac{R}{\Delta h}\frac{v_u}{v_1}\chi\phi_1^2 \tag{1.17}$$

For homogeneous blends, $\chi < 0$ and consequently the presence of another noncrystallizable polymer depresses the melting point of a polymer.

Equation (1.14) is of general utility, where the first component can be any impurity instead of a solvent. As an example, even for the case of a pure polymer, the chain ends do not readily get incorporated into the crystal structure. Therefore the chain ends can be treated as impurities. Taking $\phi_1 = 2/N$ and v_1 to be the molar volume of the end group, the melting temperature increases with the molecular weight of the polymer according to

$$\frac{1}{T_m} - \frac{1}{T_m^0} = \frac{R}{\Delta h}\frac{v_u}{v_1}\frac{2}{N} \tag{1.18}$$

in qualitative agreement with experimental observations [35]. Similarly, if the polymer chain contains branch points, then T_m is lowered in qualitative agreement with Eq. (1.16), where ϕ_1 is the volume fraction of the branch points. Another example is the class of copolymers consisting of crystallizable and noncrystallizable monomers. In this context, Eq. (1.16) leads to

$$\frac{1}{T_m} - \frac{1}{T_m^0} = -\frac{R}{\Delta h}\ln p \tag{1.19}$$

where p, called the *sequence propagation probability*, is the probability that a crystallizable unit is succeeded by another such unit. For random copolymers, $p = x_2$, where x_2 is the mole fraction of crystallizing unit. For blocky copolymers, $p > x_2$, and for alternating copolymers, $p < x_2$. The predictions of Eq. (1.19) on the sequence-dependence of T_m for copolymers have been remarkably successful [35].

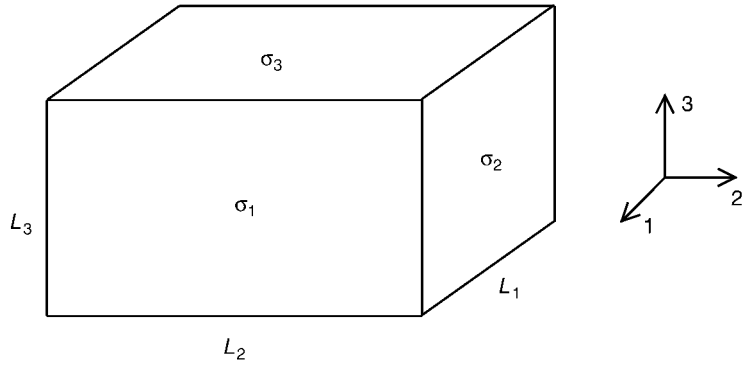

Figure 1.7. Sketch of a finite crystal.

C. Equilibrium Crystal Shape

Consider a finite crystal of thickness L_i along the ith axis, as sketched in Figure 1.7. Let σ_i be the surface free energy per unit area of surfaces perpendicular to the ith axis.

The free energy of formation of this crystal from the pure melt is

$$\Delta G = -V\Delta\mu + 2\sigma_1 L_2 L_3 + 2\sigma_2 L_3 L_1 + 2\sigma_3 L_1 L_2 \tag{1.20}$$

where $V(= L_1 L_2 L_3)$ is the volume of the crystal and $\Delta\mu$ is now per unit volume. We wish to minimize ΔG to determine the equilibrium shape. Because of the volume constraint, L_3 can be eliminated and then ΔG minimized with respect to L_1 and L_2. Eliminating $L_3(= V/L_1 L_2)$, Eq. (1.20) gives

$$\Delta G = -V\Delta\mu + \frac{2\sigma_1 V}{L_1} + \frac{2\sigma_2 V}{L_2} + 2\sigma_3 L_1 L_2 \tag{1.21}$$

Minimizing ΔG with respect to L_1 and L_2 for fixed V gives

$$\begin{aligned} \frac{\partial \Delta G}{\partial L_1} &= -\frac{2\sigma_1 V}{L_1^2} + 2\sigma_3 L_2 = 0 \\ \frac{\partial \Delta G}{\partial L_2} &= -\frac{2\sigma_2 V}{L_2^2} + 2\sigma_3 L_1 = 0 \end{aligned} \tag{1.22}$$

which simplifies to

$$\frac{\sigma_1}{L_1} = \frac{\sigma_2}{L_2} \tag{1.23}$$

By repeating the above procedure, but now eliminating L_2 instead of L_3, we obtain $\frac{\sigma_1}{L_1} = \frac{\sigma_3}{L_3}$. Therefore, based on only thermodynamic arguments, the dimensions of an equilibrium crystal in different orthogonal directions are proportional to the surface free energies of the perpendicular surfaces:

$$\frac{L_1}{\sigma_1} = \frac{L_2}{\sigma_2} = \frac{L_3}{\sigma_3} \tag{1.24}$$

For the specific case of a lamella (with thickness $L = L_3$, and lateral dimension $L_1 = L_2$)

$$\frac{L}{L_1} = \frac{\sigma_3}{\sigma_1} = \frac{\sigma_f}{\sigma_l} \tag{1.25}$$

The estimated value of the free energy of the fold surface $(\sigma_3 \equiv \sigma_f)$ is 90 $\mathrm{mJ/m^2}$ for polyethylene, whereas that of the lateral surface $(\sigma_1 \equiv \sigma_l)$ is 15 $\mathrm{mJ/m^2}$. Therefore we expect the lamellar thickness to be 6 times larger than the lateral dimension, specifically, a cylinder shape, instead of a disklike shape. This is in stark contrast to the facts described in Section II. The thermodynamic estimate of lamellar thickness is about two orders of magnitude larger than the observed values for polyethylene and other polymers. In view of this discrepancy, we are led to the conclusion that lamellae are not in equilibrium.

D. Dependence of T_m on Lamellar Thickness (Gibbs–Thompson Equation)

The free energy of a lamella, where the fold surface area $A(= L_1L_2)$ is taken to be much larger than lateral surface area $(L_3L_1 + L_2L_3)$, follows from Eq. (1.20) as

$$\Delta G = -AL\Delta\mu + 2A\sigma_f \tag{1.26}$$

where L is the lamellar thickness (L_3) and σ_f is fold surface free energy. Substituting Eq. (1.8) for $\Delta\mu$, we obtain

$$\Delta G = -AL\Delta h\frac{\Delta T}{T_m^0} + 2A\sigma_f \tag{1.27}$$

where Δh is expressed per unit volume. At the melting temperature (T_m) of a lamella of thickness L, ΔG of Eq. (1.27) is zero, yielding

$$T_m = T_m^0\left(1 - \frac{2\sigma_f}{L\Delta h}\right) \tag{1.28}$$

Therefore a plot of T_m versus $1/L$ is expected to be linear with the intercept and slope given by T_m^0 and $-2\sigma_f T_m^0/\Delta h$, respectively. This allows us to obtain the equilibrium melting temperature (T_m^0) for infinitely large lamellar thickness by extrapolation, and the fold surface free energy.

E. Minimum Lamellar Thickness

Let T_c be the crystallization temperature and $\Delta T \equiv T_m^0 - T_c$ be the supercooling. For the lamellar shape, and $\Delta T > 0$, it follows from Eq. (1.26) that $\Delta G < 0$ if

$$L > \frac{2\sigma_f}{\Delta\mu} \tag{1.29}$$

The lower limit of this inequality is the minimum possible lamellar thickness L_0:

$$L_0 = \frac{2\sigma_f}{\Delta\mu} \tag{1.30}$$

For $L > L_0$, ΔG is negative and the most stable lamella is with infinite thickness. Thus, according to the argument presented above, we expect the formation of a ''virgin lamella'' with an initial thickness L_0 for a given supercooling, and then the lamella to thicken with time. Therefore, for a given supercooling, L is given by

$$L = L_0 + \delta L \tag{1.31}$$

where δL is $L - L_0$. Substituting Eq. (1.8) for $\Delta\mu$ in Eq. (1.30), we get

$$L_0 = \frac{2\sigma_f T_m^0}{\Delta h\ \Delta T} \tag{1.32}$$

Thus, the initial lamellar thickness is inversely proportional to supercooling. Combining Eqs. (1.31) and (1.32), the dependence of lamellar thickness on the crystallization temperature T_c is given by

$$\begin{aligned} L &= \frac{2\sigma_f T_m^0}{\Delta h(T_m^0 - T_c)} + \delta L \\ &= \frac{c}{\Delta T} + \delta L \end{aligned} \tag{1.33}$$

This form is often observed experimentally.

F. Thickening (Hoffman–Weeks Plot)

If $\delta L/L_0$ is small, as observed experimentally, perhaps due to very slow kinetics of chain rearrangements, then the relationship between L_0 and T_c is the same as the Gibbs–Thompson equation:

$$T_c = T_m^0\left(1 - \frac{2\sigma_f}{L\Delta h}\right) \tag{1.34}$$

This implies that for a given lamellar thickness, the melting temperature and the crystallization temperature should be the same. In practice, this is not observed.

We now consider the role of lamellar thickening on the relation between T_c and T_m. At T_c, the initial thickness of the virgin lamella is given by Eq. (1.32) as

$$L_0 = \frac{2\sigma T_m^0}{\Delta h(T_m^0 - T_c)} \tag{1.35}$$

After certain duration of time, let the lamella have thickened by a factor of β so that $L = L_0\beta$. According to the Gibbs–Thompson equation, Eq. (1.28), the melting temperature of the thickened lamella is

$$T_m = T_m^0\left(1 - \frac{2\sigma}{\Delta h L_0 \beta}\right) \tag{1.36}$$

Substituting Eq. (1.35) in Eq. (1.36) for L_0, we obtain

$$T_m = \frac{1}{\beta}T_c + \left(1 - \frac{1}{\beta}\right)T_m^0 \tag{1.37}$$

A plot (called the *Hoffman–Weeks plot* [36]) of T_m versus T_c is linear for a constant thickening factor, and the extrapolated intersection of T_m with T_c is taken to be the equilibrium melting temperature T_m^0. While this procedure has been improved [37], the whole concept is also contested [38].

IV. NUCLEATION

When a liquid is quenched to a temperature below its melting temperature, small nuclei of different sizes and shapes are initially born as a result of fluctuations in the density of the liquid. These nuclei are stabilized by lowering of the free energy associated with the formation of the more stable crystalline phase, but destabilized by the increase in free energy associated with the creation of interfaces. As is well known, sub-critical-size nuclei dissolve back

into the liquid phase. Those nuclei larger than the critical nucleus grow and eventually complete the phase transition. In this section, we give a brief review of the classical approach without any discussion of the topological connectivity of the polymer. The polymer specificity will be discussed in Section V. Although the nuclei can have irregular shapes in the initial stages of crystallization, we restrict ourselves to spherical and cylindrical nuclei.

A. Spherical Nucleus

For a spherical nucleus of radius r, the free energy of formation of a crystal from the liquid phase, follows analogous to Eq. (1.20) as

$$\Delta G = -\frac{4}{3}\pi r^3 \Delta\mu + 4\pi r^2 \sigma \tag{1.38}$$

where σ is the interfacial tension at the spherical surface of the nucleus. $\Delta\mu$ is expressed per unit volume as given by Eq. (1.8)

$$\Delta\mu = \Delta h \frac{\Delta T}{T_m^0} \tag{1.39}$$

and is positive for $\Delta T = T_m^0 - T > 0$. A sketch of ΔG versus r is given in Figure 1.8.

The critical radius r_c is obtained from

$$\left(\frac{\partial \Delta G}{\partial r}\right)_{r=r_c} = 0 \tag{1.40}$$

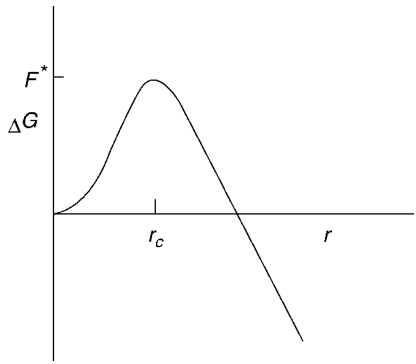

Figure 1.8. Nucleation barrier.

to be

$$r_c = \frac{2\sigma}{\Delta\mu} = \frac{2\sigma T_m^0}{\Delta h\ \Delta T} \tag{1.41}$$

The critical radius diverges inversely with supercooling. Substitution of this result for r_c into Eq. (1.38) leads to the free energy of formation of critical spherical nucleus as

$$F^* = \frac{16\pi}{3}\frac{\sigma^3}{(\Delta\mu)^2} = \frac{16\pi}{3}\frac{\sigma^3 (T_m^0)^2}{(\Delta h)^2 (\Delta T)^2} \tag{1.42}$$

diverging as $(\Delta T)^{-2}$ with the supercooling. The global free energy minimum corresponds to the infinitely large sphere of the crystalline phase.

B. Cylindrical Nucleus

Consider the cylinder sketched in Figure 1.9 with radius R and length L, where σ_f and σ_l are the fold and lateral surface free energies per unit area.

The free energy of formation of this nucleus is

$$\Delta G = -\pi R^2 L \Delta\mu + 2\pi R L \sigma_l + 2\pi R^2 \sigma_f \tag{1.43}$$

Defining R and L in units of the typical length l of a repeat unit

$$\begin{aligned} \pi R^2 &\equiv \mu l^2 \\ L &\equiv ml \end{aligned} \tag{1.44}$$

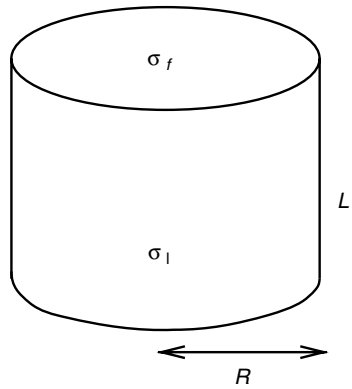

Figure 1.9. Cylindrical nucleus.

ΔG follows as

$$\Delta G = -\mu m\epsilon + m\sqrt{\mu}\sigma_l' + 2\mu\sigma_f' \tag{1.45}$$

where

$$\epsilon = l^3\Delta\mu = \frac{l^3\Delta h\Delta T}{T_m^0}$$
$$\sigma_l' = 2\sqrt{\pi}l^2\sigma_l \tag{1.46}$$
and $$\sigma_f' = l^2\sigma_f$$

Minimizing ΔG with respect to m and μ, $\frac{\partial\Delta G}{\partial m} = 0 = \frac{\partial\Delta G}{\partial\mu}$, gives the dimensions of the critical nucleus as

$$m_c = \frac{4\sigma_f'}{\epsilon} = \frac{4\sigma_f T_m^0}{l\Delta h\Delta T}$$
$$\mu_c = \left(\frac{\sigma_l'}{\epsilon}\right)^2 = \frac{4\pi\sigma_l^2(T_m^0)^2}{l^2(\Delta h)^2(\Delta T)^2} \tag{1.47}$$

The free energy of formation (F^*) of the critical nucleus is

$$F^* = \frac{\epsilon m_c\mu_c}{2} = \frac{8\pi\sigma_f\sigma_l^2(T_m^0)^2}{(\Delta h)^2(\Delta T)^2} \tag{1.48}$$

Defining $\bar{m} = m/m_c$, $\bar{\mu} = \mu/\mu_c$ and $\overline{\Delta G} = \Delta G/F^*$, the free energy of formation of the cylindrical nucleus is given by

$$\overline{\Delta G} = -2\bar{\mu}\bar{m} + 2\bar{m}\sqrt{\bar{\mu}} + \sqrt{\bar{\mu}} \tag{1.49}$$

The dependence of $\overline{\Delta G}$ on $\bar{m}$ (proportional to lamellar length) and $\bar{\mu}$ (proportional to lateral dimension) is given in Figure 1.10 as a contour plot.

The critical nucleus corresponds to $\bar{\mu} = 1 = \bar{m}$, and the global free-energy minimum corresponds to infinitely large dimensions of the cylinder in both length and radius.

Independent of the anisotropy of the shape of the crystal, it is to be recognized that the free-energy barrier required for the formation of the critical nucleus is inversely proportional to the square of supercooling

$$F^* \sim \frac{1}{(\Delta T)^2} \tag{1.50}$$

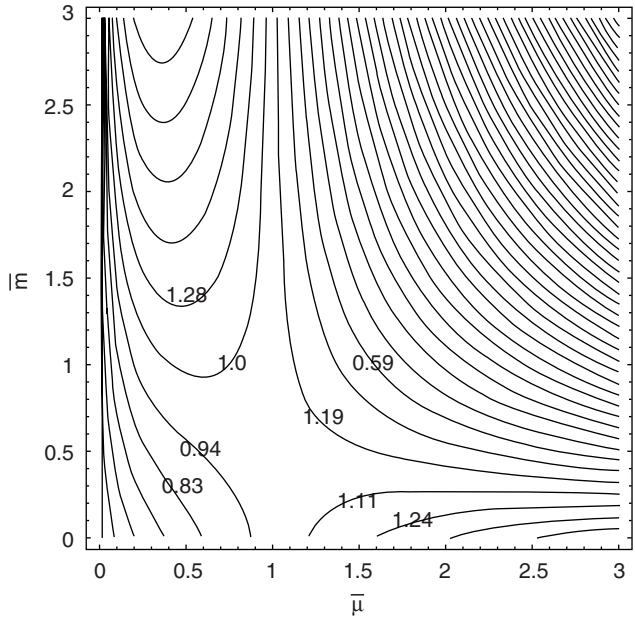

Figure 1.10. Free-energy landscape for a cylindrical nucleus.

where the prefactor depends on the geometry of the nucleus. In view of this general feature, we consider only the spherical nucleus in the following consideration of distribution of nuclei of different sizes and the rate of their formation.

C. Equilibrium Distribution of Nuclei

Expanding the free energy of formation of a spherical nucleus of radius r [given by Eq. (1.38)] around that (F^*) for a critical nucleus, we get

$$\Delta G = F^* + \frac{1}{2}\frac{\partial^2 \Delta G}{\partial r^2}\bigg|_{r=r_c} (r - r_c)^2 + \cdots \tag{1.51}$$

where the coefficient of the quadratic term follows from Eq. (1.38) as

$$\frac{1}{2}\frac{\partial^2 \Delta G}{\partial r^2}\bigg|_{r=r_c} = -4\pi(r_c \Delta\mu - \sigma) \tag{1.52}$$

Replacing $\Delta\mu$ by $2\sigma/r_c$, due to Eq. (1.41), in Eqs. (1.51) and (1.52), we obtain

$$\Delta G = \frac{4}{3}\pi\sigma r_c^2 - 4\pi\sigma(r - r_c)^2 + \cdots \tag{1.53}$$

The number of nuclei of radius r (close to r_c) in equilibrium is given by the Boltzmann distribution

$$n_0(r) = \mathcal{N} e^{-(\Delta G/kT)} = \mathcal{N} e^{-(4\pi/3kT)\sigma r_c^2 + (4\pi\sigma/kT)(r-r_c)^2} \tag{1.54}$$

where k is the Boltzmann constant, $\mathcal{N}$ is the normalization factor, and ΔG is r-dependent as given by Eq. (1.38). As a specific example, the number of critical nuclei is given by

$$n_0(r_c) = \mathcal{N} e^{-(16\pi/3)(\sigma^3/kT)\{(T_m^0)^2/[(\Delta h)^2(\Delta T)^2]\}} \tag{1.55}$$

and is strongly dependent on the supercooling. It also follows from Eqs. (1.53) and (1.54) that the mean-square fluctuation of the radius of the nucleus around r_c is inversely proportional to σ:

$$\langle (r - r_c)^2 \rangle \sim \frac{kT}{\sigma} \tag{1.56}$$

D. Nucleation Rate

In this section we give a brief summary of the classical Becker–Döring theory of nucleation [39] and then implement the results for the polymer crystallization. Let a crystalline nucleus of radius r contain N repeat units such that

$$\frac{4}{3}\pi r^3 = Nl^3 \tag{1.57}$$

In terms of N, ΔG of Eqs. (1.38) and (1.46) yield

$$F_N \equiv \Delta G = -N\epsilon + 3^{2/3}(4\pi)^{1/3}\sigma l^2 N^{2/3} \tag{1.58}$$

so that the critical number of repeat units for the formation of crystalline phase is

$$N_c = \frac{4\pi}{3}\left(\frac{2\sigma l^2}{\epsilon}\right)^3 = \frac{4}{3}\pi\left(\frac{r_c}{l}\right)^3 \tag{1.59}$$

Let the average number of nuclei of size N at time t be $n_N(t)$. We assume that the nuclei change their sizes only by the evaporation–condensation mechanism,

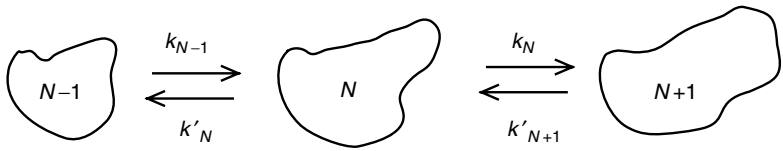

Figure 1.11. Elementary steps of growth of nuclei.

that is, in an elementary process only one repeat unit is either added or removed. This is sketched in Figure 1.11.

Let k_N represent the rate at which one repeat unit is added to a nucleus of size N. Let k'_N represent the rate at which one repeat unit is removed from a nucleus of size N. The rate of change of the number of nuclei of size N is dictated by four elementary steps (where $N-1$ becomes N, N shrinks to $N-1$, N is depleted to become $N+1$, and $N+1$ loses one repeat unit to become N) as given by

$$\begin{aligned}\frac{\partial n_N(t)}{\partial t} &= k_{N-1}n_{N-1} - k'_N n_N - k_N n_N + k'_{N+1}n_{N+1} \\ &= J_{N-1} - J_N \end{aligned} \tag{1.60}$$

where

$$J_N = k_N n_N(t) - k'_{N+1}n_{N+1} \tag{1.61}$$

is the rate per volume at which nuclei grow from size N to $N+1$.

The rate constants k_N and k'_N are phenomenological constants. If we assume that there is a local equilibrium between nuclei of different sizes, k_N and k'_N are related by the "detailed balance," that is, the ratio of the forward rate to the reverse rate is the equilibrium constant given by the exponential of the negative change in the free energy in units of kT:

$$\frac{k_N}{k'_{N+1}} = e^{-[(F_{N+1}-F_N)/kT]} \tag{1.62}$$

Substituting the expression for k'_{N+1} from Eq. (1.62) into Eq. (1.61), J_N is given by

$$J_N = k_N n_N(t) - k_N e^{(F_{N+1}-F_N)/kT} n_{N+1}(t) \tag{1.63}$$

Since N is usually very large, it can be taken as a continuous variable. Writing F_{N+1} as $F_N + \frac{\partial F_N}{\partial N} + \cdots$, and n_{N+1} as $n_N + \frac{\partial n_N}{\partial N} + \cdots$ and expanding the

exponential, J_N follows as

$$\begin{aligned} J_N &= k_N n_N(t) - k_N \left[1 + \frac{1}{kT}(F_{N+1} - F_N) + \cdots\right] n_{N+1}(t) \\ &= -k_N(n_{N+1}(t) - n_N(t)) - \frac{k_N}{kT}(F_{N+1} - F_N) n_{N+1}(t) \\ &= -k_N \frac{\partial n_N}{\partial N} - \frac{k_N}{kT}\frac{\partial F_N}{\partial N} n_N(t) + \cdots \end{aligned} \tag{1.64}$$

Within the same continuous notation for N, Eqs. (1.60) and (1.64) yield

$$\begin{aligned} \frac{\partial n_N(t)}{\partial t} &= -\frac{\partial J_N}{\partial N} \\ &= \frac{\partial}{\partial N}\left[\frac{k_N}{kT}\frac{\partial F_N}{\partial N} n_N(t) + k_N \frac{\partial n_N(t)}{\partial N}\right] \end{aligned} \tag{1.65}$$

This equation is the familiar Fokker–Planck equation for the time evolution of the distribution function for the number density of the nuclei with different sizes N.

In equilibrium, the flux in the ''size space'' J_N is zero (i.e., the square-bracket term in Eq. (1.65) vanishes). The solution of this condition is given by Eqs. (1.54) and (1.65) as

$$n_N^0 = \mathcal{N} e^{-(F_N/kT)} \tag{1.66}$$

In the steady state, the flux J_N is a constant, J, independent of N. Rearranging Eq. (1.63), we obtain

$$J_N = k_N e^{-\frac{F_N}{kT}}\left[\frac{n_N(t)}{e^{-(F_N/kT)}} - \frac{n_{N+1}(t)}{e^{-(F_{N+1}/kT)}}\right] \tag{1.67}$$

Using the result for the equilibrium distribution [Eq. (1.66)], we get

$$\frac{J_N}{k_N n_N^0} = \frac{n_N(t)}{n_N^0} - \frac{n_{N+1}(t)}{n_{N+1}^0} \tag{1.68}$$

Summing this equation over N from 1 to a large number, say, Λ, we get in the steady state ($J_N = J$)

$$J \sum_{N=1}^{\Lambda} \frac{1}{k_N n_N^0} = \frac{n_1(t)}{n_1^0} - \frac{n_{\Lambda+1}(t)}{n_{\Lambda+1}^0} \tag{1.69}$$

If we take the steady-state distribution function $n_N(t)$ to be close to n_1^0 for $N \to 1$ and to be zero for $N \to \infty$, the right-hand side of Eq. (1.69) is unity so that the flux in the steady state, called the *nucleation rate*, is given by

$$\begin{aligned} J &= \frac{1}{\sum_{N=1}^{\Lambda} \left(\frac{1}{k_N n_N^0} \right)} \\ &\cong \mathcal{N} \left[\int_0^\infty dN \frac{1}{k_N} e^{F_N/kT} \right]^{-1} \end{aligned} \tag{1.70}$$

Substituting the result of Eq. (1.54) for $n_0(r)$, we get

$$J = \mathcal{N} e^{-(4\pi\sigma/3kT)r_c^2} \left[\int_0^\infty dr \frac{e^{-(4\pi\sigma/kT)(r-r_c)^2}}{k(r)} \right]^{-1} \tag{1.71}$$

Since the integrand of the integral inside the square brackets is sharply peaked around r_c, the integral can be performed by the "saddle point approximation," and the result is

$$\begin{aligned} J &= \mathcal{N} e^{-(4\pi\sigma/3kT)r_c^2} \left(\frac{4\sigma}{kT} \right)^{1/2} k(r_c) \\ &= 2k(r_c) \left(\frac{\sigma}{kT} \right)^{1/2} n_0(r_c) \\ &\equiv J_0 e^{-(4\pi/3)(\sigma/kT)r_c^2} \\ &= J_0 \exp\left\{ -\frac{16\pi}{3} \frac{\sigma^3}{kT} \frac{(T_m^0)^2}{(\Delta h)^2 (\Delta T)^2} \right\} \\ &= J_0 \exp \frac{-F^*}{kT} \end{aligned} \tag{1.72}$$

J_0 is called the *nucleation rate prefactor.*

In general, the rate at which critical nuclei are formed, called the *homogeneous nucleation rate*, is given by the form

$$J = Ck(r_c) \left(-\frac{\Delta G''(r_c)}{kT} \right)^{1/2} e^{-F^*/kT} \tag{1.73}$$

as a product of three factors where C is a prefactor reflecting the geometry of nucleus. $k(r_c)$ is the frequency of arrival of repeat units to the critical nucleus, F^* is the nucleation barrier associated with the formation of critical nucleus, and $\Delta G''(r_c)$ is the curvature of ΔG around r_c. As discussed in Section IV.B, $F^* \sim (\Delta T)^{-2}$. The nucleation rate is very low for weak supercooling, and it

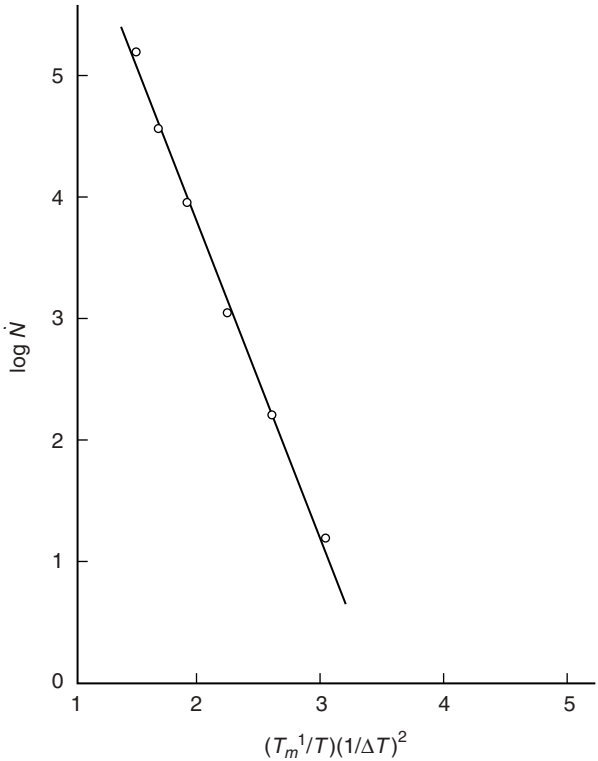

Figure 1.12. Dependence of nucleation rate on supercooling.

increases exponentially with an increase in the extent of supercooling. Therefore, a plot of log J versus $(T_m^0)^2/T(\Delta T)^2$ should be linear, in agreement with experimental data [28,40] on poly(decamethylene sebacate) as shown in Figure 1.12.

It is remarkable that the predictions of classical nucleation theory without any consideration of polymer connectivity are borne out in experiments. At higher supercooling, deviations are expected because of temperature dependence of the nucleation rate prefactor.

V. GROWTH, SECONDARY NUCLEATION, AND LAURITZEN–HOFFMAN THEORY

We now consider the growth of an already formed crystal at a given supercooling. The attachment of polymer molecules at the growth front is a very complex

process involving polymer diffusion, entanglement effects, competitive adsorption/desorption at the growth front, and other factors. The simplest approach to treat these features is to invoke a nucleation barrier for attachment of every polymer molecule at the growth front. Thus lamellar growth is assumed to occur by a nucleation process, called *secondary nucleation*. This is the basic premise of the very successful theory [4,5,16] of Lauritzen and Hoffman (LH). Although there have been several generalizations of the LH theory, we outline only the basic assumptions of the nucleation theory of LH.

A. Model

The basic model of LH theory is sketched in Figure 1.13, where polymer molecules are assumed to attach at the growth front in terms of stems, each of length comparable to the lamellar thickness L.

For each polymer molecule, the first step is to place its first stem at the growth surface, whose lateral dimension is taken as L_p. This step is assumed to be associated with a nucleation. After this step, the secondary nucleus spreads out laterally with the rate g. The thickness of the stem is a along the lateral direction and b along the growth direction with growth rate G.

Consider the attachment of the fist stem, the free-energy change accompanying this step is

$$\Delta G_1 = -abL\ \Delta\mu + 2bL\sigma_l \tag{1.74}$$

Two new lateral surfaces, each of area bL, are created in this step. Since the first stem does not generate any chain folds on the fold surfaces, the free-energy cost

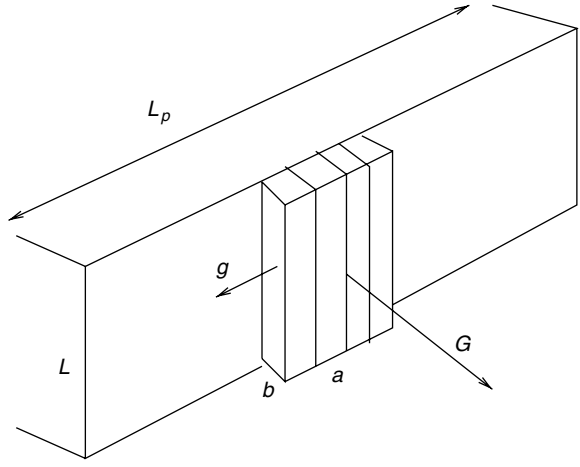

Figure 1.13. Model of growth front.

associated with fold surface areas ($2ab$) is ignored for the first stem. The initial and final states of this step are assumed to be separated by a free-energy barrier, which is taken to be the lateral surface free energy ($2bL\sigma_l$) reduced by an arbitrary fraction of the free energy of crystallization ($abL\,\Delta\mu$)

$$\Delta G_1^* = -\psi abL\ \Delta\mu + 2bL\sigma_l \tag{1.75}$$

for the forward process. For the reverse process the barrier is $(1-\psi)abL\,\Delta\mu$. ψ is called an ''apportioning'' parameter. The free-energy change associated with the second stem (i.e., first fold) is

$$\Delta G_2 = -abL\ \Delta\mu + 2ab\sigma_f \tag{1.76}$$

The initial and final stages of the deposition of the second stem are assumed to be separated by a barrier

$$\Delta G_2^* = -\psi abL\ \Delta\mu + 2ab\sigma_f \tag{1.77}$$

in the forward direction. We have assumed the apportioning parameter to be the same for both steps, for convenience. The barrier for the reverse direction of the second step is $(1-\psi)abL\,\Delta\mu$. The free-energy changes associated with the lateral attachment of subsequent stems are the same as for the second stem. The free-energy landscape of the process is illustrated in Figure 1.14.

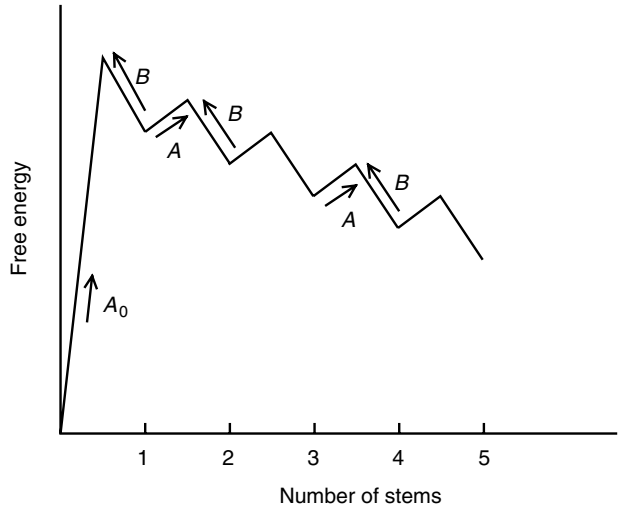

Figure 1.14. Free-energy landscape of the Lauritzen–Hoffman model.

In drawing the cartoon of Figure 1.14, we have assumed that $2\sigma_L/a > \Delta\mu$, $2\sigma_f/\Delta\mu < L$, and $0 < \psi < 1$. It is to be noted that the case of $\psi = 1$ corresponds to no barriers and that of $\psi = 0$ to the maximum barriers.

The rate of deposition of the first stem is proportional to $\exp(-\Delta G_1^*/kT)$ and is defined through

$$A_0 = \beta \exp\left[-\frac{2bL\sigma_l - \psi abL\ \Delta\mu}{kT}\right] \tag{1.78}$$

where β accounts for the approach rate of polymer segments at the growth front. The most familiar form of β is the same as that for low-molecular-weight supercooled liquids

$$\beta = CTe^{-[U^*/k(T-T_0)]} \tag{1.79}$$

where C is a constant prefactor, U^* is the free-energy barrier for local dynamics of repeat units, and T_0 is the temperature at which diffusion of polymer chains is essentially stopped. Other phenomenological expressions for β can be written, reflecting the dynamics of supercooled polymer melts. This, in itself, is not well understood, and it is presently sufficient to be content with Eq. (1.79).

The rate of removal of the first stem is given by

$$B = \beta \exp\left[-\frac{(1-\psi)abL\ \Delta\mu}{kT}\right] \tag{1.80}$$

For the particular choice of the apportioning used in the definition of barriers, B is the rate of removal of any stem (either the first or any of the subsequent stems). The rate of deposition of the second or any of the subsequent stems is given by

$$A = \beta \exp\left[-\frac{2ab\sigma_f - \psi abL\ \Delta\mu}{kT}\right] \tag{1.81}$$

B. Steady State

In the steady state, the flux of stems is a constant (S) and is given by the balance equation

$$S = \nu_0 A_0 - \nu_1 B = \nu_1 A - \nu_2 B = \nu_2 A - \nu_3 B = \cdots \tag{1.82}$$

where ν_i is the number density of systems with i stems in the growth layer. From the equality between S and the third term ($\nu_1 A - \nu_2 B$), we obtain

$$\nu_1 = \frac{1}{A}(S + \nu_2 B) \tag{1.83}$$

Substituting this result in the first identity of Eq. (1.82), we obtain

$$S\left(1+\frac{B}{A}\right)=\nu_0 A_0-\frac{B^2}{A}\nu_2 \tag{1.84}$$

Now eliminating ν_2 in terms of S and ν_3 (using the fourth term) and repeating this iteratively, we obtain

$$S\left(1+\frac{B}{A}+\frac{B^2}{A^2}+\cdots\right)=\nu_0 A_0 \tag{1.85}$$

so that the steady-state flux is given by

$$S=\nu_0 A_0\left(1-\frac{B}{A}\right) \tag{1.86}$$

Substituting the expressions for A_0, A and B from Eqs. (1.78)–(1.81), we obtain the steady-state flux of stems as an explicit function of the lamellar thickness (L)

$$S(L)=\nu_0\beta\,\exp\left(-\frac{2bL\sigma_l-\psi abL\,\Delta\mu}{kT}\right)\left[1-\exp\left(\frac{2ab\sigma_f-abL\,\Delta\mu}{kT}\right)\right] \tag{1.87}$$

where $S(L)$ is the nucleation rate for noninteracting nuclei and for the lamellar thickness L at a given supercooling. It is also the probability distribution for a crystal to have thickness L. The total flux S_T, in a collection of crystals, is calculated by summing $S(L)$ over all possible values of L. It is to be noted that the square bracket term becomes negative (i.e., the flux is unphysically negative) if $L < 2\sigma_f/\Delta\mu$ ($\equiv L_0$, obtained from the thermodynamic considerations of Section III.E). Therefore S_T follows as

$$S_T=\sum_{L_0}^{\infty}S(L)\cong\frac{1}{l_u}\int_{2\sigma_f/\Delta\mu}^{\infty}dL\;S(L) \tag{1.88}$$

where l_u is the length of the monomer repeat unit. Substituting Eq. (1.87) for $S(L)$ into the above equation, we get

$$S_T=\frac{\beta\nu_0 P}{l_u}\exp\left[\frac{2ab\psi\sigma_f}{kT}-\frac{4b\sigma_l\sigma_f}{kT\,\Delta\mu}\right] \tag{1.89}$$

with

$$P=kT\left[\frac{1}{(2b\sigma_l-ab\psi\;\Delta\mu)}-\frac{1}{(2b\sigma_l+(1-\psi)ab\;\Delta\mu)}\right] \tag{1.90}$$

The lateral spreading rate g is given by

$$g = a(A - B) \tag{1.91}$$

Substituting A and B from Eqs. (1.80) and (1.81), g becomes

$$g = a\beta Q \exp\left[-\frac{2ab\sigma_f(1-\psi)}{kT}\right] \tag{1.92}$$

with

$$Q = \exp\left[\frac{\psi ab\ \Delta\mu(L - \frac{2\sigma_f}{\Delta\mu})}{kT}\right]\left\{1 - \exp\left[-\frac{ab\,\Delta\mu(L - \frac{2\sigma_f}{\Delta\mu})}{kT}\right]\right\} \tag{1.93}$$

Using the expressions for $S(L)$, S_T, and g, average lamellar thickness and growth rates can be calculated. For small values of $\Delta\mu$, P and Q approach approximately l_u and unity, respectively. It is therefore obvious from Eqs. (1.89) and (1.92) that S_T is a strongly increasing function of $\Delta\mu$, whereas g is negligibly dependent on temperature. Thus as the supercooling increases, S_T/g increases, with significant consequences discussed in the next section.

The thermodynamic arguments of Section III show that the minimum lamellar thickness L_0 is $2\sigma_f/\Delta\mu$. The average lamellar thickness L^* follows from Eq. (1.87) as its first moment

$$\begin{aligned} L^* &= \frac{\int_{L_0}^{\infty} dL\ LS(L)}{\int_{L_0}^{\infty} dL\ S(L)} \\ &= L_0 + \frac{kT}{2b\sigma_l}\frac{\left[2 + (1-2\psi)\frac{a\Delta\mu}{2\sigma_l}\right]}{\left[1 - \frac{a\psi\Delta\mu}{2\sigma_l}\right]\left[1 + \frac{a(1-\psi)\Delta\mu}{2\sigma_l}\right]} \\ &= L_0 + \delta L \end{aligned} \tag{1.94}$$

where $L_0 = 2\sigma_f/\Delta\mu$ and δL is independent of σ_f but depends on T, $\Delta\mu$, a, b, ψ, and σ_l.

One of the successes of the LH theory is its ability to provide an explicit result for the lamellar thickness, based on kinetic considerations of secondary nucleation. In the LH theory, δL is a natural result of the steady state and not due to any subsequent thickening. The form of Eq. (1.94) is exactly the same as Eq. (1.1), observed experimentally. However, one of the serious difficulties posed by Eq. (1.94) is that it predicts a divergence in δL at

$$\frac{2\sigma_l}{a} = \psi\,\Delta\,\mu \tag{1.95}$$

Since $\Delta\mu$ is proportional to the supercooling, the LH theory predicts that as the crystallization temperature is lowered to a value when Eq. (1.95) is satisfied, the lamellar thickness would diverge. This is referred to as the "δL catastrophe." By taking reasonable experimental values for the various parameters and assuming $\psi = 1$ (no barriers for attachment of each stem), the necessary supercooling for the appearance of this catastrophe is 55 K for polyethylene. This is not observed experimentally. To fix this discrepancy, ψ is taken to be zero so that

$$\delta L = \frac{kT}{2b\sigma_l} \frac{\left(\frac{4\sigma_l}{a} + \Delta\mu\right)}{\left(\frac{2\sigma_l}{a} + \Delta\mu\right)} \tag{1.96}$$

However, this choice of ψ implies that surfaces of stems need to be formed first before any gain in the bulk free energy of the stems.

In general, in the LH model, there are two key processes: nucleation of the first stem (with a rate i per unit substrate length per unit time), and the lateral growth rate (g) for the deposition of second and subsequent stems. Depending on the relative magnitudes of i and g, three regimes can be identified. Let the dark areas in Figure 1.15 represent the growth front and each square correspond to the cross section of a stem. In regime I [Fig. 1.15(b)] secondary nucleation controls the linear growth rate $G(g \gg i)$. In regime III [Fig. 1.15(d)], prolific multiple nucleation controls G.

Sanchez and DiMarzio identified [41] a crossover regime II [Fig. 1.15(c)], where g is more rapid than in I and less than in III. On the basis of the LH model, crystallization kinetics in these three regimes are obtained as follows.

C. Regime I

In this regime, the lateral growth rate (g) is significantly greater than the secondary nucleation rate (i), so that the latter is rate-determining for the growth rate (G). For $g \gg i$, the whole substrate is covered by stems as soon as the first stem is nucleated. Thus, monolayers are added one by one. If L_p is the substrate

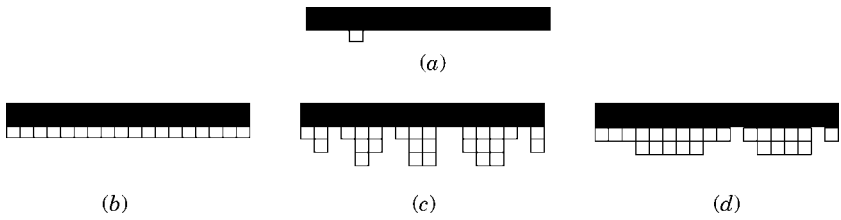

Figure 1.15. Lauritzen–Hoffman model.

length, iL_p is the rate of formation of secondary nuclei on the substrate. In regime I, each secondary nucleation leads to the formation of a monolayer of thickness b. Therefore, the linear growth rate G_{I} in regime I is given by

$$G_{\mathrm{I}} = biL_p \tag{1.97}$$

The nucleation rate i is the total flux S_T per available sites (ν_0). Substituting Eq. (1.89), for S_T, we get

$$G_{\mathrm{I}} = \frac{b\beta L_p}{l_u} P \exp\left[\frac{2ab\psi\sigma_f}{kT} - \frac{4b\sigma_l\sigma_f}{kT\,\Delta\mu}\right] \tag{1.98}$$

For small values of supercooling, P is comparable to l_u. Substituting the expression for β from Eq. (1.79), G_{I} becomes

$$G_{\mathrm{I}} = G_{\mathrm{I},0}\, e^{-[U^*/k(T-T_0)]} e^{-(4b\sigma_l\sigma_f/kT\Delta\mu)} \tag{1.99}$$

where the prefactor is

$$G_{\mathrm{I},0} = CbL_pT \exp\left(\frac{2ab\psi\sigma_f}{kT}\right) \tag{1.100}$$

Substituting the expression for $\Delta\mu$ in term of the supercooling, we obtain

$$\begin{aligned} G_{\mathrm{I}} &= G_{\mathrm{I},0} \exp\left[-\frac{U^*}{k(T-T_0)} - \frac{4b\sigma_l\sigma_f T_m^0}{kT\,\Delta h(T_m^0 - T)}\right] \\ &\equiv G_{\mathrm{I},0} G_{\mathrm{I},D} G_{\mathrm{I},n} \end{aligned} \tag{1.101}$$

where the nucleation part ($G_{\mathrm{I},n}$) of the growth rate is given by

$$G_{\mathrm{I},n} \equiv e^{-(K_g/T\,\Delta T)} \tag{1.102}$$

with

$$K_g \equiv \frac{4b\sigma_l\sigma_f T_m^0}{k\,\Delta h} \tag{1.103}$$

The expression for G_{I} nicely shows its nonmonotonic dependence on the crystallization temperature. Close to the equilibrium melting temperature, the growth is nucleation-dominated and is given essentially by $G_{\mathrm{I},n}$. For temperatures far below T_m^0, but closer to T_0, the $G_{\mathrm{I},D}$ term dominates and the growth rate precipitously decreases with supercooling.

D. Regime II

If the lateral growth rate g is comparable or smaller than the nucleation rate i, then further layers are deposited before the first layer is fully formed [as sketched in Fig. 1.15(c)]. Under these circumstances (regime II), the linear growth rate is given by

$$G_{\mathrm{II}} = b\sqrt{ig} \tag{1.104}$$

where $i = S_T/\nu_0$ and g are given in Eqs. (1.89) and (1.92). The above result emerges from the following scaling argument [41] of Sanchez and Dimarzio. Let an isolated stem undergo nucleation at time $t = 0$. As time progresses, the layer grows laterally in two opposite directions so that $2gt$ is the length of the substrate covered by the new monolayer at time t. While this patch of the monolayer tends to grow laterally, it also offers sites for nucleation of another layer. The rate at which new nuclei form on this patch is $2gti$. The total number of nuclei formed during a time τ is

$$\int_0^{\tau} 2gti\, dt = gi\tau^2 \tag{1.105}$$

assuming that g and i are independent of time. Therefore, the average time $\langle\tau\rangle$ required for the formation of a new nucleus on the growing patch is

$$\langle\tau\rangle \sim \frac{1}{\sqrt{gi}} \tag{1.106}$$

The rate at which new layers are formed is $b/\langle\tau\rangle$ so that

$$G_{\mathrm{II}} = b\sqrt{ig} \tag{1.107}$$

Substituting the results of Eqs. (1.89) and (1.92) into the above equation, we get

$$\begin{aligned} G_{\mathrm{II}} &= G_{\mathrm{II}}^0 e^{-[U^*/k(T-T_0)]} e^{-(2b\sigma_l\sigma_f/kT\,\Delta\mu)} \\ &= G_{\mathrm{II}}^0 G_{\mathrm{I},D}\sqrt{G_{\mathrm{I},n}} \end{aligned} \tag{1.108}$$

where

$$G_{\mathrm{II}}^0 = CbT \exp\left[\frac{(2\psi - 1)ab\sigma_f}{kT}\right] \tag{1.109}$$

In writing this result, we have approximated Q of Eq. (1.93) to be unity, valid for low supercoolings.

The nucleation part of the linear growth rate is

$$G_{\mathrm{II},n} = \sqrt{G_{\mathrm{I},n}} = e^{-(K_g'/T\,\Delta T)} \tag{1.110}$$

where K_g' is half of K_g:

$$K_g' = \frac{2b\sigma_l\sigma_f T_m^0}{k\,\Delta h} \tag{1.111}$$

E. Regime III

In this regime the multiple nucleation of stems is so prolific [Fig. 1.15(*d*)] that the lateral spreading rate is irrelevant, $i \gg g$. Now the growth rate is exactly of the same form as in regime I

$$\begin{aligned} G_{\mathrm{III}} &= biL_p \\ &= G_{\mathrm{III}}^0 e^{-[U^*/k(T-T_0)]-(K_g/T\Delta T)} \end{aligned} \tag{1.112}$$

with

$$\begin{aligned} G_{\mathrm{III}}^0 &= CTbL_p \exp\left(\frac{2ab\sigma_f\psi}{kT}\right) \\ K_g &= \frac{4b\sigma_l\sigma_f T_m^0}{k\Delta h} \end{aligned} \tag{1.113}$$

Equations (1.101), (1.108), and (1.112) suggest that three regimes would be manifest in a plot of $(\log G) + U^*/k(T - T_0)$ versus $1/T\Delta T$, as sketched in Figure 1.16.

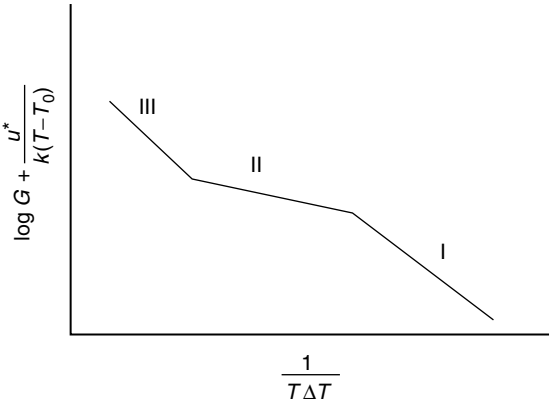

Figure 1.16. Three regimes in the LH model.

The slope of the line in regime II is predicted to be exactly half of that for regimes I and III. There is considerable experimental evidence [7] for the existence of regimes I and II and for the result, $K_g = 2K_g'$.

F. Extensions and Criticisms

The major extensions of the LH model are the following. For details, the original references should be consulted.

1. The deposition of each stem of m repeat units can be treated [8,41] as a set of m equilibria. While this generalization appears to account for more local details, the general conclusions are the same as in the LH theory. In realistic situations, we expect nonsequential deposition of repeat units into various stems. These partially formed stems will then sort out through entropic barriers to attain the lamellar thickness. We return to this issue in Section VII.

2. The kinetic factor β in Eq. (1.79) should reflect the contour length of the polymer (instead of only the monomer friction), as the polymer chains must diffuse from an entangled melt or a concentrated solution to a growth front. Based on the reptation model of polymer dynamics, an expression for β has been derived. According to this argument [22], the linear growth rate in melts is inversely proportional to the average molecular weight of the polymer, independent of the regime.

3. The LH theory has been extended [22] to account for the curvature of the growth front by incorporating the consequences of lattice strain behind the growth front.

4. When a melt of broad polydispersity in molecular weight is crystallized, lower molecular weights are rejected from growing crystals, although the temperature is below their respective melting points. This molecular fractionation has been explained [42] by the LH model, by adopting to individual molecules. This is termed *molecular nucleation*. Considering the free energy of formation of a molecular crystallite consisting of stems and surfaces (lateral and fold), the critical size of the crystalline nucleus is calculated in terms of supercooling and contour length. Nuclei smaller than the critical size will dissolve back. This leads to a critical molecular weight (below which chains do not crystallize) as an increasing function of the crystallization temperature, in good agreement with experimental data.

5. In the LH model, the stems are deposited such that the lamellar thickness is uniform throughout the growth. This restriction is partially removed by allowing the stems to diffuse by one repeat unit in the direction of layer normal, accompanied by a penalty in free energy. This model [43] is referred to as the "sliding diffusion model" and averts the "δL catastrophe."

6. In the case of crystallization of small molecules, there exists a critical temperature called the "roughening temperature [8]" T_R. For $T > T_R$, the crystalline surfaces are microscopically rough and macroscopically rounded. For $T < T_R$, the crystals are faceted. At temperatures higher than T_R, the free-energy barriers for fluctuations of density of molecules are weak, and the growth rate is proportional to the supercooling. Observation [8] of such a dependence of G for polyethylene oxide at weak supercoolings prompted Sadler to dispute the claim that nucleation is always the rate-determining factor in kinetic theories of polymer crystallization. On the other hand, for polyethylene samples, log G is proportional to $1/T\Delta T$. To explain these observations, Sadler and Gilmer proposed a model [21] for polymer crystallization by generalizing the surface roughening model for small molecules. This model is implemented by Monte Carlo simulations where repeat units at the growth front are allowed to rearrange with certain prescribed probabilities. Although the simulation results are in qualitative agreement with experimental observations, analytical expressions are not available.

7. There are many serious criticisms of the LH theory at all levels of the model and agreements with experiments. The review by Armitstead and Goldbeck-Wood [8] gives a fair and comprehensive review of this criticism. We mention only the most serious discrepancy. The value of the substrate length L_p fitted as a parameter to agree with kinetics data is unrealistically different from the experimental value measured directly by Point and collaborators [20]. They suggested that the change in K_g across the regimes I–II transition may arise from temperature dependence of interfacial energies, transport coefficients and molecular segregation, instead of validity of the LH theory.

VI. SPINODAL MODE IN POLYMER CRYSTALLIZATION

As discussed in Section II, measured excess scattering intensity, after a melt is cooled below its melting point, increases exponentially with time at all scattering wavevectors and the inverse of $q_{\max}$ (at which intensity is a maximum) diverges as $(\Delta T)^{-1/2}$. These observations are similar to those observed in mixtures undergoing phase separation by the spinodal decomposition mechanism [39], as described below. This similarity has led to the proposal of spinodal decomposition, instead of nucleation, as the primary mechanism of the very early stages of polymer crystallization. There has been extensive interest in establishing an understanding of nucleation versus spinodal decomposition in polymer crystallization. In view of this, we give below the salient features of the spinodal decomposition mechanism.

As a specific example, consider a blend (discussed in Section III.B) of n_1 chains of N_1 segments and n_2 chains of N_2 segments. The free-energy density

of mixing for this blend is obtained by dividing ΔG of Eq. (1.9) by $(n_1N_1 + n_2N_2)$

$$\frac{F}{kT} = \frac{\phi}{N_1}\ln\phi + \frac{(1-\phi)}{N_2}\ln(1-\phi) + \chi\phi(1-\phi) \tag{1.114}$$

where $\phi \equiv \phi_1$ and $\phi_2 = (1-\phi)$. Typically, χ is inversely proportional to T. Using the standard procedures to calculate the critical point for liquid–liquid demixing, Eq. (1.114) yields the critical point to be

$$\phi_c = \frac{\sqrt{N_2}}{\sqrt{N_1}+\sqrt{N_2}} \qquad \chi_c = \frac{(\sqrt{N_1}+\sqrt{N_2})^2}{2N_1N_2} \tag{1.115}$$

Defining an order parameter $\tilde{\phi}$ to be $\phi - \phi_c$, and expanding F as a Taylor series in $\tilde{\phi}$, we get

$$\frac{F}{kT} = \frac{F_0}{kT} + \frac{A}{2}\tilde{\phi}^2 + \frac{B}{4}\tilde{\phi}^4 + \cdots \tag{1.116}$$

where

$$\begin{aligned} A &= \left[\frac{1}{N_1\phi_c} + \frac{1}{N_2(1-\phi_c)}\right]\frac{T-T_c}{T_c} \equiv -a_0\,\Delta T \\ B &= \frac{1}{3}\left[\frac{1}{N_1\phi_c^3} + \frac{1}{N_2(1-\phi_c)^3}\right] \end{aligned} \tag{1.117}$$

where $\Delta T = T_c - T > 0$ is now the quench depth for phase separation. In obtaining the expression for A, χ is assumed to be strictly proportional to $1/T$. F_0 is independent of $\tilde{\phi}$.

When fluctuations are present, the system is inhomogeneous in space and $\tilde{\phi}(\mathbf{r})$ is a function of the spatial coordinate $\mathbf{r}$. Also any local gradients $\nabla\tilde{\phi}(\mathbf{r})$ cost in free energy. Now, the change in free energy to excite a fluctuation $\psi = \tilde{\phi} - \tilde{\phi}_0$ (where $\tilde{\phi}_0$ is the equilibrium value) is given by the Landau–Ginzburg form

$$\frac{\Delta F}{kT} = \int \frac{d^3r}{V}\left\{\frac{A}{2}\psi^2 + \cdots + \frac{\kappa}{2}(\nabla\psi)^2 + \cdots\right\} \tag{1.118}$$

where κ is a positive quantity proportional to interfacial tension and V is the volume of the system. Decomposition of ψ in terms of its Fourier components gives

$$\frac{\Delta F}{kT} = \frac{1}{2}\sum_q (A + \kappa q^2)\psi_q^2 \tag{1.119}$$

The time evolution of the fluctuation $\psi(\mathbf{r})$ obeys the conservation law

$$\frac{\partial \psi(\mathbf{r}, t)}{\partial t} = \nabla \cdot \left(\Lambda_0 \nabla \frac{\delta \Delta F / kT}{\delta \psi} \right) \tag{1.120}$$

so that

$$\frac{\partial \psi_q(t)}{\partial t} = -\Lambda_0 q^2 (A + \kappa q^2) \psi_q(t) \tag{1.121}$$

where Λ_0 is the Onsager coefficient reflecting the relative diffusivity of polymer chains, and nonlinear terms of ψ in Eq. (1.118) are ignored. The scattered intensity $I(q,t)$ is proportional to $\langle \psi_q^2(t) \rangle$ and follows from Eq. (1.121) as

$$I(q,t) = I(q,0) e^{2\Omega_q t} \tag{1.122}$$

where

$$\Omega_q = -\Lambda_0 q^2 (A + \kappa q^2) \tag{1.123}$$

Writing A in terms of the quench depth ΔT, given by Eq. (1.117), we get

$$\Omega_q = \Lambda_0 q^2 (a_0 \, \Delta T - \kappa q^2) \tag{1.124}$$

This result is sketched in Figure 1.17(a) for $\Delta T > 0$. For scattering wavevectors less than $q_0 = \left(\frac{a_0 \Delta T}{\kappa}\right)^{1/2}$ scattered intensity grows exponentially with time and the maximum growth occurs at $q = q_{\max} = \left(\frac{a_0 \Delta T}{2\kappa}\right)^{1/2}$. The same

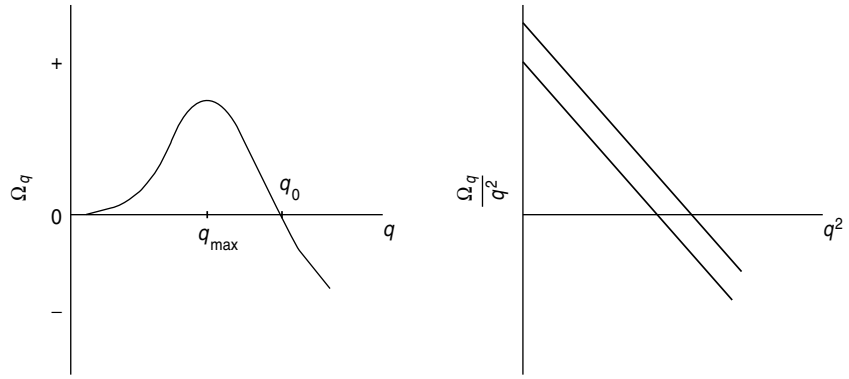

Figure 1.17. Predictions of spinodal decomposition mechanism.

result can be more conveniently written as

$$\frac{\Omega_q}{q^2} = \Lambda_0 a_0 \, \Delta T - \Lambda \kappa q^2 \tag{1.125}$$

which is sketched in Figure 1.17(*b*).

The intercept of the $(\Omega_q/q^2)/q^2$ plot is proportional to ΔT and the slope is independent of ΔT. Further, there is a cutoff wavevector q_0 delineating growing modes and decaying modes and q_0 is proportional to $\sqrt{\Delta T}$. Therefore, if spinodal decomposition occurs, all of the following features must be simultaneously observed:

1. Scattered intensity grows exponentially with time for $q < q_0$.
2. $q_{\max}$ is proportional to $(\Delta T)^{1/2}$.
3. The ordinate intercept of $\Omega_q/q^2 - q^2$ plot is proportional to ΔT.
4. The slope of $\Omega_q/q^2 - q^2$ plot is independent of ΔT.
5. The abscissa intercept of $\Omega_q/q^2 - q^2$ plot is proportional to ΔT.

If any of these features is not observed in the early stages of crystallization, the spinodal decomposition mechanism commonly encountered in phase-separating mixtures cannot be associated with polymer crystallization.

VII. RECENT ADVANCES

Availability of sensitive synchrotron radiation and atomic force microscopy (AFM) techniques have spurred recent (as of 2003) advances in following the mechanism of polymer crystallization in its early stages. Stimulated by the results of these investigations, complementary molecular modeling [44–59] of crystallization has been extensively carried out using molecular dynamics, Langevin dynamics, and Monte Carlo methods. All of these simulation methods provide converging viewpoint regarding the nature of initial stages of polymer crystallization. We review only the Langevin dynamics methodology.

Among the numerous challenges faced in understanding the formation and evolution of hierarchical structures in polymer crystallization, we restrict ourselves to explain the essential basic features of folded lamellae. Specifically, we consider (1) molecular origin of enhanced scattered intensity before any crystallographic features are apparent, (2) spontaneous selection of small lamellar thickness, (3) molecular details of growth front, and (4) formation of shish-kebab structures in the presence of a flow.

A. Molecular Modeling

In the Langevin dynamics simulations, the polymer crystallization is modeled by following the competition between the attraction among nonbonded

monomers and the torsional energies along the chain backbone. The simulation model attempts to incorporate just enough detail to observe chain folding without impeding the efficiency of the simulation. As a result, the united-atom model for polyethylene is chosen for a polymer chain, in which each methylene unit is treated as a bead in a bead–spring model of N beads. The motion of each bead is given by the Langevin equation consisting of inertial term, force field, frictional drag, and noise. The force fields include chain connectivity, bond angle, torsion angle, and nonbonded bead–bead interactions (Lennard-Jones of strength ϵ_0 and range σ_0). The force field parameters and details are given in Refs. 49, 57, and 58. The Langevin dynamics method simulates the effect of solvent through the noise, which is prescribed in accordance with the fluctuation–dissipation theorem. All simulation results given below are in reduced units (united-atom mass m of 1, equilibrium bond length ℓ_0 of 1, and Lennard-Jones ϵ_0 of 1). The reduced temperature T^* is equal to kT/ϵ_0 (with kT the Boltzmann constant times the absolute temperature), the reduced free energy is F/ϵ_0 and the reduced time is $t\sqrt{\epsilon_0/m\sigma_0^2}$. The protocol of a typical simulation is as follows. The first step is the determination of the melting temperature T_m^* for the model chains (for chosen values of N and force field parameters). An initially created random configuration is equilibrated at $T^* = 15.0$. The chain is then quenched to $T^* = 9.0$ and crystallization is allowed to take place. Once a single chain-folded structure is obtained, several runs are performed at heating rates ranging from 0.0001 to $0.002T^*$/time units. Discontinuities are observed in the slopes of both the total potential energy and global orientational order parameter at the onset and ending of melting. The equilibrium melting temperature is estimated by extrapolation of the observed melting temperatures to zero heating rate. This temperature is approximately $T^* = 11.0 \pm 0.2$. After T_m^* is determined, a collection of chains (or an individual chain) is quenched to a prescribed T^* below T_m^* and the chain configurations are followed. Attempts were made to include all hydrogen atoms explicitly in the simulations. This computationally demanding explicit-atom model shows (Fig. 1.18) that the crystal symmetry is orthorhombic, in agreement with the well-known experimental result for polyethylene single crystals, instead of the hexagonal symmetry seen in united-atom model simulations.

However, the essential mechanisms of lamellar formation and growth are found to be the same in both the united-atom and explicit-atom models. Only the united-atom model simulation results are therefore discussed below.

B. Nucleation in the Very Early Stage

We first summarize the salient features of the Langevin dynamics simulation results from the literature, and then we give a theoretical analysis.

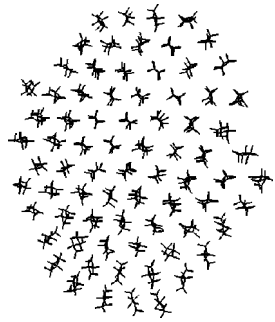

Figure 1.18. Explicit-atom model simulation.

1. Simulations

As reported in Refs. 49 and 57, Figure 1.19 shows a typical sequence of images depicting nucleation of a lamella by a single chain of $N = 700$ beads. The chain is quenched to $T^* = 9.0$ after equilibration at $T^* = 12.0$. Another example of $N = 2000$ (quenched to $T^* = 9.0$ from 20.0) is given in Figure 1.20. The timesteps shown in the sequence are selected from representative configurations during the course of crystallization.

As seen in these figures, several ''baby nuclei'' are formed, connected by the same single chain. The strands connecting these baby nuclei are flexible with

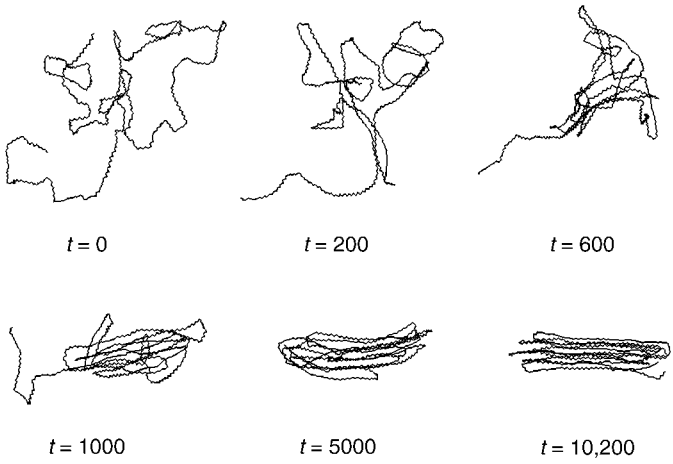

Figure 1.19. Snapshots of nucleation by a single chain ($N = 700$) [49].

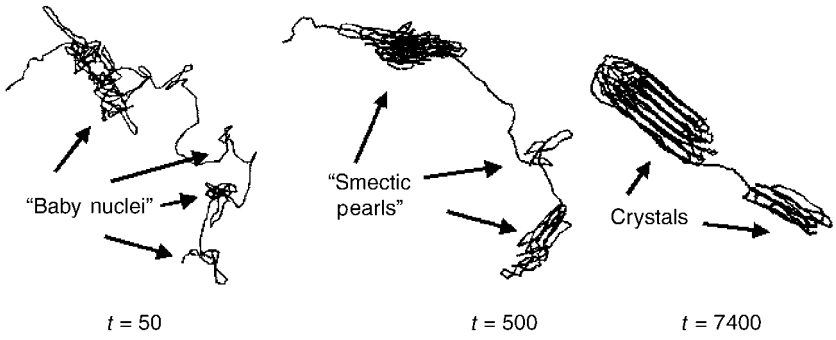

Figure 1.20. Growth of smectic pearls by reeling in the connector ($N = 2000$).

considerable configurational entropy. As time progresses, the monomers in the flexible strands are reeled into the baby nuclei while the orientational order in each nuclei increases, making them "smectic pearls." Simultaneously, the competition between nuclei for further growth dissolves some nuclei. Eventually, folded-chain structure emerges. Thus, the description is essentially the same as nucleation and growth encountered in small molecular systems, except that the polymer now is long enough to participate in several nuclei. Immediately after the quench ($t < 500$ in Fig. 1.20), we observe that the average distance between baby nuclei does not change with time. But the number of monomers in the connectors is reduced, accompanied by an increase in segmental orientation inside the nuclei as time increases.

To quantify this result, the structure factor $S(\mathbf{q}, t)$ at time t and the initial structure factor $S(\mathbf{q}, 0)$ were computed. As seen in experiments, a scattering peak at $\mathbf{q}_{\max}$ was observed. In these simulations, $\mathbf{q}_{\max}$ was found to correspond to the spacing between baby nuclei and the peak position is essentially independent of time in the very early stages.

Figure 1.21 contains a plot of Ω_q/q^2 versus q^2, where Ω_q is the rate of growth of monomer density fluctuations with wave vector $\mathbf{q}$. According to the linearized theory of spinodal decomposition for mixtures (Section VI), $S(\mathbf{q}, t) \propto \exp(2\Omega_q t)$, where $\Omega_q \propto q^2(1 - \kappa q^2)$, where κ is a positive constant. Therefore, a plot of Ω_q/q^2 versus q^2 must be linear with a negative slope if spinodal decomposition is present. Some experimentalists have used this criterion to claim that spinodal decomposition is the mechanism of polymer crystallization at the early stage. As in experiments, we also observe that Ω_q/q^2 versus q^2 is linear with a negative slope. However, this is not evidence for spinodal decomposition because this behavior is observed for only intermediate

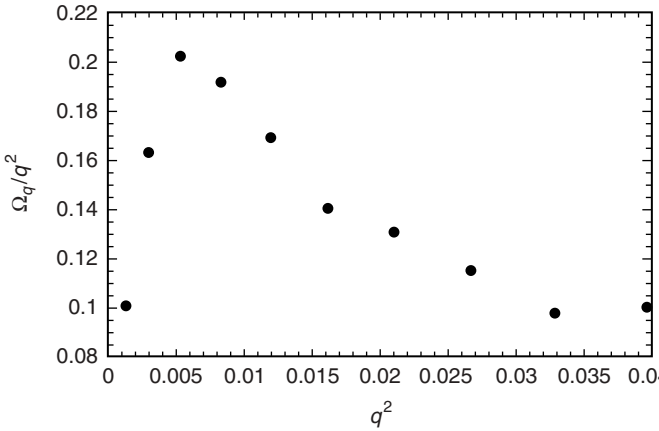

Figure 1.21. Dependence of growth rate of density fluctuations on the square of the wave-vector [57].

values of **q**. Our results show that for small **q**, $\Omega_q \propto q^4$, in agreement with experiments but in disagreement with the predictions of spinodal decomposition.

To get more insight into the further growth of smectic pearls, typical configurations at various times are presented in Figure 1.22 ($t = 500, 1550,$ 7400, 10,300, 12,850, 13,350).

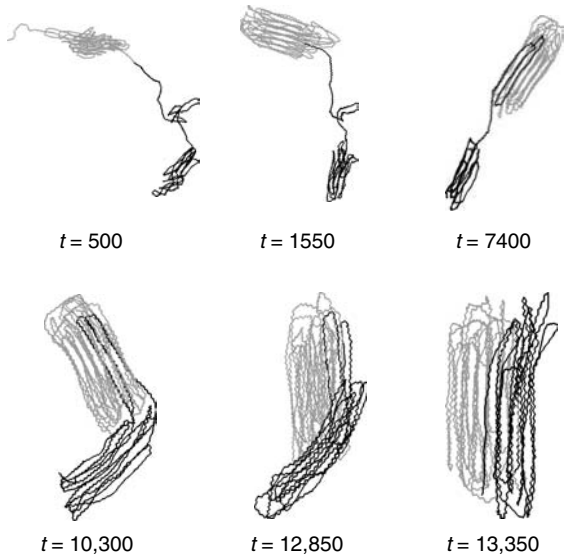

Figure 1.22. Merger of smectic pearls [57].

For the sake of clarity, we have used two shades for the polymer, although the chain is a homopolymer. As pointed out already, monomers in the connectors are transferred into the growing nuclei in the very early stage.

This process continues until the connector is essentially stretched out while keeping the average internuclei distance the same. Then, the connector is pulled into the nuclei to varying degrees until the nuclei impinge against each other. This is followed by a cooperative reorganization by which nuclei merge to form a single lamella. The mechanism of the merger is not by sequentially placing stems, but by a highly cooperative process involving all stems of the lamella.

2. *Theory*

We now present the simplest analytical model [60] for the origin of $q_{\max}$, the mechanism of growth of smectic pearls, and growth of density fluctuations in the very early stages of nucleation of lamella.

a. Origin of $q_{\max}$. To address why a certain average distance is maintained between two smectic pearls at very early times, let us consider a model chain of N beads with only two smectic pearls (containing N_1 and N_2 beads) connected by a strand of m $(= N - N_1 - N_2)$ beads (Fig. 1.23).

Let the end-to-end distance of the strand be λ, which is comparable to the average distance between the smectic pearls. Let the average energy of a bead in either of the smectic pearls be ϵ.

The free energy F_0 of this configuration is given by

$$\frac{F_0}{k_B T} = -(N - m)\epsilon + \frac{3}{2}\frac{\lambda^2}{ml^2} \tag{1.126}$$

where the second term on the right-hand side is the entropic part from the strand (assuming Gaussian chain statistics and l as the Kuhn length, a multiple of l_0). Minimization of F_0 with respect to m gives the optimum value of m $(= m^*)$ for the configuration of Figure 1.23:

$$m^* = \sqrt{\frac{3}{2\epsilon}}\left(\frac{\lambda}{l}\right) \tag{1.127}$$

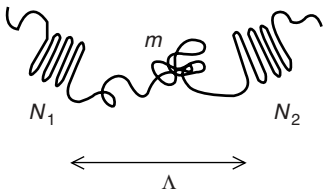

Figure 1.23. Model to consider connector entropy.

Since λ is roughly proportional to $\sqrt{m^*}$ according to the Gaussian statistics valid approximately before the quench, we expect

$$\frac{\lambda}{l} \sim \sqrt{m^*} \sim \frac{1}{\sqrt{\epsilon}} \tag{1.128}$$

Thus the initial selection of average distance between the smectic pearls is determined by ϵ (and consequently quench depth).

b. Kinetics of Growth of Smectic Pearls. Although arguments based on equilibrium are used above to estimate $q_{\max}$, the conformation discussed above is not in equilibrium and it evolves further by reeling in the connector. To address how this process takes place, let us consider the time-dependent probability $W_m(t)$ of finding m beads in the connector at time t. Let k_1 be the rate constant for one bead to detach from either of the smectic pearls, and k_1' be the rate constant for one bead to attach to either of the smectic pearls. Using detailed balance to express k_1' in terms of k_1 and letting m be a continuous variable, a mapping [60] with the standard arguments of the classical nucleation theory gives the Fokker–Planck equation

$$\frac{\partial W_m(t)}{\partial t} = k_1 \left[\frac{\partial}{\partial m} \frac{\partial (F_0/kT)}{\partial m} + \frac{\partial^2}{\partial m^2} \right] W_m(t) \tag{1.129}$$

where F_0 is given in Eq. (1.126). The prediction of Eq. (1.129) (solid curve) is compared with simulation data in Figure 1.24.

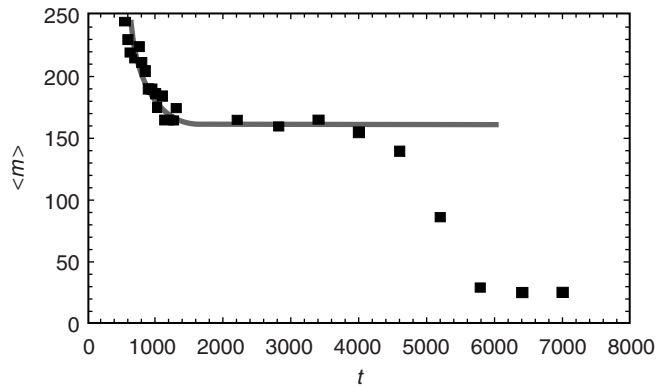

Figure 1.24. Time-dependence of average number of monomers $\langle m \rangle$ in the connector between smectic pearls. The simulation data (filled square) are from 8 simulations corresponding to the conditions of Figures 1.20 and 1.22; the solid line is calculated from Eq. (1.129).

In the comparison, λ is taken as an input from the simulations, ϵ is a parameter and the reduced time is $k_1 t$. The agreement is good, providing qualitative support to the present theoretical model, in the initial stages. For reduced times greater than 4000, the mechanism is not reeling in, and consequently, simulation data deviate from the solid curve.

c. Growth of Density Fluctuations. We now generalize the model of Figure 1.23 to account [56,60] for the wavevector dependence. There are three contributions to the free energy, F: (1) density difference ψ between the baby nuclei and the amorphous background giving free-energy contribution that is proportional to $-\Delta T\psi^2(\Delta T \equiv T_m^0 - T)$; (2) interfacial free energy given by the square gradient of ψ, proportional to $q^2\psi_q^2$ (where q is the scattering wavevector); and (3) monomer–monomer correlation arising from the chain connectivity of the connector participating in multiple nuclei, leading to a free-energy contribution that is proportional to $q^{-2}\psi_q^2$ (as in the Debye structure factor for length scales shorter than R_g). Therefore the free energy of a system with baby nuclei connected by strands is

$$F \sim \sum_{\mathbf{q}} \left(-\Delta T + q^2 + \frac{1}{q^2} \right) \psi_{\mathbf{q}}^2 \tag{1.130}$$

where all the prefactors are left out. At this juncture of the early stage of nucleation and growth, ψ evolves with time, in accordance with the relaxation of chemical potential gradients

$$\frac{\partial \psi(r,t)}{\partial t} \simeq -\nabla \cdot \left(-\nabla \frac{\partial F}{\partial \psi} \right) \tag{1.131}$$

so that

$$\frac{\partial \psi_q(t)}{\partial t} = -q^2 \left(-\Delta T + q^2 + \frac{1}{q^2} \right) \psi_q(t) \tag{1.132}$$

Therefore, we expect the scattered intensity $I(\mathbf{q}, t)$, proportional to $\langle \psi_{\mathbf{q}}^2(t) \rangle$ to be exponential in time, $I(\mathbf{q}, t) \sim \exp(2\Omega_{\mathbf{q}} t)$, with the rate $\Omega_{\mathbf{q}} = q^2(\Delta T - q^2 - \frac{1}{q^2})$ with both lower and upper cutoffs in $\mathbf{q}$. If these arguments are valid, $\Omega_{\mathbf{q}}/q^2$ should rise sharply with q^2, reach a maximum, and then decrease at higher $\mathbf{q}$ values. These predictions are fully consistent with the experimental [10] and simulation [57] observations on $I(\mathbf{q}, t)$ and $\Omega_{\mathbf{q}}$. If the mechanism is simply a spinodal decomposition into two liquid phases, then $\Omega_{\mathbf{q}}/q^2$ should show a monotonic linear decrease from a finite positive value at $\mathbf{q} \to 0$ with a slope independent of quench depth, which is not experimentally observed during

polymer crystallization. Thus, the mechanism of polymer crystallization even in the very early stage is nucleation and growth with an additional contribution arising from chain connectivity. When the original baby nuclei have grown into lamellae comparable to or larger in size than R_g, their further growth is dictated essentially by the nature of the growth front.

C. Spontaneous Selection of Lamellar Thickness

1. Simulations

Many simulations of n chains, each with N beads, such that $nN \leq 15{,}000$ and the volume fraction of the polymer $\phi \leq 0.5$, have been performed at different quench depths. The key observations are summarized below.

a. Quantization of Lamellar Thickness. The initial lamella formed as described in Section II, is typically thin and small. However, over a period of time, it thickens.

The lamellar thickening proceeds through many metastable states, each metastable state corresponding to a particular number of folds per chain, as illustrated in Figure 1.25. This quantization of number of folds has been observed in experiments [25], as already mentioned. The process by which a state with p folds changes into a state with $p + 1$ folds is highly cooperative. The

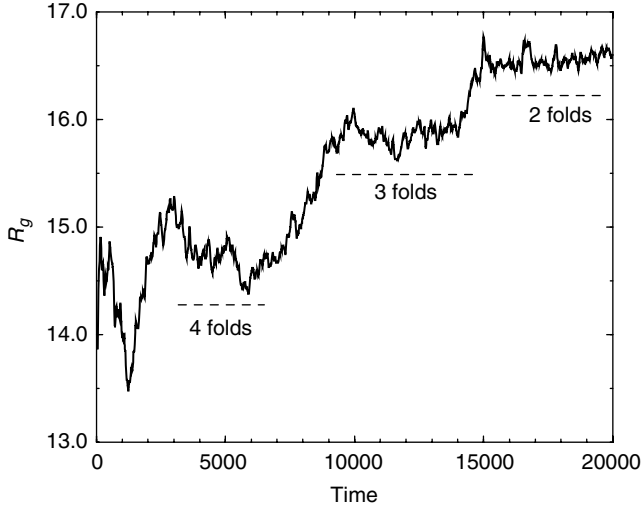

Figure 1.25. Quantized lamellar thickening, where R_g is the radius of gyration of the lamella [49].

precursor 'lives' in a quiescent state for a substantial time and ''suddenly'' it converts into the next state. By a succession of such processes, crystals thicken. If the simulation is run for a reasonably long time, the lamella settles down to the ''equilibrium'' number of folds per chain.

b. Lamellar Thickness and Quench Depth. The lamellar thickness L, after the thickening is apparently complete, is found in the simulations to obey the law

$$L = \frac{C_1}{\Delta T^*} + C_2 \tag{1.133}$$

where C_1 and C_2 are constants; for details, see Ref. 49. This relation was already observed experimentally [24]. Although the kinetic theory of Lauritzen and Hoffman predicts the same law as Eq. (1.133), it predicts a divergence in L at lower undercoolings. The simulations do not show any evidence for such a catastrophe.

c. Free-Energy Landscape. In an effort to quantify the free energies of different quantized states and free-energy barriers separating these states, the free-energy landscape has been calculated as a function of a measure, L, of lamellar thickness of single chains at a given quench depth and utilizing a histogram technique [58]. For example, the estimated free energy $F(L)$ for $N = 200$ at a quench depth of approximately 2.0 is given in Figure 1.26(a) exhibiting several wells. Each well corresponds to a different number of stems in the lamella. For example, six, five, and four stem structures are observed for chains composed of 200 united atoms. Increasing the number of united atoms results in the addition of more wells. For example, the free-energy profile [Fig. 1.26(b)] for $N = 300$ displays additional wells. As N increases, the chains increase the number of stems in the crystal to accommodate the optimum crystal thickness.

The minimum in $F(L)$ is observed to be near $L/\ell_0 \simeq 9$ for all chain lengths examined. It is to be noted that this minimum is the global minimum and the barrier between this state and other thicker lamellae increases prohibitively as the thickness increases. These simulations strongly suggest that a lamellar thickness that is much smaller than the extended chain thickness is actually an equilibrium result.

2. *Theory*

Motivated by simulation results, we now consider a theoretical model [60] that allows an exact calculation of the equilibrium lamellar thickness. Consider a nucleus sketched in Figure 1.27, of thickness $L = ml$ and radius R. For each of the n chains, let there be μ stems (and $\mu - 1$ loops and two chain tails), each of length L.

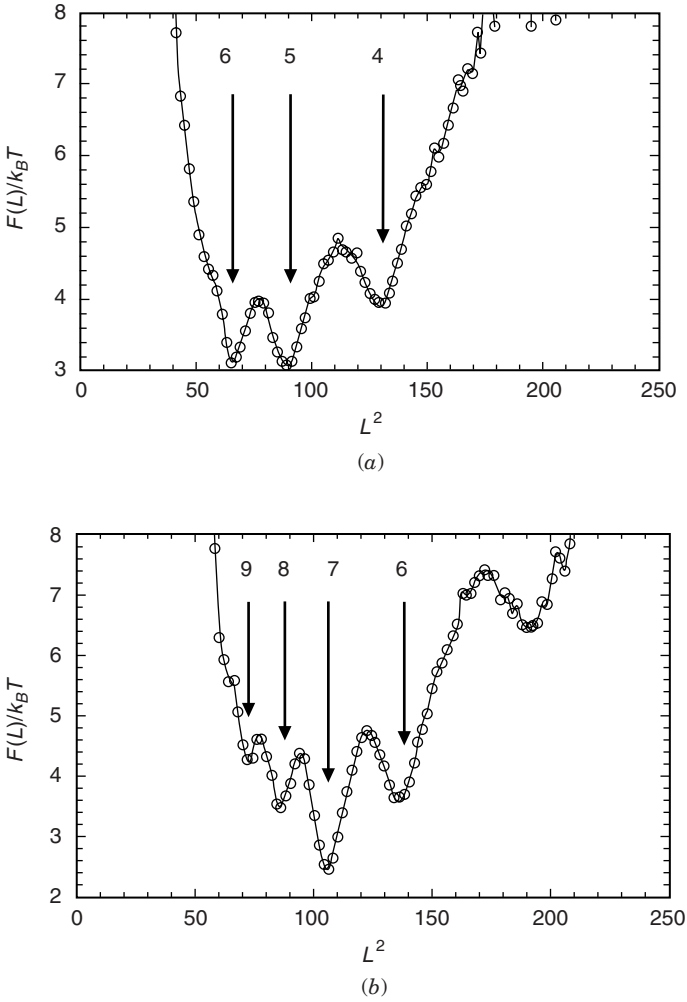

Figure 1.26. Free-energy landscape for (*a*) $N = 200$ and (*b*) $N = 300$.

Let $\epsilon > 0$ be the energy gain per segment in the nucleus (in units of kT) and σ' be the lateral surface free energy per unit area. The free energy $F_{m,\mu}$ per chain in the nucleus of Figure 1.27 is given by

$$\frac{F_{m,\mu}}{kT} = -\mu m\epsilon + \sigma\sqrt{\mu}m - \ln Z_{m,\mu} \tag{1.134}$$

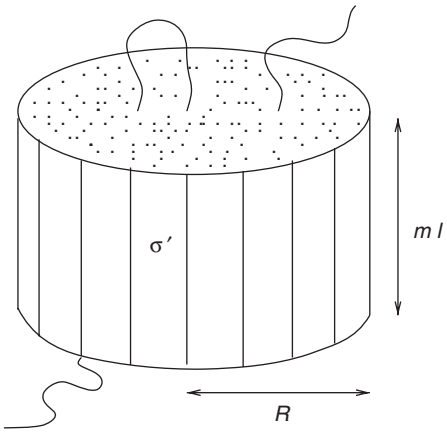

Figure 1.27. Role of loop entropy on the fold surface free energy.

where $\sigma = 2\sqrt{\pi}\sigma' l^2$. The third term on the right-hand side is due to the entropy associated with different ways of realizing loops and tails on the two fold surfaces. The partition sum of a loop of p monomers in semiinfinite space with ends at R_{11} and X_{11} (both located on the fold surface) is given by

$$g_{\text{loop}}(p) = 2\left(\frac{3}{2\pi p l^2}\right)^{3/2} \exp\left[-\frac{3(\mathbf{R_{11}} - \mathbf{X_{11}})^2}{2pl^2}\right][1 - \sqrt{\pi}\Gamma e^{\Gamma^2}\text{erfc}(\Gamma)] \quad (1.135)$$

with $\Gamma = c\sqrt{6p}$ and c is the strength of the interaction pseudopotential at the fold surface. For a tail of p segments in semiinfinite space, the partition sum is

$$g_{\text{tail}}(p) = e^{\Gamma^2}\text{erfc}(\Gamma) \quad (1.136)$$

Since the contour lengths of loops and tails are quite short ($c\sqrt{p}$ is small), as evident in the simulations, g_{loop} and g_{tail} approach the limits

$$g_{\text{loop}}(p) \to 2\left(\frac{3}{2\pi p l^2}\right)^{3/2} \exp\left[-\frac{3(\mathbf{R_{11}} - \mathbf{X_{11}})^2}{2pl^2}\right]$$

and

$$g_{\text{tail}}(p) \to 1 \quad (1.137)$$

By following the field-theoretic technology of Ref. 61 and choosing a cutoff of l_c for $(R_{11} - X_{11})$, the partition sum $Z_{m,\mu}$ for distributing $(N - m\mu)$ segments

among $(\mu - 1)$ loops and 2 tails without breaking the chain connectivity is given by

$$Z_{m,\mu} = 4\left(\frac{1}{vb_0}\right)^{\mu-1}(N - \mu m)\left[\left(\frac{z^2}{2} + \frac{1}{4}\right)\mathrm{erfc}(z) - \frac{z}{2\sqrt{\pi}}e^{-z^2}\right] \tag{1.138}$$

where

$$z = \frac{(\mu - 1)b_0}{2\sqrt{N - \mu m}} \tag{1.139}$$

with $b_0 = \sqrt{6}l_c/l$ and $v = \pi l^3/3\sqrt{6}$.

Substitution of Eq. (1.138) into Eq. (1.134) gives the free-energy landscape in terms of the lamellar thickness ($\sim m$) and width ($\sim \mu$) per chain for a given choice of ϵ, σ, and l_c. The remarkable consequence of the entropic part of $F_{m,\mu}$ is that $F_{m,\mu}$ has a global minimum for a finite value of m.

This is illustrated in Figure 1.28, where $F_{m,\mu}/k_BT$ is plotted against m and μ for a representative set of $\epsilon = 1$, $\sigma = 5$, $N = 1000$, $l_c/l = \sqrt{32/3}$, $v/l^3 = \pi/3\sqrt{6}$. For the case of Figure 1.28, the global minimum (the ground state) is at $m^* = 14.26$ and $\mu^* = 45.3$. This result is to be contrasted with the standard model of Figure 1.9, where the fold surfaces are simply treated as

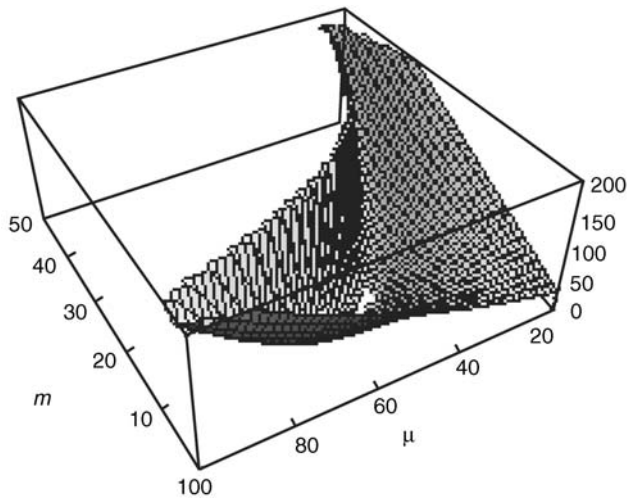

Figure 1.28. Chain entropy leads to thermodynamic stabilization of finite lamellar thickness.

planar interfaces with fold surface free energy σ_f per unit area. In the latter case, the free energy of the nucleus is given by

$$\frac{\Delta F}{k_B T} = -\mu m\epsilon + \sigma\sqrt{\mu}m + 2\mu\sigma_f \tag{1.140}$$

In terms of the critical nucleus ($m_c = 4\sigma_f/\epsilon$, $\mu_c = (\sigma/\epsilon)^2$, $\Delta F_c/k_B T = \epsilon\mu_c m_c/2$), ΔF becomes

$$\overline{\Delta F} = -2\bar{\mu}\bar{m} + 2\bar{m}\sqrt{\bar{\mu}} + \sqrt{\bar{\mu}} \tag{1.141}$$

where $\bar{m} = m/m_c$, $\bar{\mu} = \mu/\mu_c$ and $\overline{\Delta F} = \Delta F/\Delta F_c$. The free-energy landscape of Eq. (1.141) is given in Figure 1.10, and the lamella grows into infinitely large dimensions in all directions. In contrast, the exactly solved model of Figure 1.27 and Eqs. (1.126)–(1.139) show that finite lamellar thickness (much smaller than the extended chain value) is actually the equilibrium description.

D. Kinetics at Growth Front

Very long simulations have been carried out with as many as 15,000 united atoms with the following protocol. First, a single-chain crystal is placed at the origin. Next, a self-avoiding random chain is placed at a random location on a sphere whose radius is 1.5 times the radius of gyration of the crystal. The new system is equilibrated with the Langevin dynamics algorithm for 5000 time units. If the chain fails to add any segments to the crystal by the end of the addition period, the run is rejected and the crystal's coordinates are reset to their values at the beginning of the period. A new attempt to add a chain is then made. If the chain adds to the crystal, the process is repeated by moving the crystal to the origin and adding a new self-avoiding random chain to the simulation. Figure 1.29 illustrates the addition of the 40th chain to a 39 chain crystal for $k_B T/\epsilon = 9.0$.

The crystal reels in the chain one segment at a time, and then crystallographically attaches each to the growth face. This process continues until the entire chain is incorporated into the crystal. Once adsorbed, the chain continues to rearrange until its fold length is commensurate with that of the growth face. The rate-limiting step for the addition of the chain to the crystal is the diffusive contact with the surface. Once a few segments have come into contact with the crystal, the chain rapidly adds to the growth front. The numerical estimate of the free energy $F[s]$ as a function of the number of segments added to the crystal is given in Figure 1.30.

The addition of a new chain at the growth front is not hindered by a barrier, in contradiction with the underlying assumptions of the LH theory. Simultaneous to the addition of new chains at the growth front, chains inside

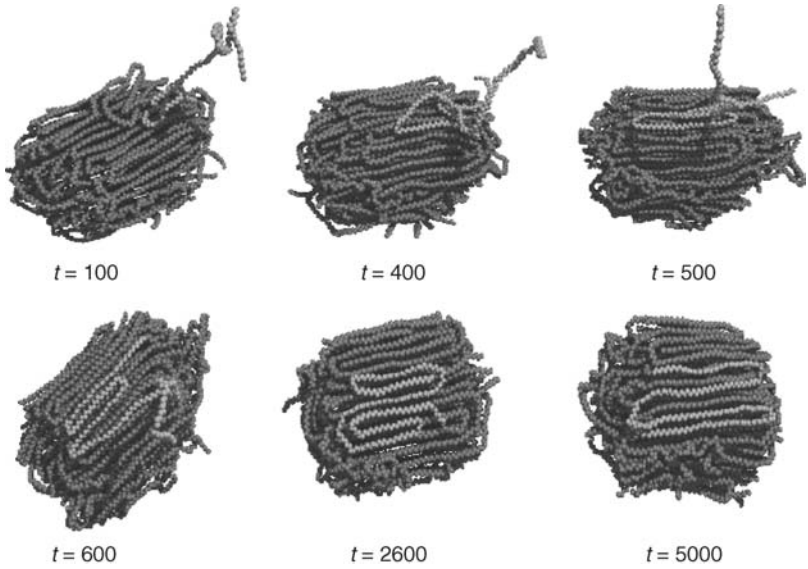

Figure 1.29. Adsorption of a new chain at the growth front [58].

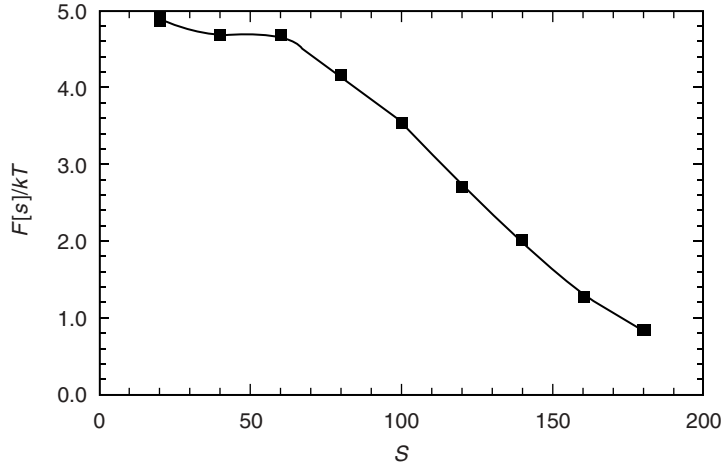

Figure 1.30. Absence of free-energy barrier for attachment of a new chain at the growth front [58].

the lamella move cooperatively. The center of mass of the lamella diffuses in space while the lamella thickens by a process of internal rearrangements; for details, see Ref. 58. The mean squared displacement of a labeled monomer varies with the elapsed time t with an effective power law of $t^{0.74}$ by shuffling back and forth between the lamellar and amorphous regions.

If the growth front is frozen, the crystallization at the growth front depends crucially on the commensurability between the thickness of the growth front and the length of crystallizing chains. For details, see Ref. 49. A collection of polydisperse chains gets effectively fractionated at the growth front.

E. Crystallization in an Elongational Flow

In the Langevin dynamics simulations [62], there is an additional force $\hat{S}\mathbf{r}_i$ acting on ith bead, where $\mathbf{r}_i$ is its position and

$$\hat{S} = \dot{\epsilon} \begin{pmatrix} -\frac{1}{2} & 0 & 0 \\ 0 & -\frac{1}{2} & 0 \\ 0 & 0 & 1 \end{pmatrix} \tag{1.142}$$

with the parameter $\dot{\epsilon}$ setting the flow rate. As expected, the chains undergo coil–stretch transition in the presence of flow and the melting temperature is elevated. For example, at the reduced temperature of 11.0 (which is the extrapolated melting temperature in reduced units for the united-atom model described above in the quiescent state) folded chains are readily formed in the presence of flow.

Several simulation runs were performed for a wide range of flow rates for chains of $N = 180$ beads. To ensure that the system is in the state of lowest free energy and to avoid the chain being in a metastable state, two initial conformations of the chain were chosen. One initial conformation is a random chain equilibrated at the given temperature without any flow. The second initial conformation is a fully extended chain obtained by equilibrating it at extremely high flow rate ($\dot{\epsilon} = 4.0$). Data were collected after the two chains with different initial conformation are in the same state, either coil or stretched polymer. The stagnation point at $\mathbf{r} = 0$ is unstable. In order to avoid the chain to be drifted away from the coordinate origin, the center of the mass of the polymer is fixed at $\mathbf{r} = 0$.

Figure 1.31 shows the square of the radius of gyration of the chain as a function of the flow rate $\dot{\epsilon}$ at relatively low temperature ($T = 9.0$).

A discontinuous coil–stretch transition is evident at $\dot{\epsilon}_c = 0.000725$. The transition point $\dot{\epsilon}_c$ was found by using two different initial conformations as described above. For values lower than $\dot{\epsilon}_c$, the random chain will eventually coil and form a folded-chain crystalline structure and stay in that conformation until the end of the run for relatively long run times. On the other hand, a prestretched chain would fluctuate and eventually form a crystallized folded chain that is

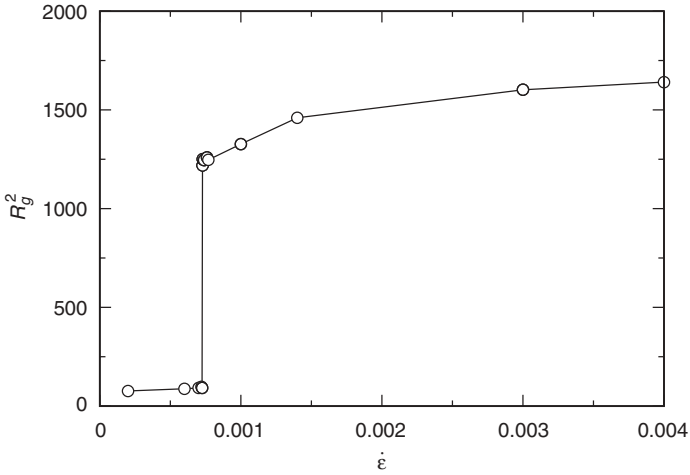

Figure 1.31. Radius of gyration squared as a function of flow rate for a chain of $N = 180$ and $T = 9.0$.

stable. Similarly, for flow rates higher than $\dot{\epsilon}_c$, a prestretched chain will never coil and a random chain will eventually stretch.

At a higher temperature $T = 11.0$, for flow rates near the transition rate $\dot{\epsilon}_c$, the free-energy barrier between the coiled and stretched conformation is much lower than for $T = 9.0$. The chain can therefore explore the phase space and jump back and forth from the coiled to the stretched states. Similar behavior has already been observed in Refs. 63 and 64. Figure 1.32 illustrates this feature.

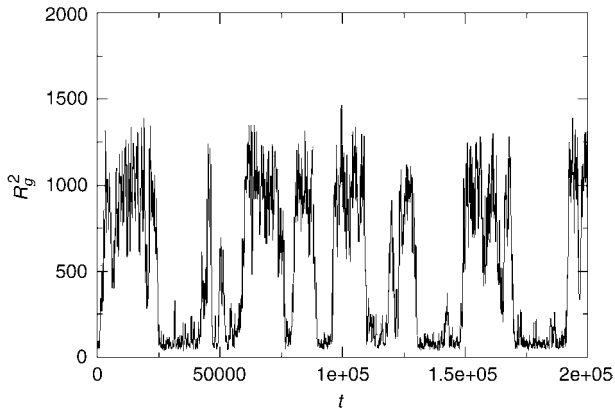

Figure 1.32. Radius of gyration squared as a function of time for $N = 180$, $T = 11.0$, and $\dot{\epsilon} = 0.00075$.

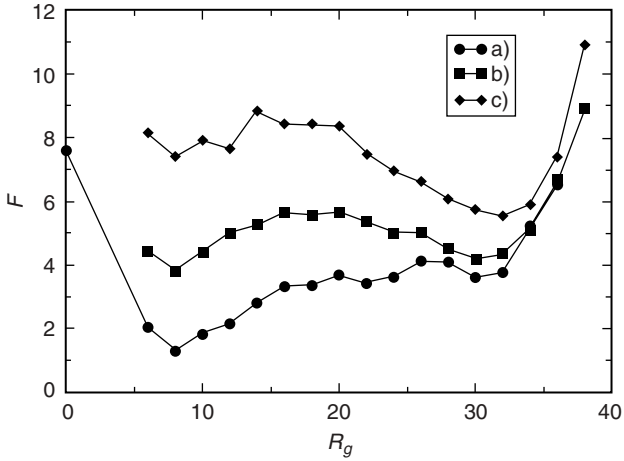

Figure 1.33. The free energy F versus $R_g(N = 180)$; (*a*) $\dot{\epsilon} = 0.0006$; (*b*) $\dot{\epsilon} = 0.00075$; (*c*) $\dot{\epsilon} = 0.0009$.

From Figure 1.32, the free energy can be calculated according to

$$F(R_g) = -kT \ln\left(\frac{\tau(R_g)}{\tau_{\text{tot}}}\right) \tag{1.143}$$

where $\tau(R_g)$ is the time the system spends in states with a radius of gyration between R_g and $R_g + \Delta R_g$ and τ_{tot} is the total time. ΔR_g is chosen to be $2r_0$. Figure 1.33 shows the free energy of the chain at $T = 11.0$ for flow rates: (1) below, (2) very close to the transition, and (3) above the transition. It is clear that at the transition the stretched and the folded state coexist.

Making the flow rate higher or lower will change from stable to metastable the folded or the stretched state, respectively. The effects of hysteresis associated with this first-order discontinuous transition play an important role in the formation of composite crystalline structures.

When simulations were performed with many chains of uniform length, some chains were stretched out and aggregated among themselves to form the shish, whereas other chains formed folded structures that in turn attached to the shish, initiating the formation of kebabs. This is attributed to the coexisting populations of stretched and coiled states. This feature is much more pronounced if the chains have different lengths. For a given flow rate, the longer chain is predominantly in the stretched state and the shorter chain is

Figure 1.34. An example of initial position of chains for the kebab formation simulation.

predominantly in the coiled state. Now the shish is formed by the crystallization of stretched chains and the kebabs are mostly from the shorter chains.

To follow the crystallization of kebabs around a shish, the dynamics of 10 short chains ($N = 180$) near a preformed shish (from seven chains of length $N = 500$) were followed at $T = 9.0$, by fixing the center of mass of the shish. The initial position of the short free chains was chosen at random in a cylinder around the shish, with radius $30r_0$ and hight of $60r_0$. Each run started with different initial conditions. Figure 1.34 shows one such initial state.

The flow rate is then maintained at $\dot{\epsilon} = 0.0001$ (lower than $\dot{\epsilon}_c$ corresponding to $N = 180$), and the short chains are allowed to assemble on the shish.

Figure 1.35 illustrates nine examples of the structures obtained in these simulations. It is clear that the chains group into crystallized kebabs on the shish surface. There are only very few areas where the chains are partially or completely stretched under the influence of the shish template. The dominant mode of crystal nucleation on the shish is growth of folded chains grouped into lamellar nuclei. Also, some of the chains do not join the central structure but drift away from it leaving a large gap on the shish between them. These simulations show clearly that the presence of ordered template (the shish) influences the nucleation of lamellae and formation of kebabs. Some of the chains, when in contact with the shish, will stretch almost completely. However, these highly stretched chains are not dominant compared to the highly folded bundles that form crystalline kebabs around the shish. Also, none of the

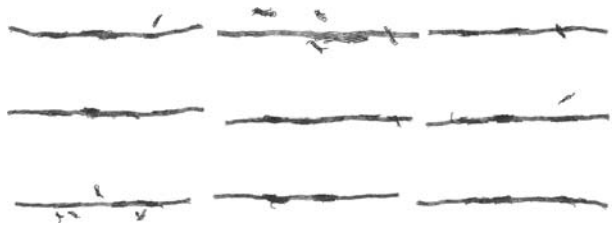

Figure 1.35. Nine examples of freely formed kebabs.

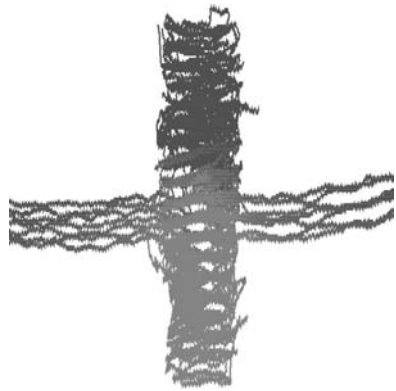

Figure 1.36. A stable shish (7 chains) and kebab (44 chains).

highly stretched chains formed a structure with part of it stretched and attached to the shish and part of it in folded crystalline lamella. The formation of kebabs in these simulations is clearly growth of lamellae, nucleated on the shish.

Next, in order to study the stability of the kebabs the flow rate was set at $\dot{\epsilon} = 0.001$ and four, initially equilibrated (i.e., in a precrystallized conformation), short chains were added per $t = 2000$ with initial position of $20r_0$ length units away from the stagnation point in the x and y directions. They form a kebab around the shish that was preformed. This procedure was repeated up to 44 short chains in the kebab as shown in Figure 1.36.

The kebab is stable even though $\dot{\epsilon}$ is larger than $\dot{\epsilon}_c$ for a single short chain. The kebab has uniform thickness and does not seem to resemble the flow contour. It must be stressed that the thickness of the kebabs formed this way is determined independent of the presence of the shish. The short chains are precrystallized before they are incorporated in the kebab. The kebab formed this way is influenced very little by the shish, except for the fact that it was nucleated on it. The presence of already formed kebabs clearly modifies the flow, a feature that is not present in these simulations. The flow, however, is modified in a way that it must be zero in the already formed shish and kebabs. This will result in greater stability of the structures that are observed and therefore only emphasize the results in this section. Finally, when the rate of addition of the chains was lowered to one per $t = 5000$, most of the short chains stretched completely as shown on Figure 1.37.

Thus kinetics of the process clearly plays an important role in the kebab formation.

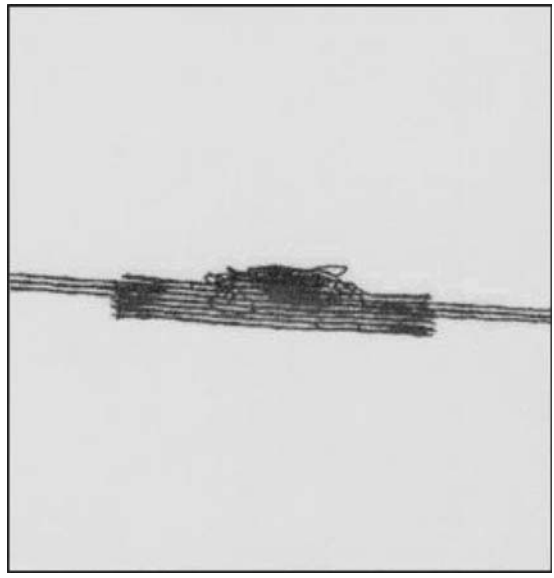

Figure 1.37. An example of completely stretched kebab grown with very slow rate.

VIII. CONCLUSIONS

The main results derived from Langevin dynamics simulations and theoretical considerations are as follows.

A. Initial Crystals

The mechanism of polymer crystallization at very early stages is nucleation and growth, although the computed scattering intensity can be superficially fitted, as in the synchrotron measurements of crystallizing polymers, to a spinodal decomposition description at intermediate wavevectors. The key feature that distinguishes polymers from small molecules at early stages of crystallization is that in the case of polymers, a single chain can participate in several nuclei. This is responsible for the spontaneous selection of a particular scattering wavevector at which the scattered intensity is a maximum.

B. Spontaneous Selection of Finite Lamellar Thickness

Historically, it had been believed that the finite lamellar thickness observed in experiments is completely due to kinetic control and that, if sufficient time is granted for the lamellae, the thickness would progressively grow to the extended chain value. The exact enumeration calculations and an exactly solvable model

discussed above show that this longstanding view might not be correct in general. The equilibrium thickness can be finite and much smaller than the extended-chain value. Before attaining the equilibrium thickness, the crystal evolves through several metastable ''quantized'' states with smaller lamellar thickness.

C. Kinetics at Growth Front

The growth at the crystalline interface is chain adsorption followed by crystallographic registry. This step is not hindered by a barrier. The newly added, folded chains undergo a rearrangement on the growth front to form stems that are commensurate with the crystal thickness at the growth front. Meanwhile, all chains in the growing lamella undergo significant dynamics, such that the center of mass of a labeled chain can be significantly displaced. These results challenge the conventional Lauritzen–Hoffman theory and its generalizations. More systematic modeling work is necessary to monitor the onset of entropic barriers at the growth front when many polymer chains are adsorbing at the growth front.

D. Molecular Origins of Shish-Kebab Morphology

Emergence of shish-kebabs in polymer crystallization under extensional flow is intimately related to the discontinuous coil–stretch transition of isolated chains. The computed free-energy landscape shows that there are in general two populations of stretched and coiled conformations at a given flow rate, even for monodisperse chains. While the stretched chains crystallize into shish, the coiled chains first form single-chain lamellae and then adsorb to the shish constituting the kebabs. Any local inhomogeneity in polymer concentration dramatically alters the population of stretched and coiled conformations, thus significantly influencing the onset of shish-kebab morphology. The propensity of kebabs is reduced by lowering the rate of crystallization and/or increasing the flow rate.

Although these results illustrate the inadequacies of the underlying assumptions of the classical theories, alternate analytically tractable theories accounting for newly discovered features have not yet emerged. The primary focus of this review is isolated lamellae. We have not discussed the fundamental issues behind the formation of hierarchy of morphological features starting from packing of monomers in unit cells at atomic length scales to packing of spherulites at macroscopic length scales. Specifically, how do lamellae branch out and form spherulites? What is the structure of the core of a spherulite, and why does the spherulite grow radially and linearly with time? Under what conditions are spherulites unstable? Why do the lamellae inside spherulites helically twist, although the lamellae are made up of achiral molecules? These are only a few of the intriguing puzzles in polymer crystallization.

Acknowledgments

This work was supported by an NSF grant DMR-0209256. The author is grateful to Chester Liu, Paul Welch and Ilija Dukovski for collaborations.

References

1. V. P. Skripov, *Metastable Liquids*, (Wiley, New York, 1973).
2. K. H. Storks, *J. Am. Chem. Soc.* **60**, 1753 (1938).
3. B. Wunderlich, *Macromolecular Physics*, Vols. I and II (Academic Press, 1973).
4. J. D. Hoffman, G. T. Davis, and J. I. Lauritzen, in *Treatise on Solid State Chemistry*, N. P. Hannay, ed., Vol. 3 (Plenum, New York, 1976), Chap. 7, pp. 497–614.
5. Special issue on the organization of macromolecules in the condensed phase, D. Y. Yoon and P. J. Flory, eds., *Disc. Faraday Soc.* **68**, 7 (1979).
6. D. C. Bassett, *Principles of Polymer Morphology*, Cambridge Univ. Press, Cambridge, U.K., (1981).
7. P. J. Phillips, *Rep. Prog. Phys.* **53**, 549 (1990).
8. K. Armitstead and G. Goldbeck-Wood, *Advances in Polymer Science*, Vol. 100 (Springer-Verlag, New York, 1992).
9. G. Strobl, *The Physics of Polymers* (Springer, 1995).
10. M. Imai, K. Kaji, and T. Kanaya, *Macromolecules* **27**, 7103 (1994).
11. T. A. Ezquerra, E. Lopez-Cabarcos, B. S. Hsiao, and F. J. Balta-Calleja, *Phys. Rev. E* **54**, 989 (1996).
12. N. J. Terrill, J. P. A. Fairclough, E. Towns-Andrews, B. U. Komanschek, R. J. Young, and A. J. Ryan, *Polymer* **39**, 2381 (1998).
13. P. D. Olmsted, W. C. K. Poon, T. C. B. McLeish, N. J. Terrill, and A. J. Ryan, *Phys. Rev. Lett.* **81**, 373 (1998).
14. A. J. Ryan, J. P. A. Fairclough, N. J. Terrill, P. D. Olmsted, and W. C. K. Poon, *Faraday Discuss.* **112**, 13 (1999).
15. Y. Akpalu, L. Kielhorn, B. S. Hsiao, R. S. Stein, T. P. Russell, J. van Egmond, and M. Muthukumar, *Macromolecules* **32**, 765 (1999).
16. J. I. Lauritzen and J. D. Hoffman, *J. Res. Nat. Bur. Std.* **64A**, 73 (1960).
17. E. A. DiMarzio, *J. Chem. Phys.* **47**, 3451 (1967).
18. G. Allegra, *J. Chem. Phys.* **66**, 5453 (1977).
19. E. Passaglio and E. A. DiMarzio, *J. Chem. Phys.* **87**, 1539 (1987).
20. J. J. Point and M. Dosière, *Macromolecules* **22**, 3501 (1989).
21. D. M. Sadler and G. H. Gilmer, *Polymer* **25**, 1446 (1984).
22. J. D. Hoffman and R. L. Miller, *Polymer* **38**, 3151 (1997).
23. A. Keller and H. W. H. Kolnaar, in *Processing of Polymers*, Vol. 18, H. E. H. Meijer, ed., (VCH, New York, 1997).
24. S. J. Organ and A. Keller, *J. Mater. Sci.* **20**, 1571 (1985).
25. G. Ungar, J. Stejny, A. Keller, I. Bidd, and M. C. Whiting, *Science* **229**, 386 (1985).
26. E. Ergoz, J. G. Fatou, and L. Mandelkern, *Macromolecules* **5**, 147 (1972).
27. G. S. Ross and L. J. Frolen, *Methods of Experimental Physics*, Vol. 16B, (Academic Press, 1980), p. 363.

28. L. Mandelkern, *Crystallization of Polymers* (McGraw-Hill, 1964).
29. A. J. Pennings and A. M. Kiel, *Kolloid Z. Z. Polym.* **205**, 160 (1965).
30. A. J. Pennings, *J. Polym. Sci., Polym. Symp.* **59**, 55 (1977).
31. T. Liu, I. Lieberwirth and J. Petermann, *Macromol. Chem. Phys.* **202**, 2921 (2001).
32. J. K. Hobbs and M. J. Miles, *Macromolecules* **34**, 353 (2001).
33. J. K. Hobbs, A. D. L. Humphris, and M. J. Miles, *Macromolecules* **34**, 5508 (2001).
34. P. J. Flory, *Principles of Polymer Chemistry* (Cornell Univ. Press, 1953).
35. L. Mandelkern, in *Physical Properties of Polymers*, J. E. Mark, ed. [American Chemical Society (ACS), Washington, DC, 1984].
36. J. D. Hoffman and J. J. Weeks, *J. Res. Natl. Bur. Std.* (U.S.) **A66**, 13 (1962).
37. H. Marand, J. Xu, and S. Srinivas, *Macromolecules* **31**, 8219 (1998).
38. G. Strobl, *Eur. Phys. J* **E3**, 165 (2000).
39. J. D. Gunton, M. San Miguel, and P. S. Sahni, The dynamics of first-order phase transitions, in *Phase Transitions*, Vol. 8 (Academic Press, 1983).
40. P. J. Flory and A. D. McIntyre, *J. Polymer Sci.* **18**, 592 (1955).
41. I. C. Sanchez and E. A. DiMarzio, *J. Chem Phys.* **55**, 893 (1971).
42. B. Wunderlich and A. Mehta, *J. Polym. Sci. Polym. Phys. Ed.* **12**, 255 (1974).
43. M. Hikosaka, *Polymer* **28**, 1257 (1987).
44. S. Toxvaerd, *J. Chem. Phys.* **93**, 4290 (1990).
45. T. A. Kavassalis and P. R. Sundararajan, *Macromolecules* **26**, 4144 (1993).
46. R. H. Boyd, R. H. Gee, J. Han, and Y. Jin, *J. Chem. Phys.* **101**, 788 (1994).
47. P. R. Sundararajan and T. A. Kavassalis, *J. Chem. Soc. Faraday Trans.* **91**, 2541 (1995).
48. L. Toma, S. Toma, and J. A. Subirana, *Macromolecules* **31**, 2328 (1998).
49. C. Liu and M. Muthukumar, *J. Chem. Phys.* **109**, 2536 (1998).
50. T. Yamamoto, *J. Chem. Phys.* **109**, 4638 (1998).
51. H. Takeuchi, *J. Chem. Phys.* **109**, 5614 (1998).
52. S. Balijepalli and G. C. Rutledge, *J. Chem. Phys.* **109**, 6523 (1998).
53. J. P. K. Doye and D. Frenkel, *J. Chem. Phys.* **110**, 2692 (1999).
54. S. Fujiwara and T. Sato, *J. Chem. Phys.* **110**, 9757 (1999).
55. J.-U. Sommer and G. Reiter, *J. Chem. Phys.* **112**, 4384 (2000).
56. M. Muthukumar, *Eur. Phys. J.* **E3**, 199 (2000).
57. M. Muthukumar and P. Welch, *Polymer* **41**, 8833 (2000).
58. P. Welch and M. Muthukumar, *Phys. Rev. Lett.* **87**, 218302 (2001).
59. T. Yamamoto, *J. Chem. Phys.* **115**, 8675 (2001).
60. M. Muthukumar, *Phil. Trans. Roy. Soc. Lond. A* **361**, 539 (2003).
61. M. Muthukumar, *J. Chem. Phys.* **104**, 691 (1996).
62. I. Dukovski and M. Muthukumar, *J. Chem. Phys.* **118**, 6648 (2003).
63. T. T. Perkins, D. E. Smith, and S. Chu, *Science* **276**, 2016 (1997).
64. A. J. Pennings, J. M. A. A. van der Mark, and H. C. Booij, *Kolloid Z. Z. Polym.* **236**, 99 (1969).

THEORY OF CONSTRAINED BROWNIAN MOTION

DAVID C. MORSE

Department of Chemical Engineering and Materials Science, University of Minnesota, Minneapolis, MN 55455

CONTENTS

Advances in Chemical Physics, Volume 128, edited by Stuart A. Rice
ISBN 0-471-44528-2

I. INTRODUCTION

The internal dynamics of polymers and other molecules in solution are often well described by mechanical models in which the relative positions and/or orientations of parts of a molecule are subject to geometric constraints. In atomistically detailed treatments, constrained classical mechanical models may be used to mimic the constraints imposed on bond lengths and/or bond angles by quantum chemistry. More phenomenological models of polymer molecules as rigid rods, rigid dumbbells, freely jointed chains, freely rotating chains, and inextensible wormlike chains also have a long history, both as illuminating toys (such as the freely jointed chain model) and as realistic but coarse-grained descriptions of certain classes of molecule (such as the rigid-rod and wormlike chain models).

Constraints may be introduced either into the classical mechanical equations of motion (i.e., Newton's or Hamilton's equations, or the corresponding inertial Langevin equations), which attempt to resolve the ballistic motion observed over short time scales, or into a theory of Brownian motion, which describes only the diffusive motion observed over longer time scales. We focus here on the latter case, in which constraints are introduced directly into the theory of Brownian motion, as described by either a diffusion equation or an inertialess stochastic differential equation. Although the analysis given here is phrased in quite general terms, it is motivated primarily by the use of constrained mechanical models to describe the dynamics of polymers in solution, for which the slowest internal motions are accurately described by a purely diffusive dynamical model.

The theory of Brownian motion for a constrained system is more subtle than that for an unconstrained system of pointlike particles, and has given rise to a substantial, and sometimes confusing, literature. Some aspects of the problem, involving equilibrium statistical mechanics and the diffusion equation, have been understood for decades [1–8]. Other aspects, particularly those involving the relationships among various possible interpretations of the corresponding stochastic differential equations [9–13], remain less thoroughly understood. This chapter attempts to provide a self-contained account of the entire theory.

The chapter is organized as follows. Section II presents most of the notation that is used here to describe constrained systems. Section III reviews the equilibrium statistical mechanics of constrained systems. There, we review the differences between the results obtained for ''rigid'' mechanical models, in which rigorous geometric constraints are introduced into the inertial equations of motion, and ''stiff'' models, in which constraints are approximately imposed by a stiff potential energy. Sections IV and V both discuss the diffusion equation for constrained systems. In Section IV, a generic diffusion equation is obtained by simple phenomenological arguments. In Section V diffusion equations for both rigid and stiff systems are instead derived from a slight extension of the phase space kinetic theory given for rigid systems by Bird, Curtiss, Armstrong, and Hassager [3,4]. Both the equilibrium distribution and diffusion equation are presented Sections III–V in generalized coordinates. Section VI introduces some of the machinery necessary to instead describe the motion of a constrained system in terms of Cartesian particle positions. Sections VII establishes a link between language of diffusion equations and the language of stochastic processes, by defining drift velocity vectors and diffusivity tensors for random diffusion process, in both generalized and Cartesian coordinates, and by giving expressions for the values required for a random process to generate a probability distribution that obeys the desired diffusion equation. Section VIII introduces the mathematical notions of generalized projection tensors and

generalized reciprocal vectors, which prove useful in the analysis of Cartesian Langevin equations for constrained systems. Section IX is a self-contained discussion of the use of nonlinear stochastic differential equations to describe Brownian motion, the relationships between several different possible ways of formulating and interpreting such equations, and their application to constrained Brownian motion, in both generalized and Cartesian coordinates. Section X discusses several algorithms for simulating constrained systems of point particles in Cartesian coordinates. Section XI presents analytic expressions for the stress tensor of a constrained system of point particles, and Section XII discusses two related methods of using the forces generated in a stochastic simulation to evaluate this stress.

II. GEOMETRY AND NOTATION

This section presents the notation for generalized coordinates, constraints, basis vectors, and tensors that is used throughout the paper. We consider a system consisting of N pointlike particles (beads) with positions $\mathbf{R}^1, \ldots, \mathbf{R}^N$ with masses $m_1, \ldots, m_N$. The positions of the beads are subject to K holonomic constraints, of the form

$$c^i(\mathbf{R}^1, \ldots, \mathbf{R}^N) = \text{const} \tag{2.1}$$

with $i = 1, \ldots, K$. The subspace within which these constraints are satisfied forms an $f = 3N - K$ dimensional hypersurface within the unconstrained 3N dimensional space, which we will refer to as the "constraint surface." In what follows, we will consider both "rigid" systems, in which the system is rigorously confined to the constraint surface; and "stiff" systems, in which the system is forced to remain very near the constraint surface by a potential function with a very steep "valley" along this surface. Bead positions in mechanical states that satisfy the constraints may be parameterized as functions

$$\mathbf{R}^\mu = \mathbf{R}^\mu(q^1, \ldots, q^f) \tag{2.2}$$

of some set of $f = 3N - K$ generalized coordinates $q^1, \ldots, q^f$, where $\mu = 1, \ldots, N$. We also define an extended set of $3N$ generalized coordinates $Q = \{Q^1, \ldots, Q^{3N}\}$ consisting of both the "soft" coordinates $q^1, \ldots, q^f$

introduced in Eq. (2.2) and K "hard" coordinates given by the constrained quantities $c^1, \ldots, c^K$, such that

$$Q^\alpha \equiv \begin{cases} q^\alpha & \text{for } \alpha = 1, \ldots, f \\ c^{\alpha - f} & \text{for } \alpha = f+1, \ldots, 3N \end{cases} \tag{2.3}$$

where $\alpha = 1, \ldots, 3N$. The following conventions will be used throughout for indices of bead positions, soft coordinates, constraints, and generalized coordinates:

$$\begin{aligned} \mu, \nu, \ldots &= 1, \ldots, N && \text{beads} \\ i, j, \ldots &= i, \ldots, K && \text{constraints} \\ a, b, \ldots &= 1, \ldots, f && \text{soft coordinates} \\ \alpha, \beta, \ldots &= 1, \ldots, 3N && \text{all coordinates} \end{aligned} \tag{2.4}$$

The symbol q^a will thus be used to indicate a soft coordinate and Q^α to indicate a coordinate that could be either soft or hard. The ranges of summation for each type of index will be those indicated above, and summation over repeated indices will be implicit, unless stated otherwise.

Placement of indices as superscripts or subscripts follows the conventions of tensor analysis. Contravariant variables, which transform like coordinates, are indexed by superscripts, and coavariant quantities, which transform like derivatives, are indexed by subscripts. Cartesian and generalized velocities $\dot{\mathbf{R}}^\mu$ and $\dot{Q}^\alpha$ are thus contravariant, while Cartesian and generalized forces, which transform like derivatives of a scalar potential energy, are covariant.

A. Basis Vectors

For each coordinate Q^α in the full space, we may define a covariant basis vector $\partial \mathbf{R}^\mu / \partial Q^\alpha$ and a contravariant basis vector $\partial Q^\alpha / \partial \mathbf{R}^\mu$, which obey orthogonality and completeness relations

$$\frac{\partial \mathbf{R}^\mu}{\partial Q^\alpha} \cdot \frac{\partial Q^\beta}{\partial \mathbf{R}^\mu} = \delta_\alpha^\beta \tag{2.5}$$

$$\frac{\partial Q^\alpha}{\partial \mathbf{R}^\mu} \frac{\partial \mathbf{R}^\nu}{\partial Q^\alpha} = \mathbf{I}_\mu^\nu \tag{2.6}$$

in the $3N$-dimensional Euclidean space of all N bead positions. Here, and in what follows

$$\mathbf{I}_{\mu}^{\nu} = \mathbf{I}\delta_{\mu}^{\nu} \tag{2.7}$$

denotes the Euclidean identity tensor, which may be labeled with either subscripted or superscripted bead indices, depending on context, so that $\mathbf{I}_{\mu}^{\nu} = \mathbf{I}_{\mu\nu} = \mathbf{I}^{\mu\nu}$.

Any $3N$-dimensional Cartesian vector that is associated with a point on the constraint surface may be divided into a "soft" component, which is locally tangent to the constraint surface; and a "hard" component, which is perpendicular to this surface. The soft subspace is the f-dimensional vector space that contains all $3N$ dimensional Cartesian vectors that are locally tangent to the constraint surface. It is spanned by f covariant tangent basis vectors

$$\mathbf{a}_{a}^{\mu} \equiv \frac{\partial \mathbf{R}^{\mu}}{\partial q^{a}} \tag{2.8}$$

with $a = 1, \ldots, f$. Cartesian bead velocities of a constrained system must, for example, lie within this soft subspace. The hard subspace is the K-dimensional space of $3N$ vectors that are perpendicular to a particular point on the constraint surface. This space is spanned by the K contravariant normal basis vectors

$$\mathbf{n}_{\mu}^{i} \equiv \frac{\partial c^{i}}{\partial \mathbf{R}^{\mu}} \tag{2.9}$$

with $i = 1, \ldots, K$. Constraint forces, by d'Alembert's principle, must lie within the hard subspace.

B. Mobility, Mass, and Metric Tensors

Hydrodynamic and frictional effects may be described by a Cartesian mobility tensor $\mathbf{H}^{\mu\nu}$, which is generally a function of all of the system coordinates. In models of systems of beads (i.e., localized centers of hydrodynamic resistance) with hydrodynamic interactions, $\mathbf{H}^{\mu\nu}$ is normally taken to be of the form

$$\mathbf{H}^{\mu\nu} = \zeta^{-1}\mathbf{I}^{\mu\nu} + \mathbf{\Omega}(\mathbf{R}^{\mu} - \mathbf{R}^{\nu}) \tag{2.10}$$

where ζ is a phenomenological friction coefficient, and $\mathbf{\Omega}$ is the Oseen or Rotne-Prager-Yamakawa tensor [14,15] for $\mu \neq \nu$. The Cartesian friction tensor $\boldsymbol{\zeta}_{\mu\nu}$ is the inverse of $\mathbf{H}^{\mu\nu}$, so that

$$\boldsymbol{\zeta}_{\lambda\mu} \cdot \mathbf{H}^{\mu\nu} = \mathbf{I}_{\lambda}^{\nu} \tag{2.11}$$

It will be assumed throughout that $\mathbf{H}^{\mu\nu}$ and $\boldsymbol{\zeta}_{\mu\nu}$ are symmetric positive-definite tensors. We write the mobility as a contravariant tensor, with raised bead indices, to reflect its function; the mobility $\mathbf{H}^{\mu\nu}$ may be contracted with a covariant force vector $\mathbf{F}_{\nu}$ (e.g., the derivative of a potential energy) to produce a resulting contravariant velocity $\mathbf{H}^{\mu\nu} \cdot \mathbf{F}_{\nu}$.

To describe inertial effects, we introduce a Cartesian mass tensor

$$\mathbf{m}_{\mu\nu} = m_{\mu}\, \mathbf{I}_{\mu\nu} \tag{2.12}$$

with no summation over μ, where the diagonal element m_{μ} is the mass of bead μ. The corresponding inverse mass tensor is given by $(\mathbf{m}^{-1})^{\mu\nu} = m_{\mu}^{-1}\mathbf{I}^{\mu\nu}$, with no summation over μ. We write the mass as a covariant tensor because it may be contracted with two contravariant velocities to produce a scalar kinetic energy

$$K = \frac{1}{2}\dot{\mathbf{R}}^{\mu} \cdot \mathbf{m}_{\mu\nu} \cdot \dot{\mathbf{R}}^{\nu} \tag{2.13}$$

or contracted with a single velocity to produce a covariant momentum $\mathbf{P}_{\mu} = \mathbf{m}_{\mu\nu} \cdot \dot{\mathbf{R}}^{\nu}$, whose time derivative is given by a covariant force $\dot{\mathbf{P}}_{\mu} = \mathbf{F}_{\mu}$.

Representations of these and other tensors in an arbitrary system of coordinates may be constructed as follows. For each contravariant rank 2 Cartesian tensor $\mathbf{T}^{\mu\nu}$ (such as $\mathbf{H}^{\mu\nu}$) or covariant tensor $\mathbf{S}_{\mu\nu}$ (such as $\mathbf{m}_{\mu\nu}$), we define corresponding Riemannian representations

$$T^{\alpha\beta} \equiv \frac{\partial Q^{\alpha}}{\partial \mathbf{R}^{\mu}} \cdot \mathbf{T}^{\mu\nu} \cdot \frac{\partial Q^{\beta}}{\partial \mathbf{R}^{\nu}} \tag{2.14}$$

$$S_{\alpha\beta} \equiv \frac{\partial \mathbf{R}^{\mu}}{\partial Q^{\alpha}} \cdot \mathbf{S}_{\mu\nu} \cdot \frac{\partial \mathbf{R}^{\nu}}{\partial Q^{\beta}} \tag{2.15}$$

A Riemannian mobility tensor $H^{\alpha\beta}$ and friction tensor $\zeta_{\alpha\beta}$, for example, are thus defined by taking $\mathbf{T}^{\mu\nu} = \mathbf{H}^{\mu\nu}$ in Eq. (2.14) and $\mathbf{S}_{\mu\nu} = \boldsymbol{\zeta}_{\mu\nu}$ in Eq. (2.15), respectively. When (as in this example) $\mathbf{T}^{\mu\nu}$ and $\mathbf{S}_{\mu\nu}$ are Cartesian inverses of one another, so that $\mathbf{T}^{\lambda\mu} \cdot \mathbf{S}_{\mu\nu} = \mathbf{I}^{\lambda}_{\nu}$, then the corresponding Riemannian tensors $T^{\alpha\beta}$ and $S_{\alpha\beta}$ are also inverses, so that $T^{\alpha\beta}S_{\beta\gamma} = \delta^{\alpha}_{\gamma}$.

A covariant metric tensor $g_{\alpha\beta}$ and contravariant inverse metric tensor $G^{\alpha\beta}$ in the full space are given by

$$g_{\alpha\beta} \equiv \frac{\partial \mathbf{R}^{\mu}}{\partial Q^{\alpha}} \cdot \frac{\partial \mathbf{R}^{\mu}}{\partial Q^{\beta}} \tag{2.16}$$

$$G^{\alpha\beta} \equiv \frac{\partial Q^{\alpha}}{\partial \mathbf{R}^{\mu}} \cdot \frac{\partial Q^{\beta}}{\partial \mathbf{R}^{\mu}} \tag{2.17}$$

These are covariant and contravariant representations of the Cartesian identity tensor, and inverses of each other.

The determinant of a tensor will be denoted in what follows by the symbol for the tensor, without indices. The determinant of the $3N \times 3N$ matrix $g_{\alpha\beta}$ is given by

$$g = \left\{ \det\left[\frac{\partial \mathbf{R}}{\partial Q}\right] \right\}^2 \tag{2.18}$$

Note that $\sqrt{g} \equiv \det\left[\frac{\partial \mathbf{R}}{\partial Q}\right]$ is the determinant of the $3N \times 3N$ transformation matrix $\partial \mathbf{R}^{\mu}/\partial Q^{\alpha}$, which gives the Jacobian for the transformation from generalized to Cartesian coordinates. This follows from the fact that the right-hand side (RHS) of Eq. (2.16) for $g_{\alpha\beta}$ is a matrix product of this transformation matrix with its transpose, and that the determinant of a matrix product is a product of determinants. By similar reasoning, we find that

$$m = (m_1 m_2 \cdots m_N)^3 g \tag{2.19}$$

where the product of bead masses is the determinant of the Cartesian mass matrix $\mathbf{m}_{\mu\nu}$. This is shown by noting that the RHS of Eq. (2.15) for $m_{\alpha\beta}$, with $\mathbf{S}_{\mu\nu} = \mathbf{m}_{\mu\nu}$, is a matrix product of the transformation matrix, the Cartesian representation of the mass tensor $\mathbf{m}_{\mu\nu}$ as a diagonal $3N \times 3N$ matrix, and the transposed transformation matrix.

C. Projected Tensors

For each covariant rank 2 tensor $\mathbf{S}_{\mu\nu}$ (with two subscripted indices) we define a projection onto the soft subspace

$$\tilde{S}_{ab} = \mathbf{a}_a^\mu \cdot \mathbf{S}_{\mu\nu} \cdot \mathbf{a}_b^\nu \tag{2.20}$$

which is denoted by the use of a tilde over the generic symbol for the tensor. The elements of this projected tensor are the same as those of the full tensor $S_{\alpha\beta}$ for subscripts $\alpha, \beta = 1, \ldots, f$. Specificially, we define projected metric, mass, and friction tensors

$$\tilde{g}_{ab} \equiv \mathbf{a}_a^\mu \cdot \mathbf{a}_b^\mu \tag{2.21}$$

$$\tilde{m}_{ab} \equiv \mathbf{a}_a^\mu \cdot \mathbf{m}_{\mu\nu} \cdot \mathbf{a}_b^\nu \tag{2.22}$$

$$\tilde{\zeta}_{ab} \equiv \mathbf{a}_a^\mu \cdot \boldsymbol{\zeta}_{\mu\nu} \cdot \mathbf{a}_b^\nu \tag{2.23}$$

for $a, b = 1, \ldots, f$.

For each rank 2 contravariant Riemannian tensors $\mathbf{T}^{\mu\nu}$ (with two raised indices) we define a $K \times K$ projection onto the hard subspace

$$\hat{T}^{ij} \equiv \mathbf{n}_\mu^i \cdot \mathbf{T}^{\mu\nu} \cdot \mathbf{n}_\nu^j \tag{2.24}$$

indicated by a caret over the symbol for the full tensor, whose elements are equal to those of the full tensor $T^{\alpha\beta}$ for subscript values $\alpha = i + f$ and $\beta = j + f$ corresponding to the hard coordinates. Specifically, we define projected inverse metric, inverse mass, and mobility tensors

$$\hat{G}^{ij} \equiv \mathbf{n}_\mu^i \cdot \mathbf{n}_\mu^j \tag{2.25}$$

$$(\widehat{m^{-1}})^{ij} \equiv \mathbf{n}_\mu^i \cdot (\mathbf{m}^{-1})^{\mu\nu} \cdot \mathbf{n}_\nu^j \tag{2.26}$$

$$\hat{H}^{ij} \equiv \mathbf{n}_\mu^i \cdot \mathbf{H}^{\mu\nu} \cdot \mathbf{n}_\nu^j \tag{2.27}$$

for indices $i, j = 1, \ldots, K$.

Fixman has shown [2] that, for any covariant symmetric tensor $S_{\alpha\beta}$ defined in the full space, with an inverse $T^{\alpha\beta} = (S^{-1})^{\alpha\beta}$ in the full space, the determinants $\tilde{S}$ and $\hat{T}$ of the projections of S and T onto the soft and hard subspaces, respectively, are related by

$$\tilde{S} = S\hat{T} \tag{2.28}$$

Specifically, this implies that $\tilde{g} = g\hat{G}$, $\tilde{m} = m\widehat{m^{-1}}$, and $\tilde{\zeta} = \zeta\hat{H}$. A proof of this theorem is given in the Appendix, Section B.

III. THERMAL EQUILIBRIUM

Here, we review the equilibrium statistical mechanics of constrained systems. Constrained models of Brownian motion may be derived from either "rigid" or "stiff" mechanical models. In a rigid model, geometric constraints are rigorously imposed at the level of the underlying inertial equations of motion. In a stiff model, values some set of "hard" variables (e.g., bond lengths, or relative bond angles) are approximately constrained by a stiff potential energy. Seemingly equivalent rigid and stiff classical mechanical models, with the same potential energy function within the constraint surface, have long been known [1–8] to yield different thermal equilibrium probability distributions for "soft" coordinates, such as the bond orientations of a linear polymer.

A. Rigid Classical Systems

The equilibrium phase space distribution $\rho(q,p)$ for a rigid system of f coordinates is given by the Boltzmann distribution

$$\rho_{\text{eq}}(q,p) \propto e^{-\mathscr{H}(q,p)/kT} \tag{2.29}$$

where $\mathscr{H}(q,p)$ is the system Hamiltonian, and where q and p are shorthand for lists of soft coordinates $q \equiv \{q^1, \ldots, q^f\}$ and canonical Hamiltonian momenta $p \equiv \{p^1, \ldots, p^f\}$. To define Hamiltonian momenta, we first expand the velocity as $\dot{\mathbf{R}}^\mu = \mathbf{a}^\mu_a \dot{q}^a$ in order to rewrite kinetic energy (2.13) in terms of generalized coordinates and velocities, as

$$K(q,\dot{q}) = \frac{1}{2}\tilde{m}_{ab}\dot{q}^a \dot{q}^b \tag{2.30}$$

where $\tilde{m}_{ab}$ is as defined in Eq. (2.22). The canonical Hamiltonian momenta are

$$p_a \equiv \frac{\partial K(q,\dot{q})}{\partial \dot{q}^a} = \tilde{m}_{ab}\,\dot{q}^b \tag{2.31}$$

The Hamiltonian for a system with potential energy U is then

$$\mathscr{H} = \frac{1}{2}(\tilde{m}^{-1})^{ab} p_a p_b + U(q) \tag{2.32}$$

where $(\tilde{m}^{-1})^{ab}$ is the matrix inverse of the $f \times f$ matrix $\tilde{m}_{ab}$.

The reduced distribution of values for the coordinates alone (e.g., of bond orientations for a linear polymer with constrained bond lengths) is given by the integral

$$\psi(q) = \int dp\, \rho(q,p) \tag{2.33}$$

in which $\int dp \equiv \int dp_1 \cdots \int dp_f$ denotes an integral over all f momenta. The equilibrium reduced distribution is obtained by substituting Eq. (2.29) for ρ in Eq. (33). Evaluating the resulting f-dimensional Gaussian momentum integral yields

$$\psi_{\text{eq}}(q) \propto \sqrt{\tilde{m}}\, e^{-U/kT} \tag{2.34}$$

where $\tilde{m} = \tilde{m}(q)$ is the determinant of the matrix $\tilde{m}_{ab}(q)$.

The corresponding analysis for an unconstrained system in Cartesian coordinates, in which all $3N$ coordinates are treated as "soft," yields a constant $\sqrt{m} = (m_1 \cdots m_N)^{3/2}$ for the determinant of the mass matrix, which affects only the constant of proportionality, and thus yields a naive Boltzmann distribution $\psi_{\text{eq}}(\mathbf{R}) \propto e^{-U(\mathbf{R})/kT}$. Analysis of an unconstrained system in generalized coordinates yields a value for $\sqrt{m}$ that depends on the system coordinates, but that, by Eq. (2.19), is simply proportional to the Jacobian $\sqrt{g}$ for the transformation between generalized and Cartesian coordinates. The result for a rigid system may be related to that for an unconstrained system by noting that $\tilde{m} = m\widehat{m^{-1}}$, by Eq. (2.28), and that $m \propto g$ in the full space, to obtain

$$\psi_{\text{eq}}(q) \propto \sqrt{g\widehat{m^{-1}}}\, e^{-U/kT} \tag{2.35}$$

where $\widehat{m^{-1}}$ is the determinant of the projected tensor defined in Eq (2.26).

B. Stiff Classical Systems

In a stiff system, no variables are constrained, but the total potential energy of the system, which will be denoted by $V(Q)$, has a sharp minimum (i.e., an f-dimensional valley) along the constraint surface. To describe slight deviations from the constraint surface, we may Taylor expand $V(Q)$ to harmonic order around its value on the constraint surface, which will be denoted by $U(q)$. This yields

$$V(Q) \simeq U(q) + \frac{1}{2} D_{ij}(q) \delta c^i \delta c^j \tag{2.36}$$

where δc^i is the deviation of a hard variable c^i from its constrained value and $D_{ij}(q)$ is a matrix of second derivatives of V with respect to the hard variables,

i.e., a matrix of generalized spring constants. The constraint surface is implicitly defined here as the surface along which $\partial V(Q)/\partial c^i = 0$ for all $i = 1, \ldots, K$.

The distribution of generalized coordinates in the full space of both soft and hard coordinates may be described by a probability distribution $\Psi(Q)$. The equilibrium distribution in the full space is obtained by integrating over the momenta, as for the rigid model, while treating all of the coordinates for this purpose as soft. This yields an equilibrium distribution

$$\Psi_{\mathrm{eq}}(Q) \propto \sqrt{m}\, e^{-V(Q)/kT} \tag{2.37}$$

where $\sqrt{m}$ is the determinant of the mass matrix $m_{\alpha\beta}$ in the full space.

The desired reduced distribution $\psi(q)$ for the soft coordinates alone is given by the integral

$$\psi(q) \equiv \int dc\, \Psi(Q) \tag{2.38}$$

where $\int dc \equiv \int dc^1 \cdots \int dc^K$ denotes an integral over all of the hard coordinates. By using the equilibrium distribution $\Psi_{\mathrm{eq}}(Q)$ in Eq. (2.38), while using approximation Eq. (2.36) for $V(Q)$, and evaluating the resulting K-dimensional Gaussian integral over the hard variables, we obtain an equilibrium reduced distribution

$$\psi_{\mathrm{eq}}(q) \propto \sqrt{gD^{-1}} e^{-U/kT} \tag{2.39}$$

in which D^{-1} is the inverse of the determinant of D_{ij} in the hard subspace, and in which we have used the fact that $m \propto g$ in the full space to replace m by g. In general, the equilibrium distribution for a stiff system thus depends on how the matrix D_{ij} of spring constants varies over the constraint surface, which controls the width of the potential energy valley to which the system is constrained. We show in the next section, however, that in the special case of a bead–spring polymer with nearest-neighbor springs, for which the determinant D is independent of the bond orientations, this prescription leads to the naive distribution of bond orientations, and to statistically independent bond orientations in the freely jointed limit $U = 0$.

C. Stiff Quantum Systems

There is a well-known precedent for the difference in the results predicted by stiff and rigid models. The constant-volume heat capacity of a diatomic ideal gas is predicted to be $\frac{7}{2}kT$ per molecule for a stiff classical model and $\frac{5}{2}kT$ for a classical rigid rotor. A quantum mechanical analysis of a diatomic gas yields the

classical result in the limit of high temperatures or slow vibrations, and the rigid rotor result for lower temperature or more rapid vibrations, and explains why the rigid-rotor result agrees well with experimental results for the most common diatomic molecules near room temperature. Questions about the realism of approximate classical models of more complicated molecules can also, in principle, be resolved by recourse to quantum mechanics, but the results are generally not so simple.

Here, we summarize a quantum mechanical analysis given by Go and Scheraga [6], in which in an effective classical model for the soft coordinates is obtained by an adiabatic (or Born–Oppenheimer) approximation for vibrations of the hard coordinates. Details of this analysis are given in the Appendix, Section D. In this approximation, one first calculates a constrained free energy from a quantum mechanical treatment of the coupled harmonic vibrations of the hard coordinates, assuming local equilibration of the vibrational modes, while treating the soft coordinates and momenta for this purpose as constant parameters. The resulting constrained free energy is then used as a classical potential for the more slowly evolving soft coordinates and momenta, which are treated classically. This analysis is found to yield an an effective classical rigid model for the remaining soft coordinates and momenta, with a Hamiltonian

$$\mathscr{H}(q,p) = \frac{1}{2}(\tilde{\boldsymbol{m}}^{-1})^{ab} p_a p_b + U_{\text{eff}}(q,T) \tag{2.40}$$

containing an effective classical potential energy

$$U_{\text{eff}}(q,T) = U(q) - kT \ln Z_{\text{vib}}(q,T) \tag{2.41}$$

given by the sum of the classical potential energy $U(q)$ on the constraint surface and a q-dependent vibrational free energy $-kT \ln Z_{\text{vib}}$, in which

$$Z_{\text{vib}}(q,T) = \prod_{k=1}^{K} \left[2 \sinh\left(\frac{\hbar \omega_k(q)}{2kT} \right) \right]^{-1} \tag{2.42}$$

is the vibrational partition function for a system of K coupled oscillators with eigenfrequencies $\omega_1(q), \ldots, \omega_K(q)$ that generally depend on the values of the soft coordinates. Classical integration over the soft momenta then yields a reduced distribution

$$\psi_{\text{eq}}(q) \propto \sqrt{\tilde{\boldsymbol{m}}} e^{-U_{\text{eff}}(q,T)/kT} \tag{2.43}$$

At very high temperatures, for which $kT \gg \hbar \omega_k(q)$ for all K vibrational eigenmodes, Eq. (2.43) is shown in the Appendix, Section D to reproduce the

results of a classical analysis of the underlying stiff model, recovering Eq. (2.39), as required by the correspondence principle. At low temperatures, for which $kT \ll \hbar\omega_k(q)$ for all the vibrational eigenmodes, Eq. (2.41) instead yields an effective potential

$$\lim_{T\to 0} U_{\text{eff}}(q,T) = U(q) + \frac{1}{2}\sum_l \hbar\omega_l(q) \tag{2.44}$$

given by the sum of the classical potential energy $U(q)$ and the vibrational ground-state energy. If $U(q)$ is small or vanishing, as in a freely jointed model, the q dependence of the ground-state vibrational energy can drastically affect $\psi_{\text{eq}}(q)$. The classical rigid result of Eq. (2.34) is recovered if and only if we approximate $U_{\text{eff}} = U$, and thus ignore the vibrational contribution to $U_{\text{eff}}(q)$.

As an example, Rallison [8] has applied this analysis to a freely jointed "trumbbell" model of three beads of equal mass connected by two stiff springs with natural vibrational frequencies ω_0, for which $U(q) = 0$. In the classical limit $kT \gg \hbar\omega_0$, this model yields uncorrelated bond orientations, in agreement with the stiff classical model. In the quantum limit $kT \ll \hbar\omega_0$, the model yields an equilibrium distribution for the cosine of the angle θ between the two bonds that becomes increasingly sharply peaked around both the parallel $\theta = 0$ and antiparallel $\theta = \pi$ configurations as the ratio $kT/\hbar\omega$ decreases, because these configurations are both found to minimize the vibrational ground state energy of this molecule. The classical rigid trumbbell model [3,4], which ignores the ground state energy, instead yields an athermal distribution $\mathscr{P}(\cos\theta) \propto \sqrt{4 - \cos^2\theta}$ that has a rather weak maximum in the perpendicular $\theta = \pi/2$ configuration, because this configuration maximizes the entropy arising from fluctuations of the bond angular momenta.

The analysis above might lead one to conclude that stiff classical models are less wrong than rigid classical models, because only a stiff classical model can be obtained as a well-defined limit of a quantum mechanical model with the same potential energy. One should keep in mind, however, that the same equilibrium distribution can be obtained from any of the above three types of model by appropriate adjustments of the potential energy used as an input to each type of model. The procedure outlined above for deriving an effective classical model from a quantum mechanical treatment of molecular vibrations is conceptually straightforward, but requires as an input an interatomic potential that must be accurate to within a small fraction of kT to resolve the rather subtle differences between stiff and rigid classical models. If trying to describe real molecules at this level of accuracy, there is little reason to require that the same potential energy be used in classical and quantum treatments of the same molecule, or to restrict the form of the interatomic potentials used in either type of treatment to arbitrarily simplified forms, such the freely joined or freely

rotating chain models, that have thus far been studied as examples. A meaningful discussion of the realism of different simplified classical models thus seems to require a degree of chemical realism greater than that that has thus far typified the study of polymer dynamics. The present discussion is thus intended only as a review of the mathematical relationships between well-defined models.

D. Linear Polymers

We now consider the example of a linear polymer of beads connected by rigid rods or stiff springs. We explicitly consider only the classical rigid bead–rod and stiff bead–spring models, since the stiff quantum model may be treated as a rigid classical model with an appropriately modified potential energy. Consider a chain of N beads numbered consecutively $\mu = 1, \ldots, N$, and bonds of fixed or nearly fixed length a between neighboring beads. To describe such a chain, we introduce a set of N vectors $\mathbf{Q}^1, \ldots, \mathbf{Q}^N$, consisting of $N-1$ bond vectors

$$\mathbf{Q}^i \equiv \mathbf{R}^{i+1} - \mathbf{R}^i \tag{2.45}$$

for $i = 1, \ldots, N-1$, and a single center-of-mass position

$$\mathbf{Q}^N \equiv \frac{1}{N}\sum_{\mu=1}^{N} \mathbf{R}^\mu \tag{2.46}$$

These definitions may be given more compactly as a linear transformation

$$\mathbf{Q}^i = \sum_\mu A^i_\mu \mathbf{R}^\mu \tag{2.47}$$

where A^i_μ is an $N \times N$ matrix with elements

$$A^i_\mu \equiv \begin{cases} \delta^{i+1}_\mu - \delta^i_\mu & i = 1, \ldots, N-1 \\ 1/N & i = N \end{cases} \tag{2.48}$$

It is straightforward to show by applying Cramer's rule recursively to chains of increasing N that the determinant of matrix $[A]$ is ± 1, with $\det[A] = -1$ for N even and $\det[A] = +1$ for N odd.

To introduce scalar coordinates, each bond vector is expressed as a product

$$\mathbf{Q}^i = c^i \mathbf{u}_i(\theta^i, \phi^i) \tag{2.49}$$

of a bond length $c^i \equiv |\mathbf{Q}^i|$ and a unit vector $\mathbf{u}_i$ that is parameterized by a polar angle θ^i and an azimuthal angle ϕ^i. The chain conformation is thereby parameterized by $K = N-1$ hard coordinates, given by the bond lengths, and $f = 2N+1$ soft coordinates, given by the $2(N-1)$ bond angles and the three

Cartesian components of $\mathbf{Q}^N$. We will also indicate the three scalar coordinates associated with each $\mathbf{Q}$ vector by the notation Q^{is}, where $i = 1, \ldots, N$ and $s = 1, \ldots, 3$. For the $N-1$ bond vectors we define

$$Q^{i1} = \theta^i \qquad Q^{i2} = \phi^i \qquad Q^{i3} = c^i \tag{2.50}$$

while for the center of mass, we take $Q^{N1}, \ldots, Q^{N3}$ to be the three Cartesian components of $\mathbf{Q}^N$. In this notation, the partial derivatives may be written

$$\frac{\partial Q^{is}}{\partial \mathbf{R}^\mu} = A^i_\mu \frac{\partial Q^{is}}{\partial \mathbf{Q}^i} \tag{2.51}$$

$$\frac{\partial \mathbf{R}^\mu}{\partial Q^{is}} = (A^{-1})^\mu_i \frac{\partial \mathbf{Q}^i}{\partial Q^{is}} \tag{2.52}$$

where $(A^{-1})^\mu_i$ is the matrix inverse of A^i_μ, and where there is no sum over i. These expressions follow from the chain rule for differentation combined with linear transformation (2.47). The contravariant normal basis vectors for the hard bond length coordinates are thus

$$\mathbf{n}^i_\mu = \frac{\partial c^i}{\partial \mathbf{R}^\mu} = A^i_\mu \mathbf{u}_i \tag{2.53}$$

for $i = 1, \ldots, N-1$, with no sum over i on the RHS. Because of the sparse structure of $[A]$, the contravariant normal vector $\mathbf{n}^i_\mu$ has nonzero values for only two neighboring beads. Because the inverse matrix $[A^{-1}]$ is dense, however, each covariant tangent basis vector $\mathbf{a}^\mu_a$ has nonzero values for all of the beads. This is a general feature of models involving constrained quantities, such as bond lengths or relative bond angles, that depend on the positions of only a few nearby beads, and provides one important motivation for formulating simulation algorithms in terms of Cartesian positions and constraints rather than generalized coordinates.

The Jacobian $\sqrt{|g|} = |\det\left[\frac{\partial \mathbf{R}}{\partial Q}\right]|$ for the transformation from generalized to Cartesian coordinates is a product of $N-1$ Jacobians for the local transformations from polar to Cartesian components for each bond vector $\mathbf{Q}^i$ for $i \leq N-1$, times the Jacobian $|\det[A^{-1}]|^3 = 1$ for the transformation of $\mathbf{Q}$ vectors to $\mathbf{R}$ vectors, in which $\det[A^{-1}] = \pm 1$ is cubed because each Cartesian component transforms independently. The Jacobian of the local transformation from polar to Cartesian coordinates for a single bond vector of length c is given by the factor $c^2 \sin(\theta)$ that appears in the relation $d^3\mathbf{Q} = c^2 \sin(\theta) dg\, d\theta\, d\phi$ between volume elements. The overall Jacobian is thus

$$\sqrt{|g|} = \prod_{i=1}^{N-1} (c^i)^2 \sin(\theta^i) \tag{2.54}$$

where $c^i = a$ for all $i = 1, \ldots, K$ on the constraint surface.

The distribution of bond orientations is most conveniently characterized by a probability distribution $\phi(\mathbf{u})$, defined such that

$$\phi(\mathbf{u})d\mathbf{u}_1 \cdots d\mathbf{u}_{N-1} \tag{2.55}$$

is the probability of finding the orientations of all $N-1$ bonds within specified ranges of solid angles around a specified set of values $\mathbf{u} \equiv \{\mathbf{u}_1, \ldots, \mathbf{u}_{N-1}\}$, where $d\mathbf{u}_i \equiv \sin(\theta^i)d\theta^i d\phi^i$ is an infinitesimal solid angle for bond i. In an ensemble in which the center-of-mass positions are uniformly distributed throughout a volume V, the distribution $\psi(q)$ is related to $\phi(\mathbf{u})$ by

$$\psi(q) = \frac{1}{V}\left(\prod_{i=1}^{N-1} \sin(\theta^i)\right)\phi(\mathbf{u}) \tag{2.56}$$

where the soft coordinates $q^1, \ldots, q^f$ include the bond angles and the components of the center of mass. By comparing Eqs. (2.56) and (2.54), we see that on the constraint surface, where $c^i = a$, we have

$$\phi(\mathbf{u}) \propto \frac{\psi(q)}{\sqrt{g}} \tag{2.57}$$

to within a prefactor that is independent of the soft coordinates.

1. *Rigid Bonds*

Consider first the case of a linear polymer with rigorously constrained bond lengths and a potential energy

$$U(q) = U(\mathbf{u}_1, \ldots, \mathbf{u}_{N-1}) \tag{2.58}$$

that may depend on the relative bond orientations (as in a wormlike chain), but not on the center of mass. The Kramers chain is a special case obtained by setting $U(q) = 0$. The equilibrium distribution of bond orientations $\phi_{\text{eq}}(\mathbf{u})$ may be obtained by combining Eq. (2.57) with Eq. (2.35) for $\psi_{\text{eq}}(q)$. This yields

$$\phi_{\text{eq}}(\mathbf{u}) \propto \sqrt{\widehat{m^{-1}}}\, e^{-U(\mathbf{u})/kT} \tag{2.59}$$

where $\widehat{m^{-1}}$ is the determinant of the $(N-1) \times (N-1)$ matrix

$$(\widehat{m^{-1}})^{ij} = \sum_{\mu} \frac{1}{m_\mu} A^i_\mu A^j_\mu \mathbf{u}_i \cdot \mathbf{u}_j \tag{2.60}$$

that is obtained by combining definition (2.26) for $\widehat{m^{-1}}$ with Eq. (2.53) for $\mathbf{n}_\mu^i$. Carrying out the sum over μ yields a symmetric tridiagonal matrix

$$(\widehat{m^{-1}})^{ij} = \begin{cases} m_{i+1}^{-1} + m_i^{-1} & i = j \\ -m_i^{-1}\mathbf{u}_i \cdot \mathbf{u}_j & i = j+1 \\ -m_j^{-1}\mathbf{u}_i \cdot \mathbf{u}_j & j = i+1 \\ 0 & \text{otherwise} \end{cases} \tag{2.61}$$

where $i,j = 1,\ldots,N-1$. In the case of beads with equal mass m, we have $(\widehat{m^{-1}})^{ij} = \hat{G}^{ij}/m$, where

$$\hat{G}^{ij} = \begin{cases} 2 & i = j \\ -\mathbf{u}_i \cdot \mathbf{u}_j & i = j \pm 1 \\ 0 & \text{otherwise} \end{cases} \tag{2.62}$$

is the projected contravariant (or inverse) metric. In the simple case of a freely jointed trumbell with three beads of equal mass, this yields a statistical weight $\sqrt{\widehat{m^{-1}}} \propto \sqrt{4 - \cos^2\theta}$, with $\cos\theta \equiv \mathbf{u}_1 \cdot \mathbf{u}_2$. Fixman [2] has given a recursion equation for the efficient calculation of the determinant $\widehat{m^{-1}}$ or $\hat{G}$ for chains of arbitrary length.

2. *Stiff Bonds*

We next consider the case of a linear polymer with stiff bonds of length $c^1,\ldots,c^{N-1}$ that are constrained to remain near a preferred value a by strong springs, giving a potential energy

$$V = U(\mathbf{u}) + \frac{1}{2}D_0(c^i - a)^2 \tag{2.63}$$

where D_0 is a spring constant and $U(\mathbf{u})$ is an unspecified function of the bond orientations, which vanishes for a freely jointed chain. The distribution of bond orientations is obtained by combining Eq. (2.57) with Eq. (2.39) for $\psi_{\text{eq}}(q)$, which yields

$$\phi_{\text{eq}}(\mathbf{u}) \propto \sqrt{D^{-1}}e^{-U(\mathbf{u})/kT} \tag{2.64}$$

The model with stiff nearest-neighbor springs is special in that the matrix

$$D_{ij} \equiv \frac{\partial^2 V}{\partial c^i \partial c^j} = \delta_{ij}D_0 \tag{2.65}$$

is both diagonal and independent of the values of the soft variables, that is, independent of the bond orientations and center-of-mass position. This leads to a

constant value for the determinant of D^{-1} in Eq. (2.39), and thus to a simple Boltzmann distribution

$$\phi_{\text{eq}}(\mathbf{u}) \propto e^{-U(\mathbf{u})/kT} \tag{2.66}$$

for the distribution of bond orientations, which become statistically independent in the case of a freely jointed chain, with $U = 0$. It is interesting to note, however, that the simplicity of this result is a consequence of the simple form assumed for the constraining potential in this particular model.

E. Summary

The equilibrium distribution of soft generalized coordinates for both stiff and rigid classical mechanical systems of point particles may be written in the generic form

$$\psi_{\text{eq}}(q) \propto \sqrt{gW}\; e^{-U(q)/kT} \tag{2.67}$$

where g is a metric tensor for the full $3N$-dimensional space, and $W(q)$ is a statistical weight given by

$$W(q) = \begin{cases} \widehat{m^{-1}} & \text{rigid} \\ D^{-1} & \text{stiff} \end{cases} \tag{2.68}$$

for rigid and stiff systems, respectively. A quantum mechanical treatment of the vibrations of the hard coordinates yields an effective classical rigid model in which the effective potential energy $U(q)$ is modified so as to include the resulting q-dependent vibrational free energy. The corresponding distribution for an unconstrained system of point particles, for which all the variables must be treated as soft, is recovered by neglecting the factor of W. The simple Boltzmann distribution with $\psi \propto e^{-U/kT}$ is obtained only for an unconstrained classical model in Cartesian coordinates, for which $g = 1$.

IV. DIFFUSION EQUATION

In this section, we use simple phenomenological arguments to construct a diffusion equation for constrained systems, in a notation that is common to both

rigid and stiff models. The diffusion equation is a continuity equation for the probability distribution $\psi(q,t)$ on the constraint surface, of the form

$$\frac{\partial \psi}{\partial t} = -\frac{\partial}{\partial q^a} J^a \tag{2.69}$$

where J^a is a probability flux within the constraint surface. We define a corresponding generalized velocity U^a and (for systems of point particles) a Cartesian bead velocity $\mathbf{U}^\mu$

$$U^a(q) \equiv \frac{J^a(q)}{\psi(q)} \tag{2.70}$$

$$\mathbf{U}^\mu(q) \equiv \mathbf{a}_a^\mu(q) U^a(q) \tag{2.71}$$

which will hereafter be referred to as generalized and Cartesian "flux velocities," respectively.

The probability flux is determined by a balance of generalized mechanical and Brownian forces, of the form

$$0 = F_a^{(\mathrm{e})} + F_a^{(\mathrm{h})} \tag{2.72}$$

in which $F_a^{(\mathrm{e})}$ is a generalized "elastic" force, which is induced by deviations of the probability distribution $\psi(q)$ from its equilibrium form, and $F_a^{(\mathrm{h})}$ is a dissipative hydrodynamic drag force.

The elastic force $F_a^{(\mathrm{e})}$ is given by the sum of a mechanical force $-\partial U/\partial q^a$ and a corresponding Brownian force. The form of the Brownian force may be inferred by requiring that $F_a^{(\mathrm{e})}$ vanish when $\psi(q) = \psi_{\mathrm{eq}}(q)$, in order to guarantee that the probability flux J^a vanishes in thermal equilibrium. This requirement yields an elastic force

$$\begin{aligned} F_a^{(\mathrm{e})} &= kT \frac{\partial}{\partial q^a} \ln\left(\frac{\psi_{\mathrm{eq}}(q)}{\psi(q)}\right) \\ &= -\frac{\partial}{\partial q^a}\left[U + kT \ln\left(\frac{\psi}{\sqrt{gW}}\right)\right] \end{aligned} \tag{2.73}$$

in which W is the statistical weight defined in Eqs. (2.67) and (2.68).

A phenomenogical expression for the hydrodynamic force $F_a^{(\mathrm{h})}$ may be constructed by assuming that this force is linear in the flux velocities and in the strength of any applied flow field. We consider a system that is subjected to a macroscopic flow field $\mathbf{v}(\mathbf{r})$ characterized by a spatially homogeneous macroscopic velocity gradient $\boldsymbol{\nabla}\mathbf{v}$. We assume that $F_a^{(\mathrm{h})}$ vanishes for all $a = 1, \ldots, f$ in the equilibrium state, where the flux velocities and the macroscopic

velocity gradient $\boldsymbol{\nabla}\mathbf{v}$ vanish, and that $F_a^{(\mathrm{h})}$ may be expanded in the creeping flow limit of interest as a linear function of the flux velocities and velocity gradient, of the form

$$F_a^{(\mathrm{h})} \simeq -K_{ab}^{-1} U^b + \mathbf{M}_a : (\boldsymbol{\nabla}\mathbf{v}) \tag{2.74}$$

with unspecified tensor coefficients $K_{ab}^{-1}(q)$ and $\mathbf{M}_a(q)$ that may depend on the system coordinates. The quantity $K_{ab}^{-1}(q)$ is a friction tensor that characterizes the generalized forces induced by motion of the system in the absence of macroscopic flow. The inverse K^{ab} of this friction tensor is a mobility tensor for the constrained system in generalized coordinates, which will be referred to here as a "constrained mobility." The relationship between $K^{ab}(q)$ and the corresponding unconstrained Cartesian mobility $\mathbf{H}^{\mu\nu}$ of a system of point particles is discussed in Section VI. The quantity $\mathbf{M}_a$ is a coupling tensor, which is a second-rank Cartesian tensor indexed by coordinate index a, that describes the generalized forces induced by a macroscopic velocity gradient on a stationary system. The force arising from the velocity gradient will be denoted by

$$F_a^{(\mathrm{f})} \equiv \mathbf{M}_a : (\boldsymbol{\nabla}\mathbf{v}) \tag{2.75}$$

and referred to as a "flow" force.

Substituting Eq. (2.74) for $F_a^{(\mathrm{h})}$ into Eq. (2.72) and solving for U^a yields a flux velocity

$$U^a = K^{ab}(F_b^{(\mathrm{e})} + F_b^{(\mathrm{f})}) \tag{2.76}$$

Substituting Eq. (2.76) into continuity equation (2.69) then yields a diffusion equation

$$\frac{\partial \psi}{\partial t} = -\frac{\partial \left[K^{ab}\left(F_b^{(\mathrm{e})} + F_b^{(\mathrm{f})}\right)\psi \right]}{\partial q^a} \tag{2.77}$$

or, more explicitly

$$\frac{\partial \psi}{\partial t} = -\frac{\partial}{\partial q^a}\left[K^{ab}\left(kT \frac{\partial \ln \psi_{\mathrm{eq}}}{\partial q^b} + F_b^{(\mathrm{f})} \right)\psi \right] + kT \frac{\partial}{\partial q^a}\left(K^{ab} \frac{\partial \psi}{\partial q^b} \right) \tag{2.78}$$

Diffusion equation (2.78) is, of course, quite generic: The discussion of this section has not specified either the form of the equilibrium distribution $\psi_{\mathrm{eq}}(q)$, which may be obtained from equilibrium statistical mechanics, or the form of the

friction tensors K_{ab}^{-1} and $\mathbf{M}_a$, which must be determined by considering the hydrodynamics of the system of interest.

V. PHASE SPACE KINETIC THEORY

In this section, we present a more microscopic derivation of the diffusion equations for both rigid and stiff models, along the lines of the ''phase space kinetic theory'' given previously for rigid and unconstrained systems by Bird, Curtiss, Armstrong, and Hassager (BCAH) [3,4]. Section V.A presents a streamlined version of the BCAH phase space theory for rigid systems. In the BCAH approach, one begins by using the underlying instantaneous equations of motion to derive an average momentum flux balance for an arbitrary classical mechanical system in contact with a solvent heat bath. The key step in this analysis is the use of an explicit assumption of ''equilibration in momentum space'' to evaluate averages over momentum fluctuations. In Section V.B, we then extend the BCAH analysis so as to also describe diffusion of the soft coordinates of stiff systems, by introducing an analogous local equilibrium hypothesis for the rapidly fluctuating hard coordinates. These analyses of rigid and stiff systems lead to coordinate space diffusion equations that both manifestly relax towards the probability distributions predicted by equilibrium statistical mechanics.

Because the resulting diffusion equation is the same as that obtained by simpler arguments in Section IV, it is possible for a reader to skip this section, if desired. The value of the analysis lies in its ability to clarify the assumptions underlying the phenomenological derivation of the previous section, the relationship between phenomenological flux velocities and underlying mechanical velocities, and the mechanical origins of the otherwise mysterious ''Brownian'' forces that drive diffusion. The extension of the kinetic theory to stiff systems is also presented here in the hopes of reducing any lingering preference for rigid models solely as a result of the rigor and completeness of the BCAH analysis.

A. Rigid Systems

We consider a rigid system of f mechanical degrees of freedom in thermal contact with a solvent. As in the discussion of equilibria, $\rho(q,p)$ is the phase space density and $\psi(q)$ is the reduced distribution for the coordinates alone. Following BCAH, we also define a conditional average $\langle A\rangle_{\mathrm{p}}$ of an arbitrary dynamical variable A with respect to the rapid fluctuations of the momenta and solvent forces, at fixed values of the coordinates q, as

$$\langle A\rangle_{\mathrm{p}} \equiv \frac{1}{\psi(q)} \int dp\ \langle A\rangle_{\mathrm{s}}\ \rho(q,p) \tag{2.79}$$

The resulting conditional average is implicitly a function $\langle A\rangle_{\mathrm{p}} = \langle A\rangle_{\mathrm{p}}(q)$ of the soft coordinates. Here and in what follows, $\langle\cdots\rangle_{\mathrm{s}}$ is used to indicate a conditional average with respect to fluctuations in the state of the surrounding solvent, for fixed values of the system's internal coordinates q and momenta p. This average over solvent degrees of freedom is unnecessary in Eq. (2.79) if $A = A(q,p)$ is a quantity (such as a bead velocity) that depends only on the system's coordinates and momenta, but is necessary if A is a quantity (such as the total force on a bead) that depends explicitly on the forces exerted on the system by surrounding solvent molecules.

The inertial equation of motion for such a system, in Cartesian coordinates, is

$$\dot{\mathbf{P}}_{\mu} = -\frac{\partial U}{\partial \mathbf{R}^{\mu}} - \mathbf{n}_{\mu}^{i}\lambda_i + \mathbf{F}_{\mu}^{(\mathrm{s})} \tag{2.80}$$

Here, $\mathbf{P}_{\mu} = m_{\mu}\dot{\mathbf{R}}^{\mu}$ is a Cartesian bead momentum, U is the internal potential energy of the system of interest, $\lambda_1,\ldots,\lambda_K$ are a set of K Lagrange multiplier constraint fields, which must be chosen so as to satisfy the K constraints, and $\mathbf{F}_{\mu}^{(\mathrm{s})}$ is the rapidly fluctuating force exerted on bead μ by interactions with surrounding solvent molecules. The corresponding Hamiltonian equation of motion is

$$\begin{aligned}\dot{p}_a &= -\frac{\partial \mathscr{H}}{\partial q^a} + F_a^{(\mathrm{s})} \\ &= -\frac{\partial U}{\partial q^a} - \frac{1}{2}\frac{\partial (\tilde{m}^{-1})^{bc}}{\partial q^a} p_b p_c + F_a^{(\mathrm{s})}\end{aligned} \tag{2.81}$$

where $\mathscr{H} = K + U$ is the system Hamiltonian of Eq. (2.32) and $F_a^{(\mathrm{s})} = \mathbf{a}_a^{\mu}\cdot\mathbf{F}_{\mu}^{(\mathrm{s})}$ is the instantaneous generalized force exerted on the system by the surrounding solvent.

1. *Evolution of Probability Densities*

The phase space density $\rho(q,p)$ evolves according to the Liouville equation

$$\frac{\partial \rho}{\partial t} = -\frac{\partial(\dot{q}^b \rho)}{\partial q^b} - \frac{\partial(\langle \dot{p}_b\rangle_{\mathrm{s}}\rho)}{\partial p_b} \tag{2.82}$$

The reduced configuration space distribution $\psi(q)$ evolves according to a continuity equation

$$\frac{\partial \psi}{\partial t} = -\frac{\partial(\langle \dot{q}^a\rangle_{\mathrm{p}}\psi)}{\partial q^a} \tag{2.83}$$

as may be confirmed by using Eq. (2.82) to evaluate $\frac{\partial \psi}{\partial t} = \int dp \frac{\partial \rho}{\partial t}$, and integrating by parts to show that the second term on the RHS of Eq. (2.82) does not contribute to the integral.

On comparing Eq. (2.83) to the continuity equation, Eq. (2.69), we may identify the average velocity $\langle \dot{q}^a \rangle_{\mathrm{p}}$ as the generalized flux velocity

$$\langle \dot{q}^a \rangle_{\mathrm{p}} = U^a \tag{2.84}$$

By noting that $\langle \dot{\mathbf{R}}^\mu \rangle_{\mathrm{p}} = \langle \mathbf{a}_a^\mu \dot{q}^a \rangle_{\mathrm{p}}$, and that the basis vector $\mathbf{a}_a^\mu(q)$ is a function of q alone that may be taken outside the average $\langle \cdots \rangle_{\mathrm{p}}$ with respect to momentum fluctuations, we may also identify

$$\langle \dot{\mathbf{R}}^\mu \rangle_{\mathrm{p}} = \mathbf{a}_\mu^a U^a = \mathbf{U}^a \tag{2.85}$$

as the Cartesian flux velocity.

2. *Evolution of Momentum Density*

We consider a balance equation for a generalized momentum density $\pi_a(q,t)$, defined by

$$\pi_a \equiv \langle p_a \rangle_{\mathrm{p}} \psi = \int dp \; p_a \rho(q,p) \tag{2.86}$$

The rate of change of π_a is

$$\frac{\partial \pi_a}{\partial t} = \int dp \; p_a \frac{\partial \rho}{\partial t} \tag{2.87}$$

$$= \int dp \; p_a \left\{ -\frac{\partial (\dot{q}^b \rho)}{\partial q^b} - \frac{\partial (\langle \dot{p}_b \rangle_{\mathrm{s}} \rho)}{\partial p_b} \right\} \tag{2.88}$$

By moving the derivative outside the integral in the first term on the RHS Eq. (2.88), and integrating the second term by parts, we obtain

$$\frac{\partial \pi_a}{\partial t} = -\frac{\partial (\langle p_a \dot{q}^b \rangle_{\mathrm{p}} \psi)}{\partial q^b} + \langle \dot{p}_a \rangle_{\mathrm{p}} \psi \tag{2.89}$$

To separate effects of a mean velocity from the effects of velocity fluctuations, we expand $\langle p_a \dot{q}^b \rangle_{\mathrm{p}}$ as a sum

$$\langle p_a \dot{q}^b \rangle_{\mathrm{p}} = \langle p_a \rangle_{\mathrm{p}} \langle \dot{q}^b \rangle_{\mathrm{p}} + \langle \delta p_a \; \delta \dot{q}^b \rangle_{\mathrm{p}} \tag{2.90}$$

where $\delta p_a \equiv p_a - \langle p_a \rangle_{\mathrm{p}}$ and $\delta \dot{q}^a \equiv \dot{q}^a - \langle \dot{q}^b \rangle_{\mathrm{p}}$ are deviations from the mean values. After substituting Eq. (2.90) into Eq. (2.89), and some straightforward manipulations similar to those used to introduce the material derivative in continuum mechanics, we obtain

$$\frac{D\langle p_a \rangle_{\mathrm{p}}}{Dt} = \langle \dot{p}_a \rangle_{\mathrm{p}} - \frac{1}{\psi} \frac{\partial (\langle \delta p_a \delta \dot{q}^b \rangle_{\mathrm{p}} \psi)}{\partial q^b} \tag{2.91}$$

where

$$\frac{D}{Dt} \equiv \frac{\partial}{\partial t} + \langle \dot{q}^c \rangle_{\mathrm{p}} \frac{\partial}{\partial q^c} \tag{2.92}$$

is the material derivative in configuration space, that is, the total time derivative measured along a configuration space trajectory with the ensemble average velocity $\langle \dot{q}^a \rangle_{\mathrm{p}}$.

The quantity $\langle \delta p_a \delta \dot{q}^b \rangle_{\mathrm{p}} \psi$ in Eq. (2.91) is a flux of generalized momentum that arises from velocity fluctuations. This quantity is closely analogous to a corresponding "kinetic" contribution to the macroscopic momentum flux (i.e., the stress tensor) in an atomic fluid. The microscopic expression for the average momentum flux across a plane in a fluid of point particles contains a kinetic contribution arising from the momentum transferred by particles whose random motions carry them (and their momentum) across this plane, in addition to a contribution arising from interparticle forces exerted across such a plane. The kinetic contribution to the stress tensor is $\rho \langle \mathbf{vp} \rangle$, where ρ is a number density of atoms, $\mathbf{v}$ and $\mathbf{p}$ are velocity and momenta, respectively, and the average is taken over particles within an infinitesimal fluid element. This kinetic contribution, which depends only on the particle density and velocity distribution, can be shown to reduce to an ideal-gas hydrostatic pressure $\rho kT\mathbf{I}$ whenever the velocity distribution is locally Maxwellian. In a fluid with a Maxwellian velocity distribution but an inhomogeneous number density, the divergence of the kinetic stress, which is analogous to the second term on the RHS of Eq. (2.91), exerts a force density on the fluid. In an ideal gas in thermal equilibrium in the presence of a gravitational field, it is this kinetic force that balances the gravitational force, thus holding up the column of gas. The same mechanism is at work here; members of a statistical ensemble contribute to the momentum contained in a volume element of f-dimensional configurational space when their random motions carry them into that volume element. Any divergence of the resulting momentum flux causes a rate of accumulation of momentum that enters the momentum balance as an effective "kinetic" force. As discussed below, this kinetic force reduces to the Brownian force that appears in the phenomenological diffusion equation when the distribution of velocities is Maxwellian.

3. Local Equilibration of Momenta

To remove momentum fluctuations from the problem, BCAH assume that in the creeping flow limit, in which a system of small mass interacts strongly with a thermally equilibrated solvent, the distribution of values for the momenta for fixed coordinate values stays very near a state of local equilibrium, in which

1. The fluctuations of the momenta have the same variance

$$\langle \delta p_a \ \delta p_b \rangle_{\mathrm{p}} \simeq kT\, \tilde{\boldsymbol{m}}_{ab} \tag{2.93}$$

   as that required in equilibrium by the equipartition theorem.
2. The average values of the generalized momenta become negligible, giving

$$\langle p_a \rangle_{\mathrm{p}} \simeq 0 \tag{2.94}$$

   for all a and all time.

In the creeping flow limit of interest, the average momenta may be assumed to be negligible without assuming that the average drift velocities are also negligible because of the assumed smallness of the system's inertia.

The assumption of equilibration in momentum space may be used to remove the momenta from momentum balance (2.91). Equation (2.93) may be used to evaluate the kinetic force, giving

$$-\frac{1}{\psi}\frac{\partial(\langle \delta p_a \delta \dot{\boldsymbol{q}}^b \rangle_{\mathrm{p}} \psi)}{\partial q^b} = -kT\frac{\partial \ln \psi}{\partial q^b} \tag{2.95}$$

The local equilibrium value of the kinetic force thus yields the "Brownian" force of the phenomelogical diffusion equation. Equation (2.94) also allows us to take $D\langle p_a \rangle_{\mathrm{p}}/Dt = 0$ on the left-hand side (LHS) of Eq. (2.91), to obtain a force balance

$$0 = \langle \dot{\boldsymbol{p}}_a \rangle_{\mathrm{p}} - kT\frac{\partial \ln \psi}{\partial q^b} \tag{2.96}$$

To evaluate the average mechanical force $\langle \dot{\boldsymbol{p}}_a \rangle_{\mathrm{p}}$, we combine Hamilton's equation for $\dot{\boldsymbol{p}}_a$, Eq. (2.81), with the preceding assumptions to obtain

$$\langle \dot{\boldsymbol{p}}_a \rangle_{\mathrm{p}} = -\frac{\partial U}{\partial q^a} - \frac{kT}{2}\frac{\partial (\tilde{\boldsymbol{m}}^{-1})^{bc}}{\partial q^a}\tilde{\boldsymbol{m}}_{bc} + \langle F_a^{(\mathrm{s})} \rangle_{\mathrm{p}} \tag{2.97}$$

Using Eq. (A.14) for the derivative of $\ln \tilde{\boldsymbol{m}}$ then yields the equivalent expression

$$\langle \dot{\boldsymbol{p}}_a \rangle_{\mathrm{p}} = -\frac{\partial (U - kT \ln \sqrt{\tilde{\boldsymbol{m}}})}{\partial q^a} + \langle F_a^{(\mathrm{s})} \rangle_{\mathrm{p}} \tag{2.98}$$

Note that the averaging with respect to momentum fluctuations has the effect of replacing the system's potential energy U by an effective potential $U - kT \ln \sqrt{\tilde{m}}$, exactly as in the equilibrium distribution for a rigid system, which is of the form $\psi_{\text{eq}}(q) \propto \exp\{-(U - kT \ln \sqrt{\tilde{m}})/kT\}$. Substituting Eq. (2.98) for the average mechanical force and Eq. (2.95) for the Brownian force into Eq. (2.96) yields an effective force balance

$$0 = F_a^{(\text{e})} + \langle F_a^{(\text{s})} \rangle_{\text{p}} \tag{2.99}$$

in which

$$F_a^{(\text{e})} \equiv -\frac{\partial}{\partial q^a}\left[U + kT \ln\left(\frac{\psi}{\sqrt{\tilde{m}}}\right)\right] \tag{2.100}$$

is an "elastic" force, given by the sum of the Brownian force and the internal contributions to the average mechanical force $\langle \dot{p}_a \rangle_{\text{p}}$, excluding the average solvent force. This elastic force vanishes when $\psi(q) = \psi_{\text{eq}}(q)$, and tends to drive ψ toward ψ_{eq}.

4. *Hydrodynamic Drag*

To obtain a closed set of equations for the evolution of $\psi(q)$, we need an approximation for the conditional ensemble average $\langle F_a^{(\text{s})} \rangle_{\text{p}}$ of the rapidly varying solvent force that appears in Eq. (2.99). The phenomenological diffusion equation given in Section IV is recovered if and only if we identify $\langle F_a^{(\text{s})} \rangle_{\text{p}}$ with the hydrodynamic drag force $F_a^{(\text{h})}$ in the phenomenological diffusion equation, and assume that it can be described by a generalized Stokes law of the form given in Eq. (2.74).

B. Stiff Systems

We now extend the preceding analysis to the case of a stiff system, by using an extended local-equilibrium hypothesis to remove both momenta and hard coordinates from the problem, and thus obtain a diffusion equation for the distribution of soft coordinates alone.

1. *Evolution of Probability Densities*

We first treat a stiff system as a generic unconstrained system. We consider a joint probability distribution $\Psi(Q)$ for all $3N$ coordinates of a stiff system, soft and hard, given by

$$\Psi(Q) \equiv \int dP_1 \cdots \int dP_{3N}\ \rho(Q, P) \tag{2.101}$$

which obeys a continuity equation

$$\frac{\partial \Psi}{\partial t} = -\frac{\partial(\langle \dot{Q}^\alpha \rangle_{\mathrm{p}} \Psi)}{\partial Q^\alpha} \tag{2.102}$$

with $\alpha = 1, \ldots, 3N$.

To construct a diffusion equation for the soft coordinates alone, we consider a reduced distribution function

$$\psi(q) \equiv \int dc\ \Psi(Q) \tag{2.103}$$

where $\int dc \equiv \int dc^1 \cdots \int dc^K$ represents an integral over all hard coordinates at fixed values of the soft coordinates. We also introduce the notation

$$\langle A \rangle_{\mathrm{f}} \equiv \frac{1}{\psi(q)} \int dc \langle A \rangle_{\mathrm{p}} \Psi(Q) \tag{2.104}$$

for an average of a variable A with respect to rapid fluctuations of the solvent degrees of freedom, system momenta, *and* hard coordinates, for fixed values of the more slowly evolving soft coordinates. The subscript "f" is used to indicate an average with respect to all "fast" dynamical degrees of freedom. In this notation, the reduced distribution $\psi(q)$ may be shown to obey a continuity equation

$$\frac{\partial \psi}{\partial t} = -\frac{\partial(\langle \dot{q}^a \rangle_{\mathrm{f}} \psi)}{\partial q^a} \tag{2.105}$$

for $a = 1, \ldots, f$.

By comparing Eq. (2.105) and continuity equation (2.69), we may identify the average soft velocity

$$\langle \dot{q}^a \rangle_{\mathrm{f}} = U^a \tag{2.106}$$

as the generalized flux velocity of a stiff system. The forces that constrain the system to remain near the constraint surface will be assumed to guarantee that the corresponding hard flux velocities vanish, that is, that

$$\langle \dot{c}^i \rangle_{\mathrm{f}} = 0 \tag{2.107}$$

for all $i = 1, \ldots, K$, so that the average values of the hard coordinates do not drift away from their constrained values. The average Cartesian velocity is given by

an expansion

$$\langle \dot{\mathbf{R}}^{\mu} \rangle_{\mathrm{f}} = \left\langle \frac{\partial \mathbf{R}^{\mu}}{\partial Q^{\alpha}} \dot{Q}^{\alpha} \right\rangle_{\mathrm{f}} \tag{2.108}$$

To relate this to the Cartesian flux velocity, we note that, in the infinitely stiff limit of interest, in which excursions from the constraint surface are negligible, the basis vectors $\partial \mathbf{R}^{\mu}/\partial Q^{a}$ may be accurately approximated by their values on the constraint surface, which are functions of the soft coordinates alone, and so may taken outside of the average average $\langle \cdots \rangle_{\mathrm{f}}$. By then using Eq. (2.107) to exclude contributions arising from the hard velocities, we identify

$$\langle \dot{\mathbf{R}}^{\mu} \rangle_{\mathrm{f}} \simeq \mathbf{a}_{a}^{\mu} \langle \dot{q}^{a} \rangle_{\mathrm{f}} = \mathbf{U}^{\mu} \tag{2.109}$$

as the Cartesian flux velocity for an infinitely stiff system.

2. *Unconstrained Force Balance*

We next consider the effective force balance for all $3N$ variables, while treating the system as an unconstrained system. For simplicity, we consider the case in which the crossover from ballistic motion to diffusion occurs at a timescale much less than any characteristic relaxation time for vibrations of the hard coordinates, so that the vibrations are overdamped, but in which the vibrational relaxation times are much less than any timescale for the diffusion of the soft coordinates. In this case, we may assume local equilibration of all $3N$ momenta at timescales of order the vibration time. Repeating the analysis of the Section V.A, while now treating all $3N$ coordinates as unconstrained, yields an effective force balance

$$0 = \mathscr{F}_{\alpha}^{(\mathrm{e})} + \langle F_{\alpha}^{(\mathrm{s})} \rangle_{\mathrm{p}} \tag{2.110}$$

for $\alpha = 1, \ldots, 3N$, in which

$$\mathscr{F}_{\alpha}^{(\mathrm{e})} \equiv -\frac{\partial}{\partial Q^{\alpha}} \left[V(Q) + kT \ln\left(\frac{\Psi}{\sqrt{g}} \right) \right] \tag{2.111}$$

is a generalized elastic force in the unconstrained space.

3. *Local Equilibration of Hard Coordinates*

To evaluate averages with respect to the hard coordinates, we must introduce an additional hypothesis of local equilibrium for the distribution of values for these

coordinates. We postulate a local-equilibrium distribution $\Psi(Q)$ of the form

$$\Psi(Q) \simeq \psi(q) \frac{\sqrt{g}\ e^{-[V - c^i \tau_i]/kT}}{\int\ dc\ \sqrt{g}\ e^{-[V - c^i \tau_i]/kT}} \tag{2.112}$$

Here $\tau_i = \tau_i(q)$ is one of K Lagrange multiplier fields that are functions of the soft coordinates alone, which must be chosen so as to satisfy condition (2.107) for all of the hard coordinates. Equation (2.112) has the following properties:

1. Equation (2.112) is a normalized distribution that reduces exactly to the equilibrium distribution

$$\Psi_{\text{eq}}(Q) \propto \sqrt{g}\ e^{-V/kT} \tag{2.113}$$

when $\tau_i = 0$ for all $i = 1, \ldots, K$ and $\psi(q)$ equals the equilibrium reduced distribution

$$\psi_{\text{eq}}(q) \propto \int\ dc\ \sqrt{g}\ e^{-V/kT} \tag{2.114}$$

Equation (2.114) reduces to Eq. (2.39) when $V(Q)$ is approximated by harmonic form (2.36).

2. Equation (2.112) yields generalized elastic forces along the hard directions, defined by

$$\mathscr{F}^{(\text{e})}_{i+f}(Q) \equiv -\frac{\partial}{\partial c^i}\left[V(Q) + kT \ln\left(\frac{\Psi}{\sqrt{g}}\right)\right] \tag{2.115}$$

for $i = 1, \ldots, K$, with values

$$\mathscr{F}^{(\text{e})}_{i+f}(Q) = -\tau_i(q) \tag{2.116}$$

These hard forces are thus functions of the soft coordinates q alone, and completely independent of the values of $c^1, \ldots, c^K$. This is because, for this local-equilibrium distribution, the rapid variation of the hard mechanical force $-\partial V/\partial c^i$ along the hard directions is canceled by a compensating variation in the Brownian contribution to $\mathscr{F}^{(\text{e})}_{i+f}$.

3. The average $\langle \mathscr{F}^{(\text{e})}_a \rangle_{\text{f}}$ of the soft elastic force $\mathscr{F}_a$ with respect to variations in the hard coordinates, for $a = 1, \ldots, f$, which we will denote by

$$F^{(\text{e})}_a \equiv \langle \mathscr{F}^{(\text{e})}_a \rangle_{\text{f}} \tag{2.117}$$

is given by

$$F^{(\text{e})}_a = -\frac{\partial}{\partial q^a}\left[U(q) + kT \ln\left(\frac{\psi}{\sqrt{gD^{-1}}}\right)\right] \tag{2.118}$$

To obtain Eq. (2.118), $V(Q)$ has been approximated by Eq. (2.36), and $g(Q)$ by its value on the constraint surface. Equation (2.118) for $F_a^{(e)}$ is closely analogous to Eq. (2.100) for the elastic force in a rigid system, except for the replacement of $\widetilde{m^{-1}}$ by D^{-1}. Like the corresponding elastic force for a rigid system, this force vanishes when $\psi(q) = \psi_{eq}(q)$.

Using distribution (2.112) to evaluate the average of both sides of Eq. (2.110) with respect to fluctuations in the hard coordinates thus yields an effective force balance with soft and hard components

$$0 = F_a^{(e)} + \langle F_a^{(s)} \rangle_f \tag{2.119}$$

$$0 = -\tau_i + \langle F_{i+f}^{(s)} \rangle_f \tag{2.120}$$

where $F_a^{(e)}$ is given by Eq. (2.118). The values of the parameters $\tau_1(q), \ldots, \tau_K(q)$ must be chosen so that the underlying diffusion equation for the unconstrained space satisfies Eq. (2.107) for all $i = 1, \ldots, K$.

A dynamical argument for the validity of Eq. (2.112) may be obtained by considering the evolution of the $3N$-dimensional distribution $\Psi(Q)$ of a stiff system, as determined by the $3N$ dimensional diffusion equation. In order for a distribution that is tightly localized near the constraint surface at one instant to remain so at later times, the probability fluxes along the hard directions must have both vanishing average values (when averaged with respect to fluctuations of the hard coordinates), in order to prevent drift in the average values of the hard coordinates, and also very small gradients with respect to the hard coordinates, in order to prevent rapid changes in the width of the distribution. These requirements imply that the hard components of the probability flux and flux velocity vectors must nearly vanish throughout the vicinity of the constraint surface in which $\Psi(Q)$ is non-negligible. The flux velocity along a hard direction $\mathbf{n}_i$ is given by a matrix product $H^{i+f,\beta}[\mathscr{F}_\beta^{(e)} + \mathscr{F}_\beta^{(f)}]$, in which $\beta = 1, \ldots, 3N$. The mobility tensor $\mathscr{H}^{\alpha\beta}$, the flow force $\mathscr{F}_\beta^{(f)}$, and the soft components of the elastic force $\mathscr{F}_\alpha^{(e)}$, with $\alpha = 1, \ldots, f$, all remain slowly varying functions of the hard components in the limit of a stiff confining potential, which may be adequately approximated very near the constraint surface by their values on the constraint surface. For the hard flux velocities to remain small and nearly independent of the hard coordinates throughout a narrow region near the constraint surface, however, the hard components of the elastic force, given by $\mathscr{F}_{j+f}^{(e)}$ with $j = 1, \ldots, K$, must also be nearly independent of the hard coordinates, and have values (which are given by the parameters τ_j) that are chosen so as to yield vanishing values for the hard flux velocities on the constraint surface. The requirement that the sum of the hard mechanical force $-\partial V/\partial c^j$ and the hard Brownian force $-kT\partial \ln \Psi/\partial c^j$ remain approximately independent of the hard coordinates in the limit of an infinitely stiff confining potential, despite the divergence of the derivatives of the mechanical hard forces

with respect to the hard coordinates in this limit, uniquely selects Eq. (2.212) as the asymptotic dependence of $\Psi(Q)$ on the hard coordinates.

4. *Hydrodynamic Drag*

To construct a closed set of equations for the evolution of $\psi(q)$ in a stiff system, we need an expression for the average solvent force $\langle F_\alpha^{(\mathrm{s})}\rangle_\mathrm{f}$ that appears in Eq. (2.119). A diffusion equation of the form given in Section IV is recovered if and only if we identify $\langle F_\alpha^{(\mathrm{s})}\rangle_\mathrm{f}$ as a hydrodynamic drag force $F_\alpha^{(\mathrm{h})}$, and (as for the rigid system) assume that it may be described by a generalized Stokes equation of the form given in Eq. (2.74), where U^a is defined for a stiff system by Eq. (2.106).

VI. CARTESIAN FORCES AND TENSORS

In the preceding two sections, the balance of mechanical and Brownian forces that is implicit in the diffusion equation has been presented in generalized coordinates. In this section, these generalized forces are related to corresponding Cartesian forces, and the generalized flux velocities to Cartesian flux velocities. The resulting Cartesian equation of motion is introduced here within the context of the diffusion equation description of Brownian motion, in which Brownian forces are represented by derivatives of a distribution function, rather than by stochastic forces. The mathematical machinery introduced here to describe a constrained system of point particles is, however, essentially identical to that used in earlier treatments of the corresponding stochatic differential equations by Fixman [9], Hinch [10], and Öttinger [11].

The effective balance of soft forces obtained in Section IV may be generalized to a corresponding Cartesian force balance of the form

$$0 = \mathbf{F}_\mu^{(\mathrm{e})} - \mathbf{n}_\mu^i \tau_i + \mathbf{F}_\mu^{(\mathrm{h})} \tag{2.121}$$

in which the τ terms are constraint forces, $\mathbf{F}_\mu^{(\mathrm{h})}$ is a Cartesian drag force given by Eq. (2.74), and

$$\begin{aligned}\mathbf{F}_\mu^{(\mathrm{e})} &\equiv -\frac{\partial q^a}{\partial \mathbf{R}^\mu} F_a^{(\mathrm{e})} \\ &= -\frac{\partial}{\partial \mathbf{R}^\mu}\left[U + kT \ln\left(\frac{\psi}{\sqrt{gW}}\right)\right]\end{aligned} \tag{2.122}$$

is a Cartesian generalization of the effective elastic force. Here, and in what follows, we define the Cartesian gradient of quantities that depends only on the soft coordinates, such as $U(q)$ and $\psi(q)$, by the expansion $\frac{\partial}{\partial \mathbf{R}^\mu} \equiv \frac{\partial q^a}{\partial \mathbf{R}^\mu}\frac{\partial}{\partial q^a}$.

The preceding division of the hard components of the total nonhydrodynamic force $\mathbf{F}_\mu^{(\mathrm{e})} - \mathbf{n}_\mu^i \tau_i$ in Eq. (2.121) between an elastic force $\mathbf{F}_\mu^{(\mathrm{e})}$ and a sum of constraint forces $\mathbf{n}_\mu^i \tau_i$ is a matter of convention. Arbitrary shifts in the values of hard components of $\mathbf{F}_\mu^{(\mathrm{e})}$ could be absorbed into compensating shifts in the

values of $\tau_1, \ldots, \tau_K$ without affecting the overall Cartesian force balance, or the values of the corresponding flux velocities. Only the Cartesian hydrodynamic force $\mathbf{F}_\mu^{(h)}$, the soft components of the elastic force, which are given explicitly by Eq. (2.73), and the hard components of the total nonhydrodynamic force, which must balance the corresponding components of $\mathbf{F}_\mu^{(h)}$, are unambiguously defined by the physics of the problem. The definition of $\mathbf{F}_\mu^{(e)}$ given in Eq. (2.122) has been chosen because it yields expressions for the $\tau(q)$ values that are equivalent to those obtained from in the formalism developed for stiff systems in Section V.B, for which $\mathbf{F}_\mu^{(e)}$ and $\tau_1, \ldots, \tau_K$ all vanish in thermal equilibrium.

A. Hydrodynamic Forces

We assume that, in the creeping flow limit, the Cartesian drag force on bead μ may be expanded to linear order in $\mathbf{U}^\nu$ and $\boldsymbol{\nabla}\mathbf{v}$, as

$$\mathbf{F}_\mu^{(h)} \simeq -\boldsymbol{\zeta}_{\mu\nu} \cdot \mathbf{U}^\nu + \mathbf{F}_\mu^{(f)} \tag{2.123}$$

where $\boldsymbol{\zeta}_{\mu\nu}(q)$ is a second rank Cartesian friction tensor, and

$$\mathbf{F}_\mu^{(f)} \equiv \mathbf{M}_\mu : (\boldsymbol{\nabla}\mathbf{v}) \tag{2.124}$$

is a Cartesian flow force, in which $\mathbf{M}_\mu(q)$ is a rank 3 Cartesian coupling tensor. The inverse of $\boldsymbol{\zeta}_{\mu\nu}(q)$ is the corresponding unconstrained mobility tensor $\mathbf{H}^{\mu\nu}(q)$. In the case of a system of hydrodynamically interacting pointlike particles, the unconstrained mobility $\mathbf{H}^{\mu\nu}$ is normally given for $\mu \neq \nu$ by the Oseen tensor (or some approximation to the Oseen tensor) and

$$\mathbf{F}_\mu^{(h)} \simeq -\boldsymbol{\zeta}_{\mu\nu} \cdot [\mathbf{U}^\nu - \mathbf{R}^\nu \cdot (\boldsymbol{\nabla}\mathbf{v})] \tag{2.125}$$

This corresponds to a flow force $\mathbf{F}_\mu^{(f)} \equiv \boldsymbol{\zeta}_{\mu\nu} \cdot (\boldsymbol{\nabla}\mathbf{v})^T \cdot \mathbf{R}^\nu$, or to a third-rank coupling tensor $\mathbf{M}_\mu = \boldsymbol{\zeta}_{\mu\nu}\mathbf{R}^\nu$.

The generalized hydrodynamic force $F_a^{(h)}$ and flow force $F_b^{(f)}$ used in Sections IV and V are given by

$$\begin{aligned} F_a^{(h)} &= \mathbf{a}_a^\mu \cdot \mathbf{F}_\mu^{(h)} \\ F_a^{(f)} &= \mathbf{a}_a^\mu \cdot \mathbf{F}_\mu^{(f)} \end{aligned} \tag{2.126}$$

By contracting Eq. (2.123) with $\mathbf{a}_a^\mu$, while using expansion (2.71) for $\mathbf{U}^\mu$, and comparing the result with Eq. (2.74), we may identify

$$\mathbf{M}_a = \mathbf{a}_a^\mu \cdot \mathbf{M}_\mu \tag{2.127}$$

where $\mathbf{M}_a$ is a second-rank tensor, and

$$K_{ab}^{-1} = \tilde{\zeta}_{ab} \tag{2.128}$$

where $\tilde{\zeta}_{ab} \equiv \mathbf{a}_a^\mu \boldsymbol{\zeta}_{\mu\nu} \mathbf{a}_b^\nu$ is the projected friction tensor defined in Eq. (2.23). The expression for the constrained mobility given by Eq. (2.128) is identical to that used by Fixman [9], but somewhat different from the definition of a closely related mobility tensor defined by BCAH [3,4], which is also used by Öttinger [11,12]. The relationship between the two definitions is discussed in detail in the Appendix, Section E.

B. Cartesian Constrained Mobility

By solving for the Cartesian flux velocities that appear in Eq. (2.123) for $\mathbf{F}_\mu^{(\mathrm{h})}$, Eq. (2.121) may be rewritten as an equation of motion

$$\mathbf{U}^\mu = \mathbf{H}^{\mu\nu} \cdot [\mathbf{F}_\nu^{(\mathrm{e})} - \mathbf{n}_\nu^i \tau_i + \mathbf{F}_\nu^{(\mathrm{f})}] \tag{2.129}$$

where $\mathbf{F}_\nu^{(\mathrm{f})}$ is given by Eq. (2.124). Values for the constraint forces $\tau_1, \ldots, \tau_K$ are obtained by requiring that Eq. (2.129) yield a Cartesian flux velocity that is tangent to the constraint surface, so that

$$\mathbf{n}_\mu^i \cdot \mathbf{U}^\mu = 0 \tag{2.130}$$

for all $i = 1, \ldots, K$. Substituting Eq. (2.129) for $\mathbf{U}^\mu$ into Eq. (2.130) yields the set of K linear equations

$$\hat{H}^{ij} \tau_j = \mathbf{n}_\mu^i \cdot \mathbf{H}^{\mu\nu} \cdot [\mathbf{F}_\nu^{(\mathrm{e})} + \mathbf{F}_\nu^{(\mathrm{f})}] \tag{2.131}$$

where $\hat{H}^{ij}$ is the projected mobility tensor defined in Eq. (2.27). Substituting the solution of Eq. (2.131) for the constraint forces back into Eq. (2.121) yields a velocity

$$\mathbf{U}^\mu = \mathbf{K}^{\mu\nu} \cdot [\mathbf{F}_\nu^{(\mathrm{e})} + \mathbf{F}_\nu^{(\mathrm{f})}] \tag{2.132}$$

where

$$\mathbf{K}^{\lambda\rho} \equiv \mathbf{H}^{\lambda\rho} - \mathbf{H}^{\lambda\mu} \cdot \hat{\mathbf{H}}_{\mu\nu}^{-1} \cdot \mathbf{H}^{\nu\rho} \tag{2.133}$$

and where

$$\hat{\mathbf{H}}_{\mu\nu}^{-1} \equiv \mathbf{n}_\mu^i \hat{H}_{ij}^{-1} \mathbf{n}_\nu^j \tag{2.134}$$

is a Cartesian representation of $\hat{H}_{ij}^{-1}$. It is straightforward to confirm, using the above definition of $\mathbf{K}^{\mu\nu}$, that

$$0 = \mathbf{n}_\mu^i \cdot \mathbf{K}^{\mu\nu} = \mathbf{K}^{\mu\nu} \cdot \mathbf{n}_\nu^i \tag{2.135}$$

thus showing that $\mathbf{K}^{\mu\nu}$ has nonzero components only in the soft subspace. The first equality in Eq. (2.135) confirms that the Cartesian flux velocities in Eqs. (2.132) are parallel to the hypersurface. The second implies that the hard components of $\mathbf{F}_{\mu}^{(e)}$ and $\mathbf{F}_{\mu}^{(f)}$ (if any) have no effect on these velocities.

The tensor $\mathbf{K}^{\lambda\rho}$ defined by Eq. (2.133) is a Cartesian representation of the constrained mobility tensor $K^{ab} = (\tilde{\zeta}^{-1})^{ab}$, which may also be represented by the expansion

$$\mathbf{K}^{\mu\nu} = \mathbf{a}_a^{\mu}\, K^{ab}\, \mathbf{a}_b^{\nu} \tag{2.136}$$

The equivalence of Eqs. (2.133) and (2.136) for $\mathbf{K}^{\mu\nu}$ is a special case of a more general theorem relating inverses of projected tensors, which is stated and proved in the Appendix, Section B. Both Eqs. (2.133) and (2.136) yield tensors that satisfy Eq. (2.135), and that thus have vanishing hard components. The equivalence of the soft components of these tensors may be confirmed by substituting expansion (2.136) into the RHS of Eq. (2.132), expanding $\mathbf{U}^{\mu} = \mathbf{a}_a^{\mu} U^a$ on the LHS and showing that this yields Eq. (2.76) for the generalized velocity U^a.

C. Dynamical Projection Tensor

Cartesian equation of motion (2.132) may also be rewritten as

$$\mathbf{U}^{\mu} = \mathbf{P}^{\mu}{}_{,\nu} \cdot \mathbf{H}^{\nu\rho} \cdot [\mathbf{F}_{\rho}^{(e)} + \mathbf{F}_{\rho}^{(f)}] \tag{2.137}$$

where

$$\begin{aligned} \mathbf{P}^{\lambda}{}_{,\nu} &\equiv \mathbf{K}^{\lambda\mu} \cdot \boldsymbol{\zeta}_{\mu\nu} \\ &= \mathbf{I}_{\nu}^{\lambda} - \mathbf{H}^{\lambda\mu} \cdot \hat{\mathbf{H}}_{\mu\nu}^{-1} \end{aligned} \tag{2.138}$$

The tensor $\mathbf{P}_{,\nu}^{\lambda}$ is a "dynamical projection tensor," which operates on the unprojected flux velocity $\mathbf{H}^{\nu\rho} \cdot [\mathbf{F}_{\rho}^{(e)} + \mathbf{F}_{\rho}^{(f)}]$ that would be obtained in the absence of constraint forces to produce a projected velocity that is tangent to the constraint surface. The dynamical projection tensor is easily shown to have the properties

$$\mathbf{n}_{\mu}^{i} \cdot \mathbf{P}^{\mu}{}_{,\nu} = 0 \tag{2.139}$$

$$\mathbf{P}^{\mu}{}_{,\nu} \cdot \mathbf{a}_a^{\nu} = \mathbf{a}_a^{\mu} \tag{2.140}$$

Because $\mathbf{P}_{,\nu}^{\mu}$ is not symmetric under simultaneous transposition of bead indices and (implicit) Cartesian indices, a comma is used before the bead subscript to indicate that the Cartesian component associated with this index operates to the right.

The notation

$$\mathbf{P}_{\lambda}{}^{,\nu} \equiv (\mathbf{P}^{\nu}{}_{,\lambda})^{T} = \boldsymbol{\zeta}_{\lambda\mu} \cdot \mathbf{K}^{\mu\nu} \tag{2.141}$$

will be used for the transposed dynamical projection tensor. Note that Eq. (2.132) can also be expressed in terms of this transposed tensor as a product

$$\mathbf{U}^{\mu} = \mathbf{H}^{\mu\nu} \cdot \mathbf{P}_{\nu}{}^{,\rho} \cdot [\mathbf{F}^{(e)}_{\rho} + \mathbf{F}^{(f)}_{\rho}] \tag{2.142}$$

Using Eq. (2.131), it is straightforward to show that

$$\mathbf{P}_{\nu}{}^{,\rho} \cdot [\mathbf{F}^{(e)}_{\rho} + \mathbf{F}^{(f)}_{\rho}] = \mathbf{F}^{(e)}_{\nu} + \mathbf{F}^{(f)}_{\nu} - \mathbf{n}^{i}_{\nu}\tau_{i} \tag{2.143}$$

More generally, contracting the transposed projection tensor with a force to its right (or the projection tensor with a force to its left) produces a ''constrained'' force given by the sum of the original force and the constraint force induced by it. Such constrained forces may have nonzero hard components, but, on contraction with $\mathbf{H}^{\mu\nu}$, induce velocities that do not.

D. Dynamical Reciprocal Vectors

We also define dynamical reciprocal basis vectors that are closely related to the dynamical projection tensor defined above. We define a set of f vectors

$$\mathbf{b}^{a}_{\nu} \equiv K^{ab}\mathbf{a}^{\mu}_{b} \cdot \boldsymbol{\zeta}_{\mu\nu} \tag{2.144}$$

with $a = 1, \ldots, f$, that are ''reciprocal'' to the tangent vectors $\mathbf{a}^{\mu}_{1}, \ldots, \mathbf{a}^{\mu}_{f}$, and a corresponding set of K vectors

$$\mathbf{m}^{\nu}_{i} \equiv \hat{H}^{-1}_{ij}\mathbf{n}^{j}_{\mu} \cdot \mathbf{H}^{\mu\nu} \tag{2.145}$$

with $i = 1, \ldots, K$, that are reciprocal to the normal vectors $\mathbf{n}^{1}_{\mu}, \ldots, \mathbf{n}^{f}_{\mu}$. It is straightforward to show, using the definitions above, that these vectors obey the biorthogonality relations

$$\mathbf{a}^{\mu}_{a} \cdot \mathbf{b}^{b}_{\mu} = \delta^{b}_{a} \tag{2.146}$$

$$\mathbf{m}^{\mu}_{i} \cdot \mathbf{n}^{j}_{\mu} = \delta^{j}_{i} \tag{2.147}$$

$$\mathbf{m}^{\mu}_{i} \cdot \mathbf{b}^{a}_{\mu} = 0 \tag{2.148}$$

If the set $3N$ contravariant Cartesian vectors given by the f $\mathbf{a}^{\mu}_{a}$ vectors and K $\mathbf{m}^{\mu}_{i}$ vectors are linearly independent, and thus span the full $3N$ space of Cartesian

vectors (which we will hereafter assume to be the case), then such a set of basis vectors obey a completeness relation

$$\mathbf{I}^{\mu}_{\nu} = \mathbf{a}^{\mu}_{a}\mathbf{b}^{a}_{\nu} + \mathbf{m}^{\mu}_{i}\mathbf{n}^{i}_{\nu} \tag{2.149}$$

This may be confirmed by expanding an arbitary contravariant Cartesian vector (with a raised bead index) in a basis of **a** and **m** vectors and confirming that one recovers the original vector if such an expansion vector is left-multiplied by the RHS of Eq. (2.149).

The tensor $\mathbf{P}^{\mu}{}_{,\nu}$ may be expanded as

$$\mathbf{P}^{\mu}{}_{,\nu} = \mathbf{a}^{\mu}_{a}\,\mathbf{b}^{a}_{\nu} \tag{2.150}$$

as may be shown by using expansion (2.136) for $\mathbf{K}^{\mu\lambda}$ and the definition of $\mathbf{b}^{a}_{\nu}$ to rewrite the RHS of the preceding as $\mathbf{K}^{\mu\lambda}\cdot\boldsymbol{\zeta}_{\lambda\nu}$. Alternatively, $\mathbf{P}^{\mu}{}_{,\nu}$ may be expanded as

$$\mathbf{P}^{\mu}{}_{,\nu} = \mathbf{I}^{\mu}_{\nu} - \mathbf{m}^{\mu}_{i}\mathbf{n}^{i}_{\nu} \tag{2.151}$$

as may be shown by using either the second line of Eq. (2.138) and definition (2.145) or expansion (2.150) and completeness relation (2.149).

The reciprocal basis vector $\mathbf{m}^{\mu}_{i}$ may be used to express Eq. (2.131) for the constraint forces more compactly, as

$$\tau_i = \mathbf{m}^{\nu}_{i}\cdot[\mathbf{F}^{(\mathrm{e})}_{\nu} + \mathbf{F}^{(\mathrm{f})}_{\nu}] \tag{2.152}$$

More generally, $\mathbf{m}^{\nu}_{i}\cdot\mathbf{F}_{\nu}$ is the constraint force induced by an unconstrained force $\mathbf{F}_{\nu}$.

The dynamical reciprocal basis vectors $\mathbf{b}^{1}_{\mu},\ldots,\mathbf{b}^{f}_{\mu}$ defined above are closely related to the "modified" reciprocal basis vectors defined in Eq. (16.3-6) of the monograph by BCAH [4] (see the table on p. 188 of BCAH for definitions), and to a set of corresponding basis vectors used by Öttinger, which he refers to by the notation $\partial Q_i/\partial\mathbf{R}_{\mu}$ introduced in Eq. (5.29) of his monograph, in which Q_i refers in Öttinger's notation to one of the soft coordinates. The dynamical reciprocal vectors $\mathbf{m}^{\mu}_{1},\ldots,\mathbf{m}^{\mu}_{K}$ defined here are identical to another set of vectors defined by Öttinger, which he refers to by the notation $\partial\mathbf{R}_{\mu}/\partial g_i$ introduced in Eq. (5.50) of his monograph, where g_i is his notation for one of the hard coordinates. Öttinger's use of the purely formal notation $\partial Q_i/\partial\mathbf{R}_{\mu}$ and $\partial\mathbf{R}_{\mu}/\partial g_i$ for these reciprocal vectors appears to be inspired by the fact that they obey biorthogonality and completeness relations identical to those obeyed by the true partial derivatives.

VII. DRIFT VELOCITIES AND DIFFUSIVITIES

In this section, we begin the description of Brownian motion in terms of stochastic process. Here, we establish the link between stochastic processes and diffusion equations by giving expressions for the drift velocity and diffusivity of a stochastic process whose probability distribution obeys a desired diffusion equation. The drift velocity vector and diffusivity tensor are defined here as statistical properties of a stochastic process, which are proportional to the first and second moments of random changes in coordinates over a short time period, respectively. In Section VII.A, we describe Brownian motion as a random walk of the soft generalized coordinates, and in Section VII.B as a constrained random walk of the Cartesian bead positions.

A. Generalized Coordinates

Constrained Brownian motion may be represented as a continuous Markov process of the f soft variables $q^1, \ldots, q^f$. A standard result of the theory of random processes [16,17] tells us that the evolution of the probability distribution $\psi(q,t)$ generated by a Markov diffusion process of a set of f random variables $q^1(t), \ldots, q^f(t)$ is described by a Fokker–Planck (or forward Kolmogorov) equation

$$\frac{\partial \psi(q)}{\partial t} = -\frac{\partial (V^a \psi)}{\partial q^a} + \frac{\partial^2 (D^{ab}\psi)}{\partial q^a \partial q^b} \tag{2.153}$$

in which $V^a(q)$ is a drift velocity vector and $D^{ab}(q)$ is a diffusivity tensor given by the moments

$$V^a(q) \equiv \lim_{\Delta t \to 0} \frac{\langle \Delta q^a \rangle_0}{\Delta t} \tag{2.154}$$

$$D^{ab}(q) \equiv \lim_{\Delta t \to 0} \frac{\langle \Delta q^a \Delta q^b \rangle_0}{2\Delta t} \tag{2.155}$$

where

$$\Delta q^a \equiv q^a(\Delta t) - q^a(0) \tag{2.156}$$

is a random change in the coordinate value over a time interval $0 < t < \Delta t$. The notation $\langle \cdots \rangle_0$ is used here and hereafter to indicate an average over random trajectories for a stochastic initial value problem in which the system coordinates

start from known initial values $q = q(0)$ at an initial time $t = 0$. The result of an average $\langle \cdots \rangle_0$ is thus always implicitly a function of the initial condition q.

By comparing Eq. (2.153) to Eq. (2.78) for the desired diffusion equation, while taking due care with the order of derivatives, we find that the two forms of the diffusion equation become equivalent if and only if

$$V^a(q) = K^{ab}\left[kT\frac{\partial \ln \psi_{\text{eq}}}{\partial q^b} + F_b^{(\text{f})}\right] + kT\frac{\partial K^{ab}}{\partial q^b} \tag{2.157}$$

$$D^{ab}(q) = kTK^{ab} \tag{2.158}$$

Equation (2.158) is the Einstein relation relating the mobility and diffusivity tensors.

The drift velocity $V^a(q)$ defined above is both conceptually and algebraically different from the flux velocity $U^a(q)$ given in Eq. (2.76). Note that the RHS of Eq. (2.76) for the generalized flux velocity $U^a(q)$ contains a diffusive contribution, arising from the Brownian contribution to $F_b^{(\text{e})}$, that is proportional to the gradient $\partial\psi/\partial q^a$ of the distribution $\psi(q)$. The flux velocity $U^a(q)$ is thus not a unique function of q, but also depends on $\partial\psi/\partial q^a$: It a property not of an isolated system but of a statistical ensemble. The drift velocity is instead a unique function of q, which is defined as an ensemble average rate of change of the coordinates for a hypothetical system that is prepared in a known mechanical state q, and that then begins to drift away from that initial state.

An equivalent definition of the drift velocity V^a may be obtained by using the diffusion equation alone to calculate the average flux velocity in a statistical ensemble characterized by a probability distribution

$$\psi(q') \propto \delta(q' - q) \tag{2.159}$$

that is localized infinitely tightly around a prescribed state q. The drift velocity $V^a(q)$ is given by the ensemble average

$$V^a(q) \equiv \int dq'\, \psi(q') U^a(q') \tag{2.160}$$

for an ensemble characterized by Eq. (2.159). To evaluate the RHS of Eq. (2.160), we first use the diffusion equation to calculate the ensemble average

$$\langle U^a \rangle = \left\langle K^{ab}\left[F_b^{(\text{e})} + F_b^{(\text{f})}\right]\right\rangle \tag{2.161}$$

for a generic ensemble $\psi(q')$, where $\langle \cdots \rangle \equiv \int dq' \cdots \psi(q')$ is used here to indicate an average over values of q'. Using Eq. (2.73) for $F_b^{(\text{e})}$ yields the more

explicit expression

$$\langle U^a \rangle = \left\langle K^{ab} \left[kT \frac{\partial \ln \psi_{\rm eq}}{\partial q^b} + F_b^{\rm (f)} \right] \right\rangle - kT \int dq' \; K^{ab} \frac{\partial \psi(q')}{\partial q'^b} \tag{2.162}$$

Integrating the second line by parts, and then using the δ-function distribution of Eq. (2.159) to evaluate the result then yields Eq. (2.157) for $V^a(q)$, thus confirming the equivalence of the definition given in Eq. (2.160) to that given in Eq. (2.154).

The conceptual difference between the flux and drift velocity may thus be illustrated further by considering a dilute colloidal suspension in thermal equilibrium in the presence of a gravitational field. In equilibrium, this system adopts a single-particle probability density $\psi(\mathbf{R}) \propto e^{-U(\mathbf{R})/kT}$, with $U = \Delta m g R_z$, where Δm is the difference between the colloid mass and the mass of the displaced fluid, g is the gravitational acceleration, and R_z is a vertical coordinate. In the equilibrium state, the upward diffusive flux balances the downward flux arising from the gravitational field, giving a vanishing flux velocity $\mathbf{U}^{\mu}(\mathbf{R})$ for all $\mathbf{R}$. If one were to instead label a small number of particles with positions localized around some point $\mathbf{R}$ in the solution at some time t, creating a δ-function "ink drop," and then follow the evolution of this localized ensemble, one would find that over very short periods of time, for which the ensemble remains localized, the average position of the labeled particles (i.e., the center of mass of the ink drop) would drift downward with a nonzero drift velocity $\mathbf{V}^{\mu} = -\hat{\mathbf{z}} \Delta m \, g/\zeta$, where ζ is a Stokes friction coefficient.

B. Cartesian Coordinates

Brownian motion of a constrained system of N point particles may also be described by an equivalent Markov process of the Cartesian bead positions $\mathbf{R}^1(t), \ldots, \mathbf{R}^N(t)$. The constrained diffusion of the Cartesian coordinates may be characterized by a Cartesian drift velocity vector and diffusivity tensor

$$\mathbf{V}^{\mu} \equiv \lim_{\Delta t \to 0} \frac{1}{\Delta t} \langle \Delta \mathbf{R}^{\mu} \rangle_0 \tag{2.163}$$

$$\mathbf{D}^{\mu\nu} \equiv \lim_{\Delta t \to 0} \frac{1}{2\Delta t} \langle \Delta \mathbf{R}^{\mu} \Delta \mathbf{R}^{\nu} \rangle_0 \tag{2.164}$$

To relate these quantities to the corresponding moments of Δq^a to the required accuracy of $\mathcal{O}(\Delta t)$, we Taylor expand $\Delta \mathbf{R}^{\mu}$ to quadratic order in Δq^a as

$$\Delta \mathbf{R}^{\mu} \simeq \mathbf{a}_a^{\mu} \Delta q^a + \frac{1}{2} \frac{\partial^2 \mathbf{R}^{\mu}}{\partial q^a \partial q^b} \Delta q^a \Delta q^b \tag{2.165}$$

Using this expansion to calculate the first and second moments of $\Delta\mathbf{R}^{\mu}$, while retaining only terms of $\mathcal{O}(\Delta t)$, yields a drift velocity and diffusivity

$$\mathbf{V}^{\mu} = \mathbf{a}_a^{\mu} V^a + \frac{\partial^2 \mathbf{R}^{\mu}}{\partial q^a \partial q^b} D^{ab} \tag{2.166}$$

$$\mathbf{D}^{\mu\nu} = kT\mathbf{K}^{\mu\nu} \tag{2.167}$$

where Eq. (2.158) for D^{ab} and Eq. (2.136) for $\mathbf{K}^{\mu\nu}$ have been used to obtain Eq. (2.167). Equation (2.166) implies that, unlike the flux velocities U^a and $\mathbf{U}^{\mu}$, the drift velocities V^a and $\mathbf{V}^{\mu}$ do not transform as normal contravariant vectors, since

$$\mathbf{V}^{\mu} \neq \mathbf{a}_a^{\mu} V^a \tag{2.168}$$

The transformation rule given in Eq. (2.166) is instead an example to the so-called Ito formula for the transformation of the drift coefficients in Ito stochastic differential equations [16]. It is shown in Section IX that $V^a(q)$ and $\mathbf{V}^{\mu}(q)$ are equal to the drift coefficients that appear in the Ito formulation of the stochastic differential equations for the generalized and Cartesian coordinates, respectively.

The Cartesian drift velocity $\mathbf{V}^{\mu}(q)$ may also be defined as the ensemble average

$$\mathbf{V}^{\mu}(q) \equiv \int dq'\, \psi(q') \mathbf{U}^{\mu}(q') \tag{2.169}$$

of the Cartesian flux velocity $\mathbf{U}^{\mu}(q')$ in a hypothetical localized ensemble in which $\psi(q')$ is given by Eq. (2.159). To evaluate the RHS of Eq. (2.169), we first evaluate the average

$$\langle \mathbf{U}^{\mu} \rangle = \langle \mathbf{a}_a^{\mu} U^a \rangle \tag{2.170}$$

for an arbitrary distribution $\psi(q')$, and then take the limit of a δ-function distribution. Using Eq. (2.76) for $U^a(q')$, for an arbitrary $\psi(q')$, yields

$$\begin{aligned} \langle \mathbf{U}^{\mu} \rangle = & \left\langle \mathbf{a}_a^{\mu} K^{ab} \left[kT \frac{\partial \ln \psi_{\mathrm{eq}}}{\partial q^b} + F_b^{(\mathrm{f})} \right] \right\rangle \\ & - kT \int dq'\, \mathbf{a}_a^{\mu} K^{ab} \frac{\partial \psi}{\partial q'^b} \end{aligned} \tag{2.171}$$

By using expansion (2.136) for $\mathbf{K}^{\mu\nu}$ and the expansion $\frac{\partial}{\partial q^a} = \mathbf{a}^{\mu} \cdot \frac{\partial}{\partial \mathbf{R}^{\mu}}$ to obtain a Cartesian expression for the first line in Eq. (2.171), while integrating the second line by parts, and then using a delta-function distribution to evaluate the integral, we obtain a Cartesian velocity

$$\mathbf{V}^{\mu} = \mathbf{K}^{\mu\nu} \left[kT \frac{\partial \ln \psi_{\mathrm{eq}}}{\partial \mathbf{R}^{\nu}} + \mathbf{F}_{\nu}^{(\mathrm{f})} \right] + kT \frac{\partial (\mathbf{a}_a^{\mu} K^{ab})}{\partial q^b} \tag{2.172}$$

Expanding the derivative of $\mathbf{a}_a^\mu K^{ab}$ then yields Eq. (2.166), thus confirming the equivalence of the definitions given in Eqs. (2.163) and (2.169).

Applying the identity $\partial \ln \sqrt{g}/\partial q^b = (\partial \sqrt{g}/\partial q^b)/\sqrt{g}$ to the factor of $\ln \sqrt{g}$ in $\ln \psi_{\text{eq}}(q)$ in Eq. (2.172) yields the equivalent expression

$$\mathbf{V}^\mu = \mathbf{K}^{\mu\nu}\left[-\frac{\partial(U - kT \ln \sqrt{W})}{\partial \mathbf{R}^\nu} + \mathbf{F}_\nu^{(\text{f})}\right] + \frac{kT}{\sqrt{g}}\frac{\partial(\sqrt{g}\mathbf{a}_a^\mu K^{ab})}{\partial q^b} \tag{2.173}$$

which will be useful in what follows.

1. *Diffusion in Unconstrained Space*

To obtain a more compact expression for the Cartesian drift velocity, it is useful to generalize the underlying diffusion equation in the f-dimensional constraint surface to a diffusion equation in the unconstrained $3N$ dimensional space. To define a mobility tensor throughout the unconstrained space, we adopt Eq. (2.133) as the definition of the constrained Cartesian mobility $\mathbf{K}^{\mu\nu}$ everywhere. To allow Eqs. (2.133) and (2.134) to be evaluated away from the constraint surface, we must also define $\mathbf{n}_\mu^i \equiv \partial c^i/\partial \mathbf{R}^\mu$ everywhere, and specify definitions of the constrained quantities $c^1, \ldots, c^K$ throughout the unconstrained space. This yields a tensor for which $\mathbf{K}^{\mu\nu} \cdot \mathbf{n}_\mu^i = 0$ for all $i = 1, \ldots, K$ throughout the unconstrained space. In the system of $3N$ generalized coordinates defined in Eq. (2.3), the corresponding Riemannian tensor

$$K^{\alpha\beta} \equiv \frac{\partial Q^\alpha}{\partial \mathbf{R}^\mu} \cdot \mathbf{K}^{\mu\nu} \cdot \frac{\partial Q^\beta}{\partial \mathbf{R}^\nu} \tag{2.174}$$

thus has elements that vanish if either α or β corresponds to a hard variables, with $\alpha > f$ or $\beta > f$.

Using this definition of $K^{\alpha\beta}$, we may generalize the diffusion equation for the distribution $\psi(q)$ on the f-dimensional constraint surface to an equivalent diffusion equation for a distribution $\Psi(Q)$ in the $3N$-dimensional unconstrained space. We consider a model in which a system of $3N$ coordinates undergoes Brownian motion in the full unconstrained space under the influence of the mobility, $K^{\alpha\beta}$ defined above, as described by a diffusion equation

$$\frac{\partial \Psi}{\partial t} = -\frac{\partial}{\partial Q^\alpha}\left[K^{\alpha\beta}\left(-\frac{\partial \ln \Psi_{\text{eq}}}{\partial Q^\beta} + F_\beta^{(\text{f})}\right)\Psi\right] + kT\frac{\partial}{\partial Q^\alpha}\left(K^{\alpha\beta}\frac{\partial \Psi}{\partial Q^\beta}\right) \tag{2.175}$$

where $\alpha, \beta = 1, \ldots, 3N$, and where $\Psi_{\text{eq}}(Q)$ is an equilibrium distribution in the unconstrained space. The singular nature of the mobility for this model allows no

probability flux along the hard directions. In a corresponding stochastic process, the values of the hard coordinates would be rigorous constants of the motion. To describe a constrained system, we thus consider the evolution of a distribution that is initially confined to an infinitesimal region around the constraint surface, and which remains confined to this region thereafter as a result of the peculiar dynamics of the model.

We may recover a diffusion equation for the reduced distribution $\psi(q) \equiv \int dc\, \Psi(Q)$ by integrating both sides of Eq. (2.175) with respect to the hard coordinates, while approximating the functions $K^{\alpha\beta}(Q)$, $F^{(\mathrm{f})}_{\beta}(Q)$, and $\partial \ln \Psi_{\mathrm{eq}}/\partial q^b$ by their values on the constraint surface. This yields a diffusion equation

$$\frac{\partial \psi}{\partial t} = -\frac{\partial}{\partial q^a}\left[K^{ab}\left(-\frac{\partial \ln \Psi_{\mathrm{eq}}}{\partial q^b} + F^{(\mathrm{f})}_b\right)\psi\right] + kT\frac{\partial}{\partial q^a}\left(K^{ab}\frac{\partial \psi}{\partial q^b}\right) \tag{2.176}$$

By comparing Eq. (2.176) to Eq. (2.78) for the desired diffusion equation, we may identify the reduced equilibrium distribution $\psi_{eq}(q)$ at each point on the constraint surface, to within a constant of proportionality, with the value of $\Psi_{\mathrm{eq}}(Q)$ on the constraint surface. In this model, the behavior of $\Psi_{\mathrm{eq}}(Q)$ away from the constraint surface is dynamically irrelevant, since only the values of the derivatives of $\ln \Psi_{\mathrm{eq}}(Q)$ with respect to the soft coordinates, evaluated infinitesimally close to the constraint surface, enter diffusion Eq. (2.175).

The behavior of a constrained system may thus be correctly described by a $3N$-dimensional model with a mobility $K^{\alpha\beta}$, an initial distribution that is confined to within an infinitesimal region around the constraint surface, and an equilibrium distribution $\Psi_{\mathrm{eq}}(Q)$ whose value at each point the constraint surface is proportional to the desired value of $\psi_{eq}(q)$, giving

$$\Psi_{\mathrm{eq}}(Q) \propto \sqrt{gW}e^{-U/kT} \tag{2.177}$$

on the constraint surface. Equation (2.177) is also the equilibrium distribution $\Psi_{\mathrm{eq}}(Q) \propto \sqrt{g}e^{-U_{\mathrm{eff}}(Q)/kT}$ for a $3N$-dimensional model with an effective potential energy $U_{\mathrm{eff}}(Q)$ given by

$$U_{\mathrm{eff}} = U - kT \ln \sqrt{W} \tag{2.178}$$

on the constraint surface.

The content of diffusion equation (2.175) for such a model is, moreover, independent of our choice of a system of $3N$ coordinates for the unconstrained space. Constrained Brownian motion may thus be described by a model with a mobility $K^{\alpha\beta}$ and an effective potential U_{eff} in any system of $3N$ coordinates for

the unconstrained space, including Cartesian coordinates, by using an equilibrium distribution $\Psi_{\rm eq}(Q)$ in Eq. (2.175) whose behavior on the constraint surface is given by the RHS of Eq. (2.177) with g equal to the determinant of the metric tensor for the chosen system of coordinates.

2. *Compact Cartesian Expression*

Using this generalized definition of $K^{\alpha\beta}$, we may use the fact that $K^{\alpha\beta}$ and its derivatives $\partial K^{\alpha\beta}/\partial Q^{\gamma}$ vanish for any α or $\beta > f$ to extend the implied summations over the soft indices $a, b = 1, \ldots, f$ in the last term of Eq. (2.173) to summations over generic indices $\alpha, \beta = 1, \ldots, 3N$, giving

$$\frac{1}{\sqrt{g}}\frac{\partial(\sqrt{g}K^{ba}\,\mathbf{a}_a^{\mu})}{\partial q^b} = \frac{1}{\sqrt{g}}\frac{\partial}{\partial Q^{\beta}}\left(\sqrt{g}K^{\beta\alpha}\frac{\partial \mathbf{R}^{\mu}}{\partial Q^{\alpha}}\right) \tag{2.179}$$

We then note that each $3N$ Cartesian component of the RHS of Eq. (2.179) is a covariant divergence in the unconstrained space, of the standard form [36]

$$\frac{1}{\sqrt{g}}\frac{\partial}{\partial Q^{\beta}}(\sqrt{g}X^{\beta}) \tag{2.180}$$

for a contravariant vector

$$X^{\beta} \equiv K^{\beta\alpha}\frac{\partial \mathbf{R}^{\mu}}{\partial Q^{\alpha}} \cdot \hat{\mathbf{e}}_s \tag{2.181}$$

that is defined for fixed values of the bead index μ and a Cartesian index s, where $\hat{\mathbf{e}}_s$ is a unit vector parallel to Cartesian axis s, for $s = 1, \ldots, 3$. This covariant divergence retains the same form in any system of coordinates, including Cartesian coordinates, for which $\sqrt{g} = 1$, and so may also be expressed in Cartesian coordinates as

$$\frac{1}{\sqrt{g}}\frac{\partial}{\partial Q^{\beta}}\left(\sqrt{g}\,K^{\beta\alpha}\frac{\partial \mathbf{R}^{\mu}}{\partial Q^{\alpha}}\right) = \frac{\partial}{\partial \mathbf{R}^{\nu}} \cdot \mathbf{K}^{\nu\mu} \tag{2.182}$$

A proof of Eq. (2.182) by elementary means is given in the Appendix, Section F.

Substituting Eq. (2.182) into Eq. (2.173) yields a drift velocity

$$\mathbf{V}^{\mu} = \mathbf{K}^{\mu\nu} \cdot \left[-\frac{\partial U_{\rm eff}}{\partial \mathbf{R}^{\nu}} + \mathbf{F}_{\nu}^{(\rm f)}\right] + kT\frac{\partial}{\partial \mathbf{R}^{\nu}} \cdot \mathbf{K}^{\nu\mu} \tag{2.183}$$

where $U_{\rm eff}$ is defined in Eq. (2.178). The form of Eq. (2.183) is identical to that obtained for the Cartesian drift velocity of an unconstrained system of point

particles, except for the replacement of the unconstrained mobility $\mathbf{H}^{\mu\nu}$ by $\mathbf{K}^{\mu\nu}$ and of the true potential energy U by U_{eff}, as in the $3N$-dimensional model of constrained diffusion discussed above. Equation (2.183) could thus have been obtained more directly by analyzing this $3N$-dimensional model in Cartesian coordinates from the outset. Equation (2.183) has been given previously by Peters, as the last line of Eq. (2.33) in his Ph.D. thesis, who obtained this result by quite different methods.

3. *Öttinger's Expression*

Öttinger [11,12] has given a more explicit expression for $\mathbf{V}^{\mu}$. Öttinger's expression may be recovered by using expansion (2.133) for $\mathbf{K}^{\mu\nu}$ in the last term of Eq. (2.183), and expanding the divergence. The required expansion is presented in the Appendix, Section F, and yields

$$\mathbf{V}^{\mu} = \mathbf{K}^{\mu\nu} \cdot \left[-\frac{\partial U_{\text{eff}}}{\partial \mathbf{R}^{\nu}} + \mathbf{F}_{\nu}^{(\text{f})} \right] - kT\mathbf{K}^{\mu\nu} \cdot \frac{\partial^2 c^i}{\partial \mathbf{R}^{\lambda} \partial \mathbf{R}^{\nu}} \cdot \mathbf{m}_i^{\lambda} - kT\mathbf{K}^{\lambda\nu} : \frac{\partial^2 c^i}{\partial \mathbf{R}^{\nu} \partial \mathbf{R}^{\lambda}} \mathbf{m}_i^{\mu} + kT\mathbf{P}_{\nu}{}^{,\lambda} : \frac{\partial \mathbf{H}^{\nu\rho}}{\partial \mathbf{R}^{\lambda}} \cdot \mathbf{P}_{\rho}{}^{,\mu} \tag{2.184}$$

This equation is equivalent to the result given by Öttinger for the Ito drift velocity of an arbitrary rigid system, generalized here by the use of an unspecified value of W so as to also apply to stiff systems. This drift velocity appears as the drift coefficient (i.e., the prefactor of dt) in the Ito SDE given in Eq. (29) of Ref. 11 and Eq. (5.61) of Ref. 12.

C. Summary

The connection between a diffusion equation and a corresponding Markov diffusion process may be established through expressions for drift velocities and diffusitivities. The drift velocity for both unconstrained and constrained systems may be expressed in an arbitrary system of coordinates in the generic form

$$V^{\alpha} = K^{\alpha\beta} \left[kT \frac{\partial \ln \mathscr{P}_{\text{eq}}(X)}{\partial X^{\beta}} + F_{\beta}^{(\text{f})} \right] + kT \frac{\partial K^{\beta\alpha}}{\partial X^{\beta}} \tag{2.185}$$

where $X^1, X^2, \ldots, X^L$ represents some generic system of L coordinates, which may be taken to be either $L = f$ soft coordinates for the constraint surface or a set of $L = 3N$ coordinates for the unconstrained space, and where $\mathscr{P}_{\text{eq}}(X)$ is the equilibrium distribution in the chosen system of coordinates.

To describe an unconstrained system of N particles, we take $X^1, \ldots, X^L$ to be any system of $L = 3N$ generalized or Cartesian coordinates for the

unconstrained space, take $K^{\alpha\beta}$ equal to the unconstrained mobility $H^{\alpha\beta}$ in the chosen system of coordinates, and take $\mathscr{P}_{\rm eq} \propto \sqrt{g}e^{-U/kT}$.

To describe a constrained system of N particles, we must instead take $K^{\alpha\beta}$ be the constrained mobility and take $\mathscr{P}_{\rm eq} \propto \sqrt{gW}e^{-U/kT}$ within the constraint surface. In this case, the variables $X^1, \ldots, X^L$ may, moreover, be interpreted either as a set f soft coordinates for the constraint surface or as an arbitrary set of $3N$ coordinates for the unconstrained space. In the latter case, the mobility $K^{\alpha\beta}$ must be interpreted as an extension of the tensor K^{ab} for which the hard subspace is a null subspace, namely, for which $K^{\alpha\beta} = 0$ if α or β is greater than f in the system of $3N$ generalized coordinates defined in Section II, or for which $\mathbf{K}^{\mu\nu} \cdot \mathbf{n}^i_\nu = 0$ for all $i = 1, \ldots, K$ in Cartesian coordinates. Applying Eq. (2.185) to a set of soft coordinates yields Eq. (2.157) for the generalized drift velocity V^a. Applying Eq. (2.185) to Cartesian coordinates yields Eq. (2.183) for the Cartesian drift velocity $\mathbf{V}^\mu$.

VIII. RECIPROCAL VECTORS AND PROJECTION TENSORS

In this section, we introduce generalized definitions of sets of reciprocal basis vectors, and of corresponding projection tensors, which include the dynamical reciprocal vectors and the dynamical projection tensor introduced in Section VI as special cases. These definitions play an essential role in the analysis of the constrained Langevin equation given in Section IX.

A. Reciprocal Vectors

A generalized set of reciprocal vectors for a constrained system is defined here to be any set of f contravariant basis vectors $\bar{\mathbf{b}}^1_\mu, \ldots, \bar{\mathbf{b}}^f_\mu$ and K covariant basis vectors $\bar{\mathbf{m}}^\mu_1, \ldots, \bar{\mathbf{m}}^\mu_K$ that satisfy the biorthogonality conditions

$$\mathbf{a}^\mu_a \cdot \bar{\mathbf{b}}^b_\mu = \delta^b_a \tag{2.186}$$

$$\bar{\mathbf{m}}^\mu_i \cdot \mathbf{n}^j_\mu = \delta^j_i \tag{2.187}$$

$$\bar{\mathbf{m}}^\mu_i \cdot \bar{\mathbf{b}}^a_\mu = 0 \tag{2.188}$$

$$\mathbf{a}^\mu_a \cdot \mathbf{n}^i_\mu = 0. \tag{2.189}$$

If the set $3N$ contravariant Cartesian vectors given by the f $\mathbf{a}$ vectors and K $\bar{\mathbf{m}}$ vectors form a complete basis for 3N space of Cartesian vectors, which we will hereafter assume to be true, then they must also obey a completeness relation

$$\mathbf{I}^\mu_\nu = \mathbf{a}^\mu_a \bar{\mathbf{b}}^a_\nu + \bar{\mathbf{m}}^\mu_i \mathbf{n}^i_\nu \tag{2.190}$$

as may be confirmed by the reasoning already applied to the special case of dynamical basis vectors. Here and hereafter, we use an overbar to indicate a

generic set of such vectors, and reserve the corresponding symbols without overbars to indicate the dynamical reciprocal vectors.

The biorthogonality and completeness relations presented above do not uniquely define the reciprocal basis vectors $\bar{\mathbf{b}}^a_\mu$ and $\bar{\mathbf{m}}^\mu_i$; a list of $(3N)^2$ scalar components is required to specify the $3N$ components of these $3N$ reciprocal basis vectors, but only $(3N)^2 - fK$ equations involving the reciprocal vectors are provided by Eqs. (2.186–2.188), leaving fK more unknowns than equations. The source of the resulting arbitrariness may be understood by decomposing the reciprocal vectors into soft and hard components. The f^2 soft components of the f $\bar{\mathbf{b}}$ vectors are completely determined by the f^2 equations of Eq. (2.186). Similarly, the K^2 hard components of the $\bar{\mathbf{m}}$ vectors are determined by Eq. (2.187). These two restrictions leave undetermined both the fK hard components of the f $\bar{\mathbf{b}}$ vectors and the Kf soft components of the K $\bar{\mathbf{m}}$ vectors. Equation (2.188) provides another fK equations, but still leaves fK more equations than unknowns. Equation (2.189) does not involve the reciprocal vectors, and so is irrelevant for this purpose. We show below that a choice of reciprocal basis vectors may be uniquely specified by specifying arbitrary expressions for either the hard components of the $\bar{\mathbf{b}}$ vectors or the soft components of $\bar{\mathbf{m}}$ vectors (but not both).

B. Projection Tensors

A generalized projection tensor $\bar{\mathbf{P}}^\lambda_{,\mu}$ is defined to be any tensor for which

$$\bar{\mathbf{P}}^\lambda{}_{,\mu} \cdot \bar{\mathbf{P}}^\mu{}_{,\nu} = \bar{\mathbf{P}}^\lambda{}_{,\nu} \tag{2.191}$$

and for which

$$\bar{\mathbf{P}}^\mu{}_{,\nu} \cdot \mathbf{a}^\nu_a = \mathbf{a}^\mu_a \tag{2.192}$$

$$\mathbf{n}^i_\mu \cdot \bar{\mathbf{P}}^\mu{}_{,\nu} = 0 \tag{2.193}$$

for all $a = 1, \ldots, f$ and all $i = 1, \ldots, K$. The dynamical projection tensor $\mathbf{P}^\mu{}_{,\nu}$ satisfies this definition. As for the special case of the dynamical projection tensor, we use the notation

$$\bar{\mathbf{P}}_\nu{}^{,\mu} = (\bar{\mathbf{P}}^\mu{}_{,\nu})^T \tag{2.194}$$

to denote a transposed projection tensor.

For any set of reciprocal vectors that satisfy Eqs. (2.186–2.190), a corresponding projection tensor can be constructed as a sum:

$$\begin{aligned} \bar{\mathbf{P}}^\lambda{}_{,\nu} &= \mathbf{a}^\lambda_a \bar{\mathbf{b}}^a_\nu \\ &= \mathbf{I}^\lambda_\nu - \bar{\mathbf{m}}^\lambda_i \mathbf{n}^i_\nu \end{aligned} \tag{2.195}$$

The resulting tensor satisfies

$$\bar{\mathbf{b}}^a_\mu \cdot \bar{\mathbf{P}}^\mu{}_{,\nu} = \bar{\mathbf{b}}^a_\nu \tag{2.196}$$

$$\bar{\mathbf{P}}^\mu{}_{,\nu} \cdot \bar{\mathbf{m}}^\nu_i = 0 \tag{2.197}$$

in addition to Eqs. (2.191–2.193).

We now show, conversely, that for each projection tensor $\bar{\mathbf{P}}^\mu{}_{,\nu}$, there exists a unique set of corresponding reciprocal basis vectors that are related to $\bar{\mathbf{P}}^\mu{}_{,\nu}$ by Eq. (2.195). To show this, we show that the set of arbitrary numbers required to uniquely define such a projection tensor at a point on the constraint surface is linearly related to the set of fK arbitrary numbers required to uniquely specify a system of reciprocal vectors. A total of $(3N)^2$ coefficients are required to specify a tensor $\bar{\mathbf{P}}^\mu{}_{,\nu}$. Equation (2.193) yields a set of $3NK$ scalar equations that require vanishing values of both the K^2 "hard–hard" components, which are given by the quantities $\mathbf{n}^i_\mu \cdot \bar{\mathbf{P}}^\mu{}_{,\nu} \cdot \mathbf{n}^j_\nu = 0$, and of the fK mixed "hard–soft" components, which are given by $\mathbf{n}^i_\mu \cdot \bar{\mathbf{P}}^\mu{}_{,\nu} \cdot \mathbf{a}^\nu_b = 0$. Equation (2.192) yields another f^2 equations, which determine the f^2 "soft–soft" components given by $\mathbf{a}^\mu_a \cdot \bar{\mathbf{P}}^\mu{}_{,\nu} \cdot \mathbf{a}^\nu_b = \tilde{g}_{ab}$. These conditions thus leave unspecified the values of the fK mixed "soft–hard" components, given by the quantities $\mathbf{a}^\mu_a \cdot \bar{\mathbf{P}}^\mu{}_{,\nu} \cdot \mathbf{n}^j_\nu$. By using both forms of expansion (2.195) for $\bar{\mathbf{P}}^\mu{}_{,\nu}$ to calculate $\mathbf{a}^\mu_a \cdot \bar{\mathbf{P}}^\mu{}_{,\nu} \cdot \mathbf{n}^j_\nu$, we may obtain a set of fK equations

$$\mathbf{a}^\mu_a \cdot \bar{\mathbf{P}}^\mu{}_{,\nu} \cdot \mathbf{n}^j_\nu = \tilde{g}_{ab} \bar{\mathbf{b}}^b_\nu \cdot \mathbf{n}^j_\nu = -\mathbf{a}^\mu_a \cdot \bar{\mathbf{m}}^\mu_i \hat{G}^{ij} \tag{2.198}$$

that relate the fK arbitrary soft-hard components of $\bar{\mathbf{P}}^\mu{}_{,\nu}$ to both the fK arbitrary hard components of the $\bar{\mathbf{b}}$ vectors and to the fK arbitrary soft components of the $\bar{\mathbf{m}}$ vectors, while also relating the arbitrary components of the $\bar{\mathbf{b}}$ and $\bar{\mathbf{m}}$ vectors to one another.

C. Cartesian Drift Velocity (Revisited)

A useful class of alternative expressions for $\mathbf{V}^\mu$ may be derived by inserting an arbitrary projection tensor into the divergence of $\mathbf{K}^{\mu\nu}$ on the RHS of (2.183). We note that

$$\mathbf{K}^{\nu\mu} = \bar{\mathbf{P}}^\nu{}_{,\lambda} \cdot \mathbf{K}^{\lambda\mu} \tag{2.199}$$

because any projection tensor $\bar{\mathbf{P}}^\nu{}_{,\lambda}$ acts like the identity when operating to the right on a soft vector. We may thus insert an arbitrary projection tensor into the divergence in Eq. (2.183) to express the Cartesian divergence as a sum

$$\frac{\partial}{\partial \mathbf{R}^\nu} \cdot \mathbf{K}^{\nu\mu} = \frac{\partial}{\partial \mathbf{R}^\nu} \cdot (\bar{\mathbf{P}}^\nu{}_{,\lambda} \cdot \mathbf{K}^{\lambda\mu}) \tag{2.200}$$

$$= \bar{\mathbf{P}}_\lambda{}^{,\nu} : \frac{\partial \mathbf{K}^{\lambda\mu}}{\partial \mathbf{R}^\nu} + \mathbf{K}^{\mu\lambda} \cdot \left(\frac{\partial}{\partial \mathbf{R}^\nu} \cdot \bar{\mathbf{P}}^\nu{}_{,\lambda} \right) \tag{2.201}$$

of a projected divergence (the first term on the RHS) plus a term involving the divergence of the projection tensor. Note that the values of both terms on the RHS of Eq. (2.201) depend upon an arbitrary definition for the projection tensor $\bar{\mathbf{P}}^{\mu}{}_{,\lambda}$, or of the corresponding reciprocal basis vectors, but that the sum of the two terms can not, since the value of $\mathbf{V}^{\mu}$ on the LHS of the equation is independent of this choice.

Substituting Eq. (2.201) into Eq. (2.183) for $\mathbf{V}^{\mu}$ yields

$$\mathbf{V}^{\mu} = \mathbf{K}^{\mu\nu} \cdot \left[-\frac{\partial U_{\text{eff}}}{\partial \mathbf{R}^{\nu}} + \mathbf{F}^{(\text{f})}_{\nu} + \mathbf{F}^{(\text{ps})}_{\nu} \right] + kT \bar{\mathbf{P}}_{\nu}{}^{,\lambda} : \frac{\partial \mathbf{K}^{\mu\nu}}{\partial \mathbf{R}^{\lambda}} \tag{2.202}$$

Here, $\mathbf{F}^{(\text{ps})}_{\nu}$ is a "pseudoforce" that is defined by the relation

$$\mathbf{K}^{\mu\lambda} \cdot \mathbf{F}^{(\text{ps})}_{\lambda} = \mathbf{K}^{\mu\lambda} \cdot \left(kT \frac{\partial}{\partial \mathbf{R}^{\nu}} \cdot \bar{\mathbf{P}}^{\nu}{}_{,\lambda} \right) \tag{2.203}$$

Because $\mathbf{K}^{\mu\nu}$ has only soft components, this is equivalent to the requirement that

$$\mathbf{a}^{\lambda}_{a} \cdot \mathbf{F}^{(\text{ps})}_{\lambda} = \mathbf{a}^{\lambda}_{a} \cdot \left(kT \frac{\partial}{\partial \mathbf{R}^{\nu}} \cdot \bar{\mathbf{P}}^{\nu}{}_{,\lambda} \right) \tag{2.204}$$

that is, that the soft components of $\mathbf{F}^{(\text{ps})}_{\lambda}$ be equal to the soft components of the divergence of $kT\bar{\mathbf{P}}^{\nu}{}_{,\lambda}$. Because $\mathbf{F}^{(\text{ps})}_{\nu}$ is contracted with $\mathbf{K}^{\mu\nu}$ in Eq. (2.202), the hard components of $\mathbf{F}^{(\text{ps})}_{\nu}$ have no effect on the drift velocity, and so are left arbitrary by this definition.

A more explicit expression for $\mathbf{F}^{(\text{ps})}_{\nu}$ may be obtained by expanding $\bar{\mathbf{P}}^{\nu}{}_{,\lambda} = \mathbf{I}^{\nu}_{\lambda} - \bar{\mathbf{m}}^{\nu}_{i}\mathbf{n}^{i}_{\lambda}$ within the divergence, and expanding the derivative, to show that

$$\mathbf{F}^{(\text{ps})}_{\lambda} = -kT \frac{\partial \mathbf{n}^{i}_{\lambda}}{\partial \mathbf{R}^{\nu}} \cdot \bar{\mathbf{m}}^{\nu}_{i} = -kT \frac{\partial^2 c^{i}}{\partial \mathbf{R}^{\lambda} \partial \mathbf{R}^{\nu}} \cdot \bar{\mathbf{m}}^{\nu}_{i} \tag{2.205}$$

to within arbitrary hard components. The second equality in Eq. (2.205) follows from the definition $\mathbf{n}^{i}_{\nu} \equiv \partial c^{i} / \partial \mathbf{R}^{\nu}$.

D. Useful Choices

We now consider several possible ways of defining a system of reciprocal vectors and a corresponding projection tensor.

Biorthogonality conditions (2.186–2.189) and completeness relation (2.190) are equivalent to the biorthogonality and completeness relations (2.5) and (2.6) obeyed by partial derivatives in the full space, if we identify

$$\bar{\mathbf{b}}^{a}_{\mu} \equiv \frac{\partial q^{a}(\mathbf{R})}{\partial \mathbf{R}^{\mu}} \qquad \bar{\mathbf{m}}^{\mu}_{i} \equiv \frac{\partial \mathbf{R}^{\mu}(Q)}{\partial c^{i}} \tag{2.206}$$

This is perhaps the most obvious definition of a set of reciprocal vectors.

Other definitions may be constructed by the following generalization of the relationship between the dynamical reciprocal vectors and the mobility tensor: Given any invertible symmetric covariant Cartesian tensor $\mathbf{S}_{\mu\nu}$ with an inverse $\mathbf{T}^{\mu\nu} = (\mathbf{S}^{-1})^{\mu\nu}$, we may take

$$\bar{\mathbf{b}}^{a}_{\nu} \equiv (\tilde{S}^{-1})^{ab}\mathbf{a}^{\mu}_{b} \cdot \mathbf{S}_{\mu\nu} \tag{2.207}$$

and

$$\bar{\mathbf{m}}^{\nu}_{i} \equiv (\hat{T}^{-1})_{ij}\mathbf{n}^{j}_{\mu} \cdot \mathbf{T}^{\mu\nu} \tag{2.208}$$

By repeating the reasoning applied in Section VI to the dynamical reciprocal vectors, we may confirm that any vectors so defined will satisfy Eqs. (2.186)–(2.189). It will hereafter be assumed that (except for pathological choices of $\mathbf{S}_{\mu\nu}$) they also satisfy completness relation (2.190). A few choices for the tensors $\mathbf{S}_{\mu\nu}$ and $\mathbf{T}^{\mu\nu}$ yield useful reciprocal vectors and projection tensors, for which we introduce special notation:

1. *Dynamical Projection*

Dynamical reciprocal vectors $\mathbf{b}^{a}_{\mu}$ and $\mathbf{m}^{\nu}_{i}$, which were introduced in Section VI, are defined by taking $\mathbf{T}^{\mu\nu} = \mathbf{H}^{\mu\nu}$ in Eq. (2.208). The corresponding projection tensor is the dynamical projection tensor $\mathbf{P}^{\mu}{}_{,\nu}$.

The pseudoforce associated with the dynamical projection tensor may be calculated by using dynamical reciprocal vectors to evaluate Eq. (2.205). In the simple case of a coordinate-independent mobility $\mathbf{H}^{\mu\nu}$, as in a free-draining model or a model with an equilibrium preaveraged mobility, we may use Eq. (A.17) to express $\mathbf{F}^{(\mathrm{ps})}_{\lambda}$ as a derivative

$$\mathbf{F}^{(\mathrm{ps})}_{\lambda} = -kT\frac{\partial \ln\sqrt{\hat{H}}}{\partial \mathbf{R}^{\lambda}} \qquad (\text{for } \mathbf{H}^{\mu\nu} = \text{const}) \tag{2.209}$$

In the general case of a coordinate-dependent mobility $\mathbf{H}^{\mu\nu}(q)$, as in a model with full hydrodynamic interactions, the resulting pseudoforce cannot be expressed as the derivative of any corresponding pseudopotential.

The use of a dynamical projection tensor in Eq. (2.202) also leads naturally to Öttinger's expression for $\mathbf{V}^{\mu}$, Eq. (2.184). To show this, we expand $\mathbf{K}^{\nu\mu}$ as a product $\mathbf{H}^{\nu\rho} \cdot \mathbf{P}_{\rho}{}^{,\mu}$ in the last term in Eq. (2.202), and expand the derivative as

$$\begin{aligned}\mathbf{P}_{\nu}{}^{,\lambda} : \frac{\partial \mathbf{K}^{\nu\mu}}{\partial \mathbf{R}^{\lambda}} &= \mathbf{P}_{\nu}{}^{,\lambda} : \frac{\partial(\mathbf{H}^{\nu\rho} \cdot \mathbf{P}_{\rho}{}^{,\mu})}{\partial \mathbf{R}^{\lambda}} \\ &= \mathbf{P}_{\nu}{}^{,\lambda} : \frac{\partial \mathbf{H}^{\nu\rho}}{\partial \mathbf{R}^{\lambda}} \cdot \mathbf{P}_{\rho}{}^{,\mu} - \mathbf{K}^{\rho\lambda} : \frac{\partial \mathbf{n}^{i}_{\rho}}{\partial \mathbf{R}^{\lambda}}\mathbf{m}^{\mu}_{i}\end{aligned} \tag{2.210}$$

where we have used the expansion $\mathbf{P}_{\rho}^{\ \mu} = \mathbf{I}_{\rho}^{\mu} - \mathbf{n}_{\rho}^{i}\bar{\mathbf{m}}_{i}^{\mu}$ to obtain the second term in the second line. Equation (2.184) is obtained by substituting Eq. (2.210) into Eq. (2.202). The second line on the RHS of Eq. (2.184) is the term arising from $\mathbf{F}_{\nu}^{(\mathrm{ps})}$.

2. *Geometric Projection*

Geometric reciprocal basis vectors, which will be denoted by $\tilde{\mathbf{b}}_{\mu}^{a}$ and $\hat{\mathbf{m}}_{i}^{\mu}$, are defined by instead taking $\mathbf{T}^{\mu\nu} = \mathbf{I}^{\mu\nu}$ in Eq. (2.208). This yields

$$\tilde{\mathbf{b}}_{\mu}^{a} \equiv (\tilde{g}^{-1})^{ab}\mathbf{a}_{b}^{\mu} \tag{2.211}$$

$$\hat{\mathbf{m}}_{i}^{\mu} \equiv \hat{G}_{ij}^{-1}\mathbf{n}_{\mu}^{j} \tag{2.212}$$

Note that the soft reciprocal vectors $\tilde{\mathbf{b}}_{\mu}^{a}$ are expanded in a basis of tangent vectors, and so are manifestly parallel to the constraint surface (as indicated by the use of a tilde), while the hard reciprocal vectors $\hat{\mathbf{m}}_{i}^{\mu}$ are expanded in normal vectors, and so lie entirely normal to the constraint surface (as indicated by the use of a caret). These basis vectors may be used to construct a "geometric" projection tensor

$$\begin{aligned}\tilde{\mathbf{P}}_{\mu}^{\nu} &\equiv \tilde{\mathbf{b}}_{\mu}^{a}\mathbf{a}_{a}^{\nu} = \mathbf{a}_{a}^{\nu}\tilde{\mathbf{b}}_{\mu}^{a} \\ &= \mathbf{I}_{\mu}^{\nu} - \hat{G}_{ij}^{-1}\mathbf{n}_{\mu}^{i}\mathbf{n}_{\nu}^{j}\end{aligned} \tag{2.213}$$

The product of any $3N$ vector with this geometric projection tensor isolates the soft component of that vector. The geometrical projection tensor is a symmetric tensor, like the Euclidean identity and unlike the dynamical projection tensor. To reflect this fact, its bead indices are written directly above and below one another, with no offset to indicate whether the implicit Cartesian index associated with each bead index acts to the right or left.

The pseudoforce that is obtained by using geometric reciprocal vectors in Eq. (2.205) may be expressed, using Eq. (A.19), as a derivative

$$\mathbf{F}_{\lambda}^{(\mathrm{ps})} = -kT\frac{\partial \ln\sqrt{\hat{G}}}{\partial \mathbf{R}^{\lambda}} \tag{2.214}$$

of a pseudo-potential $kT\ln\sqrt{\hat{G}}$. This is the "metric" pseudoforce found previously by both Fixman [9] and Hinch [10] in their analyses of the Langevin equation for constrained systems.

3. *Inertial Projection*

Inertial reciprocal vectors, which will be denoted by $\breve{\mathbf{b}}_{\mu}^{a}$ and $\breve{\mathbf{m}}_{i}^{\mu}$, are obtained by setting $\mathbf{S}_{\mu\nu} = \mathbf{m}_{\mu\nu}$. This yields

$$\breve{\mathbf{b}}_{\mu}^{a} \equiv (\tilde{m}^{-1})^{ab}\mathbf{a}_{b}^{\mu}m_{\mu} \tag{2.215}$$

$$\breve{\mathbf{m}}_{i}^{\mu} \equiv (\hat{m}^{-1})_{ij}^{-1}\mathbf{n}_{\mu}^{i}m_{\mu}^{-1} \tag{2.216}$$

with no summation with respect to μ, where m_μ is the mass of bead μ. The corresponding inertial projection tensor is given by

$$\breve{\mathbf{P}}^{\nu}{}_{,\mu} \equiv \mathbf{I}^{\nu}_{\mu} - (\widehat{m^{-1}})^{-1}_{ij} m_{\nu}^{-1} \mathbf{n}^{i}_{\nu} \mathbf{n}^{i}_{\mu} \tag{2.217}$$

The inertial and geometrical projection tensors, and associated reciprocal vectors, are identical for models with equal masses for all beads, in which the mass tensor is proportional to the identity.

The corresponding pseudoforce is

$$\mathbf{F}^{(\mathrm{ps})}_{\lambda} = -kT \frac{\partial \ln \sqrt{\widehat{m^{-1}}}}{\partial \mathbf{R}^{\lambda}} \tag{2.218}$$

When applied to a rigid model, for which $W \propto \widehat{m^{-1}}$, this pseudoforce exactly cancels the force arising from the derivative of $kT \ln \sqrt{W}$ within U_{eff} in Eq. (2.202), yielding a drift velocity

$$\mathbf{V}^{\mu} = \mathbf{K}^{\mu\nu} \cdot \left[-\frac{\partial U}{\partial \mathbf{R}^{\nu}} + \mathbf{F}^{(\mathrm{f})}_{\nu} \right] + kT \breve{\mathbf{P}}_{\nu}{}^{,\lambda} : \frac{\partial \mathbf{K}^{\mu\nu}}{\partial \mathbf{R}^{\lambda}} \tag{2.219}$$

that contains neither of these cancelling forces. The same result obviously applies for geometric projection in the case of rigid models with equal bead masses. This expression for the drift velocity has been given previously by Peters [13], as the drift coefficient in the Ito SDE given in the first line of Eq. (3.33) of his Ph.D. thesis.

E. Summary

The main result of this section is the derivation of a class of alternative expressions for the Cartesian drift velocity $\mathbf{V}^{\mu}$ that is based on an expansion of the divergence of the diffusivity of $kT\mathbf{K}^{\mu\nu}$ as a sum

$$\frac{\partial}{\partial \mathbf{R}^{\nu}} \cdot \mathbf{K}^{\nu\mu} = \bar{\mathbf{P}}_{\nu}{}^{,\lambda} : \frac{\partial \mathbf{K}^{\nu\mu}}{\partial \mathbf{R}^{\lambda}} + \frac{1}{kT} \mathbf{K}^{\mu\nu} \cdot \mathbf{F}^{(\mathrm{ps})}_{\nu} \tag{2.220}$$

in which the projected divergence of the first term is defined using an generalized projection tensor $\bar{\mathbf{P}}_{\nu}{}^{,\lambda}$, and in which $\mathbf{F}^{(\mathrm{ps})}_{\nu}$ is a corresponding pseudoforce with soft components

$$F^{(\mathrm{ps})}_{a} = \mathbf{a}^{\nu}_{a} \cdot \left(kT \frac{\partial}{\partial \mathbf{R}^{\lambda}} \cdot \bar{\mathbf{P}}^{\lambda}{}_{,\nu} \right) \tag{2.221}$$

Because $\mathbf{F}_{\mathrm{v}}^{(\mathrm{ps})}$ appears contracted with $\mathbf{K}^{\mu\nu}$ in the equation of motion, the hard components of $\mathbf{F}_{\mathrm{v}}^{(\mathrm{ps})}$ have no dynamical effect, and are arbitrary. The values of the soft components of $\mathbf{F}_{\mathrm{v}}^{(\mathrm{ps})}$ depend on the form chosen for the generalized projection tensor, and reduce to the metric pseudoforce found by Fixman and Hinch in the case of geometric projection.

The expression for $\mathbf{V}^{\mu}$ that is obtained by substituting the preceding into Eq. (2.183) is found to include as special cases all of the correct results for the Cartesian drift velocity obtained by previous authors: Expressions obtained previously by Öttinger [11,12], Hinch [10], and Peters [13] are recovered in the cases of dynamical, geometrical, and inertial projection, respectively. This expression for $\mathbf{V}^{\mu}$ also plays an essential role in the analyses of constrained Langevin equations and constrained kinetic SDEs given in Section IX, in which constrained fluctuations are found to give rise naturally to a contribution to the drift velocity proportional to a projected divergence of the mobility, but in which a correspondng pseudoforce must be added to the SDE by hand to obtain the correct drift velocity.

IX. STOCHASTIC DIFFERENTIAL EQUATIONS (SDEs)

In this section, we consider the description of Brownian motion by Markov diffusion processes that are the solutions of corresponding stochastic differential equations (SDEs). This section contains self-contained discussions of each of several possible interpretations of a system of nonlinear SDEs, and the relationships between different interpretations. Because most of the subtleties of this subject are generic to models with coordinate-dependent diffusivities, with or without constraints, this analysis may be more broadly useful as a review of the use of nonlinear SDEs to describe Brownian motion. Because each of the various possible interpretations of an SDE may be defined as the limit of a discrete jump process, this subject also provides a useful starting point for the discussion of numerical simulation algorithms, which are considered in the following section.

The present analysis builds directly on three previous analyses of SDEs for constrained systems by Fixman [9], Hinch [10], and Öttinger [11]. Fixman and Hinch both considered an interpretation of the inertialess Langevin equation as a limit of an ordinary differential equation with a finite, continuous random force. Both authors found that, to obtain the correct drift velocity and equilibrium distribution, it was necessary to supplement forces arising from derivatives of $U_{\mathrm{eff}} = U - kT \ln \sqrt{W}$ by an additional corrective pseudoforce, but obtained inconsistent results for the form of the required correction force. Öttinger [11] based his analysis on an Ito interpretation of SDEs for both generalized and Cartesian coordinates, and thereby obtained results that

(although correct) bore no obvious resemblance to those obtained by Fixman or Hinch.

The present analysis follows the approach taken by all three of these authors, in which SDEs are constructed by choosing the drift and diffusivity coefficients so as to yield a desired diffusion equation. Peters [13] has pioneered an alternative approach, in which expressions for the drift and diffusivity are derived from a direct, but rather subtle, analysis of the underlying inertial equations of motion, in which (for rigid systems) he integrates the instantaneous equations of motion over time intervals much greater than the autocorrelation time of the particle velocities. Peters has expressed his results both as standard Ito SDEs and in a nonstandard interpretation that he describes heuristically as a mixture of Stratonovich and Ito interpretations. Peters' mixed Ito–Stratonovich interpretation is equivalent to the ''kinetic'' interpretation discussed here. Here, we recover several of Peters' results, but do not imitate his method.

Sections IX.A–IX.D discuss four different possible interpretations of a set of nonlinear SDEs, and the relationships between them. SDEs are mathematically ambiguous unless they are supplemented by a rule for their interpretation, because their solutions are not differentiable functions of time. Each of the different possible interpretations of a set of SDEs may defined as the limit of an underlying discrete jump process in the limit of infinitesimal time step. Sections IX.A and IX.B review the standard Ito and Stratonovich interpretations. Section IX.C discusses the traditional interpretation of an inertialess Langevin equation as a limit of an ordinary differential equation with rapidly varying random forces, clarifies its relationship to the Stratonovich interpretation, and identifies some of the potential pitfalls of this interpretation. Subsection IX.D discusses a ''kinetic'' interpretation that is constructed so as to lead naturally, in the absence of constraints, to a diffusion equation of the form required by statistical mechanics. The definition of the kinetic interpretation given here is a formalization of a suggestion by Fixman [9] of a particular mid-step algorithm for integration of the Langevin equation.

Throughout this section, we will use the notation $X^1(t), \ldots, X^L(t)$ to denote a unspecified set of L Markov diffusion processes when discussing mathematical properties that are unrelated to the physics of constrained Brownian motion, or that are not specific to a particular set of variables. The variables q^a, Q^α, and $\mathbf{R}^\mu$ will be reserved to refer specifically to soft coordinates, generalized coordinates for a system of N point particles, and Cartesian particle positions, respectively. The generic variables $X^1, \ldots, X^L$ will be indexed by integer variables $\alpha, \beta, \ldots = 1, \ldots, L$.

The normalized joint probability distribution for an ensemble of such generic variables will be denoted by $\mathscr{P}(X)$, which is normalized such that $\int dX^1 \cdots dX^L \mathscr{P}(X) = 1$. The evolution of such a probability distribution is

described by a Fokker–Planck, or forward Kolmogorov, equation [16,17]

$$\frac{\partial \mathscr{P}}{\partial t} = -\frac{\partial (V^{\alpha}\mathscr{P})}{\partial X^{\alpha}} + \frac{\partial^2 (D^{\alpha\beta}\mathscr{P})}{\partial X^{\alpha}\partial X^{\beta}} \tag{2.222}$$

in which the drift velocity V^a and diffusivity tensor $D^{\alpha\beta}$ are given by the moments

$$V^{\alpha}(X) \equiv \lim_{\Delta t \to 0} \frac{1}{\Delta t} \langle \Delta X^{\alpha} \rangle_0 \tag{2.223}$$

$$D^{\alpha\beta}(X) \equiv \lim_{\Delta t \to 0} \frac{1}{2\Delta t} \langle \Delta X^{\alpha} \Delta X^{\beta} \rangle_0 \tag{2.224}$$

of the deviation $\Delta X^{\alpha} \equiv X^{\alpha}(\Delta t) - X^0(0)$ of $X^{\alpha}(t)$ over a time interval of length Δt from an arbitrary origin of time at $t = 0$. As in Section VII, the notation $\langle \cdots \rangle_0$ represents the conditional average of a dynamical variable at some specified time, such as the value of $X(t)$ at $t = \Delta t$, for an ensemble of systems for which the set of variables $X(t) = \{X^1(t), \ldots, X^L(t)\}$ has a known set of initial values X at an earlier time $t = 0$. The value of an average $\langle \cdots \rangle_0$ thus depends upon the chosen initial condition X.

In what follows, we distinguish between the drift velocity V^{α} associated with a random variable X^{α}, which is defined by Eq. (2.223), and the corresponding drift coefficient that appears explicitly in a corresponding SDE for X^{α}, which will be denoted by $A^{\alpha}(X)$, and which is found to be equal to V^{α} only in the case of an Ito SDE. The values of the generalized and Cartesian drift velocities required to force each type of SDE to mimic constrained Brownian motion are determined in what follows by requiring that the resulting drift velocities have the values obtained in Section VII.

In both the Ito and Stratonovich formulations, the randomness in a set of SDEs is generated by an auxiliary set of statistically independent Wiener processes [12,16]. The solution of an SDE is defined by a limiting process (which is different in different interpretations) that yields a unique solution to any stochastic initial value problem for each possible realization of this underlying set of Wiener processes. A Wiener process $W(t)$ is a Gaussian Markov diffusion process for which the change in value $W(t) - W(t')$ between any two times t' and t has a mean and variance

$$\begin{aligned} \langle W(t) - W(t') \rangle &= 0 \\ \langle |W(t) - W(t')|^2 \rangle &= |t - t'| \end{aligned} \tag{2.225}$$

Wiener processes are continuous but not differentiable. To generate a particular time history for a set of L random variables, we use some set of M statistically independent Wiener processes $W_1(t), \ldots, W_M(t)$, which will herafter be labeled by indices $m, n, \ldots = 1, \ldots, M$. The number of Weiner processes M used to generate random processes for L coordinates need not always equal L.

A. Ito SDEs

We first consider a generic set of L Ito SDEs for some set of variables $X^1, \ldots, X^L$, which are specified by the standard notation

$$dX^\alpha = A^\alpha(X)dt + B^{\alpha m}(X)dW_m(t) \tag{2.226}$$

with $\alpha = 1, \ldots, L$, where $A^\alpha(X)$ and $B^{\alpha m}(X)$ are coefficients that are differentiable functions of the system coordinates. Because $W_m(t)$ is not differentiable, Eq. (2.226) is mathematically meaningless until one specifies an interpretation of the term involving the differential dW_m. In the Ito interpretation, the solution of Eq. (2.226), for a given set of initial conditions and a given set of Wiener processes, is given by the limit $\Delta t \to 0$ of a sequence of discrete processes with timesteps of length Δt, in which the change $\Delta X_n^\alpha = X_{n+1}^\alpha - X_n^\alpha$ in the value of $X_n^\alpha \equiv X^\alpha(t_n)$ during a step between times t_n and $t_{n+1} = t_n + \Delta t$ is given by

$$\Delta X_n^\alpha = A^\alpha(X_n)\Delta t + B^{\alpha m}(X_n)\Delta W_{m,n} \tag{2.227}$$

where $\Delta W_{m,n} \equiv W_m(t_{n+1}) - W_m(t_n)$. A unique solution of the SDE is defined by taking $\Delta t \to 0$, while calculating the increments $\Delta W_{m,n}$ from increasingly fine discretizations of the same set of random functions $W_1(t), \ldots, W_m(t)$. It is essential to the Ito interpretation that the functions $A^\alpha(X)$ and $B^{\alpha m}(X)$ in the underlying discrete process be evaluated using the value X_n obtained at the *beginning* of the timestep, as in an explicit forward Euler algorithm for numerical integration.

Expressions for the drift velocity and diffusivity of the solution of Ito SDE (2.226) may be obtained by calculating the first and second moments of ΔX^α for the underlying discrete process. Taking the average of ΔX^α in Eq. (2.227) immediately yields a drift velocity, as defined by Eq. (2.223), that is equal to the drift coefficient $A^\alpha(X)$ that appears in the Ito SDE:

$$V^\alpha(X) = A^\alpha(X) \tag{2.228}$$

By using Eq. (2.227) to evaluate the second moment $\langle \Delta X^\alpha \Delta X^\beta \rangle_0$, and taking the limit $\Delta t \to 0$, one finds a diffusivity

$$D^{\alpha\beta}(X) = \frac{1}{2} B^{\alpha m}(X) B^{\beta m}(X) \tag{2.229}$$

For $L > 1$, $B^{\alpha m}$ is generally not a unique function of the diffusivity $D^{\alpha\beta}$, as discussed further below.

1. *Summary of Properties*

The essential properties of an Ito SDE are:

1. *Fokker–Planck Equation.* The ensemble of trajectories generated by SDE (2.226) obeys a Fokker–Planck equation of the form given in Eq. (2.222), with a drift velocity $V^\alpha(X) = A^\alpha(X)$ given in Eq. (2.228) and the diffusivity given by Eq. (2.229).
2. *Change of Variables.* A change of coordinates from the variables $X^1, \ldots, X^L$ that appear in Eq. (226) to another set of L variables $\bar{X}^1(X), \ldots, \bar{X}^L(X)$ yields a set of L equivalent SDEs for the new coordinates, of the form

$$d\bar{X}^\beta = \bar{A}^\beta dt + \bar{B}^{\beta m} dW_m \tag{2.230}$$

with coefficients given by the transformation formulas

$$\bar{A}^\beta = \frac{\partial \bar{X}^\beta}{\partial X^\alpha} V^\alpha + \frac{\partial^2 \bar{X}^\beta}{\partial X^\alpha \partial X^\gamma} D^{\alpha\gamma} \tag{2.231}$$

$$\bar{B}^{\beta m} = \frac{\partial \bar{X}^\beta}{\partial X^\alpha} B^{\alpha m} \tag{2.232}$$

and a transformed diffusivity tensor

$$\bar{D}^{\gamma\delta} = \frac{\partial \bar{X}^\gamma}{\partial X^\alpha} D^{\alpha\beta} \frac{\partial \bar{X}^\delta}{\partial X^\beta} \tag{2.233}$$

The nontrivial transformation rule of Eq. (2.231) for the Ito drift coefficient (or the drift velocity) is sometimes referred to as the "Ito formula." Note that Eq. (2.166) is a special case of the Ito formula, as applied to a transformation from generalized coordinates to Cartesian bead coordinates. The method used above to derive Eq. (2.166) thus constitutes a poor person's derivation of the Ito formula, which is readily generalized to obtain the general transformation formula of Eq. (2.231).

Analysis of a physical problem involving Brownian motion can normally determine only the values of the coefficients V^α and $D^{\alpha\beta}$ that appear in the Fokker–Planck equation. The matrix of coefficients $B^{\alpha m}$ is required only to satisfy Eq. (2.229), which is generally not sufficient to determine a unique value for $B^{\alpha m}$. For $L > 1$ and $M = L$, there are generally an infinite number of ways of

decomposing $D^{\alpha\beta}$ as a matrix product of the form given in Eq. (2.229). For example, if $L = M$ and $D^{\alpha\beta}$ is symmetric and positive-definite, we could obtain uniquely defined values for $B^{\alpha m}$ by either arbitrarily requiring that $B^{\alpha m}$ be a real symmetric matrix, giving the symmetric "square root" of D^{ab}, or requiring that it be lower diagonal, giving a Cholesky decomposition. Ito SDEs based on different decompositions of the same diffusivity yield different trajectories but generate ensembles described by the same Fokker–Planck equation.

When formulating an SDE to produce a desired Fokker–Planck equation, one also has some freedom to choose the number of Wiener processes M used to generate random motion. The only general requirement is that M be taken large enough to guarantee that it possible to construct a matrix B^{am} that will yield the desired diffusivity D^{ab}. For a symmetric positive-definite diffusivity, any $M \geq f$ will satisfy this requirement. To describe the constrained motion of a system of N beads with f degrees of freedom, one might thus consider using either $M = f$ Wiener processes or $M = 3N$ processes. To construct purely Cartesian SDEs and simulation algorithms, however, it is convenient to use $M = 3N$ processes, each of which can be mentally associated with a single Cartesian coordinate of a single bead.

2. *Constrained Brownian Motion*

Constrained Brownian motion may be described in generalized cordinates as the solution of a set of f Ito SDEs for the soft generalized coordinates $q^1, \ldots, q^f$, of the form

$$dq^a = A^a(q)\, dt + B^{am}(q) dW_m(t) \tag{2.234}$$

with a drift coefficient $A^a(q) = V^a(q)$ and a matrix $B^{am}(q)$ that must be chosen so that Eq. (2.229) yields the diffusivity $D^{ab} = kTK^{ab}$ required by Eq. (2.158).

Alternatively, constrained Brownian motion of a set of pointlike particles may be described as a set of N vector SDEs for the bead positions, of the form

$$d\mathbf{R}^\mu = \mathbf{A}^\mu dt + \mathbf{B}^{\mu m} dW_m. \tag{2.235}$$

The coefficients $\mathbf{V}^\mu$ and $\mathbf{B}^{\mu n}$ may be chosen so as to yield the correct Cartesian diffusivity, or may be obtained by applying the Ito transformation formulae to the transformation from generalized to Cartesian coordinates. Either method yields a drift coefficient

$$\mathbf{A}^\mu = \mathbf{V}^\mu \tag{2.236}$$

equal to the Cartesian drift velocity given explicitly in Eq. (2.166), and a matrix $\mathbf{B}^{\mu m} \equiv \mathbf{a}_a^{\mu} B^{am}$ that yields the Cartesian diffusivity

$$\mathbf{D}^{\mu\nu} \equiv \frac{1}{2}\mathbf{B}^{\mu m} \cdot \mathbf{B}^{\nu m} = kT\mathbf{K}^{\mu\nu} \tag{2.237}$$

required by Eq. (2.167).

The Ito SDEs for either generalized or Cartesian coordinates can be numerically simulated by implementing the forward Euler timestepping algorithm used to define an Ito SDE in Eq. (2.226). Calculation of the coefficient B^{am} or $\mathbf{B}^{\mu m}$ can be accomplished by carrying out Cholesky decomposition of the corresponding tensor K^{ab} or $\mathbf{K}^{\mu\nu}$ [29]. Implementation of any integration scheme in generalized coordinates requires a calculation of the elements of the generalized forces and constrained mobility tensor in the chosen system of coordinates, which can become complicated. Implentation of the forward Euler algorithm in either generalized or Cartesian coordinates also requires a potentially costly evalution of a term in the drift velocity proportional to the divergence $\frac{\partial K^{ab}}{\partial q^b}$ or $\frac{\partial}{\partial \mathbf{R}^{\nu}} \cdot \mathbf{K}^{\nu\mu}$ of the constrained mobility in the chosen system of coordinates. The constrained mobility generally has a complex dependence on coordinates in either type of coordinate system, even in the absence of hydrodynamic interactions. Because there exist other algorithms that avoid the need to evaluate sums of derivatives of the constrained mobility, this forward Euler algorithm is generally a poor choice for the simulation of a constrained system.

The simple Cartesian Euler algorithm is, however, useful for simulating some common models of unconstrained systems of point particles for which the divergence of the unconstrained mobility $\mathbf{H}^{\mu\nu}$ vanishes. In the simple cases of free draining unconstrained models, such as the Rouse model, and of models with equilibrium preaveraged hydrodynamic interactions, such as the Zimm model, $\mathbf{H}^{\mu\nu}$ is approximated by a coordinate-independent tensor, and thus has no divergence. In addition, hydrodynamic interactions between pointlike beads are typically described by either the Oseen or Rotne–Prager–Yamakawa tensor, both of which have a vanishing divergence as a result of the assumed incompressibility of the solvent. The use of the Euler algorithm to describe unconstrained systems of hydrodynamically interacting particles has been discussed in detail by Ermak and McCammon [29].

B. Stratonovich SDEs

The Stratonovich interpretation of a generic set of L SDEs driven by M Wiener processes will be indicated in what follows by the notation

$$dX^{\alpha} = A^{\alpha}(X)\, dt + B^{\alpha m}(X) \circ dW_m \tag{2.238}$$

The notation "$\circ$" (the "Stratonovich circle") is used to distinguish this from the corresponding set of Ito SDEs. The Stratonovich interpretation of such a set of equations may be defined by either of two limiting procedures, which have been shown to yield equivalent limits, and are discussed separately below:

1. *Limit of a Discrete Process*

The solution of SDE (2.238) was originally defined by Stratonovich [30] as the limit $\Delta t \to 0$ of a sequence of discrete Markov processes, for which

$$\Delta X_n^\alpha = A^\alpha(X_n)\Delta t + B^{\alpha m}\left(\frac{X_n + X_{n+1}}{2}\right)\Delta W_m \tag{2.239}$$

Note that, in this interpretation, $B^{\alpha m}$ must be evaluated at a position midway between X_n and X_{n+1}, as in an implicit midstep algorithm for numerical integration, rather than at the position obtained at the beginning of the step, as in the Ito interpretation.

The drift velocity and diffusivity for a Stratonovich SDE may be obtained by using Eq. (2.239) to calculate the first and second moments of ΔX^α to an accuracy of $\mathcal{O}(\Delta t)$. To calculate the drift velocity, we evaluate the average of the RHS of Eq. (2.244) for ΔX^α. To obtain the required accuracy of $\mathcal{O}(\Delta t)$, we must Taylor expand the midpoint value of $B^{\alpha m}$ that appears in Eq. (2.244) to first order in ΔX^β about its value at the initial position X_n, giving the approximation

$$\langle \Delta X_n^\alpha \rangle_0 \simeq A^\alpha \Delta t + \left\langle \left[B^{\alpha m} + \frac{1}{2}\Delta X_n^\beta \frac{\partial B^{\alpha m}}{\partial X^\beta} \right] \Delta W_{m,n} \right\rangle_0 \tag{2.240}$$

in which A^α, $B^{\alpha m}$ and $\partial B^{\alpha m}/\partial X^\beta$ are all evaluated at the initial position X_n. The contributions $\langle B^{\alpha m}(X_n)\Delta W_{m,n}\rangle_0$ vanishes, because $\langle \Delta W_{m,n}\rangle = 0$. To evaluate the term involving $\partial B^{\alpha m}/\partial X^\beta$, we may approximate ΔX^β inside the average value by the approximation

$$\Delta X_n^\beta \simeq B^{\beta m}(X_n)\Delta W_{m,n} \tag{2.241}$$

which captures the dominant $\mathcal{O}(\sqrt{\Delta t})$ fluctuations in ΔX_n^α, while neglecting all $\mathcal{O}(\Delta t)$ contributions. Using approximation (2.241) for ΔX_n^α within the RHS of Eq. (2.240), while using Eq. (2.225) for the variance of $\Delta W_{m,n}$, yields an average value

$$\langle \Delta X_n^\alpha \rangle_0 \simeq \left[A^\alpha + \frac{1}{2} B^{\beta m} \frac{\partial B^{\alpha m}}{\partial X^\beta} \right] \Delta t \tag{2.242}$$

and a corresponding the drift velocity

$$V^\alpha = A^\alpha + \frac{1}{2} B^{\beta m} \frac{\partial B^{\alpha m}}{\partial X^\beta} \tag{2.243}$$

Note that for a Stratonovich SDE, unlike an Ito SDE, the drift velocity V^α generally differs from the drift coefficient A^α that appears in the SDE.

To calculate $\langle \Delta X^\alpha \Delta X^\beta \rangle_0$ to an accuracy of $\mathcal{O}(\Delta t)$, we need only the $\mathcal{O}(\sqrt{\Delta t})$ approximation of Eq. (2.241) for ΔX^α. This yields a diffusivity identical to that given for the Ito SDE in Eq. (2.229).

2. *Limit of an Ordinary Differential Equation*

The Stratonovich interpretation of Eq. (2.238) may also be obtained [31,32] from the white-noise limit of a sequence of stochastic ordinary differential equations (ODEs) of the form

$$\dot{X}^\alpha(t) = A^\alpha(X) + B^{\alpha m}(X) f_m(t) \tag{2.244}$$

in which $f_m(t)$ is one of a set of M statistically independent continuous random functions, indexed by $m = 1, \ldots, M$, with statistical properties

$$\langle f_m(t) \rangle = 0 \qquad \langle f_m(t) f_n(t') \rangle = \delta(t - t') \delta_{mn} \tag{2.245}$$

Here, $\delta(t - t')$ represents a sharply peaked but finite and differentiable autocorrelation function with a small but nonzero autocorrelation time, which is assumed to be an even function of $t - t'$. The Stratonovich interpretation is obtained in the limit of vanishing autocorrelation time.

To construct a sequence of ODEs whose solutions converge to that of a corresponding Stratonovich SDE driven by a known set of Weiner processes $W_1(t), \ldots, W_M(t)$, the random functions $f_m(t)$ may be taken as the time derivatives $f_m^{(\epsilon)}(t) \equiv dW_m^{(\epsilon)}(t)/dt$ of a sequence of differentiable functions $W_m^{(\epsilon)}(t)$ that approach the specified Weiner processes $W_m(t)$ in the limit $\epsilon \to 0$, so that

$$\lim_{\epsilon \to 0} \int_{t'}^{t} f_m^{(\epsilon)}(t'') dt'' = W_m(t) - W_m(t') \tag{2.246}$$

where ϵ is a parameter proportional to the autocorrelation time of $f_m^{(\epsilon)}(t)$. An ϵ-smoothed Weiner process $W_m^{(\epsilon)}(t)$ may be constructed [32] by convoluting $W_m(t)$ with a normalized smoothing function of the form $\epsilon^{-1} F(|t - t'|/\epsilon)$, with $\int dx F(x) = 1$, that "smears" the values of $W_m(t)$ over a range $|t - t'| \lesssim \epsilon$.

To calculate the drift velocity and diffusivity for such a process, we imagine a discrete sequence of coordinates values $X_n^\alpha = X^\alpha(t_n)$ sampled at times $t_1, t_2, t_3, \ldots$ separated by Δt, and then take the limit $\Delta t \to 0$. Such a sequence could be generated by integrating Eq. (2.244) over each timestep to obtain the change ΔX_n^α for that step. Such a sequence will be approximately Markovian

when the autocorrelation time ϵ for the random force is much less than Δt. We thus consider a limiting process in which we first take the limit of vanishing autocorrelation time ϵ for $f_m(t)$, to obtain a Markov process, and only then take the limit of vanishing Δt. The change in $X^\alpha(t)$ during the course of a single timestep may be characterized by an increment

$$\Delta X^\alpha(t) \equiv \int_0^t dt' \, \dot{X}^\alpha(t') \tag{2.247}$$

for any $0 \leq t \leq \Delta t$, in which $\dot{X}^\alpha(t')$ is given by Eq. (2.244). To simplify notation, we set $t = 0$ at the beginning of the single timestep of interest.

To calculate $\Delta X^\alpha(t)$ to $\mathcal{O}(t)$, we may approximate $A^\alpha(t')$ by its value at $t = 0$ in the drift term, but must expand $B^{\alpha m}(t')$ to linear order in $\Delta X^\gamma(t')$ around its $t = 0$ value. This yields the $\mathcal{O}(t)$ approximation

$$\Delta X^\alpha(t) \simeq A^\alpha t + \int_0^{t'} dt' \left\{ B^{\alpha m} + \Delta X^\beta(t') \frac{\partial B^{\alpha m}}{\partial X^\beta} \right\} f_m(t') \tag{2.248}$$

in which A^α, $B^{\alpha m}$, and $\partial B^{\alpha m}/\partial X^\beta$ are all evaluated at $t = 0$. The dominant $\mathcal{O}(\sqrt{t})$ contribution to Eq. (2.248) is given by the integral

$$\Delta X^\alpha(t) \simeq B^{\alpha m} \int_0^{t'} dt' f_m(t') \tag{2.249}$$

in which $B^{\alpha m}$ is evaluated at $t = 0$.

To calculate the drift velocity, we evaluate the average of Eq. (2.248), while approximating $\Delta X^\beta(t')$ within the RHS by Eq. (249). This yields

$$\langle \Delta X^\alpha(t) \rangle_0 \simeq A^\alpha t + B^{\beta n} \frac{\partial B^{\alpha m}}{\partial X^\beta} \int_0^t dt' \int_0^{t'} dt'' \, \langle f_m(t') f_n(t'') \rangle \tag{2.250}$$

To evaluate the double integral, we set

$$\int_0^{t'} dt'' \langle f_m(t') f_n(t'') \rangle = \frac{1}{2} \delta_{mn} \tag{2.251}$$

consistent with the Stratonovich interpretation of $\delta(t' - t'')$ as an even function of $t' - t''$. This yields

$$\langle \Delta X^\alpha(t) \rangle_0 \simeq \left[A^\alpha + \frac{1}{2} B^{\beta m} \frac{\partial B^{\alpha m}}{\partial X^\beta} \right] t \tag{2.252}$$

from which we immediately recover Eq. (2.243) for V^α.

To calculate the second moment $\langle \Delta X^\alpha \Delta X^\beta \rangle_0$ to $\mathcal{O}(t)$, it is sufficient to approximate $\Delta X^\alpha(t')$ by the dominant $\mathcal{O}(\sqrt{t})$ contribution given in Eq. (2.249). This yields

$$\langle \Delta X^\alpha(t) \Delta X^\beta(t) \rangle_0 = B^{\alpha m} B^{\beta m} t \tag{2.253}$$

consistent with Eq. (2.229), which yields the correct diffusivity for either an Ito or Stratonovich SDE.

3. *Summary of Properties*

The essential properties of a Stratonovich SDE, which may be derived from either of the two limiting processes presented above, are

1. *Relation to Ito SDE.* A Stratonovich SDE (2.238) is equivalent to an Ito SDE of the form given in Eq. (2.226), with the same coefficient $B^{\alpha m}$, but with an Ito drift coefficient equal to the drift velocity V^α given in Eq. (2.243). We may summarize this equivalence by the statement

$$B^{\alpha m} \circ dW_m \equiv B^{\alpha m} dW_m + \frac{1}{2} B^{\beta m} \frac{\partial B^{\alpha m}}{\partial X^\beta} dt \tag{2.254}$$

   where the notation $B^{\alpha m} dW_m$ (with no Stratonovich circle) indicates an Ito differential.

2. *Fokker–Planck Equation.* A Stratonovich SDE obeys a Fokker–Planck equation of the form given in Eq. (2.222) with the drift velocity $V^\alpha(X)$ given in Eq. (2.243), and the diffusivity given in Eq. (2.229). The resulting diffusion equation may be written in terms of the drift coefficient A^α as

$$\frac{\partial \mathscr{P}}{\partial t} = -\frac{\partial (A^\alpha \mathscr{P})}{\partial X^\alpha} + \frac{1}{2} \frac{\partial}{\partial X^\alpha} \left(B^{\alpha m} \frac{\partial (B^{\beta m} \mathscr{P})}{\partial X^\beta} \right) \tag{2.255}$$

   Note the differences between the form of the diffusion term that appears in this Stratonovich form of the diffusion equation and those that appear in the Ito (or forward Kolmogorov) form of Eq. (2.222) and in the physical diffusion equation of Eq. (2.78).

3. *Change of Variables.* A change of coordinates from the variables $X^1, \ldots, X^L$ that appear in Eq. (2.238) to another set of L variables $\bar{X}^1(X), \ldots, \bar{X}^L(X)$ yields an equivalent SDEs for the new coordinates, of the form

$$d\bar{X}^\gamma = \bar{A}^\gamma dt + \bar{B}^{\gamma m} \circ dW_m \tag{2.256}$$

with coefficients that transform as contravariant tensors, using the chain rule

$$\bar{A}^{\gamma} = \frac{\partial \bar{X}^{\gamma}}{\partial X^{\alpha}} A^{\alpha} \tag{2.257}$$

$$\bar{B}^{\gamma m} = \frac{\partial \bar{X}^{\gamma}}{\partial X^{\alpha}} B^{\alpha m} \tag{2.258}$$

Stratonovich SDEs, unlike Ito SDEs, may thus be manipulated using the familiar calculus of differentiable functions, rather than the Ito calculus. This property of a Stratonovich SDE may be shown to follow from the Ito transformation rule for the equivalent Ito SDE. It also follows immediately from the definition of the Stratonovich SDE as the white-noise limit of an ordinary differential equation, since the coefficients in the underlying ODE may be legitimately manipulated by the usual rules of calculus.

4. Constrained Brownian Motion

A set of Stratonovich SDEs for a constrained mechanical system may be formulated either as a set of f SDEs for the soft coordinates or as a corresponding set of $3N$ SDEs for the Cartesian bead positions. The Stratonovich SDEs for the generalized coordinates are of the form given in Eq. (2.238), with a drift coefficient

$$A^{a} = V^{a} - \frac{1}{2} B^{bm} \frac{\partial B^{am}}{\partial X^{b}} \tag{2.259}$$

chosen as to correspond to an Ito SDE with a drift coefficient V^{a}. Equivalent Stratonovich SDEs for the bead positions may be obtained either by applying a change of variables to Eq. (2.259) or, more directly, by simply choosing the coefficients in the Cartesian Stratonovich SDE so as to yield the correct Cartesian drift velocity and diffusity. Either method yields a set of SDEs of the form

$$d\mathbf{R}^{\mu} = \mathbf{A}^{\mu} dt + \mathbf{B}^{\mu m} \circ dW_{m} \tag{2.260}$$

with a Cartesian drift coefficient

$$\mathbf{A}^{\mu} = \mathbf{V}^{\mu} - \frac{1}{2} \mathbf{B}^{\nu m} \cdot \frac{\partial \mathbf{B}^{\mu m}}{\partial \mathbf{R}^{\nu}} \tag{2.261}$$

and with a matrix $\mathbf{B}^{\mu m} = \mathbf{a}_{a}^{\mu} B^{am}$ identitical to that in the corresponding Cartesian Ito SDE.

Note that, in either system of coordinates, the value of the Stratonovich drift coefficient required to produce a given drift velocity depends on derivatives of

the coefficients B^{am} or $\mathbf{B}^{\mu m}$, which are not uniquely determined by the diffusivity. The required value of the drift coefficient in the Stratonovich SDE thus depends on arbitrary details of how the random velocities are constructed, which are not determined by the physics of the underlying model. We show in the next subsection that the same arbitrariness appears in a different guise in the traditional interpretation of the Langevin equation.

The Stratonovich SDEs for either generalized or Cartesian coordinates could be numerically simulated by implementing the midstep algorithm of Eq. (2.238). Evaluation of the required drift velocities would, however, require the evaluation of sums of derivatives of B^{am} or $\mathbf{B}^{\mu n}$ whose values will depend on the decomposition of the mobility used to define these quantities. This provides a worse starting point for numerical simulation than the forward Euler algorithm interpretation.

C. Inertialess Langevin Equations

It is traditional in the physical science literature to represent Brownian motion in terms of Langevin equations, which are SDEs with rapidly varying random forces. These are usually interpreted as limits of corresponding ODEs, in the limit of a vanishing autocorrelation time for the random forces. The original Langevin equation was a second-order ODE, which was obtained by adding friction and a rapidly fluctuating random force to Newton's equation. Such an inertial Langevin equation yields non-differentiable velocities, but differentiable coordinate trajectories, which exhibit ballistic behavior over very short time scales and diffusive behavior over longer times. We focus here instead on the case of inertialess Langevin equations, which are first order differential equations in which terms proportional to the particle masses are neglected, and that produce purely diffusive coordinate trajectories.

We consider a generic set of L inertialess Langevin equations of the form

$$\dot{X}^{\alpha} = A^{\alpha}(X) + K^{\alpha\beta}(X)\eta_{\beta}(t) \tag{2.262}$$

where $A^{\alpha}(X)$ is a drift coefficient, $K^{\alpha\beta}(X)$ is a mobility tensor, and $\eta_{\beta}(t)$ is a random force. The statistical properties of the random force $\eta_{\beta}(t)$ are typically specified by requiring that its first and second moments satisfy conditions of the form

$$\langle \eta_{\alpha}(t) \rangle = 0 \tag{2.263}$$

$$\langle \eta_{\alpha}(t)\eta_{\beta}(t') \rangle = 2kTK^{-1}_{\alpha\beta}(t)\delta(t-t') \tag{2.264}$$

where $\delta(t-t')$ is interpreted as a sharply peaked but differentiable function. As expressed above, however, these conditions are mathematically ambiguous, because we have not specified either what ensemble of trajectories should be

used to calculate the average values indicated by the notation $\langle \cdots \rangle$, or precisely what value of X should be used to evaluate $K^{-1}_{\alpha\beta}(X(t))$ on the RHS of Eq. (2.264). This ambiguity may be removed by instead requiring that

$$\langle \eta_\alpha(t) \rangle_t = 0 \tag{2.265}$$

$$\langle \eta_\alpha(t)\eta_\beta(t') \rangle_t = 2kTK^{-1}_{\alpha\beta}(t)\delta(t-t') \tag{2.266}$$

The notation $\langle \cdots \rangle_t$ is a generalization of the notation $\langle \cdots \rangle_0$ introduced previously, and represents a conditional average for an ensemble of trajectories for which the system coordinates have a known set of values at the specified time t, but a distribution of values at any $t' \neq t$. The distribution of values of $X(t')$ at $t' \neq t$ may be generated by integrating the SDE forward (or backward) in time from the specified initial (or final) value X, using different realizations of the random force to generate different trajectories. We will show in what follows that conditions (2.265) and (2.266) give a description of the statistical properties of the random forces that, while not ambiguous, is incomplete, insofar as it is found to contain insufficient information to uniquely determine the value of the drift velocity that appears in the corresponding Fokker–Planck equation.

The preceding formulation of the Langevin equation requires that the mobility tensor $K^{\alpha\beta}(X)$ be invertible, in order for the friction tensor $K^{-1}_{\alpha\beta}(X)$ used in Eq. (2.266) to exist. The study of constrained systems will, however, force us to consider sets of SDE for which the mobility tensor is singular. The mobility of a constrained system of N beads with f unconstrained degrees of freedom will generally be nonsingular when expressed as an $f \times f$ matrix in the soft subspace, as required for the formulation of the problem as a set of f SDEs for the soft generalized coordinates. The same mobility will be singular, however, when viewed as a $3N \times 3N$ matrix in the space of Cartesian bead coordinates. In this representation, the constrained mobility has a K-dimensional null space, corresponding to the hard subspace, since $\mathbf{K}^{\mu\nu} \cdot \mathbf{n}^i_\nu = 0$ for all $i = 1, \ldots, K$.

In the case of a singular mobility tensor, we will replace condition (266) by the weaker condition

$$\langle \eta_\alpha(t)\eta_\beta(t') \rangle_t = 2kTZ_{\alpha\beta}(t)\delta(t-t') \tag{2.267}$$

in which the force variance tensor $Z_{\alpha\beta}(X)$ is required to satisfy the condition

$$K^{\alpha\delta} = K^{\alpha\beta}Z_{\beta\gamma}K^{\gamma\delta} \tag{2.268}$$

This requires that $Z_{\alpha\beta}(X) = K^{-1}_{\alpha\beta}(X)$ if $K^{\alpha\beta}(X)$ is invertible, but requires only that the projection of $Z_{\alpha\beta}(X)$ onto the nonnull subspace equal the inverse of $K^{\alpha\beta}$

within this subspace when $K^{\alpha\beta}$ is singular. This weaker condition is found to be necessary and sufficient to obtain the desired diffusivity.

The interpretation of the Langevin equation presents conceptual difficulties that are not present in the Ito and Stratonovich interpretation. These difficulties are the result of the fact that the probability distribution for the random force $\eta_\beta(t)$ cannot be fully specified a priori when the diffusivity and friction tensors are functions of the system coordinates. The resulting dependence of the statistical properties of the random forces on the system's trajectories is not present in the Ito and Stratonovich interpretations, in which the randomness is generated by standard Wiener processes $W_m(t)$ whose complete probability distribution is known *a priori*.

1. *Relation to Stratonovich SDE*

A completely unambiguous formulation of the Langevin equation may, however, be constructed by relating the random Langevin forces to random functions $f_m(t)$ of the type used in our discussion of the Stratonovich SDE, by taking

$$\eta_\beta(t) = \sqrt{2kT}C_\beta^m(X(t))f_m(t) \tag{2.269}$$

where $C_\beta^m(X)$ is a matrix of coefficients chosen such that

$$Z_{\alpha\beta}(X) \equiv C_\alpha^m(X)C_\beta^m(X) \tag{2.270}$$

where $Z_{\alpha\beta}$ satisfies Eq. (2.268). This prescription is easily shown to yield random forces that obeys conditions (2.265) and (2.266).

When supplemented by Eq. (2.269) for $\eta_\beta(t)$, the Langevin equation becomes equivalent to a standard Stratonovich SDE with a drift coefficient A^α and a coefficient

$$B^{\alpha m} = \sqrt{2kT}K^{\alpha\beta}C_\beta^m \tag{2.271}$$

The drift velocity may then be derived by using Eq. (2.243) for the drift velocity of a Stratonovich SDE. We consider the cases of singular and nonsingular mobility matrices separately.

In the case of an invertible mobility matrix, expanding the required derivative of the matrix product on the RHS of Eq. (271) yields a drift velocity

$$V^\alpha = A^\alpha + kT\left(\frac{\partial K^{\beta\alpha}}{\partial X^\beta} + C_\delta^m K^{\delta\gamma}\frac{\partial C_\beta^m}{\partial X^\gamma}K^{\beta\alpha}\right) \tag{2.272}$$

Note that the divergence of $kTK^{\alpha\beta}$ in Eq. (2.272) also appears in Eq. (2.157) for the desired drift velocity V^α. The appearance of this term is thus a desirable

feature of the traditional interpretation of the Langevin equation. The term involving derivatives of C is, however, both undesirable, since it does not appear in Eq. (2.157), and arbitrary, since its value depends on the arbitrary form chosen for the matrix $C^m_\beta(X)$, which is not a unique function of the diffusivity.

In the case of a singular mobility, we obtain

$$V^\alpha = A^\alpha + kT\left(\bar{P}^\gamma_\beta \frac{\partial K^{\beta\alpha}}{\partial X^\gamma} + C^m_\delta K^{\delta\gamma}\frac{\partial C^m_\beta}{\partial X^\gamma}K^{\beta\alpha}\right) \tag{2.273}$$

where

$$\bar{P}^\alpha_\beta \equiv K^{\alpha\gamma}Z_{\gamma\beta} \tag{2.274}$$

The quantity $\bar{P}^\alpha_\beta$ is a projection tensor, which reduces to the identity δ^α_β in the case of an invertible mobility matrix, and which is always idempotent, since

$$\bar{P}^\alpha_\beta \bar{P}^\beta_\gamma = \bar{P}^\alpha_\gamma \tag{2.275}$$

as a consequence of condition (2.268) for $Z_{\alpha\beta}$. It will be confirmed in what follows that the Cartesian representation of this quantity for a constrained system of point particles is indeed a generalized projection tensor of the type introduced in Section VIII. The Langevin equation for a system with a singular mobility thus yields a drift velocity that contains a projected divergence of the diffusivity, in which the form of the projection operator depends on the form chosen for the variance $Z_{\alpha\beta}$ of the random Langevin forces.

2. *Drift and Diffusivity*

We now instead calculate the drift velocity and diffusivity by directly integrating the traditional formulation of the Langevin equation in terms of random forces, and compare the results to those obtained above by rewriting the Langevin equation as a standard Stratonovich SDE. As in the analysis of the Stratonovich SDE, we calculate the first and second moments of an increment $\Delta X^\alpha(t) = X^\alpha(t) - X^\alpha(0)$ by integrating Eq. (2.262) from a known initial condition at $t = 0$.

To approximate the random quantity $\Delta X^\alpha(t)$ to $\mathcal{O}(t)$, we use Langevin Eq. (2.262) in integral (2.247), and expand $K^{\alpha\beta}(X(t'))$ to first order in $\Delta X^\gamma(t')$ around its value at $t = 0$. This yields the $\mathcal{O}(t)$ approximation

$$\Delta X^\alpha(t) \simeq A^\alpha t + \int_0^{t'} dt' \left\{K^{\alpha\beta} + \Delta X^\gamma(t')\frac{\partial K^{\alpha\beta}}{\partial X^\gamma}\right\}\eta_\beta(t') \tag{2.276}$$

in which A^α, $K^{\alpha\beta}$, and $\partial K^{\alpha\beta}/\partial X^\gamma$ are all evaluated at $t = 0$. The dominant $\mathcal{O}(\sqrt{t})$ contribution to Eq. (2.248) is given by

$$\Delta X^\alpha(t) \simeq K^{\alpha\beta} \int_0^{t'} dt' \, \eta_\beta(t') \tag{2.277}$$

where $K^{\alpha\beta}$ is evaluated at $t = 0$.

To calculate the diffusivity, we may use the $\mathcal{O}(\sqrt{t})$ approximation of Eq. (2.277) for $\Delta X^\alpha(t')$ to calculate the moment

$$\langle \Delta X^\alpha(t) \Delta X^\beta(t) \rangle_0 \simeq K^{\alpha\gamma} K^{\beta\delta} \int_0^t dt' \int_0^t dt'' \langle \eta_\gamma(t') \eta_\delta(t'') \rangle_0 \tag{2.278}$$

Taking

$$\lim_{t\to 0} \frac{1}{t} \int_0^t dt' \int_0^t dt'' \langle \eta_\alpha(t') \eta_\beta(t'') \rangle_0 = 2kTZ_{\alpha\beta}(0) \tag{2.279}$$

immediately yields the standard result $D^{\alpha\beta} = kTK^{\alpha\beta}$, for either singular or nonsingular mobility.

To evaluate the drift velocity, we take the average of Eq. (2.276), while using (2.277) for $\Delta X^\gamma(t')$ within the last term on the RHS. To evaluate this last term, we take

$$\lim_{t\to 0} \frac{1}{t} \int_0^t dt' \int_0^{t'} dt'' \langle \eta_\alpha(t') \eta_\gamma(t'') \rangle_0 = kTZ_{\alpha\beta}(0) \tag{2.280}$$

consistent with the use of a Stratonovich interpretation of the integral $\int_0^{t'} dt''$ $\delta(t' - t'') = \frac{1}{2}$. This yields a drift velocity

$$V^\alpha = A^\alpha + K^{\alpha\beta} \overline{\langle \eta_\beta \rangle}_0 + kT \frac{\partial K^{\beta\alpha}}{\partial X^\beta} \tag{2.281}$$

in the case of a nonsingular mobility, or

$$V^\alpha = A^\alpha + K^{\alpha\beta} \overline{\langle \eta_\beta \rangle}_0 + kT \bar{P}^\gamma_\beta \frac{\partial K^{\beta\alpha}}{\partial X^\gamma} \tag{2.282}$$

in the general case. Here and in what follows, we use the notation

$$\overline{\langle \eta_\beta \rangle}_0 \equiv \lim_{t\to 0} \frac{1}{t} \int_0^t dt' \langle \eta_\beta(t') \rangle_0 \tag{2.283}$$

to indicate the ensemble and time average of the random force η_β over an infinitesimal time interval. This quantity will be referred to as a "bias" in the random Langevin force.

3. *Force Bias*

A naive application of Eq. (2.263) might suggest that the force bias $\overline{\langle \eta_\beta \rangle}_0$ must vanish. One might suppose that the integrand in the RHS of Eq. (2.283) must vanish for all t' as a result of Eq. (2.263), and thus that the integral must also vanish. Neglect of the term arising from the force bias in Eq. (2.282) would yield a convenient expression for the drift velocity, in which the quantity $kT\frac{\partial K^{\alpha\beta}}{\partial X^\beta}$, which also appears in the desired expression for V^α, appears automatically.

The supposition that $\overline{\langle \eta_\beta \rangle}_0$ must vanish is incorrect. The problem with the argument presented above is that it is based on Eq. (2.263), which is ambiguous unless supplemented by a specification of the ensemble used to define the average value of η_β. The unambiguous condition given in Eq. (2.265), however, requires only that the integrand $\langle \eta_\beta(t') \rangle_0$ in Eq. (2.283) vanish at $t' = 0$, and not at any $t' \neq 0$, and thus does not require the integral to vanish.

The fact that $\overline{\langle \eta_\beta \rangle}_0$ need not vanish may be demonstrated by using prescription (2.269) for $\eta_\beta(t)$ to calculate this quantity. By substituting Eq. (2.269) into definition (2.283), and expanding $C^m_\beta(t')$ to first order in $\Delta X^\gamma(t')$ about its $t = 0$ value, we obtain

$$\overline{\langle \eta_\beta \rangle}_0 = \lim_{t\to 0} \frac{1}{t} \int_0^{t'} dt' \left\{ C^m_\beta + \Delta X^\gamma(t') \frac{\partial C^m_\beta}{\partial X^\gamma} \right\} f_m(t') \tag{2.284}$$

where C^m_β and $\partial C^m_\beta / \partial X^\gamma$ are evaluated at $t = 0$. Evaluating the average of the second term on the RHS then yields a bias

$$\overline{\langle \eta_\beta \rangle}_0 = C^m_\delta K^{\delta\gamma} \frac{\partial C^m_\beta}{\partial X^\gamma} \tag{2.285}$$

whose value depends on the spatial derivatives of $C^m_\beta(X)$.

Substitution of Eq. (2.285) into Eq. (2.282) produces an expression for V^α identical to that given in Eq. (2.273), which was obtained by using the Stratonovich interpretation of the Langevin equation. The last term in Eq. (2.273) may thus be interpreted, in the traditional formulation of the Langevin equation, as a drift velocity arising from the bias $\overline{\langle \eta_\beta \rangle}_0$ in the random force. Inclusion of a force bias in the Langevin equation is thus found to be necessary to maintain equivalence between the Langevin and Stratonovich SDEs. It thus must be included to produce an SDE whose coefficients, like those of a Stratonovich SDE, can be manipulated according to the usual chain rule of calculus.

A deeper argument for the existence of a nonzero force bias may be obtained by considering how the force bias $\overline{\langle \eta_\alpha \rangle}_0$ transforms under an invertible coordinate transformation from a set of L coordinates $X^1, \ldots, X^L$ to a set $\bar{X}^1, \ldots, \bar{X}^L$. Such a transformation induces a trivial tensor transformation for the instantaneous force $\eta_\beta(t)$. We show in the Appendix, Section H, by evaluating the time and ensemble average of the instantaneous force over a short time interval, that, in the case of a nonsingular mobility matrix, such a transformation creates a transformed force bias

$$\overline{\langle \bar{\eta}_\alpha \rangle}_0 = \frac{\partial X^\beta}{\partial \bar{X}^\alpha} \overline{\langle \eta_\beta \rangle}_0 - kT \frac{\partial \ln J}{\partial \bar{X}^\alpha} \tag{2.286}$$

in which J is the determinant of the Jacobian matrix

$$J^\alpha_\beta \equiv \frac{\partial \bar{X}^\alpha}{\partial X^\beta} \tag{2.287}$$

for the transformation from X to $\bar{X}$. The existence of the second term on the RHS of Eq. (2.286) indicates that the force bias (unlike the instantaneous force) does not transform like a covariant tensor, and so cannot vanish in an arbitrary system of coordinates. A generalization of this result to the case of a constrained system with a singular mobility is given below, where we relate the bias in the Cartesian random forces for a constrained system to the bias in the corresponding generalized random forces.

4. Constrained Motion—Cartesian Coordinates

The inertialess Langevin equation for the Cartesian bead positions of a constrained system may be formulated as a limit of a set of ODEs containing rapidly varying constraint forces, which must be chosen so as keep the instantaneous bead velocities always tangent to the constraint surface. We consider a Langevin equation

$$\dot{\mathbf{R}}^\mu = \mathbf{H}^{\mu\nu} \cdot \left[-\frac{\partial U_{\text{eff}}}{\partial \mathbf{R}^\nu} - \mathbf{n}^i_\nu \lambda_i + \mathbf{F}^{(\text{f})}_\mu + \mathbf{F}^{(\text{c})}_\mu + \boldsymbol{\eta}_\mu \right] \tag{2.288}$$

in which $U_{\text{eff}} \equiv U - kT \ln \sqrt{W}$ is the effective potential energy defined in Eq. (2.178), $\boldsymbol{\eta}_\mu$ is a finite continuous random force, and $\lambda_1, \ldots, \lambda_K$ are instantaneous constraint forces. The force $\mathbf{F}^{(\text{c})}_\mu$ is a "correction force" whose form will be chosen so as to produce the desired Cartesian drift velocity. The values of the constraint forces may be determined by requiring that

$$0 = \dot{c}^i = \mathbf{n}^i_\mu \cdot \dot{\mathbf{R}}^\mu \tag{2.289}$$

for all $i = 1, \ldots, K$ at each instant of time. By repeating the procedure used to remove constraint forces from the effective Cartesian force balance in Section VI, we find that the instantaneous tensions obey a system of equations

$$\hat{H}^{ij}\lambda_j = \mathbf{n}^i_\mu \cdot \mathbf{H}^{\mu\nu} \cdot \left[-\frac{\partial U_{\text{eff}}}{\partial \mathbf{R}^\nu} + \mathbf{F}^{(\text{f})}_\mu + \mathbf{F}^{(\text{c})}_\mu + \boldsymbol{\eta}_\mu \right] \tag{2.290}$$

Substituting these constraint forces back into Eq. (2.288) then yields the alternative form

$$\dot{\mathbf{R}}^\mu = \mathbf{A}^\mu + \mathbf{K}^{\mu\nu} \cdot \boldsymbol{\eta}_\nu \tag{2.291}$$

where

$$\mathbf{A}^\mu = \mathbf{K}^{\mu\nu} \cdot \left[-\frac{\partial U_{\text{eff}}}{\partial \mathbf{R}^\nu} + \mathbf{F}^{(\text{f})}_\nu + \mathbf{F}^{(\text{c})}_\nu \right] \tag{2.292}$$

is a Cartesian drift coefficient. The random forces are taken to have statistical properties

$$\langle \boldsymbol{\eta}_\mu(t) \rangle_t = 0 \tag{2.293}$$

$$\langle \boldsymbol{\eta}_\mu(t) \boldsymbol{\eta}_\nu(t') \rangle_t = 2kT\mathbf{Z}_{\mu\nu}(t)\delta(t - t') \tag{2.294}$$

where $\mathbf{Z}_{\mu\nu}(t)$ is a positive-definite symmetric tensor that is required to satisfy

$$\mathbf{K}^{\lambda\rho} = \mathbf{K}^{\lambda\mu} \cdot \mathbf{Z}_{\mu\nu} \cdot \mathbf{K}^{\nu\rho} \tag{2.295}$$

in order to obtain the correct diffusivity. Equation (2.295) is equivalent to a requirement that the projections of $\mathbf{Z}_{\mu\nu}$ and $\boldsymbol{\zeta}_{\mu\nu}$ onto the soft subspace be equal, that is, that $\tilde{\zeta}_{ab} = \mathbf{a}^\mu_a \cdot \mathbf{Z}_{\mu\nu} \cdot \mathbf{a}^\nu_b$ for all $a, b = 1, \ldots, f$.

The Cartesian drift velocity and diffusivity may be obtained by applying the general analysis to this system of Cartesian SDEs, which contains a singular mobility $\mathbf{K}^{\mu\nu}$. This yields a diffusivity $\mathbf{D}^{\mu\nu} = kT\mathbf{K}^{\mu\nu}$, and a drift velocity

$$\mathbf{V}^\mu = \mathbf{A}^\mu + kT\,\bar{\mathbf{P}}_\nu{}^{,\lambda} : \frac{\partial \mathbf{K}^{\nu\mu}}{\partial \mathbf{R}^\lambda} + \mathbf{K}^{\mu\nu} \cdot \overline{\langle \boldsymbol{\eta}_\nu \rangle_0} \tag{2.296}$$

where

$$\overline{\langle \boldsymbol{\eta}_\nu \rangle_0} \equiv \lim_{t \to 0} \frac{1}{t} \int_0^t dt' \, \langle \boldsymbol{\eta}_\nu(t') \rangle_0 \tag{2.297}$$

is a bias in the Cartesian random force, and $\bar{\mathbf{P}}_{\nu}{}^{,\lambda} \equiv (\bar{\mathbf{P}}^{\lambda}{}_{,\nu})^T$ is the transpose of a projection tensor

$$\bar{\mathbf{P}}^{\lambda}{}_{,\nu} \equiv \mathbf{K}^{\lambda\mu} \cdot \mathbf{Z}_{\mu\nu} \tag{2.298}$$

It is straightforward to show that $\bar{\mathbf{P}}^{\lambda}{}_{,\nu}$ fits the definition of a generalized projection tensor given in Section VIII, by using Eq. (2.295) to show that $\bar{\mathbf{P}}^{\lambda}{}_{,\nu}$ is idempotent, and using expansion (2.136) for $\mathbf{K}^{\lambda\mu}$ and the relationship $K^{-1}_{ab} = \mathbf{a}^{\mu}_{a} \cdot \mathbf{Z}_{\mu\nu} \cdot \mathbf{a}^{\mu}_{b}$ to show that $\bar{\mathbf{P}}^{\lambda}{}_{,\nu} \cdot \mathbf{a}^{\nu}_{a} = \mathbf{a}^{\lambda}_{a}$ and that $\mathbf{n}^{i}_{\lambda} \cdot \bar{\mathbf{P}}^{\lambda}{}_{,\nu} = 0$.

Note that the form of the projection tensor $\bar{\mathbf{P}}^{\lambda}_{,\nu}$ depends on the form chosen for the hard components of $\mathbf{Z}_{\mu\nu}$. Specifically, values of the mixed soft–hard components of $\bar{\mathbf{P}}^{\lambda}{}_{,\mu}$, which are not specified by the definition of a generalized projection tensor given in Section VIII, are determined in this context by the values chosen for the mixed components of $\mathbf{Z}_{\mu\nu}$, which specify correlations between hard and soft components of the random forces that are not specified by Eq. (2.295) for $\mathbf{Z}_{\mu\nu}$.

An expression for the correction force $\mathbf{F}^{(\mathrm{c})}_{\nu}$ in Eq. (2.292) may be obtained by comparing Eq. (2.296) to Eq. (2.202) for the desired drift velocity $\mathbf{V}^{\mu}$, while taking the generalized projection tensor in Eq. (2.202) to be that defined in Eq. (2.298). Both expressions for $\mathbf{V}^{\mu}$ contain identical terms involving a projected divergence of $\mathbf{K}^{\mu\nu}$, but the term arising from $\mathbf{F}^{(\mathrm{ps})}_{\nu}$ in Eq. (2.202) is absent from Eq. (2.296), while the term arising from $\overline{\langle \boldsymbol{\eta} \rangle_0}$ in Eq. (2.296) is absent from (2.202). Equating these two expressions thus yields a required correction force

$$\mathbf{F}^{(\mathrm{c})}_{\nu} = \mathbf{F}^{(\mathrm{ps})}_{\nu} - \overline{\langle \boldsymbol{\eta}_{\nu} \rangle_0} \tag{2.299}$$

in which the second term on the RHS is required to cancel the force bias in Eq. (2.296), and in which $\mathbf{F}^{(\mathrm{ps})}_{\nu}$ is the pseudoforce corresponding to the projection tensor defined in Eq. (2.298), which may be calculated by using the corresponding reciprocal vectors to evaluate Eq. (2.205).

The results given above are essentially identical to those obtained by Hinch [10] by a similar method, except for the fact that Hinch did not retain any of the terms involving the force bias $\overline{\langle \boldsymbol{\eta}_{\nu} \rangle_0}$, which he presumably assumed to vanish. An apparent contradiction in Hinch's results may be resolved by correcting his neglect of this bias. In a traditional interpretation of the Langevin equation as a limit of an underlying ODE, the bead velocities are rigorously independent of the hard components of the random forces, since the random forces in Eq. (2.291) appear contracted with $\mathbf{K}^{\mu\nu}$, which has nonzero components only in the soft subspace. Physically, the hard components of the random forces are instantaneously canceled by the constraint forces, and thus can have no effect

on the motion. Hinch distinguished between what we will call "unprojected random forces," with $\mathbf{Z}_{\mu\nu} = \boldsymbol{\zeta}_{\mu\nu}$, which contain hard components, and "projected random forces," for which the hard components are absent. A projected random force $\tilde{\boldsymbol{\eta}}_\mu(t)$ may be generated from a corresponding unprojected random force $\boldsymbol{\eta}_\mu(t)$ by contraction with the geometric projection tensor:

$$\tilde{\boldsymbol{\eta}}_\mu(t) = \tilde{\mathbf{P}}^\nu_\mu(t) \cdot \boldsymbol{\eta}_\nu(t) \tag{2.300}$$

Hinch's analysis yields a drift velocity given by Eq. (2.296) without the force bias term, which (as he notes on the top of p. 229) yields different results for projected and unprojected random forces. Hinch resolves this amibiguity by asserting at the outset of his analysis that the random forces should be taken to be projected forces: As he puts it, on p. 223, "Now there can be no components of the random forcing parallel to the constraints, because they would have no dynamical effect." With this choice, Hinch recovered the earlier result of Fixman [9] for the pseudoforce. The dependence of Hinch's results on the form chosen for the random forces is, however, inconsistent with a traditional interpretation of the Langevin equation, precisely because the hard components of the random forces *should* have no dynamical effect. We show in the Appendix, Section J that identical results for the drift velocity $\mathbf{V}^\mu$ are indeed obtained with projected and unprojected random forces related by Eq. (2.300), if one allows for the existence of a nonzero force bias in both cases. It is found that the value of this bias is generally changed by projection, and that the resulting difference between the values obtained for $\overline{\langle \boldsymbol{\eta}_\nu \rangle}_0$ and $\overline{\langle \tilde{\boldsymbol{\eta}}_\nu \rangle}_0$ exactly cancels the differences in drift velocity found by Hinch. Inclusion of a force bias is thereby shown to be *necessary* to obtain logically consistent results for the traditional interpretation of the constrained Langevin equation.

5. *Constrained Motion—Generalized Coordinates*

The first analysis of the constrained Langevin equation was given by Fixman [9], who worked primarily in generalized coordinates. In order to resolve a discrepancy between Fixman's results and those of Hinch [10], we now follow Fixman by considering a Langevin equation for the soft coordinates $q^1, \ldots, q^L$. We consider the Langevin equation

$$\dot{q}^a = K^{ab}\left[-\frac{\partial U_{\text{eff}}}{\partial q^b} + F_b^{(\text{f})} + F_b^{(\text{c})} + \eta_b \right] \tag{2.301}$$

that is obtained by a simple coordinate transformation of the Cartesian Langevin equation of Eq. (2.291). Equation (2.282) for the drift velocity of a set of

Stratonovich SDEs with a nonsingular mobility yields a drift velocity

$$V^a = K^{ab}\left[-\frac{\partial U_{\text{eff}}}{\partial q^b} + F_b^{(\text{f})} + F_b^{(\text{c})}\right] + K^{ab}\overline{\langle \eta_b \rangle}_0 + kT\frac{\partial K^{ab}}{\partial q^b} \tag{2.302}$$

in which $F_b^{(\text{c})}$ is an unspecified generalized correction force. Comparison of Eq. (2.302) to Eq. (2.157) for the desired drift velocity then yields a correction force

$$F_b^{(\text{c})} = kT\frac{\partial \ln \sqrt{g}}{\partial q^b} - \overline{\langle \eta_b \rangle}_0 \tag{2.303}$$

Note that, in this system of coordinates, the correction force includes a term involving the Jacobian of the transformation from generalized to Cartesian coordinates, which arises from the $\ln \sqrt{g}$ contribution to $\ln \psi_{\text{eq}}$ in Eq. (2.157) for V^a.

The subtle part of Fixman's calculation is his calculation of the relation between the bias $\overline{\langle \eta_b \rangle}_0$ in the generalized random force and that for an underlying Cartesian random force. Fixman calculates the drift velocity in generalized coordinates, but imagines that there exists an underlying Cartesian Langevin equation containing Cartesian random force vectors $\boldsymbol{\eta}_\mu$, to which the generalized random forces are related by the instantaneous transformation

$$\eta_b(t) \equiv \mathbf{a}_b^\mu(t) \cdot \boldsymbol{\eta}_\mu(t) \tag{2.304}$$

By expanding the basis vector $\mathbf{a}_b^\mu(t')$ to linear order in the displacement $\Delta q^a(t')$ from its value at $t = 0$, Fixman showed that

$$\overline{\langle \eta_b \rangle}_0 \simeq \lim_{t\to 0}\frac{1}{t}\int_0^t dt' \left\langle \left[\mathbf{a}_b^\mu + \Delta q^c(t')\frac{\partial \mathbf{a}_b^\mu}{\partial q^c}\right] \cdot \boldsymbol{\eta}_\mu(t') \right\rangle_0 \tag{2.305}$$

where $\mathbf{a}_b^\mu$ and its derivative are evaluated at $t = 0$. Averaging over the Cartesian noise then yields

$$\overline{\langle \eta_b \rangle}_0 \simeq \mathbf{a}_b^\mu \cdot \overline{\langle \boldsymbol{\eta}_\mu \rangle}_0 + \frac{\partial \mathbf{a}_b^\mu}{\partial q^c} \cdot \mathbf{Z}_{\mu\nu} \cdot \mathbf{a}_d^\nu K^{dc} \tag{2.306}$$

This equation agrees with Fixman's Eq. (3.26), except for the fact that Fixman, like Hinch, implicitly assumed that $\overline{\langle \boldsymbol{\eta}_\mu \rangle}_0 = 0$ for the Cartesian random forces, and so did not retain the first term on the RHS of Eq. (2.306). Fixman correctly emphasized, however, that the transformation from Cartesian to generalized

coordinates can generate a bias in the generalized random forces, given by the second term on the RHS of Eq. (2.306), even if (as he assumed) no such bias exists for the Cartesian random forces.

Equation (2.306) may be expressed more compactly by defining a set of reciprocal basis vectors

$$\bar{\mathbf{b}}^c_\mu \equiv \mathbf{Z}_{\mu\nu} \cdot \mathbf{a}^\nu_d K^{dc} \tag{2.307}$$

These are the reciprocal basis vectors corresponding to the generalized projection tensor $\bar{\mathbf{P}}^\mu{}_{,\nu} = \mathbf{K}^{\mu\lambda} \cdot \mathbf{Z}_{\lambda\nu}$ identified in Eq. (2.298). With this definition, we may write

$$\overline{\langle \eta_b \rangle}_0 \simeq \mathbf{a}^\mu_b \cdot \overline{\langle \boldsymbol{\eta}_\mu \rangle}_0 + kT \frac{\partial \mathbf{a}^\mu_b}{\partial q^c} \cdot \bar{\mathbf{b}}^c_\mu \tag{2.308}$$

In the Appendix, Section G, we prove that

$$\frac{\partial \mathbf{a}^\nu_b}{\partial q^c} \cdot \bar{\mathbf{b}}^c_\nu = \frac{\partial \ln \sqrt{g}}{\partial q^b} + \frac{\partial \mathbf{n}^i_\mu}{\partial q^b} \cdot \bar{\mathbf{m}}^\mu_i \tag{2.309}$$

for any valid system of reciprocal vectors $\bar{\mathbf{b}}^a_\nu$ and $\bar{\mathbf{m}}^\mu_i$. This theorem is the key to a correct treatment of the problem in generalized coordinates. Substituting Eq. (2.309) into Eq. (2.308) yields a force bias

$$\overline{\langle \eta_b \rangle}_0 \simeq \mathbf{a}^\mu_b \cdot \overline{\langle \boldsymbol{\eta}_\mu \rangle}_0 + kT \frac{\partial \ln \sqrt{g}}{\partial q^b} - F^{(\mathrm{ps})}_b \tag{2.310}$$

in which

$$F^{(\mathrm{ps})}_b \equiv -kT \frac{\partial \mathbf{n}^i_\mu}{\partial q^b} \cdot \bar{\mathbf{m}}^\mu_i \tag{2.311}$$

is a soft component of the Cartesian pseudoforce $\mathbf{F}^{(\mathrm{ps})}_\nu$ defined in Eq. (2.205). Note that Eq. (2.310) is a generalization of Eq. (2.286), which describes the transformation of the force bias for system with a nonsingular mobility matrix, and which is generalized here by the addition of a pseudoforce in order to correctly describe the transformation from Cartesian to generalized coordinates for a system with a singular mobility. Using Eq. (2.310) in Eq. (2.303) yields a total correction force

$$F^{(\mathrm{c})}_b = F^{(\mathrm{ps})}_b - \mathbf{a}^\mu_b \cdot \overline{\langle \boldsymbol{\eta}_\mu \rangle}_0 \tag{2.312}$$

This force is related to the Cartesian correction force of Eq. (2.299) by a trivial transformation $F_b^{(c)} = \mathbf{a}_b^\mu \cdot \mathbf{F}_\mu^{(c)}$, and so is completely equivalent to that obtained above by working in Cartesian coordinates.

Fixman [9] and Hinch [10], however, did not obtain fully consistent results. Fixman seems to have analyzed a Langevin equation with unprojected random forces [see Fixman's Eqs. (2.14) and (3.25)], but obtained an expression for the pseudoforce equal to that which Hinch (correctly) found only in the case of projected random forces. The pseudoforce reported by both authors is the metric force of Eq. (2.214), which is the pseudoforce corresponding to the geometric projection operator. We show in Section IX.E, where we consider different possible forms for $\mathbf{Z}_{\mu\nu}$ below that a Langevin equation with unprojected random forces actually requires the corrective pseudoforce corresponding to the dynamical projection operator, which may be calculated by using dynamical reciprocal vectors to evaluate the RHS of Eq. (2.205). The source of this discrepancy is traced in the Appendix, Section K to a subtle error in Fixman's use of differential geometry.

D. Kinetic SDEs

Statistical mechanics requires that Brownian motion yield a diffusion equation of the form given in Eq. (2.78), in which the diffusivity appears in a term of the form

$$\frac{\partial \mathscr{P}}{\partial t} = \cdots + \frac{\partial}{\partial X^\alpha}\left(D^{\alpha\beta}\frac{\partial \mathscr{P}}{\partial X^\beta}\right) \tag{2.313}$$

Neither the Ito nor the Stratonovich interpretation of an SDE leads naturally to a term of this form. The Ito interpretation yields a diffusion equation of the form given in Eq. (2.222), in which the diffusivity instead appears inside two derivatives, while the Stratonovich interpretation yields Eq. (2.255), in which $D^{\alpha\beta}$ is decomposed into two factors of B, one of which appears inside both derivatives and the other between them.

We now discuss an alternative interpretation of a set of SDEs that is designed so as to automatically generate the form of the diffusion equation required by statistical mechanics. Following a suggestion by Klimontovich [33], we will refer to this as a "kinetic" interpretation of the Langevin equation. The definition presented here is a slight generalization (generalized to the case of a singular mobility) of that given by Hütter and Öttinger [34], who formalized the earlier suggestion by Fixman [9] that the desired behavior could be obtained by the use of an appropriate midstep integration algorithm.

The kinetic interpretation of a set of L SDEs characterized by a diffusivity $D^{\alpha\beta} \equiv kTK^{\alpha\beta}$ will be specfied here by the notation

$$dX^\alpha = A^\alpha(X)\,dt + \sqrt{2kT}K^{\alpha\beta}(X) \diamond C_\beta^m(X)dW_m \tag{2.314}$$

in which the matrix $C^m_\beta(X)$ is required to satisfy Eqs. (2.270) and (2.268). The solution to such a set of kinetic SDEs is defined as the $\Delta t \to 0$ limit of a sequence of discrete processes in which

$$\Delta X^\alpha_n = A^\alpha(X_n)\Delta t + \sqrt{2kT}K^{\alpha\beta}\left(\frac{X_n + X_{n+1}}{2}\right)C^m_\beta(X_n)\,\Delta W_{m,n} \tag{2.315}$$

Here, we have borrowed Hütter and Öttinger's use of a "$\diamond$" symbol to indicate a kinetic interpretation of the stochastic term, but adopted a more explicit notation for its use. The $\diamond$ is used here to indicate that the function to its left should be evaluated at a midstep position, as in a Stratonovich SDE, but that the random quantity to the right of the diamond should be evaluated by evaluating the function $C^m_\beta(X)$ at the beginning of each timestep, as in an Ito SDE. This notation is similar to that used by Peters [13] to denote a "mixed" interpretation that is identical to the kinetic interpretation defined above, which Peters indicates by using a Stratonovich circle in the position where we use a diamond.

The preceding definition of a kinetic SDE reduces to that given by Hütter and Öttinger [34] in the case of an invertible mobility matrix $K^{\alpha\beta}$, for which Eq. (2.268) reduces to the requirement that $Z_{\alpha\beta} = K^{-1}_{\alpha\beta}$. In the case of a singular mobility, the present definition requires that the projection of $Z_{\alpha\beta}$ onto the nonnull subspace of K (corresponding to the soft subspace of a constrained system) equal the inverse of $K^{\alpha\beta}$ within this subspace, while leaving the components of $Z_{\alpha\beta}$ outside this subspace unspecified.

Equation (2.315) may be interpreted as a peculiar discretization of the Langevin equation, which is constructed so as to avoid the force bias that arises in the traditional interpretation. We identify random forces

$$\eta_{\alpha,n} \equiv \sqrt{2kT}C^m_\alpha(X_n)\frac{\Delta W_{m,n}}{\Delta t} \tag{2.316}$$

for timestep n, which may be shown to satisfy the conditions

$$\langle \eta_{\alpha,n}\rangle_0 = 0, \quad \langle \eta_{\alpha,n}\eta_{\beta,n'}\rangle_0 = \frac{2kT}{\Delta t}Z_{\alpha\beta}(X_n)\delta_{nn'} \tag{2.317}$$

in which $Z_{\alpha\beta}$ is evaluated at the beginning of each time step.

Using this definition, Eq. (2.315) may be rewritten as

$$\Delta X^\alpha_n = \left[A^\alpha(X_n) + K^{\alpha\beta}\left(\frac{X_n + X_{n+1}}{2}\right)\eta_{\beta,n}\right]\Delta t \tag{2.318}$$

The kinetic interpretation thus corresponds to a discretization of Langevin equation (2.262) in which the mobility is evaluated at a midstep position, as first suggested by Fixman [9], but in which the random force η_β is constructed at the

beginning of the timestep, with a variance determined by the value $Z_{\alpha\beta}(X_n)$ obtained at the beginning of the step. This differs from a true Stratonovich interpretation of the Langevin equation, which would require that we use midstep values of both the mobility $K^{\alpha\beta}(X)$ *and* the matrix $C^m_\alpha(X)$. In this discrete Stratonovich interpretation of the Langevin equation, it is the use of a midstep value of $C^m_\alpha(X)$ that causes the unwanted bias in the random forces.

1. *Drift and Diffusivity*

To evaluate the drift velocity, we take the average of Eq. (2.315) for ΔX^α, while Taylor-expanding the midpoint value of $D^{\alpha\beta}$ to first order in ΔX about its value at X_n. This yields

$$\langle \Delta X^\alpha_n \rangle_0 \simeq A^\alpha \Delta t + \left\langle \left[K^{\alpha\beta} + \frac{1}{2} \Delta X^\gamma \frac{\partial K^{\alpha\beta}}{\partial X^\gamma} \right] \eta_{\beta,n} \right\rangle_0 \Delta t \tag{2.319}$$

in which A^α, D^α, and $\partial D^{\alpha\beta}/\partial X^\gamma$ are all evaluated using the value X_n obtained at the beginning of the timestep. We then use Eq. (2.318) for ΔX^α_n and Eq. (2.317) for the variance of η, to show that

$$\langle \Delta X^\gamma_n \eta_\beta \rangle_0 \simeq 2kT \bar{P}^\gamma_\beta \tag{2.320}$$

to the required accuracy of $\mathcal{O}(\Delta t)$. Substituting this into Eq. (2.319) yields an average value

$$\langle \Delta X^\alpha_n \rangle_0 \simeq \left(A^\alpha + kT \bar{P}^\gamma_\beta \frac{\partial K^{\beta\alpha}}{\partial X^\gamma} \right) \Delta t \tag{2.321}$$

giving a drift velocity

$$V^\alpha = A^\alpha + kT \frac{\partial K^{\beta\alpha}}{\partial X^\beta} \tag{2.322}$$

in the case of a nonsingular mobility, or

$$V^\alpha = A^\alpha + kT \bar{P}^\gamma_\beta \frac{\partial K^{\beta\alpha}}{\partial X^\gamma} \tag{2.323}$$

in the general case of a singular mobility. The only difference between these results for the drift velocity and the corresponding results for the traditional interpretation of the Langevin equation is the absence in the kinetic interpretation of terms involving the Langevin force bias $\overline{\langle \eta_\beta \rangle}_0$. The calculation of the diffusivity is essentially identical to that for the Stratonovich SDE, and again yields the diffusivity $D^{\alpha\beta} = \frac{1}{2} B^{\alpha m} B^{\beta m}$ given in Eq. (2.229).

Using the fact that $K^{\alpha\beta} = \bar{P}^{\alpha}_{\gamma} K^{\gamma\beta}$, we may write (2.323) in the alternative form

$$V^{\alpha} = A^{\alpha} - K^{\alpha\beta} F^{(\mathrm{ps})}_{\beta} + kT \frac{\partial K^{\beta\alpha}}{\partial X^{\beta}} \tag{2.324}$$

where $F^{(\mathrm{ps})}_{\beta}$ is a pseudoforce that may be defined for any system of equations with a singular mobility matrix by the requirement

$$K^{\alpha\beta} F^{(\mathrm{ps})}_{\beta} = K^{\alpha\beta} \left(kT \frac{\partial \bar{P}^{\gamma}_{\beta}}{\partial X^{\gamma}} \right) \tag{2.325}$$

The term involving the pseudoforce in Eq. (2.324) may be compensated by the inclusion of a corresponding term (with a positive sign) in the expression chosen for A^{α}.

2. *Summary of Properties*

The essential properties of a kinetic SDE are

1. *Relation to Ito SDE.* Kinetic SDE (2.314) is equivalent to an Ito SDE with a drift coefficient A^{α} equal to the drift velocity given in Eq. (2.323), and with

$$B^{\alpha m} = \sqrt{2kT} K^{\alpha\beta} C^{m}_{\beta} \tag{2.326}$$

   This relationship may be summarized by the relation

$$\sqrt{2kT} K^{\alpha\beta} \diamond C^{m}_{\beta} dW_m \equiv B^{\alpha m} dW_m + \bar{P}^{\gamma}_{\beta} \frac{\partial D^{\beta\alpha}}{\partial X^{\gamma}} dt \tag{2.327}$$

   where $\bar{P}^{\gamma}_{\beta}$ is as defined by Eq. (2.274). This relation could be taken as a mathematically adequate definition of a kinetic SDE, although such a definition would, by itself, provide no guidance in the design of a corresponding integration algorithm.
2. *Fokker–Planck Equation.* The preceding identification of the kinetic SDE with an equivalent Ito SDE yields a Fokker–Planck equation of the desired form

$$\frac{\partial \mathscr{P}}{\partial t} = - \frac{\partial (A^{\alpha} \mathscr{P})}{\partial X^{\alpha}} + \frac{\partial}{\partial X^{\alpha}} \left(D^{\alpha\beta} \frac{\partial \mathscr{P}}{\partial X^{\beta}} \right) \tag{2.328}$$

   in the case of a nonsingular diffusivity $D^{\alpha\beta} = kTK^{\alpha\beta}$, and

$$\frac{\partial \mathscr{P}}{\partial t} = - \frac{\partial}{\partial X^{\alpha}} \left[\left(A^{\alpha} + \bar{P}^{\gamma}_{\beta} \frac{\partial D^{\beta\alpha}}{\partial X^{\gamma}} \right) \mathscr{P} \right] + \frac{\partial^2 (D^{\alpha\beta} \mathscr{P})}{\partial X^{\alpha} \partial X^{\beta}} \tag{2.329}$$

   in the case of a singular diffusivity.

3. *Change of Variables.* It is shown in the Appendix, Section I that, for a set of kinetic SDEs with an nonsingular mobility matrix, a transformation from the L variables $X^1, \ldots, X^L$ to another set of variables $\bar{X}^1(X), \ldots, \bar{X}^L(X)$ yields a transformed set of kinetic SDEs of the form

$$d\bar{X}^\gamma = \bar{A}^\gamma dt + \bar{B}^{\gamma m} \diamond dW_m \tag{2.330}$$

with transformed coefficients

$$\bar{A}^\gamma = \frac{\partial \bar{X}^\gamma}{\partial X^\alpha} A^\alpha - \bar{D}^{\gamma\alpha} \frac{\partial \ln J}{\partial \bar{X}^\alpha} \tag{2.331}$$

$$\bar{B}^{\gamma m} = \frac{\partial \bar{X}^\gamma}{\partial X^\alpha} B^{\alpha m} \tag{2.332}$$

where J is the determinant of the Jacobian matrix defined in Eq. (2.287).

Note that the term involving a derivative of $\ln J$ in Eq. (2.331) is identical to the velocity arising from the second term on the RHS of Eq. (2.286) for the transformed force bias in the traditional interpretation of the Langevin equation. The traditional interpretation of the Langevin equation yields a simple tensor transformation rule for the drift coefficient A^α, but also yields a contribution to Eq. (2.282) for the drift velocity V^α that is driven by the force bias. The kinetic interpretation yields an expression for the drift velocity from which the term involving the force bias is absent, but, correspondingly, yields a nontrivial transformation rule for the overall drift coefficient.

3. *Constrained Motion—Generalized Coordinates*

Constrained Brownian motion may be described in generalized coordinates by a set of f kinetic SDEs for the soft coordinates, of the form given in Eq. (2.314). The required drift coefficient is

$$A^a = K^{ab} \left[kT \frac{\partial \ln \psi_{\text{eq}}}{\partial q^b} + F_b^{(\text{f})} \right] \tag{2.333}$$

which easily shown to yield the drift velocity V^a given in Eq. (2.157). The matrix C_a^m must be chosen as to give $Z_{ab} = \tilde{\zeta}_{ab}$. Because the mobility matrix K^{ab} for this set of coordinates is generally nonsingular, no pseudoforce is required in this formulation; the form of the equations is the same as that for an unconstrained system, except for differences arising from different expressions for $\psi_{\text{eq}}(q)$.

It is interesting to consider how the RHS of Eq. (2.333) transforms under a transformation from a set of soft coordinates $q = \{q^1, \ldots, q^f\}$ to a different set

$\bar{q} = \{\bar{q}^1, \ldots, \bar{q}^f\}$. A nontrivial transformation rule is obtained for the derivative of $\ln \psi_{\text{eq}}$ because $\psi_{\text{eq}}(q)$ is not a scalar invariant, but a probability density, which transforms like an inverse volume element

$$\bar{\psi}_{\text{eq}}(\bar{q}) = J^{-1}\psi_{\text{eq}}(q) \tag{2.334}$$

in order that $\bar{\psi}_{\text{eq}}(\bar{q})d^f\bar{q} = \psi_{\text{eq}}(q)d^f q$. Using this transformation for ψ_{eq}, it is straightforward to show that the RHS of Eq. (2.333) does indeed obey the transformation law required by Eq. (2.331).

The discrete Markov process used to define a kinetic SDE in Eq. (2.315) or (2.318) can be directly implemented as a numerical algorithm for the integration of a set of SDEs. The resulting simulation algorithm would require the evaluation of neither derivatives of the mobility nor any corrective pseudoforce. It would, however, require an efficient method of calculating the elements of the mobility tensor K^{ab} and derivatives of U and $\ln\sqrt{gW}$ in the chosen system of generalized coordinates.

4. Constrained Motion—Cartesian Coordinates

Constrained motion may also be described by a corresponding set of Cartesian kinetic SDEs

$$d\mathbf{R}^\mu = \mathbf{A}^\mu dt + \sqrt{2kT}\,\mathbf{K}^{\mu\nu} \diamond \mathbf{C}^m_\nu dW_m \tag{2.335}$$

with a singular mobility $\mathbf{K}^{\mu\nu}$, where $\mathbf{C}^m_\nu$ is chosen so as to yield

$$\mathbf{Z}_{\mu\nu} \equiv \mathbf{C}^m_\mu \mathbf{C}^m_\nu \tag{2.336}$$

for some $\mathbf{Z}_{\mu\nu}$ that satisfies Eq. (2.295). By applying the analysis given above for a generic kinetic SDE, we find a

$$\mathbf{V}^\mu \simeq \mathbf{A}^\mu + kT\bar{\mathbf{P}}_\nu{}^{,\lambda} : \frac{\partial \mathbf{K}^{\nu\mu}}{\partial \mathbf{R}^\lambda} \tag{2.337}$$

in which $\bar{\mathbf{P}}_\nu{}^{,\lambda}$ is given by Eq. (2.298). Equating the RHS of Eq. (2.323) to the RHS of Eq. (2.202) for $\mathbf{V}^\mu$ then yields a required drift coefficient

$$\mathbf{A}^\mu = \mathbf{K}^{\mu\nu} \cdot \left[-\frac{\partial U_{\text{eff}}}{\partial \mathbf{R}^\nu} + \mathbf{F}^{(\text{f})}_\nu + \mathbf{F}^{(\text{ps})}_\nu \right] \tag{2.338}$$

where $\mathbf{F}^{(\text{ps})}_\nu$ is a pseudoforce corresponding to the projection tensor of Eq. (2.298). The only difference between Eqs. (2.338) and (2.296), which gives the corresponding drift velocity for the traditional interpretation of the Langevin equation, is the absence in the kinetic interpretation of a term arising from the force bias.

E. Types of Random Force

In both traditional and kinetic interpretations of the Cartesian Langevin equation for a constrained system, one retains some freedom to specify the hard and mixed components of the force variance tensor $\mathbf{Z}_{\mu\nu}$. Several forms for $\mathbf{Z}_{\mu\nu}$ have been considered in previous work, corresponding to different types of random force, which generally require the use of different corrective pseudoforces:

1. *Unprojected* random forces have a variance

$$\mathbf{Z}_{\mu\nu} = \boldsymbol{\zeta}_{\mu\nu} \tag{2.339}$$

given by the unprojected Cartesian friction tensor. This choice yields a generalized projection tensor

$$\bar{\mathbf{P}}^{\mu}{}_{,\nu} = \mathbf{K}^{\mu\lambda} \cdot \mathbf{Z}_{\lambda\nu} = \mathbf{P}^{\mu}_{,\nu} \tag{2.340}$$

equal to the dynamical projection tensor $\mathbf{P}^{\mu}{}_{,\nu}$. The pseudoforce required by unprojected random forces is thus that corresponding to dynamical projection, which is obtained by using a dynamical basis vector $\mathbf{m}_i^{\nu}$ in Eq. (2.205).

2. *Geometrically projected* random forces, which were introduced by Hinch [10], have a variance given by the geometrically projected friction tensor

$$\mathbf{Z}_{\mu\nu} = \tilde{\mathbf{P}}^{\lambda}_{\mu} \cdot \boldsymbol{\zeta}_{\lambda\rho} \cdot \tilde{\mathbf{P}}^{\rho}_{\nu} = \tilde{\mathbf{b}}^{a}_{\mu} \tilde{\zeta}_{ab} \tilde{\mathbf{b}}^{b}_{\nu} \tag{2.341}$$

This choice for $\mathbf{Z}_{\mu\nu}$ yields a projection tensor

$$\bar{\mathbf{P}}^{\mu}_{,\nu} = \tilde{\mathbf{P}}^{\mu}_{\nu} \tag{2.342}$$

equal to the soft geometric projection tensor. The required pseudoforce for this case is thus obtained by using the geometric basis vector $\hat{\mathbf{m}}_i^{\mu}$ in Eq. (2.205), which yields the metric pseudoforce given in Eq. (2.214).

3. *Inertially projected* random forces have a variance $\mathbf{Z}_{\mu\nu}$ calculated using an inertial projection tensor in place of the geometric projection tensor in Eq. (2.341). This results in a generalized projection tensor equal to the inertial projection tensor, and thus requires a pseudoforce given by the inertial pseudoforce of Eq. (2.218). Use of inertially projected random forces in the Cartesian kinetic SDE for a rigid system yields a very simple drift coefficient vector

$$\mathbf{A}^{\mu} = \mathbf{K}^{\mu\nu} \cdot \left[-\frac{\partial U}{\partial \mathbf{R}^{\nu}} + \mathbf{F}^{(\mathrm{f})}_{\nu} \right] \tag{2.343}$$

in which $\mathbf{F}^{(\mathrm{ps})}_{\nu}$ and $kT\, \partial \ln \sqrt{W} / \partial \mathbf{R}^{\nu}$ are absent because they cancel. The kinetic SDE with inertially projected forces is equivalent to the convenient "mixed" representation of rigid systems discovered by Peters [13].

Cartesian kinetic SDEs with unprojected, geometrically projected, and inertially projected random forces require the same correction forces in certain special cases. Inertial and geometric projections are completely equivalent for models with an equal bead mass m for all beads, for which the mass tensor $\mathbf{m}_{\mu\nu} = m\mathbf{I}_{\mu\nu}$ is proportional to the identity. Unprojected and geometrically projected random forces require identical correction forces in the case of local, isotropic friction with an equal friction coefficient ζ for all beads, as in the Rouse or Kramers model, for which the friction tensor $\boldsymbol{\zeta}_{\mu\nu} = \zeta\mathbf{I}_{\mu\nu}$ is proportional to the identity. In this case, the dynamical projection tensor $\mathbf{P}^{\mu}{}_{,\nu}$ becomes equal to the geometric projection tensor $\tilde{\mathbf{P}}^{\mu}_{\nu}$, and thus leads to the same pseudoforce, which is given by the metric force of Eq. (2.214). All three types of random force lead to this same pseudoforce for models with isotropic friction, equal friction coefficients, and equal bead masses.

F. Summary

In this section, we have considered four possible ways of formulating and interpreting a set of SDE to describe Brownian motion, and tried to clarify the relationships among them. Because each interpretation may be defined as the $\Delta t \to 0$ limit of a discrete Markov processes, this discussion of SDEs provides a useful starting point for the discussion of possible simulation algorithms.

The value of the drift coefficients required by each type of SDE may be obtained by comparing the value of the drift velocity V^{α} generated by the SDE to that required by statistical mechanics. The desired drift velocity vector for a system of coordinates $X^{\alpha}, \ldots, X^{L}$ may be expressed in generic form as a sum

$$V^{\alpha} = V^{\alpha}_{(0)} + \frac{\partial D^{\alpha\beta}}{\partial X^{\beta}} \tag{2.344}$$

where $D^{\alpha\beta} = kTK^{\alpha\beta}$, and

$$V^{\alpha}_{(0)} \equiv K^{\alpha\beta}\left[kT\frac{\partial \ln \mathscr{P}_{\mathrm{eq}}}{\partial X^{\beta}} + F^{(\mathrm{f})}_{\beta}\right] \tag{2.345}$$

Here, $K^{\alpha\beta}$ is the mobility tensor in the chosen system of coordinates, which is a constrained mobility for a constrained system and an unconstrained mobility $K^{\alpha\beta} = H^{\alpha\beta}$ for an unconstrained system. As discussed in Section VII, in the case of a constrained system, Eq. (2.344) may be applied either to the drift velocities for the f soft coordinates, for which $K^{\alpha\beta}$ is a nonsingular $f \times f$ matrix, or to the drift velocities for a set of $3N$ unconstrained generalized or Cartesian coordinates, for a probability distribution $\mathscr{P}(X)$ that is dynamically constrained to the constraint surface, for which $K^{\alpha\beta}$ is a singular $3N \times 3N$ matrix. The equilibrium distribution is $\mathscr{P}(X) \propto \sqrt{g}e^{-U/kT}$ for unconstrained systems and $\mathscr{P}(X) \propto \sqrt{gW}e^{-U/kT}$ for constrained systems. Expressions for the drift velocities

TABLE II.1
Drift Velocity and Coefficient[a]

SDE	V^α (Drift Velocity)	A^α (Drift Coefficient)
I	A^α	$V^\alpha_{(0)} + \frac{\partial}{\partial X^\beta} D^{\beta\alpha}$
S	$A^\alpha + \frac{1}{2} B^{\beta m} \frac{\partial}{\partial X^\beta} B^{\alpha m}$	$V^\alpha_{(0)} + \frac{1}{2} B^{\alpha m} \frac{\partial}{\partial X^\beta} B^{\beta m}$
L	$A^\alpha + \bar{P}^\gamma_\beta \frac{\partial}{\partial X^\gamma} D^{\beta\alpha} + K^{\alpha\beta} \overline{\langle \eta_\beta \rangle}_0$	$V^\alpha_{(0)} + K^{\alpha\beta} [F^{(\mathrm{ps})}_\beta - \overline{\langle \eta_\beta \rangle}_0]$
K	$A^\alpha + \bar{P}^\gamma_\beta \frac{\partial D^{\beta\alpha}}{\partial X^\gamma}$	$V^\alpha_{(0)} + K^{\alpha\beta} F^{(\mathrm{ps})}_\beta$

[a] Expressions for the drift velocity V^α produced by Ito (I), Stratonovich (S), Langevin (L), and kinetic (K) SDEs, and for the drift coefficient A^α required for each type of SDE to produce the predicted drift velocity of Eq. (2.344), in a generic system of coordinates. $V^\alpha_{(0)}$ is as defined in Eq. (2.345). For systems of equations with a nonsingular mobility $K^{\alpha\beta}, F^{(\mathrm{ps})}_\beta = 0$ and $\bar{P}^\gamma_\beta = \delta^\gamma_\beta$.

produced by the different types of SDE, and the drift velocities required to mimic Brownian motion, are listed in this generic notation in Table II.1.

Ito and Stratonovich SDEs are defined as different interpretations of equations of the form

$$dX^\alpha = A^\alpha(X)dt + B^{\alpha m}(X)dW_m(t) \tag{2.346}$$

in which random components of the motion are generated by an underlying set of standard Weiner processes. Ito SDEs are obtained by interpreting Eq. (2.346) as the limit of an underlying discrete process in which $B^{am}(X)$ is evaluated at the beginning of each timestep. Stratonovich SDEs may be defined either by as the limit of a discrete process in which $B^{\alpha m}(X)$ is instead evaluated at a midstep position, or as the limit of a corresponding sequence of ODEs, in which dW_m is intepreted as the differential of a smoothed, differentiable approximation to $W_m(t)$. The Ito interpretation yields a drift velocity $V^\alpha(X)$ equal to the drift coefficient A^α in the SDE, while the Stratonovich interpretation yields a drift velocity that differs from A^α by a term involving derivatives of the matrix $B^{\alpha m}(X)$, as indicated in Table II.1. To describe Brownian motion, both interpretations require values of A^α that involve computationally awkward sums of derivatives of $K^{\alpha\beta}(X)$, in the Ito interpretation, or of $B^{\alpha m}(X)$, in the Stratonovich interpretation.

The traditional intepretation of the Langevin equation and kinetic SDEs may instead be defined as different interpretations of the generic Langevin equation

$$\dot{X}^\alpha = A^\alpha + K^{\alpha\beta}\eta_\beta \tag{2.347}$$

in which η_β is a random Langevin force. Fluctuations of the random force are characterized by a force variance tensor $Z_{\alpha\beta}(X)$, where $Z_{\alpha\beta} = K^{-1}_{\alpha\beta}$ when $K_{\alpha\beta}$ is not singular. The traditional interpretation of the Langevin equation may be obtained by interpreting Eq. (2.347) either as the limit of an ODE with rapidly varying random forces or as the limit of a discretized process in which both the mobility $K^{\alpha\beta}(X)$ and the variance tensor $Z_{\alpha\beta}(X)$ used to construct the random forces are evaluated at a midstep position. This interpretation of the Langevin equation is equivalent to a corresponding Stratonovich SDE in which the random Langevin forces are linearly related to the underlying Weiner processes. The kinetic interpretation of Eq. (2.347) is defined as the limit of a discretization in which the mobility $K^{\alpha\beta}$ is evaluated at a midstep position, but in which the random forces are constructed using the value of $Z_{\alpha\beta}$ obtained at the beginning of each timestep.

When applied to a system of SDEs with a nonsingular mobility matrix $K^{\alpha\beta}$ (i.e., those for an unconstrained system or for the unconstrained soft coordinates of a constrained system), the traditional interpretation of the Langevin equation produces an expression for V^α that contains both a divergence of the diffusivity, which also appears in the desired expression for V^α, and an unwanted (and previously unrecognized) term arising from the existence of a nonzero bias $\overline{\langle \eta_\alpha \rangle}_0$ in the random force. The value of this bias depends on details of how the random forces are constructed that are not specified by the traditional formulation of the Langevin equation. The nonunique contribution to V^α that arises from this force bias is shown to be equivalent to a corresponding nonunique contributions to the drift velocity of the equivalent Stratonovich SDE, which arises in the Stratonovich SDE from terms involving derivatives of the nonunique tensor B^{am}.

A kinetic interpretation of Eq. (2.347) for a system with a nonsingular mobility produces a drift velocity that contains the desired divergence of the diffusivity, without the unwanted force bias. Brownian motion of such a system may thus be described by a set of kinetic SDEs with a drift coefficient equal to the "naive" drift coefficient $V^\alpha_{(0)}$ of Eq. (2.345), which may be simulated by implementing the kinetic discretization of the Langevin equation as a numerical integration algorithm. Abandonment of the traditional Stratonovich interpretation of the Langevin equation necessarily leads, however, to an interpretation in which the drift coefficient does not transform according to a simple chain rule under coordinate transformations.

A problem peculiar to constrained systems arises when either the traditional or kinetic interpretation of the Langevin equation is applied to a system of equations containing a singular mobility tensor, such as the Cartesian Langevin equations for a constrained system of point particles. In this case, the drift velocity produced by either interpretation contains a term given by a *projected* divergence of the diffusivity, which is defined using a generalized projection

tensor $\bar{P}^{\alpha}_{\gamma} \equiv K^{\alpha\beta} Z_{\beta\gamma}$. Because the drift velocity predicted by statistical mechanics contains an unprojected divergence of the diffusivity, the drift coefficient for the kinetic SDEs must be supplemented in this case by a correction term arising from a pseudoforce of the kind identified in Section VIII, which is designed to correct for the difference between the projected and unprojected divergence of the diffusivity.

In either interpretation of the Langevin equation, the form of the required pseudoforce depends on the values of the mixed components of $Z_{\beta\gamma}$, and thus on the statistical properties of the hard components of the random forces. The definition of a pseudoforce given here is a generalization of the metric force found by both Fixman [9] and Hinch [10]. An apparent discrepancy between the results of Fixman, who considered the case of unprojected random forces, and those of Hinch, who was able to reproducd Fixman's expression for the pseudoforce only in the case of projected random forces, is traced here to an error in Fixman's use of differential geometry.

In the traditional interpretation of the Langevin equation for a constrained system, the overall drift velocity is insensitive to the presence or absence of hard components of the random forces, since these components are instantaneously canceled in the underlying ODE by constraint forces. This insensitivity to the presence of hard forces is obtained, however, only if both the projected divergence of the mobility and the force bias are retained in the expression for the drift velocity. The drift velocity for a kinetic interpretation of a constrained Langevin equation does not contain a force bias, and does depend on statistical properties of the hard random force components. Both Fixman and Hinch nominally considered the traditional interpretation of the Langevin equation for the Cartesian bead coordinates as a limit of an ordinary differential equation. Both authors, however, neglected the possible existence of a bias in the Cartesian random forces. As a result, both obtained a drift velocity that (after correcting the error in Fixman's expression for the pseudoforce) is actually the appropriate expression for a kinetic interpretation.

X. CARTESIAN SIMULATION ALGORITHMS

To construct a simulation algorithm for a constrained system of point particles, one must first choose whether to formulate the underlying equations of motion in terms of soft generalized coordinates or in terms of Cartesian coordinates. The use of generalized coordinates makes it unnecessary to calculate constraint forces. It also avoids any subtleties in the treatment of the Langevin equation that arise from the existence of a singular mobility matrix. The correct drift velocity for a set of generalized coordinates can be obtained by implementing the midstep algorithm that is used above to define a kinetic SDE. The use of generalized coordinates thus reduces the design of a simulation algorithm to that

of formulating the appropriate set of f kinetic SDEs for the chosen set of coordinates. The main disadvantage with this approach is the potential complexity of the calculation of the required generalized forces and of the elements of the constrained mobility matrix K^{ab} in such a system of coordinates.

We focus here instead on the analysis of several algorithms that have been proposed for the simulation of constrained systems of point particles in Cartesian coordinates. Section X.A discusses a generalization of the midstep algorithm originally proposed by Fixman [9], which implements the discrete timestepping scheme used above to define a kinetic SDE. Section X.B discusses a different two-step algorithm proposed by Öttinger, which provides a useful alternative for the simulation of systems described by a divergence-free unconstrained mobility tensor such as the Rotne–Prager–Yamakawa tensor. Section X.C discuses a more specialized algorithm introduced by Liu [22], which is valid only for simulations of free-draining rigid systems with beads of equal mass, such as the Kramers chains.

All three of these algorithms have been used to study polymer dynamics. The midstep algorithm has been used by Grassia and Hinch [20] to study free-draining freely jointed chains and by several other groups [24–27] to study free-draining wormlike chains. Öttinger's algorithm has been used by Petera and Muthukumar to study steady flow properties of freely jointed bead–rod chains with full hydrodynamic interactions [28]. Liu's algorithm has been used by both Liu [22] and Doyle et al. [23] to study Kramers chains in steady flows.

A. Fixman's Algorithm

We now present a generalization of the Cartesian algorithm originally proposed by Fixman [9], which is the based on the midstep scheme used above to define kinetic SDEs.

1. *Algorithm*

We consider a single timestep of length Δt, at the beginning of which the beads are in initial positions $\mathbf{R}^1_{(0)}, \ldots, \mathbf{R}^N_{(0)}$. A full timestep requires the following sequence of operations:

1. At the beginning of the step, discrete random forces $\boldsymbol{\eta}_\mu$ are generated, which must be constructed to have mean and variance

$$\begin{aligned} \langle \boldsymbol{\eta}_\mu \rangle_0 &= 0 \\ \langle \boldsymbol{\eta}_\mu \boldsymbol{\eta}_\nu \rangle_0 &= \frac{2kT}{\Delta t} \mathbf{Z}^{(0)}_{\mu\nu} \end{aligned} \tag{2.348}$$

where $\mathbf{Z}^{(0)}_{\mu\nu} = \mathbf{Z}_{\mu\nu}(\mathbf{R}^1_{(0)}, \ldots, \mathbf{R}^N_{(0)})$ is the value of $\mathbf{Z}_{\mu\nu}$ at the initial bead positions, which must satisfy Eq. (2.295).

2. Predicted midstep positions, denoted by $\mathbf{R}^{\mu}_{(\mathrm{m})}$, are given by

$$\mathbf{R}^{\mu}_{(\mathrm{m})} = \mathbf{R}^{\mu}_{(0)} + \dot{\mathbf{R}}^{\mu}_{(0)}(\Delta t/2) \tag{2.349}$$

where $\dot{\mathbf{R}}^{\mu}_{(0)}$ is an instantaneous velocity calculated using (2.291) with mobilities and nonrandom forces evaluated at the initial bead positions. In practice, this velocity is calculated by first solving system of equations (2.290) for the instantaneous tensions, and then using Eq. (2.288) for $\dot{\mathbf{R}}^{\mu}$.

3. Updated bead positions are given by

$$\mathbf{R}^{\mu}_{(1)} = \mathbf{R}^{\mu}_{(0)} + \dot{\mathbf{R}}^{\mu}_{(\mathrm{m})}\,\Delta t \tag{2.350}$$

where $\dot{\mathbf{R}}^{\mu}_{(\mathrm{m})}$ is an instantaneous velocity that is calculated using the values of the mobility and nonrandom forces obtained at the midstep positions, while retaining the same set of Cartesian random forces as those used in Eq. (2.349), which were generated at the beginning of the timestep.

At the end of each timestep of this basic algorithm, the constraints are not satisified exactly, but are satisfied to an accuracy of $\mathcal{O}(\Delta t)$. This is sufficient to guarantee convergence to the desired solution over any finite time interval in the limit $\Delta t \to 0$. To keep the algorithm with a nonzero value of Δt from drifting slowly away from the constraint surface over long periods of time, however, the algorithm must be supplemented by a correction operation that returns the system to the constraint surface. This may be accomplished by requiring that the values of the constraint forces used to calculate $\dot{\mathbf{R}}^{\mu}_{(\mathrm{m})}$ at the midstep be chosen so as to exactly satisfy the constraints at the end of a step. This requirement yields a set of weakly nonlinear equations for the midstep constraint forces, which can be either iterated to completion, using the constraint forces obtained in the basic algorithm as the first iteration; or iterated a small fixed number of times, which is sufficient to suppress the drift. Alternatively, for a linear polymer with constrained bond lengths, Grassia and Hinch have used a procedure in which they periodically rescale bond lengths without changing bond orientations, and calculate corresponding bead positions by ''regrowing'' the chain from one end.

This algorithm differs from the Markov process used in Section IX to define a kinetic SDE only in that an explicitly predicted midstep position, rather than an implicitly defined midstep position, is used to calculate the midstep velocity for the final update. To the accuracy needed to calculate the drift velocity and diffusivity, the analyses of the explicit and implicit midstep schemes are identical. As a result, the preceding calculation of the diffusivity and drift for a kinetic SDE also applies to this algorithm.

2. *Generation of Random Forces*

The analysis of kinetic SDEs for constrained systems allows for the use of several kinds of random forces, corresponding to different values of $\mathbf{Z}_{\mu\nu}$, which require different corrective pseudoforces. We consider the problem of efficiently generating random forces in situations in which the mobility $\mathbf{H}^{\mu\nu}$ may be calculated directly, as for a model with hydrodynamic interactions.

To efficiently generate unprojected random forces, with $\mathbf{Z}_{\mu\nu} = \mathbf{H}^{-1}_{\mu\nu}$, one must calculate a Cholesky decomposition of $\mathbf{H}^{\mu\nu}$, of the form

$$\mathbf{H}^{\mu\nu} = \mathbf{L}^{\mu m}(\mathbf{L}^T)^{m\nu} \tag{2.351}$$

and then solve the set of $3N$ equations

$$(\mathbf{L}^T)^{m\nu} \cdot \boldsymbol{\eta}_\nu = \frac{\sqrt{2kT}}{\Delta t} f^m \tag{2.352}$$

by backsubstitution, where the $f^1, \ldots, f^{3N}$ is a vector of $3N$ random numbers for which $\langle f^m \rangle = 0$ and $\langle f^m f^n \rangle = \delta^{mn}$.

Geometrically or inertially projected random forces may be generated from unprojected random forces. As an example, we consider the case of geometric projection. Let $\boldsymbol{\eta}_1, \ldots, \boldsymbol{\eta}_N$ be a set of unprojected forces, generated by the procedure described above, and $\tilde{\boldsymbol{\eta}}_1, \ldots, \tilde{\boldsymbol{\eta}}_N$ be the desired projected random forces, which are given by

$$\tilde{\boldsymbol{\eta}}_\mu = \tilde{\mathbf{P}}^\nu_\mu \cdot \boldsymbol{\eta}_\nu \tag{2.353}$$

In the usual case in which $\boldsymbol{n}^i_\mu$ and $\hat{\boldsymbol{G}}^{ij}$ are sparse matrices produced by constraints involving only a few nearby beads, the projection may be completed in $\mathcal{O}(N)$ operations by first solving the system of equations

$$\hat{\boldsymbol{G}}^{ij}\hat{\eta}_j = \mathbf{n}^i_\nu \cdot \boldsymbol{\eta}_\nu \tag{2.354}$$

for $\hat{\eta}_j$, by LU decomposition, and then setting

$$\tilde{\boldsymbol{\eta}}_\mu = \boldsymbol{\eta}_\mu - \mathbf{n}^i_\mu \hat{\eta}_i \tag{2.355}$$

Inertially projected random forces may be produced by an analogous procedure, in which $\hat{\boldsymbol{G}}^{ij}$ is replaced by $(\widehat{\boldsymbol{m}^{-1}})^{ij}$ and $\mathbf{n}^i_\nu$ is replaced by $m_\nu^{-1}\mathbf{n}^i_\nu$ in Eq. (2.354). In the case of a linear polymer with constrained bond lengths, both $\hat{\boldsymbol{G}}^{ij}$ and $(\widehat{\boldsymbol{m}^{-1}})^{ij}$ are tridiagonal.

A free-draining model with equal bead friction coefficients and $W = \text{const}$, such as a stiff bead–spring polymer, may be efficiently simulated with

unprojected random forces and the metric pseudoforce of Eq. (2.214). Efficient $O(N)$ algorithms for the calculation of this metric force for linear polymers with constrained link lengths have been given by both Grassia and Hinch [20] and Pasquali and Morse [25]. Models with $W = \text{const.}$ and more complicated mobility tensors, such as infinitely stiff bead–spring polymers with hydrodynamic interactions or anisotropic mobilities, may be efficiently simulated with geometrically projected random forces and a metric pseudoforce. Rigid models with arbitrary bead masses and arbitrary mobility tensors may be most efficiently simulated with inertially projected random forces, which make the calculation of a pseudoforce unnecessary.

In models of beads with full hydrodynamic interactions, for which the mobility tensor is represented by a dense matrix, the Cholesky decomposition of $\mathbf{H}^{\mu\nu}$ requires $(3N)^3/6$ operations. For large N, this appears to be the most expensive operation in the entire algorithm. The only other unavoidable $O(N^3)$ operation is the LU decomposition of the $K \times K$ matrix $\hat{H}^{ij}$ that is required to solve for the K constraint forces, which requires $K^3/3$ operations, or roughly $N^3/3$ for a linear chain with constrained bond lengths, which must be carried out twice each timestep. The $\mathcal{O}(N)$ costs of projecting the random forces and calculating a metric pseudopotential force for a polymer with constrained bond lengths would be negligible by comparison. Models of free-draining chains can be simulated in $\mathcal{O}(N)$ operations per timestep.

B. Öttinger's Algorithm

Öttinger [11,12] has proposed a diffferent two-step algorithm in which the first step (the ''predictor'') is actually an unconstrained move appropriate to an explicit Euler algorithm for the corresponding unconstrained system, rather than a move tangent to the constraint surface. Because Öttinger gave few details of his analysis of this algorithm, and because it contains a slight error (although one that vanishes in the most common applications, as discussed below), a detailed analysis is presented here.

1. *Algorithm*

In this algorithm, the change $\Delta\mathbf{R}^\mu$ between between bead positions at successive timesteps is given by

$$\Delta\mathbf{R}^\mu = \Delta\mathbf{R}^\mu_{(\mathrm{u})} - [\mathbf{H}^{\mu\nu} \cdot \mathbf{n}^i_\nu]_\mathrm{c} \lambda_i \Delta t \tag{2.356}$$

where $\Delta\mathbf{R}^\mu_{(\mathrm{u})}$ is an unconstrained random displacement, and λ_i is a constraint force that must be chosen such that the constraints are exactly satisfied at the end of the step. The quantity $\Delta\mathbf{R}^\mu_{(\mathrm{u})}$ is a random displacement appropriate to an

explicit Euler algorithm for the corresponding unconstrained system, which has a mean value

$$\left\langle \Delta \mathbf{R}^{\mu}_{(\mathrm{u})} \right\rangle_0 = \mathbf{H}^{\mu\nu} \cdot \left(-\frac{\partial U_{\mathrm{eff}}}{\partial \mathbf{R}^{\nu}} + \mathbf{F}^{(\mathrm{f})}_{\nu} \right) \Delta t + kT \frac{\partial}{\partial \mathbf{R}^{\nu}} \cdot \mathbf{H}^{\nu\mu} \Delta t \tag{2.357}$$

and, to $\mathcal{O}(\Delta t)$, a variance

$$\left\langle \Delta \mathbf{R}^{\mu}_{(\mathrm{u})} \Delta \mathbf{R}^{\nu}_{(\mathrm{u})} \right\rangle_0 = 2kT \mathbf{H}^{\mu\nu} \Delta t \tag{2.358}$$

All quantities in Eq. (2.358) and elsewhere in this analysis, unless otherwise noted, are evaluated using the bead positions at the beginning of the time step. The subscript "c" is used in Eq. (2.356) to indicate that the quantity in square brackets is instead evaluated (and the constraint forces thus are applied) at auxiliary bead positions

$$\mathbf{R}^{\mu}_{(\mathrm{c})} \equiv \mathbf{R}^{\mu}_{(0)} + c\, \Delta \mathbf{R}^{\mu}_{(\mathrm{u})} \tag{2.359}$$

where $\mathbf{R}^{\mu}_{(0)}$ is the bead position at the beginning of the timestep, and c is a fraction $0 \leq c \leq 1$. As in Öttinger's analysis, the value of the constant c will be unspecified until the end of the analysis, where it will be shown that a useful algorithm is obtained by setting $c = \frac{1}{2}$.

The algorithm described above differs from that described by Öttinger only in that Öttinger failed to include the term proportional to the divergence of $\mathbf{H}^{\mu\nu}$ in Eq. (2.357). The inclusion of this term is, in general, found to be necessary in order to obtain the correct drift velocity from this algorithm. In the usual cases in which $\mathbf{H}^{\mu\nu}$ is taken to be the Oseen or the Rotne–Prager tensor, however, the divergence $\frac{\partial}{\partial \mathbf{R}^{\nu}} \cdot \mathbf{H}^{\nu\mu}$ vanishes (either with or without the summation over the bead index ν) as a result of the assumed incompressibility of the solvent, and so this term vanishes.

2. *Linear Approximation*

Here, we construct approximations for the random quantities $\Delta \mathbf{R}^{\mu}$ and λ_i to linear order in $\Delta \mathbf{R}^{\mu}_{(\mathrm{u})}$. Because λ_i appears multiplied by Δt throughout this analysis, we define a variable

$$\Lambda_i \equiv \lambda_i \Delta t \tag{2.360}$$

A linear approximation for $\Delta\mathbf{R}^\mu$ is obtained by approximating the quantity in square brackets in Eq. (2.356) by its value at the initial bead positions, giving

$$\Delta\mathbf{R}^\mu_{(1)} = \Delta\mathbf{R}^\mu_{(u)} - \mathbf{H}^{\mu\nu}\cdot\mathbf{n}^i_\nu\Lambda^{(1)}_i \tag{2.361}$$

Here and in what follows, we use super- and subscripts of "(1)" to indicate approximations valid to linear order in $\Delta\mathbf{R}^\mu_{(u)}$. The required linear approximation for Λ_i is obtained by expanding the change in c^i to linear order in $\Delta\mathbf{R}^\mu$, as $0 = \Delta c^i \simeq \Delta\mathbf{R}^\mu_{(1)}\cdot\mathbf{n}^i_\mu$, to obtain

$$0 = \Delta\mathbf{R}^\mu_{(u)}\cdot\mathbf{n}^i_\mu - \hat{\boldsymbol{H}}^{ij}\Lambda^{(1)}_j \tag{2.362}$$

Substituting the solution of Eq. (2.362) into Eq. (2.361) then yields

$$\Delta\mathbf{R}^\mu_{(1)} = \mathbf{P}^\mu{}_{,\nu}\cdot\Delta\mathbf{R}^\nu_{(u)} \tag{2.363}$$

where we have used Eq. (2.138) for the dynamical projection tensor $\mathbf{P}^\mu{}_{,\nu}$. This quantity is easily shown to have a mean and variance

$$\left\langle\Delta\mathbf{R}^\mu_{(1)}\right\rangle_0 = \mathbf{P}^\mu{}_{,\nu}\cdot\left\langle\Delta\mathbf{R}^\nu_{(u)}\right\rangle_0 \tag{2.364}$$

$$\left\langle\Delta\mathbf{R}^\mu_{(1)}\Delta\mathbf{R}^\nu_{(1)}\right\rangle_0 = 2kT\mathbf{K}^{\mu\nu}\Delta t \tag{2.365}$$

This approximation yields the variance $\langle\Delta\mathbf{R}^\mu\Delta\mathbf{R}^\nu\rangle_0$ to the required accuracy of $\mathcal{O}(\Delta t)$, but an expansion to second order in $\Delta\mathbf{R}^\nu_{(u)}$, given below, is required to calculate $\langle\Delta\mathbf{R}^\mu\rangle_0$ to the same accuracy. To evaluate this second-order approximation, we will also need the correlation

$$\begin{aligned}\left\langle\Lambda^{(1)}_i\Delta\mathbf{R}^\mu_{(u)}\right\rangle_0 &= \hat{\boldsymbol{H}}^{-1}_{ij}\mathbf{n}^j_\nu\cdot\left\langle\Delta\mathbf{R}^\nu_{(u)}\Delta\mathbf{R}^\mu_{(u)}\right\rangle_0\\ &= 2kT\mathbf{m}^\mu_i\Delta t\end{aligned} \tag{2.366}$$

in which we have used Eq. (2.358) for the variance of $\Delta\mathbf{R}^\mu_{(u)}$ and definition (2.145) for the dynamical reciprocal vector $\mathbf{m}^\mu_i$ to obtain the second line.

3. *Second-Order Approximation*

An approximation for $\Delta\mathbf{R}^\mu$ to second order in $\Delta\mathbf{R}^\mu_{(u)}$, which is accurate to first order in Δt, may be obtained by expanding the quantity in square brackets in Eq. (2.356) to first order in $\Delta\mathbf{R}^\mu_{(u)}$ around its value at the initial bead positions. This yields

$$\Delta\mathbf{R}^\mu = \Delta\mathbf{R}^\mu_{(u)} - \Lambda_i\mathbf{n}^i_\nu\cdot\mathbf{H}^{\nu\mu} - c\Lambda^{(1)}_i\Delta\mathbf{R}^\lambda_{(u)}\cdot\frac{\partial(\mathbf{n}^i_\nu\cdot\mathbf{H}^{\nu\mu})}{\partial\mathbf{R}^\lambda} \tag{2.367}$$

where Λ_i denotes the corresponding second-order approximation for the constraint force. At this order of approximation, all quantities that are quadratic in $\Delta\mathbf{R}_{(u)}$ may be approximated using the linear approximation for $\Delta\mathbf{R}$ and Λ, as has been

done for the product $\Lambda_i \Delta\mathbf{R}^{\lambda}_{(\mathrm{u})}$ in the last term on the RHS of Eq. (2.367). To calculate Λ_i to second order in $\Delta\mathbf{R}^{\mu}_{(\mathrm{u})}$, we expand Δc^i to second order in $\Delta\mathbf{R}^{\mu}$, as

$$0 = \Delta\mathbf{R}^{\mu} \cdot \frac{\partial c^i}{\partial \mathbf{R}^{\mu}} + \frac{1}{2} \Delta\mathbf{R}^{\nu}\, \Delta\mathbf{R}^{\mu} : \frac{\partial^2 c^i}{\partial \mathbf{R}^{\mu}\, \partial \mathbf{R}^{\nu}} \tag{2.368}$$

while using the second-order expansion of Eq. (2.367) for $\Delta\mathbf{R}^{\mu}$ in the term linear in $\Delta\mathbf{R}^{\mu}$ and a linear approximation for $\Delta\mathbf{R}^{\mu}$ in the term quadratic in $\Delta\mathbf{R}$. This yields

$$\begin{aligned} \hat{H}^{ij}\Lambda_j \simeq & \left[\Delta\mathbf{R}^{\mu}_{(\mathrm{u})} - c\Lambda_j^{(1)} \Delta\mathbf{R}^{\lambda}_{(\mathrm{u})} \cdot \frac{\partial(\mathbf{n}^j_{\nu} \cdot \mathbf{H}^{\nu\mu})}{\partial \mathbf{R}^{\lambda}}\right] \cdot \mathbf{n}^i_{\mu} \\ & + \frac{1}{2} \Delta\mathbf{R}^{\mu}_{(1)}\, \Delta\mathbf{R}^{\nu}_{(1)} : \frac{\partial^2 c^i}{\partial \mathbf{R}^{\nu} \partial \mathbf{R}^{\mu}} \end{aligned} \tag{2.369}$$

Substituting the solution of Eq. (2.369) into Eq. (2.367) then yields

$$\begin{aligned} \Delta\mathbf{R}^{\mu} = & \left[\Delta\mathbf{R}^{\sigma}_{(\mathrm{u})} - c\Lambda_j^{(1)} \Delta\mathbf{R}^{\lambda}_{(\mathrm{u})} \cdot \frac{\partial(\mathbf{n}^j_{\nu} \cdot \mathbf{H}^{\nu\sigma})}{\partial \mathbf{R}^{\lambda}}\right] \cdot \mathbf{P}_{\sigma}^{\ ,\mu} \\ & - \frac{1}{2} \Delta\mathbf{R}^{\nu}_{(1)}\, \Delta\mathbf{R}^{\sigma}_{(1)} : \frac{\partial^2 c^i}{\partial \mathbf{R}^{\sigma} \partial \mathbf{R}^{\nu}} \mathbf{m}^{\mu}_i \end{aligned} \tag{2.370}$$

where $\Delta\mathbf{R}^{\nu}_{(1)}$ is as given by Eq. (2.363).

To calculate the drift velocity, we evaluate the average of Eq. (2.370) for $\Delta\mathbf{R}^{\mu}$ with respect to fluctuations of $\Delta\mathbf{R}^{\nu}_{(\mathrm{u})}$, and divide the result by Δt. Using Eqs. (2.357), (2.365), and (2.366) to evaluate the required averages yields a drift velocity

$$\begin{aligned} \mathbf{V}^{\mu} = & \mathbf{K}^{\mu\nu} \cdot \left(-\frac{\partial U_{\mathrm{eff}}}{\partial \mathbf{R}^{\nu}} + \mathbf{F}^{(\mathrm{f})}_{\nu}\right) + kT\mathbf{P}^{\mu}{}_{,\nu} \cdot \left(\frac{\partial}{\partial \mathbf{R}^{\lambda}} \cdot \mathbf{H}^{\lambda\nu}\right) \\ & - 2ckT\, \mathbf{m}^{\lambda}_i \cdot \frac{\partial(\mathbf{n}^i_{\nu} \cdot \mathbf{H}^{\nu\sigma})}{\partial \mathbf{R}^{\lambda}} \cdot \mathbf{P}_{\sigma}^{\ ,\mu} - kT\, \mathbf{K}^{\nu\sigma} : \frac{\partial^2 c^i}{\partial \mathbf{R}^{\sigma} \partial \mathbf{R}^{\nu}} \mathbf{m}^{\mu}_i \end{aligned} \tag{2.371}$$

Expanding the derivative in the first term of the second line of Eq. (2.371) yields the final result

$$\begin{aligned} \mathbf{V}^{\mu} = & \mathbf{K}^{\mu\nu} \cdot \left[-\frac{\partial U_{\mathrm{eff}}}{\partial \mathbf{R}^{\nu}} + \mathbf{F}^{(\mathrm{f})}_{\nu}\right] + kT\mathbf{P}^{\mu}{}_{,\nu} \cdot \left(\frac{\partial}{\partial \mathbf{R}^{\lambda}} \cdot \mathbf{H}^{\lambda\nu}\right) \\ & - 2ckT\mathbf{m}^{\lambda}_i \cdot \frac{\partial^2 c^i}{\partial \mathbf{R}^{\lambda} \partial \mathbf{R}^{\nu}} \cdot \mathbf{K}^{\nu\mu} + 2ckT(\mathbf{P}_{\nu}^{\ ,\lambda} - \mathbf{I}^{\lambda}_{\nu}) : \frac{\partial \mathbf{H}^{\nu\sigma}}{\partial \mathbf{R}^{\lambda}} \cdot \mathbf{P}_{\sigma}^{\ ,\mu} \\ & - kT\mathbf{m}^{\mu}_i \frac{\partial^2 c^i}{\partial \mathbf{R}^{\sigma} \partial \mathbf{R}^{\nu}} : \mathbf{K}^{\nu\sigma} \end{aligned} \tag{2.372}$$

in which we have used the identity $-\mathbf{n}_\nu^i \mathbf{m}_i^\lambda = \mathbf{P}_\nu^{\ \lambda} - \mathbf{I}_\nu^\lambda$ to write the second term of the second line. On equating Eq. (2.372) with Eq. (2.184) for $\mathbf{V}^\mu$, we find that the two expressions can be made equivalent by taking

$$c = \frac{1}{2} \tag{2.373}$$

Equation (2.372) largely agrees with Öttinger's final result, except for the absence in Öttinger's result of the terms in the first and second lines involving the unprojected divergence of $\mathbf{H}$. The term in the first line is absent because of the absence of a corresponding term in Öttinger's original algorithm. The term in the second line is absent because of an oversight in his analysis. When applied to a problem without constraints, for which there is no need to calculate constraint forces, this algorithm reduces to an explicit forward Euler integration algorithm. The required drift coefficient reduces in this case to that given by the first line of Eq. (2.372), with $\mathbf{K}^{\mu\nu}$ replaced by the unconstrained mobility $\mathbf{H}^{\mu\nu}$. Consideration of the special case of an unconstrained model thus makes clear the need to include the divergence of $\mathbf{H}^{\mu\nu}$ in the RHS of expression (2.357) for $\langle \Delta \mathbf{R}_{(\mathrm{u})} \rangle_0$, since this term is required by the explicit Euler algorithm for the corresponding unconstrained system.

This corrected version of Öttinger's algorithm requires that the divergence of $\mathbf{K}^{\mu\nu}$ be calculated at each timestep, in order to calculate an average value for $\Delta \mathbf{R}_{(\mathrm{u})}^\mu$. As a result, this algorithm, like the explicit Euler algorithm for unconstrained systems to which it is closely related, provides an efficient integration scheme only for models in which the divergence of $\mathbf{H}^{\mu\nu}$ vanishes, that is, for models with a coordinate-independent mobility $\mathbf{H}^{\mu\nu}$, or for which a divergence-free approximation to the Oseen tensor is used to describe hydrodynamic interactions between particles. The application of Öttinger's algorithm to a broader class of models by Elsgaeter and coworkers [21] may need to be reconsidered in light of this conclusion. For this important class of models, however, Öttinger's algorithm requires no correction forces beyond those arising from the derivatives of the contribution $-kT \ln \sqrt{W}$ to U_{eff}. For an infinitely stiff bead–spring polymer, for which W is constant, the algorithm requires no nontrivial correction forces at all.

C. Liu's Algorithm

A more specialized algorithm has been proposed by Liu for the simulation of rigid free-draining systems with an equal friction coefficient ζ and bead mass m for every bead. The displacement in Liu's algorithm is given by

$$\Delta \mathbf{R}^\mu = \mathbf{H}^{\mu\nu} \cdot \left(-\frac{\partial U}{\partial \mathbf{R}^\nu} + \mathbf{F}_\nu^{(\mathrm{f})} + \boldsymbol{\eta}_\nu - \mathbf{n}_\nu^i \lambda_i \right) \Delta t \tag{2.374}$$

where $\mathbf{H}^{\mu\nu} = \mathbf{I}^{\mu\nu}/\zeta$, and $\boldsymbol{\eta}_\mu$ is an unprojected random force with $\langle \boldsymbol{\eta}_\mu \boldsymbol{\eta}_\nu \rangle = 2kT\zeta \mathbf{I}_{\mu\nu}/\Delta t$. In this algorithm, both $\frac{\partial U}{\partial \mathbf{R}^\mu}$ and $\mathbf{n}_\nu^i$ are evaluated at the initial bead positions, so that the constraint forces are applied along the initial normal directions. The values of $\lambda_1, \ldots, \lambda_K$ are chosen so that the constraints are satisfied exactly at the end of the timestep. Liu's algorithm is thus a special case of the class of implicit algorithm's analyzed above, with $U_{\text{eff}} = U$, and with

$$c = 0 \tag{2.375}$$

rather than $c = \frac{1}{2}$ as in Öttinger's algorithm. By setting $c = 0$ in Eq. (2.372), while dropping all terms involving derivatives of $\mathbf{H}^{\mu\nu}$ and setting $U_{\text{eff}} = U$, we find a drift velocity

$$\mathbf{V}^\mu = \mathbf{K}^{\mu\nu} \cdot \left(-\frac{\partial U}{\partial \mathbf{R}^\nu} + \mathbf{F}_\nu^{(\text{f})} \right) - kT \mathbf{m}_i^\mu \frac{\partial^2 c^i}{\partial \mathbf{R}^\sigma \partial \mathbf{R}^\nu} : \mathbf{K}^{\nu\sigma} \tag{2.376}$$

We compare this to Eq. (2.184) for the desired drift velocity. For this class of systems, Eq. (2.184) is simplified by the absence of the last term on the RHS, which involves derivatives of $\mathbf{H}^{\mu\nu}$, and by a cancellation between the second term on the RHS, which is the velocity arising from the pseudoforce $\mathbf{F}_\mu^{(\text{ps})}$, and the velocity arising from the force $kT\partial \ln \sqrt{W}/\partial \mathbf{R}^\mu$, which in this case is equal and opposite to $\mathbf{F}_\mu^{(\text{ps})}$. All that remains is a drift velocity equal to that given in Eq. (2.376), thus confirming the validity of the algorithm.

XI. STRESS TENSOR

In this section, we use the Cartesian force of Section VI to derive several equivalent expressions for the stress tensor of a constrained system of pointlike particles in a flow field with a macroscopic velocity gradient $\boldsymbol{\nabla}\mathbf{v}$. The excess stress of any system of interacting beads (i.e., point centers of hydrodynamic resistance) in a Newtonian solvent, beyond the Newtonian contribution that would be present at the applied deformation rate in the absence of the beads, is given by the Kramers–Kirkwood expression [1,4,18]

$$\boldsymbol{\sigma} = \frac{1}{V} \left\langle \mathbf{R}^\mu \mathbf{F}_\mu^{(\text{h})} \right\rangle \tag{2.377}$$

where V is the total volume of a macroscopic system and where the sum is taken over all beads in such a system. Using Cartesian force balance (2.121), this may be rewritten in terms of nonhydrodynamic forces as

$$\boldsymbol{\sigma} = \frac{-1}{V} \left\langle \mathbf{R}^\mu \left(\mathbf{F}_\mu^{(\text{e})} - \mathbf{n}_\mu^i \tau_i \right) \right\rangle \tag{2.378}$$

In a dilute solution of M identical molecules, the sum over all of the beads in the system may be restricted to a sum over all beads of a single molecule, if the prefactor of $1/V$ is replaced by the molecular number density M/V.

By dividing the constraint forces into components induced by the elastic and flow forces, the total stress may be expressed as the sum

$$\boldsymbol{\sigma} = \boldsymbol{\sigma}_{\mathrm{e}} + \boldsymbol{\sigma}_{\mathrm{v}} \tag{2.379}$$

of an elastic stress

$$\boldsymbol{\sigma}_{\mathrm{e}} = -\frac{1}{V}\langle \mathbf{R}^{\mu}\mathbf{P}_{\mu}{}^{,\nu} \cdot \mathbf{F}_{\nu}^{(\mathrm{e})}\rangle \tag{2.380}$$

that arises from the elastic forces and the constraint forces induced by them, and a viscous stress

$$\begin{aligned}\boldsymbol{\sigma}_{\mathrm{v}} &= \frac{1}{V}\langle \mathbf{R}^{\mu}\mathbf{n}_{\mu}^{i}\mathbf{m}_{i}^{\nu} \cdot \mathbf{F}_{\nu}^{(\mathrm{f})}\rangle \\ &= \frac{1}{V}\langle \mathbf{R}^{\mu}(\mathbf{I}_{\mu}^{\nu} - \mathbf{P}_{\mu}{}^{,\nu}) \cdot \mathbf{F}_{\nu}^{(\mathrm{f})}\rangle \end{aligned} \tag{2.381}$$

that arises from the constraint forces induced by $\mathbf{F}_{\nu}^{(\mathrm{f})}$, which are given by $\tau_i^{(\mathrm{f})} \equiv \mathbf{m}_i^{\nu} \cdot \mathbf{F}_{\nu}^{(\mathrm{f})}$.

A. Modified Kramers Expression

We now focus on Eq. (2.380) for the elastic stress, which may be expressed more explicitly as

$$\boldsymbol{\sigma}_{\mathrm{e}} = \frac{1}{V}\left\langle \mathbf{R}^{\mu}\mathbf{P}_{\mu}{}^{,\nu} \cdot \frac{\partial\left[U + kT\ln\left(\frac{\psi}{\sqrt{gW}}\right)\right]}{\partial \mathbf{R}^{\nu}}\right\rangle \tag{2.382}$$

We may rewrite the Brownian term, using Eq. (2.150) for $\mathbf{P}_{\mu}{}^{,\nu} = \mathbf{b}_{\mu}^{a}\mathbf{a}_{a}^{\nu}$ and the chain rule $\frac{\partial}{\partial q^a} = \mathbf{a}_a^{\nu} \cdot \frac{\partial}{\partial \mathbf{R}^{\nu}}$, as

$$\boldsymbol{\sigma}_{\mathrm{e}} = \frac{kT}{V}\left\langle \mathbf{R}^{\mu}\mathbf{P}_{\mu}{}^{,\nu} \cdot \frac{\partial \ln \psi_{\mathrm{eq}}}{\partial \mathbf{R}^{\nu}}\right\rangle + \frac{kT}{V}\int dq\, \mathbf{R}^{\mu}\mathbf{b}_{\mu}^{a}\frac{\partial \psi}{\partial q^a} \tag{2.383}$$

Integrating the second term by parts then yields

$$\boldsymbol{\sigma}_{\mathrm{e}} = \frac{kT}{V}\left\langle \mathbf{R}^{\mu}\mathbf{P}_{\mu}{}^{,\nu} \cdot \frac{\partial \ln \psi_{\mathrm{eq}}}{\partial \mathbf{R}^{\nu}}\right\rangle - \frac{kT}{V}\left\langle \frac{\partial(\mathbf{R}^{\mu}\mathbf{b}_{\mu}^{a})}{\partial q^a}\right\rangle \tag{2.384}$$

In the case of rigid systems, for which $gW \propto \tilde{m}$, the sum of Eq. (384) for the elastic stress and Eq. (2.381) for the viscous stress is equivalent to Eq. (16.3-11) for the total stress in the monograph of Bird et al. [4], and Eq. (5.68) in Öttinger's

monograph [12], which these authors refer to as a "modified Kramers expression" for the stress.

B. Cartesian Expressions

A fully Cartesian form for the stress tensor may be obtained by using Eq. (2.182) to expand terms arising from the generalized divergence of K^{ab} in Eq. (2.384). To begin, we move the derivative of $\ln\sqrt{g}$ within $\ln\psi_{\text{eq}}$ into the second term in Eq. (2.384), to obtain the equivalent expression

$$\boldsymbol{\sigma}_{\text{e}} = \frac{1}{V}\left\langle \mathbf{R}^{\mu}\mathbf{P}_{\mu}{}^{,\nu}\cdot\frac{\partial U_{\text{eff}}}{\partial \mathbf{R}^{\nu}}\right\rangle - \frac{kT}{V}\left\langle \frac{1}{\sqrt{g}}\frac{\partial(\sqrt{g}\,\mathbf{R}^{\mu}\mathbf{b}_{\mu}^{a})}{\partial q^{a}}\right\rangle \tag{2.385}$$

Definition (2.144) for the dynamical reciprocal vector $\mathbf{b}_{\mu}^{a}$ may then be used to expand the second term in Eq. (2.384) as

$$\frac{1}{\sqrt{g}}\frac{\partial(\sqrt{g}\,\mathbf{R}^{\mu}\mathbf{b}_{\mu}^{a})}{\partial q^{a}} = \mathbf{a}_{a}^{\mu}\mathbf{b}_{\mu}^{a} + \frac{\mathbf{R}^{\mu}}{\sqrt{g}}\frac{\partial(\sqrt{g}\,K^{ab}\mathbf{a}_{b}^{\nu}\cdot\boldsymbol{\zeta}_{\nu\mu})}{\partial q^{a}} \tag{2.386}$$

By using expansion (2.150) to identify the first term on the RHS as $\mathbf{P}^{\mu}{}_{,\mu}$, and expanding the derivative in the second, we obtain

$$\frac{1}{\sqrt{g}}\frac{\partial(\sqrt{g}\,\mathbf{R}^{\mu}\mathbf{b}_{\mu}^{a})}{\partial q^{a}} = \mathbf{P}^{\mu}{}_{,\mu} + \mathbf{R}^{\mu}\mathbf{K}^{\nu\lambda}{:}\frac{\partial\boldsymbol{\zeta}_{\nu\mu}}{\partial\mathbf{R}^{\lambda}} + \frac{\mathbf{R}^{\mu}}{\sqrt{g}}\frac{\partial(\sqrt{g}\,K^{ab}\mathbf{a}_{b}^{\nu})}{\partial q^{a}}\cdot\boldsymbol{\zeta}_{\nu\mu} \tag{2.387}$$

where we have used the expansion $\frac{\partial}{\partial q^{a}} = \mathbf{a}_{a}^{\lambda}\cdot\frac{\partial}{\partial\mathbf{R}^{\lambda}}$ and expansion (2.136) for $\mathbf{K}^{\nu\lambda}$ to obtain a Cartesian expression for the second term on the RHS of (2.387). Using Eq. (2.182) for the covariant divergence of $\mathbf{K}^{\lambda\nu}$ in the last term then yields

$$\begin{aligned}\frac{1}{\sqrt{g}}\frac{\partial(\sqrt{g}\,\mathbf{R}^{\mu}\mathbf{b}_{\mu}^{a})}{\partial q^{a}} &= \mathbf{P}^{\mu}{}_{,\mu} + \mathbf{R}^{\mu}\mathbf{K}^{\nu\lambda}{:}\frac{\partial\boldsymbol{\zeta}_{\nu\mu}}{\partial\mathbf{R}^{\lambda}} + \mathbf{R}^{\mu}\left(\frac{\partial}{\partial\mathbf{R}^{\lambda}}\cdot\mathbf{K}^{\lambda\nu}\right)\cdot\boldsymbol{\zeta}_{\nu\mu}\\ &= \mathbf{P}^{\mu}{}_{,\mu} + \mathbf{R}^{\mu}\frac{\partial}{\partial\mathbf{R}^{\lambda}}\cdot\mathbf{P}^{\lambda}{}_{,\mu}\end{aligned} \tag{2.388}$$

where we have used the chain rule expansion of the product $\mathbf{P}^{\lambda}{}_{,\mu} \equiv \mathbf{K}^{\lambda\nu}\cdot\boldsymbol{\zeta}_{\nu\mu}$ to combine the last two terms on the first line of the RHS. Substituting this into the modified Kramers expression then yields the fully Cartesian expression

$$\begin{aligned}\boldsymbol{\sigma}_{\text{e}} = \frac{1}{V}&\left\langle \mathbf{R}^{\mu}\mathbf{P}_{\mu}{}^{,\nu}\cdot\left(\frac{\partial(U - kT\ln\sqrt{W})}{\partial\mathbf{R}^{\nu}}\right)\right\rangle\\ &- \frac{kT}{V}\langle\mathbf{P}^{\mu}{}_{,\mu}\rangle - \frac{kT}{V}\left\langle\mathbf{R}^{\mu}\frac{\partial}{\partial\mathbf{R}^{\nu}}\cdot\mathbf{P}^{\nu}{}_{,\mu}\right\rangle\end{aligned} \tag{2.389}$$

The sum of the two terms in the last line of this equation is the Brownian stress of a constrained system.

An alternative class of expressions for the stress tensor, analogous to those obtained in Section VIII for the drift velocity, may be obtained by using Eqs. (2.201) to expand the divergence of $\mathbf{K}^{\lambda\nu}$ in the first line of Eq. (2.388). This expansion yields an elastic stress

$$\boldsymbol{\sigma}_e = \frac{1}{V}\left\langle \mathbf{R}^{\mu}\mathbf{P}_{\mu}{}^{,\nu}\cdot\left(\frac{\partial(U - kT\ln\sqrt{W})}{\partial\mathbf{R}^{\nu}} - \mathbf{F}_{\nu}^{(ps)}\right)\right\rangle - \frac{kT}{V}\langle\mathbf{P}^{\mu}{}_{,\mu}\rangle - \frac{kT}{V}\left\langle \mathbf{R}^{\mu}\bar{\mathbf{P}}_{\nu}{}^{,\lambda}:\frac{\partial\mathbf{P}^{\nu}{}_{,\mu}}{\partial\mathbf{R}^{\lambda}}\right\rangle \tag{2.390}$$

in which $\bar{\mathbf{P}}_{\nu}{}^{,\lambda}$ can be any generalized projection tensor, and $\mathbf{F}_{\nu}^{(ps)}$ is the corresponding pseudoforce.

In the case of an unconstrained system, the dynamical projection tensor $\mathbf{P}_{\nu}{}^{,\lambda}$ becomes equal to the identity $\mathbf{I}_{\nu}^{\lambda}$. Also, in the absence of constraint forces, there is is no viscous stress. In this case Eq. (2.389) reduces to a well-known expression [4,18]

$$\boldsymbol{\sigma} = \frac{1}{V}\left\langle \mathbf{R}^{\mu}\frac{\partial U}{\partial\mathbf{R}^{\mu}}\right\rangle - \frac{NkT}{V}\mathbf{I} \tag{2.391}$$

for the total excess stress of an unconstrained system of N interacting Stokeslets.

C. Modified Giesekus Expression

Öttinger [11,12] has also given an expression relating the total polymer stress to the drift velocity $\mathbf{V}^{\mu}$, which is analogous to the Giesekus expression [4] for the stress in a system without constraints. Note that Eqs. (2.387) and the first line of Eq. (2.388) contain divergences of the mobility identical to those found in Eqs. (2.173) and (2.183) for the drift velocity $\mathbf{V}^{\nu}$, respectively. By using either of these expression to expand the modified Kramers expression for the elastic stress, and, comparing either result to the corresponding expressions for $\mathbf{V}^{\mu}$, one may show that the sum of this elastic stress and the viscous stress of Eq. (2.381) yields a total stress

$$\boldsymbol{\sigma} = \frac{1}{V}\langle\mathbf{R}^{\mu}(\mathbf{V}^{\nu}\cdot\boldsymbol{\zeta}_{\nu\mu} - \mathbf{F}_{\mu}^{(f)})\rangle - \frac{kT}{V}\langle\mathbf{P}^{\mu}{}_{,\mu}\rangle - \frac{kT}{V}\left\langle \mathbf{R}^{\mu}\mathbf{K}^{\rho\nu}:\frac{\partial\boldsymbol{\zeta}_{\rho\mu}}{\partial\mathbf{R}^{\nu}}\right\rangle \tag{2.392}$$

In the case of rigid systems of pointlike particles, for which $\mathbf{F}_{\mu}^{(f)} = \boldsymbol{\kappa}\cdot\mathbf{R}^{\nu}\cdot\boldsymbol{\zeta}_{\nu\mu}$, this is equivalent to the expression given by Öttinger in Eq. (29) of Ref. 11 and in Eq. (5.70) of Ref. 12.

XII. STOCHASTIC STRESS ALGORITHMS

Here, we consider two closely related algorithms proposed by Grassia and Hinch [20] and Doyle et al. [23] for evaluating the stress tensor within simulations based on two of the algorithms discussed in Section X. Grassia and Hinch's [20] method is designed for use with Fixman's timestepping algorithm, while Doyle et al.'s [23] is intended for use with Liu's algorithm. In both methods, one defines a stochastic stress $\boldsymbol{\sigma}$ for each timestep of the associated timestepping algorithm, whose ensemble average is shown to be equivalent to the macroscopic stress obtained in Section XI. In both cases, this stress is given by a stochastic interpretation of Eq. (2.378) in which the nonhydrodynamic force used to calculate $\boldsymbol{\sigma}$ is taken to include the rapidly fluctuating random forces, and in which Brownian contributions to the stress are obtained as appropriately defined averages of the resulting random stresses. Both sets of authors also introduced similar methods of filtering the otherwise divergent $\mathcal{O}(1/\sqrt{\Delta t})$ fluctuations of the random forces, in order to obtain average stresses that are not swamped by random noise. Neither set of authors, however, provided a proof of the validity of their proposed method. It is confirmed here that Grassia and Hinch's method is valid for all valid variants of Fixman's algorithm, and that Doyle et al.'s method is valid for the class of rigid free-draining models to which Liu's timestepping algorithm applies. Because Fixman's algorithm is essentially identical to the definition of a kinetic SDE, Grassia and Hinch's method implicitly provides a stochastic definition of the stress tensor within the context of a kinetic interpretation of the Langevin equation for any constrained or unconstrained system of point particles.

A. Grassia and Hinch (in Fixman's Algorithm)

The stochastic stress $\boldsymbol{\sigma}$ in Grassia and Hinch's algorithm is given by a discrete approximation to the time average of Eq. (2.378) over one timestep, as

$$\boldsymbol{\sigma} = -\frac{1}{2V}\left[(\mathbf{R}^{\mu}\mathbf{F}_{\mu}^{(\mathrm{nh})})_0 + (\mathbf{R}^{\mu}\mathbf{F}_{\mu}^{(\mathrm{nh})})_1\right] \tag{2.393}$$

where

$$\mathbf{F}^{(\mathrm{nh})} = -\frac{\partial U_{\mathrm{eff}}}{\partial \mathbf{R}^{\mu}} + \mathbf{F}_{\nu}^{(\mathrm{ps})} + \boldsymbol{\eta}_{\nu} - \lambda_i \mathbf{n}_{\mu}^{i} \tag{2.394}$$

is the total nonhydrodynamic force on a bead, including both the rapidly varying random forces and constraint forces, and the corrective pseudoforce. Here and in the rest of this section, we use of sub- or superscripts of "0" and "1" on variables and parentheses to represent quantities that are evaluated using the bead

positions at the beginning and end of a single timestep, respectively. To define a instantaneous force at the ''end'' of the timestep (which is not needed in the timestepping algorithm), one calculates the instantaneous force that would be felt by a system evolving continuously in time, using the smooth forces, mobility, and normal vectors at the specified set of final bead positions, while taking the instantaneous random force $\boldsymbol{\eta}_\mu$ at both the beginning and end of the step to be that used to advance the bead positions during that timestep. In what follows, we calculate the conditional average $\langle \boldsymbol{\sigma} \rangle_0$ of the stochastic tension for a single timestep for with known bead positions at the beginning of the timestep. The macroscopic stress is given by an ensemble average of this conditional average with respect to bead positions.

It is useful to express the total nonhydrodynamic force $\mathbf{F}_\mu^{(\mathrm{nh})}$ as a sum

$$\mathbf{F}_\mu^{(\mathrm{nh})} = \mathbf{F}_\mu^{(\mathrm{s})} + \mathbf{F}_\mu^{(\mathrm{r})} \tag{2.395}$$

of smooth and random components

$$\mathbf{F}_\mu^{(\mathrm{s})} = \mathbf{P}_\mu{}^{,\nu} \cdot \left(-\frac{\partial U_{\mathrm{eff}}}{\partial \mathbf{R}^\nu} + \mathbf{F}_\nu^{(\mathrm{ps})} \right) + (\mathbf{P}_\mu{}^{,\nu} - \mathbf{I}_\mu^\nu) \cdot \mathbf{F}_\nu^{(\mathrm{f})} \tag{2.396}$$

$$\mathbf{F}_\mu^{(\mathrm{r})} = \mathbf{P}_\mu{}^{,\nu} \cdot \boldsymbol{\eta}_\nu \tag{2.397}$$

respectively. The stress is then divided into a corresponding smooth stress $\boldsymbol{\sigma}_{(\mathrm{s})}$ and random stress $\boldsymbol{\sigma}_{(\mathrm{r})}$, which are obtained by using smooth and random components of $\mathbf{F}_\mu^{(\mathrm{nh})}$, respectively, in Eq. (2.393). The smooth stress includes both the viscous stress, which is the contribution that arises from the last term in Eq. (2.396), and a smooth elastic contribution arising from the potential U_{eff} and pseudoforces, and the constraint forces induced by them. The random stress $\boldsymbol{\sigma}_{(\mathrm{r})}$ is a Brownian contribution to the elastic stress, which arises from stochastic fluctuations of $\mathbf{F}_\mu^{(\mathrm{r})}$.

The smooth component requires no particular care, and can be approximated equally well in the limit $\Delta t \to 0$ by using either inital or final values of the positions and forces. This yields a smooth stress

$$\boldsymbol{\sigma}_{(\mathrm{s})} = \frac{1}{V} \mathbf{R}^\mu \mathbf{P}_\mu{}^{,\nu} \cdot \left(\frac{\partial U_{\mathrm{eff}}}{\partial \mathbf{R}^\nu} - \mathbf{F}_\nu^{(\mathrm{ps})} \right) - \frac{1}{V} \mathbf{R}^\mu (\mathbf{P}_\mu{}^{,\nu} - \mathbf{I}_\mu^\nu) \cdot \mathbf{F}_\nu^{(\mathrm{f})} \tag{2.398}$$

in which all quantities on the RHS are evaluated at the initial bead positions. The first term of the RHS Eq. (2.398) is the smooth elastic stress, which is equal to the quantity being averaged in the first line of Eq. (2.390). The second term is the viscous stress.

We focus herafter on the random elastic stress, which is obtained by replacing $\mathbf{F}_\mu^{(\mathrm{nh})}$ by $\mathbf{F}_\mu^{(\mathrm{r})}$ in Eq. (2.393). To evaluate the required average over

random forces, we follow both Grassia and Hinch [20] and Doyle et al. [23] by noting that the contribution from the beginning of the timestep has fluctuations of $\mathcal{O}(1/\sqrt{t})$ but a vanishing mean value

$$\langle (\mathbf{R}^{\mu}\mathbf{F}^{(\mathrm{r})}_{\mu})_0 \rangle_0 = 0 \tag{2.399}$$

because the initial random force $\mathbf{F}^{(\mathrm{r})}_{\mu}$ is a linear function of $\boldsymbol{\eta}_1, \ldots, \boldsymbol{\eta}_N$ terms, which have vanishing mean values. We may thus remove the $\mathcal{O}(1/\sqrt{\Delta t})$ fluctuations from the stochastic stress, without changing the desired conditional average value, by changing the sign on this vanishing contribution, to obtain the "filtered" expression

$$\langle \boldsymbol{\sigma}_{(\mathrm{r})} \rangle_0 = -\frac{1}{2V} \left\langle \left(\mathbf{R}^{\mu}\mathbf{F}^{(\mathrm{r})}_{\mu} \right)_1 - \left(\mathbf{R}^{\mu}\mathbf{F}^{(\mathrm{r})}_{\mu} \right)_0 \right\rangle_0 \tag{2.400}$$

This quantity has fluctuations of $\mathcal{O}(1)$, and a nonvanishing mean value of the same order. The use of this filtered expression is essential to the construction of a practical stochastic algorithm for the stress.

To evaluate Eq. (2.400), we expand the final bead positions $\mathbf{R}^{\mu}_{(1)}$ and random forces $\mathbf{F}^{(\mathrm{r},1)}_{\mu}$ around their values at the beginning of the timestep, as

$$\begin{aligned} \mathbf{R}^{\mu}_{(1)} &= \mathbf{R}^{\mu}_{(0)} + \Delta\mathbf{R}^{\mu} \\ \mathbf{F}^{(\mathrm{r},1)}_{\mu} &= \mathbf{F}^{(\mathrm{r},0)}_{\mu} + \Delta\mathbf{F}_{\mu} \end{aligned} \tag{2.401}$$

and keep only terms of $\mathcal{O}(1)$ to obtain

$$\langle \boldsymbol{\sigma}_{(r)} \rangle_0 \simeq -\frac{1}{2V} \langle \Delta\mathbf{R}^{\mu}\mathbf{F}^{(r)}_{\mu} + \mathbf{R}^{\mu}\Delta\mathbf{F}^{(r)}_{\mu} \rangle_0 \tag{2.402}$$

Here and hereafter, we drop the superscript 0 in quantities that are evaluated at the initial position. To evaluate the first term in Eq. (2.402) to an accuracy of $\mathcal{O}(1)$, we need only the dominant $\mathcal{O}(\sqrt{\Delta t})$ approximation for $\Delta\mathbf{R}$:

$$\Delta\mathbf{R}^{\mu} \simeq \mathbf{K}^{\mu\nu} \cdot \boldsymbol{\eta}_{\nu} \Delta t \tag{2.403}$$

Together wtih Eq. (2.397) for the $\mathbf{F}^{(\mathrm{r})}_{\mu}$, and (2.348) for the variance of the noise, this yields

$$\begin{aligned} \langle \Delta\mathbf{R}^{\mu}\mathbf{F}^{(r)}_{\mu} \rangle_0 &\simeq \mathbf{K}^{\mu\nu} \cdot \langle \boldsymbol{\eta}_{\nu}\boldsymbol{\eta}_{\lambda} \rangle_0 \cdot \mathbf{P}^{\lambda}{}_{,\mu} \Delta t \\ &\simeq 2\,kT\,\mathbf{P}^{\mu}{}_{,\mu} \end{aligned} \tag{2.404}$$

The second expression here follows from the fact that $\bar{\mathbf{P}}^{\mu}{}_{,\lambda} \cdot \mathbf{P}^{\lambda}{}_{,\mu} = \mathbf{P}^{\mu}{}_{,\mu}$ for $\bar{\mathbf{P}}^{\mu}{}_{,\lambda} = \mathbf{K}^{\mu\nu} \cdot \mathbf{Z}_{\nu\lambda}$.

To evaluate the second term in Eq. (2.402), we must evaluate the average $\Delta\mathbf{F}_{\mu}^{(\mathrm{r})}$ for one timestep. Because $\boldsymbol{\eta}_{\nu}$ is regarded as constant over a timestep, the change in Eq. (2.397) for $\mathbf{F}_{\mu}^{(\mathrm{r})}$ arises from the change in $\mathbf{P}_{\mu}{}^{,\nu}$ during the step, which causes a change in the constraint force induced by $\boldsymbol{\eta}_{\nu}$. Taylor-expanding $\mathbf{P}_{\mu}{}^{,\nu}$ to first order in $\Delta\mathbf{R}^{\lambda}$ yields

$$\Delta\mathbf{F}_{\mu}^{(\mathrm{r})} = \Delta\mathbf{R}^{\lambda} \cdot \frac{\partial \mathbf{P}_{\mu}{}^{,\nu}}{\partial \mathbf{R}^{\lambda}} \cdot \boldsymbol{\eta}_{\nu} \tag{2.405}$$

Using approximation (2.403) for $\Delta\mathbf{R}^{\lambda}$ averaging then yields

$$\left\langle \Delta\mathbf{F}_{\mu}^{(\mathrm{r})} \right\rangle_0 = 2kT\bar{\mathbf{P}}_{\nu}{}^{,\lambda} : \frac{\partial \mathbf{P}^{\nu}{}_{,\mu}}{\partial \mathbf{R}^{\lambda}} \tag{2.406}$$

where $\bar{\mathbf{P}}_{\nu}{}^{,\lambda}$ is given by Eq. (2.298). Combining this with Eqs. (2.402) and (2.404) then yields a total random stress

$$\langle \boldsymbol{\sigma}_{(\mathrm{r})} \rangle_0 = -\frac{kT}{V}\left(\mathbf{P}^{\mu}{}_{,\mu} + \mathbf{R}^{\mu}\bar{\mathbf{P}}_{\nu}{}^{,\lambda} : \frac{\partial \mathbf{P}^{\nu}{}_{,\mu}}{\partial \mathbf{R}^{\lambda}} \right) \tag{2.407}$$

Equation (2.407) is identical to sum of quantities averaged in the second line of Eq. (2.390) for the elastic stress. Adding this Brownian stress to Eq. (2.398) for the smooth stress yields a total stress whose ensemble average is equal to the sum of Eq. (2.390) for the elastic stress and Eq. (2.381) for the smooth viscous stress.

B. Doyle et al. (in Liu's Algorithm)

Doyle et al. [23] have proposed a similar stochastic method of evaluating the stress in Liu's algorithm for rigid free-draining systems. The stochastic stress is given in this algorithm as

$$\boldsymbol{\sigma} = -\frac{1}{2V}\left(\mathbf{R}_{(0)}^{\mu} + \mathbf{R}_{(1)}^{\mu} \right) \mathbf{F}_{\mu}^{(\mathrm{nh})} \tag{2.408}$$

where

$$\mathbf{F}_{\nu}^{(\mathrm{nh})} = -\frac{\partial U}{\partial \mathbf{R}^{\nu}} + \boldsymbol{\eta}_{\nu} - \lambda_i \mathbf{n}_{\nu}^{i} \tag{2.409}$$

is the total nonhydrodynamic force exerted during the timestep, in which $\partial U/\partial \mathbf{R}^{\mu}$, and $\mathbf{n}_{\nu}^{i}$ are evaluated at the initial bead positions, and λ_i is chosen so as

to satisfy the constraints at the end of the step. This stress may be divided into a smooth part, which is adequately approximated as

$$\boldsymbol{\sigma}_{(\mathrm{s})} = \frac{1}{V}\mathbf{R}^{\mu}\mathbf{P}_{\mu}{}^{,\nu}\cdot\frac{\partial U}{\partial \mathbf{R}^{\nu}} - \frac{1}{V}\mathbf{R}^{\mu}(\mathbf{P}_{\mu}{}^{,\nu} - \mathbf{I}_{\mu}^{\nu})\cdot\mathbf{F}_{\nu}^{(\mathrm{f})} \tag{2.410}$$

with all quantities evaluated at the initial bead positions, and a random part

$$\boldsymbol{\sigma}_{(r)} = -\frac{1}{2V}\left(\mathbf{R}_{(0)}^{\mu} + \mathbf{R}_{(1)}^{\mu}\right)\left(\mathbf{P}_{\mu}{}^{,\nu}\cdot\boldsymbol{\eta}_{\nu} - \mathbf{n}_{\mu}^{i}\Delta\lambda_{i}\right) \tag{2.411}$$

where

$$\Delta\lambda_{i} \equiv \lambda_{i} - \lambda_{i}^{(1)} \tag{2.412}$$

and where $\lambda_{i}^{(1)}$ is a linear approximation to λ_{i}, given by the solution of

$$\hat{H}^{ij}\lambda_{i}^{(1)} = \mathbf{n}_{\mu}^{i}\cdot\mathbf{H}^{\mu\nu}\left(-\frac{\partial U}{\partial \mathbf{R}^{\nu}} + \mathbf{F}_{\nu}^{(\mathrm{f})} + \boldsymbol{\eta}_{\nu}\right) \tag{2.413}$$

with $\mathbf{H}^{\mu\nu} = \mathbf{I}^{\mu\nu}/\zeta$. The $\mathcal{O}(1/\sqrt{t})$ fluctuations of the random stress may be removed from the calculation of the average value $\langle\boldsymbol{\sigma}_{(r)}\rangle_{0}$ by subtracting

$$-\left\langle\mathbf{R}_{(0)}^{\mu}\mathbf{P}_{\mu}{}^{,\nu}\cdot\boldsymbol{\eta}_{\nu}\right\rangle = 0 \tag{2.414}$$

from the average, to obtain the "filtered" expression

$$\langle\boldsymbol{\sigma}_{(r)}\rangle_{0} \simeq -\frac{1}{2V}\langle\Delta\mathbf{R}^{\mu}\mathbf{P}_{\mu}{}^{,\nu}\cdot\boldsymbol{\eta}_{\nu} - \mathbf{R}^{\mu}\mathbf{n}_{\mu}^{i}\Delta\lambda_{i}\rangle_{0} \tag{2.415}$$

The first term on the RHS of Eq. (2.415) yields

$$-\frac{1}{2V}\langle\Delta\mathbf{R}^{\mu}\mathbf{P}_{\mu}{}^{,\nu}\cdot\boldsymbol{\eta}_{\nu}\rangle_{0} \simeq -\frac{kT}{V}\mathbf{P}^{\mu}{}_{,\mu} \tag{2.416}$$

as in Grassia and Hinch's algorithm. To calculate the second term in Eq. (2.415), we use Eq. (2.369) for $\Lambda_{i} = \lambda_{i}\Delta t$, with $c = 0$, to show that

$$\Delta\lambda_{i} \simeq \frac{1}{2\Delta t}\Delta\mathbf{R}^{\nu}\Delta\mathbf{R}^{\rho}\colon\frac{\partial c^{j}}{\partial\mathbf{R}^{\rho}\partial\mathbf{R}^{\nu}}\hat{H}_{ji}^{-1} \tag{2.417}$$

Evaluating the average of the second term in Eq. (2.415) and adding it to Eq. (2.416) then yields a random stress

$$\langle \boldsymbol{\sigma}_{(r)} \rangle_0 \simeq -\frac{kT}{V}\mathbf{P}^{\mu}{}_{,\mu} - \frac{kT}{V}\mathbf{R}^{\mu}\mathbf{K}^{\nu\rho} : \frac{\partial c^j}{\partial \mathbf{R}^{\rho}\,\partial \mathbf{R}^{\nu}}\hat{H}^{-1}_{ji}\mathbf{n}^i_{\mu} \tag{2.418}$$

We then compare Eq. (2.418) to the second line on the RHS of Eq. (2.390), for the case of a generalized projection tensor $\bar{\mathbf{P}}_{\nu}{}^{,\lambda} = \mathbf{P}_{\nu}{}^{,\lambda}$, which is the same as the inertial or geometric projection tensor in this simple class of models. After some straightforward algebra, we find that, for the class of models to which Liu's algorithm applies, the last term in Eq. (2.390) may be written more explicitly as

$$-\mathbf{R}^{\mu}\mathbf{P}_{\nu}{}^{,\lambda} : \frac{\partial \mathbf{P}^{\nu}{}_{,\mu}}{\partial \mathbf{R}^{\lambda}} \simeq -kT\mathbf{R}^{\mu}\mathbf{K}^{\nu\rho} : \frac{\partial c^j}{\partial \mathbf{R}^{\rho}\partial \mathbf{R}^{\nu}}\hat{H}^{-1}_{ji}\mathbf{n}^i_{\mu} \tag{2.419}$$

thus confirming that the random stress given in Eq. (2.418) is equal to the Brownian stress given by the second line in Eq. (2.390). For this class of models, with this choice for $\bar{\mathbf{P}}_{\nu}{}^{,\lambda}$, the forces $\mathbf{F}^{(\mathrm{ps})}_{\nu}$ and $kT\partial \ln \sqrt{W}/\partial \mathbf{R}^{\mu}$ cancel in the first line of Eq. (2.390). Adding Eq. (2.418) to the smooth stress then yields the correct total stress, given by the sum of Eq. (2.390) for the elastic stress and Eq. (2.381) for the viscous stress.

Acknowledgments

This work was supported by NSF Grants DMR-9973976 and PHY99-07949, the latter of which supports the Kavli Institute for Theoretical Physics, where much of this work was completed. I would also like to acknowledge Marshall Fixman and Hans-Christian Öttinger for helpful correspondence, and Shriram Ramanathan for reading and commenting on an earlier draft of the manuscript.

APPENDIX

A. Nomenclature

The last column of the following table of symbols lists either the equation or equations (Arabic numbers in parentheses) or the section (Roman numerals) in which the symbol is introduced and defined.

Symbol	Meaning	Introduced
N	Number of beads	II
K	Number of holonomic constraints	II
f	$= 3N - K$, number of soft coordinates	II
$\mathbf{R}^{\mu}$	Position of bead $\mu = 1, \ldots, N$	II
c^i	Constrained (hard) coordinate $i = 1, \ldots, K$	(2.1)
q^a	Unconstrained (soft) coordinate $a = 1, \ldots, f$	(2.2)
Q^{α}	General coordinate $\alpha = 1, \ldots, 3N$	(2.3)
$\mathbf{a}^{\mu}_a$	Tangent (soft) basis vector	(2.8)

$\mathbf{n}_\mu^i$	Normal (hard) basic vector	(2.9)
$\mathbf{H}^{\mu\nu}$	Cartesian mobility tensor	(2.10)
$\boldsymbol{\zeta}_{\mu\nu}$	Cartesian friction tensor	(2.11)
$\mathbf{m}_{\mu\nu}$	Cartesian mass tensor	(2.12)
$g_{\alpha\beta}$	Covariant metric in full space	(2.16)
$G^{\alpha\beta}$	Contravariant (inverse) metric in full space	(2.17)
$\tilde{S}_{ab}$	Projection of $S_{\alpha\beta}$ in soft subspace	(2.20)
$\hat{T}^{ij}$	Projection of $T^{\alpha\beta}$ in hard subspace	(2.24)
p^a	Hamiltonian momentum	(2.31)
$\rho(q,p)$	Phase space distribution	(2.29)
$\psi(q)$	Distribution of soft coordinates	(2.33)
$\mathscr{H}(q,p)$	Hamiltonian	(2.32)
$U(q)$	Potential energy on constraint surface	(2.32)
$V(Q)$	Potential energy of stiff system	(2.36)
$D_{ij}(q)$	Spring constants $= \partial^2 V/\partial c_i \partial c_j$	(2.36)
$W(q)$	Prefactor in $\psi_{\text{eq}}(q)$	(2.67),(2.68)
U^a	Flux velocity (soft coordinates)	(2.70)
U^μ	Flux velocity (Cartesian coordinates)	(2.71)
$F_a^{(\text{e})}$	Elastic force (soft coordinates)	(2.73)
$F_a^{(\text{h})}$	Hydrodynamic force (soft coordinates)	(2.74)
$F_a^{(\text{f})}$	Flow force (soft coordinates)	(2.75)
K^{ab}	Constrained mobility (soft coordinates)	(2.74),(2.128)
$\langle\cdots\rangle_{\text{s}}$	Average over solvent forces, at fixed q and p	(2.79)
$\langle\cdots\rangle_{\text{p}}$	Average over solvent forces and p, at fixed q	(2.79)
$\langle\cdots\rangle_{\text{f}}$	Average over fast variables, at fixed q	(2.104)
τ_i	Constraint force	(2.121),(2.131)
$\mathbf{F}_\mu^{(\text{e})}$	Elastic force (Cartesian)	(2.122)
$\mathbf{F}_\mu^{(\text{h})}$	Hydrodynamic force (Cartesian)	(2.123)
$\mathbf{F}_\mu^{(\text{f})}$	Flow force (Cartesian)	(2.124)
$\mathbf{K}^{\mu\nu}$	Constrained mobility (Cartesian)	(2.133),(2.136)
V^a	Drift velocity (soft coordinates)	(2.154),(2.160)
D^{ab}	Diffusivity (soft coordinates)	(2.155)
$\mathbf{V}^\mu$	Drift velocity (Cartesian coordinates)	(2.163),(2.169)
$\mathbf{D}^{\mu\nu}$	Diffusivity (Cartesian coordinates)	(2.164)
$\langle\cdots\rangle_0$	Average given known coordinates at $t = 0$	(2.154–2.155)
$\bar{\mathbf{b}}_\mu^a, \bar{\mathbf{m}}_i^\mu$	Generalized reciprocal vectors	(2.186–2.190)
$\mathbf{b}_\mu^a, \mathbf{m}_i^\mu$	Dynamical reciprocal vectors	(2.144),(2.145)
$\mathbf{b}_\mu^a, \mathbf{m}_i^\mu$	Geometric reciprocal vectors	(2.211),(2.212)
$\bar{\mathbf{P}}^\mu{}_\nu$	Generalized projection tensor	(2.191)–(2.195)
$\mathbf{P}^\mu{}_\nu$	Dynamical projection tensor	(2.138)
$\tilde{\mathbf{P}}^\mu{}_\nu$	Geometric projection tensor	(2.213)
$\breve{\mathbf{P}}^\mu{}_\nu$	Inertial projection tensor	(2.217)

$\mathbf{F}_{\nu}^{(\mathrm{ps})}$	Pseudoforce	(2.203–2.205)
X^{α}	Generic coordinate $\alpha = 1, \ldots, L$	IX
$\mathscr{P}(X)$	Probability distribution (generic coordinates)	(2.222)
V^{α}	Drift velocity (generic coordinates)	(2.223)
$D^{\alpha\beta}$	Diffusivity (generic coordinates)	(2.224)
A^{α}	Drift coefficient (generic coordinates)	IX
A^{a}	Drift coefficient (soft coordinates)	IX
$\mathbf{A}^{\mu}$	Drift coefficient (Cartesian coordiantes)	IX
$\langle \cdots \rangle_t$	Average given known coordinates at time t	(2.265),(2.266)
η_{β}	Random Langevin forces (generic)	(2.262–2.268)
$Z_{\alpha\beta}$	Variance tensor for random forces (generic)	(2.267),(2.268)
$\overline{\langle \eta_{\beta} \rangle_0}$	Langevin force bias (generic)	(2.283)
$\boldsymbol{\eta}_{\nu}$	Random Langevin forces (Cartesian)	(2.288)–(2.294)
$\mathbf{Z}_{\mu\nu}$	Variance tensor for random forces (Cartesian)	(2.294),(2.295)
$\overline{\langle \boldsymbol{\eta}_{\beta} \rangle_0}$	Langevin force bias (Cartesian)	(2.297)

B. Projected Tensors

In this section, we develop some useful relationships involving the determinants and inverses of projected tensors. Let $S_{\alpha\beta}$ be the Riemannian representation of an arbitrary symmetric covariant tensor with a Cartesian representation $\mathbf{S}_{\mu\nu}$. We may write the Riemannian representation in block matrix form, using the indices a,b to denote blocks in which α or β runs over the soft coordinates and i,j to represent hard coordinates, as

$$S = \begin{bmatrix} \tilde{S}_{ab} & S_{aj} \\ S_{ib} & S_{ij} \end{bmatrix} \tag{A.1}$$

where upper left block is the projected tensor $\tilde{S}_{ab}$ defined in Eq. (2.20). Let $T^{\alpha\beta} = (S^{-1})^{\alpha\beta}$, which we may write in the corresponding form

$$T = \begin{bmatrix} T^{ab} & T^{aj} \\ T^{ib} & \hat{T}^{ij} \end{bmatrix} \tag{A.2}$$

where the lower right block is the projected tensor $\hat{T}^{ij}$ defined in Eq. (2.24).

1. *Determinants*

We first prove a theorem given by Fixman relating the determinants of projected tensors S_{ab} and T^{ij}, which is stated in Eq. (2.28). The proof given here follows that given for the mass matrix in Ref. 35. Define a $3N \times 3N$ matrix

$$X = \begin{bmatrix} \tilde{S}_{ab} & 0 \\ S_{ib} & 1 \end{bmatrix} \tag{A.3}$$

By expanding the determinant in minors, we find that

$$\det(X) = \det(\tilde{S}) \tag{A.4}$$

Also note that

$$T \cdot X = \begin{bmatrix} 1 & T^{aj} \\ 0 & \hat{T}^{ij} \end{bmatrix} \tag{A.5}$$

which has a determinant

$$\det(T \cdot X) = \det(T)\det(X) = \det(\hat{T}) \tag{A.6}$$

Using Eq. (A.4) for $\det(X)$ in the second equality of Eq. (A.6) then yields Eq. (2.28).

2. *Inversion*

We next present a relationship between the inverses of the projected tensors $\tilde{S}$ and $\hat{T}$ within the soft and hard subspaces, respectively. By requiring that the matrix product of the block matrices (A.1) and (A.2) yield the identity tensor, it is straightforward to show that the elements of the matrix

$$(\tilde{S}^{-1})^{\alpha\beta} \equiv T^{\alpha\beta} - T^{\alpha i}\, \hat{T}^{-1}_{ij}\, T^{j\beta} \tag{A.7}$$

within the soft subspace, where $\alpha, \beta = 1, \ldots, f$, yield the inverse of $\tilde{S}_{ab}$ within this subspace. Furthermore, if the RHS of Eq. (A.7) is interpreted as a matrix in the full space, then all elements outside of the soft subspace (for which $\alpha > f$ and/or $\beta > f$) are easily shown to vanish. Similarly

$$\hat{T}^{-1}_{\alpha\beta} \equiv S_{\alpha\beta} - S_{\alpha a}\, (\tilde{S}^{-1})^{ab}\, S_{b\beta} \tag{A.8}$$

is a $3N \times 3N$ matrix that is the inverse of $\hat{T}_{ij}$ within the hard subspace, and that has vanishing elements outside of this subspace.

We define Cartesian representations of these inverse projected tensors as sums:

$$(\tilde{\mathbf{S}}^{-1})^{\mu\nu} \equiv \mathbf{a}^{\mu}_{a} (\tilde{S}^{-1})^{ab} \mathbf{a}^{\nu}_{b} \tag{A.9}$$

$$(\tilde{\mathbf{T}}^{-1})_{\mu\nu} \equiv \mathbf{n}^{i}_{\mu} (\hat{T}^{-1})_{ij} \mathbf{n}^{j}_{\nu} \tag{A.10}$$

Because Eq. (A.7) and (A.8) yield expressions for the corresponding Reimannian tensors that vanish outside of the soft and hard subspaces, respectively, we may use these expressions for $(\tilde{S}^{-1})^{\alpha\beta}$ and $(\hat{T}^{-1})_{\alpha\beta}$ in Eqs. (A.9) and (A.10), and extend the summations over indices to include all $3N$ generalized coordinates,

while generalizing $\mathbf{a}_a^\mu$ to $\partial\mathbf{R}^\mu/\partial Q^\alpha$ and $\mathbf{n}_\mu^i$ to $\partial Q^\alpha/\partial\mathbf{R}^\mu$, without changing the result. Carrying out these expansions yield

$$(\tilde{\mathbf{S}}^{-1})^{\lambda\rho} = \mathbf{T}^{\lambda\rho} - \mathbf{T}^{\lambda\mu}\cdot\tilde{\mathbf{T}}^{-1}_{\mu\nu}\cdot\mathbf{T}^{\nu\rho} \tag{A.11}$$

$$\tilde{\mathbf{T}}^{-1}_{\lambda\rho} = \mathbf{S}_{\lambda\rho} - \mathbf{S}_{\lambda\mu}\cdot(\tilde{\mathbf{S}}^{-1})^{\mu\nu}\cdot\mathbf{S}_{\nu\rho} \tag{A.12}$$

which are Cartesian representations of (A.7) and (A.8). Equation (2.133) for the Cartesian modified mobility $\mathbf{K}^{\mu\nu} \equiv (\tilde{\boldsymbol{\zeta}}^{-1})^{\mu\nu}$ is an application of Eq. (A.11) to the case $\mathbf{T}^{\mu\nu} = \mathbf{H}^{\mu\nu}$.

The reciprocal vectors defined in Section VIII may be used to construct a more direct derivation. Let $\bar{\mathbf{b}}$ and $\bar{\mathbf{m}}$ refer to reciprocal basis vectors defined using $\mathbf{S}_{\mu\nu}$ and $\mathbf{T}^{\mu\nu}$ in Eqs. (2.207) and (2.208), respectively. By substituting definitions (2.207) and (2.208) into completeness relation (2.190), we find that

$$\mathbf{I}_\nu^\lambda = (\tilde{\mathbf{S}}^{-1})^{\lambda\mu}\cdot\mathbf{S}_{\mu\nu} + \mathbf{T}^{\lambda\mu}\cdot(\tilde{\mathbf{T}}^{-1})_{\mu\nu} \tag{A.13}$$

for arbitrary $\mathbf{T}$ and $\mathbf{S} = \mathbf{T}^{-1}$. Multiplying Eq. (A.13) on the right by $\mathbf{T}$ or on the left by $\mathbf{S}$ then yields Eqs. (A.11) or (A.12), respectively.

C. Derivatives of Determinants

In this section, we derive expressions for derivatives of various determinants, all of which are evaluated by using the identity

$$\frac{\partial \ln M}{\partial X} = M_{ij}^{-1}\frac{\partial M_{ij}(X)}{\partial X} \tag{A.14}$$

for a derivative of the determinant $M \equiv \det[M]$ of an $N \times N$ square nonsingular matrix $M_{ij}(X)$ whose elements are functions of some parameter X.

We first consider derivatives with respect to curvilinear coordinates of the determinant g of the metric tensor $g_{\alpha\beta}$ in the unconstrained space. Using Eq. (A.14) and definition (2.16) for $g_{\alpha\beta}$ yields

$$\begin{aligned}\frac{\partial \ln g}{\partial Q^\gamma} &= G^{\alpha\beta}\frac{\partial g_{\alpha\beta}}{\partial Q^\gamma}\\ &= G^{\alpha\beta}\frac{\partial}{\partial Q^\gamma}\left(\frac{\partial\mathbf{R}^\mu}{\partial Q^\alpha}\cdot\frac{\partial\mathbf{R}^\mu}{\partial Q^\beta}\right)\\ &= 2G^{\alpha\beta}\frac{\partial\mathbf{R}^\mu}{\partial Q^\alpha}\cdot\frac{\partial^2\mathbf{R}^\mu}{\partial Q^\beta\partial Q^\gamma}\\ &= 2\frac{\partial Q^\beta}{\partial\mathbf{R}^\mu}\cdot\frac{\partial^2\mathbf{R}^\mu}{\partial Q^\beta\partial Q^\gamma}\end{aligned} \tag{A.15}$$

where $G^{\alpha\beta} = (g^{-1})^{\alpha\beta}$.

Derivatives of the determinants $\tilde{S}$ and $\hat{T}$ of the generic projected tensors $\tilde{S}_{ab}$ and $\hat{T}_{ij}$ defined in Eqs. (2.20) and (2.24) may be expressed compactly in terms of the reciprocal vectors that are generated by applying Eqs. (2.207) and (2.208) to the corresponding Cartesian tensors $\mathbf{S}_{\mu\nu}$ and $\mathbf{T}^{\mu\nu}$, respectively. Using Eq. (A.14) to differentiate $\ln \tilde{S}$ with respect to a soft variable gives

$$\begin{aligned}\frac{\partial \ln \tilde{S}}{\partial q^a} &= (\tilde{S}^{-1})^{bc} \frac{\partial \left(\mathbf{a}_b^\mu \cdot \mathbf{S}_{\mu\nu} \cdot \mathbf{a}_c^\nu\right)}{\partial q^a} \\ &= 2\bar{\mathbf{b}}_\mu^b \cdot \frac{\partial \mathbf{a}_b^\mu}{\partial q^a} + (\tilde{S}^{-1})^{bc} \mathbf{a}_b^\mu \cdot \frac{\partial \mathbf{S}_{\mu\nu}}{\partial q^a} \cdot \mathbf{a}_c^\nu \end{aligned} \tag{A.16}$$

where $\bar{\mathbf{b}}_\mu^b$ is related to $\mathbf{S}_{\mu\nu}$ by Eq. (2.207). Similar reasoning may be used to show that

$$\frac{\partial \ln \hat{T}}{\partial q^a} = 2\bar{\mathbf{m}}_i^\mu \cdot \frac{\partial \mathbf{n}_\mu^i}{\partial q^a} + \hat{T}_{ij}^{-1} \mathbf{n}_\mu^i \cdot \frac{\partial \mathbf{T}^{\mu\nu}}{\partial q^a} \cdot \mathbf{n}_\nu^j \tag{A.17}$$

where $\bar{\mathbf{m}}_i^\mu$ is related to $\mathbf{T}^{\mu\nu}$ by Eq. (2.208).

Simpler expressions for the derivatives of $\tilde{S}$ and $\tilde{H}$ are obtained if $\mathbf{S}_{\mu\nu}$ and $\mathbf{T}^{\mu\nu}$ are constants, so that the terms involving derivatives of the Cartesian tensors vanish in Eqs. (A.16) and (A.17). In particular, for $\mathbf{S}_{\mu\nu} = \mathbf{I}_{\mu\nu}$, we obtain

$$\frac{\partial \ln \sqrt{\tilde{g}}}{\partial q^a} = \tilde{\mathbf{b}}_\mu^b \cdot \frac{\partial \mathbf{a}_b^\mu}{\partial q^a} \tag{A.18}$$

$$\frac{\partial \ln \sqrt{\hat{G}}}{\partial q^a} = \hat{\mathbf{m}}_i^\mu \cdot \frac{\partial \mathbf{n}_\mu^i}{\partial q^a} \tag{A.19}$$

where $\tilde{\mathbf{b}}_\mu^b$ and $\hat{\mathbf{m}}_i^\mu$ are geometrical reciprocal vectors defined in Eqs. (2.211) and (2.212).

D. Stiff Quantum Systems

Here, we review an adiabatic approximation for the statistical mechanics of a stiff quantum mechanical system, in which vibrations of the hard coordinates are first treated quantum mechanically, while treating the more slowly evolving soft coordinates and momenta for this purpose as parameters, and in which the constrained free energy obtained by summing over vibrational quantum states is then used as a potential energy in a classical treatment of the soft coordinates and momenta.

We first construct an adiabatic approximation for the classical Hamiltonian equations of motion. We start from an unconstrained model with a classical

Hamiltonian $\mathscr{H}(Q,P) = K(Q,P) + V(Q)$, in which the inverse mass tensor in the kinetic energy $K = \frac{1}{2}(m^{-1})^{\alpha\beta}P_\alpha P_\beta$ may be expressed in block form

$$m^{-1} = \begin{bmatrix} (m^{-1})^{ab} & (m^{-1})^{aj} \\ (m^{-1})^{ib} & (\widehat{m^{-1}})^{ij} \end{bmatrix} \tag{A.20}$$

as in Section B of this appendix. To approximately decouple the dynamics of soft and hard coordinates, it is useful to define modified hard momenta

$$\hat{P}_i \equiv P_{i+f} + (\widehat{m^{-1}})^{-1}_{ij}(m^{-1})^{ja}p_a \tag{A.21}$$

in which P_{i+f} is the Hamiltonian momentum conjugate to the hard coordinate $Q^{i+f} = c^i$, and p_a is conjugate to the soft coordinate $Q^a = q^a$. It is straightforward to confirm that the rates of change of the hard coordinates may be expressed in terms of these quantities as

$$\frac{dc^i}{dt} = (m^{-1})^{i\beta}P_\beta = (\widehat{m^{-1}})^{ij}\hat{P}_j \tag{A.22}$$

where $\beta = 1, \ldots, 3N$ and $i,j = 1, \ldots, K$

An appropriate approximation for the rate change of the modified hard momenta may then be obtained by assuming that

1. The soft coordinates and momenta may be treated as constants for the purpose of describing the rapid vibrations of the hard coordinates. This is the adiabatic approximation.
2. Elements of the inverse mass matrix may be approximated in the stiff limit by their values on the constraint surface, which are functions only of the soft coordinates, thus ignoring the slight variations arising from fluctuations in hard coordinates. This is a generalization of the neglect of the effect of centrifugal force on the vibrations in the rigid-rotor harmonic oscillator approximator for a classical diatomic molecule.
3. The potential energy $V(Q)$ may be approximated by the harmonic approximation of Eq. (2.36).

Assumptions (1) and (2) allow us to assume that the rate of change of the second term on the RHS of Eq. (A.21) is negligible compared to the rate of change of the canonical hard momentum P_{i+f}, and thus that

$$\frac{d\hat{P}_i}{dt} \simeq \frac{dP_{i+f}}{dt} = -\frac{\partial V}{\partial c^i} \tag{A.23}$$

Combining this with the harmonic approximation for $V(Q)$ yields the approximation

$$\frac{d\hat{\boldsymbol{P}}_i}{dt} \simeq -D_{ij}\delta c^j \tag{A.24}$$

Combining Eqs. (A.22) and (A.24), while again treating $(\widehat{m^{-1}})^{ij}$ as a constant, yields an approximate vibrational equation of motion

$$\frac{d^2}{dt^2}\delta c^i \simeq -F^i_{,j}\delta c^j \tag{A.25}$$

with a dynamical matrix

$$F^i_{,j} \equiv (\widehat{m^{-1}})^{ik} D_{kj} \tag{A.26}$$

The corresponding vibrational eigenmodes and eigenfrequencies at a given point q on the constraint surface are given by the solutions of the eigenvalue equation

$$F^i_{,j}(q)\delta c^j_k = \delta c^j_k \omega^2_k(q) \tag{A.27}$$

where $\omega_k(q)$ with $k = 1, \ldots, K$ are the K classical vibration frequencies.

We now consider the equilibrium distribution. Definition (A.21) may be used to rewrite the kinetic energy K as a sum

$$K = \frac{1}{2}(\widehat{m^{-1}})^{ij}\hat{\boldsymbol{P}}_i\hat{\boldsymbol{P}}_j + \frac{1}{2}(\tilde{\boldsymbol{m}}^{-1})^{ab}p_a p_b \tag{A.28}$$

in which we have used the identity

$$(\tilde{\boldsymbol{m}}^{-1})^{ab} = (m^{-1})^{ab} - (m^{-1})^{ai}(\widehat{m^{-1}})^{-1}_{ij}(m^{-1})^{jb} \tag{A.29}$$

to obtain the second term. By combining Eq. (A.28) for the kinetic energy and harmonic approximation (2.36) for $V(Q)$, we may thus write the classical Hamiltonian as a sum

$$\mathscr{H} = \mathscr{H}_{\text{vib}} + \mathscr{H}_{\text{rigid}} \tag{A.30}$$

where

$$\mathscr{H}_{\text{vib}} = \frac{1}{2}(\widehat{m^{-1}})^{ij}\hat{\boldsymbol{P}}_i\hat{\boldsymbol{P}}_j + \frac{1}{2}D_{ij}\delta c^i \delta c^j \tag{A.31}$$

is a vibrational Hamiltonian, and

$$\mathscr{H}_{\text{rigid}} = \frac{1}{2}(\tilde{\boldsymbol{m}}^{-1})^{ab}p_a p_b + U(q) \tag{A.32}$$

is the Hamiltonian of a corresponding classical rigid model. A quantum statistical mechanical treatment of the vibrations, in which soft coordinates and momenta are treated as parameters, yields the q-dependent vibrational partition function given in Eq. (2.42). Using $Z_{\rm vib}(q)$ as a statistical weight in a classical treatment of the remaining soft coordinates and momenta then yields a reduced phase space density

$$\rho_{\rm eq}(q,p) \propto e^{-\mathscr{H}_{\rm rigid}(q,p)/kT} Z_{\rm vib}(q) \tag{A.33}$$

which is equivalent to that of a rigid classical model with the effective potential energy $U_{\rm eff}(q) = U(q) - kT \ln Z_{\rm vib}(q)$ defined in Eq. (2.41).

In the high-temperature limit, where $kT \gg \hbar\omega_k$ for all K eigenmodes, Eq. (A.33) recovers the classical stiff result of Eq. (2.39). To show this, we first note that, in this limit

$$\prod_{k=1}^{K} \left[2 \sinh\left(\frac{\hbar\omega_k(q)}{2kT} \right) \right]^{-1} \simeq \prod_{k=1}^{K} \frac{kT}{\hbar\omega_k(q)} \tag{A.34}$$

We then note that the determinant $F(q)$ of the dynamical matrix $F^i_{,j}(q)$ is given by the product of all K eigenvalues of Eq. (A.27), and thus that

$$\prod_{k=1}^{K} \omega_k(q) = \sqrt{F} = \sqrt{\widehat{m^{-1}} D} \tag{A.35}$$

By substituting Eqs. (A.34) and (A.35) into Eqs. (2.41) and (2.43), while noting that $\widehat{m^{-1}} = \tilde{m}/m$, we recover Eq. (2.39) for the distribution $\psi_{\rm eq}(q)$ of a stiff classical system.

E. Internal and Central Coordinates

The results given here for the constrained mobility tensor and related quantities are superficially different from those given by BCAH [4]. These differences exist because BCAH explicitly divide the soft coordinates for a rigid molecule with f mechanical degrees of freedom into a set of three Cartesian coordinates that give the overall location of the molecule in space (which BCAH take to be the components of the center of mass), and a remaining set of $f-3$ internal soft coordinates. We instead treat all f soft coordinates on an equal footing, and distinguish only between soft and hard coordinates.

To clarify the relationship between these approaches, we consider an expansion of the bead position $\mathbf{R}^\mu$ as

$$\mathbf{R}^\mu = \mathbf{r}^\mu(q^1, \ldots, q^{f-3}) + \mathbf{R}_{(c)} \tag{A.36}$$

Here $\mathbf{R}_{(c)}$ is a "central" position vector for a molecule, and $\mathbf{r}^{\mu}$ is the position of bead μ relative is this central position, which depends only on the $f-3$ internal coordinates $q^1, \ldots, q^{f-3}$. The analysis given here does not depend on the use of a particular definition of $\mathbf{R}_{(c)}$, which could be the center of mass, the center of hydrodynamic resistance, or the position of a specified bead. The three Cartesian components of $\mathbf{R}_{(c)}$ will be denoted by $R^s_{(c)}$, with $s = 1, \ldots, 3$. In this parameterization, the tangent vectors $\mathbf{a}^{\mu}_a$ may be divided into a set of $f-3$ vectors basis vectors

$$\frac{\partial \mathbf{R}^{\mu}}{\partial q^a} = \frac{\partial \mathbf{r}^{\mu}}{\partial q^a} \tag{A.37}$$

for $a = 1, \ldots, f-3$, associated with the internal coordinates, and a set

$$\frac{\partial \mathbf{R}^{\mu}}{\partial R^s_{(c)}} = \mathbf{e}_s \tag{A.38}$$

of three more associated with the three Cartesian components of the center position, where $\mathbf{e}_s$ is a unit vector parallel to Cartesian direction $s = 1, \ldots, 3$.

The projection $\tilde{\zeta}_{ab}$ of the friction tensor onto the f dimensional soft subspace may be divided into corresponding blocks

$$\tilde{\zeta} = \begin{bmatrix} \zeta_{ab} & \zeta_{as} \\ \zeta_{sa} & \zeta_{st} \end{bmatrix} \tag{A.39}$$

where $a, b = 1, \ldots, f-3$ and $s, t = 1, \ldots, 3$, and

$$\begin{aligned} \zeta_{ab} &= \sum_{\mu\nu} \frac{\partial \mathbf{r}^{\mu}}{\partial q^a} \cdot \boldsymbol{\zeta}_{\mu\nu} \cdot \frac{\partial \mathbf{r}^{\mu}}{\partial q^b} \\ \zeta_{as} &= \sum_{\mu\nu} \frac{\partial \mathbf{r}^{\mu}}{\partial q^a} \cdot \boldsymbol{\zeta}_{\mu\nu} \cdot \mathbf{e}_s \\ \zeta_{st} &= \mathbf{e}_s \cdot \boldsymbol{\zeta}^{(c)} \cdot \mathbf{e}_t \end{aligned} \tag{A.40}$$

in which

$$\boldsymbol{\zeta}^{(c)} \equiv \sum_{\mu\nu} \boldsymbol{\zeta}_{\mu\nu} \tag{A.41}$$

is what BCAH refer to as the total effective friction tensor, which they denote by the symbol $\mathbf{Z}$.

The constrained mobility K^{ab} defined in this chapter is given by the inverse of $\tilde{\zeta}_{ab}$ within the entire f-dimensional soft subspace. In any translationally invariant problem, in which there is no mechanical force or overall concentration gradient present to induced a generalized elastic force conjugate to the central position, one is typically interested only in the projection of K^{ab} onto the $(f-3)$-dimensional subspace of internal coordinates, which we will

call $K^{ab}_{(\mathrm{int})}$. This quantity cannot be obtained by simply inverting the projection of $\tilde{\zeta}$ onto the internal subspace. However, by using the results given in Section B of this appendix for the inverse of block matrices, it can be shown that the inverse of $K^{ab}_{(\mathrm{int})}$ within the $(f-3)$-dimensional internal subspace is given by a tensor

$$\zeta^{(\mathrm{int})}_{ab} \equiv [K_{(\mathrm{int})}]^{-1}_{ab} = \mathbf{a}^{\mu}_{a} \cdot \boldsymbol{\zeta}^{(\mathrm{int})}_{\mu\nu} \cdot \mathbf{a}^{\nu}_{b} \tag{A.42}$$

with a Cartesian representation

$$\boldsymbol{\zeta}^{(\mathrm{int})}_{\lambda\rho} \equiv \boldsymbol{\zeta}_{\lambda\rho} - \sum_{\mu\nu} \boldsymbol{\zeta}_{\lambda\mu} \cdot [\boldsymbol{\zeta}^{(\mathrm{c})}]^{-1} \cdot \boldsymbol{\zeta}_{\nu\rho} \tag{A.43}$$

If this definition of $\zeta^{(\mathrm{int})}_{ab}$ is extended to the full soft subspace, by letting $a, b = 1, \ldots, f$ in Eq. (A.42), then all elements of $\zeta^{(\mathrm{int})}_{ab}$ for which a or b corresponds to a component of the central position may be shown to vanish. Correspondingly, in the Cartesian representation, it is easily confirmed that

$$\sum_{\rho} \boldsymbol{\zeta}^{(\mathrm{int})}_{\lambda\rho} = \sum_{\lambda} \boldsymbol{\zeta}^{(\mathrm{int})}_{\lambda\rho} = 0 \tag{A.44}$$

BCAH refer to $\boldsymbol{\zeta}^{(\mathrm{int})}_{\lambda\rho}$ as the "modified effective friction tensor," which they denote by the symbol $\tilde{\boldsymbol{\zeta}}_{\lambda\rho}$. (See p. 188 of Ref. 4 for a table of these and related definitions.)

The expression given by BCAH for elements of the constrained mobility within the internal subspace is based on inversion of the projection $\zeta^{(\mathrm{int})}_{ab}$ of the modified mobility within the internal subspace, rather than inversion of the projection $\tilde{\zeta}_{ab}$ of the mobility within the entire soft subspace. BCAH first define a tensor given by the projection of the modified friction tensor onto the internal subspace, which they denote by the symbol $\tilde{g}_{ab}$ and refer to as a "modified covariant metric" tensor, which is equivalent to our $\zeta^{(\mathrm{int})}_{ab}$. They then define an inverse of this quantity within the subspace of internal coordinates, which they denote by $\tilde{g}^{ab}$ and refer to as a "modified contravariant metric tensor," which is equivalent to our $K^{ab}_{(\mathrm{int})}$ for $ab = 1, \ldots, f-3$. It is this last quantity that appears in their diffusion equation, given in Eq. (16.2-6) of Ref. 4, in place of our constrained mobility K^{ab}. Within the space of internal coordinates, the two quantities are completely equivalent.

F. Divergence of Constrained Mobility

In this section, we first give an elementary derivation of Eq. (2.182) for the covariant divergence of $\mathbf{K}^{\mu\nu}$, and then derive an expansion for the resulting Cartesian divergence of $\mathbf{K}^{\mu\nu}$, in order to recover the more explicit expression for $\mathbf{V}^{\mu}$ given in Eq. (2.184).

1. Covariant Form

To prove Eq. (2.182), we start with the Cartesian divergence, and expand $\mathbf{K}^{\nu\mu}$ in covariant basis vectors, and the Cartesian gradient in covariant basis vectors, to obtain

$$\frac{\partial}{\partial \mathbf{R}^{\nu}} \cdot \mathbf{K}^{\nu\mu} = \frac{\partial Q^{\gamma}}{\partial \mathbf{R}^{\nu}} \cdot \frac{\partial}{\partial Q^{\gamma}} \left(\frac{\partial \mathbf{R}^{\nu}}{\partial Q^{\beta}} K^{\beta\alpha} \frac{\partial \mathbf{R}^{\nu}}{\partial Q^{\alpha}} \right) \tag{A.45}$$

By using the chain rule for differentiation and the orthogonality of the basis vectors, we then obtain

$$\frac{\partial}{\partial \mathbf{R}^{\nu}} \cdot \mathbf{K}^{\nu\mu} = \frac{\partial}{\partial Q^{\beta}} \left(K^{\beta\alpha} \frac{\partial \mathbf{R}^{\nu}}{\partial Q^{\alpha}} \right) + \Gamma^{\gamma}_{\gamma\beta} K^{\beta\alpha} \frac{\partial \mathbf{R}^{\nu}}{\partial Q^{\alpha}} \tag{A.46}$$

where

$$\Gamma^{\gamma}_{\alpha\beta} \equiv \frac{\partial Q^{\gamma}}{\partial \mathbf{R}^{\nu}} \cdot \frac{\partial^2 \mathbf{R}^{\nu}}{\partial Q^{\alpha}\, \partial Q^{\beta}} \tag{A.47}$$

is the Christoffel symbol for the unconstrained space with a metric g. By using the identity

$$\frac{1}{\sqrt{g}} \frac{\partial \sqrt{g}}{\partial Q^{\beta}} = \Gamma^{\gamma}_{\gamma\beta} \tag{A.48}$$

which is proved in appendix Section C, and rearranging terms in Eq. (A.46), we obtain the geometrical identity given in Eq. (2.182).

2. Explicit Expansion

We now expand the RHS of the divergence:

$$\frac{\partial}{\partial \mathbf{R}^{\nu}} \cdot \mathbf{K}^{\nu\mu} = \frac{\partial}{\partial \mathbf{R}^{\nu}} \cdot \left(\mathbf{H}^{\nu\mu} - \mathbf{H}^{\nu\kappa} \cdot \widehat{\mathbf{H}}^{-1}_{\kappa\lambda} \cdot \mathbf{H}^{\lambda\mu} \right) \tag{A.49}$$

Applying the chain rule to the RHS, while using Eq. (2.145) to show that $\hat{\mathbf{H}}^{-1}_{\kappa\lambda} \cdot \mathbf{H}^{\lambda\mu} = \mathbf{n}^{i}_{\kappa} \mathbf{m}^{\mu}_{i}$, yields

$$\begin{aligned} \frac{\partial}{\partial \mathbf{R}^{\nu}} \cdot \mathbf{K}^{\nu\mu} = & \frac{\partial}{\partial \mathbf{R}^{\nu}} \cdot \mathbf{H}^{\nu\mu} \\ & - \left(\frac{\partial}{\partial \mathbf{R}^{\nu}} \cdot \mathbf{H}^{\nu\kappa} \right) \cdot \mathbf{n}^{i}_{\kappa} \mathbf{m}^{\mu}_{i} - \cdot \mathbf{n}^{j}_{\lambda} \mathbf{m}^{\nu}_{j} : \frac{\partial}{\partial \mathbf{R}^{\nu}} \mathbf{H}^{\lambda\mu} \\ & - \mathbf{H}^{\kappa\nu} : \left(\frac{\partial}{\partial \mathbf{R}^{\nu}} \widehat{\mathbf{H}}^{-1}_{\kappa\lambda} \right) \cdot \mathbf{H}^{\lambda\mu} \end{aligned} \tag{A.50}$$

Focusing attention on the last term of expansion (A.50), we expand

$$-\mathbf{H}^{\kappa\nu}:\left(\frac{\partial}{\partial \mathbf{R}^{\nu}}\hat{\mathbf{H}}^{-1}_{\kappa\lambda}\right)\cdot\mathbf{H}^{\lambda\mu}=-\mathbf{H}^{\kappa\nu}:\frac{\partial\left(\mathbf{n}^{i}_{\kappa}\hat{H}^{-1}_{ij}\mathbf{n}^{j}_{\lambda}\right)}{\partial\mathbf{R}^{\nu}}\cdot\mathbf{H}^{\lambda\mu} \tag{A.51}$$

to rewrite the RHS of Eq. (A.51) as

$$-\mathbf{H}^{\kappa\nu}:\frac{\partial^2 c^{i}}{\partial\mathbf{R}^{\nu}\mathbf{R}^{\kappa}}\mathbf{m}^{\mu}_{i}-\mathbf{m}^{\nu}_{j}\cdot\frac{\partial^2 c^{j}}{\partial\mathbf{R}^{\nu}\mathbf{R}^{\lambda}}\cdot\mathbf{H}^{\lambda\mu}+\mathbf{m}^{\nu}_{k}\cdot\frac{\partial\hat{H}^{kl}}{\partial\mathbf{R}^{\nu}}\mathbf{m}^{\mu}_{l} \tag{A.52}$$

Here, we have used the definition of $\mathbf{m}$, and the identity

$$\frac{\partial^2 c^{i}}{\partial\mathbf{R}^{\mu}\partial\mathbf{R}^{\nu}}=\frac{\partial\mathbf{n}^{i}_{\mu}}{\partial\mathbf{R}^{\nu}}=\frac{\partial\mathbf{n}^{i}_{\nu}}{\partial\mathbf{R}^{\mu}} \tag{A.53}$$

which follows from the definition of $\mathbf{n}$, to obtain the first two terms, and the identity

$$\frac{\partial\hat{H}^{-1}_{ij}}{\partial\mathbf{R}^{\nu}}=-\hat{H}^{-1}_{ik}\frac{\partial\hat{H}^{kl}}{\partial\mathbf{R}^{\nu}}\hat{H}^{-1}_{lj} \tag{A.54}$$

to obtain the last term. By then expanding

$$\frac{\partial\hat{H}^{kl}}{\partial\mathbf{R}^{\nu}}=\frac{\partial\left(\mathbf{n}^{k}_{\rho}\cdot\mathbf{H}^{\rho\sigma}\cdot\mathbf{n}^{l}_{\sigma}\right)}{\partial\mathbf{R}^{\nu}} \tag{A.55}$$

and combining terms involving second derivatives of c with the first two terms in Eq. (A.52), we may rewrite (A.52) as

$$\begin{aligned}&-\mathbf{K}^{\kappa\nu}:\frac{\partial^2 c^{i}}{\partial\mathbf{R}^{\nu}\mathbf{R}^{\kappa}}\mathbf{m}^{\mu}_{i}-\mathbf{m}^{\nu}_{j}\cdot\frac{\partial^2 c^{j}}{\partial\mathbf{R}^{\nu}\mathbf{R}^{\lambda}}\cdot\mathbf{K}^{\lambda\mu}\\&+\mathbf{m}^{\nu}_{k}\mathbf{n}^{k}_{\rho}:\frac{\partial\mathbf{H}^{\rho\sigma}}{\partial\mathbf{R}^{\nu}}\cdot\mathbf{n}^{l}_{\sigma}\mathbf{m}^{\mu}_{l}\end{aligned} \tag{A.56}$$

Substituting this for the last term in Eq. (A.50), while using expansion for $\mathbf{P}_{\nu}{}^{,\lambda}$ to combine terms involving derivatives of $\mathbf{H}$, then yields

$$\begin{aligned}\frac{\partial}{\partial\mathbf{R}^{\nu}}\cdot\mathbf{K}^{\nu\mu}=&-\mathbf{K}^{\mu\nu}\cdot\frac{\partial^2 c^{i}}{\partial\mathbf{R}^{\lambda}\partial\mathbf{R}^{\nu}}\cdot\mathbf{m}^{\lambda}_{i}\\&-\mathbf{K}^{\lambda\nu}:\frac{\partial^2 c^{i}}{\partial\mathbf{R}^{\nu}\partial\mathbf{R}^{\lambda}}\mathbf{m}^{\mu}_{i}\\&+\mathbf{P}_{\nu}{}^{,\lambda}:\frac{\partial\mathbf{H}^{\nu\rho}}{\partial\mathbf{R}^{\lambda}}\cdot\mathbf{P}_{\rho}{}^{,\mu}\end{aligned} \tag{A.57}$$

Substituting this into Eq. (2.183) yields Eq. (2.184).

G. Relations among Derivatives of Basis Vectors

In this section, we derive a set of relations involving derivatives of any set of tangent, normal, and generalized reciprocal vectors. The main result, which is given in Eq. (A.73), is a generalization of Eq. (A.15) for derivatives of $\ln g$.

Differentiation of bi-orthogonality conditions (2.186)–(2.189) with respect to an arbitrary soft coordinates q^c yields the relations

$$\mathbf{a}_a^\mu \cdot \frac{\partial \bar{\mathbf{b}}_\mu^b}{\partial q^c} = -\frac{\partial \mathbf{a}_a^\mu}{\partial q^c} \cdot \bar{\mathbf{b}}_\mu^b = \mathbf{a}_c^\mu \cdot \frac{\partial \bar{\mathbf{b}}_\mu^a}{\partial q^b} \tag{A.58}$$

$$\bar{\mathbf{m}}_i^\mu \cdot \frac{\partial \mathbf{n}_\mu^j}{\partial q^c} = -\frac{\partial \bar{\mathbf{m}}_i^\mu}{\partial q^c} \cdot \mathbf{n}_\mu^j \tag{A.59}$$

$$\bar{\mathbf{m}}_i^\mu \cdot \frac{\partial \bar{\mathbf{b}}_\mu^b}{\partial q^c} = -\frac{\partial \bar{\mathbf{m}}_i^\mu}{\partial q^c} \cdot \bar{\mathbf{b}}_\mu^b \tag{A.60}$$

$$\mathbf{a}_a^\mu \cdot \frac{\partial \mathbf{n}_\mu^j}{\partial q^c} = -\frac{\partial \mathbf{a}_a^\mu}{\partial q^c} \cdot \mathbf{n}_\mu^j \tag{A.61}$$

Here, we have used the identity

$$\frac{\partial^2 \mathbf{R}^\mu}{\partial q^a \partial q^c} = \frac{\partial \mathbf{a}_a^\mu}{\partial q^c} = \frac{\partial \mathbf{a}_c^\mu}{\partial q^a} \tag{A.62}$$

which follows from the definition of $\mathbf{a}$, in order to interchange the indices a and c in Eq. (A.58), and thereby obtain the second equality in that equation.

We next divide the reciprocal basis vectors into components tangent and normal to the constraint surface, as

$$\bar{\mathbf{b}}_\mu^a = \tilde{\mathbf{b}}_\mu^a + \hat{\mathbf{b}}_\mu^a \tag{A.63}$$

$$\bar{\mathbf{m}}_i^\mu = \tilde{\mathbf{m}}_i^\mu + \hat{\mathbf{m}}_i^\mu \tag{A.64}$$

such that $\tilde{\mathbf{b}}$ and $\tilde{\mathbf{m}}$ are purely tangent (or soft) while $\hat{\mathbf{b}}$ and $\hat{\mathbf{m}}$ are purely normal (or hard). By expanding $\tilde{\mathbf{b}}$ in tangent vectors and $\hat{\mathbf{b}}_\mu^i$ in normal vectors, it is straightforward to show that orthogonality conditions (2.186) and (2.187) requires that the soft component of a generic $\bar{\mathbf{b}}$ be equal to the geometric reciprocal vector $\tilde{\mathbf{b}}$ and that the hard compoment of a generic $\bar{\mathbf{m}}$ be equal to the hard geometric reciprocal vector $\hat{\mathbf{m}}$ defined in Eq. (2.212), which is why we use the same notation for these components of generic basis vectors $\bar{\mathbf{b}}$ and $\bar{\mathbf{m}}$ that we used earlier for the geometric reciprocal vectors.

By substituting the preceding expansions in Eq. (2.188), we find that the remaining "mixed" components must satisfy

$$\hat{\mathbf{m}}_i^{\mu} \cdot \hat{\mathbf{b}}_{\mu}^{b} = -\tilde{\mathbf{m}}_i^{\mu} \cdot \tilde{\mathbf{b}}_{\mu}^{b} \tag{A.65}$$

for all i and b. By substituting expansions (A.63) and (A.64) into Eqs. (A.58) and (A.59), to give

$$\mathbf{a}_a^{\mu} \cdot \frac{\partial \bar{\mathbf{b}}_{\mu}^{b}}{\partial q^c} = -(\tilde{\mathbf{b}}_{\mu}^{a} + \hat{\mathbf{b}}_{\mu}^{a}) \cdot \frac{\partial \mathbf{a}_a^{\mu}}{\partial q^c} \tag{A.66}$$

$$\mathbf{n}_{\mu}^{j} \cdot \frac{\partial \bar{\mathbf{m}}_i^{\mu}}{\partial q^c} = -(\tilde{\mathbf{m}}_i^{\mu} + \hat{\mathbf{m}}_i^{\mu}) \cdot \frac{\partial \mathbf{n}_{\mu}^{i}}{\partial q^c} \tag{A.67}$$

and considering the case $a = b$ in Eq. (A.66) and $i = j$ in Eq. (A.67), while summing over repeated indices, we obtain

$$\mathbf{a}_a^{\mu} \cdot \frac{\partial \bar{\mathbf{b}}_{\mu}^{a}}{\partial q^c} + \frac{\partial \ln \sqrt{\bar{g}}}{\partial q^c} = -\hat{\mathbf{b}}_{\mu}^{a} \cdot \frac{\partial \mathbf{a}_a^{\mu}}{\partial q^c} \tag{A.68}$$

$$\mathbf{n}_{\mu}^{i} \cdot \frac{\partial \bar{\mathbf{m}}_i^{\mu}}{\partial q^c} + \frac{\partial \ln \sqrt{\hat{G}}}{\partial q^c} = -\tilde{\mathbf{m}}_i^{\mu} \cdot \frac{\partial \mathbf{n}_{\mu}^{j}}{\partial q^{\gamma}} \tag{A.69}$$

where we have used Eqs. (A.62) and (A.63) to obtain the terms involving $\ln \sqrt{\bar{g}}$ and $\ln \sqrt{\hat{G}}$. By inserting a redundant factor of $\mathbf{I}_{\nu}^{\mu} - \tilde{\mathbf{P}}_{\nu}^{\mu} = \hat{\mathbf{m}}_j^{\mu} \mathbf{n}_{\nu}^{j}$ between the two vectors on the RHS of Eq. (A.68) and a redundant factor of $\tilde{\mathbf{P}}_{\mu}^{\nu} = \tilde{\mathbf{b}}_{\mu}^{b} \mathbf{a}_b^{\nu}$ into the RHS of Eq. (A.69), we may rewrite this as

$$\mathbf{a}_a^{\mu} \cdot \frac{\partial \bar{\mathbf{b}}_{\mu}^{a}}{\partial q^{\gamma}} + \frac{\partial \ln \sqrt{\bar{g}}}{\partial q^{\gamma}} = -\hat{\mathbf{b}}_{\mu}^{a} \cdot \hat{\mathbf{m}}_j^{\mu} \mathbf{n}_{\nu}^{j} \cdot \frac{\partial \mathbf{a}_a^{\nu}}{\partial q^{\gamma}} \tag{A.70}$$

$$\mathbf{n}_{\mu}^{i} \cdot \frac{\partial \bar{\mathbf{m}}_i^{\mu}}{\partial q^{\gamma}} + \frac{\partial \ln \sqrt{\hat{G}}}{\partial q^{\gamma}} = -\tilde{\mathbf{m}}_i^{\mu} \cdot \tilde{\mathbf{b}}_{\mu}^{b} \mathbf{a}_b^{\nu} \cdot \frac{\partial \mathbf{n}_{\nu}^{j}}{\partial q^{\gamma}} \tag{A.71}$$

On comparing these expressions to Eqs. (A.61) and (A.65), we find that the RHSs of Eqs. (A.70) and (A.71) are equal. Equating the LHSs yields the relation

$$\mathbf{a}_a^{\mu} \cdot \frac{\partial \bar{\mathbf{b}}_{\mu}^{a}}{\partial q^{\gamma}} + \frac{\partial \ln \sqrt{\bar{g}}}{\partial q^{\gamma}} = \mathbf{n}_{\mu}^{i} \cdot \frac{\partial \bar{\mathbf{m}}_i^{\mu}}{\partial q^{\gamma}} + \frac{\partial \ln \sqrt{\hat{G}}}{\partial q^{\gamma}} \tag{A.72}$$

By using Eq. (2.28) to combine the two determinants, and applying Eq. (A.58) to the first term on the LHS, we obtain our main result:

$$\frac{\partial \ln \sqrt{g}}{\partial q^{\gamma}} = \bar{\mathbf{b}}_{\nu}^{a} \cdot \frac{\partial \mathbf{a}_a^{\nu}}{\partial q^{\gamma}} + \mathbf{n}_{\mu}^{i} \cdot \frac{\partial \bar{\mathbf{m}}_i^{\mu}}{\partial q^{\gamma}} \tag{A.73}$$

This is a generalization of Eq. (A.15), which may be recovered as a special case by taking the reciprocal vectors to be conventional partial derivatives. By using Eqs. (A.58) and/or (A.59) to replace either of the terms on the LHS, several equivalent expressions can be obtained, one of which is presented in Eq. (2.309).

H. Transformation of Langevin Force Bias

We consider the transformation of the force bias $\overline{\langle \eta_\beta \rangle_0}$ in the Stratonovich interpretation of the Langevin under a change of variables. We consider an invertible transformation from coordinates $X^1, \ldots, X^L$ to another set of f coordinates $\bar{X}^1, \ldots, \bar{X}^L$, and restrict ourselves in this appendix to the case of a nonsingular mobility. The *instantaneous* Langevin force $\eta_\beta(t)$ transforms as a covariant vector, giving a transformed force

$$\bar{\eta}_\alpha(t) = [J^{-1}(t)]^\beta_\alpha \eta_\beta(t) \tag{A.74}$$

where $(J^{-1})^\beta_\alpha = \partial X^\beta / \partial \bar{X}^\alpha$ is the inverse of the Jacobian matrix defined in Eq. (2.287). The transformed force bias is thus given by the integral

$$\overline{\langle \bar{\eta}_\alpha \rangle_0} = \lim_{t\to 0} \frac{1}{t} \int_0^t dt' [J^{-1}(t')]^\beta_\alpha \eta_\beta(t') \tag{A.75}$$

Expanding $J^{-1}(t') = J^{-1}(\bar{X}(t'))$ to first order in $\Delta\bar{X}^\alpha(t')$ about its $t' = 0$ value yields an $\mathcal{O}(t)$ approximation for the integral as

$$\overline{\langle \bar{\eta}_\alpha \rangle_0} = \lim_{t\to 0} \frac{1}{t} \int_0^t dt' \left\{ (J^{-1})^\beta_\alpha + \Delta\bar{X}^\gamma(t') \frac{\partial (J^{-1})^\beta_\alpha}{\partial \bar{X}^\gamma} \right\} \eta_\beta(t') \tag{A.76}$$

where J^{-1} and its derivative are evaluated at $t = 0$. Approximating $\Delta\bar{X}^\gamma(t')$ to lowest order as $\Delta\bar{X}^\gamma(t') \simeq J^\gamma_\delta(0)\Delta X^\delta(t')$, while using approximation (2.277) for $\Delta X^\delta(t')$ and averaging over the noise, then yields

$$\overline{\langle \bar{\eta}_\alpha \rangle_0} = (J^{-1})^\beta_\alpha \overline{\langle \eta_\beta \rangle_0} + kTJ^\gamma_\delta \frac{\partial X^\delta}{\partial \bar{X}^\alpha \partial \bar{X}^\gamma} \tag{A.77}$$

The assumption of a nonsingular mobility has been used to obtain this last result. By using Eq. (A.14) for the derivative of a determinant, to show that

$$\frac{\partial \ln J^{-1}}{\partial X^\alpha} = J^\gamma_\delta \frac{\partial (J^{-1})^\gamma_\delta}{\partial \bar{X}^\alpha} = J^\gamma_\delta \frac{\partial X^\delta}{\partial \bar{X}^\alpha \partial \bar{X}^\gamma} \tag{A.78}$$

we obtain Eq. (2.286).

I. Transformation of Kinetic SDEs

Here, we consider the transformation of the set of f kinetic SDEs given in Eq. (2.314) under a coordinate transformation to a set of f variables $\bar{X}^1, \ldots, \bar{X}^L$. As in Section H of this appendix, we restrict ourselves in this section to the case of a nonsingular mobility tensor. By combining Eq. (2.323) for the drift velocites in the original coordinate system with the Ito transformation rule for drift velocities, we find that the variables $\bar{X}^1, \ldots, \bar{X}^L$ experience drift velocities

$$\begin{aligned}\bar{V}^\alpha &= \frac{\partial \bar{X}^\alpha}{\partial X^\beta}\left(A^\beta + \frac{\partial D^{\gamma\beta}}{\partial X^\gamma}\right) + D^{\beta\gamma}\frac{\partial^2 \bar{X}^\alpha}{\partial X^\beta\,\partial X^\gamma} \\ &= \frac{\partial \bar{X}^\alpha}{\partial X^\beta}A^\beta + \frac{\partial}{\partial X^\gamma}\left(D^{\gamma\beta}\frac{\partial \bar{X}^\alpha}{\partial X^\beta}\right)\end{aligned} \tag{A.79}$$

in which the quantity in parentheses in the first line is V^β. The drift coefficients for the transformed kinetic SDEs can then be obtained by applying Eq. (2.323) to the transformed SDEs, which yields

$$\bar{A}^\alpha = \bar{V}^\alpha - \frac{\partial \bar{D}^{\delta\alpha}}{\partial \bar{X}^\delta} \tag{A.80}$$

where

$$\bar{D}^{\delta\alpha} = \frac{\partial \bar{X}^\delta}{\partial X^\gamma}D^{\gamma\beta}\frac{\partial \bar{X}^\alpha}{\partial X^\beta} \tag{A.81}$$

is the transformed diffusivity tensor. Expanding the divergence of $\bar{D}$ then yields

$$\begin{aligned}\frac{\partial \bar{D}^{\delta\alpha}}{\partial \bar{X}^\delta} &= \frac{\partial X^\epsilon}{\partial \bar{X}^\delta}\frac{\partial}{\partial X^\epsilon}\left(\frac{\partial \bar{X}^\delta}{\partial X^\gamma}D^{\gamma\beta}\frac{\partial \bar{X}^\alpha}{\partial X^\beta}\right) \\ &= \frac{\partial}{\partial X^\gamma}\left(D^{\gamma\beta}\frac{\partial \bar{X}^\alpha}{\partial X^\beta}\right) + \frac{\partial X^\epsilon}{\partial \bar{X}^\delta}\frac{\partial \bar{X}^\delta}{\partial X^\epsilon\,\partial X^\gamma}D^{\gamma\beta}\frac{\partial \bar{X}^\alpha}{\partial X^\beta}\end{aligned} \tag{A.82}$$

By substituting Eqs. (A.79) and (A.82) into Eq. (A.80), and canceling terms, then yields

$$\bar{A}^\alpha = \frac{\partial \bar{X}^\alpha}{\partial X^\beta}\left(A^\beta - D^{\beta\gamma}\frac{\partial \bar{X}^\delta}{\partial X^\gamma\,\partial X^\epsilon}\frac{\partial X^\epsilon}{\partial \bar{X}^\delta}\right) \tag{A.83}$$

Finally, by applying Eq. (A.14) to the determinant of the Jacobian matrix of Eq. (2.287) to show that

$$\frac{\partial \ln J}{\partial X^\gamma} = \frac{\partial J^\delta_\epsilon}{\partial X^\gamma}(J^{-1})^\epsilon_\delta = \frac{\partial \bar{X}^\delta}{\partial X^\gamma\,\partial X^\epsilon}\frac{\partial X^\epsilon}{\partial \bar{X}^\delta} \tag{A.84}$$

we obtain Eq. (2.331).

J. Projected versus Unprojected Random Forces

We now show that the same drift velocity is obtained from a Stratonovich interpretation of the Langevin equation with unprojected and projected random forces that have the same soft components but different hard components. We consider an unprojected random force $\boldsymbol{\eta}_\mu(t)$ and a corresponding projected random force $\bar{\boldsymbol{\eta}}_\mu(t)$ that are related by a generalization of Eq. (2.300), in which

$$\bar{\boldsymbol{\eta}}_\mu(t) = \bar{\mathbf{P}}_\mu{}^{,\nu}(t) \cdot \boldsymbol{\eta}_\nu(t) \tag{A.85}$$

in which $\bar{\mathbf{P}}_\mu{}^{,\nu}(t)$ is a generic projection tensor. We calculate the difference $\delta\mathbf{V}^\mu$ between the drift velocity obtained by applying Eq. (2.296) to the Langevin equation with an unprojected random force $\boldsymbol{\eta}_\mu$ and that obtained, for the same value of the Stratonovich drift coefficient $\mathbf{A}^\mu$, by using the corresponding projected force $\bar{\boldsymbol{\eta}}_\mu$. This difference may be expanded as a sum

$$\delta\mathbf{V}^\mu = \delta\mathbf{V}^\mu_{(1)} + \delta\mathbf{V}^\mu_{(2)} \tag{A.86}$$

where

$$\delta\mathbf{V}^\mu_{(1)} \equiv kT(\mathbf{P}_\nu{}^{,\lambda} - \bar{\mathbf{P}}_\nu{}^{,\lambda}) : \frac{\partial \mathbf{K}^{\nu\mu}}{\partial \mathbf{R}^\lambda} \tag{A.87}$$

is the difference arising from the use of different projection tensors in the projected derivative of $\mathbf{K}$ on the RHS of Eq. (2.296), and where

$$\delta\mathbf{V}^\mu_{(2)} \equiv \lim_{t\to 0} \frac{1}{t} \mathbf{K}^{\mu\nu} \cdot \int_0^t dt' \langle \boldsymbol{\eta}_\nu(t') - \bar{\boldsymbol{\eta}}_\nu(t') \rangle_0 \tag{A.88}$$

is a difference arising from the different values obtained for the force bias in the two cases. Focusing on $\delta\mathbf{V}^\mu_{(2)}$ we may use Eq (A.85) for $\bar{\boldsymbol{\eta}}_\mu$ to rewrite this as an integral:

$$\delta\mathbf{V}^\mu_{(2)} = \lim_{t\to 0} \frac{1}{t} \mathbf{K}^{\mu\nu} \cdot \int_0^t dt' \left\langle [\mathbf{I}^\rho_\nu - \bar{\mathbf{P}}_\nu{}^{,\rho}(t')] \cdot \boldsymbol{\eta}_\rho(t') \right\rangle_0 \tag{A.89}$$

Taylor-expanding $\mathbf{I}^\rho_\nu - \bar{\mathbf{P}}_\nu{}^{,\rho}(t')$ to linear order in $\Delta\mathbf{R}^\lambda(t')$ around its value at $t' = 0$ within the integrand, we find that the contribution involving the value of this tensor at $t' = 0$ vanishes, but that the next term in the expansion yields

$$\delta\mathbf{V}^\mu_{(2)} = \frac{-1}{t} \mathbf{K}^{\mu\nu} \cdot \int_0^t dt' \left\langle \Delta\mathbf{R}^\lambda(t') \cdot \frac{\partial \bar{\mathbf{P}}_\nu{}^{,\rho}}{\partial \mathbf{R}^\lambda} \cdot \boldsymbol{\eta}_\rho(t') \right\rangle_0 \tag{A.90}$$

where $\mathbf{K}^{\mu\nu}$ and $\partial\bar{\mathbf{P}}_{\nu}^{\ ,\rho}/\partial\mathbf{R}$ are evaluated at $t = 0$. Evaluating the average then yields

$$\delta\mathbf{V}_{(2)}^{\mu} = -kT\,\mathbf{P}_{\rho}^{\ ,\lambda}\colon \frac{\partial\bar{\mathbf{P}}^{\rho}_{\ ,\nu}}{\partial\mathbf{R}^{\lambda}} \cdot \mathbf{K}^{\nu\mu} \tag{A.91}$$

By differentiating $(\mathbf{I}_{\nu}^{\rho} - \bar{\mathbf{P}}^{\rho}_{\ ,\nu}) \cdot \mathbf{K}^{\nu\mu} = 0$ with respect to $\mathbf{R}^{\lambda}$, we may show that

$$\frac{\partial\bar{\mathbf{P}}^{\rho}_{\ ,\nu}}{\partial\mathbf{R}^{\lambda}} \cdot \mathbf{K}^{\nu\mu} = (\mathbf{I}_{\nu}^{\rho} - \bar{\mathbf{P}}^{\rho}_{\ ,\nu}) \cdot \frac{\partial\mathbf{K}^{\nu\mu}}{\partial\mathbf{R}^{\lambda}} \tag{A.92}$$

to obtain the equivalent expression

$$\delta\mathbf{V}_{(2)}^{\mu} = -kT\left[(\mathbf{I}_{\nu}^{\rho} - \bar{\mathbf{P}}_{\nu}^{\ ,\rho}) \cdot \mathbf{P}_{\rho}^{\ ,\lambda}\right]\colon \frac{\partial\mathbf{K}^{\nu\mu}}{\partial\mathbf{R}^{\lambda}} \tag{A.93}$$

Using the fact that $\bar{\mathbf{P}}_{\nu}^{\ ,\rho} \cdot \mathbf{P}_{\rho}^{\ ,\lambda} = \bar{\mathbf{P}}_{\nu}^{\ ,\lambda}$, we then obtain

$$\delta\mathbf{V}_{(2)}^{\mu} = -kT(\mathbf{P}_{\nu}^{\ ,\lambda} - \bar{\mathbf{P}}_{\nu}^{\ ,\lambda})\colon \frac{\partial\mathbf{K}^{\nu\mu}}{\partial\mathbf{R}^{\lambda}} \tag{A.94}$$

Since this is opposite to Eq. (A.87) for $\delta\mathbf{V}_{(1)}^{\mu}$, we conclude that

$$\delta\mathbf{V}^{\mu} = \delta\mathbf{V}_{(1)}^{\mu} + \delta\mathbf{V}_{(2)}^{\mu} = 0 \tag{A.95}$$

and thus that the same overall drift velocity is obtained with either type of random force.

K. Fixman's Analysis

The analysis given in Section III of Fixman's 1978 article [9] is consistent with that given Section IX.C.5 of this chapter through Fixman's Eq. (3.26), which is consistent with our Eq. (2.306), aside from the difference caused by Fixman's neglect of any bias in the Cartesian random forces. In Fixman's Eq. (3.27), he then asserts that

$$\frac{\partial\mathbf{a}_{b}^{\mu}}{\partial q^{c}} = \left\{ \begin{matrix} d \\ bc \end{matrix} \right\}\mathbf{a}_{d}^{\mu} \tag{A.96}$$

where

$$\left\{ \begin{matrix} d \\ bc \end{matrix} \right\} \equiv \frac{1}{2}(\tilde{\mathbf{g}}^{-1})^{de}\left(\frac{\partial\tilde{g}_{eb}}{\partial q^{c}} + \frac{\partial\tilde{g}_{ec}}{\partial q^{b}} - \frac{\partial\tilde{g}_{bc}}{\partial q^{e}}\right) \tag{A.97}$$

$$= \tilde{\mathbf{b}}_{\mu}^{d} \cdot \frac{\partial\mathbf{a}_{b}^{\mu}}{\partial q^{c}} \tag{A.98}$$

is the Christoffel symbol for the constraint surface with a metric $\tilde{g}_{ab}$. Equation (A.97) is the standard definition of a Christoffel symbol [36]. Equation (A.98)

may be obtained by using Eq. (2.21) for $\tilde{g}_{ab}$ in Eq. (A.97) and differentiating. Substituting expansion (A.96) into Eq. (2.306) and using Eq. (A.18) for $\partial \ln \tilde{g}/dq^b$, yields an average value

$$\overline{\langle \eta_b \rangle}_0 \simeq \mathbf{a}_b^\mu \cdot \overline{\langle \boldsymbol{\eta}_\mu \rangle}_0 + kT \frac{\partial \ln \sqrt{\tilde{g}}}{\partial q^b} t \tag{A.99}$$

This equation is identical to Fixman's Eq. (3.29), except for the absence in Fixman's expression of the term proportional to $\overline{\langle \boldsymbol{\eta}_\mu \rangle}_0$.

Equations (A.96) and (A.99) are, however, incorrect. The RHS of Eq. (A.96), and of Fixman's Eq. (3.27), is a vector that is manifestly parallel to the constraint surface, since it is expressed as an expansion in tangent vectors. The vector $\frac{\partial \mathbf{a}_b^\mu}{\partial q^c}$ on the LHS can instead have nonzero components normal to this surface, which reflect the curvature of the constraint surface. For example, in the simple case of a two-dimensional surface $\mathbf{R}(q^1, q^2)$ in three dimensions, for which there is only one normal direction, the normal components of $\frac{\partial \mathbf{a}_b}{\partial q^c}$ define an extrinsic curvature tensor

$$C_{bc} \equiv \mathbf{n} \cdot \frac{\partial \mathbf{a}_b}{\partial q^c} = \mathbf{n} \cdot \frac{\partial^2 \mathbf{R}}{\partial q^b \partial q^c} \tag{A.100}$$

which vanishes only for a flat surface. By using Eq. (A.98) for the Christoffel symbol and Eq. (2.213) for the projection tensor $\tilde{\mathbf{P}}_\nu^\mu$, it is straightforward to show that the RHS of Eq. (A.96) gives only the projection of $\frac{\partial \mathbf{a}_b^\mu}{\partial q^c}$ onto a plane parallel to the constraint surface

$$\tilde{\mathbf{P}}_\nu^\mu \cdot \frac{\partial \mathbf{a}_b^\nu}{\partial q^c} = \left\{ \begin{array}{c} d \\ bc \end{array} \right\} \mathbf{a}_d^\mu \tag{A.101}$$

and thus neglects any perpendicular components of $\frac{\partial \mathbf{a}_b^\nu}{\partial q^c}$.

Equation (A.99) may, however, also be obtained by explicitly using projected random forces, as Hinch did in order to reproduce Fixman's result. The use of the projected friction tensor for $\mathbf{Z}_{\mu\nu}$ in Eq. (2.306), rather than the unprojected tensor $\boldsymbol{\zeta}_{\mu\nu}$, has the same effect in that equation as did Fixman's neglect of the hard components of $\frac{\partial \mathbf{a}_b^\nu}{\partial q^c}$, because the RHS of Eq. (2.306) depends only on the dot product $\frac{\partial \mathbf{a}_b^\mu}{\partial q^c} \cdot \mathbf{Z}_{\mu\nu}$. Hinch was thus able to recover Fixman's result by introducing the notion of a projected random force.

References

1. H. A. Kramers, *J. Chem. Phys.* **14**, 415 (1946).
2. M. Fixman, *Proc. Nat. Acad. Sci. USA* **74**, 3050 (1974).
3. C. Curtiss, R. Bird, and O. Hassager, *Adv. Chem. Phys.* **35**, 31–117 (1976).
4. R. Bird, C. Curtiss, R. Armstrong, and O. Hassager, *Dynamics of Polymeric Fluids* (Wiley, New York, 1987).

5. M. Gottlieb and R. B. Bird, *J. Chem. Phys.* **65**, 2467 (1976).
6. N. Go and H.A. Scheraga, *Macromolecules* **9**, 535 (1976).
7. E. Helfand, *J. Chem. Phys.* **71**, 5000 (1979).
8. J. M. Rallison, *J. Fluid Mech.* **93**, 251–279 (1979).
9. M. Fixman, *J. Chem. Phys.* **69**, 1527 (1978).
10. E. J. Hinch, *J. Fluid Mech.* **271**, 219 (1994).
11. H.-Ch. Öttinger, *Phys. Rev. E* **50**, 2696 (1994).
12. H.-Ch. Öttinger, *Stochastic Processes in Polymer Fluids: Tools and Examples for Developing Simulation Algorithms*, (Springer-Verlag, Berlin, 1996).
13. E. A. J. F. Peters, *Polymers in Flow: Modelling and Simulation*, Ph.D. thesis, Technische Universiteit Delft (2000).
14. J. Rotne and S. Prager, *J. Chem. Phys.* **50**, 4831 (1969).
15. H. Yamakawa, *J. Chem. Phys.* **53**, 436 (1970).
16. C. W. Gardiner, *Handbook of Stochastic Methods* (Springer-Verlag, Berlin, 1985).
17. H. Risken, *The Fokker-Planck Equation* (Springer-Verlag, 1989).
18. M. Doi and S. F. Edwards, *The Theory of Polymer Dynamics* (Oxford Univ. Press, London, 1986).
19. P. S. Grassia, E. J. Hinch, and L. C. Nitsche, *J. Fluid. Mech.* **282**, 373 (1995).
20. P. S. Grassia and E. J. Hinch, *J. Fluid Mech.* **308**, 255 (1996).
21. G. H. Nyland, P. Sketne, A. Mikkelsen, and A. Elgsaeter, *J. Chem. Phys.* **105**, 1198 (1996); E. Klaveness and A. Elsgaeter, *J. Chem. Phys.* **110**, 11608 (1999).
22. T. W. Liu, *J. Chem. Phys.* **90**, 5826 (1989).
23. P. S. Doyle, E. S. G. Shaqfeh, and A. P. Gast, *J. Fluid Mech.* **334**, 251 (1997).
24. R. Everaers, F. Julicher, A. Ajdari, and A. C. Maggs, *Phys. Rev. Lett.* **82**, 3717 (1999).
25. M. Pasquali, V. Shankar, and D. C. Morse, *Phys. Rev. E* **64**, 020802(R) (2001).
26. V. Shankar, M. Pasquali, and D. C. Morse, *J. Rheol.* **46**, 1111–1154 (2002).
27. P. Dimitrakopoulos, J. F. Brady, and Z.-G. Wang, *Phys. Rev. E* **64**, 050803(R) (2001).
28. D. Petera and M. Muthukumar, *J. Chem. Phys.* **111**, 7614 (1999).
29. D. L. Ermak and J. McCammon, *J. Chem. Phys.* **69**, 1352 (1978).
30. R. L. Stratonovich, *SIAM J. Control* **4**, 362 (1966).
31. E. Wong and M. Zakai, *Ann. Math. Stat.* **3**, 1560 (1965).
32. N. Ikeda and S. Watanabe, *Stochastic Differential Equations and Diffusion Processes* (North-Holland, Amsterdam, 1981).
33. Yu. L. Klimontovich, *Physica A* **163**, 515–532 (1990); *Physica A* **182**, 121–132 (1992).
34. M. Hütter and H. C. Öttinger, *J. Chem. Soc., Faraday Trans.* **94**, 1403 (1998).
35. D. Frenkel and B. Smit, *Understanding Molecular Simulations* (*from Algorithms to Applications*) (Academic Press, San Diego, 1996).
36. See, e.g., I. V. Sokolnikoff, *Tensor Analysis, Theory and Applications to Geometry and Mechanics of Continua* (Wiley, New York, 1964); L. D. Landau and E. M. Lifschitz, *The Classical Theory of Fields* (Pergamon Press, New York, 1979).

SUPERPARAMAGNETISM AND SPIN GLASS DYNAMICS OF INTERACTING MAGNETIC NANOPARTICLE SYSTEMS

PETRA E. JÖNSSON*

Department of Materials Science, Uppsala University, Uppsala, Sweden

CONTENTS

*Present address: Institute for Solid State Physics, University of Tokyo, Kashiwa-no-ha 5-1-5, Kashiwa, Chiba 277-8581, Japan.

Advances in Chemical Physics, Volume 128, edited by Stuart A. Rice
ISBN 0-471-44528-2

The physical properties of magnetic nanoparticles have been investigated with focus on the influence of dipolar interparticle interaction. For weakly coupled nanoparticles, thermodynamic perturbation theory is employed to derive analytical expressions for the linear equilibrium susceptibility, the zero-field specific heat and averages of the local dipolar fields. By introducing the averages of the dipolar fields in an expression for the relaxation rate of a single particle, a nontrivial dependence of the superparamagnetic blocking on the damping coefficient is evidenced. This damping dependence is interpreted in terms of the nonaxially symmetric potential created by the transverse component of the dipolar field.

Strongly interacting nanoparticle systems are investigated experimentally in terms of spin glass behavior. Disorder and frustration arise in samples consisting of frozen ferrofluids from the randomness in particle position and anisotropy axis orientation. A strongly interacting FeC system is shown to exhibit critical dynamics characteristic of a spin glass phase transition. Aging, memory, and rejuvenation phenomena similar to those of conventional spin glasses are observed, albeit with much weaker rejuvenation effects than in both a Ag(11 at% Mn) Heisenberg and an $Fe_{0.5}Mn_{0.5}TiO_3$ Ising spin glass. Differences in the nonequilibrium dynamics of the strongly interacting nanoparticle system and the two spin glass samples are discussed in terms of anisotropy and different timescales, due to the much longer microscopic flip time of a magnetic moment than of an atomic spin.

I. INTRODUCTION

Ferro- and ferrimagnetic nanoparticles are important examples of how a reduction in size changes the properties of a magnetic material. For small particles it is energetically favorable to avoid domain walls and form only one magnetic domain. The magnetism of such single-domain particles has been an active field of research since the pioneering work of Stoner and Wohlfarth [1] and Néel [2] in the late 1940s. Because of new fabrication methods and characterization techniques, understanding of and interest in nanosized materials have increased explosively within the disciplines of physics, chemistry, material science, and medicine. This development is driven by a large number of applications; nanosized magnetic materials are used in, for example, magnetic recording media, ferrofluids, catalysts, and refrigerators; as well as by a large interest of fundamental nature. Nanomagnets made up of a small number of spins can be used to study quantum tunneling of magnetization [3]. In ferrofluids the dipolar interparticle interaction can be tuned by the particle concentration, and frozen ferrofluids have been shown to change their magnetic behavior from superparamagnetic at low concentrations to spin-glass-like in dense systems.

The research on spin glasses started in the 1970s after the discovery by Cannella and Mydosh [4] of a peak in the alternating-current (ac)-susceptibility of diluted gold–iron alloys. Several different materials with various interaction mechanisms were soon found to exhibit this ''new'' magnetic behavior, all with two properties in common—disorder and frustration. Spin glasses have since been widely studied, partly because they are excellent model systems of materials with quenched disorder. An understanding of spin glasses can thus contribute to the understanding of other, more complex disordered systems, such as ceramic superconductors, polymers, gels, and dense nanoparticle systems.

This article reviews the dynamic properties of magnetic nanoparticle systems with different interparticle interaction strength. In Section II we discuss basic properties of noninteracting particle systems, and thermodynamic perturbation theory is used to study weakly interacting particle systems. In Section III we discuss the behavior of strongly interacting magnetic nanoparticle systems in the light of recent results in the field of spin glasses.

II. SINGLE-DOMAIN MAGNETIC NANOPARTICLES

The study of single-domain magnetic particles has been an active field of research since the pioneering work of Stoner and Wohlfarth [1], who studied the hysteretic rotation of the magnetization over the magnetic–anisotropy energy barrier under the influence of an applied field, and Néel [2], who predicted that at nonzero temperature the magnetization can overcome the energy barrier as a

result of thermal agitation. Later, Brown [5] derived the Fokker–Planck equation for the probability distribution of spin orientations, starting from the stochastic Landau–Lifshitz equation, and calculated approximate expression for the relaxation time of particles with uniaxial anisotropy. The theoretically most well studied systems are noninteracting classical spins (representing the magnetization of the nanoparticles) with axially symmetric magnetic anisotropy. A great step forward in comparing experiments and theory was taken when measurements on individual particles were reported [6]. A profound knowledge of the physical properties of isolated particles is a prerequisite for further studies of phenomena such as quantum tunneling in molecular nanomagnets or dipole–dipole interaction in dense samples.

In this section, some general properties of magnetic nanoparticles are first recalled (for more details, see, e.g., Refs. 7–9). The definition of a magnetic nanoparticle is rather wide and includes ferro- and ferrimagnetic materials (e.g., γ-Fe_2O_3, Fe_3O_4, and $Fe_{1-x}C_x$) as well as magnetic nanoclusters (e.g., Mn_{12} and Fe_8). Subsequently, thermodynamic properties of spins weakly coupled by the dipolar interaction are calculated. Dipolar interaction is, due to its long range and reduced symmetry, difficult to treat analytically; most previous work on dipolar interaction is therefore numerical [10–13]. Here thermodynamic perturbation theory will be used to treat weak dipolar interaction analytically. Finally, the dynamical properties of magnetic nanoparticles are reviewed with focus on how relaxation time and superparamegnetic blocking are affected by weak dipolar interaction. For notational simplicity, it will be assumed throughout this section that the parameters characterizing different nanoparticles are identical (e.g., volume and anisotropy).

A. General Properties

The current studies of magnetic single-domain nanoparticles are limited to systems where the particles are fixed in space (realized, e.g., in frozen ferrofluids, single crystals of molecular magnets, and magnetic nanoparticles in a solid matrix). We will also assume that every single-domain nanoparticle is in internal thermodynamic equilibrium and that its constituent spins rotate coherently. Moreover, we are considering only temperatures much lower than the Curie temperature, so the spontaneous magnetization is approximately constant with temperature. Hence, the only relevant degree of freedom is the *orientation* of the net magnetic moment.

The Hamiltonian of a single isolated nanoparticle consists of the magnetic anisotropy (which creates preferential directions of the magnetic moment orientation) and the Zeeman energy (which is the interaction energy between the magnetic moment and an external field). In the ensembles, the nanoparticles are supposed to be well separated by a nonconductive medium [i.e., a ferrofluid in which the particles are coated with a surfactant (surface-active agent)]. The

only relevant interparticle interaction mechanism is therefore the dipole–dipole interaction.

1. Magnetic Anisotropy

The term *magnetic anisotropy* is used to describe the dependence of the internal energy on the direction of the spontaneous magnetization of the ferro/ferrimagnetic nanoparticle, creating "easy" and "hard" directions of magnetization. In general, a bulk sample of a ferromagnet exhibits magnetic anisotropy with the same symmetry as in the crystal structure. This anisotropy energy originates from spin–orbit coupling and is called *magnetocrystalline anisotropy* [14]. The two most common symmetries are uniaxial and cubic. For uniaxial symmetry the energy is given by

$$E_a^{\text{uni}} = K_1 V \sin^2\theta + K_2 V \sin^4\theta + \cdots \tag{3.1}$$

where V is the particle volume, K_1 and K_2 are anisotropy constants, and θ is the angle between the magnetic moment and the symmetry axis. For cubic symmetry the anisotropy can be expressed in terms of the direction cosines (α_i) as

$$E_a^{\text{cubic}} = K_1 V(\alpha_1^2\alpha_2^2 + \alpha_2^2\alpha_3^2 + \alpha_3^2\alpha_1^2) + K_2 V\alpha_1^2\alpha_2^2\alpha_3^2 + \cdots \tag{3.2}$$

where the α_i are defined through $\alpha_1 = \sin\theta\cos\phi$, $\alpha_2 = \sin\theta\sin\phi$ and $\alpha_3 = \cos\theta$, θ is the angle between the magnetization and the z axis, and ϕ is the azimuthal angle.

For a single-domain ferromagnet, any nonspherical particle shape gives rise to *shape anisotropy* due to the internal magnetostatic energy. The magnetostatic energy, for an ellipsoid of revolution, is equal to

$$E_m = \tfrac{1}{2}\mu_0 V M_s^2(N_z\cos^2\theta + N_x\sin^2\theta) \tag{3.3}$$

where θ is the angle between the magnetic moment and the polar axis $\hat{z}$, M_s is the saturation magnetization, N_z is the demagnetization factor along the polar axis, and $N_x = N_y$ is the demagnetization factor along an equatorial axis. Both the magnetostatic energy for an ellipsoid and the uniaxial magnetocrystalline anisotropy energy [Eq. (3.1)] can, to first order—except for a constant term—be written as

$$E_a = -A\cos^2\theta \tag{3.4}$$

where $A = KV$ is the anisotropy energy barrier and the uniaxial anisotropy constant $K = \frac{1}{2}\mu_0 M_s^2(N_x - N_z)$ in the case of shape anisotropy. For a prolate ellipsoid, $K > 0$ and the anisotropy is of "easy axis" type, since there exist two

minima of the anisotropy energy along $\pm\hat{z}$ (the anisotropy axis). For an oblate ellipsoid, $K < 0$ and the anisotropy energy has its minimum in the whole xy plane. In this case the anisotropy is of "easy plane" type.

With decreasing particle size, the magnetic contributions from the surface will eventually become more important than those from the bulk of the particle, and hence *surface anisotropy* energy will dominate over the magnetocrystalline anisotropy and magnetostatic energies. A uniaxial anisotropy energy proportional to the particle surface S

$$E_a^{\text{surface}} = K_s S \cos^2 \theta \tag{3.5}$$

has been observed experimentally by ferromagnetic resonance [15].

Hereafter, we will assume uniaxial anisotropy, of easy-axis type, given by Eq. (3.4) (if not otherwise indicated), since it is the simplest symmetry that contains the basic elements (potential minima, barriers) responsible for the important role of magnetic anisotropy in superparamagnets. Experimental evidence for uniaxial anisotropy is given in Refs. 15 and 16.

2. *Superparamagnetic Relaxation*

The uniaxial anisotropy energy creates two potential wells separated by the energy barrier A. The magnetic moment is subjected to thermal fluctuations and may undergo a Brownian-type rotation surmounting the potential barriers. This relaxation process was proposed and studied by Néel in 1949 [2] and further developed by Brown in 1963 [5]. In the high potential barrier range, $\beta A \gg 1$, where $\beta = 1/k_B T$, the characteristic time for the overbarrier rotation τ can approximately be written in the Arrhenius form

$$\tau \simeq \tau_0 \exp(\beta A) \tag{3.6}$$

where $\tau_0 \sim 10^{-9} - 10^{-12}$ s. For observation times t_{obs} much longer than the relaxation time, $\vec{m}$ maintains the thermal equilibrium distribution of orientations as in a classical paramagnet; however, because of the much larger magnetic moment than a single spin, this phenomenon was called *superparamagnetism* [17]. The condition of superparamagnetism ($t_{\text{obs}} \gg \tau$) corresponds to a temperature range that fulfills $\ln(t_{\text{obs}}/\tau_0) > \beta A$. For $t_{\text{obs}} \sim 10$ s, due to the small value of τ_0, this equilibrium range extends down to low thermal energies compared to the anisotropy energy ($25 > \beta A$). Hence, *within the equilibrium regime*, the system displays an isotropic behavior at high temperatures ($\beta A \ll 1$), but a strongly anisotropic behavior at low temperatures ($\beta A \gg 1$).

If $t_{\text{obs}} \ll \tau$, the magnetic moment is *blocked* in one of the potential wells, a state that corresponds to stable magnetization in a bulk magnet. If the measurement time is of the same order as the relaxation time ($t_{\text{obs}} \sim \tau$), dynamical time-dependent effects are observed.

3. *Effects of a Magnetic Field*

The Hamiltonian of a noninteracting nanoparticle with uniaxial anisotropy is given by

$$\mathscr{H} = -\frac{A}{m^2}(\vec{m}\cdot\vec{n})^2 - \mu_0\vec{m}\cdot\vec{H} \tag{3.7}$$

where $\vec{m}$ is the magnetic moment with $m = M_s V$, $A = KV$ and $\vec{n}$ is a unit vector along the symmetry axis of the anisotropy energy (anisotropy direction). By introducing unit vectors for the magnetic moment ($\vec{s} = \vec{m}/m$) and the external magnetic field ($\hat{h} = \vec{H}/H$) and defining dimensionless parameters for the anisotropy and magnetic field

$$\sigma = \beta A, \qquad \xi = \beta\mu_0 mH \tag{3.8}$$

we can write a dimensionless Hamiltonian as

$$-\beta\mathscr{H} = \sigma(\vec{s}\cdot\vec{n})^2 + \xi(\vec{s}\cdot\hat{h}) \tag{3.9}$$

The bistable character of the zero-field Hamiltonian will be destroyed by a sufficiently large field. The critical field for $\vec{n}||\hat{h}$ is called the *anisotropy field*, and is expressed by

$$H_K = \frac{2A}{\mu_0 m} = \frac{2K}{\mu_0 M_s} \tag{3.10}$$

We can define another dimensionless field quantity

$$h = \frac{H}{H_K} = \frac{\xi}{2\sigma} \tag{3.11}$$

which is the field measured in units of the anisotropy field. The Hamiltonian, as a function of the angle θ between the anisotropy axis and the magnetic moment ($\vec{s}\cdot\vec{n} = \cos\theta$), is shown in Figure 3.1 for different values of the longitudinal field.

4. *Interparticle Interaction*

Dipole–dipole interaction is present in all magnetic spin systems, but usually other interaction mechanisms such as exchange interaction dominate. The relative weakness of the dipolar coupling between magnetic ions in paramagnetic systems results in characteristic temperatures lying in the range of 0.01–0.1 K. For superparamagnetic nanoparticles (for which care has been taken to avoid direct contact between the particles by, e.g., applying a surfactant to a ferrofluid), exchange interaction and other interaction mechanisms can usually be discarded so that the dipolar interaction is the only relevant interparticle

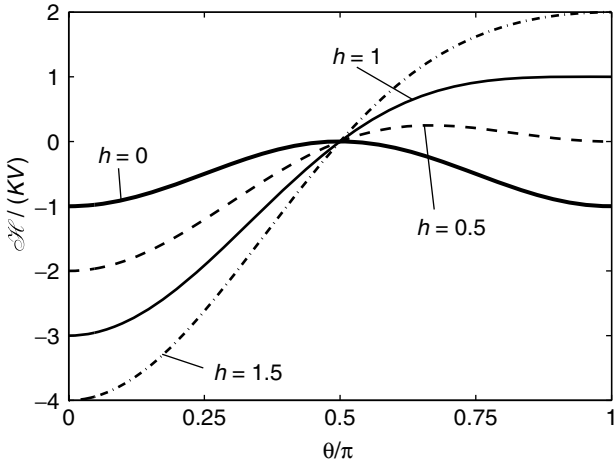

Figure 3.1. Magnetic energy versus θ in the case of a longitudinal field for different values of the reduced field $h = H/H_K$.

interaction. In addition, the size of the typical magnetic moment ($S \sim 10^2 - 10^5$ magnetic spins) shifts the relevant temperatures up to the range of a few kelvins, making it possible to observe effects of dipolar interaction in conventional magnetization experiments.

The dipolar field, created by all other spins, at the position $\vec{r}_i$ of the spin $\vec{s}_i$, is given by

$$\vec{H}_i = \frac{m}{4\pi a^3} \sum_j \mathbf{G}_{ij} \cdot \vec{s}_j \tag{3.12}$$

where the term $j = i$ is omitted from the summation, a is defined in such a way that a^3 is the mean volume around each spin, and

$$\mathbf{G}_{ij} = \frac{1}{r_{ij}^3} \left(3\,\hat{r}_{ij}\hat{r}_{ij} - \mathbf{1} \right) \tag{3.13}$$

$$\vec{r}_{ij} = \vec{r}_i - \vec{r}_j, \quad \hat{r}_{ij} = \frac{\hat{r}_{ij}}{r_{ij}} \tag{3.14}$$

where $\mathbf{1}$ is the unit tensor.

By introducing the dimensionless coupling constant

$$\xi_{\mathrm{d}} = \frac{\mu_0 m^2}{4\pi a^3} \frac{1}{k_{\mathrm{B}} T} \tag{3.15}$$

and noting that the dipolar energy $E_{\mathrm{d}} = \frac{\mu_0}{2}\sum_{i\neq j}\vec{m}\cdot\vec{H}_i$, we can write the total dimensionless Hamiltonian of an interacting nanoparticle system as

$$-\beta\mathscr{H} = \sigma\sum_i(\vec{s}_i\cdot\vec{n}_i)^2 + \xi\sum_i(\vec{s}_i\cdot\hat{h}) + \xi_{\mathrm{d}}\sum_{i>j}\omega_{ij} \tag{3.16}$$

where $\omega_{ij} = \vec{s}_i\cdot\mathbf{G}_{ij}\cdot\vec{s}_j$. Note that the interaction strength can also be measured by the temperature independent coupling parameter

$$h_{\mathrm{d}} = \frac{\xi_{\mathrm{d}}}{2\sigma} = \frac{M_{\mathrm{s}}}{4\pi H_K}c \tag{3.17}$$

which is the magnitude of the field, measured in units of the anisotropy field H_K, produced at a given position by a dipole at a distance a. Here, $c = V/a^3$ is the volume concentration of particles.

Dipole–dipole interaction is long-ranged and anisotropic, which makes it cumbersome to treat both analytically and numerically. Randomness in particle positions and anisotropy directions yields frustration and magnetic disorder leading to glassy dynamics for strongly interacting systems [18]. We will therefore use analytical and numerical treatment only for weakly interacting particle systems, while strongly interacting systems will be discussed in terms of collective spin glass behavior in Section III.

B. Thermal Equilibrium Properties

The thermal equilibrium average of any quantity $B(\vec{s}_1,\ldots,\vec{s}_N)$ is given by

$$\langle B\rangle = \frac{1}{\mathscr{Z}}\int d\Gamma B\,\exp(-\beta\mathscr{H}) \tag{3.18}$$

where $\mathscr{Z} = \int d\Gamma\,\exp(-\beta\mathscr{H})$ is the partition function and $d\Gamma = \prod_i d\Omega_i$, with the solid angle $d\Omega_i = d^2\vec{s}_i/2\pi$. In the case of non-interacting spins, Eq. (3.18) has already been solved analytically for different quantities and anisotropies (for a review, see, e.g., Ref. 8). For isotropic spins, the magnetization is given by the Langevin function and the linear susceptibility follows a $1/T$ dependence, $\chi_{\mathrm{iso}} = \frac{1}{3}\beta\mu_0 m^2$, while the nonlinear susceptibility follows a $1/T^3$ dependence, $\chi_{\mathrm{iso}}^{(3)} = -\frac{1}{45}\beta^3\mu_0^3 m^4$. Magnetic anisotropy generally causes deviations from these well-known laws [8,19–21] and also dipole–dipole interparticle interaction will cause deviations from the Langevin behavior [22,23]. It is important to know the nature of such deviations in order to avoid confusion with, for example, deviations due to quantum effects [24–26].

In the case of dipole–dipole interaction, the calculation of any thermodynamic property becomes a many-body problem and approximations and/or

numerical simulations are needed in order to solve Eq. (3.18). Here we will use thermodynamic perturbation theory to expand the Boltzmann distribution in the dipolar coupling parameter—an approximation that is valid for weakly coupled spins.

The analysis presented in this section is restricted to spins with Hamiltonians having inversion symmetry [$\mathscr{H}(\vec{m}) = \mathscr{H}(-\vec{m})$]. This assumption is valid for any kind of anisotropy or dipolar interaction, but if a bias field is applied in addition to the probing field, the condition of inversion symmetry breaks down.

1. *Thermodynamic Perturbation Theory for Weakly Interacting Superparamagnets*

We will consider dipolar interaction in zero field so that the total Hamiltonian is given by the sum of the anisotropy and dipolar energies $\mathscr{H} = E_\mathrm{a} + E_\mathrm{d}$. By restricting the calculation of thermal equilibrium properties to the case $\xi_\mathrm{d} \ll 1$, we can use thermodynamical perturbation theory [27,28] to expand the Boltzmann distribution in powers of ξ_d. This leads to an expression of the form [23]

$$W = W_\mathrm{a}\left(1 + \xi_\mathrm{d}F_1 + \tfrac{1}{2}\xi_\mathrm{d}^2F_2 + \cdots\right) \tag{3.19}$$

where F_1 is linear in E_d and F_2 is (up to) quadratic in E_d, while

$$W_\mathrm{a} = \mathscr{Z}_a^{-1}\exp(-\beta E_\mathrm{a}) \tag{3.20}$$

is the Boltzmann distribution of the noninteracting ensemble. Expressions for F_1 and F_2 in are given in the Appendix, Section A.1. By keeping all averages weighted with W_a, the thermal-equilibrium quantities calculated with this method will be exact in the anisotropy and only perturbational in the dipolar interaction. An ordinary high-temperature expansion corresponds to expanding Eq. (3.20) further in powers of β.

All results obtained below with the thermodynamic perturbation theory are limited to the case of axially symmetric anisotropy potentials (see the Appendix, Section A.2), and all explicit calculations are done assuming uniaxial anisotropy (see the Appendix, Section B).

2. *Linear Susceptibility*

The equilibrium linear susceptibility is, in the absence of an external bias field, given by

$$\chi = \frac{\mu_0 m^2}{k_\mathrm{B}T}\frac{1}{N}\langle s_z^2\rangle, \qquad s_z = \sum_i(\vec{s}_i\cdot\hat{\boldsymbol{h}}) \tag{3.21}$$

where $\hat{\boldsymbol{h}}$ is a unit vector along the probing field direction and s_z is the field projection of the net magnetic moment. Calculating $\langle s_z^2\rangle$ using thermodynamic

perturbation theory yields an expansion of the susceptibility of the form

$$\chi = \frac{\mu_0 m^2}{k_B T}\left(a_0 + \xi_d a_1 + \tfrac{1}{2}\xi_d^2 a_2\right) \tag{3.22}$$

with the general expressions for the coefficients a_n given in the Appendix, Section A.3. Simplified expressions for the coefficients can be obtained for some orientational distributions of the anisotropy axes, such as parallel anisotropy axes and randomly distributed axes.

For systems with parallel axes (e.g., single crystals of magnetic molecular clusters or a ferrofluid frozen in a strong field), the coefficients for the longitudinal response read

$$a_{0,\parallel} = \frac{1 + 2S_2}{3} \tag{3.23}$$

$$a_{1,\parallel} = \frac{1 + 4S_2 + 4S_2^2}{9}\mathscr{C} \tag{3.24}$$

$$\begin{aligned}\tfrac{1}{2}a_{2,\parallel} = &-\frac{1 + 4S_2 + 4S_2^2}{27}\left[(1 - S_2)\left(\bar{\mathscr{R}} - \mathscr{S}\right) + 3S_2(\mathscr{T} - \mathscr{U})\right] \\ &+ \frac{7 + 10S_2 - 35S_2^2 + 18S_4}{315}\left[(1 - S_2)\left(\bar{\mathscr{R}} - \mathscr{R}\right) + 3S_2\left(\mathscr{T} - \tfrac{1}{3}\bar{\mathscr{R}}\right)\right]\end{aligned} \tag{3.25}$$

where $\mathscr{C}$, $\mathscr{R}$ ($\bar{\mathscr{R}}$), $\mathscr{S}$, $\mathscr{T}$, and $\mathscr{U}$ are *lattice sums* whose properties are discussed in Section II.B.5. The properties of $S_l(\sigma)$ are discussed in the Appendix, Section B.

A common experimental situation is an ensemble of nanoparticles with the anisotropy axes oriented randomly (e.g., frozen ferrofluids). To obtain the susceptibility when the anisotropy axes are distributed at random, we average the general expressions for the a_n over $\vec{n}$, getting

$$a_{0,\text{rand}} = \tfrac{1}{3} \tag{3.26}$$

$$a_{1,\text{rand}} = \tfrac{1}{9}\mathscr{C} \tag{3.27}$$

$$\tfrac{1}{2}a_{2,\text{rand}} = -\frac{1}{27}\left(\bar{\mathscr{R}} - \mathscr{S}\right) + \frac{1}{45}(1 - S_2^2)\left(\bar{\mathscr{R}} - \mathscr{R}\right) \tag{3.28}$$

Note that in the limit of isotropic spins (where $S_l \to 0$), the results for coherent axes and for random anisotropy duly coincide and agree with ordinary high-temperature expansions.

It can easily be shown that $a_{0,\text{rand}}$ is independent of anisotropy for any type of anisotropy, not only axially symmetric [21]. Changing the coordinate system of Eq. (3.21) to the local one determined by the anisotropy direction of each spin,

the field becomes a randomly distributed vector and by performing random averaging with respect to $\hat{h}$ by means of Eq. (A.14), one obtains

$$\chi = \frac{\mu_0 m^2}{k_B T} \frac{1}{3N} \left\langle \sum_i (\vec{s}_i \cdot \vec{s}_i) \right\rangle = \frac{\mu_0 m^2}{3 k_B T} \tag{3.29}$$

which is same expression as for isotropic spins. It is, however, only for the linear susceptibility term that randomly distributed anisotropy axes erase all traces of the anistropy. For the nonlinear susceptibility, the anisotropy is of importance even for systems with randomly distributed anistropy axis [8,19–21].

3. *Specific Heat*

The specific heat at constant volume can be obtained directly from the partition function

$$\frac{c_v}{k_B} = \beta^2 \frac{\partial^2}{\partial \beta^2} (\ln \mathscr{Z}) = \sigma^2 \frac{\partial^2}{\partial \sigma^2} (\ln \mathscr{Z}) \tag{3.30}$$

where, to take the σ derivative, the coupling parameter ξ_d is expressed as $\xi_d = 2\sigma h_d$ [Eq. (3.17)]. As in the calculation of χ, we consider only the zero-field specific heat. In that case, the term linear in ξ_d vanishes and the expansion of the specific heat to second order in ξ_d reads

$$\frac{c_v}{N k_B} = \sigma^2 b_0 + \tfrac{1}{2} \xi_d^2 b_2 \tag{3.31}$$

where the zeroth-order coefficient

$$b_0 = \frac{4}{315} (18 S_4 - 35 S_2^2 + 10 S_2 + 7) \tag{3.32}$$

gives the specific heat in the absence of interaction [8]. The general formula for b_2 is given in the Appendix, Section A.4. Again, it is possible to obtain simplified formulas for coherent anisotropy axes and for random anisotropy. In the first case ($\vec{n}_i = \vec{n}$, $\forall\ i$), we obtain

$$\begin{aligned} b_{2,\parallel} = {} & \tfrac{1}{3} \left\{ 1 - S_2^2 - 4\sigma S_2 S_2' - \sigma^2 [S_2 S_2'' + (S_2')^2] \right\} \mathscr{R} \\ & + \tfrac{1}{3} \big(2 S_2 (1 - S_2) + 4\sigma S_2' (1 - 2 S_2) \\ & + \sigma^2 \{ S_2'' - 2 [S_2 S_2'' + (S_2')^2] \} \big) (\bar{\mathscr{R}} - \mathscr{R}) \\ & + \left\{ S_2^2 + 4\sigma S_2 S_2' + \sigma^2 [S_2 S_2'' + (S_2')^2] \right\} \mathscr{T} \end{aligned} \tag{3.33}$$

where $S_2' = dS_2/d\sigma$. For randomly distributed axes, on averaging the general expression for b_2 over $\vec{n}$, one simply gets

$$b_{2,\text{rand}} = \tfrac{1}{3}\mathscr{R} \tag{3.34}$$

This is the same correction term as that obtained for *isotropic* spins by Waller [29] and van Vleck [30] using ordinary high-temperature expansions.

4. *Dipolar Fields*

We are interested in calculating thermodynamical averages of the dipolar field, to introduce them in the expression for the relaxation rate in a weak but arbitrary oriented field, in order to obtain an expression for the relaxation rate of weakly interacting dipoles (we will argue in Section II.C.3 that the effect of weak dipolar interaction can be accounted for by the thermodynamic averages of the dipolar field). Because of the inversion symmetry of the anisotropy, only the square of the field will enter the low-field expression for the relaxation rate and not the field itself. In addition, the effects of longitudinal and transversal fields will be different. To be able to calculate the dipolar field is also of interest in the study of quantum tunneling of the magnetization of molecular magnets (e.g., Fe_8 and Mn_{12}) [3,31].

The general expressions for $\langle \xi_{i,\parallel}^2 \rangle$ and $\langle \xi_{i,\perp}^2 \rangle = \langle \xi_i^2 \rangle - \langle \xi_{i,\parallel}^2 \rangle$ to second order in ξ_d are given in the Appendix, Section A.5. If we consider infinite systems, the index i can be removed since all spins have the same surroundings. For a system with aligned anisotropy axes, the averaged fields are given in terms of the lattice sums by

$$\begin{aligned} \langle \xi_\parallel^2 \rangle &= \frac{\xi_\text{d}^2}{3}[(1 - S_2)\bar{\mathscr{R}} + 3S_2\mathscr{T}] \\ \langle \xi_\perp^2 \rangle &= \frac{\xi_\text{d}^2}{3}[3\mathscr{R} - (1 - S_2)\bar{\mathscr{R}} + 3S_2(\mathscr{R} - \bar{\mathscr{R}} - \mathscr{T})] \end{aligned} \tag{3.35}$$

while for randomly distributed anisotropy axes they read

$$\overline{\langle \xi_\parallel^2 \rangle} = \frac{\xi_\text{d}^2}{3}\mathscr{R}, \qquad \overline{\langle \xi_\perp^2 \rangle} = \frac{\xi_\text{d}^2}{3}2\mathscr{R} \tag{3.36}$$

Note that the result for random anisotropy is identical to the result for isotropic dipoles.

5. *The Lattice Sums*

An essential element of the expressions derived for χ, c_v, and the dipolar fields are the following "lattice sums:"[1]

$$\mathscr{C} = \frac{1}{N}\sum_i \sum_{j\neq i} \hat{\boldsymbol{h}} \cdot \mathbf{G}_{ij} \cdot \hat{\boldsymbol{h}} \tag{3.37}$$

$$\mathscr{R} = \frac{2}{N}\sum_i \sum_{j\neq i} r_{ij}^{-6} \tag{3.38}$$

$$\bar{\mathscr{R}} = \frac{1}{N}\sum_i \sum_{j\neq i} \hat{\boldsymbol{h}} \cdot \mathbf{G}_{ij} \cdot \mathbf{G}_{ij} \cdot \hat{\boldsymbol{h}} \tag{3.39}$$

$$\mathscr{S} = \frac{1}{N}\sum_i \sum_{j\neq i} \sum_{k\neq j} \hat{\boldsymbol{h}} \cdot \mathbf{G}_{ij} \cdot \mathbf{G}_{jk} \cdot \hat{\boldsymbol{h}} \tag{3.40}$$

$$\mathscr{T} = \frac{1}{N}\sum_i \sum_{j\neq i} (\hat{\boldsymbol{h}} \cdot \mathbf{G}_{ij} \cdot \hat{\boldsymbol{h}})^2 \tag{3.41}$$

$$\mathscr{U} = \frac{1}{N}\sum_i \sum_{j\neq i} \sum_{k\neq j} (\hat{\boldsymbol{h}} \cdot \mathbf{G}_{ij} \cdot \hat{\boldsymbol{h}})\,(\hat{\boldsymbol{h}} \cdot \mathbf{G}_{jk} \cdot \hat{\boldsymbol{h}}) \tag{3.42}$$

The long range of the dipole–dipole interaction leads to a sample shape[2] dependence of the physical quantities dependent on an external magnetic field [32,33]. In the expressions obtained for the susceptibility, this sample shape dependence is borne by the slowly convergent lattice sums $\mathscr{C}$, $\mathscr{S}$, and $\mathscr{U}$. If we consider "sufficiently isotropic" lattices, in the sense of fulfilling $\sum(r_x)^n = \sum(r_y)^n = \sum(r_z)^n$, such as cubic and completely disordered lattices (incidentally, the type of arrangements for which in the classical Lorentz cavity–field calculation the contribution of the dipoles inside the "small sphere" vanishes) these lattice sums vanish for large spherical samples. The sums $\mathscr{R}$, $\bar{\mathscr{R}}$, and $\mathscr{T}$, on the other hand, contain r_{ij}^{-6}, which make them rapidly convergent and sample shape-independent. For sufficiently symmetric lattices $\bar{\mathscr{R}} = \mathscr{R} = 16.8,\ 14.5,\ 14.5$ for simple cubic (sc), body-centered cubic (bcc), and face-centered cubic (fcc) structures, respectively [34], and $\mathscr{T} = 13.54$ (sc), 3.7 (bcc), 4.3 (fcc). Note that since $\bar{\mathscr{R}} - \mathscr{R} = 0$, some terms vanish in the above expressions for χ, c_v, and the dipolar fields.

[1] $\hat{\boldsymbol{h}}$ should be replaced by $\vec{\boldsymbol{n}}$ in the formulas for c_v and the dipolar fields.

[2] Sample shape refers to the shape of the whole ensemble of nanoparticles, *not* to the shape of the individual particles. The linear susceptibility exhibits a sample shape dependence, while the zero-field specific heat and the dipolar fields do not.

a. Sample Shape and Anisotropy Dependence. The sample shape dependence of the linear susceptibility is illustrated in Figure 3.2. The susceptibility is calculated for small systems using both thermodynamic perturbation theory and a Monte Carlo technique [35], taking the dipolar interaction into account

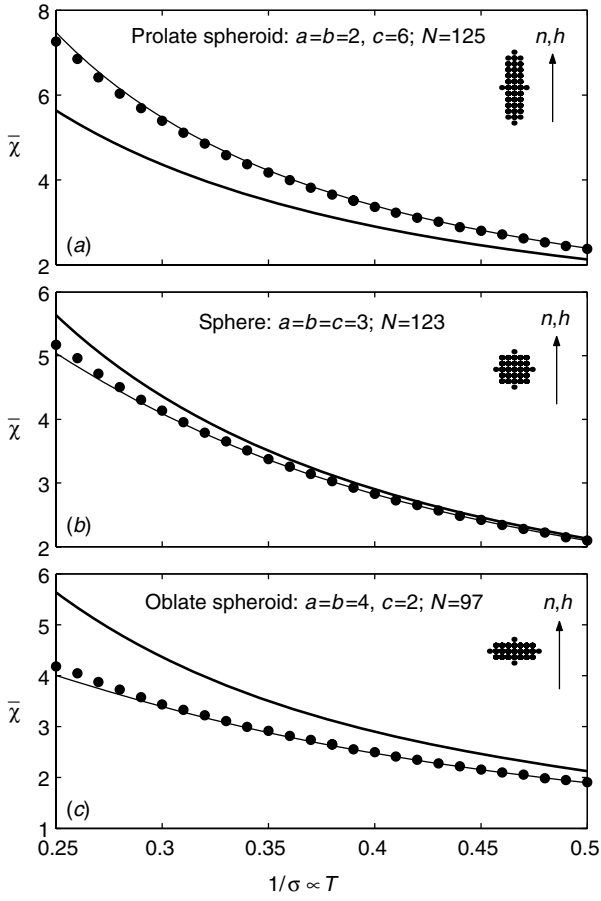

Figure 3.2. Equilibrium linear susceptibility in reduced units $\bar{\chi} = \chi(H_K/m)$ versus temperature for three different ellipsoidal systems with equation $x^2/a^2 + y^2/b^2 + z^2/c^2 \leq 1$, resulting in a system of N dipoles arranged on a simple cubic lattice. The points shown are the projection of the spins to the xz plane. The probing field is applied along the anisotropy axes, which are parallel to the z axis. The thick lines indicate the equilibrium susceptibility of the corresponding noninteracting system (which does not depend on the shape of the system and is the same in the three panels); thin lines show the susceptibility including the corrections due to the dipolar interaction obtained by thermodynamic perturbation theory [Eq. (3.22)]; the symbols represent the susceptibility obtained with a Monte Carlo method. The dipolar interaction strength is $h_{\rm d} = \xi_{\rm d}/2\sigma = 0.02$.

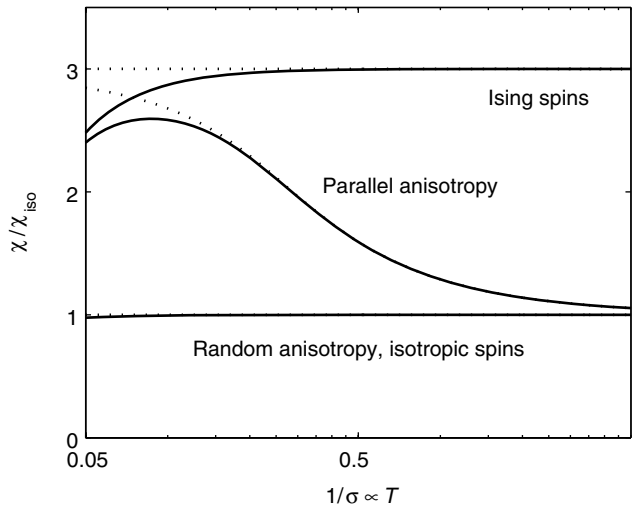

Figure 3.3. Equilibrium linear susceptibility (χ/χ_{iso}) versus temperature for an infinite spherical sample on a simple cubic lattice. The dotted lines are the results for independent spins, while the solid lines show the results for parallel and random anisotropy calculated with thermodynamic perturbation theory, as well as for Ising spins calculated with an ordinary high-temperature expansions. We notice in this case that the linear susceptibility for systems with random anisotropy is the same as for isotropic spins calculated with an ordinary high-temperature expansion. The dipolar interaction strength is $h_d = \xi_d/2\sigma = 0.004$.

without any approximation. It can be seen that χ obtained by thermodynamic perturbation theory accurately describes the simulated susceptibility at high temperatures, while the results start to deviate at the lowest temperatures displayed. An estimate of the lowest temperature attainable by the thermodynamic perturbation theory is $\xi_d \sim 1/6$, which is milder than the a priori restriction $\xi_d \ll 1$.

For the linear susceptibility, the zero-field specific heat as well as the dipolar fields, the anisotropy dependence cancels out in the case of randomly distributed anisotropy (at least for sufficiently symmetric lattices). In other cases the anisotropy is a very important parameter as shown for the linear susceptibility in Figure 3.3 for an infinite (macroscopic) spherical sample. The susceptibility is divided by $\chi_{iso} = \frac{1}{3}\beta\mu_0 m^2$ in order to single out effects of anisotropy and dipolar interaction. It can be seen in this figure that the effect of the dipolar interaction is much stronger for a system with parallel anisotropy axes than for a system with random anistropy (which coincide with the case of isotropic spins). At low temperatures, the susceptibility of a system with parallel anisotropy approaches that of Ising spins (calculated with an ordinary high-temperature expansion), while at high temperatures it is close to that of isotropic spins.

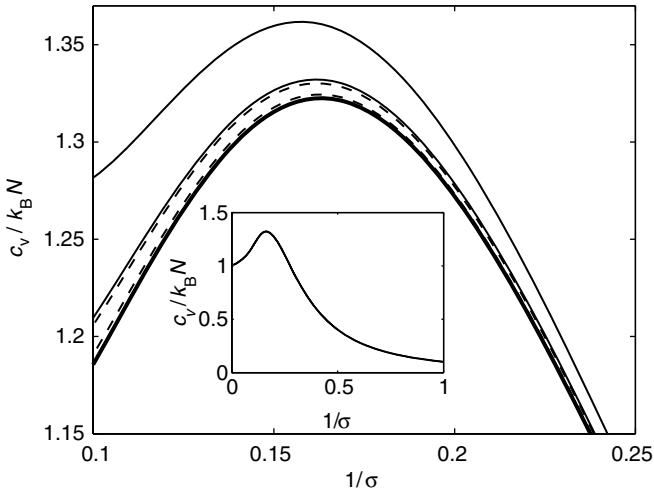

Figure 3.4. The specific heat per spin versus temperature for noninteracting spins (thick line) and weakly interacting spins with randomly distributed anisotropy axes (dashed lines) and parallel axes (thin lines) arranged on a simple cubic lattice. In each case, $h_d = \xi_d/2\sigma = 0.003$ and 0.006 from bottom to top. The inset shows the specific heat for noninteracting spins over a wider temperature interval.

The specific heat for uncoupled spins does not depend on the orientations of the anisotropy axes; however, the corrections due to the dipolar coupling do, as can be seen in Figure 3.4. As for the linear susceptibility, the effect of dipolar interaction is stronger in the case of parallel anistropy than for random anistropy.

C. Dynamic Properties

At high temperatures, a nanoparticle is in a superparamagnetic state with thermal equilibrium properties as described in the previous section. At low temperatures, the magnetic moment is blocked in one potential well with a small probability to overcome the energy barrier, while at intermediate temperatures, where the relaxation time of a spin is comparable to the observation time, dynamical properties can be observed, including magnetic relaxation and a frequency-dependent ac susceptibility.

For applications, such as magnetic recording media, it is necessary to know how different parameters will affect the relaxation time in order to avoid spontaneous data erasure (caused by thermal fluctuations) on the lifetime of the device. Because of the ongoing effort to increase the information/volume ratio, it is of special importance to know how the dipolar interaction of densely packed nanoparticles will affect the relaxation time.

In 1963 Brown [5] derived the Fokker–Planck equation for the probability distribution of the spin orientation, starting from the stochastic Gilbert equation, and calculated the relaxation time for particles with uniaxial anisotropy in a longitudinal field. More recent work on spins with nonaxially symmetric potential revealed a large dependence of the relaxation time on the damping coefficient λ in the medium–weak damping regime [36–38]. Experiments on individual nanoparticles analyzed with accurate asymptotes of the relaxation time [39] gave damping coefficients in the range $\lambda \approx 0.05 - 0.5$. Nonaxially symmetric potentials are, for example, created when applying a field at an oblique angle to a uniaxial spin. This oblique field can either be a bias field [40] or a nonlinear probing field [41]. In the case of interacting particles a transverse field component arises from the dipolar field of the surrounding particles. This explains the dependence on λ of the blocking temperature that was first observed in numerical simulations by Berkov and Gorn [13] (see Fig. 3.5).

The importance of including the damping in models describing the dynamic response of spins with nonaxially symmetric potentials (e.g., interacting uniaxial spins) tells us that models based only on how the energy barriers change [42,43] necessarily overlook the precession of the magnetic moment ($\lambda \to \infty$) and therefore cannot account for the numerical results of Berkov and Gorn. A simple approach to include the damping in the dynamics of weakly coupled spin systems was proposed in Ref. 44.

1. *The Equation of Motion*

We will present the equation of motion for a classical spin (the magnetic moment of a ferromagnetic single-domain particle) in the context of the theory of stochastic processes. The basic Langevin equation is the stochastic Landau–Lifshitz(–Gilbert) equation [5,45]. More details on this subject and various techniques to solve this equation can be found in the reviews by Coffey et al. [46] and García-Palacios [8].

a. Deterministic Equations. The motion of a magnetic moment can be described by the Gilbert equation [47]

$$\frac{1}{\gamma}\frac{d\vec{m}}{dt} = \vec{m} \times \vec{H}_{\text{eff}} - \frac{\lambda}{\gamma m}\vec{m} \times \frac{d\vec{m}}{dt} \tag{3.43}$$

where γ is the gyromagnetic ratio (which includes μ_0), λ is a dimensionless damping coefficient, and the effective field is given by

$$\vec{H}_{\text{eff}} = -\frac{\mu_0^{-1}\partial \mathscr{H}}{\partial \vec{m}} \tag{3.44}$$

The first term on the right side of Eq. (3.43) represents the precession of the magnetic moment about the axis of the effective field, while the second one is

[Image not available in this electronic edition.]

Figure 3.5. The out-of-phase component of the ac susceptibility versus temperature for two different values of the damping $\lambda = 0.1$ and 1.0. $\gamma M_s \omega = 0.03$, $E_{dem} = M_s^2 V/k_B$, and $h_d = (\mu_0/4\pi)(c/\beta)$ with $\beta = 2.0$. From Ref. 13.

the damping term, which rotates $\vec{m}$ toward the potential minima and is responsible for the dissipation of the energy.

The Gilbert equation can be cast into the Landau–Lifshitz form [48]

$$\frac{1}{\gamma}\frac{d\vec{m}}{dt} = \vec{m} \times \vec{H}_{\text{eff}} - \frac{\lambda}{m}\vec{m} \times (\vec{m} \times \vec{H}_{\text{eff}}) \tag{3.45}$$

with a ''renormalized'' gyromagnetic ratio $\gamma \rightarrow \gamma/(1+\lambda^2)$ [8,48]. In the case of uniaxial anisotropy and a Hamiltonian given by Eq. (3.7), $\vec{H}_{\text{eff}} = (H_K/m)(\vec{m}\cdot\vec{n})\vec{n} + \vec{H}$, where H_K is the anisotropy field and $\vec{H}$ is an external field. The ferromagntic resonance frequency ω for the precession about $\vec{H}_{\text{eff}}$ is given by $\omega = \gamma\mu_0 H_{\text{eff}}$ [49].

b. Stochastic Equations. At $T \neq 0$ the magnetic moment will interact with the microscopic degrees of freedom (phonons, conducting electrons, nuclear spins, etc.). The complexity of this interaction allows an idealization, namely, to introduce them through a stochastic model. The simplest model is the Brownian, in which the interaction of $\vec{m}$ with the surroundings is represented by a randomly fluctuating magnetic field. This fluctuating field is necessarily combined with a dissipation (damping) term, and these two terms are linked by fluctuation–dissipation relations [50].

In the work of Brown [5] and Kubo and Hashitsume [45] the starting equation is the Gilbert equation (3.43), in which the effective field is increased by a fluctuating field yielding the stochastic Gilbert equation. This equation can, as in the deterministic case, be cast into the Landau–Lifshitz form as

$$\frac{1}{\gamma}\frac{d\vec{m}}{dt} = \vec{m}\times[\vec{H}_{\text{eff}} + \vec{b}_{\text{fl}}(t)] - \frac{\lambda}{m}\vec{m}\times\{\vec{m}\times[\vec{H}_{\text{eff}} + \vec{b}_{\text{fl}}(t)]\} \tag{3.46}$$

known as the stochastic Landau–Lifshitz–Gilbert (LLG) equation. The fluctuating field is assumed to be Gaussian distributed white noise

$$\langle b_{\text{fl},\alpha}(t)\rangle = 0, \qquad \langle b_{\text{fl},\alpha}(t) b_{\text{fl},\beta}(t')\rangle = 2D\delta_{\alpha\beta}\delta(t-t') \tag{3.47}$$

with $\alpha, \beta = x, y, z$. García-Palacios and Lázaro [51] showed that the stochastic Landau–Lifshitz–Gilbert equation [Eq. (3.46)] and the simpler stochastic Landau–Lifshitz (LL) equation

$$\frac{1}{\gamma}\frac{d\vec{m}}{dt} = \vec{m}\times[\vec{H}_{\text{eff}} + \vec{b}_{\text{fl}}(t)] - \frac{\lambda}{m}\vec{m}\times(\vec{m}\times\vec{H}_{\text{eff}}) \tag{3.48}$$

both give rise to the same Fokker–Planck equation, describing the average properties of the magnetic moment, but with different Einstein-type relations between the amplitude of the fluctuating field and the temperature:

$$D_{\text{LLG}} = \frac{\lambda}{1+\lambda^2}\frac{k_{\text{B}}T}{\gamma m}, \qquad D_{\text{LL}} = \lambda\frac{k_{\text{B}}T}{\gamma m} \tag{3.49}$$

2. *Relaxation Time in a Weak but Arbitrary Field*

We are interested in knowing how the relaxation time of uniaxial spins is affected by a weak field at an arbitrary direction, since it will allow us to study how the superparamagnetic blocking is affected by a field. This field dependence of the relaxation time can be obtained by expanding the relaxation rate $\Gamma = 1/\tau$ in powers of the field components. As the spins have inversion symmetry in the absence of a field, Γ should be an even function of the field components, and to third order it is given by

$$\Gamma \simeq \Gamma_0(1 + c_\parallel \xi_\parallel^2 + c_\perp \xi_\perp^2) \tag{3.50}$$

where $\xi_\parallel$ and $\xi_\perp$ respectively are the longitudinal and transversal components of the field [given in temperature units, see Eq. (3.8)] with respect to the anisotropy axis. Γ_0 is the zero-field relaxation rate, which for low temperatures ($\sigma > 1$) is given by Brown's result [5]

$$\Gamma_0 = \frac{1}{\tau_D}\frac{2}{\sqrt{\pi}}\sigma^{3/2}e^{-\sigma} \tag{3.51}$$

where $\tau_D = m/(2\gamma\lambda k_B T)$ is the relaxation time of isotropic spins. The coefficient $c_\parallel$ can be obtained by expanding the expression for Γ in the presence of a longitudinal field [5,52]

$$\begin{aligned}\Gamma(\xi_\parallel, \xi_\perp = 0) &= \frac{1}{\tau_D}\frac{\sigma^{3/2}}{\sqrt{\pi}}\left[(1+h)e^{-\sigma(1+h)^2} + (1-h)e^{-\sigma(1-h)^2}\right] \\ &\simeq \Gamma_0\left(1 + \tfrac{1}{2}\xi_\parallel^2\right)\end{aligned} \tag{3.52}$$

There is no general expression for the relaxation rate in the presence of a nonzero transversal field valid for all values of the relevant parameters [53], but Garanin et al. have derived a low-temperature formula valid for weak transversal fields [38], which can be used to determine the coefficient $c_\perp$:

$$\Gamma(\xi_\parallel = 0, \xi_\perp) \simeq \Gamma_0\left[1 + \tfrac{1}{4}F(\alpha)\xi_\perp^2\right] \tag{3.53}$$

$$F(\alpha) = 1 + 2(2\alpha^2 e)^{1/(2\alpha^2)}\gamma\left(1 + \frac{1}{2\alpha^2}\,,\,\frac{1}{2\alpha^2}\right) \tag{3.54}$$

Here $\alpha = \lambda\,\sigma^{1/2}$ and $\gamma(a,z) = \int_0^z dt\, t^{a-1}\, e^{-t}$ is the incomplete gamma function. It can be noted that for the axially symmetric potential with a longitudinal field, the only dependence on λ is the trivial one in τ_D, while in the nonaxially symmetric potential obtained with a transversal field the relaxation rate will strongly depend on λ through $F(\alpha)$, which is plotted in Figure 3.6.

Collecting these results, we can finally write the expression for the relaxation rate in a weak field [44]:

$$\Gamma \simeq \Gamma_0\left[1 + \tfrac{1}{2}\xi_\parallel^2 + \tfrac{1}{4}F(\alpha)\xi_\perp^2\right] \tag{3.55}$$

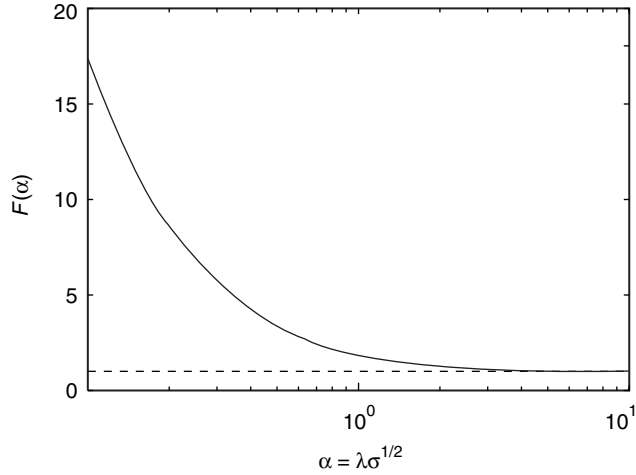

Figure 3.6. F versus $\alpha = \lambda\sigma^{1/2}$ (solid line) and the overdamped value $F = 1$ (dashed line).

3. *Relaxation Time of Weakly Interacting Nanoparticles*

The relaxation time for weakly interacting nanoparticles with uniaxial anisotropy can be obtained by inserting the thermodynamical averages of the dipolar fields (calculated in Section II.B.4) in the expression for the relaxation rate in a weak field [Eq. (3.55)], yielding $\Gamma \simeq \Gamma_0[1 + \frac{1}{2}\langle\xi_\parallel^2\rangle + \frac{1}{4}F(\alpha)\langle\xi_\perp^2\rangle]$. Other models [42,43,54] are energy-barrier-based and therefore neglect the λ dependence on relaxation time. For instance, the model by Mørup and Tronc [43] is basically the same as the one presented here in the particular case of high damping and random anisotropy. The Mørup–Tronc model predicts a decrease of the blocking temperature with increasing interaction strength for weak interaction as was observed in high-frequency Mössbauer experiments, while the Dormann–Bessias–Fiorani model [42] predicts an increase of the blocking temperature with increasing interaction strength as commonly observed in magnetization measurements. These discrepancies led to some controversy [55,56]. Berkov and Gorn [13] showed, by numerical integration of the stochastic LLG equation [Eq. (3.46)], that for strong anisotropy (or weak interaction) the blocking temperature decreases with interaction (see Fig. 3.5), while for weak anisotropy (or moderate–high interaction) the energy barriers are governed by the interaction and hence grow with h_d. An increase of the apparent blocking temperature is clearly the case for the strongly interacting nanoparticle samples (see Section III) in which the relaxation time increases with h_d due to spin–spin correlations (see Fig. 3.21).

In order to determine the characteristics of the superparamagnetic blocking we use the equilibrium susceptibility χ_{eq} calculated using the thermodynamic

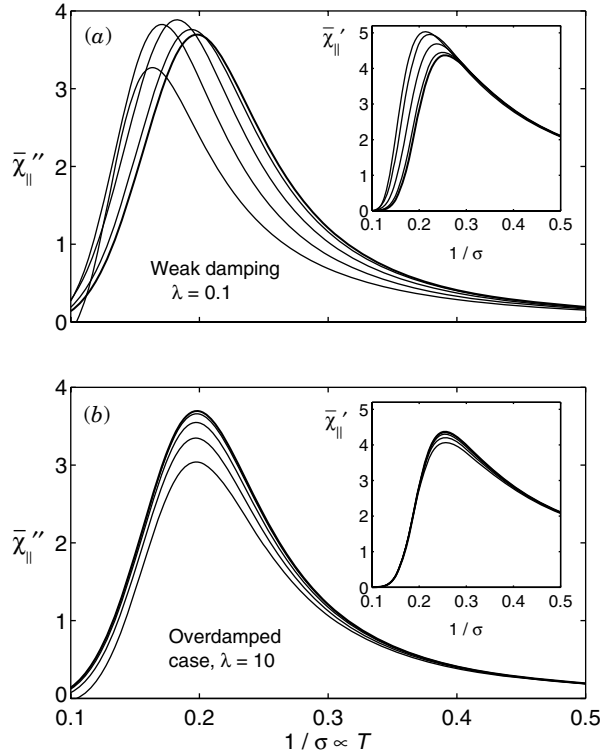

Figure 3.7. Imaginary component of the dynamical susceptibility versus temperature (the real component is shown in the inset) for a spherical sample and spins placed in a simple cubic lattice. The anisotropy axes are all parallel, and the response is probed along their common direction. The dipolar interaction strength $h_d = \xi_d/2\sigma$ is $h_d = 0$ (thick lines), 0.004, 0.008, 0.012, and 0.016 from (*a*) right to left and (*b*) top to bottom. The frequency is $\omega\tau_D/\sigma = 2\pi \times 0.003$.

perturbation theory Eq. (3.22) and the relaxation rate Γ obtained when the dipolar fields [Eq. (3.35) or (3.36)] are introduced in Eq. (3.55). Combining these expressions in a Debye-type formula

$$\chi = \chi_{eq} \frac{\Gamma}{\Gamma + i\omega} \tag{3.56}$$

provides us with a simple model for the dynamic response. The dynamic susceptibility of a large spherical sample with parallel anisotropy axis and a simple cubic structure is shown in Figure 3.7. In the overdamped case, the blocking temperature is not noticeably affected by the dipolar interaction, while for low damping the blocking temperature decreases significantly as the

interaction strength increases. These results are in agreement with the simulations by Berkov and Gorn [13] shown in Figure 3.5.

An interpretation of the strong damping dependence found in the presence of a transverse field component was given in Ref. 41—the transverse field creates a saddle point in the potential barrier. A thermally excited spin with high damping will ''fall'' directly back to the bottom of the potential well if the thermal excitation is not sufficient for an overbarrier jump. On the other hand, a weakly damped spin in the same situation will precess ($\sim 1/\lambda$ times) about the anisotropy axis and therefore has an increased probability for overbarrier jumps each time it passes close to the saddle point. In the case of noninteracting particles the transverse field component must come from either a nonlinear probing field [41] or a bias field [40], while the transverse field here naturally arises from the dipolar interaction.

D. Numerical Methods

Because of the long-range and reduced symmetry of the dipole–dipole interaction, analytical methods such as the thermodynamic perturbation theory presented in Section II.B.1. will be applicable only for weak interaction. Numerical simulation techniques are therefore indispensable for the study of interacting nanoparticle systems, beyond the weak coupling regime.

The Monte Carlo (MC) method can be used to efficiently calculate thermal equilibrium properties (see Fig. 3.2). However, since it is an energy-barrier-based method, it will fail to generate dynamic features such as the precession of the spins, and will be able to generate the dynamic magnetization in the overdamped limit ($\lambda \to \infty$) only if an appropriate algorithm is used [35].

Using a Langevin dynamics approach, the stochastic LLG equation [Eq. (3.46)] can be integrated numerically, in the context of the Stratonovich stochastic calculus, by choosing an appropriate numerical integration scheme [51]. This method was first applied to the dynamics of noninteracting particles [51] and later also to interacting particle systems [13] (see Fig. 3.5).

Because of the long-range nature of the dipolar interaction, care must be taken in the evaluation of the dipolar field. For finite systems the sums in Eq. (3.12) are performed over all particles in the system. For systems with periodic boundary conditions the Ewald method [57–59], can be used to correctly calculate the conditionally convergent sum involved. However, in most work [12,13] the simpler Lorentz-cavity method is used instead.

III. STRONGLY INTERACTING NANOPARTICLE SYSTEMS—SPIN-GLASS-LIKE BEHAVIOR

A large number of applications use densely packed magnetic nanoparticles. It is thus important to know how interparticle interaction affects the physical

properties of magnetic nanoparticle systems. In particular, it is important to understand how the thermal stability of magnetic recording media is changed by interparticle interactions due to the current effort of shrinking the volume of storage devices.

It has been suggested that dense nanoparticle samples may exhibit glassy dynamics due to dipolar interparticle interaction [18]; disorder and frustration are induced by the randomness in the particle positions and anisotropy axis orientations. In order to investigate such systems, one needs to use the experimental techniques (protocols) developed in studies of spin glasses. Examination of the effects of dipolar interactions using standard experimental protocols (zero-field-cooled (ZFC)/field-cooled (FC) magnetization) indicates no dramatic change in these quantities, and one can be misled to believe that the only effect of the dipolar interaction is to increase the blocking temperature due to enhanced energy barriers. However, glassy dynamics has been observed in strongly interacting nanoparticle systems [60–62], and for strongly interacting systems with narrow size distributions, evidence has been given for a spin-glass-like phase transition [63–66].

In frozen ferrofluids the strength of the dipolar interaction between the single-domain nanoparticles can be continuously varied by changing the particle concentration. With increasing particle concentration the magnetic behavior may evolve from superparamagnetic to spin-glass-like. We will begin this section by recalling some fundamental properties of spin glasses. Furthermore, experimental results will be presented on a ferrofluid of $Fe_{1-x}C_x$ nanoparticles. The glassy dynamics of dense nanoparticle samples will be compared with those of an Ising and a Heisenberg spin glass.

A. Spin Glasses

This section is intended as a brief introduction to spin glasses, focusing on the most recent work. For reviews on spin glasses, see, for example, Refs. 67–69.

1. *Material*

The canonical spin glass consists of a noble metal (Au, Ag, Cu, or Pt) diluted with a transition metal ion, such as Fe or Mn. The magnetic interaction in such systems is mediated by the conduction electrons, leading to an indirect exchange interaction—the RKKY (Ruderman and Kittel [70], Kasuya [71], and Yosida [72]) interaction, whose coupling constant $J(R)$ oscillates strongly with distance r between the spins as

$$J(r) = J_0 \frac{\cos(2k_F r + \varphi_0)}{(k_F r)^3} \tag{3.57}$$

Here J_0 and φ_0 are constants and k_F is the Fermi wavevector of the host metal. Since the spins are randomly placed in the host metal, some spin–spin interaction will be positive and favor parallel alignment, while other will be negative, thus favoring antiparallel alignment.

The pure RKKY interaction is isotropic, and the canonical spin glass systems are therefore often referred to as *Heisenberg spin glasses*. However, some anisotropy is also present in those systems originating from dipolar interaction and interaction of the Dzyaloshinsky–Moriya (DM) type [73]. The latter is due to spin–orbit scattering of the conduction electrons by non-magnetic impurities and reads

$$E_{\mathrm{DM}} = -\vec{D}_{ij} \cdot (\vec{s}_i \times \vec{s}_j), \qquad \vec{D}_{ij} \propto \vec{r}_i \times \vec{r}_j \tag{3.58}$$

where $\vec{D}_{ij}$ is a random vector due to the randomness of the spin positions $\vec{r}_i$. The dipolar interaction is, as discussed in Section II.A.4, weak for atomic spin systems, while the DM interaction is enhanced by the presence of nonmagnetic transition-metal impurities [73,74]. However, for macroscopic spins (magnetic moments), the dipolar interaction is important, and if the particles are dispersed in a nonconductive medium (e.g., a frozen ferrofluid), it is the dominating interparticle interaction. If the magnetic particles are randomly placed, the dipolar interaction will be both positive and negative.

A widely studied model system for an Ising spin glass is single crystals of $Fe_xMn_{1-x}TiO_3$ with $x \approx 0.5$ [75–77]. Both $FeTiO_3$ and $MnTiO_3$ are antiferromagnets having the easy axis along the hexagonal c axis of the ilmenite structure. The Fe^{2+} spins in $FeTiO_3$ are coupled ferromagnetically within a c layer and antiferromagnetically between adjacent c layers. In $MnTiO_3$, on the other hand, both the intralayer and interlayer coupling of Mn^{2+} spins are antiferromagnetic. The compound $Fe_xMn_{1-x}TiO_3$ behaves as an Ising spin glass for $0.4 \lesssim x \lesssim 0.57$, due to the mixing of ferromagnetic and antiferromagnetic interaction [77].

There are essential differences between the systems we have presented here, even in the limit of very strong anisotropy. The RKKY spin glasses are Heisenberg systems with *random unidirectional* anisotropy. Ferrofluids frozen under zero field are Heisenberg systems with *random uniaxial* anisotropy, while an Ising system is characterized by *parallel uniaxial* anisotropy.

2. *Spin Glass Models*

The Hamiltonian of an Ising spin glass, given by Edwards and Anderson (EA) [78], is

$$\mathscr{H} = -\tfrac{1}{2}\sum_{i,j} J_{ij} s_i s_j - H \sum_{i=1}^{N} s_i \tag{3.59}$$

where the spin $s_i = \pm 1$ and the coupling constants J_{ij} are chosen from some random distribution fulfilling $\sum_{i,j} J_{ij} = 0$ in the case of a symmetric spin glass. In the EA model the spin–spin interaction is only of the nearest-neighbor type. The Sherrington–Kirpatrick (SK) model [79] is the infinite-range version of the EA model. It is most useful as a basis for mean-field calculations. One such solution is the replica symmetry breaking theory of Parisi [80–82].

For a ferromagnet the order parameter is the magnetization, while for antiferromagnets it is the sublattice magnetization. For spin glasses the magnetization is zero at all temperatures, and an appropriate order parameter was proposed by Edwards and Anderson [78] as the average value of the autocorrelation function

$$q_{\mathrm{EA}} = \lim_{t\to\infty} \langle \vec{s}_i(0) \cdot \vec{s}_i(t) \rangle \tag{3.60}$$

The order parameter susceptibility, which diverges at the transition temperature, is the nonlinear susceptibility χ_2, defined as $M/h = \chi_0 + \chi_2 h^2 + \cdots$, where χ_0 is the linear susceptibility [83]. The divergency of the nonlinear susceptibility was first shown on a Au(Fe) spin glass in 1977 by Chikazawa et al. [84] and more recently for a strongly interacting nanoparticle system by Jonsson et al. [64].

3. *Critical Dynamics*

Close to the transition temperature T_{g}, the dynamics of a spin glass system will be governed by critical fluctuations, but critical fluctuations are also of importance on experimental timescales quite far from T_{g}. At temperatures both below and above T_g, length scales shorter than the coherence length of the critical fluctuations

$$\xi \sim L_0 |\epsilon|^{-\nu} \tag{3.61}$$

will be dominated by critical fluctuations. Here L_0 is a microscopic length scale and the reduced temperature $\epsilon = (1 - T/T_{\mathrm{g}})$. The coherence length can be transformed into a timescale according to conventional critical slowing down; the critical correlation time is given by

$$\tau_c \sim \tau_m \left(\frac{\xi(T)}{L_0} \right)^z \sim \tau_m |\epsilon|^{-z\nu} \tag{3.62}$$

where τ_m is a microscopic timescale. For spin glasses, $\tau_m \sim 10^{-13}$ s is the fluctuation time of an atomic moment. For nanoparticles, τ_m can be assigned to the superparamagnetic relaxation time of a single particle of average size, which, in the relevant temperature range for our studies, can be approximated by the Arrhenius–Néel expression [Eq. (3.6)].

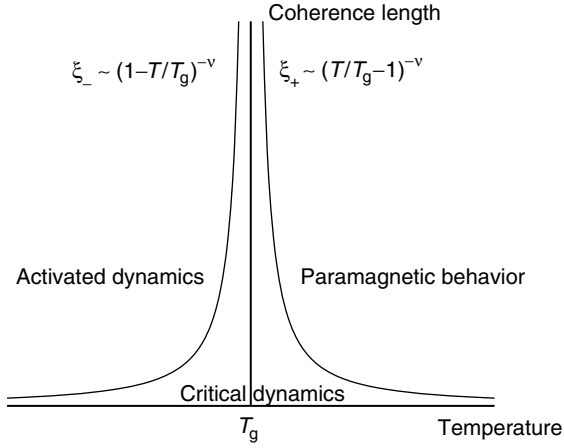

Figure 3.8. Illustration of length (time) scales in spin glasses.

At temperatures below T_g, there is a crossover between critical dynamics on short length (time) scales and activated dynamics on long length (time) scales. The length scale of critical dynamics as a function of temperature is illustrated in Figure 3.8. For $T > T_g$, the system is in equilibrium on length (time) scales longer than ξ (τ_c) and hence the magnetic response is paramagnetic. The "freezing" temperature ($T_f(\tau_c)$) of the crossover from a paramagnetic response to slow spin glass dynamics, as a function of observation time, can be obtained from experiments. Such a dynamic scaling analysis is performed in Section III.B.2 for two samples of a nanoparticle system with two different volume concentrations. Dynamic scaling analyzes have given evidence for critical slowing down in a wide range of spin glass materials [67,68,85]. The critical exponents obtained are rather scattered. However, the critical exponents of Ising and Heisenberg systems are clearly different [86,87].

4. Nonequilibrium Dynamics

Aging phenomena in glassy materials were first discovered and thoroughly investigated in the field of structural glasses [88]. Magnetic aging in spin glasses was first observed by Lundgren et al. in 1983 [89]. It was found that the ZFC relaxation depends on the wait time t_w during which the system has been allowed to age at the measurement temperature, before applying the probing field and recording the magnetization as a function of time t. The measurement protocol is illustrated in Figure 3.9 and ZFC relaxation measurements on a Ag(11 atomic percent (at%) Mn) spin glass are shown in Figure 3.10. It can be seen that the relaxation rate $S(t) = h^{-1}dM/d\log t$ exhibits a maximum at $t \sim t_w$

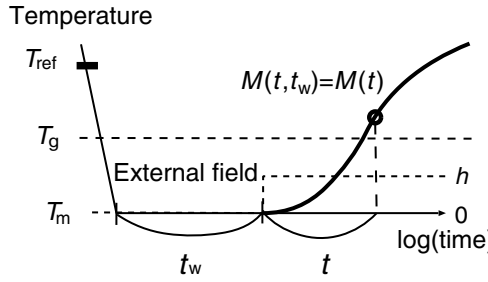

Figure 3.9. Schematic representation of a ZFC relaxation experiment. The sample is cooled to the measurement temperature T_m under zero field, after a wait time t_w, a small probing field h is applied and the ZFC magnetization is recorded as a function of time.

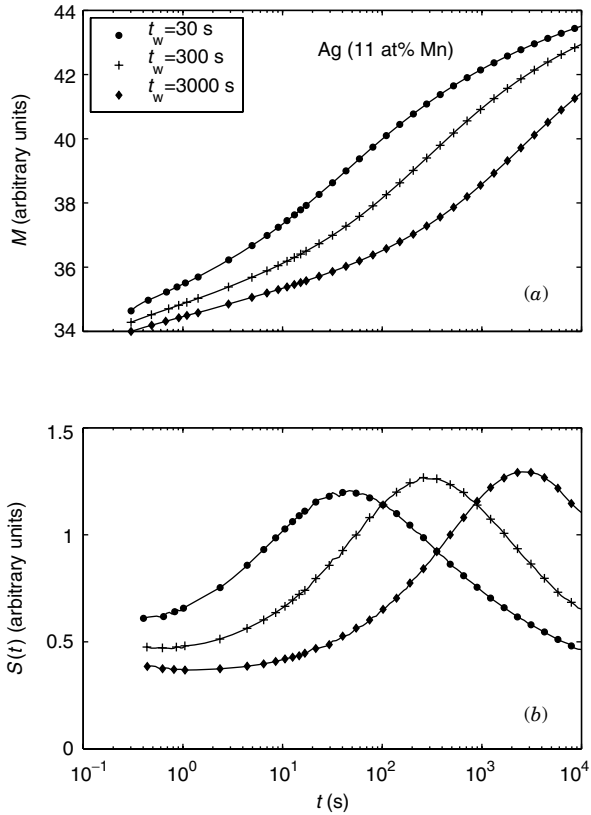

Figure 3.10. (*a*) ZFC susceptibility versus time on a logarithmic scale for the Ag(11 at% Mn) spin glass. $T_m = 30$ K and $h = 0.5$ G. (*b*) Relaxation rate $S(t) = h^{-1}\frac{\partial M}{\partial \log t}$ of the ZFC susceptibility curves shown in (*a*).

[89,90]. Many different types of materials were later shown to exhibit aging and nonequilibrium dynamics, including polymers [91], orientational glasses [92], gels [93], and ceramic superconductors [94].

Spin glass systems represent ideal model systems for studying nonequilibrium dynamics experimentally, numerically, and theoretically. The dynamic properties of spin glasses can accurately be investigated by *superconductive quantum interference device* (SQUID) magnetometry on specially designed magnetometers with low-background field (<1 mOe) and optimized temperature control ($\Delta T < 100\,\mu\text{K}$) [95]. Spin glasses exhibit nonequilibrium dynamics on all timescales from τ_m to infinity. Experimental studies are, however, limited to a finite time window $t/\tau_m \sim 10^8 - 10^{17}$, while numerical simulations are limited to much shorter timescales $t/\tau_m \sim 1 - 10^5$. Because of the larger spin–flip time of a magnetic moment compared to an atomic spin, interacting nanoparticle systems can be investigated in an experimental time window in between those of ordinary spin glasses and numerical simulations. In addition, the strength of the dipolar interaction can be tuned by the particle concentration of the nanoparticle system. Strongly interacting nanoparticle systems are therefore also interesting as model systems for glassy dynamics.

a. The Droplet Model. The ''droplet'' theory [96–100] is a real-space theory, based on renormalization group arguments for the Ising EA model with a continuous distribution of independent exchange. It makes predictions concerning the nonequilibrium dynamics within the spin glass phase. Important concepts are domain growth—growth of the coherence length for equilibrium spin-glass order, and temperature chaos. Both these concepts can also be applied to less anisotropic spin glasses [87,101–103] and generalized to other glassy systems [104].

At each temperature the equilibrium spin glass state is considered to consist of a ground state plus thermally activated droplet excitations of various sizes. A droplet is a low-energy cluster of spins with a volume L^d and a fractal surface area L^{d_s}. The typical droplet free-energy scales as

$$F_L^{\text{typ}} \sim \Upsilon(T)\left(\frac{L}{L_0}\right)^{\theta}, \qquad \Upsilon(T) \sim J\epsilon^{\theta\nu} \tag{3.63}$$

where θ is the stiffness exponent and $\Upsilon(T)$ is the stiffness. The droplet free energy is broadly distributed, and because of the presence of configurations that are almost degenerate with the ground state, the distribution of F_L will have weight down to zero energy:

$$\rho_L(F_L) \approx \frac{\tilde{\rho}(F_L/F_L^{\text{typ}})}{F_L^{\text{typ}}} \qquad \tilde{\rho}(0) > 0 \tag{3.64}$$

If $\theta < 0$, large droplets can be flipped at a low energy cost so that the large droplets will not be stable against small fluctuations and the system will be paramagnetic. Hence, a negative value of θ indicates that the system is below its lower critical dimension [96,105]. On the other hand, if $\theta > 0$, very few of the large-scale droplets will be thermally activated since $F_L^{\mathrm{typ}} > k_{\mathrm{B}}T$. Since $\rho_L(F_L)$ has non-zero weight near zero energy, a certain fraction of droplets will be thermally active and dominate most of the equilibrium physics.

The dynamics of droplets is considered to be a thermally activated process. The energy barrier for annihilation of a droplet will scale as

$$B_L^{\mathrm{typ}} \sim \Delta(T)\left(\frac{L}{L_0}\right)^{\psi}, \qquad \Delta(T) \sim J\epsilon^{\psi\nu} \tag{3.65}$$

where $\Delta(T)$ sets the free-energy scale of the barriers and ψ is an exponent satisfying $\theta < \psi < d-1$. The characteristic time τ_L that a thermally activated droplet will last for is given by an Arrhenius law

$$\ln\frac{\tau_L}{\tau_0(T)} \sim \frac{B_L}{k_{\mathrm{B}}T} \tag{3.66}$$

where $\tau_0(T)$ is the unit timescale for the activated process. For activated hopping processes the unit timescale is *not* simply given by the real microscopic timescale [106], which is $\tau_m \sim \hbar/J \sim 10^{-13}$ s in spin systems. A plausible choice for $\tau_0(T)$ is instead the critical correlation time τ_c [Eq. (3.62)] as proposed in Ref. 100. The Arrhenius law implies that droplets of length scale $L = L_T(t)$

$$L_T(t) \sim \left[\frac{k_{\mathrm{B}}T\ln(t/\tau_0(T))}{\Delta(T)}\right]^{1/\psi} \tag{3.67}$$

can be activated within a timescale t.

$L_T(t_{\mathrm{w}})$ will be the characteristic length scale of equilibrium spin glass order at a time t_{w} after a quench from a temperature above T_{g} to a temperature T in the spin glass phase. In a magnetization measurement the system is probed by applying a small magnetic field. The magnetization arises through the polarization of droplets. Since this polarization also is a thermally activated process, it will affect droplets of size $L(t)$, where t is the time elapsed after the application of the magnetic field in a ZFC relaxation experiment or $t = 1/\omega$ in an ac experiment at a given angular frequency ω. The peak observed in the relaxation rate of the ZFC magnetization at $t \approx t_{\mathrm{w}}$ (see Fig. 3.10) has, within the droplet model, been interpreted as a crossover from quasiequilibrium dynamics at $L(t) < L(t_{\mathrm{w}})$ to nonequilibrium dynamics at $L(t) > L(t_{\mathrm{w}})$ (see Ref. 107 for a detailed discussion).

According to the droplet theory, typical spin configurations of a pair of equilibrium states at two different temperatures, say, T_1 and T_2, are essentially

the same on short length scales much below the so-called overlap length $L_{\Delta T}$, but completely different on large length scales much beyond $L_{\Delta T}$. This temperature chaos is due to a subtle competition between energy and entropy in the spin glass phase. In the limit of small temperature differences $|\Delta T/J| \ll 1$, the overlap length between the two temperatures T_1 and $T_2 = T_1 + \Delta T$ is supposed to scale as [99,100,108]

$$L_{\Delta T} \sim L_0 \left| \frac{\Delta T}{J} \right|^{-\zeta}, \qquad \zeta = \frac{2}{d_s - 2\theta} \tag{3.68}$$

where ζ is the chaos exponent.

Experimentally, temperature chaos can be evidenced by aging the system at a temperature T_i and changing the temperature to a $T_i + \Delta T$. If the temperature shift is large enough, the equilibrium domain configurations at T_i and $T_i + \Delta T$ are completely different on the length scales relevant for the experiment. Hence, if the magnetic response at $T_i + \Delta T$ is the same as after a direct quench, the system appears *rejuvenated*.

b. Experiments: Aging, Memory, and Rejuvenation. After discovery of the aging effect in the spin glass phase, experimental protocols with temperature steps and cyclings were proposed [109]. These experiments showed not only rejuvenation effects but also that spin glass order, characteristic of different temperatures, can coexist on different length scales; hence the spin glass keeps a *memory* of its thermal history.

A simple experimental protocol [85] was employed to illustrate memory and rejuvenation effects [110–113]; the sample is cooled from a high temperature with one (or more) halts of the cooling at one (or more) temperatures in the spin

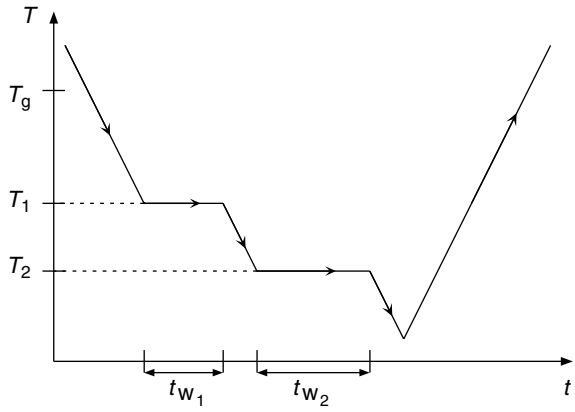

Figure 3.11. The experimental procedure of a "memory" experiment with two halts on cooling.

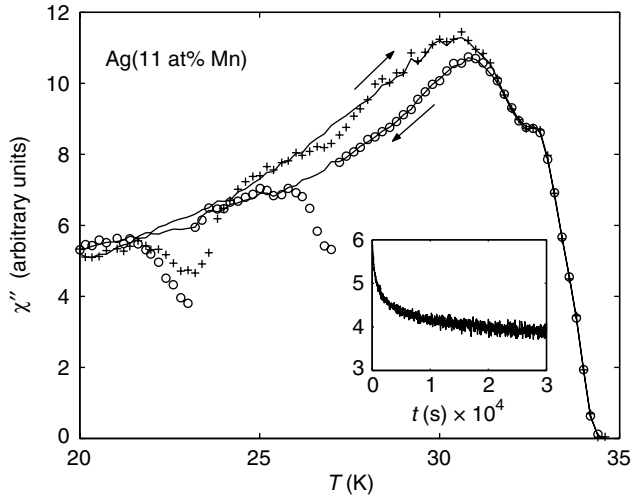

Figure 3.12. $\chi''(\omega)$ versus temperature for the Ag(11 at% Mn) sample measured during cooling (circles) and during the subsequent reheating (pluses). Two intermittent halts were made during the cooling: one at 27 K for 10,000 s and another at 23 K for 30,000 s. The susceptibility measured on constant cooling and on constant heating is shown as reference (solid lines). The arrows indicate the cooling and heating curves, respectively. The inset shows $\chi''(\omega)$ versus time during the halt at $T = 23$ K; $\omega/2\pi = 510$ mHz. The cooling and heating rate is ~ 0.2 K/min.

glass phase. The experimental procedure of a double-stop experiment is illustrated in Figure 3.11. The ac susceptibility is subsequently recorded on heating. An ''ac memory'' experiment is shown in Figure 3.12 for a Ag(11 at% Mn) spin glass and in Figure 3.13 for an $Fe_{0.50}Mn_{0.50}TiO_3$ spin glass. The ac susceptibility is measured on cooling with two intermittent stops. During a stop the ac susceptibility relaxes downward as shown in the inset of Figure 3.12. The level of the ac susceptibility is hence related to the age of the system (a lower susceptibility indicates an older system). As the cooling is resumed, the ac susceptibility merges (quite rapidly) with the reference curve, and the system is *rejuvenated*. On subsequent reheating the ac susceptibility shows a dip around each aging temperature—the system has kept a *memory* of each equilibration at constant temperature. The memory experiment is an efficient tool to study spin-glass-like properties in various materials [114–118].

For the Ag(11 at% Mn) sample, the ac susceptibility curve measured on cooling lies below the curve subsequently measured on heating, except close to the lowest temperature (see Fig. 3.12). If the aging at different temperatures is accumulative, the heating curve would appear older than the cooling curve and therefore lower in amplitude. For the $Fe_{0.50}Mn_{0.50}TiO_3$ sample this is indeed the case (see Fig. 3.13). The nonaccumulative behavior observed in the

cooling–heating curves of the ac susceptibility of the Ag(11 at% Mn) sample can qualitatively be explained by rejuvenation during cooling and heating due to strong temperature chaos. For the $Fe_{0.50}Mn_{0.50}TiO_3$ sample, the double-memory experiment shown in Figure 3.13 indicates that temperature chaos does exist, but that it is much weaker than for Ag(11 at% Mn).

The memory experiments presented above yield, in a simple and illustrative way, information about aging, memory, and rejuvenation effects for the two spin glass systems. However, cooling and heating rate effects as well as memory and rejuvenation phenomena are all mixed in a nontrivial way. Specially designed thermal protocols have been used to quantitatively investigate aging and rejuvenation proprieties of the $Fe_{0.50}Mn_{0.50}TiO_3$ and Ag(11 at% Mn) sample [87,102,103,119]. It was shown that the temperature dependence of $L_T(t)$ is stronger for the Ag(11 at% Mn) sample than for the $Fe_{0.50}Mn_{0.50}TiO_3$ sample. Also, the rejuvenation effects are much stronger for the Ag(11 at% Mn) sample.

B. FeC Nanoparticle Systems

We now focus on a ferrofluid of single-domain particles of the amorphous alloy $Fe_{1-x}C_x$ ($x \approx 0.2$–0.3). The particles were coated with a surfactant (oleic acid) and dispersed in a carrier liquid (xylene). The particle shape is nearly spherical (see Fig 3.14) and the average particle diameter $d = 5.3 \pm 0.3$ nm. The

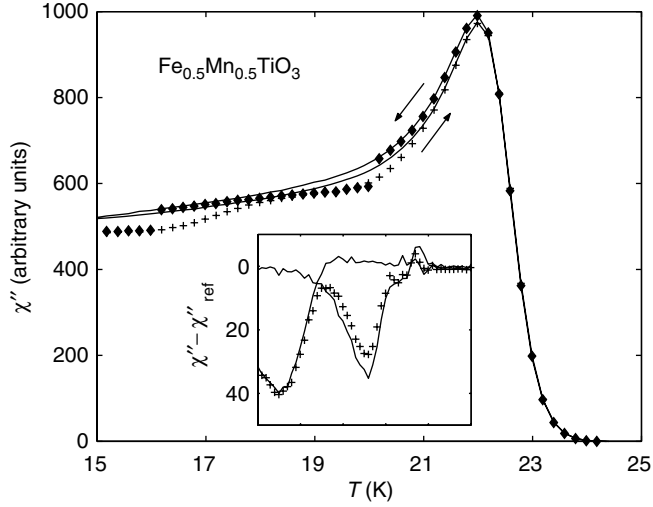

Figure 3.13. (*a*) χ'' versus temperature measured on cooling (diamonds), with two intermittent stops at 20 K for 10,000 s and at 16 K for 30,000 s, and on the subsequent reheating (pluses), for the $Fe_{0.50}Mn_{0.50}TiO_3$ sample. The reference cooling and heating curves are drawn with solid lines. Inset: $\chi'' - \chi''_{\text{ref}}$ versus temperature derived from the heating curves for single and double stops. $\omega/2\pi = 510$ mHz.

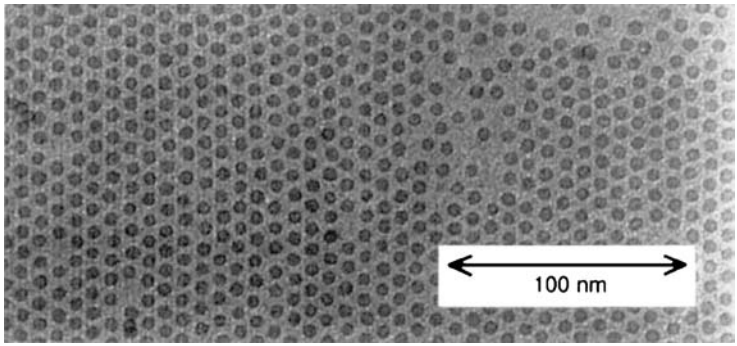

Figure 3.14. TEM picture of typical $Fe_{1-x}C_x$ nanoparticles.

saturation magnetization was estimated to $M_s = 1 \times 10^6$ A/m, the microscopic flip time to $\tau_0 = 1 \times 10^{-12}$ s, and the uniaxial anisotropy constant $K = 0.9 \times 10^5$ J/m^3 [65]. The interparticle interaction can be varied by changing the particle concentration of the ferrofluid. The strength of the interaction for a given concentration is determined by the anisotropy constant and the saturation magnetization according to Eq. (3.17) with the parameters given above $h_d \approx 0.56c$, where c is the volume concentration of nanoparticles. The samples studied here originate from the same batch as those in Refs. 65, 114, 120, and 121. Earlier studies use samples from different batches having slightly different physical properties [63,64,122–124].

Figure 3.15 shows the real and imaginary part of ac susceptibility versus temperature for three different particle concentrations of the FeC sample: $c = 0.06$, 5, and 17 vol%. With increasing concentration, the peak in the ac susceptibility is shifted to higher temperatures and the curve is simultaneously suppressed. This behavior is different from that of the weakly interacting nanoparticle systems shown in Figures 3.5 and 3.7. In this section we will argue that the dynamics of the 5 and 17 vol% samples is spin-glass-like, and hence fundamentally different from the superparamagnetic behavior of noninteracting and weakly interacting nanoparticle systems.

1. Nonequilibrium Dynamics

Magnetic aging can be evidenced by measuring the ZFC relaxation at constant temperature after a fast cooling through the transition temperature using different wait times before applying the magnetic field. The experimental procedure was depicted in Figure 3.9 together with a typical measurement on a Ag(11 at% Mn) spin glass in Figure 3.10. In a noninteracting nanoparticle system, the low-field ZFC relaxation is governed only by the distribution of relaxation times of the particles and their temperature dependence. It does not

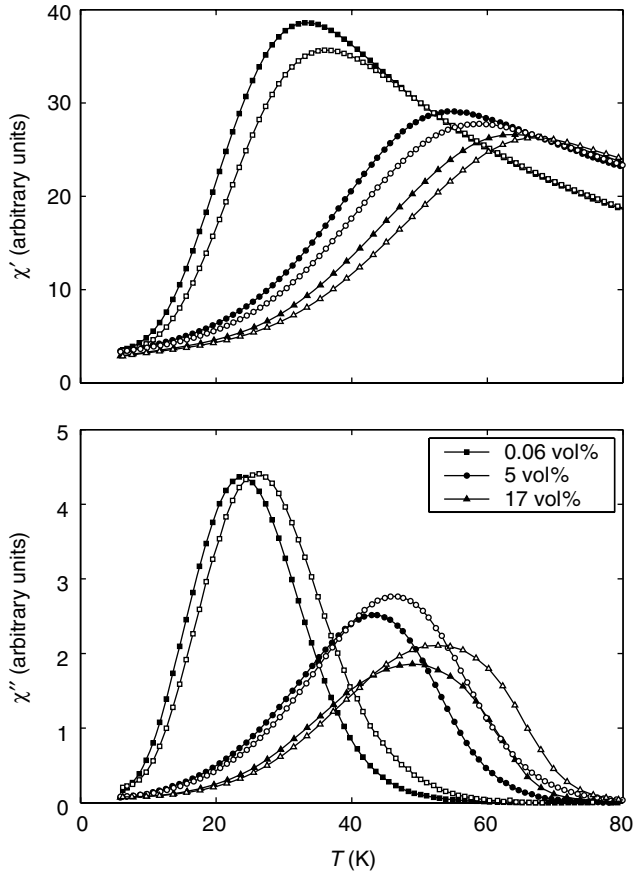

Figure 3.15. Ac susceptibility versus temperature at frequencies $\omega/2\pi = 125$ Hz (filled symbols) and $\omega/2\pi = 1000$ Hz (open symbols).

depend on the wait time at T_m before applying the probing field,[3] as was shown experimentally in Ref. 60. The relaxation rate $S(t)$ of the ZFC magnetization measured at different temperatures between 20 and 40 K are shown in Figure 3.16 for the 5 vol% sample. The measurements are repeated for two different wait times 300 and 3000 s. A clear difference between the $S(t, t_w)$

[3] The only wait time dependence that could exist is the adjustment of the position of the magnetic moment to the Boltzmann distribution at T_m. This adjustment does however only involve intrawell rotation and is therefore a much faster process than the slow cooling to T_m and the time needed to stabilize the temperature.

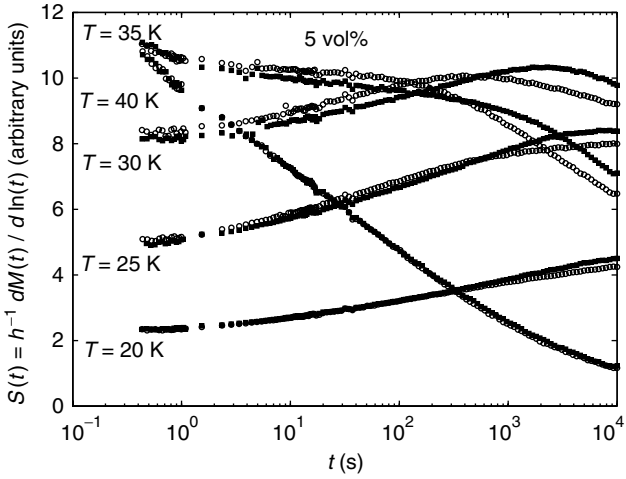

Figure 3.16. $S(t)$ versus time on a logarithmic scale for the 5 vol% sample obtained from ZFC relaxation measurements with $t_w = 300$ s (open symbols) and 3000 s (filled symbols); $h = 0.05$ Oe.

curves for $t_w = 300$ and 3000 s can be seen for all temperatures <40 K, presenting evidence for glassy nonequilibrium dynamics at those temperatures. The shapes of the $S(T)$ curves are, however, rather different from those of canonical spin glasses (see Fig. 3.10). A peak in $S(t)$ at $t \sim t_w$ as in ordinary spin glasses is observed only at $T = 30$ K. The difference arises largely from the strong temperature dependence of the individual particle relaxation time compared to the almost temperature independent relaxation time of individual spins.

The 5 vol% sample has also been investigated with ac susceptibility measurements. $\chi'(T)$ is shown in Figure 3.17 for a low frequency. The insets show how the ac susceptibility relaxes with time if the cooling is halted at $T_s = 33$ or 23 K. The relative relaxation of the ac susceptibility is smaller than for ordinary spin glasses. χ' relaxes more in absolute units than χ'' and χ' has therefore been chosen to illustrate the nonequilibrium dynamics. For a waiting time of 30,000 s at low temperature $\Delta\chi''/\chi''_{\text{ref}} \approx 3\%$ compared to $\approx 8\%$ for the $Fe_{0.50}Mn_{0.50}TiO_3$ sample (see Fig. 3.13) and $\approx 30\%$ for the Ag(11 at% Mn) sample (see Fig. 3.12).

Memory experiments with one and two temporary stops during cooling are shown in Figure 3.18. The nonequilibrium effects are more clearly revealed by subtracting the reference curves obtained on constant cooling and reheating. The features are qualitatively similar to those of ordinary spin glasses (see Section III.A.4); during a halt in the cooling, the system ages—the ac susceptibility decreases. When the cooling is resumed, the ac susceptibility slowly regains the reference level. On the subsequent heating, the

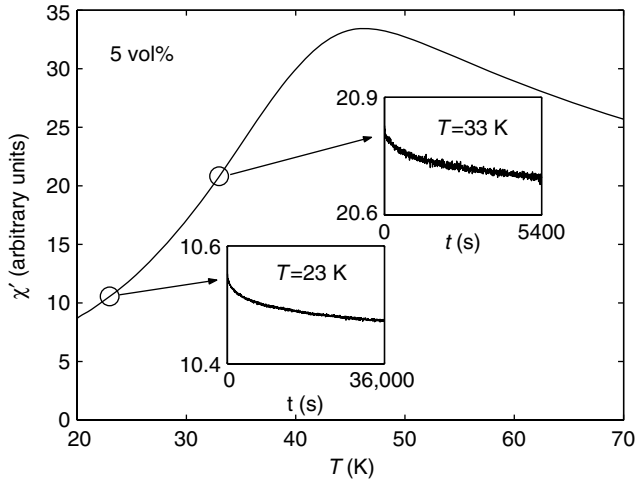

Figure 3.17. χ' versus temperature for the 5 vol% sample. The insets show how χ' relaxes with time if the cooling is halted at 33 or 23 K. $f = 510$ mHz.

ac susceptibility exhibits a "dip" centered around T_s in a single-stop experiment. In a double-stop experiment it exhibits two dips if the two halts are well separated in temperature [Fig. 3.18(*a*)], but if the two halts are close in temperature [Fig. 3.18(*b*)], only one large dip is observed on heating as a result of the two aging processes. In both cases, the difference curve $\chi' - \chi'_{\text{ref}}$ of the double-stop experiment equals the sum of $\chi' - \chi'_{\text{ref}}$ of the two single-stop experiments. As for the $Fe_{0.50}Mn_{0.50}TiO_3$ sample, the ac susceptibility measured on heating lies below the one measured on cooling. In conclusion, the rejuvenation effect in particle systems is weaker than in ordinary spin glasses and as a consequence, the memory of both one and two aging processes is better preserved on reheating than in the spin glass case.

This nanoparticle sample exhibits strong anisotropy, due to the uniaxial anisotropy of the individual particles and the anisotropic dipolar interaction. The relative timescales (t/τ_m) of the experiments on nanoparticle systems are shorter than for conventional spin glasses, due to the larger microscopic flip time. The nonequilibrium phenomena observed here are indeed rather similar to those observed in numerical simulations on the Ising EA model [125,126], which are made on much shorter time (length) scales than experiments on ordinary spin glasses [127].

2. *A Spin Glass Phase Transition?*

Aging and nonequilibrium dynamics indicate but give by no means evidence for a thermodynamic phase transition at finite temperature to a low-temperature

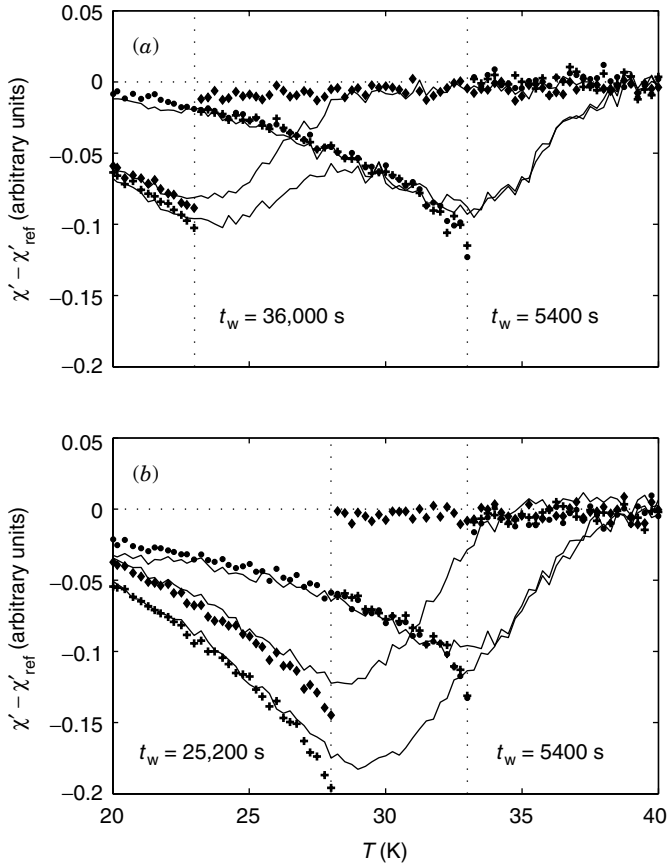

Figure 3.18. $\chi'(T) - \chi'_{\text{ref}}(T)$ versus T measured on cooling (symbols) and heating (lines) for the 5 vol% sample. Circles—the cooling was halted at 33 K for 5400 s; diamonds—the cooling was halted at (*a*) 23 K for 36,000 s (*b*) 28 K for 25, 200 s; pluses—the cooling was halted at $T_1 = 33$ K for $t_{w_1} = 5400$ s and at (*a*) $T_2 = 23$ K for $t_{w_2} = 36,000$ s (*b*) $T_2 = 28$ K for $t_{w_2} = 25{,}200$ s. χ'_{ref} is shown in Fig. 3.17. $\omega/2\pi = 510$ mHz.

spin-glass-like phase. For example, two-dimensional (2D) spin glasses ($T_g = 0$) have been shown to exhibit similar nonequilibrium dynamics as 3D spin glasses [128,129]. A detailed analysis of the magnetic response close to the assumed transition temperature is needed in order to evidence a spin glass phase transition (see, e.g., Ref. 85 and references cited therein).

The existence of a second-order phase transition can be evidenced from critical slowing down [Eq. (3.62)] approaching the phase transition from the

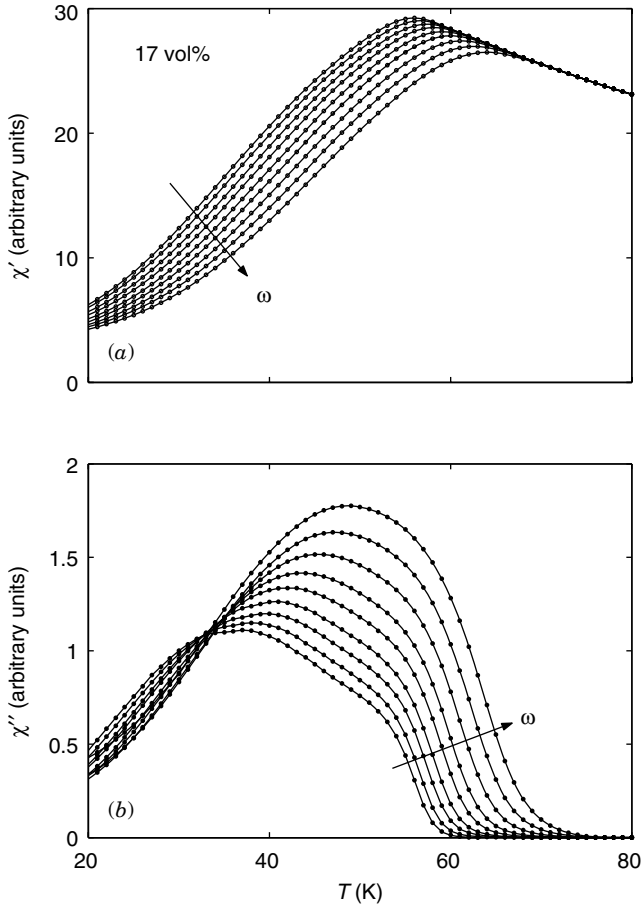

Figure 3.19. Alternating-current susceptibility versus temperature for the 17 vol% sample. $\omega/2\pi = 0.017, 0.051, 0.17, 0.51, 1.7, 5.1, 17, 55, 170$ Hz.

paramagnetic phase. Defining a criterion to determine the freezing temperature T_f associated with a certain relaxation time, it is possible to derive the ''transition'' line (τ_c) between thermodynamic equilibrium and critical dynamics as in Figure 3.8. In ac susceptibility measurements the relaxation time $\tau = 1/\omega$, and a possible criterion for the freezing is where $\chi''(T, \omega)$ attains a certain fraction, say, 15%, of its maximum value.

Ac susceptibility data for a large set of frequencies are shown in Figure 3.19 for the 17 vol% sample and in Figure 3.20 for the 5 vol% sample. These curves

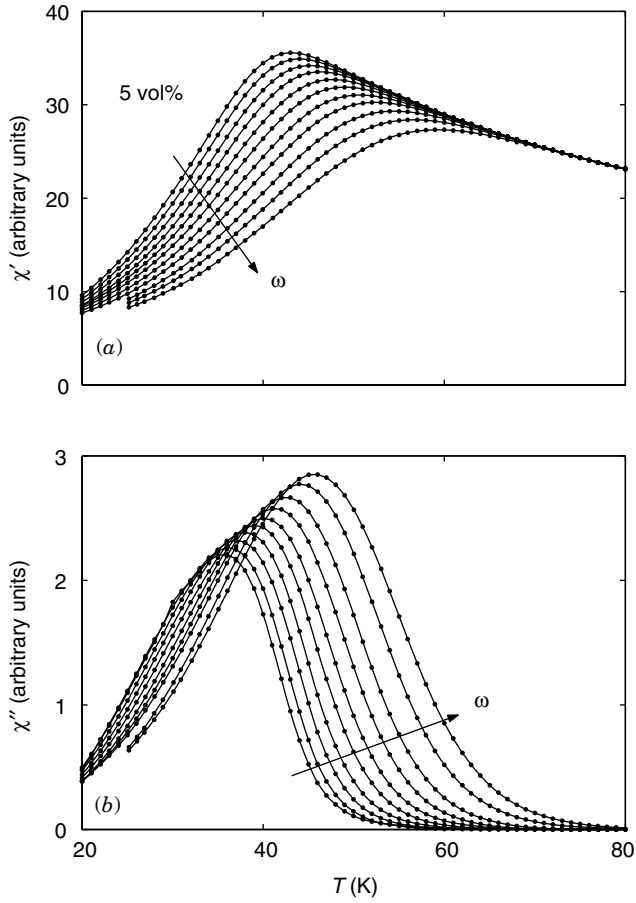

Figure 3.20. Alternating-current susceptibility versus temperature for the 5 vol% sample. $\omega/2\pi = 0.017$, 0.051, 0.17, 0.51, 1.7, 5.1, 17, 55, 170, 510, 1700 Hz.

were used to extract the $T_f(1/\omega)$ plotted in Figure 3.21. The corresponding blocking temperatures for the 0.06 vol% sample are plotted in the same figure as a reference for the behavior of a noninteracting system of the same particle ensemble. A dynamic scaling analysis according to critical slowing down [Eq. (3.62)] with the microscopic timescale given by an Arrhenius law [Eq. (3.6)], $\tau_c(T_f) = \tau_0 \exp(A/k_B T_f)(T_f/T_g - 1)^{z\nu}$, was performed for the two concentrated samples. Two assumptions concerning the anisotropy energy was used: (1) $A = 0$, which correspond to a temperature-independent

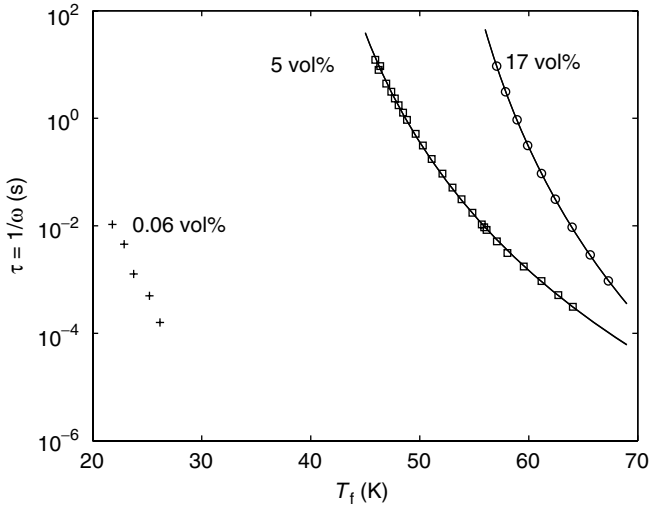

Figure 3.21. Relaxation time $\tau = \omega^{-1}$ versus T_f. For the 5 vol% and 17 vol% samples the lines are fits to the critical slowing down relation [Eq. (3.62)] with the parameters given in Table III.1. The assumptions $E = 0$ and $E = 500$ yield exactly the same line. For the 0.06 vol% sample T_f is the superparamagnetic blocking temperature defined as the maximum of χ''.

microscopic flip time; and (2) $A/k_B = 500$ K, which is approximately the anisotropy barrier energy for a particle of average size. The values obtained for $z\nu$, T_g, and τ_0 in each case are given in Table III.1. The quality of the fits of the experimental data to Eq. (3.62) are equally good for assumptions (1) and (2). In fact, in Figure 3.21, the line corresponds to both assumptions; in the experimental temperature–frequency interval the two assumptions cannot be distinguished. In addition, the values of T_g and the critical exponents depend quite strongly on the criterion used when determining T_f. The error bars on the exponents obtained are therefore large.

TABLE III.1
Parameters Obtained from Dynamic Scaling Analysis

Sample (vol%)	E/k_B (K)	$z\nu$	T_g (K)	τ_0 (s)
17	0	11.4	48.8	2×10^{-8}
17	500	8.8	49.9	5×10^{-11}
5	0	10.3	36.0	2×10^{-5}
5	500	6.4	37.9	1×10^{-8}

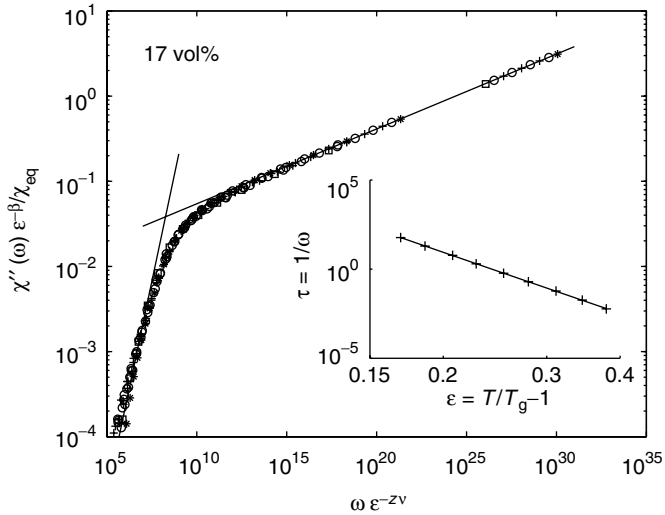

Figure 3.22. Scaling of $\epsilon^{-\beta}\chi''(T,\omega)/\chi_{\rm eq}$ data for $T > T_{\rm g}$ for the 17 vol% sample. The assumption $A = 0$ is used and $\beta = 1.0$. The other parameters are those of Table I. The two lines are the asymptotic behavior $G(x) \propto x$ for small values of x and $G(x) \propto x^{\beta/z\nu}$ for large x. Inset: critical slowing down analysis on a log–log scale.

In a full dynamics scaling analysis, the imaginary component of the dynamic susceptibility of a spin glass is scaled according to [130]

$$\frac{\chi''(T,\omega)}{\chi_{\rm eq}(T)} = \epsilon^{\beta} G(\omega\tau_c), \qquad T > T_{\rm g} \tag{3.69}$$

where $\omega = 1/t$ and $G(x)$ is a scaling function. The asymptotic behavior of $G(x) \propto x^y$ with $y = 1$ and $\beta/z\nu$ for small and large values of x, respectively. It is shown in Figure 3.22 that the χ'' data for the 17 vol% sample could be collapsed into a master curve according to this relation. In this figure the assumption $A = 0$ is used, but an equally good collapse could be obtained by assuming $A = 500$ K (and changing ϵ^{β} to $\tau_m^{\beta/z\nu}$). The critical exponent $\beta = 1.0 \pm 0.3$. For the 5 vol% sample, the dynamic susceptibility could not be scaled according to Eq. (3.69). In addition, if data for larger values of τ (obtained from ZFC relaxation data) are included in the critical slowing-down analysis, deviations from the power law is observed [65]. To conclude, the dynamic scaling analysis indicates that the 5 vol% sample does not exhibit a thermodynamic phase transition although it clearly exhibits spin glass dynamics. Because of the temperature dependence of τ_m, a static scaling analysis as performed in Ref. 64 is a crucial additional tool to disclose a possible spin glass phase transition in interacting nanoparticle systems.

The time dependence of the dynamic correlation function $q(t)$ was investigated numerically on the Ising EA model by Ogielski [131]. An empirical formula for the decay of $q(t)$ was proposed as a combination of a power law at short times and a stretched exponential at long times

$$q(t) = ct^{-x}e^{-wt^{y}} \tag{3.70}$$

where c, x, w, and y are temperature-dependent parameters. $q(t)$ follows a pure power-law behavior below T_g. It was shown in Ref. 132 that $[\chi_{eq} - \chi'(t)]/\chi_{eq}$ measured on the $Fe_{0.50}Mn_{0.50}TiO_3$ spin glass sample also behaves according to Eq. (3.70). In Figure 3.23 $[\chi_{eq} - \chi'(t)]/\chi_{eq}$ is shown for the 17 vol% sample at temperatures around T_g. The temperature dependence of the exponent x is shown in the inset. The behavior of the 17 vol% sample shown here is similar to that observed in the numerical simulation on the EA Ising model [131] and to the experimental result obtained for the $Fe_{0.50}Mn_{0.50}TiO_3$ spin glass [132]. However, the stretched–exponential behavior is less pronounced than for the $Fe_{0.50}Mn_{0.50}TiO_3$ spin glass. One reason for this is that the investigated timescales t/τ_m are shorter for the nanoparticle sample because of the larger value of τ_m. In the numerical simulation, performed on even shorter timescales, it was possible to observe the stretched–exponential behavior by investigating $q(t)$ far from T_g. The resolution of our experimental data does not allow such an investigation.

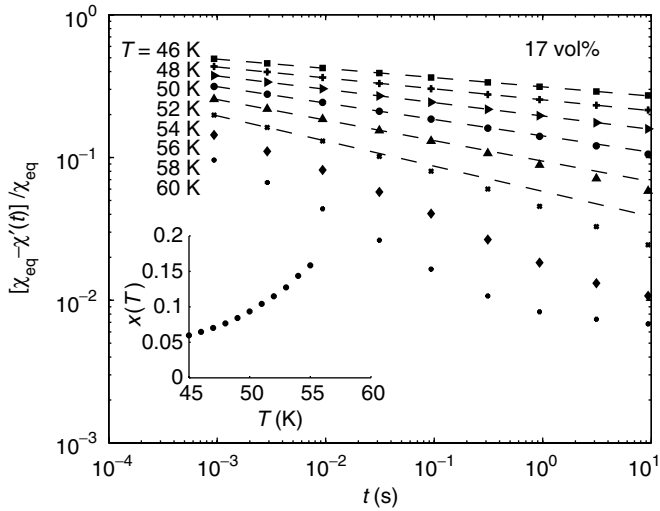

Figure 3.23. $[\chi_{eq} - \chi'(t)]/\chi_{eq}$ versus time for the 17 vol% sample. Inset: Temperature dependence of the exponent x in Eq. (3.70).

3. *Dynamics in a Field*

All measurements presented so far are performed with a probing field in the linear response regime and without an external bias field. We will now investigate the effect of a nonzero bias field on the nonequilibrium dynamics (still probing the system with a weak magnetic field in the linear response regime). The question as to whether a spin glass-like phase exists under a finite field in a strongly interacting nanoparticle system will not be addressed. Figure 3.24 shows the ac susceptibility as a function of temperature with bias dc fields in the range 0–250 G for 1 and a 5 vol% samples. The magnetic field affects the superparamagnetic behavior of individual spins (as discussed in Section II) as well as the nonequilibrium dynamics. It can be seen in the figure that the dynamic response of the two systems in low fields is rather different, while with increasing bias field the dynamic response of the two systems

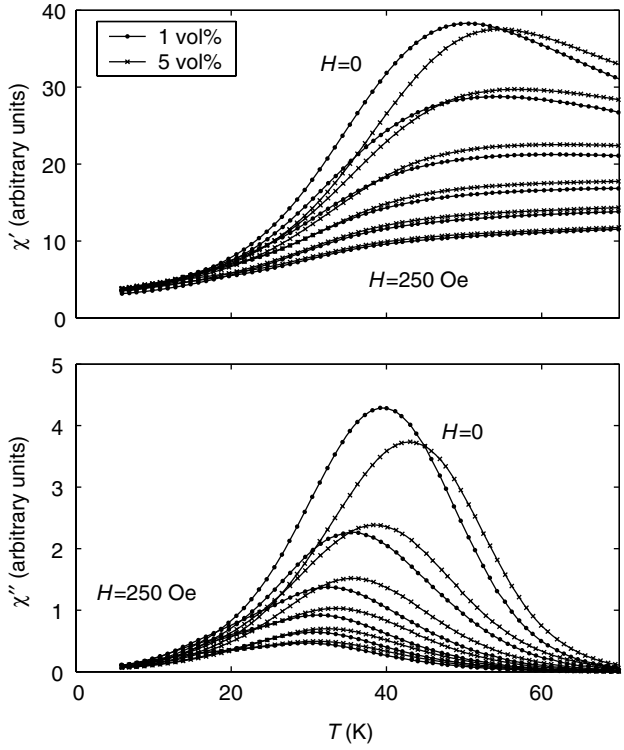

Figure 3.24. Alternating-current susceptibility versus temperature for different superimposed dc fields; $H = 0$, 50, 100, 150, 200, 250 Oe. $\omega/2\pi = 125$ Hz.

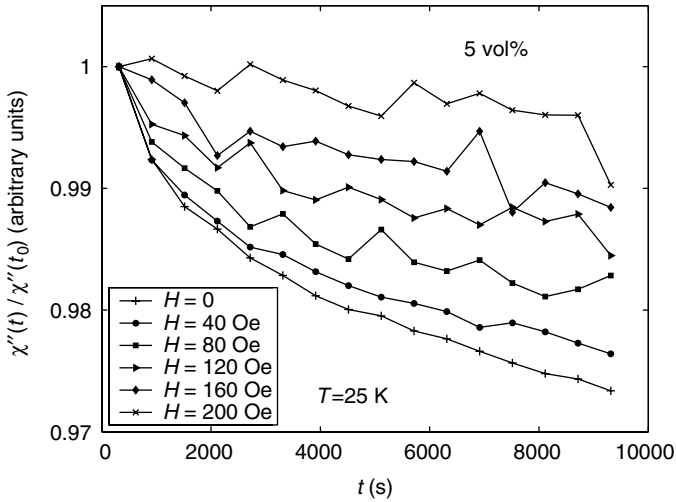

Figure 3.25. Alternating-current susceptibility versus time for different superimposed dc fields; $H = 0$, 40, 80, 120, 160, 200 Oe. $\omega/2\pi = 510$ Hz.

becomes more and more similar. This indicates that the effects of dipolar interaction are suppressed by a sufficiently strong magnetic field.

The effect of an external field on the glassy dynamics can be studied by recording the ac susceptibility as a function of time for different bias fields. χ'' normalized by its value just after the quench, $\chi''(t_0)$, is shown in Figure 3.25 for the 5 vol% sample. It can be seen in this figure that the ac relaxation diminishes with increasing bias field. For the highest field, almost no relaxation exists. The field has in addition the effect that it makes the measurement more noisy. The effects of the field is also temperature-dependent and the ac susceptibility is more affected by a field at high temperatures. A qualitatively similar result was found for the $(Fe_{0.15}Ni_{0.85})_{75}P_{16}B_6Al_3$ spin glass [121].

C. Discussion

We have seen that the magnetic properties of a strongly interacting nanoparticle system are of spin-glass-like nature, and hence very different from the superparamagnetic behavior of noninteracting systems and weakly interacting spins discussed in Section II. Any model for interparticle interaction based on a modified superparamagnetic behavior [42–44,54] will therefore fail to describe the dynamics of a strongly interacting nanoparticle system.

The value of the dipolar coupling parameter h_d [Eq. (3.17)] determines the strength of the dipolar interaction, but the width of the distribution of energy barriers is equally important for the dynamic properties. For example, Jonsson

et al. studied [133] a γ-Fe_2O_3 nanoparticle sample that had a value of ξ_d comparable to the 17 vol% sample investigated here, but with a much broader energy barrier distribution. That sample showed glassy dynamics, but it did not exhibit a spin glass phase transition.

It would be interesting to examine the nonequilibrium dynamics of a strongly interacting system for different concentrations (different dipolar coupling strengths). Such a study could give more detailed insight into how the aging and rejuvenation phenomena depend on the interaction strength and the experimental timescale.

IV. SUMMARY AND CONCLUSION

The effects of interparticle dipolar interaction in magnetic nanoparticle systems have been investigated. For weak dipolar coupling strengths equilibrium quantities can be calculated using thermodynamic perturbation theory, treating the anisotropy exactly and the dipolar interaction perturbatively. Such an approach is always valid at sufficiently high temperatures, but it is valid around the blocking temperature only in the case of weak dipolar coupling. In a simple model, the relaxation rate is modified by the dipolar interaction in the same way as by a field, where the field components of the dipolar field can be calculated using thermodynamic perturbation theory [44]. The dipolar field also plays an important role for quantum tunneling of the magnetization of crystals of magnetic molecules [3].

Superparamagnetic blocking depends strongly on the damping parameter in the case of weak–medium damping due to the transverse component of the dipolar field [38]. Any energy-barrier-based model overlooks that damping dependence and can therefore only be valid in the overdamped case. The effect of a magnetic field is to decrease the relaxation time. Hence, in the case of weak interparticle interaction, a decrease of the blocking temperature is predicted and also observed in high-frequency measurements, such as Mössbauer spectroscopy [43] and Langevin dynamics simulations [13]. However, for stronger interparticle interaction, the dipolar interaction does not modify but creates energy barriers, and hence the blocking temperature increases with increasing interaction strength. A blocking temperature that increases with the interaction strength is commonly observed in magnetization measurements.

The existence of glassy dynamics in dense frozen ferrofluids, specifically, strongly interacting nanoparticle systems with randomness in the particle positions and anisotropy axes, has been evidenced by experimental techniques developed in the study of conventional spin glasses. Hence, the dynamics of such systems is radically different from simple superparamagnetic blocking. The nonequilibrium dynamics observed in strongly interacting nanoparticle

systems exhibits qualitatively similar aging, memory, and rejuvenation effects as ordinary spin glasses, but the aging and rejuvenation effects are weaker. The differences observed can be explained at least qualitatively by the longer microscopic relaxation time of a magnetic moment compared to an atomic spin. Only strongly interacting nanoparticle systems with a narrow anisotropy barrier distribution have been shown to exhibit a phase transition to a low-temperature spin glass phase.

Acknowledgments

The author is indebted to J. L. García-Palacios, M. F. Hansen, and P. Nordblad for their contribution to the work presented in this chapter. The author also acknowledges H. Aruga Katori, S. Felton, A. Ito, T. Jonsson, R. Mathieu, P. Svedlindh, and H. Yoshino for collaboration and I. A. Campbell, H. Mamiya, T. Sato, H. Takayama, and E. Vincent for helpful discussions.

This work has partially been financed by the Swedish Research Council (VR).

APPENDIX

A. Thermodynamic Perturbation Theory

1. *Expansion of the Boltzmann Distribution in the Dipolar Coupling Parameter*

Thermodynamic perturbation theory is used to expand the Boltzmann distribution in the dipolar interaction, keeping it exact in the magnetic anisotropy (see Section II.B.1). A convenient way of performing the expansion in powers of ξ_d is to introduce the Mayer functions f_{ij} defined by $1 + f_{ij} = \exp(\xi_d \omega_{ij})$, which permits us to write the exponential in the Boltzmann factor as

$$\exp(-\beta\mathscr{H}) = \exp(-\beta E_a) \prod_{i>j} (1 + f_{ij}) \tag{A.1}$$

Expanding the product to second order in the f_{ij} gives

$$\prod_{i>j} (1 + f_{ij}) = 1 + \xi_d G_1 + \tfrac{1}{2}\xi_d^2 G_2 + O(\xi_d^3) \tag{A.2}$$

where [134]

$$G_1 = \sum_{i>j} \omega_{ij} \tag{A.3}$$

$$G_2 = \sum_{i>j} \omega_{ij}^2 + \sum_{i>j} \sum_{k>l} \omega_{ij}\omega_{kl} q_{ik:jl} q_{il:jk} \tag{A.4}$$

and the symbol $q_{ik:jl}$ annihilates terms containing duplicate pairs: $q_{ik:jl} = \frac{1}{2}(2 - \delta_{ik} - \delta_{jl})(1 + \delta_{ik})(1 + \delta_{jl})$.

To obtain the average of any quantity B, we introduce the expansion (A.2) in both the numerator and denominator of $\langle B\rangle = \int d\Gamma B \exp(-\beta\mathscr{H})/\int d\Gamma \exp(-\beta\mathscr{H})$, and work out the expansion of the quotient, getting

$$\langle B\rangle \simeq \langle B\rangle_{\rm a} + \xi_{\rm d}\langle BG_1\rangle_{\rm a} + \tfrac{1}{2}\xi_{\rm d}^2[\langle BG_2\rangle_{\rm a} - \langle B\rangle_{\rm a}\langle G_2\rangle_{\rm a}] \tag{A.5}$$

Here we have utilized the fact that the single-spin anisotropy has inversion symmetry $[W_{\rm a}(-\vec{s}_i) = W_{\rm a}(\vec{s}_i)]$ in the absence of a bias field and that $\langle G_1\rangle_{\rm a} = \langle\sum_{i>j}\omega_{ij}\rangle_{\rm a} = 0$ since a dipole does not interact with itself.

We have now obtained expressions for F_1 and F_2 in Eq. (3.19):

$$F_1 = G_1, \qquad F_2 = G_2 - \langle G_2\rangle_{\rm a} \tag{A.6}$$

To complete the calculation, we need to obtain averages of low-grade powers of $\vec{s}$ weighted by the noninteracting distribution (moments), which is the only place where one needs to specify the form of $E_{\rm a}$. In the next section we will do that for systems with axially symmetric anisotropy.

2. *Averages Weighted with an Axially Symmetric Boltzmann Factor*

Assuming an axially symmetric potential, the anisotropy energy of $E_{\rm a}(\vec{s}\cdot\vec{n})$ will be an *even* function of the longitudinal component of the magnetic moment $\vec{s}\cdot\vec{n}$. The averages we need to calculate are all products of the form $I_m = \langle\prod_{n=1}^m(\vec{c}_n\cdot\vec{s})\rangle_{\rm a}$, where the $\vec{c}_n$ are arbitrary constant vectors. Introducing the polar and azimuthal angles of the spin (ϑ,φ), we can write I_m as

$$I_m = \frac{\int_0^{2\pi}d\varphi\int_0^{\pi}d\vartheta\sin\vartheta\prod_{n=1}^m(\vec{c}_n\cdot\vec{s})\exp[-\beta E_{\rm a}(\vec{s}\cdot\vec{n})]}{\int_0^{2\pi}d\varphi\int_0^{\pi}d\vartheta\sin\vartheta\exp[-\beta E_{\rm a}(\vec{s}\cdot\vec{n})]}$$

For odd m, I_m is an integral of an odd function over a symmetric interval and hence $I_m = 0$. To calculate the susceptibility and specific heat to second order in $\xi_{\rm d}$, we require I_2 and I_4, which will be calculated using symmetry arguments similar to those employed to derive the $\sigma = 0$ unweighted averages (see, e.g., arguments in Ref. 135).

Note that I_2 is a scalar bilinear in $\vec{c}_1$ and $\vec{c}_2$. The most general scalar with this property that can be constructed with the vectors of the problem ($\vec{c}_1$, $\vec{c}_2$, and $\vec{n}$) has the form

$$I_2 = A\,\vec{c}_1\cdot\vec{c}_2 + B\,(\vec{c}_1\cdot\vec{n})(\vec{c}_2\cdot\vec{n})$$

To find the coefficients A and B, one chooses particular values for the $\vec{c}_n$:

1. If $\vec{c}_1 \parallel \vec{c}_2 \perp \vec{n}$ then $I_2 = A$. Thus, setting $\vec{n} = \hat{z}$ and $\vec{c}_1 = \vec{c}_2 = \hat{x}$, one has $\vec{s}\cdot\vec{n} = \cos\vartheta \equiv z$ and $(\vec{c}_1\cdot\vec{s})(\vec{c}_2\cdot\vec{s}) = (1-z^2)\cos^2\varphi$, so the integral reads

$$A = \frac{\int_0^{2\pi} d\varphi \cos^2\varphi \int_{-1}^{1} dz(1-z^2)\exp[-\beta E_a(z)]}{\int_0^{2\pi} d\varphi \int_{-1}^{1} dz\, \exp[-\beta E_a(z)]}$$

$$= \tfrac{1}{2}[1 - \langle z^2\rangle_a] = \frac{1-S_2}{3}$$

   where $S_2 = \langle P_2(z)\rangle_a$ is the average of the second Legendre polynomial $P_2(z) = \frac{1}{2}(3z^2-1)$ over the noninteracting distribution.
2. If $\vec{c}_1 \parallel \vec{c}_2 \parallel \vec{n}$, then $I_2 = A + B$. Putting $\vec{n} = \vec{c}_1 = \vec{c}_2 = \hat{z}$, the integral is given by

$$A + B = \frac{\int_{-1}^{1} dz\, z^2 \exp[-\beta E_a(z)]}{\int_{-1}^{1} dz \exp[-\beta E_a(z)]} = \langle z^2\rangle_a = \frac{1+2S_2}{3}$$

Therefore, since $I_2 = \langle(\vec{c}_1\cdot\vec{s})(\vec{c}_2\cdot\vec{s})\rangle_a$, we get the following for the second-order moment:

$$\langle(\vec{c}_1\cdot\vec{s})(\vec{c}_2\cdot\vec{s})\rangle_a = \frac{1-S_2}{3}\vec{c}_1\cdot\vec{c}_2 + S_2(\vec{c}_1\cdot\vec{n})(\vec{c}_2\cdot\vec{n}) \tag{A.7}$$

We can similarly calculate I_4 by constructing the most general scalar fulfilling certain properties, getting

$$\begin{aligned}\langle(\vec{c}_1\cdot\vec{s})(\vec{c}_2\cdot\vec{s})(\vec{c}_3\cdot\vec{s})(\vec{c}_4\cdot\vec{s})\rangle_a = {}& \Delta_4[(\vec{c}_1\cdot\vec{c}_2)(\vec{c}_3\cdot\vec{c}_4) + (\vec{c}_1\cdot\vec{c}_3)(\vec{c}_2\cdot\vec{c}_4)\\ &+ (\vec{c}_1\cdot\vec{c}_4)(\vec{c}_2\cdot\vec{c}_3)] + \Delta_2[(\vec{c}_1\cdot\vec{c}_2)(\vec{c}_3\cdot\vec{n})(\vec{c}_4\cdot\vec{n})\\ &+ (\vec{c}_1\cdot\vec{c}_3)(\vec{c}_2\cdot\vec{n})(\vec{c}_4\cdot\vec{n}) + (\vec{c}_1\cdot\vec{c}_4)(\vec{c}_2\cdot\vec{n})(\vec{c}_3\cdot\vec{n})\\ &+ (\vec{c}_2\cdot\vec{c}_3)(\vec{c}_1\cdot\vec{n})(\vec{c}_4\cdot\vec{n}) + (\vec{c}_2\cdot\vec{c}_4)(\vec{c}_1\cdot\vec{n})(\vec{c}_3\cdot\vec{n})\\ &+ (\vec{c}_3\cdot\vec{c}_4)(\vec{c}_1\cdot\vec{n})(\vec{c}_2\cdot\vec{n})] + S_4(\vec{c}_1\cdot\vec{n})(\vec{c}_2\cdot\vec{n})(\vec{c}_3\cdot\vec{n})(\vec{c}_4\cdot\vec{n})\end{aligned} \tag{A.8}$$

where Δ_2 and Δ_4 are combinations of the first $S_l(\sigma)$

$$\Delta_2 = \tfrac{1}{7}(S_2 - S_4), \qquad \Delta_4 = \frac{S_4}{35} - \frac{2S_2}{21} + \frac{1}{15} \tag{A.9}$$

Therefore, Eq. (A.8) involves S_2 as well as $S_4 = \langle P_4(z)\rangle_{\rm a}$, the average of the fourth Legendre polynomial $P_4(z) = \frac{1}{8}(35\,z^4 - 30\,z^2 + 3)$ with respect to $W_{\rm a}$.

Finally, introducing the following tensor and scalar shorthands

$$\mathbf{\Gamma} = \frac{1 - S_2}{3}\mathbf{1} + S_2 \vec{n}\vec{n} \tag{A.10}$$

$$\mathbf{\Lambda} = \sqrt{\Delta_4}\mathbf{1} + \frac{\Delta_2}{\sqrt{\Delta_4}}\vec{n}\,\vec{n}, \quad \Omega = S_4 - 3\,\frac{\Delta_2^2}{\Delta_4} \tag{A.11}$$

where $\mathbf{1}$ is the identity tensor, the results for the moments can compactly be written as

$$\langle(\vec{c}_1 \cdot \vec{s})(\vec{c}_2 \cdot \vec{s})\rangle_{\rm a} = (\vec{c}_1 \cdot \mathbf{\Gamma} \cdot \vec{c}_2) \tag{A.12}$$

$$\begin{aligned}\langle(\vec{c}_1 \cdot \vec{s})(\vec{c}_2 \cdot \vec{s})(\vec{c}_3 \cdot \vec{s})(\vec{c}_4 \cdot \vec{s})\rangle_{\rm a} = {} & (\vec{c}_1 \cdot \mathbf{\Lambda} \cdot \vec{c}_2)(\vec{c}_3 \cdot \mathbf{\Lambda} \cdot \vec{c}_4) \\ & + (\vec{c}_1 \cdot \mathbf{\Lambda} \cdot \vec{c}_3)(\vec{c}_2 \cdot \mathbf{\Lambda} \cdot \vec{c}_4) \\ & + (\vec{c}_1 \cdot \mathbf{\Lambda} \cdot \vec{c}_4)(\vec{c}_2 \cdot \mathbf{\Lambda} \cdot \vec{c}_3) \\ & + \Omega(\vec{c}_1 \cdot \vec{n})(\vec{c}_2 \cdot \vec{n})(\vec{c}_3 \cdot \vec{n})(\vec{c}_4 \cdot \vec{n})\end{aligned} \tag{A.13}$$

which facilitates the manipulation of the observables.

The quantities S_l are calculated in the case of uniaxial anisotropy in this appendix, Section B. Note finally that in the isotropic limit ($S_l \to 0$), Eqs. (A.7) and (A.8) reduce to the known moments for the isotropic distribution [134,135]

$$\langle(\vec{c}_1 \cdot \vec{s})(\vec{c}_2 \cdot \vec{s})\rangle_{\rm iso} = \tfrac{1}{3}\vec{c}_1 \cdot \vec{c}_2 \tag{A.14}$$

$$\begin{aligned}\langle(\vec{c}_1 \cdot \vec{s})(\vec{c}_2 \cdot \vec{s})(\vec{c}_3 \cdot \vec{s})(\vec{c}_4 \cdot \vec{s})\rangle_{\rm iso} = {} & \tfrac{1}{15}[(\vec{c}_1 \cdot \vec{c}_2)(\vec{c}_3 \cdot \vec{c}_4) \\ & + (\vec{c}_1 \cdot \vec{c}_3)(\vec{c}_2 \cdot \vec{c}_4) + (\vec{c}_1 \cdot \vec{c}_4)(\vec{c}_2 \cdot \vec{c}_3)]\end{aligned} \tag{A.15}$$

These expressions are formally identical to those for the average of a quantity involving the anisotropy axes $\vec{n}_i$, when these are distributed at random $\frac{1}{N}\sum_i f(\vec{n}_i) \to \int \frac{d^2\vec{n}}{4\pi} f(\vec{n}) \equiv \overline{f}$. For instance, for arbitrary $\vec{n}$-independent vectors $\vec{v}_1$ and $\vec{v}_2$, we have

$$\frac{1}{N}\sum_i (\vec{v}_1 \cdot \vec{n}_i)(\vec{v}_2 \cdot \vec{n}_i) \longrightarrow \overline{(\vec{v}_1 \cdot \vec{n})(\vec{v}_2 \cdot \vec{n})} = \tfrac{1}{3}\vec{v}_1 \cdot \vec{v}_2 \tag{A.16}$$

3. General Formulas for the Coefficients of Susceptibility

The general expression for the equilibrium linear susceptibility is given by Eq. (3.22) with the following expressions for the coefficients

$$a_0 = \frac{1}{N}\sum_i \hat{\boldsymbol{h}}\cdot\boldsymbol{\Gamma}_i\cdot\hat{\boldsymbol{h}} \tag{A.17}$$

$$a_1 = \frac{1}{N}\sum_i\sum_{j\neq i}\hat{\boldsymbol{h}}\cdot(\boldsymbol{\Gamma}_i\cdot\mathbf{G}_{ij}\cdot\boldsymbol{\Gamma}_j)\cdot\hat{\boldsymbol{h}} \tag{A.18}$$

$$\begin{aligned} a_2 = &-\frac{2}{N}\sum_i\sum_{j\neq i}\hat{\boldsymbol{h}}\cdot(\boldsymbol{\Gamma}_i\cdot\mathbf{G}_{ij}\cdot\boldsymbol{\Gamma}_j\cdot\mathbf{G}_{ij}\cdot\boldsymbol{\Gamma}_i)\cdot\hat{\boldsymbol{h}} \\ &+\frac{2}{N}\sum_i\sum_{j\neq i}\sum_{k\neq j}\hat{\boldsymbol{h}}\cdot(\boldsymbol{\Gamma}_i\cdot\mathbf{G}_{ij}\cdot\boldsymbol{\Gamma}_j\cdot\mathbf{G}_{jk}\cdot\boldsymbol{\Gamma}_k)\cdot\hat{\boldsymbol{h}} \\ &+\frac{1}{N}\sum_i\sum_{j\neq i}\left\{\frac{1-S_2}{r_{ij}^6}[(\hat{\boldsymbol{h}}\cdot\boldsymbol{\Lambda}_i\cdot\hat{\boldsymbol{h}})(\hat{\boldsymbol{r}}_{ij}\cdot\boldsymbol{\Lambda}_i\cdot\hat{\boldsymbol{r}}_{ij})+2(\hat{\boldsymbol{h}}\cdot\boldsymbol{\Lambda}_i\cdot\hat{\boldsymbol{r}}_{ij})^2\right. \\ &+\Omega(\hat{\boldsymbol{h}}\cdot\vec{\boldsymbol{n}}_i)^2(\vec{\boldsymbol{n}}_i\cdot\hat{\boldsymbol{r}}_{ij})^2]+S_2[(\hat{\boldsymbol{h}}\cdot\boldsymbol{\Lambda}_i\cdot\hat{\boldsymbol{h}})(\vec{\boldsymbol{n}}_j\cdot\mathbf{G}_{ij}\cdot\boldsymbol{\Lambda}_i\cdot\mathbf{G}_{ij}\cdot\vec{\boldsymbol{n}}_j) \\ &\left.+2(\hat{\boldsymbol{h}}\cdot\boldsymbol{\Lambda}_i\cdot\mathbf{G}_{ij}\cdot\vec{\boldsymbol{n}}_j)^2+\Omega(\hat{\boldsymbol{h}}\cdot\vec{\boldsymbol{n}}_i)^2(\vec{\boldsymbol{n}}_i\cdot\mathbf{G}_{ij}\cdot\vec{\boldsymbol{n}}_j)^2]\right\} \\ &-\frac{1}{N}\sum_i\sum_{j\neq i}(\hat{\boldsymbol{h}}\cdot\boldsymbol{\Gamma}_i\cdot\hat{\boldsymbol{h}})\left[\frac{1-S_2}{r_{ij}^6}(\hat{\boldsymbol{r}}_{ij}\cdot\boldsymbol{\Gamma}_i\cdot\hat{\boldsymbol{r}}_{ij})\cdot\right. \\ &\left.+\ S_2(\vec{\boldsymbol{n}}_j\cdot\mathbf{G}_{ij}\cdot\boldsymbol{\Gamma}_i\cdot\mathbf{G}_{ij}\cdot\vec{\boldsymbol{n}}_j)\right] \end{aligned} \tag{A.19}$$

where $\mathbf{G}_{ij}$, $\vec{\boldsymbol{r}}_{ij}$ and $\hat{\boldsymbol{r}}_{ij}$ are defined in Eq. (3.13), and $\boldsymbol{\Gamma}$, $\boldsymbol{\Lambda}$, and Ω in Eqs. (A.10) and (A.11) and also involve the $S_l(\sigma)$.

When calculating these coefficients, the same type of averages appear as in the isotropic case (see Refs. 30 and 134 for details of the calculation) and with the same multiplicities. The only difference is the weight function and hence the formulas required to calculate those averages [Eqs. (A.7) and (A.8) instead of Eqs. (A.14) and (A.15)].

4. General Formula for the Coefficient b_2 of Specific Heat

In the general expression (3.31) for the specific heat the coefficient b_0 is given by Eq. (3.32), while b_2 reads

$$\begin{aligned} Nb_2 = &\tfrac{1}{3}\{2(1-S_2)-4\sigma S_2'-\sigma^2 S_2''\}\sum_i\sum_{j\neq i}r_{ij}^{-6}+\tfrac{1}{2}\{2S_2(1-S_2)+4\sigma S_2'(1-2S_2) \\ &+\sigma^2[S_2''(1-2S_2)-2(S_2')^2]\}\sum_i\sum_{j\neq i}r_{ij}^{-6}[(\hat{\boldsymbol{r}}_{ij}\cdot\vec{\boldsymbol{n}}_i)^2+(\hat{\boldsymbol{r}}_{ij}\cdot\vec{\boldsymbol{n}}_j)^2] \\ &+\{S_2^2+4\sigma S_2S_2'+\sigma^2[S_2S_2''+(S_2')^2]\}\sum_i\sum_{j\neq i}(\vec{\boldsymbol{n}}_i\cdot\mathbf{G}_{ij}\cdot\vec{\boldsymbol{n}}_j)^2 \end{aligned} \tag{A.20}$$

where $f' = df/d\sigma$. General formulas for S_l' in the case of uniaxial anisotropy are given in Section B of this appendix.

5. *Dipolar Field*

The dipolar field averages we want to calculate are $\langle \xi_{i,\parallel}^2 \rangle = \langle (\vec{\xi}_i \cdot \vec{n}_i)^2 \rangle$ and $\langle \xi_{i,\perp}^2 \rangle = \langle \xi_i^2 \rangle - \langle \xi_{i,\parallel}^2 \rangle$. The general expressions for these quantities are [44]

$$\langle \xi_{i,\parallel}^2 \rangle = \frac{\xi_d^2}{3} \sum_j [(1 - S_2)\,(\vec{n}_i \cdot \mathbf{G}_{ij} \cdot \mathbf{G}_{ij} \cdot \vec{n}_i) + 3S_2 (\vec{n}_i \cdot \mathbf{G}_{ij} \cdot \vec{n}_j)^2] \tag{A.21}$$

$$\langle \xi_{i,\perp}^2 \rangle = \frac{\xi_d^2}{3} \sum_j [6 r_{ij}^{-6} + 3S_2 r_{ij}^{-3} (\vec{n}_j \cdot \mathbf{G}_{ij} \cdot \vec{n}_j) - (1 - S_2)(\vec{n}_i \cdot \mathbf{G}_{ij} \cdot \mathbf{G}_{ij} \cdot \vec{n}_i) - 3S_2\,(\vec{n}_i \cdot \mathbf{G}_{ij} \cdot \vec{n}_j)^2] \tag{A.22}$$

Since we want to use the dipolar fields in order to examine the blocking behavior (see Section II.C.3), one may wonder about the validity of these field averages below the superparamagnetic blocking, where the spins are not in complete equilibrium. However, since at those temperatures the spins are still in quasiequilibrium confined to one of the two wells, we can repeat the derivation of the algorithm (A.7) restricting the phase space for integration to one well. In this case, averages of the form $\langle \vec{s} \cdot \vec{v}_1 \rangle_a$ do not vanish, and should be considered together with $\langle (\vec{s} \cdot \vec{v}_1)(\vec{s} \cdot \vec{v}_2) \rangle_a$, which, being even in $\vec{s}$ is not modified. The extra terms associated with $\langle \vec{s} \cdot \vec{v}_1 \rangle_a$ will, however, vanish if the overall state is demagnetized, and Eqs. (A.21) and (A.22) are recovered.

B. S_l for Uniaxial Anisotropy

The thermodynamical average $S_l(\sigma)$ over the Legendre polynomials P_l occur in the expressions for the susceptibilities, the specific heat, and the dipolar fields in Section II.B. For uniaxial anisotropy these averages read

$$S_l(\sigma) = \langle P_l \rangle_a = \frac{1}{\mathscr{Z}_a} \int_{-1}^{1} dz P_l(z) e^{\sigma z^2} \tag{A.23}$$

In particular, $S_0 = 1$ and $S_2 = \frac{1}{2} \langle 3z^2 - 1 \rangle_a$ can be written

$$S_2 = \frac{3}{2} \left(\frac{e^\sigma}{\sigma \mathscr{Z}_a} - \frac{1}{2\sigma} \right) - \frac{1}{2} \tag{A.24}$$

The one-spin partition function $\mathscr{Z}_a = \int_{-1}^{1} dz\, \exp(\sigma z^2)$ can be written in terms of *error* functions of real and "imaginary" argument as

$$\mathscr{Z}_a = \begin{cases} \sqrt{\pi/\sigma}\,\mathrm{erfi}(\sqrt{\sigma}), & \sigma > 0 \\ \sqrt{\pi/|\sigma|}\,\mathrm{erf}(\sqrt{|\sigma|}), & \sigma < 0 \end{cases} \tag{A.25}$$

The less familiar $\mathrm{erfi}(x)$ is related to the Dawson integral $D(x)$, so in the easy-axis case one can write $Z_a = (2e^{\sigma}/\sqrt{\sigma})D(\sqrt{\sigma})$ and compute $D(x)$ with the subroutine DAWSON of Ref. 136.

For $l > 2$, the S_l can be computed using the following homogeneous three-term recurrence relation [137]:

$$\left[1 - \frac{2\sigma}{(2l-1)(2l+3)}\right] S_l - \frac{2\sigma}{2l+1}\left[\frac{l-1}{2l-1} S_{l-2} - \frac{l+2}{2l+3} S_{l+2}\right] = 0 \tag{A.26}$$

The derivative of any S_l can be computed by means of the differential recurrence relation [23]

$$\begin{aligned} S_l' = \frac{dS_l}{d\sigma} = {} & \frac{(l-1)l}{(2l-1)(2l+1)} S_{l-2} + \frac{2l(l+1)}{3(2l-1)(2l+3)} S_l \\ & + \frac{(l+1)(l+2)}{(2l+1)(2l+3)} S_{l+2} - \frac{2}{3} S_2 S_l \end{aligned} \tag{A.27}$$

The approximate behavior of S_2 and S_4 for weak ($|\sigma| \ll 1$) and strong ($|\sigma| \gg 1$) anisotropy are

$$S_2(\sigma) = \begin{cases} \frac{2}{15}\sigma + \frac{4}{315}\sigma^2 + \cdots & |\sigma| \ll 1 \\ 1 - \frac{3}{2\sigma} - \frac{3}{4\sigma^2} + \cdots & \sigma \gg 1 \\ -\frac{1}{2}\left(1 + \frac{3}{2\sigma}\right) + \cdots & \sigma \ll -1 \end{cases} \tag{A.28}$$

$$S_4(\sigma) = \begin{cases} \frac{4}{315}\sigma^2 + \cdots & |\sigma| \ll 1 \\ 1 - \frac{5}{\sigma} + \frac{25}{4\sigma^2} + \cdots & \sigma \gg 1 \\ \frac{3}{8}\left(1 + \frac{5}{\sigma} + \frac{35}{4\sigma^2}\right) + \cdots & \sigma \ll -1 \end{cases} \tag{A.29}$$

References

1. E. C. Stoner and E. P. Wohlfarth, *Philos. Trans. Roy. Soc. Lond. A* **240**, 599 (1948).
2. L. Néel, *Ann. Geophys.* **5**, 99 (1949).
3. W. Wernsdorfer, *Adv. Chem. Phys.* **118**, 99 (2001).
4. V. Cannella and J. A. Mydosh, *Phys. Rev. B* **6**, 4220 (1972).
5. W. F. Brown, Jr., *Phys. Rev.* **130**, 1677 (1963).

6. W. Wernsdorfer, E. B. Orozco, K. Hasselbach, A. Benoit, B. Barbara, N. Demoncy, A. Loiseau, H. Pascard, and D. Mailly, *Phys. Rev. Lett.* **78**, 1791 (1997).
7. J. L. Dormann, D. Fiorani, and E. Tronc, *Adv. Chem. Phys*. **98**, 283 (1997).
8. J. L. García-Palacios, *Adv. Chem. Phys*. **112**, 1 (2000).
9. X. Batlle and A. Labarta, *J. Phys. D, Appl. Phys*. **35**, R15 (2002).
10. M. A. Załuska-Kotur and M. Cieplak, *Europhys. Lett*. **23**, 85 (1993).
11. M. A. Załuska-Kotur, *Phys. Rev. B* **54**, 1064 (1996).
12. J.-O. Andersson, C. Djurberg, T. Jonsson, P. Svedlindh, and P. Nordblad, *Phys. Rev. B* **56**, 13 983 (1997).
13. D. V. Berkov and N. L. Gorn, *J. Phys.*; *Condens. Matter* **13**, 9369 (2001).
14. S. Chikazumi, *Physics of Ferromagnetism*, 2nd ed. (Oxford Univ. Press, Oxford, 1997).
15. F. Gazeau, J. C. Bacri, F. Gendron, R. Perzynski, Y. L. Raĭkher, V. I. Stepanov, and E. Dubois, *J. Magn. Magn. Mater.* **186**, 175 (1998).
16. R. V. Upadhyay, D. Srinivas, and R. V. Mehta, *J. Magn. Magn. Mater.* **214**, 105 (2000).
17. C. P. Bean and J. D. Livingston, *J. Appl. Phys*. **30**, 120s (1959).
18. W. Luo, S. R. Nagel, T. F. Rosenbaum, and R. E. Rosensweig, *Phys. Rev. Lett*. **67**, 2721 (1991).
19. J. L. García-Palacios and F. J. Lázaro, *Phys. Rev. B* **55**, 1006 (1997).
20. Y. L. Raĭkher and V. I. Stepanov, *Phys. Rev. B* **55**, 15 005 (1997).
21. J. L. García-Palacios, P. Jönsson, and P. Svedlindh, *Phys. Rev. B* **61**, 6726 (2000).
22. B. Huke and M. Lücke, *Phys. Rev. E* **62**, 6875 (2000).
23. P. E. Jönsson and J. L. García-Palacios, *Phys. Rev. B* **64**, 174416 (2001).
24. M. Hanson, C. Johansson, and S. Mørup, *Phys. Rev. Lett*. **81**, 735 (1998).
25. J. Tejada, X. X. Zhang, E. del Barco, J. M. Hernández, and E. M. Chudnovsky, *Phys. Rev. Lett*. **81**, 736 (1998).
26. H. Mamiya, I. Nakatani, and T. Furubayashi, *Phys. Rev. Lett*. **88**, 067202 (2002).
27. R. Pierls, *Z. Phys*. **80**, 763 (1933).
28. L. D. Landau and E. M. Lifshitz, *Statistical Physics*, 2nd ed. (Pergamon Press, Oxford, 1970).
29. I. Waller, *Z. Phys*. **104**, 132 (1936).
30. J. H. van Vleck, *J. Chem. Phys*. **5**, 320 (1937).
31. N. V. Prokof'ev and P. C. E. Stamp, *Phys. Rev. Lett*. **80**, 5794 (1998).
32. R. B. Griffiths, *Phys. Rev.* **176**, 655 (1968).
33. S. Banerjee, R. B. Griffiths, and M. Widom, *J. Stat. Phys*. **93**, 109 (1998).
34. J. A. Pople, *Phil. Mag*. **44**, 1276 (1953).
35. U. Nowak, R. W. Chantrell, and E. C. Kennedy, *Phys. Rev. Lett*. **84**, 163 (2000).
36. W. T. Coffey, D. S. F. Crothers, J. L. Dormann, L. J. Geoghegan, and E. C. Kennedy, *Phys. Rev. B* **58**, 3249 (1998).
37. W. T. Coffey, D. S. F. Crothers, J. L. Dormann, L. J. Geoghegan, E. C. Kennedy, and W. Wernsdorfer, *J. Phys.: Condens. Matter* **10**, 9093 (1998).
38. D. A. Garanin, E. C. Kennedy, D. S. F. Crothers, and W. T. Coffey, *Phys. Rev. E* **60**, 6499 (1999).
39. W. T. Coffey, D. S. F. Crothers, J. L. Dormann, Y. P. Kalmykov, E. C. Kennedy, and W. Wernsdorfer, *Phys. Rev. Lett*. **80**, 5655 (1998).
40. W. T. Coffey, D. S. F. Crothers, Y. P. Kalmykov, and S. V. Titov, *Phys. Rev. B* **64**, 012411 (2001).
41. J. L. García-Palacios and P. Svedlindh, *Phys. Rev. Lett*. **85**, 3724 (2000).

42. J. L. Dormann, L. Bessais, and D. Fiorani, *J. Phys. C* **21**, 2015 (1988).
43. S. Mørup and E. Tronc, *Phys. Rev. Lett*. **72**, 3278 (1994).
44. P. E. Jönsson and J. L. García-Palacios, *Europhys. Lett*. **55**, 418 (2001).
45. R. Kubo and N. Hashitsume, *Prog. Theor. Phys*. **46**, 210 (1970).
46. W. T. Coffey, P. J. Cregg, and Y. P. Kalmykov, *Adv. Chem. Phys*. **83**, 263 (1993).
47. T. L. Gilbert, *Phys. Rev*. **100**, 1243 (1955).
48. L. D. Landau and E. M. Lifshitz, *Z. Phys. Sowjet*. **8**, 153 (1935).
49. Y. L. Raĭkher and V. I. Stepanov, *Phys. Rev. B* **50**, 6250 (1994).
50. R. Kubo, *Rep. Prog. Phys*. **29**, 255 (1966).
51. J. L. García-Palacios and F. J. Lázaro, *Phys. Rev. B* **58**, 14 937 (1998).
52. A. Aharoni, *Phys. Rev*. **177**, 793 (1969).
53. W. T. Coffey, D. A. Garanin, H. Kachkachi, and D. J. McCarthy, *J. Magn. Magn. Mater*. **221**, 110 (2000).
54. F. Luis, F. Petroff, J. M. Torres, L. M. García, J. Bartolomé, J. Carrey, and A. Vaurès, *Phys. Rev. Lett*. **88**, 217205 (2002).
55. M. F. Hansen and S. Mørup, *J. Magn. Magn. Mater*. **184**, 262 (1998).
56. J. L. Dormann, D. Fiorani, and E. Tronc, *J. Magn. Magn. Mater*. **202**, 251 (1999).
57. P. Ewald, *Ann. Phys*. **64**, 253 (1921).
58. E. Madelung, *Phys. Z*. **19**, 524 (1918).
59. S. W. de Leeuw, J. W. Perram, and E. R. Smith, *Proc. Roy. Soc. Lond. A* **373**, 27 (1980).
60. T. Jonsson, J. Mattsson, C. Djurberg, F. A. Khan, P. Nordblad, and P. Svedlindh, *Phys. Rev. Lett*. **75**, 4138 (1995).
61. H. Mamiya, I. Nakatani, and T. Furubayashi, *Phys. Rev. Lett*. **82**, 4332 (1999).
62. J. L. Dormann, D. Fiorani, R. Cherkaoui, E. Tronc, F. Lucari, F. D'Orazio, L. Spinu, M. Noguès, H. Kachkachi, and J. P. Jolivet, *J. Magn. Magn. Mater*. **203**, 23 (1999).
63. C. Djurberg, P. Svedlindh, P. Nordblad, M. F. Hansen, F. Bødker, and S. Mørup, *Phys. Rev. Lett*. **79**, 5154 (1997).
64. T. Jonsson, P. Svedlindh, and M. F. Hansen, *Phys. Rev. Lett*. **81**, 3976 (1998).
65. M. F. Hansen, P. Jönsson, P. Nordblad, and P. Svedlindh, *J. Phys.; Condens. Matter* **14**, 4901 (2002).
66. S. Sahoo, O. Petracic, C. Binek, W. Kleemann, J. B. Sousa, S. Cardoso, and P. P. Freitas, *Phys. Rev. B* **65**, 134406 (2002).
67. K. Binder and A. P. Young, *Rev. Mod. Phys*. **58**, 801 (1986).
68. K. H. Fischer and J. A. Hertz, *Spin Glasses* (Cambridge Univ. Press, Cambridge, U.K., 1991).
69. A. P. Young, ed., *Spin Glasses and Random Fields*, (World Scientific, Singapore, 1997).
70. M. A. Ruderman and C. Kittel, *Phys. Rev*. **96**, 99 (1954).
71. T. Kasuya, *Prog. Theor. Phys*. **16**, 45, 58 (1956).
72. K. Yosida, *Phys. Rev*. **106**, 893 (1957).
73. A. Fert and P. M. Levy, *Phys. Rev. Lett*. **44**, 1538 (1980).
74. J. J. Prejean, M. J. Joliclerc, and P. Monod, *J. Physique* **41**, 427 (1980).
75. A. Ito, H. Aruga, E. Torikai, M. Kikuchi, Y. Syono, and H. Takei, *Phys. Rev. Lett*. **57**, 483 (1986).

76. A. Ito, E. Torikai, S. Morimoto, H. Aruga, M. Kikuchi, Y. Syono, and H. Takei, *J. Phys. Soc. Jpn.* **59**, 829 (1990).
77. H. Aruga Katori and A. Ito, *J. Phys. Soc. Jpn.* **62**, 4488 (1993).
78. S. F. Edwards and P. W. Anderson, *J. Phys. F* **5**, 965 (1975).
79. D. Sherrington and S. Kirkpatrick, *Phys. Rev. Lett.* **35**, 1792 (1975).
80. G. Parisi, *Phys. Rev. Lett.* **43**, 1754 (1979).
81. G. Parisi, *J. Phys. A* **13**, 1101 (1980).
82. G. Parisi, *Phys. Rev. Lett.* **50**, 1946 (1983).
83. M. Suzuki, *Prog. Theor. Phys.* **58**, 1151 (1977).
84. S. Chikazawa, T. Saito, T. Sato, and Y. Miyako, *J. Phys. Soc. Jpn.* **47**, 335 (1979).
85. P. Nordblad and P. Svedlindh, in *Spin Glasses and Random Fields*, A. P. Young, ed. (World Scientific, Singapore, 1997), pp. 1–27.
86. D. Petit, Ph.D. thesis, Université Paris XI, 2002.
87. P. E. Jönsson, H. Yoshino, P. Nordblad, H. A. Katori, and A. Ito, *Phys. Rev. Lett.* **88**, 257204 (2002).
88. L. C. A. Struik, *Physical Aging in Amorphous Polymers and Other Materials* (Elsevier, Amsterdam, 1978).
89. L. Lundgren, P. Svedlindh, P. Nordblad, and O. Beckman, *Phys. Rev. Lett.* **51**, 911 (1983).
90. J. O. Andersson, J. Mattsson, and P. Svedlindh, *Phys. Rev. B* **46**, 8297 (1992).
91. L. Bellon, S. Ciliberto, and C. Laroche, *Europhys. Lett.* **51**, 551 (2000).
92. P. Doussineau, T. de Lacerda-Arôso, and A. Levelut, *Europhys. Lett.* **46**, 401 (1999).
93. V. Normand, S. Muller, J.-C. Ravey, and A. Parker, *Macromolecules* **33**, 1063 (2000).
94. E. L. Papadopoulou, P. Nordblad, P. Svedlindh, R. Schöneberger, and R. Gross, *Phys. Rev. Lett.* **82**, 173 (1999).
95. J. Magnusson, C. Djurberg, P. Granberg, and P. Nordblad, *Rev. Sci. Instrum.* **68**, 3761 (1997).
96. W. L. McMillan, *J. Phys. C* **17**, 3179 (1984).
97. A. J. Bray and M. A. Moore, in *Heidelberg Colloquium on Glassy Dynamics*, J. L. van Hemmen and I. Morgenstern, eds. (Springer, Berlin, 1986).
98. D. S. Fisher and D. A. Huse, *Phys. Rev. Lett.* **56**, 1601 (1986).
99. D. S. Fisher and D. A. Huse, *Phys. Rev. B* **38**, 386 (1988).
100. D. S. Fisher and D. A. Huse, *Phys. Rev. B* **38**, 373 (1988).
101. J.-P. Bouchaud, V. Dupuis, J. Hammann, and E. Vincent, *Phys. Rev. B* **65**, 024439 (2001).
102. V. Dupuis, E. Vincent, J.-P. Bouchaud, J. Hammann, A. Ito, and H. Aruga Katori, *Phys. Rev. B* **64**, 174204 (2001).
103. P. Jönsson, H. Yoshino, and P. Nordblad, *Phys. Rev. Lett.* **89**, 097201 (2002).
104. L. Berthier, V. Viasnoff, O. White, V. Orlyanchik, and F. Krzakala, cond-mat/0211106.
105. A. J. Bray and M. A. Moore, *J. Phys. C* **17**, L463 (1984).
106. H. Risken, *The Fokker–Planck Equation*, 2nd ed. (Springer, Berlin, 1989).
107. H. Yoshino, K. Hukushima, and H. Takayama, *Phys. Rev. B* **66**, 064431 (2002).
108. A. J. Bray and M. A. Moore, *Phys. Rev. Lett.* **58**, 57 (1987).
109. P. Granberg, L. Sandlund, P. Nordblad, P. Svedlindh, and L. Lundgren, *Phys. Rev. B* **38**, 7079 (1988).

110. K. Jonason, E. Vincent, J. Hammann, J.-P. Bouchaud, and P. Nordblad, *Phys. Rev. Lett*. **81**, 3243 (1998).
111. T. Jonsson, K. Jonason, P. Jönsson, and P. Nordblad, *Phys. Rev. B* **59**, 8770 (1999).
112. R. Mathieu, P. Jönsson, D. N. H. Nam, and P. Nordblad, *Phys. Rev. B* **63**, 092401 (2001).
113. R. Mathieu, P. E. Jönsson, P. Nordblad, H. A. Katori, and A. Ito, *Phys. Rev. B* **65**, 012411 (2002).
114. P. Jönsson, M. F. Hansen, and P. Nordblad, *Phys. Rev. B* **61**, 1261 (2000).
115. E. V. Colla, L. K. Chao, M. B. Weissman, and D. D. Viehland, *Phys. Rev. Lett*. **85**, 3033 (2000).
116. L. Bellon, S. Ciliberto, and C. Laroche, *Eur. Phys. J. B* **25**, 223 (2002).
117. A. V. Kityk, M. C. Rheinstädter, K. Knorr, and H. Rieger, *Phys. Rev. B* **65**, 144415 (2002).
118. A. Gardchareon, R. Mathieu, P. E. Jönsson, and P. Nordblad, *Phys. Rev. B* **67**, 052505 (2003).
119. P. E. Jönsson, R. Mathieu, H. Yoshino, P. Nordblad, H. A. Katori, and A. Ito, cond-mat/0307640.
120. P. Jönsson, P. Svedlindh, P. Nordblad, and M. F. Hansen, *J. Magn. Magn. Mater.* **226–230**, 1315 (2001).
121. P. Jönsson, S.Felton, P. Svedlindh, P. Nordblad, and M. F. Hansen, *Phys. Rev. B* **64**, 212402 (2001).
122. M. Hanson, C. Johansson, and S. Mørup, *J. Phys., Condens. Matter* **7**, 9263 (1995).
123. M. Hanson, C. Johansson, M. S. Pedersen, and S. Mørup, *J. Phys., Condens. Matter* **7**, 9269 (1995).
124. M. F. Hansen, F. Bødker, S. Mørup, C. Djurberg, and P. Svedlindh, *J. Magn. Magn. Mater.* **177–181**, 928 (1998).
125. T. Komori, H. Yoshino, and H. Takayama, *J. Phys. Soc. Jpn*. **69** (Suppl. A), 228 (2000).
126. M. Picco, F. Ricci-Tersenghi, and F. Ritort, *Phys. Rev. B* **63**, 174412 (2001).
127. L. Berthier and J. P. Bouchaud, *Phys. Rev. B* **66**, 054404 (2002).
128. J. Mattsson, C. Djurberg, P. Nordblad, L. Hoines, R. Stubi, and J. A. Cowen, *Phys. Rev. B* **47**, 14626 (1993).
129. A. G. Schins, E. M. Dons, A. F. M. Arts, H. W. Wijn, E. Vincent, L. Leylekian, and J. Hammann, *Phys. Rev. B* **48**, 16524 (1993).
130. C. Rigaux, *Ann. Phys. Fr.* **20**, 445 (1995).
131. A. T. Ogielski, *Phys. Rev. B* **32**, 7384 (1985).
132. K. Gunnarsson, P. Svedlindh, P. Nordblad, L. Lundgren, H. Aruga, and A. Ito, *Phys. Rev. Lett*. **61**, 754 (1988).
133. T. Jonsson, P. Nordblad, and P. Svedlindh, *Phys. Rev. B* **57**, 497 (1998).
134. R. Rosenberg and M. Lax, *J. Chem. Phys*. **21**, 424 (1952).
135. J. Mathews and R. L. Walker, *Mathematical Methods of Physics*, 2nd ed. (Benjamin/Cummings, Menlo Park, CA, 1970).
136. W. H. Press, S. A. Teukolsky, W. T. Vetterling, and B. P. Flannery, *Numerical Recipes*, 2nd ed. (Cambridge Unive. Press, New York, 1992).
137. Y. P. Kalmykov and W. T. Coffey, *Phys. Rev. B* **56**, 3325 (1997).

WAVEPACKET THEORY OF PHOTODISSOCIATION AND REACTIVE SCATTERING

GABRIEL G. BALINT-KURTI

School of Chemistry, The University of Bristol, Bristol BS8 1TS, United Kingdom

CONTENTS

Advances in Chemical Physics, Volume 128, edited by Stuart A. Rice
ISBN 0-471-44528-2

I. INTRODUCTION

This chapter deals with the theory underlying the application of wavepackets to molecular photodissociation and reactive scattering. The objective will be to derive and gather together the equations and theoretical methods needed in such calculations. No attempt will be made to reference all calculations that have been undertaken in this very popular field. Several alternative related methods will be discussed, but it will not be possible to do full justice to all the different methods that have been proposed, many of which are being successfully used.

Photodissociation has been referred to as a ''half-collision.'' The molecule starts in a well-defined initial state and ends up in a final scattering state. The intial bound-state vibrational–rotational wavefunction provides a natural initial wavepacket in this case. It is in connection with this type of spectroscopic process that Heller [1–3] introduced and popularized the use of wavepackets.

In a reactive scattering process both the initial and final states of the system are scattering states. In this case the initial wavepacket, representing the nuclear wavefunction of the reactive system, must be artificially introduced. This initial wavepacket is located in the entrance valley of the potential energy surface and must be given an inward momentum toward the strong interaction region. As the momentum eigenfunctions are of the form e^{ikx}, the initial wavepacket is intrinsically complex. The wavepacket is localized in space and consequently, as a result of Heisenberg's uncertainty principle, it contains a range of energies. The power of wavepacket techniques rests on this observation. As the energy is a conserved quantity, each energy component within the wavepacket propagates independently. Thus, by correctly analyzing the results of the dynamics of the wavepacket, it should be possible to compute observable quantities, such as cross sections, for all energies contained within the initial wavepacket. A single calculation of the wavepacket dynamics should therefore yield cross sections over a wide range of energies. Both photodissociation theory and reactive scattering theory were initially treated using methods of time-independent scattering theory [4–7]. It is evident from the number of wavepacket calculations now appearing in the literature that time-dependent methods have become increasingly popular.

The review is divided into two major parts. The first deals with photodissociation theory and the second, with reactive scattering methods.

Many aspects of these two parts overlap, as the dynamics and analysis of the wavepacket is the same in the two cases. This should be borne in mind when reading the review. Photodissociation theory is in many ways simpler than the theory of reactive scattering. This is because the initial wavepacket in the photodissociation process has a well-defined total angular momentum, which is conserved throughout (see text below for a more precise discussion), while the calculation of a reactive scattering cross section requires the calculation of wavepacket dynamics over a wide range of total angular momenta [8–10]. Some technical aspects of the theory are covered in detail in three appendix sections, and a short conclusion is given at the end of the chapter.

II. PHOTODISSOCIATION THEORY

Three reviews [11–13], a book [14], and a conference proceedings [15] have been published on the subject of photodissociation theory. A review on time-dependent quantum dynamics [16] and several important papers comparing the different methods for evaluating the action of the time evolution operator on a wavepacket [17–19] have also appeared, as well as a review on the use of grid methods in photodissociation and reactive scattering [20]. The first quantum mechanical treatments of photodissociation theory [21–35] were based on time-independent quantum scattering techniques [4–6]. In 1978 Heller [1,2,36] introduced both an exact and an approximate semiclassical time-dependent quantum mechanical computational method for the calculation of photodissociation cross sections. In 1983 Kosloff proposed the very stable and numerically accurate Chebyshev expansion technique [37–40] for evaluating the action of the time evolution operator on a wavepacket. These publications led a huge advance in both time-dependent [41–61] and time-independent [62–74] theoretical molecular dynamics.

In this section of the review the time-dependent wavepacket approach for the treatment of photodissociation processes is outlined. The time-dependent theory of photodissociation has been thoroughly discussed elsewhere [1–3,20,37, 75,76]. I start with a definition of the energy-dependent photodissociation cross sections. This is followed by discussion of how the integral cross section can be computed using a time-dependent formalism and of the construction of the initial wavepacket and finally a derivation of a time-dependent treatment of the partial and differential cross sections for the production of the different final quantum states of the photofragments. Important technical aspects concerning the details of the body-fixed form of the energy normalized scattering wavefunction, the construction of the initial wavepacket, and the derivation of the time-dependent theory of the partial and differential photofragmentation cross sections are treated in three appendixes. In all cases I specialize the

treatment to that for a triatomic system, although the principles and the general approach may easily be generalized to larger molecules.

A. Definition of Cross Sections

1. *Total Integral Cross Section*

Within the semiclassical, perturbational treatment of the interaction of radiation with matter [77,78] and within the dipole approximation [79], the total energy absorption cross section may be written in the form [11,12,20,80]

$$\sigma_{\text{tot}}(E) = \frac{2\pi^2 \nu}{c\epsilon_0} \sum_f \int d\hat{\mathbf{k}} |\langle \psi_f | \vec{\epsilon} \cdot \vec{\mu} | \psi_i \rangle|^2 \tag{4.1}$$

where ψ_i and ψ_f are the wavefunctions of the nuclear motion corresponding to the initial and final states, respectively; $\vec{\epsilon}$ is the polarization vector of the electric field of the light; and $\vec{\mu}$ is the transition dipole vector (which depends on the nuclear geometry). Note that the factor of $\frac{1}{3}$, which is often present on the right-hand side of this equation, is absent. This is because it is assumed that the customary average over the initial M_J states (z components of the total angular momentum) and the sum over all final $M_{J'}$ states has not yet been performed. The integration over $\hat{\mathbf{k}}$ is an integration over all scattering directions. This is needed as the final-state wavefunctions ψ_f correspond to scattering into the direction $\hat{\mathbf{k}}$ (see discussion below).

The cross section is defined by the relationship

$$\sigma_{\text{tot}}(E) = \frac{\text{radiative energy absorbed per second}}{\text{incident radiative energy flux}} \tag{4.2}$$

and has the units of area.

a. The Continuum Wavefunction. For a photodissociation process the final-state wavefunction ψ_f is a continuum wavefunction, and it is important that it be normalized correctly. The correct normalization is ''normalization on the energy scale'' [81]. In order to give a concrete framework to the derivation of the equations of photodissociation theory, we specialize to the case of the photodissociation of a triatomic molecule to form an atom plus a diatomic molecule, neither of which have any electronic angular momentum. The final-state quantum numbers, f, [see Eq. (4.1)] therefore become the vibrational–rotational quantum numbers of the fragment diatomic (v,j). If $\psi^-_{vjm_j}(\mathbf{r},\mathbf{R};\hat{\mathbf{k}},E)$ is the continuum wavefunction, which replaces ψ_f in Eq. (4.1), we can write its

asymptotic form as [80]

$$\psi_f \equiv \psi^-_{vjmj}(\mathbf{r},\mathbf{R};\hat{\mathbf{k}},E) \underset{R\to\infty}{\sim} \left(\frac{\mu k_{vj}}{\hbar^2(2\pi)^3}\right)^{1/2} \left\{ e^{i\mathbf{k}\cdot\mathbf{R}}\chi_{vj}(r)Y_{jm_j}(\hat{\mathbf{r}}) + \sum_{v'j'm'_j} f_{v'j'm'_j,vjm_j}(\mathbf{k},\hat{\mathbf{R}}) \frac{e^{-ik_{v'j'}R}}{R}\chi_{v'j'}(r)Y_{j'm'_j}(\hat{\mathbf{r}}) \right\} \tag{4.3}$$

where $\hat{\mathbf{k}}$ denotes the direction of observation (i.e., the direction in which the two fragments scatter), $\mathbf{r}$ is the vector joining the two atoms of the diatom fragment, and R is the distance between the center of mass of the diatom and the atomic fragment.

The summation over final states in Eq. (4.1) also includes an integration over all the directions of dissociation, $\hat{\mathbf{k}}$. The boundary conditions of the wavefunction $\psi^-_{vjm_j}(\mathbf{r},\mathbf{R};\hat{\mathbf{k}},E)$ correspond to a pure outgoing wave where the diatomic fragment has vibrational–rotational quantum numbers vj and is associated with the wavefunction $\chi_{vj}(r)Y_{jm}(\hat{\mathbf{r}})$.

The total angular momentum is a conserved quantity and the initial wavefunction, ψ_i in Eq. (4.1), also has a well-defined total angular momentum. For these reasons it is highly advantageous, both theoretically and computationally, to reexpress the final state wavefunction in terms of a basis of angular functions that are eigenfunctions of the total angular momentum J and of its z component, M. It is only through such a reformulation that we are able to benefit from the immense numerical simplifications that stem from the fact that J is a ''good'' quantum number. It is also convenient to work in a body-fixed coordinate system, rather than in the space-fixed system [4] used in Eq. (4.3). The transformation from the space-fixed to the body-fixed coordinate system is discussed in detail in Ref. 80 and also in the books of Edmonds [82] and Zare [83] and in a previous review by the present author [4]. Using these techniques, we can show that the continuum wavefunction can be written in the form (see the Appendix, Section A):

$$\psi^-_{vjm_j}(\mathbf{r},\mathbf{R};\hat{\mathbf{k}},E) = \sum_{JM}\sum_{lm_lp} Y^*_{lm_l}(\hat{\mathbf{k}})(jlJM|jm_jlm_l)\sum_{K=\lambda}^{J}(Jjl0|JKj-K) \times \sum_{K'=\lambda}^{J}\Phi^{-JvjKp}_{K'}(r,R,\theta;E)|J,K',M,p\rangle \tag{4.4}$$

where

$$\Phi^{-JvjKp}_{K'}(r,R,\theta;E) = \left(\frac{\mu k_{vj}}{\hbar^2(2\pi)^3}\right)^{1/2} 4\pi \sum_{v'j'}\left\{\frac{2(-1)^{j-K}}{\sqrt{2(1+\delta_{0,K})}}\right\} \times \frac{\Phi^{(JvjKp)}_{v'j'K'}(R)}{R}\Theta_{j'K'}(\theta)\chi_{v'j'}(r) \tag{4.5}$$

and $|J,K,M,p\rangle$ are parity-adapted eigenfunctions [84] of the total angular momentum (J) corresponding to specified space-fixed (M) and body-fixed (K) z components; $\Phi^{-Jvjkp}(r,R,\theta;E)$ is a body-fixed wavefunction with the correct boundary conditions [80] so as to yield the asymptotic behavior specified in Eq. (4.3); $(Jjl0|JKj-K)$ are Clebsch Gordan angular momentum coupling coefficients [82,83]; and the coordinates r,R,θ are the body-fixed Jacobi coordinates where θ is the angle between the scattering coordinate **R** and the diatomic molecular axis direction, **r** [84].

The parity-adapted total angular momentum eigenfunctions [84] are defined as

$$|J,K,M,p\rangle = \sqrt{\frac{2J+1}{8\pi^2}}\frac{1}{\sqrt{2(1+\delta_{0,K})}}\left\{D^J_{K,M}(\omega)+(-1)^{J+K+p}D^J_{-K,M}(\omega)\right\} \tag{4.6}$$

and

$$\lambda = \frac{1-(-1)^{J+p}}{2} \tag{4.7}$$

The parity is given by $(-1)^{J+K+p}$, where p can take the values $p=1$ or $p=2$, thereby yielding positive or negative parity states, depending on the values of J and $|K|$. The $D^J_{K,M}(\omega)$s are Wigner D matrices and are functions of the three Euler angles, $\omega(\equiv \alpha,\beta,\gamma)$, which orient the three-atom system in the space-fixed frame [82]. The $D^J_{K,M}(\omega)$ matrix elements corresponding to the same absolute value, but different signs, of K must be combined to form parity eigenfunctions [80,83].

The asymptotic form of the body-fixed radial scattering wavefunction, $\Phi^{(JvjK)}_{v'j'K'}(R)$, is [4,80]

$$\Phi^{(JvjK)}_{v'j'K'}(R)\underset{R\to\infty}{\sim}\frac{1}{2ik_{vj}}\left[e^{ik_{v'j'}R}\delta_{vv'}\delta_{jj'}\delta_{KK'}-S^{Jp*}_{vjK,v'j'K'}\left(\frac{k_{v'j'}}{k_{vj}}\right)^{1/2}e^{-ik_{v'j'}R}\right] \tag{4.8}$$

The **S** matrix elements, which occur in Eq. (4.8), contain information about the dynamics or scattering on the final or upper-state electronic energy surface. As they refer only to the asymptotic form of the continuum wavefunction, they do not contain information about the probability of the photodissociation process.

The form of the scattering wavefunction has been represented in a very general manner, specifically, as a product of a function in body-fixed coordinates $[\Phi^{-Jvjkp}(r,R,\theta;E)]$, the parity-adapted total angular momentum

eigenfunctions ($|J, K, M, p\rangle$), and angular momentum coupling coefficients. This is exactly the form needed in the time-dependent wavepacket formulation discussed below.

b. The Initial Wavefunction. The initial wavefunction, ψ_i, appearing in Eq. (4.1) is also an eigenfunction of the total angular momentum J, of its space-fixed z component M and of the parity, $(-1)^{J+K+p}$. It may be written in the form

$$\psi_i \equiv \Psi^{J_i,M_i,p}(r, R, \theta, \omega) = \sum_{K=\lambda}^{J_i} \psi^{J_i,K_i,p}(r, R, \theta)|J_i, K, M_i, p\rangle \tag{4.9}$$

where the functions $|J, K, M, p\rangle$ have been defined above [see Eq. (4.6)].

2. *Partial Integral Cross Section*

We will be interested not only in the total absorption cross section [Eqs. (4.1) and (4.2)], which gives us a measure of the total probability that the molecule will absorb light and dissociate, but also in the probability that different product quantum states will be formed. This probability is given by a *partial* cross section $\sigma_f(E)$. From Eq. (4.1) we see that this partial integral cross section may be written as

$$\sigma_f(E) = \frac{2\pi^2\nu}{c\epsilon_0} \int d\hat{\mathbf{k}} |\langle \psi_f | \vec{\epsilon} \cdot \vec{\mu} | \psi_i \rangle|^2 \tag{4.10}$$

The partial cross section gives the probability of absorbing light and producing a particular final product quantum state. The total photodissociation cross section is clearly given by the sum over all partial photodissociation cross sections:

$$\sigma_{\text{tot}}(E) = \sum_f \sigma_f(E) \tag{4.11}$$

3. *Partial Differential Cross Section*

The definition of the final quantum state [see Eqs. (4.3) and (4.4)] of the system includes the direction $\hat{\mathbf{k}}$ into which the separating fragments are scattered. If we omit the integrals over all final scattering directions in Eqs. (4.1) and (4.10), we obtain a cross section for scattering into a specific final direction. These are called *differential cross sections*. Below I will briefly outline the definition and properties of the partial differential cross section, which is the probability of producing a specific final quantum state of the system scattered into a well-specified direction.

The partial differential cross section may be defined, in analogy to Eqs. (4.1) and (4.10), as

$$\sigma_{vjm_j}(E;\hat{\mathbf{k}}) = \frac{2\pi^2\nu}{c\,\epsilon_0}\left|\langle\psi^-_{vjm_j}(\mathbf{r},\mathbf{R};\hat{\mathbf{k}},E)|\,\vec{\epsilon}\cdot\vec{\mu}\,|\psi_i\rangle\right|^2 \tag{4.12}$$

where I have used a specific form [see Eq. (4.4)] for the final-state wavefunction ψ_f to emphasize its directional properties.

Substituting Eq. (4.4) into Eq. (4.12), we obtain

$$\sigma_{vjm_j}(E;\hat{\mathbf{k}}) = \frac{2\pi^2\nu}{c\,\epsilon_0}\left|\sum_{JM}\sum_{KK'p}\left\{\sum_{lm_l} Y^*_{lm_l}(\hat{\mathbf{k}})(jlJM|jm_jlm_l)(Jjl0|JKj-K)\right\}\right.$$
$$\left.\times\,\langle J,K',M,p|\Phi^{-JvjKp}_{K'}(r,R,\theta;E)\,|\vec{\epsilon}\cdot\vec{\mu}|\psi_i\rangle\right|^2 \tag{4.13}$$

where $Y^*_{lm_l}(\hat{\mathbf{k}}) = Y^*_{lm_l}(\theta_k,\phi_k)$. Using Eq. (33) of Ref. 80, we can rewrite the curly bracket in Eq. (4.13) as follows:

$$\sum_{lm_l} Y^*_{lm_l}(\hat{\mathbf{k}})(jlJM|jm_jlm_l)(Jjl0|JKj-K)$$
$$= \left(\frac{2J+1}{4\pi}\right)^{1/2}(-1)^{j-m_j}D^J_{K,M}(\phi_k,\theta_k,0)D^j_{-K,-m_j}(\phi_k,\theta_k,0) \tag{4.14}$$

Substituting Eq. (4.14) into Eq. (4.13), we obtain

$$\sigma_{vjm_j}(E;\hat{\mathbf{k}}) = \frac{2\pi^2\nu}{c\,\epsilon_0}\frac{1}{4\pi}\left|\sum_{JM}\sum_{KK'p}(2J+1)^{1/2}D^J_{K,M}(\phi_k,\theta_k,0)D^j_{-K,-m_j}(\phi_k,\theta_k,0)\right.$$
$$\left.\times\,\langle J,K',M,p|\Phi^{-JvjKp}_{K'}(r,R,\theta;E)\,|\vec{\epsilon}\cdot\vec{\mu}|\psi_i\rangle\right|^2 \tag{4.15}$$

The product of Wigner D matrix elements in Eq. (4.15) $[D^J_{K,M}(\theta_k,\phi_k,0)\,D^j_{-K,-m_j}(\theta_k,\phi_k,0)]$ determines the form of the angular distribution of the photofragments [80,85]. In particular, this form shows clearly that if either the polarization of the initial molecular state (i.e., the M_i quantum number) or the polarization of the product diatomic rotational state m_j is selected, then the angular distribution of the photofragments is more complex than is normally assumed. In particular, if linearly polarized light is used to accomplish the photodissociation, the angular distribution will require terms of the form $P_4(\cos(\theta_k)$ (i.e., fourth-order Legendre polynomials in the scattering angle) for its description and the conventional β parameter, associated with second-order Legendre polynomials will not be sufficient [80]. Also, more recently Pe'er, Shapiro and the author have argued [85] that the backward–forward symmetry

of the angular distribution of the photofragments may be destroyed under the same circumstances. The integral on the right-hand side (RHS) of Eq. (4.15) contains the essential molecular dynamics of the photodissociation process. The form of this integral has been analyzed in some detail in two previous publications, first in conjunction with a time-independent formulation [80] and later in the context of a time-dependent formulation [84]. We will develop the form of the expression for the partial differential cross sections further after we have discussed the time-dependent wavepacket treatment of photodissociation processes.

B. The Time-Dependent Formulation; Total Integral Photodissociation Cross Section

The key to reexpressing the integral cross section [Eq. (4.1)] in terms of time-dependent quantities is the recognition that the continuum functions $\psi^-_{vjm_j}(\mathbf{r}, \mathbf{R}; \hat{\mathbf{k}}, E)$ [Eqs. (4.3) and (4.4)] form a complete set for the space of functions with energy E. This fact can be expressed as follows [1,2,86]:

$$\sum_{vjm_j} \int d\hat{\mathbf{k}} |\psi^-_{vjm_j}(\mathbf{r}, \mathbf{R}; \hat{\mathbf{k}}, E)\rangle \langle \psi^-_{vjm_j}(\mathbf{r}, \mathbf{R}; \hat{\mathbf{k}}, E)| = \delta(\hat{\mathbf{H}} - E)\hat{\mathbf{I}} \tag{4.16}$$

The Dirac delta function may be represented as a Fourier transform over time:

$$\delta(\hat{\mathbf{H}} - E) = \frac{1}{2\pi\hbar} \int_{-\infty}^{\infty} dt \exp\left[\frac{-i(\hat{\mathbf{H}} - E)t}{\hbar}\right] \tag{4.17}$$

Replacing the final-state wavefunction ψ_f in Eq. (4.1) by $\psi^-_{v'j'm_{j'}}(\mathbf{r}, \mathbf{R}; \hat{\mathbf{k}}, E)$ [see Eqs. (4.3) and (4.4)] and replacing the summation over the final states f in Eq. (4.1) by a summation over v', j', and $m_{j'}$ together with an integration over all continuum channels, we can write

$$\begin{aligned}
\sigma_{\text{tot}}(E) &= \frac{2\pi^2 \nu}{c\,\epsilon_0} \sum_{v'j'm_{j'}} \int d\hat{\mathbf{k}} \left| \langle \psi^-_{v'j'm_{j'}}(\mathbf{r}, \mathbf{R}; \hat{\mathbf{k}}, E) | \vec{\epsilon} \cdot \vec{\mu} | \psi_i \rangle \right|^2 \\
&= \frac{2\pi^2 \nu}{c\,\epsilon_0} \sum_{v'j'm_{j'}} \int d\hat{\mathbf{k}} \langle \psi_i | \vec{\epsilon} \cdot \vec{\mu} | \psi^-_{v'j'm_{j'}}(\mathbf{r}, \mathbf{R}; \hat{\mathbf{k}}, E) \rangle \langle \psi^-_{v'j'm_{j'}}(\mathbf{r}, \mathbf{R}; \hat{\mathbf{k}}, E) | \vec{\epsilon} \cdot \vec{\mu} | \psi_i \rangle \\
&= \frac{2\pi^2 \nu}{c\,\epsilon_0} \langle \psi_i | \vec{\epsilon} \cdot \vec{\mu} \left\{ \sum_{v'j'm_{j'}} \int d\hat{\mathbf{k}} \left| \psi^-_{v'j'm_{j'}}(\mathbf{r}, \mathbf{R}; \hat{\mathbf{k}}, E) \right\rangle \left\langle \psi^-_{v'j'm_{j'}}(\mathbf{r}, \mathbf{R}; \hat{\mathbf{k}}, E) \right| \right\} \\
&\quad \times \vec{\epsilon} \cdot \vec{\mu} | \psi_i \rangle
\end{aligned} \tag{4.18}$$

Inserting Eqs. (4.16) and (4.17) into Eq. (4.18) then yields

$$\sigma_{\text{tot}}(E) = \frac{\pi\nu}{c\,\epsilon_0\hbar}\langle\psi_i|\vec{\epsilon}\cdot\vec{\mu}|\left\{\int_{-\infty}^{\infty} dt \exp\left[\frac{-i(\hat{\mathbf{H}}-E)t}{\hbar}\right]\right\}|\vec{\epsilon}\cdot\vec{\mu}|\psi_i\rangle \tag{4.19}$$

If we now define the ''initial wavepacket'' as

$$|\Phi_i(\mathbf{r},\mathbf{R},t=0)\rangle = \vec{\epsilon}\cdot\vec{\mu}|\psi_i\rangle \tag{4.20}$$

we can reexpress the energy-dependent total photodissociation cross section as

$$\begin{aligned}\sigma_{\text{tot}}(E) &= \frac{\pi\nu}{c\,\epsilon_0\hbar}\langle\Phi_i(\mathbf{r},\mathbf{R},t=0)|\left\{\int_{-\infty}^{\infty} dt \exp\left[\frac{-i(\hat{\mathbf{H}}-E)t}{\hbar}\right]\right\}|\Phi_i(\mathbf{r},\mathbf{R},t=0)\rangle \\ &= \frac{\pi\nu}{c\,\epsilon_0\hbar}\int_{-\infty}^{\infty} dt \exp\left[\frac{iEt}{\hbar}\right]\langle\Phi_i(\mathbf{r},\mathbf{R},t=0)|\exp\left[\frac{-i\hat{\mathbf{H}}t}{\hbar}\right]|\Phi_i(\mathbf{r},\mathbf{R},t=0)\rangle\end{aligned} \tag{4.21}$$

The time-dependent Schrödinger equation is

$$i\hbar\frac{\partial\Phi(t)}{\partial t} = \hat{\mathbf{H}}\Phi(t) \tag{4.22}$$

If the Hamiltonian $\hat{\mathbf{H}}$ does not depend on time, this equation has the analytic solution:

$$\Phi(t) = \exp\left[\frac{-i\hat{\mathbf{H}}t}{\hbar}\right]\Phi(t=0) \tag{4.23}$$

Using Eq. (4.23) in the RHS of Eq. (4.21), we can rewrite the expression for the total absorption cross section as follows:

$$\sigma_{\text{tot}}(E) = \frac{\pi\nu}{c\,\epsilon_0\hbar}\int_{-\infty}^{\infty} dt \exp\left[\frac{iEt}{\hbar}\right]\langle\Phi_i(\mathbf{r},\mathbf{R},t=0)|\Phi_i(\mathbf{r},\mathbf{R},t)\rangle \tag{4.24}$$

The time-dependent quantity in the integrand of Eq. (4.24), $\langle\Phi_i(\mathbf{r},\mathbf{R},t=0)|\Phi_i(\mathbf{r},\mathbf{R},t)\rangle$, is called the *autocorrelation function*. It is the integral over all space of the product of the initial wavepacket with the wavepacket at time t. Rama Krishna and Coalson [86] have shown that the Fourier transform over time in Eq. (4.24) can be replaced by twice the half–Fourier transform where the time integral runs from $t = 0$ to $t = \infty$. Using this result we obtain the final expression:

$$\sigma_{\text{tot}}(E) = \frac{2\pi\nu}{c\,\epsilon_0\hbar}\int_{0}^{\infty} dt \exp\left[\frac{iEt}{\hbar}\right]\langle\Phi_i(\mathbf{r},\mathbf{R},t=0)|\Phi_i(\mathbf{r},\mathbf{R},t)\rangle \tag{4.25}$$

This equation expresses the total absorption cross section as the half–Fourier transform of an autocorrelation function, $\langle\Phi(t=0)|\Phi(t)\rangle$, where the angular brackets indicate integration over all spatial coordinates.

C. The Initial Wavepacket

The initial wavefunction of the molecule, ψ_i in Eq. (4.1), before the absorption of the light is taken to be a pure quantum state or eigenstate of the system, with a well-defined value of the initial total angular momentum J_i and its space-fixed z component M_i [see Eq. (4.9)]. This initial state can be expanded as a linear combination of the parity-adapted total angular momentum eigenfunctions [84] $|J_i, K, M_i, p\rangle$, as defined in Eq. (4.6). The initial wavepacket, $\Phi_i(\mathbf{r}, \mathbf{R}, t=0)$ [Eq. (4.20)], is obtained by multiplying the initial wavefunction by $\vec{\epsilon}\cdot\vec{\mu}$, where $\vec{\epsilon}$ is the electric field polarization vector of the linearly (or circularly) polarised light and $\vec{\mu}$ is the transition dipole moment for the electronic transition involved and depends on the molecular geometry (i.e., on R, r, and θ). Note that $\vec{\epsilon}$ is defined in the space-fixed reference frame and must be rotated to the body-fixed frame using Wigner D matrices. Despite the fact that the direction or sense of the electric field of the lightwave oscillates, the vector $\vec{\epsilon}$ takes on a constant, although maybe arbitrarily defined, direction. For linearly polarized light, this direction defines the space-fixed z axis. The oscillations of the electric field are fully taken into account through the semiclassical theory [77–79] of the interaction of light with matter. The derivation of the detailed form of the initial wavepacket and its relationship to the initial bound-state wavefunction are fully discussed in Ref. 84 [see also the Appendix, Section B (below)]. As expected, from the vector property of the polarization vector of the incident lightbeam, the result is that the initial wavepacket becomes a linear combination of functions with up to three possible values of the total angular momentum, differing from J_i by at most one

$$
\begin{aligned}
\Phi_i(\mathbf{r}, \mathbf{R}, t=0) &= \vec{\epsilon}\cdot\vec{\mu}\,|\psi_i\rangle \\
&= \vec{\epsilon}\cdot\vec{\mu}\sum_{K=\lambda}^{J_i}\psi^{J_i,K_i,p}(r,R,\theta)|J_i,K,M_i,p\rangle \\
&= \sum_{J'=J_i-1}^{J_i+1}(-1)^{m+M_i}\begin{pmatrix} 1 & J_i & J' \\ m & M_i & -(m+M_i)\end{pmatrix} \\
&\quad\times\left\{\sum_{K=\lambda'}^{J'}\Phi_i^{J'K}(r,R,\theta,t=0)|J',K,M_i+m,p'\rangle\right\} \qquad (4.26)
\end{aligned}
$$

where the detailed form of $\Phi_i^{J'K}(r,R,\theta,t=0)$ is given in the Appendix, Section B.

It should be noted that K, which is the z component of the total angular momentum along the body-fixed z axis, is not a good quantum number and in general the initial wavefunction ψ_i will be a linear combination of parity-adapted total angular momentum eigenfunctions corresponding to different values of K but the same J_i. The label m relates to the nature of the space-fixed electric field polarization vector. $m = 0$ denotes linearly polarized light with the electric field vector pointing along the space-fixed z axis, while $m = \pm 1$ corresponds to circularly polarised light, with the space-fixed z axis pointing along the propagation direction of the lightbeam. The parity factor, $(-1)^{p'}$, of the wavefunction for nuclear motion is the same as that of the initial wavefunction if the electronic transition is perpendicular, that is, if the transition dipole moment is perpendicular to the molecular plane and is opposite to the initial parity for a parallel electronic transition.

The functions $\Phi_i^{J'K}(r, R, \theta, t = 0)$ involve a product of the initial wavefunction and the internal coordinate-dependent vector components of the transition dipole moment (see the Appendix, Section B and Ref. 84). As the total angular momentum is a conserved quantity during the time propagation of the wavepacket, we may divide up the initial wavepacket [Eq. (4.26)] into three components, one for each of the allowed values of J'. Thus Eq. (4.26) may be rewritten as

$$\Phi_i(\mathbf{r}, \mathbf{R}, t = 0) = \sum_{J'=J_i-1}^{J_i+1} (-1)^{m+M_i} \begin{pmatrix} 1 & J_i & J' \\ m & M_i & -(m + M_i) \end{pmatrix} \Phi_i^{J'}(\mathbf{r}, \mathbf{R}, t = 0) \tag{4.27}$$

where the function $\Phi_i^{J'}(\mathbf{r}, \mathbf{R}, t = 0)$ corresponds to the curly bracket in Eq. (4.26):

$$\Phi_i^{J'}(\mathbf{r}, \mathbf{R}, t = 0) = \sum_{K=\lambda'}^{J'} \Phi_i^{J'K}(r, R, \theta, t = 0) |J', K, M_i + m, p'\rangle \tag{4.28}$$

and λ' takes on the value of 0 or 1 depending on the parity number p' (see Eq. (4.7)). Each of the wavepackets $\Phi_i^{J'}(\mathbf{r}, \mathbf{R}, t = 0)$ corresponds to a single total angular momentum value J', and each may be propagated forward in time independently of the other component wavepackets.

It should be noted that for values of $J' > 0$ there will be J' or $J' + 1$ different values of K (depending on the value of p') involved in the summation of Eq. (4.28)). The set of body-fixed wavepackets, $\Phi_i^{J'K}(r, R, \theta, t = 0)$, corresponding to the same value of J' but to different values of K, must be propagated together as they are coupled or mixed during the propagation process by the centrifugal coupling [80,93].

If we substitute Eqs. (4.27) and (4.28) into Eq. (4.25), average over the z components of the initial total angular momentum, and sum over the z components of the final total angular momentum, we obtain [84] (note that the proof in Ref. 84 is specialized to the case of linearly polarized light, $m = 0$)

$$\sigma_{\text{tot}}(E) = \frac{2\pi\nu}{3\,c\,\epsilon_0\hbar} \sum_{J'=J_i-1}^{J_i+1} \delta(J', J_i, 1) \times \sum_{K=0}^{J'} \int_0^\infty dt \exp\left[\frac{iEt}{\hbar}\right] \left\langle \Phi_i^{J'K}(r, R, \theta, t=0) | \Phi_i^{J'K}(r, R, \theta, t) \right\rangle \quad (4.29)$$

D. Partial Cross Sections, Product State Distributions, and Differential Cross Sections

Equation (4.25) and its widespread application [1,3,36,43,76,84,87] clearly show that total absorption cross sections may be computed by propagating an initial wavepacket forward in time. The initial wavepacket is localized in space; therefore, by Heisenberg's uncertainty principle, it necessarily contains a range of relative momenta and kinetic energies. This range of initial energies is reflected in the fact that the use of Eq. (4.25) immediately yields the cross section over the full range of energies from a single calculation (i.e., based on the motion of a single wavepacket). The autocorrelation function is a time-dependent function. The Fourier transform of a time-dependent function yields an energy, or frequency, dependent quantity, namely, in this case, the total absorption cross section.

It seems reasonable to suppose that some alternative analysis of the properties of the same time-dependent wavepacket might also yield more detailed information, such as the partial cross sections or the probability of producing different quantum states of the products. This was realized at a very early stage by Kulander and Heller [2], who discuss the evaluation of partial cross sections by projection onto the final scattering states of the system. Related methods have been developed by Kouri and coworkers [88,89] in the context of inelastic scattering and were applied to photodissociation problems at an early stage by the groups of Gray [90] and Schinke [91]. In this section an alternative approach, which is ideally suited for use in conjunction with a grid or discrete-variable representation (DVR) [92] of the final scattering coordinate is presented.

Figure 4.1 shows a schematic of an excited-state potential energy surface and superimposed on it is a wavepacket, which is the initial wavepacket for a photodissociation process. An ''analysis line'' is drawn perpendicular to the contour lines in the asymptotic region of the surface, where there is no longer any substantial interaction between the separating fragments and the contour

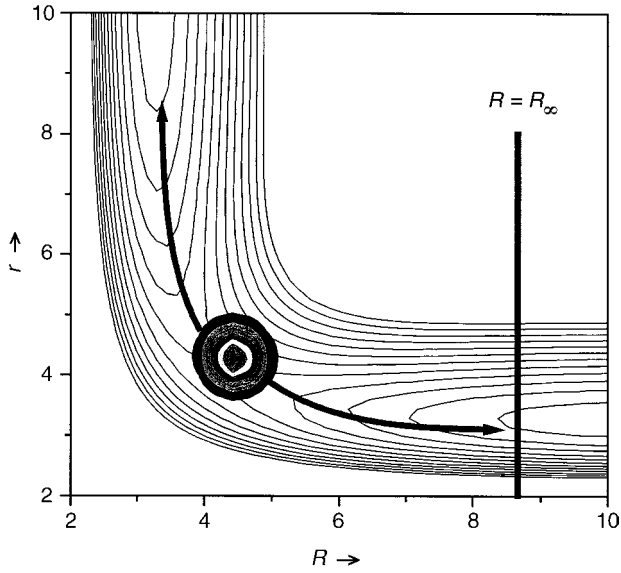

Figure 4.1. Schematic diagram of an excited-state potential energy surface showing an initial wavepacket for a photodissociation calculation and indicatng its path toward the dissociation products. The line marked R_∞ is the "analysis line."

lines have become parallel. This line or surface is drawn at a constant value of the scattering coordinate $R = R_\infty$.

The basic philosophy is that if the wavepacket is analyzed, at each timestep, as it passes by the analysis line, it should be possible to extract from this information all necessary measurable cross sections arising out of the breakup process. The analysis consists in fixing the scattering coordinate at its value on the analysis line ($R = R_\infty$) and then expressing the cut through the wavepacket along this line as a linear combination of fragment eigenfunctions. This yields a set of time-dependent coefficients. The half–Fourier transform of these time-dependent coefficients yields energy-dependent photofragmentation **T** matrix elements in terms of which all the experimentally measurable cross sections may be expressed. The theory is outlined in detail in the Appendix, Section C. The treatment relies in turn on theoretical developments first published in Ref. 75.

The most detailed possible photofragmentation cross section is the detailed final-state resolved differential photofragmentation cross section defined in Eq. (4.12), which measures the probability of the formation of a particular final state, v, j, m_j scattered into a specified scattering direction, $\hat{\mathbf{k}} = \theta_k, \phi_k$. This cross section has been discussed in Ref. 80 in the context of time-independent

theory of photodissociation. In the Appendix, Section C the theory is developed in the context of a time-dependent formalism. The partial differential cross section may be written as [see Eqs. (4.15) and (A.46)]

$$\sigma_{vjm_j}(E;\hat{\mathbf{k}}) = \frac{2\pi^2\nu}{c\,\epsilon_0}\frac{1}{4\pi}\left|\sum_{J=J_i-1}^{J_i+1}\sum_{K}(2J+1)^{1/2}D^{J}_{K,M_i+m}(\phi_k,\theta_k,0)D^{j}_{-K,-m_j}(\phi_k,\theta_k,0)\right.$$
$$\left.\times\begin{pmatrix}1 & J_i & J\\ m & M_i & -(m+M_i)\end{pmatrix}T^{JKp'}_{vj}\right|^2 \tag{4.30}$$

where

$$T^{JKp'}_{vj} = \sum_{K'}\langle\Phi^{-Jvjkp'}_{K'}(r,R,\theta;E)|\Phi^{JK'}_{i}(r,R,\theta,t=0)\rangle \tag{4.31}$$

Equations (4.30) and (4.31) have been developed and defined within a time-dependent framework. These equations are identical to Eqs. (35) and (32), respectively, of Ref. 80. They differ only in that a different, more appropriate, normalization has been used here for the continuum wavefunction and that the transition dipole moment function has not been expanded in terms of a spherical harmonic basis of angular functions. All the analysis given in Ref. 80 continues to be valid. In particular, the details of the angular distributions of the various differential cross sections and the relationships between the various possible integral and differential cross sections have been described in that paper.

The photofragmentation **T** matrix elements in Eq. (4.31) contain all possible information concerning the dynamics of the photodissociation process. In the Appendix, Section C, the time-dependent theory needed for evaluating these centrally important matrix elements is developed. The first step is the calculation of a set of time-dependent coefficients. This is done by fixing the scattering coordinate in the time-dependent wavepacket at its value on the analysis line R_∞, and then multiplying by the fragment eigenfunctions and integrating over all the other coordinates

$$C^{JK}_{vj}(t) = \left\langle \Theta_{jK}(\theta)\chi_{vj}(r)\left|\left\{\sum_{K'}\Phi^{JK'}_{i}(r,R=R_\infty,\theta,t)\right\}\right.\right\rangle \tag{4.32}$$

where the angular brackets $\langle\ \rangle$ indicate integration over the variables r and θ and it is implied that $\Theta_{jK}(\theta)$ on the left of the integral must only be associated with the same value of K on the right. The sum over all the radial wavepackets corresponding to the various different values of K are kept together in Eq. (A.34) because the wavepackets corresponding to these different values interact and amplitude or flux is exchanged between them as time progresses.

We now take the half–Fourier transform of this integral over time to give us an energy-dependent quantity:

$$A_{vj}^{JK}(E) = \frac{1}{2\pi}\int_{t=0}^{\infty} \exp(iEt/\hbar) C_{vj}^{JK}(t) \tag{4.33}$$

In Section C of the Appendix I show that the **T** matrix elements are related to the $A_{vj}^{JK}(E)$ coefficients by

$$T_{vj}^{JKp'} = i(-1)^{K-j} A_{vj}^{JK}(E) \left(\frac{2\pi k_{vj}}{\mu}\right)^{1/2} \left\{\frac{\sqrt{2(1+\delta_{0,K})}}{2}\right\} e^{-ik_{vj}R_{\infty}} \tag{4.34}$$

These equations enable us to compute all the possible photofragmentation cross sections. An example of the use of these equations applied to the photodissociation of HOBr may be found in Ref. 84, and similar applications to electronically nonadiabatic photofragmentation of HF, DF, and HCl can be found in Refs. 76, 97, and 96. Time-dependent methods have been used most recently to compute vector correlations and alignment parameters [98,99]

III. REACTIVE SCATTERING THEORY

As in the case of photodissociation, the quantum theory of reactive molecular scattering was initially entirely based on time-independent scattering theory [4–7,100–123]. There were several early attempts to apply time-dependent quantum theory to reactive scattering processes [124–131]. But the modern era of the field really began with the seminal work of Kosloff et al. [37] and the subsequent application of his grid-based methods to the reactive scattering problem by Neuhauser and Baer and coworkers [45,132]. There have been many developments in the field [93,133–138], and several reviews and a book have been written on the topic [10,139–141]. My aim in the next section will be to outline the basic methods of time-dependent quantum theory used in reactive scattering calculations. While the review will cover many aspects of the theory, it will not cover all the approaches currently in use (as of 2003).

A. Reactant and Product Coordinates

Jacobi coordinates involve the scattering coordinate R, which is the distance between the centers of mass of the two fragments, the internal coordinates of the fragment, and the angles between the fragment axes and the scattering coordinate. Figure 4.2 shows the reactant and product Jacobi coordinates for the atom–diatom reaction $A + BC \rightarrow AB + C$. These coordinates are by far the most convenient because of the simplicity of the form of kinetic energy operator when expressed in these coordinates [80,142]. The figure clearly illustrates one

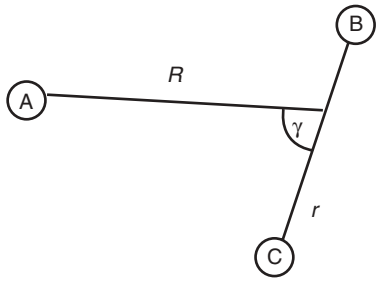

Reactant Jacobi coordinates for A + BC → AB + C

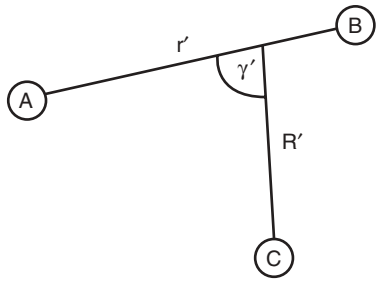

Product Jacobi coordinates for A + BC → AB + C

Figure 4.2. Jacobi coordinates for reactants and products in the reaction A + BC → AB + C.

of the main difficulties bedevilling the quantum theory of chemical reactions [101], namely, that the most appropriate coordinates for expressing the quantum states of the reactants and the products are different. This has a particularly significant effect on time-dependent wavepacket calculations, as in this case the wavefunction of the system spreads over all of coordinate space, and may simultaneously include both reactantlike and productlike nuclear coordinates.

In our work we have approached this problem in two ways. The first was to start the wavepacket motion in reactant Jacobi coordinates, and to propagate the wavepacket inward until the entire wavepacket is in the strongly interacting region. At this stage the wavepacket is transformed to a grid in product Jacobi coordinates. This method [47,132,143] involved setting up an initial wavepacket that was specifically designed to yield a compact wavepacket in the strong interaction part of the coordinate space. This property of the wavepacket assists the process of transforming the wavepacket from a grid specified in terms of reactant coordinates to one defined in terms of product coordinates. This

transformation is in any case difficult and quite computationally demanding. It is also difficult to generalize it to the case $J > 0$. This method has therefore not been generally adopted. The second method we have adopted is to use only one of the two coordinate systems illustrated in Figure 2.4. When we are interested only in the total reaction cross section, we can use reactant Jacobi coordinates [149,150]. In contrast, when information is needed about the product quantum state distribution or state-to-state cross sections, then we have to use product Jacobi coordinates [144]. This creates its own problems because it implies that the initial reactant eigenfunctions must be described in terms of a product coordinate grid, which in turn requires a very fine grid in these coordinates.

An alternative technique for handling this problem is to separate the reactant and product parts of the process. This can be done by creating *source* and *sink* terms to absorb the wavepacket as it leaves the reactant region and to reemit it as a source term in product coordinates in the strong interaction or product region of the potential [136,145]. There is, however, a fundamental problem with this approach in that it implicitly assumes that there will be relatively little recrossing of the chosen dividing line between the reactant and product regions.

B. The Initial Wavepacket

Figure 4.3 shows an initial wavepacket for a reactive scattering calculation superimposed on a potential energy surface for the $Li + HF \rightarrow LiF + H$ reaction. The initial wavepacket is placed in the asymptotic region of the reactant channel, where there is no force between the reactant molecules. It is constructed by calculating the desired initial vibrational–rotational eigenfunctions of the reactant fragments and multiplying the product of these by a one-dimensional wavepacket $g(R)$, where R is the scattering coordinate, which is the distance between the centers of mass of the two reactants. This wavepacket is then multiplied by $\exp[-ikR]$ so as to give it a momentum of magnitude $k\hbar$ toward the strong interaction or reactive region. This leads to an initial wavepacket which is intrinsically complex (in the mathematical sense).

The most common form of the one-dimensional wavepacket in R is a Gaussian wavepacket [133,144]. This wavepacket has a Gaussian shape in both coordinate and momentum space. We have proposed the use of an alternative form of wavepacket, a sinc wavepacket [146,147]. The two forms of wavepacket are shown in Figure 4.4 as a function of initial collision energy for the case of $D + H_2$. In general we will be interested in computing reactive scattering cross sections over a range of initial collision energies. Using the sinc wavepacket, we can see that the amplitude of the wavepacket is roughly constant over most of the energy range of the wavepacket. The Gaussian wavepacket in contrast has a long tail at both high and low energies. This makes it more difficult to determine the energy range covered accurately by the Gaussian wavepacket, as cross sections corresponding to energies associated with a small amplitudes of the

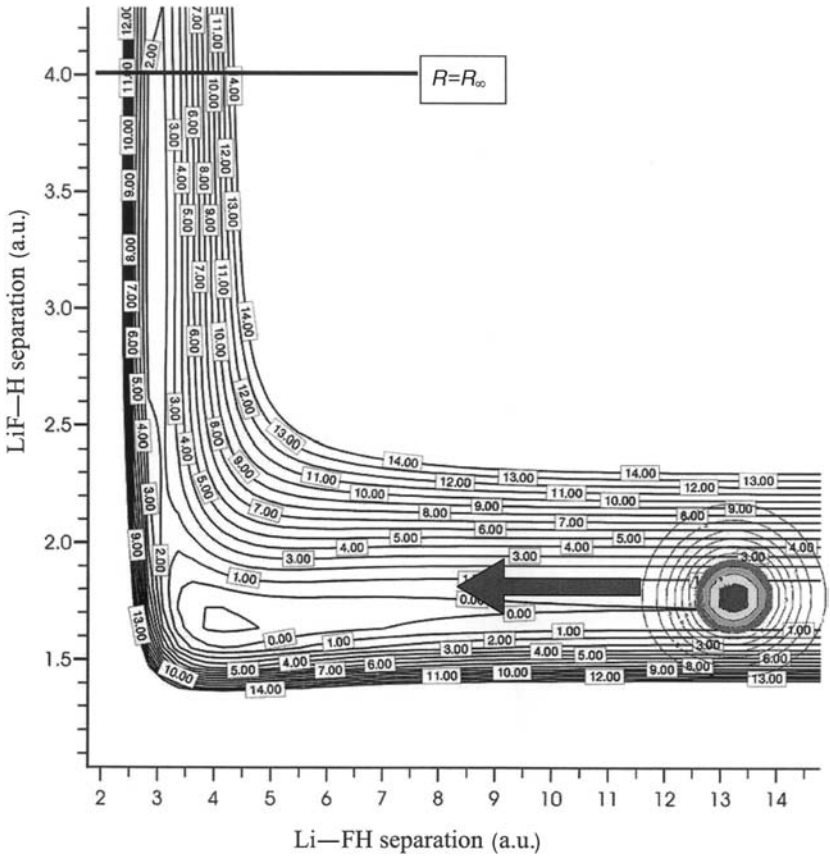

Figure 4.3. The initial wavepacket superimposed on an Li+HF potential energy surface. Also shown (in a schematic manner) is the analysis line, marked R_∞, in the product channel. In an actual calculation the analysis line would be placed at a much larger value of the product scattering coordinate.

initial wavepacket will be subject to greater round-off errors and cannot be considered reliable. In principle, this is certainly the case, but for our typical calculations, which are carried out entirely in double-precision arithmetic, we have not observed a marked numerical benefit from the use of the sinc wavepacket.

C. Analysis of the Wavepacket and Computation of Integral Cross Sections

One of the key aspects of time-dependent reactive scattering theory arises from the conservation of the total energy. This has the consequence that each energy

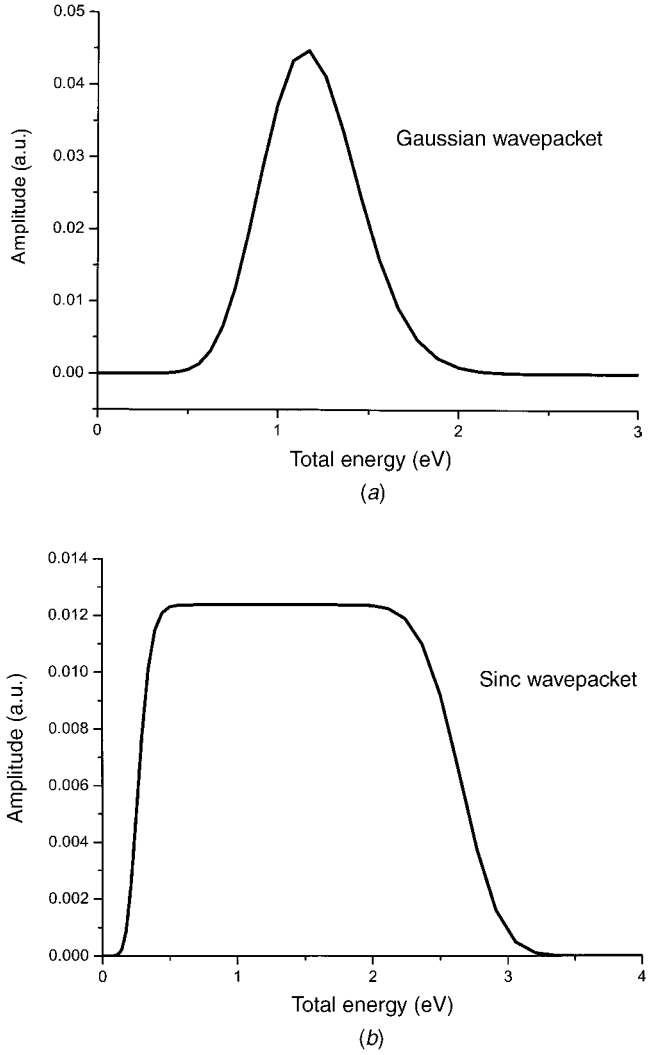

Figure 4.4. One-dimensional wavepackets in the reactant scattering coordinate for use in constructing the initial wavepacket. The wavepackets are shown as a function of the initial translational energy. (*a*) A Gaussian wavepacket; (*b*) a sinc wavepacket.

component of the wavepacket propagates independently. In order to calculate the cross sections, we must therefore know the amplitude of the initial wavepacket with a given energy. Let us denote the initial one-dimensional wavepacket by $g(R)$. The component of this wavepacket with momentum component $-k\hbar$ pointed toward the strong interaction or reactive scattering

region is

$$g(-k) = \frac{1}{2\pi}\int_0^\infty e^{ikR} g(R) dR \tag{4.35}$$

The analysis of the wavepacket proceeds in exactly the same way as described above for the case of photodissociation theory [47,133,148] (see Section II.D). An analysis line is drawn corresponding to a fixed value of the product Jacobi scattering coordinate R' perpendicularly across the exit channel in the the asymptotic region of the potential energy surface (see Figs. 4.1 and 4.3). Specializing the formulas as before to the case of an atom–diatom reaction (i.e., a three-atom system), we may write the body-fixed wavepacket as $\Phi^{JK'}(r', \theta', R', t)$, where the primes on the coordinates indicate the use of product Jacobi coordinates and the wavepackets corresponding to the different K' values are coupled by the propagation dynamics (see below). We must first take a cut through the wavepacket along the analysis line and project this cut through the wavepacket onto the product vibrational–rotational eigenfunctions. This yields a time-dependent coefficient, $C_{v'j'}^{JK'}(t)$:

$$C_{v'j'}^{JK'}(t) = \langle \Theta_{j'K'}(\theta')\, \chi_{v'j'}(r') | \Phi^{JK'}(r', \theta', R' = R'_\infty, t) \rangle \tag{4.36}$$

We then take the half–Fourier transform of this to obtain an energy-dependent quantity, $A_{v'j'}^{JK'}(E)$:

$$A_{v'j'}^{JK'}(E) = \frac{1}{2\pi}\int_0^\infty \exp\frac{iEt}{\hbar} C_{v'j'}^{JK'}(t) dt \tag{4.37}$$

Analysis of Ref. 75 (see also Ref. 133) enables us to relate this to the reactive **S** matrix elements through the expression

$$S^J_{v'j'K',vjK}(E) = -\left(\frac{\hbar^2 k_{vj} k'_{v'j'}}{\mu\mu'}\right)^{1/2} \exp(-ik'_{v'j'}R'_\infty)\frac{A_{v'j'}^{JK'}(E)}{g(-k_{vj})} \tag{4.38}$$

where the primed variables indicate quantities relating to the products and the unprimed to the reactants. Note the presence of the term $g(-k_{vj})$ in the denominator and the fact that the quantum numbers K and K' are associated with the z components of the total angular momentum, referred to as *body-fixed reactant* and *product axes*, respectively. I have purposely included here the initial-state quantum numbers, vjK, which relate to the construction of the initial wavepacket as they will be needed later when we discuss the calculation of differential cross sections.

The total reaction probability for a particular value of the total angular momentum J, averaged over all values of m_j and M for the reactants and summed over all values of $m_{j'}$ and M' for the products, is given by

$$P^J_{\text{react}}(E) = \frac{1}{2j+1} \sum_{v'j'} \sum_{KK'} \left| S^J_{v'j'K',vjK}(E) \right|^2 \tag{4.39}$$

The total integral reactive cross section for reaction from a particular initial state to all possible final states is then given by a summation over all total angular momenta that can contribute to the reaction:

$$\sigma^{\text{tot}}_{\text{all}\leftarrow vj} = \frac{\pi}{k^2_{vj}} \sum_J (2J+1) P^J_{\text{react}}(E) \tag{4.40}$$

1. *Reactant Coordinate Calculations for the Total Reactive Cross Sections*

Calculation of the total reactive cross section does not necessarily require a knowledge of the wavepacket dynamics in the exit channel of the reaction. All that is required is a knowledge of the particle flux that results in the creation of products. This can be accomplished by calculating the flux of particles passing through a plane corresponding to a large constant value of the reactant diatom separation [149–151]. This allows us to use reactant coordinates instead of product coordinates and often greatly simplifies the calculation. It also permits the use of the helicity decoupling or centrifugal sudden approximation [149,150], in which we ignore the coupling between different K components corresponding to a single J value (see discussion below for further details). This important simplifying approximation is much more difficult to justify when there is a transformation from reactant to product coordinates [93].

2. *Capture Model and Total Reactive Cross Sections*

The problem with Eqs. (4.39) and (4.40) is that they require exact calculation of the scattering dynamics and the **S** matrix elements for many values of J. As we will see below, when we discuss the propagation of the wavepacket, the computational effort required for exact $J > 0$ calculations is very great. For $J > 0$, $|K|$ takes on either $(J+1)$ or J values depending on the parity. The wavepackets corresponding to each of these K values will be coupled by the propagation dynamics of the wavepacket. In general, quite large values of J are important for calculation of the total reactive cross section. Thus, in the case of $O(^1D) + H_2$, J values up to 66 were required [144] in one calculation and up to $J = 40$ in another [149,150], while for heavier collision partners much higher values of J are needed [152] [up to $J = 140$ for $N(^2D) + O_2$]. These figures depend, of course, on the range of collision energies covered by the

calculations, but they clearly illustrate that $J > 0$ calculations are far more computationally demanding than $J = 0$ calculations.

The calculation of total reaction cross sections may be greatly simplified by using any one of a family of approximations known as *J-shifting approximations* [155,156]. In this type of approximation the reaction probability is calculated for a limited number of J values, or even just for $J = 0$, and approximate methods are used to estimate the reaction probability for required values of J other than those for which more accurate calculations have been performed. J-shifting approximations rely on the identification of a ''bottleneck'' geometry, such as a transition state. The changes in rotational energy of the system, when fixed at this geometry, provide an energy shift, E_{shift}, which is used in estimating the reaction probabilities:

$$\tilde{P}^{J}_{\text{react}}(E) = P^{J=0}_{\text{react}}(E - E^{J}_{\text{shift}}) \tag{4.41}$$

where $P^{J=0}_{\text{react}}(E)$ is the accurately computed reaction probability for $J = 0$, at the collision energy E, and $\tilde{P}^{J}_{\text{react}}(E)$ is the estimated reaction probability for another value of J.

The J-shifting method depends on our ability to identify a unique bottleneck geometry and is particularly well suited to reactions that have a barrier in the entrance channel. For cases where there is no barrier to reaction in the potential energy surface, a capture model [149,150,152] approach has been developed. In this approach the energy of the centrifugal barrier in an effective one-dimensional potential is used to define the energy shift needed in Eq. (4.41). For the case of $K = 0$, we define the one-dimensional effective potential as (see Ref. 150 for the case of $|K| > 0$)

$$V^{J}_{\text{eff}}(R) = \langle vj|V|vj\rangle + \frac{\hbar^2 J(J+1)}{2\mu R^2} \tag{4.42}$$

where $\langle vj|V|vj\rangle$ is the potential averaged over the initial vibrational–rotational state of the reactants and is a function of the reactant scattering Jacobi coordinate. ϵ_{vj} is the vibrational–rotational energy of the initial state of the diatomic. The effective potential exhibits a centrifugal barrier in the entrance channel. Let V^{J*} be the height of the effective potential barrier corresponding to a total angular momentum quantum number J. In the capture model, the reaction probability is now estimated as

$$\tilde{P}^{J}_{\text{react}}(E) = P^{J=0}_{\text{react}}(E - V^{J*}) \tag{4.43}$$

In both the J-shifting model and the capture model it is assumed that the reaction probabilities are a function of the available energy, which is the energy

in excess of the barrier height. This function of the excess energy is assumed to be universal (i.e., the same for all J values). One can then take the results for some particular J values and use them to define how reaction probability varies as a function of the excess energy.

Rather than using just calculations for $J = 0$ as a basis for approximating reaction probabilities for all higher values of J, we have adopted the technique of calculating reaction probabilities for a reasonably large number of J values, in general using the helicity decoupling approximation [149,153,154], and using capture model techniques to interpolate between the J values for which more accurately computed reaction probabilities are available. Suppose that we have calculated the reaction probability for J_1 and J_2 and that J lies between these two J values ($J_1 < J < J_2$). Then the reaction probability for J can be estimated as

$$\tilde{P}^J_{\text{react}}(E) = P^{J_1}_{\text{react}}\left(E - [V^{J*} - V^{J_1*}]\right)\frac{(J_2 - J)}{(J_2 - J_1)} + P^{J_2}_{\text{react}}\left(E + [V^{J_2*} - V^{J*}]\right)\frac{(J - J_1)}{(J_2 - J_1)} \tag{4.44}$$

For values of J greater than any for which actual dynamical calculations have been performed, the reaction probability may be extrapolated from that calculated for this highest value using the formula

$$\tilde{P}^J_{\text{react}}(E) = P^{J_1}_{\text{react}}\left(E - [V^{J*} - V^{J_1*}]\right) \tag{4.45}$$

where, in this case, J_1 is the highest value of J for which helicity decoupled wavepacket calculations were carried out.

3. *Backward Propagation Method*

The theory used to analyze the wavepacket and to determine the reaction probability requires that the initial wavepacket be placed in the asymptotic region, where there is very little interaction between the reactants [133,151]. This is because we require knowledge of the amplitude of the initial wavepacket associated with a given relative translational energy in this asymptotic region. For large values of the total angular momentum the centrifugal potential is very long-ranged and it is in practice impossible to place the initial wavepacket at sufficiently large separations so as to render the centrifugal potential unimportant. In order to overcome this problem and other problems arising from the intrinsically long-range nature of the potential energy surfaces, we place the initial wavepacket at a large but manageable separation of the reactants, and after calculating an effective potential, as in Eq. (4.42), we propagate the R-dependent part of the initial wavepacket [i.e., $g(R)$ as discussed in Eq. (4.35);

see Section III.B] backward in one dimension. We then analyze the backward-propagated wavepacket and use the resulting momentum distribution in the analysis of the final wavepacket to yield the total reaction probability [133,150,152].

4. *Differential Reactive Cross Sections*

The differential reactive state-to-state cross section may be written in the following form [4,101,103,157]:

$$\sigma_{v',j'\leftarrow v,j}(E,\theta) = \frac{1}{2j+1}\sum_{KK'}\frac{1}{4k_{vj}^2}\left|\sum_J (2J+1)\,S^J_{v'j'K',vjK}(E)\,d^J_{KK'}(\theta)\right|^2 \quad (4.46)$$

As we have given an explicit expression for the **S** matrix in Eq. (4.38), there would seem to be no problem in calculating the reactive differential cross section. This is, however, not entirely true. The problem arises because the definition of the cross section relates to the large R asymptotic form of the wavefunction. Furthermore, the method I have presented for analysis of the wavepacket relies on an analysis line R_∞ drawn in the asymptotic region of the potential. The problem arises, as indicated in Section III.C.3, for larger values of the total angular momentum J. In such cases the centrifugal potential and the centrifugal coupling terms are very long-ranged. The long-range nature of these terms is a result of using the body-fixed coordinate system rather than the space-fixed one [80], and it is essential to transform back to the space-fixed system as part of the process of calculating the **S** matrix elements. This was clearly recognised in the recent reactive wavepacket scattering calculations of Althorpe [136,158,159], and the discussion below borrows heavily from this work and from the Ph.D. thesis of M. Hankel [160].

In the space-fixed axis system the channel quantum numbers for an atom–diatom collision are jl, where j refers to the rotational quantum number of the diatomic and l is the quantum number for the orbital angular momentum of the relative motion of the two fragments. We have ignored the vibrational quantum number for the purposes of this discussion. The part of the Hamiltonian with the longest range, when working in this axis system, is the effective centrifugal repulsion term $[\hbar^2 l(l+1))/2\mu R^2]$. There is no kinetic energy coupling between the different jl channels, and the long-range part of the effective centrifugal repulsion is fully accounted for analytically through the use of the spherical Bessel functions and of their analytic behavior at in the asymptotically large R region [4,161]. In contrast, as we will discuss more explicitly in the next section, the channels are labeled with the quantum numbers jK when body-fixed axes are used, where K is the z component of the total angular momentum with respect to the body-fixed z axis. Rotation to the body-fixed axes simplifies the coupling arising from the potential energy term, but it creates new couplings in the

kinetic energy term [4,80]. Thus there are couplings between different K quantum numbers when the Hamiltonian is expressed in the body-fixed axes. These couplings are, furthermore, very long-ranged and there is no satisfactory means of including them analytically in the scattering formulation [80].

The solution to this problem is to transform, or half-transform, the **S** matrix from the body-fixed to the space-fixed axis system; then to use the known analytic properties of the spherical Bessel functions, which are the solutions to the potential-free scattering problem in the space-fixed axes; and finally to transform back to the body-fixed axes and then to use Eq. (4.46) to calculate the differential cross section.

For a given value of J and the parity p, the first step is to calculate the transformation matrix from the body-fixed jK basis to the space-fixed jl basis. This transformation matrix has in fact already been derived in Eq. (A.17) of the Appendix. Alternatively, the transformation matrix may be computed by using the matrix elements of the kinetic energy operator in the body-fixed axis system. These are just the diagonal and off-diagonal elements of the centrifugal coupling, which we will discuss in more detail below (see also Ref. 80). If we then diagonalize this matrix, the eigenvectors of this matrix form the desired transformation matrix from the body-fixed to the space-fixed bases. This must be the case because the kinetic energy operator is diagonal in the space-fixed basis [162]. We denote this transformation matrix by T^{Jp}_{lK}, where p denotes the parity, $(-1)^{J+K+p} = (-1)^{j+l}$. The **S** matrix in the space-fixed axes may then be written as

$$\begin{aligned} S^{Jp}_{v'j'l',vjl}(E) &= \sum_{KK'} T^{Jp}_{l'K'} S^{J}_{v'j'K',vjK}(E) T^{Jp}_{lK} \\ &= -i^{l-l'} \left(\frac{\hbar^2 k_{vj} k'_{v'j'}}{\mu\mu'} \right)^{1/2} \frac{\exp(-ik'_{v'j'} R'_\infty)}{g(-k_{vj})} \left\{ \sum_{KK'} T^{Jp}_{l'K'} A^{JK'p}_{v'j'K}(E) T^{Jp}_{lK} \right\} \end{aligned} \tag{4.47}$$

where the extra phase factor of $i^{l-l'}$ is discussed below.

As the kinetic energy operator has no off-diagonal elements in the space-fixed axis representation we may more easily correct for the fact that the analysis line is not truly in the asymptotic region as far as the centrifugal representation is concerned. We do this first by subtracting the residual centrifugal repulsion, $l'(l'+1)/(2\mu' R'^2)$, from the radial kinetic energy at the analysis line in the product channel. Thus we use the expression

$$k'_{v'j'} = \sqrt{2\,\mu' \left(E - \left(\varepsilon_{v'j'} + \frac{l'(l'+1)}{2\,\mu' R'^2_\infty} \right) \right)} \tag{4.48}$$

to calculate the wavenumber of the products at the analysis line, which we use in evaluating the **S** matrix elements in Eq. (4.47).

The analysis underlying the evaluation of the **S** matrix elements was formulated for the $J = 0$ (and $l = 0$) case [75] and did not take proper account of the correct asymptotic phases of the spherical Bessel functions [161]. This phase should have been $\exp(-i(k'_{v'j'}R'_\infty - l'\pi/2)$ rather than the phase given in Eq. (4.47). To correct for this omission in both the reactant and product channels, we must multiply by a phase of $\exp(-il'\pi/2) = i^{-l'}$ for the products and i^l for the reactants. These factors are included on the RHS of Eq. (4.47).

After making these adjustments to allow for the fact that the analysis line cannot be located in the region of space where the centrifugal coupling in the body-fixed coordinates is negligible, and also for the fact that the analysis of Ref. 75 did not account for the long-range analytic form of the spherical Bessel functions, the space-fixed **S** matrix of Eq. (4.47) must be transformed back to the body-fixed axes and Eq. (4.46) must be used to compute the state-to-state differential cross sections [136,160].

D. Propagation of the Wavepacket in Time

For an atom–diatom collision the initial wavepacket, in body-fixed coordinates, is defined as [47,133]

$$\Phi^{JK}(R, r, \theta, t = 0) = g(R)\chi_{vj}(r)\Theta_{jK}(\theta) \tag{4.49}$$

where $g(R)$ is the one-dimensional wavepacket in the reactant scattering coordinate (see Section III.B), $\chi_{vj}(r)$ is the initial vibrational wavefunction, and $\Theta_{jK}(\theta)$ is a normalized associated Legendre polynomial that represents the rotational wavefunction of the diatomic in the body-fixed coordinate system.

If reactant coordinates are to be used for the propagation, then this function is propagated forward in time and analyzed [151] after it has reached the product region at large values of r. If state-to-state reactive probabilities and cross sections are required, the initial wavepacket must be transformed to the product Jacobi coordinates and the propagation must be performed in these coordinates. The general form of the transformation from reactant to product Jacobi coordinates is

$$\Phi^{JK'}(R', r', \theta') = \sum_K \Phi^{JK}(R, r, \theta)\, \frac{R'\, r'}{R\, r}\, d^J_{KK'}(\beta) \tag{4.50}$$

but as the initial value of K has been specified by the choice of initial conditions, the summation over K may be omitted, and the equation becomes

$$\Phi^{JK'}(R', r', \theta') = \Phi^{JK}(R, r, \theta)\, \frac{R'\, r'}{R\, r} d^J_{KK'}(\beta) \tag{4.51}$$

where β is the angle between the reactant and product Jacobi scattering coordinates.

Our main concern in this section is with the actual propagation forward in time of the wavepacket. The standard ways of solving the time-dependent Schrödinger equation are the Chebyshev expansion method proposed and popularised by Kossloff [16,18,20,37–40] and the split-operator method of Feit and Fleck [19,163,164]. I will not discuss these methods here as they have been amply reviewed in the references just quoted. Comparative studies [17–19] show conclusively that the Chebyshev expansion method is the most accurate and stable but the split-operator method allows for explicit time dependence in the Hamiltonian operator and is often faster when ultimate accuracy is not required. All methods for solving the time propagation of the wavepacket require the repeated operation of the Hamiltonian operator on the wavepacket. It is this aspect of the propagation that I will discuss in this section.

The action of the Hamiltonian on a wavepacket may be accomplished in many ways. An important decision to make is how the wavepacket will be represented. I will opt here for a grid-based representation of the wavepacket. As elegantly shown by Light et al. [92], when a grid or discrete-variable representation (DVR) method is used, the potential is diagonal and we only need to evaluate it at the specified grid points. In the present discussion we will assume that we are using a uniform evenly spaced grid of points for the radial variables and Gauss-Legendre points for the angular variable. The action of the hamiltonian on the wavepacket may be written as

$$\begin{aligned}\hat{H}\Phi^{JK}(R,r,\theta,t) = &\left\{-\frac{\hbar^2}{2\mu}\frac{\partial^2}{\partial R^2} - \frac{\hbar^2}{2\mu_r}\frac{\partial^2}{\partial r^2}\right\}\Phi^{JK}(R,r,\theta,t)\\ &- \left(\frac{\hbar^2}{2\mu R^2} + \frac{\hbar^2}{2\mu_r r^2}\right)\left\{\frac{1}{\sin\theta}\frac{\partial}{\partial\theta}\sin\theta\frac{\partial}{\partial\theta} - \frac{K^2}{\sin^2\theta}\right\}\Phi^{JK}(R,r,\theta,t)\\ &+ V(R,r,\theta)\Phi^{JK}(R,r,\theta,t) + \left(\frac{\hbar^2}{2\mu R^2}\right)\left(J(J+1) - 2K^2\right)\\ &\times \Phi^{JK}(R,r,\theta,t) - \frac{\hbar^2 C^+_{JK}}{2\mu R^2}\left\{\frac{\partial}{\partial\theta} - K\cot\theta\right\}\Phi^{J(K+1)}(R,r,\theta,t)\\ &- \frac{\hbar^2 C^-_{JK}}{2\mu R^2}\left\{-\frac{\partial}{\partial\theta} - K\cot\theta\right\}\Phi^{J(K-1)}(R,r,\theta,t) \qquad (4.52)\end{aligned}$$

where

$$C^{\pm}_{JK} = \left[J(J+1) - K(K\pm 1)\right]^{1/2} \qquad (4.53)$$

I will now discuss the evaluation of the first two of these terms in some detail.

1. The Radial Terms

The action of the radial differential operator is accomplished through the use of discrete Fourier transforms as proposed by Kosloff [20,37]. If we take the example of the action of the differential operator in the scattering coordinate, then

$$\left\{-\frac{\hbar^2}{2\mu}\frac{\partial^2}{\partial R^2}\right\}\Phi^{JK}(R,r,\theta,t) \tag{4.54}$$

The Fourier transform of the wavepacket over R and its inverse are

$$\Phi^{JK}(k_R,r,\theta,t) = \frac{1}{\sqrt{2\pi}}\int_0^\infty \exp(-ik_R R)\,\Phi^{JK}(R,r,\theta,t)dR \tag{4.55}$$

$$\Phi^{JK}(R,r,\theta,t) = \frac{1}{\sqrt{2\pi}}\int_{-\infty}^\infty \exp(ik_R R)\Phi^{JK}(k_R,r,\theta,t)dk_R \tag{4.56}$$

Substituting Eq. (4.56) into Eq. (4.54), we can write:

$$\begin{aligned}\left\{-\frac{\hbar^2}{2\mu}\frac{\partial^2}{\partial R^2}\right\}\Phi^{JK}(R,r,\theta,t) &= \left\{-\frac{\hbar^2}{2\mu}\frac{\partial^2}{\partial R^2}\right\}\frac{1}{\sqrt{2\pi}}\int_{-\infty}^\infty \exp(ik_R R)\,\Phi^{JK}(k_R,r,\theta,t)dk_R \\ &= \left\{\frac{\hbar^2}{2\mu}\right\}\frac{1}{\sqrt{2\pi}}\int_{-\infty}^\infty k_R^2\exp(ik_R R)\Phi^{JK}(k_R,r,\theta,t)dk_R\end{aligned} \tag{4.57}$$

Now using Eq. (4.55) in the equations above, we obtain

$$\begin{aligned}&\left\{-\frac{\hbar^2}{2\mu}\frac{\partial^2}{\partial R^2}\right\}\Phi^{JK}(R,r,\theta,t) = \left\{\frac{\hbar^2}{2\mu}\right\}\frac{1}{\sqrt{2\pi}}\int_{-\infty}^\infty k_R^2\exp(ik_R R)\,\Phi^{JK}(k_R,r,\theta,t)dk_R \\ &= \left\{\frac{\hbar^2}{2\mu}\right\}\frac{1}{\sqrt{2\pi}}\int_{-\infty}^\infty k_R^2\exp(ik_R R)\left\{\frac{1}{\sqrt{2\pi}}\int_0^\infty \exp(-ik_R R')\,\Phi^{JK}(R',r,\theta,t)dR'\right\}dk_R\end{aligned} \tag{4.58}$$

We can describe the mathematics in the above process as follows:

1. Fourier-transform the wavepacket over R.
2. Multiply by $-\frac{\hbar^2 k_R^2}{2\mu}$
3. Back-Fourier-transform.

All of these operations may be performed very simply. The radial differential operator in r is treated in exactly the same manner as described above.

2. *First Angular Term*

We now turn our attention to the first angular term in Eq. (4.52):

$$-\left(\frac{\hbar^2}{2\mu R^2}+\frac{\hbar^2}{2\mu_r r^2}\right)\left\{\frac{1}{\sin\theta}\frac{\partial}{\partial\theta}\sin\theta\frac{\partial}{\partial\theta}-\frac{K^2}{\sin^2\theta}\right\}\Phi^{JK}(R,r,\theta,t) \tag{4.59}$$

In order to perform this operation, we expand the wavepacket in terms of normalized associated Legendre polynomials

$$\Phi^{JK}(R,r,\theta,t)=\sum_j \Phi_j^{JK}(R,r,t)\Theta_{jK}(\theta) \tag{4.60}$$

and use the fact that the associated Legendre polynomials are eigenfunctions of the operator in Eq. (4.59):

$$-\left(\frac{\hbar^2}{2\mu R^2}+\frac{\hbar^2}{2\mu_r r^2}\right)\left\{\frac{1}{\sin\theta}\frac{\partial}{\partial\theta}\sin\theta\frac{\partial}{\partial\theta}-\frac{K^2}{\sin^2\theta}\right\}\Theta_{jK}(\theta)=\hbar^2 j(j+1)\Theta_{jK}(\theta) \tag{4.61}$$

In practice we represent the wavepacket on an angular grid. We follow the DVR philosophy of Light et al. [92] as extended by Leforestier [165] and by Corey and Lemoine [166]. These authors show how we can use a single set of angular Gauss–Legendre grid points for all values of K. The method we use is explained more fully in Ref. 87. For convenience, we include a weighting of $\sqrt{w_\alpha}$ in the grid representation of the wavepacket, where $w_\alpha=\sin\theta_\alpha$ are the Gauss–Legendre weights and θ_α are the grid points. The grid representation for the wavepacket, $\bar{\Phi}^{JK}(R_i,r_j,\theta_\alpha,t)$, is therefore

$$\bar{\Phi}^{JK}(R_i,r_j,\theta_\alpha,t)=\sqrt{w_\alpha}\Phi^{JK}(R_i,r_j,\theta_\alpha,t) \tag{4.62}$$

The normalised associated Legendre functions constitute our fixed basis representation (FBR) [92]. The transformation matrix from the DVR to the FBR representation is given by

$$T_{j\alpha}^K=\sqrt{w_\alpha}\Theta_{jK}(\theta_\alpha) \tag{4.63}$$

Using these equations, we can write one term in the expansion of the wavepacket in terms of the associated Legendre polynomials [Eq. (4.60)] as

$$\Phi_j^{JK}(R_i,r_j,t)\Theta_{jK}(\theta)=\sum_\alpha T_{j\alpha}^K\bar{\Phi}^{JK}(R_i,r_j,\theta_\alpha,t) \tag{4.64}$$

Armed with these equations, our strategy is as follows:

1. Use Eq. (4.64) to transform from the DVR representation to the expansion of the wavepacket over the FBR basis.
2. Use the analytic properties of the FBR basis to act with the Hamiltonian on the wavepacket, that is, multiply by $j(j+1)\hbar^2$.
3. Backtransform the resultant function using the orthogonal transformation matrix of Eq. (4.63).

The general philosophy is in fact identical to that used for the radial variables. The reader is referred to Ref. 87 for further details of the manner in which the operation of the Hamiltonian operator on the wavepacket is accomplished.

E. The Grid and the Absorbing Potential

In both photodissociation and reactive scattering theory the wavepacket is eventually propagated to large values of the scattering coordinate. As we are forced to use finite-sized grids for numerical reasons, the problem arises as to what is to be done with the wavepacket when it approaches the edge of the grid. If Fourier transforms are used to compute the action of the radial derivatives in the Hamiltonian operator, then serious errors will arise if the wavepacket is allowed to reach the edge of the grid. This arises from the fact that the Fourier transform method implicitly assumes a cyclic boundary condition and, if the function is nonzero at the grid edge, it will be reflected to the opposite side of the grid, causing well-documented "aliasing" problems [167]. It is therefore imperative that something be done to prevent the wavefunction reaching the grid edge.

Arbitrarily setting the wavepacket to zero at some large value of the scattering coordinate is not an acceptable solution, because this would cause reflection waves that would impact on the wavepacket in the physically important inner region of coordinate space. Therefore the crucial criterion for handling this problem is that any alteration of the wavepacket must be sufficiently gentle so as not to change the computed values of the physical observables of interest. But at the same time no part of the wavepacket must be allowed to reach the edge of the grid.

There are two general methods for addressing this problem. The first is the "gobbler" method, which involves multiplying the part of the wavepacket near the edges of the grid, at each timestep, by a positive function which is smaller than unity and which will generally decrease toward grid edge [43,48,90, 168,169]. The other is the "negative imaginary potential" (NIP) method, in which a negative imaginary potential, which is nonzero only in an absorbing region close to the grid edge, is added to the potential. This method has a long tradition within scattering theory and was previously known as the "optical potential" method [170,171]. It has been popularized within the context of

time-dependent and time-independent scattering theory through the work of Neuhauser and Bear [172,173]. Several papers have been written suggesting optimal forms and parameterisations for the NIPs [17,40,131,174–178] and discussing the effectiveness of different functional forms of the negative imaginary potentials [177,179].

In general we use a complex absorbing potential of the form

$$V_{\text{damp}}(R) = \begin{cases} 0.0 & ; \quad R < R_{\text{damp}} \\ -iA_{\text{damp}}\left(\frac{R-R_{\text{damp}}}{R_{\text{max}}-R_{\text{damp}}}\right)^{n_{\text{damp}}} & ; \quad R_{\text{damp}} \leq R \leq R_{\text{max}} \end{cases} \tag{4.65}$$

where n_{damp} is set equal to 2 or 3, and we choose the parameters A_{damp} and R_{damp} in accordance with the recommendations given in Refs. 177 and 178.

There have also been attempts to find optimal complex (as opposed to purely imaginary) absorbing potentials [180–182] and to relate these to the gobbler method [183]. Manolopoulos [184] has proposed a very interesting simple potential of this type that guarantees zero transmission of the wavepacket. The main practical problem with absorbing potentials is that it is very difficult to find appropriate potentials that can absorb a component of a wavepacket with a low translational energy, and therefore a long wavelength. This is at present the major challenge to the wavepacket theory of reactive scattering (see, however, Ref. 148, where stable threshold reactive scattering probabilities were successfully computed).

F. The Real Wavepacket Method

The initial wavepacket, described in Section III.B is intrinsically complex (in the mathematical sense). Furthermore, the solution of the time-dependent Schrödinger equation [Eq. (4.23)] also involves an intrinsically complex time evolution operator, $\exp(-i\hat{\mathbf{H}}t/\hbar)$. It therefore seems reasonable to assume that all the numerical operations involved with generating and analyzing the time-dependent wavefunction will involve complex arithmetic. It therefore comes as a surprise to realize that this is in fact not the case and that nearly all aspects of the calculation can be performed using entirely real wavefunctions and real arithmetic. The theory of the *real wavepacket method* described in this section has been developed by S. K. Gray and the author [133].

Consider the propagation of a wavepacket forward in time, from time t to $(t+\tau)$ [see Eq. (4.23)]:

$$\begin{aligned} \Phi(t+\tau) &= \exp\left[\frac{-i\hat{\mathbf{H}}\tau}{\hbar}\right]\Phi(t) \\ &= \cos\left[\frac{\hat{\mathbf{H}}\tau}{\hbar}\right]\Phi(t) - i\sin\left[\frac{\hat{\mathbf{H}}\tau}{\hbar}\right]\Phi(t) \end{aligned} \tag{4.66}$$

The corresponding expression for the back propagation, from t to $t-\tau$ is

$$\Phi(t-\tau)=\cos\left[\frac{\hat{\mathbf{H}}\tau}{\hbar}\right]\Phi(t)+i\sin\left[\frac{\hat{\mathbf{H}}\tau}{\hbar}\right]\Phi(t) \tag{4.67}$$

By adding Eqs. (4.66) and (4.67), we obtain:

$$\Phi(t+\tau)=-\Phi(t-\tau)+2\cos\left[\frac{\hat{\mathbf{H}}\tau}{\hbar}\right]\Phi(t) \tag{4.68}$$

This equation is exact and constitutes an iterative equation equivalent to the time-dependent Schrödinger equation [185,186]. The iterative process itself does not involve the imaginary number i; therefore, if $\Phi(t)$ and $\Phi(t-\tau)$ were the real parts of the wavepacket, then $\Phi(t+\tau)$ would also be real and would be the real part of the exact wavepacket at time $(t+\tau)$. Thus, if $\Phi(t)$ is complex, we can use Eq. (4.68) to propagate the real part of $\Phi(t)$ forward in time without reference to the imaginary part.

In Ref. 133 we show that all the observable cross sections and reaction probabilities may be obtained from an analysis of the real part of the wavepacket, with no reference to the imaginary part. The analysis itself is identical to that described in Section III.C, but when the real part of the wavepacket is used to compute $A_{v'j'}^{JK'}(E)$ in Eq. (4.38), we must multiply by an extra factor of 2.

The iterative relationship in Eq. (4.68) is still very difficult to apply, just as much so in fact as the original form of the evolution operator [Eq. (4.23)]. The relationship can be dramatically simplified by applying a functional mapping of the Hamiltonian. The presence of the cosine term in Eq. (4.68) suggests an inverse cosine type of mapping. If such a mapping is to be used, it is necessary to ensure that it is single-valued. So the next step is to shift and scale the Hamiltonian operator in exactly the same way as in the Chebyshev expansion of the evolution operator [20,37,133]. This shifting and scaling ensures that the spectrum (or eigenvalues) of the Hamiltonian falls entirely within the range $(-1,1)$. The shifted and scaled Hamiltonian, $\hat{\mathbf{H}}_s$, is then subject to the following mapping:

$$f(\hat{\mathbf{H}}_s)=-\frac{\hbar}{\tau}\cos^{-1}(\hat{\mathbf{H}}_s) \tag{4.69}$$

The use of this mapping means that we are no longer solving the time-dependent Schrödinger equation, but rather a modified equation of the form:

$$i\hbar\frac{\partial\Phi_f(t)}{\partial t}=f(\hat{\mathbf{H}}_s)\,\Phi_f(t) \tag{4.70}$$

where a subscript f has been placed on the wavefunction to emphasize that it is the solution of a mapped equation rather than of the original time-dependent Schrödinger equation. The same arguments that led to the iterative equation, Eq. (4.68), now lead to the simplified form:

$$\Phi_f(t+\tau) = -\Phi_f(t-\tau) + 2\,\hat{\mathbf{H}}_s\Phi_f(t) \tag{4.71}$$

In Ref. 133 we showed that analysis of the real part of $\Phi_f(t)$, the solution of the mapped Schrödinger equation, can yield all the observable cross sections. We also showed that the arbitrary timestep τ cancels out in all expressions for the cross sections and can effectively be set to unity, namely, $\tau = 1$.

In order to carry out the iteration process in Eq. (4.71), we need the wavepacket at two previous iterations (i.e., at $t-\tau$ and at t). If the initial wavepacket is taken to be $\Phi_f(t-\tau)$, the mapped version of Eq. (4.66)

$$\Phi_f(t) = \hat{\mathbf{H}}_s\Phi_f(t-\tau) - i\sqrt{1-\hat{\mathbf{H}}_s^2}\Phi_f(t-\tau) \tag{4.72}$$

can be used to find $\Phi(t)$, where the operator $\sqrt{1-\hat{\mathbf{H}}_s^2}$ is evaluated using a Chebyshev expansion [187]:

$$\sqrt{1-\hat{\mathbf{H}}_s^2} = \frac{2}{\pi}\left[1 - 2\sum_{s=1}^{s_{\max}}(4s^2-1)^{-1}T_{2s}(\hat{\mathbf{H}}_s)\right] \tag{4.73}$$

where $T_{2s}(x)$ is a Chebyshev polynomial of the first kind.

Taken together, the use of the real part of the wavepacket and the mapping of the time-dependent Schrödinger equation lead to a very significant reduction of the computational work needed to accomplish the calculation of reactive cross sections using wavepacket techniques.

To summarize, a real wavepacket calculation proceeds as follows:

1. Define an initial complex wavepacket, $\Phi^{JK'}(r', \theta', R', t=0)$, as described in Section III.B.
2. Use Eq. (4.72) to obtain the complete wavepacket after the first iteration at $t = \tau$, $\Phi^{JK'}(r', \theta', R', t=\tau)$.
3. Use Eq. (4.68) to propagate the real part of $\Phi^{JK'}(r', \theta', R', t)$ forward in time. For $D + H_2$, 1000–1500 iterations are reqired [133]; while for a system such as $N + O_2$, about 40,000 iterations are required [152].
4. The analysis proceeds as in section IIIC, except that iteration numbers are used in performing a discrete Fourier transform rather than a trapezoid rule integration over time.

Techniques similar to the those described in this section and in Ref. 133, but used within a time-independent framework, have been developed by Kouri and coworkers [188,189] and by Mandelshtam and Taylor [62,63]. Kroes and Neuhauser [65–68] have used the methods developed in these papers to perform time-independent wavepacket calculations using only real arithmetic. The iterative equation that lies at the heart of the real wavepacket method, Eq. (4.68), is in fact simply the Chebyshev recursion relationship [187]. This was realized by Guo, who developed similar techniques based on Chebyshev iterations [50,51].

IV. CONCLUSIONS

The review has discussed some of the methods underlying the use of wavepackets in molecular dynamics. This field, which was initially popularized through the work of Heller [1–3], has now reached maturity and is probably the main technique currently used in the quantum theory of photodissociation and reactive scattering. I have not attempted to cover every aspect of the field or to list the vast number of applications in the literature. Nor have I done justice to the areas of multiconfiguration time-dependent Hartree (MCTDH) theory [190–193] or to that of collisions with surfaces [135,194–198], to name only two areas inadequately covered in this review. The review has instead focused on some of the basic aspects of time-dependent wavepacket theory. To make the discussion more specific, and so as to avoid generalizations, I have concentrated on the photodissociation of triatomic molecules and on atom–diatom reactive scattering collisions. Many aspects of the theory discussed within this context apply quite generally also to larger systems.

Time-independent and time-dependent theories are not really separate disciplines. This should be clear from the work of Kouri [188,189] and Althorpe [136,158], who use time-independent wavepacket techniques. These are easily derived from the more natural time-dependent versions by Fourier transforming the propagator over time. This is equivalent to transforming from the time domain to the energy domain at the beginning rather than the end of the calculation.

The first part of the review deals with aspects of photodissociation theory and the second, with reactive scattering theory. Three appendix sections are devoted to important technical details of photodissociation theory, namely, the detailed form of the parity-adapted body-fixed scattering wavefunction needed to analyze the asymptotic wavefunction in photodissociation theory, the definition of the initial wavepacket in photodissociation theory and its relationship to the initial bound-state wavepacket, and finally the theory of differential state-specific photofragmentation cross sections. Many of the details developed in these appendix sections are also relevant to the theory of reactive scattering.

Key topics covered in the review are the analysis of the wavepacket in the exit channel to yield product quantum state distributions, photofragmentation **T** matrix elements, state-to-state **S** matrices, and the real wavepacket method, which we have applied only to reactive scattering calculations.

Exciting new developments, not discussed in the review are the extension of time-dependent wavepacket reactive scattering theory to full dimensional four-atom systems [137,199–201], the adaptation of the codes to use the power of parallel computers [202], and the development of new computational techniques for acting with the Hamiltonian operator on the wavepacket [138].

Perhaps the most problematic area for the wavepacket theory of reactive scattering is the treatment of the reactive scattering probabilities close the threshold, where the wavelength of the relative translational motion of the products is extremely large and it is very difficult to absorb the wavepacket near the edge of the grid. This problem provides a strong motivation for developing improved absorbing potentials [184].

Acknowledgments

I would like to thank my many colleagues and friends who have collaborated with me over many years for their essential part in developing the methods outlined in this chapter. In particular I thank Alex Brown, Richard N. Dixon, László Füsti-Molnár, Simon C. Givertz, Stephen K. Gray, Marlies Hankel, Clay C. Marston, Alison Offer, and Moshe Shapiro, for their long and close collaboration.

APPENDIX

A. Body-Fixed Form of Scattering Wavefunction

This section of the appendix is based on Appendix B of Ref. 80. It outlines the transformation of the space-fixed form of the continuum wavefunction, Eq. (4.3), to a body-fixed form. It differs from the previous development in that the angular functions used in the final equations are all parity-adapted.

The plane wave appearing in Eq. (4.3) may be expanded as follows [81]:

$$e^{i\mathbf{k}\cdot\mathbf{R}} = 4\pi \sum_{lm_l} i^l Y^*_{lm_l}(\hat{\mathbf{k}}) Y_{lm_l}(\hat{\mathbf{R}}) j_l(k_{vj}R) \tag{A.1}$$

In Eq. (4.3) the plane wave is multiplied by the internal rotational wavefunction $Y_{jm_j}(\hat{\mathbf{r}})$. Multiplying Eq. (A.1) by this function, we obtain

$$e^{i\mathbf{k}\cdot\mathbf{R}} Y_{jm_j}(\hat{\mathbf{r}}) = 4\pi \sum_{lm_l} i^l Y^*_{lm_l}(\hat{\mathbf{k}}) \left\{ Y_{lm_l}(\hat{\mathbf{R}}) Y_{jm_j}(\hat{\mathbf{r}}) \right\} j_l(k_{vj}R) \tag{A.2}$$

The term in curly brackets in this equation can be rewritten in terms of total angular momentum eigenfunctions, $\mathscr{Y}^{JM}_{jl}(\hat{\mathbf{R}}, \hat{\mathbf{r}})$, which are obtained by coupling

the angular functions $Y_{lm_l}(\hat{\mathbf{R}})$ and $Y_{jm_j}(\hat{\mathbf{r}})$:

$$Y_{lm_l}(\hat{\mathbf{R}})Y_{jm_j}(\hat{\mathbf{r}}) = \sum_{JM} \mathscr{Y}_{jl}^{JM}(\hat{\mathbf{R}},\hat{\mathbf{r}})(jlJM|jm_jlm_l) \tag{A.3}$$

Substituting into Eq. (A.2), we obtain

$$e^{i\mathbf{k}\cdot\mathbf{R}}Y_{jm_j}(\hat{\mathbf{r}}) = 4\pi \sum_{JM}\sum_{lm_l} Y_{lm_l}^{*}(\hat{\mathbf{k}})(jlJM|jm_jlm_l)\mathscr{Y}_{jl}^{JM}(\hat{\mathbf{R}},\hat{\mathbf{r}})i^l j_l(k_{vj}R) \tag{A.4}$$

Comparing this with the form of the scattering wavefunction given in Eq. (4.3), we can write the scattering wavefunction in the following form:

$$\begin{aligned}\psi_{vjm_j}^{-}(\mathbf{r},\mathbf{R};\hat{\mathbf{k}},E) = &\left(\frac{\mu k_{vj}}{\hbar^2(2\pi)^3}\right)^{1/2} 4\pi \sum_{JM}\sum_{lm_l} Y_{lm_l}^{*}(\hat{\mathbf{k}})(jlJM|jm_jlm_l) \\ &\times \sum_{l'v'j'} i^l \frac{F_{v'j'l'}^{(Jvjl)}(R)}{R}\mathscr{Y}_{j'l'}^{JM}(\hat{\mathbf{R}},\hat{\mathbf{r}})\chi_{v'j'}(r)\end{aligned} \tag{A.5}$$

The total angular momentum eigenfunctions, $\mathscr{Y}_{jl}^{JM}(\hat{\mathbf{R}},\hat{\mathbf{r}})$, have parity $(-1)^{j+l}$; therefore, the summation in Eqs. (A.4) and (A.5) extends over both positive and negative parities. The function $F_{v'j'l'}^{(Jvjl)}(R)$ is the space-fixed radial scattering function. It obeys the following boundary conditions:

$$\begin{aligned}F_{v'j'l'}^{(Jvjl)}(R) &\underset{R\to 0}{\sim} 0 \\ &\underset{R\to\infty}{\sim} \left(\frac{1}{2ik_{vj}}\right)\left\{e^{i(k_{vj}-l\pi/2)}\delta_{vv'}\delta_{jj'}\delta_{ll'} - S_{vjl,v'j'l'}^{J*}\left(\frac{k_{vj}}{k_{v'j'}}\right)^{1/2} e^{-i(k_{v'j'}-l'\pi/2)}\right\}\end{aligned} \tag{A.6}$$

In the absence of any scattering, $S_{vjl,v'j'l'}^{J*} = \delta_{v,v'}\delta_{j,j'}\delta_{l,l'}$ and the right-hand side (RHS) of Eq. (A.5) reduces to $e^{i\mathbf{k}\cdot\mathbf{R}}Y_{jm_j}(\hat{\mathbf{r}})\chi_{v'j'}(r)$. We will want to work in a body-fixed frame [4], where the scattering channels will be specified by the quantum numbers jK (i.e., the rotational quantum number of the diatomic and the body-fixed z component of its angular momentum) rather than jl as is the space-fixed frame.

In order to transform to the body-fixed representation, we will need to relate the angular functions $\mathscr{Y}_{jl}^{JM}(\hat{\mathbf{R}},\hat{\mathbf{r}})$ to angular functions defined relative to the body-fixed axes [i.e.,$|J,K,M,p\rangle\Theta_{jK}(\theta)$, where $|J,K,M,p\rangle$ are the parity-adapted total angular momentum eigenfunctions of Eq. (4.5) and $\Theta_{jK}(\theta)$ are the normalized associated Legendre polynomials of the body-fixed Jacobi angle].

The function $\mathscr{Y}_{jl}^{JM}(\hat{\mathbf{R}},\hat{\mathbf{r}})$ can be defined by using the inverse of Eq. (A.3):

$$\mathscr{Y}_{j'l'}^{JM}(\hat{\mathbf{R}},\hat{\mathbf{r}}) = \sum_{m_{l'}m_{j'}} Y_{l'm_{l'}}(\hat{\mathbf{R}})Y_{j'm_{j'}}(\hat{\mathbf{r}})(j'm_{j'}l'm_{l'}|j'l'JM) \tag{A.7}$$

If we now rotate the axis system for the two functions on the RHS of the equation so that they are referred to the body-fixed, rather than space-fixed, z axes, we can write

$$\begin{aligned} Y_{l'm_{l'}}(\hat{\mathbf{R}}) &= Y_{l'0}(0,0)D^{l'}_{0m_{l'}}(\omega) \\ &= \left(\frac{2l'+1}{4\pi}\right)^{1/2} D^{l'}_{0m_{l'}}(\omega) \end{aligned} \tag{A.8}$$

where we have explicitly utilized the fact that the orbital angular momentum l' is by definition perpendicular to the body-fixed z axis $\hat{\mathbf{R}}$, and consequently its body-fixed z component is zero.

Also

$$\begin{aligned} Y_{j'm_{j'}}(\hat{\mathbf{r}}) &= \sum_K Y_{j'K}(\theta,0)D^{j'}_{Km_{j'}}(\omega) \\ &= \left(\frac{1}{2\pi}\right)^{1/2} \sum_K \Theta_{j'K}(\theta)D^{j'}_{Km_{j'}}(\omega) \end{aligned} \tag{A.9}$$

where the body-fixed axis system is oriented so that the axis of the diatomic molecules lies in the zx plane, and $\Theta_{j'K}(\theta)$ is a normalized associated Legendre polynomial.

Substituting Eqs. (A.8) and (A.9) back into Eq. (A.7), we obtain

$$\mathscr{Y}_{j'l'}^{JM}(\hat{\mathbf{R}},\hat{\mathbf{r}}) = \left(\frac{2l'+1}{8\pi^2}\right)^{1/2} \sum_K \left\{ \sum_{m_{l'}m_{j'}} D^{l'}_{0m_{l'}}(\omega)D^{j'}_{Km_{j'}}(\omega)(j'm_{j'}l'm_{l'}|j'l'JM) \right\} \Theta_{j'K}(\theta) \tag{A.10}$$

We may now use the following relationship (see Ref. 82, Eqs. 4.3.1, 4.3.4, and 3.5.16):

$$\begin{aligned} &\left\{ \sum_{m_{l'}m_{j'}} D^{l'}_{0m_{l'}}(\omega)D^{j'}_{Km_{j'}}(\omega)(j'm_{j'}l'm_{l'}|j'l'JM) \right\} \\ &= D^{J}_{KM}(\omega)(j'l'JK|j'Kl'0) = D^{J}_{KM}(\omega)(-1)^{j'-K}\left(\frac{2J+1}{2l'+1}\right)^{1/2} \times (Jj'l'0|JKj'-K) \end{aligned} \tag{A.11}$$

Substituting this into Eq. (A.10), we now obtain

$$\mathscr{Y}^{JM}_{j'l'}(\hat{\mathbf{R}},\hat{\mathbf{r}}) = \left(\frac{2J+1}{8\pi^2}\right)^{1/2} \sum_{K=-J}^{J} D^{J}_{KM}(\omega)(-1)^{j'-K}(Jj'l'0|JKj'-K)\Theta_{j'K}(\theta) \tag{A.12}$$

In order to cast the RHS in terms of parity-adatpted functions, we now need to restrict the summation to positive values of K:

$$\begin{aligned}
\mathscr{Y}^{JM}_{j'l'}(\hat{\mathbf{R}},\hat{\mathbf{r}}) &= \left(\frac{2J+1}{8\pi^2}\right)^{1/2} \sum_{K=0}^{J} \Big\{ D^{J}_{KM}(\omega)(-1)^{j'-K}(Jj'l'0|JKj'-K)\Theta_{j'K}(\theta) \\
&\quad + D^{J}_{-KM}(\omega)(-1)^{j'+K}(Jj'l'0|J-Kj'K)\Theta_{j'-K}(\theta)\Big\}\left(\frac{1}{1+\delta_{0,K}}\right) \\
&= \left(\frac{2J+1}{8\pi^2}\right)^{1/2} \sum_{K=0}^{J} \Big\{ D^{J}_{KM}(\omega)(-1)^{j'-K}(Jj'l'0|JKj'-K) \\
&\quad + D^{J}_{-KM}(\omega)(-1)^{j'+2K}(Jj'l'0|J-Kj'K)\Big\}\Theta_{j'K}(\theta)\left(\frac{1}{1+\delta_{0,K}}\right) \\
&= \left(\frac{2J+1}{8\pi^2}\right)^{1/2} (-1)^{j'} \sum_{K=0}^{J} (-1)^{-K}\Big\{ D^{J}_{KM}(\omega) + (-1)^{3K+J+j'-l} D^{J}_{-KM}(\omega)\Big\} \\
&\quad \times (Jj'l'0|JKj'-K)\Theta_{j'K}(\theta)\left(\frac{1}{1+\delta_{0,K}}\right)
\end{aligned} \tag{A.13}$$

Note that we have used the symmetry properties $\Theta_{j'-K}(\theta) = (-1)^{K}\Theta_{j'K}(\theta)$ (see Ref. 82, Eqs. 2.5.18 and 2.5.26) and $(Jj'l'0|JKj'-K) = (-1)^{J+j'-l'}(Jj'l'0|J-Kj'K)$ (see Ref. 82, Eq. 3.5.17).

We now use the fact that the space-fixed functions $\mathscr{Y}^{JM}_{j'l'}(\hat{\mathbf{R}},\hat{\mathbf{r}})$ have parity $(-1)^{p} = (-1)^{j'+l'}$. We can therefore multiply the second Wigner D matrix element in the curly bracket in Eq. (A.11) by $1 = (-1)^{p-j'-l'}$. This yields

$$\begin{aligned}
\mathscr{Y}^{JM}_{j'l'}(\hat{\mathbf{R}},\hat{\mathbf{r}}) &= \left(\frac{2J+1}{8\pi^2}\right)^{1/2} (-1)^{j'} \sum_{K=0}^{J} (-1)^{-K}\Big\{ D^{J}_{KM}(\omega) + (-1)^{3K+J-2l'+p} D^{J}_{-KM}(\omega)\Big\} \\
&\quad \times (Jj'l'0|JKj'-K)\left(\frac{1}{1+\delta_{0,K}}\right)\Theta_{j'K}(\theta)
\end{aligned} \tag{A.14}$$

We now assume that $(-1)^{2K-2l'} = 1$, which leads to

$$\begin{aligned}
\mathscr{Y}^{JM}_{j'l'}(\hat{\mathbf{R}},\hat{\mathbf{r}}) &= \left(\frac{2J+1}{8\pi^2}\right)^{1/2} (-1)^{j'} \sum_{K=0}^{J} (-1)^{-K}\Big\{ D^{J}_{KM}(\omega) + (-1)^{J+K+p} D^{J}_{-KM}(\omega)\Big\} \\
&\quad \times (Jj'l'0|JKj'-K)\left(\frac{1}{1+\delta_{0,K}}\right)\Theta_{j'K}(\theta)
\end{aligned} \tag{A.15}$$

The parity-adapted total angular momentum eigenfunctions are defined as follows [see Eq. (4.5)]:

$$|J,K,M,p\rangle = \sqrt{\frac{2J+1}{8\pi^2}}\frac{1}{\sqrt{2(1+\delta_{0,K})}}(D^J_{K,M}(\omega) + (-1)^{J+K+p}D^J_{-K,M}(\omega)) \tag{A.16}$$

Substituting this into Eq. (A.15), we obtain

$$\mathscr{Y}^{JM}_{j'l'}(\hat{\mathbf{R}},\hat{\mathbf{r}}) = \sum_{K=\lambda}^{J}\left\{\frac{2(-1)^{j'-K}}{\sqrt{2(1+\delta_{0,K})}}(Jj'l'0|JKj'-K)\right\}|J,K,M,p\rangle\Theta_{j'K}(\theta) \tag{A.17}$$

This equation corresponds to a unitary transformation from the space-fixed basis functions $\mathscr{Y}^{JM}_{j'l'}(\hat{\mathbf{R}},\hat{\mathbf{r}})$ to the body-fixed functions $|J,K,M,p\rangle\Theta_{j'K}(\theta)$.

The inverse transforamtion is

$$|J,K,M,p\rangle\Theta_{j'K}(\theta) = \sum_{l'=0}^{J}\left\{\frac{2(-1)^{j'-K}}{\sqrt{2(1+\delta_{0,K})}}(Jj'l'0|JKj'-K)\right\}\mathscr{Y}^{JM}_{j'l'}(\hat{\mathbf{R}},\hat{\mathbf{r}}) \tag{A.18}$$

This implies the orthogonality relationships

$$\sum_{l'=0}^{J}\left\{\frac{2(-1)^{j-K}}{\sqrt{2(1+\delta_{0,K})}}(Jjl'0|JKj-K)\right\}\left\{\frac{2(-1)^{j-K'}}{\sqrt{2(1+\delta_{0,K'})}}(Jjl'0|JK'j-K')\right\} = 2\,\delta_{K,K'} \tag{A.19}$$

and

$$\sum_{K=\lambda}^{J}\left\{\frac{2(-1)^{j-K}}{\sqrt{2(1+\delta_{0,K})}}(Jjl0|JKj-K)\right\}\left\{\frac{2(-1)^{j-K}}{\sqrt{2(1+\delta_{0,K})}}(Jjl'0|JKj-K)\right\} = \delta_{l,l'} \tag{A.20}$$

Using Eq. (A.17) in Eq. (A.5), we obtain

$$\psi^{-}_{vjm_j}(\mathbf{r},\mathbf{R};\hat{\mathbf{k}},E) = \left(\frac{\mu k_{vj}}{\hbar^2(2\pi)^3}\right)^{1/2} 4\pi \sum_{JM}\sum_{lm_l} Y^*_{lm_l}(\hat{\mathbf{k}})(jlJM|jm_jlm_l) \sum_{v'j'}\sum_{l'} \times \sum_{p} i^l \frac{F^{(Jvjl)}_{v'j'l'}(R)}{R} \sum_{K'=\lambda}^{J} \left\{ \frac{2(-1)^{j'-K'}}{\sqrt{2(1+\delta_{0,K'})}} (Jj'l'0|JK'j'-K') \right\} \times |J,K',M,p\rangle \Theta_{j'K'}(\theta)\chi_{v'j'}(r) \tag{A.21}$$

An extra summation over p has been added as Eq. (A.5) contains a summation over both parities (i.e., $\sum_{l'j'}$). We need to transform the radial functions $F^{(Jvjl)}_{v'j'l'}(R)$ to the body-fixed basis (i.e., from using l to K). To accomplish this, we insert

$$\sum_{l''=0}^{J} \delta_{l,l''} = 1 \tag{A.22}$$

to the left of $F^{(Jvjl)}_{v'j'l'}(R)$ in Eq. (A.21):

$$\psi^{-}_{vjm_j}(\mathbf{r},\mathbf{R};\hat{\mathbf{k}},E) = \left(\frac{\mu k_{vj}}{\hbar^2(2\pi)^3}\right)^{1/2} 4\pi \sum_{JM}\sum_{lm_l} Y^*_{lm_l}(\hat{\mathbf{k}})(jlJM|jm_jlm_l) \sum_{v'j'}\sum_{l''=0}^{J} \delta_{l,l''} \times \sum_{l'p} i^l \frac{F^{(Jvjl'')}_{v'j'l'}(R)}{R} \sum_{K'=\lambda}^{J} \left\{ \frac{2(-1)^{j'-K'}}{\sqrt{2(1+\delta_{0,K'})}} (Jj'l'0|JK'j'-K') \right\} \times |J,K',M,p\rangle \Theta_{j'K'}(\theta)\chi_{v'j'}(r) \tag{A.23}$$

Substituting Eq. (A.20) into Eq. (A.23), we obtain

$$\psi^{-}_{vjm_j}(\mathbf{r},\mathbf{R};\hat{\mathbf{k}},E) = \left(\frac{\mu k_{vj}}{\hbar^2(2\pi)^3}\right)^{1/2} 4\pi \sum_{JM}\sum_{lm_lp} Y^*_{lm_l}(\hat{\mathbf{k}})(jlJM|jm_jlm_l) \sum_{v'j'}\sum_{K=\lambda}^{J}\sum_{K'=\lambda}^{J} \times \left\{ \frac{2(-1)^{j-K}}{\sqrt{2(1+\delta_{0,K})}} (Jjl0|JKj-K) \right\} \frac{1}{R} \times \left[\sum_{l''=0}^{J}\sum_{l'=0}^{J} \left\{ \frac{2(-1)^{j-K}}{\sqrt{2(1+\delta_{0,K})}} (Jjl''0|JKj-K) \right\} \times i^l F^{(Jvjl'')}_{v'j'l'}(R) \left\{ \frac{2(-1)^{j'-K'}}{\sqrt{2(1+\delta_{0,K'})}} (Jj'l'0|JK'j'-K') \right\} \right] \times |J,K',M,p\rangle \Theta_{j'K'}(\theta)\chi_{v'j'}(r) \tag{A.24}$$

The term in square brackets is the body-fixed radial wavefunction and has been discussed previously (see Ref. 80, Appendix B). Defining this body-fixed radial wavefunction as

$$\Phi^{(JvjKp)}_{v'j'K'}(R) = \sum_{l''=0}^{J}\sum_{l'=0}^{J}\left\{\frac{2(-1)^{j-K}}{\sqrt{2(1+\delta_{0,K})}}(Jjl''0|JKj-K)\right\} \times i^{l}F^{(Jvjl'')}_{v'j'l'}(R)\left\{\frac{2(-1)^{j'-K'}}{\sqrt{2(1+\delta_{0,K'})}}(Jj'l'0|JK'j'-K')\right\} \tag{A.25}$$

Inserting this into Eq. (A.24), we obtain

$$\psi^{-}_{vjm_j}(\mathbf{r},\mathbf{R};\hat{\mathbf{k}},E) = \left(\frac{\mu k_{vj}}{\hbar^2(2\pi)^3}\right)^{1/2} 4\pi\sum_{JM}\sum_{lm_l p} Y^{*}_{lm_l}(\hat{\mathbf{k}})(jlJM|jm_j lm_l)\sum_{v'j'}\sum_{K=\lambda}^{J} \times\left\{\frac{2(-1)^{j-K}}{\sqrt{2(1+\delta_{0,K})}}(Jjl0|JKj-K)\right\}\sum_{K'=\lambda}^{J}\frac{\Phi^{(JvjKp)}_{v'j'K'}(R)}{R} \times|J,K',M,p\rangle\Theta_{j'K'}(\theta)\chi_{v'j'}(r) \tag{A.26}$$

B. Detailed Definition of the Initial Wavepacket for Photodissociation of a Triatomic Molecule

The results presented here follow the analysis presented in Ref. 84. It is possible to define the functions $\Phi^{J'K}_{i}(r,R,\theta,t=0)$ only when we have specified whether the electronic transition involved is perpendicular or parallel (i.e., whether the transition dipole moment is perpendicular to or lies in the molecular plane).

For the case of a perpendicular transition when the transition dipole is in the body-fixed y direction (perpendicular to molecular plane), we obtain the following:

$$\Phi^{J'K}_{i}(r,R,\theta,t=0) = i(2J_i+1)^{1/2}(2J'+1)^{1/2}\mu_y\delta_{p,p'}\psi^{J_i,K_i,p}(r,R,\theta) \times\left\{\frac{(-1)^{-K}}{\sqrt{2}}\begin{pmatrix}1 & J_i & J'\\ 1 & (K-1) & -K\end{pmatrix}\delta_{K,K_i+1}(1-\delta_{K_i,0}) +\sqrt{\frac{(1+\delta_{0,K})}{2}}(-1)^{-K+J_i+J'+1}\begin{pmatrix}1 & J_i & J'\\ 1 & -(K+1) & K\end{pmatrix} \times\delta_{K,K_i-1}(1-\delta_{K_i,0}) - \begin{pmatrix}1 & J_i & J'\\ 1 & 0 & -1\end{pmatrix}\delta_{K,1}\delta_{K_i,0}\delta_{\lambda,0}\right\} \tag{A.27}$$

For the case of a parallel transition when the transition dipole lies in the molecular plane xz, we obtain

$$\Phi_i^{J'K}(r,R,\theta,t=0) = (2J_i+1)^{1/2}(2J'+1)^{1/2}\delta_{p,p'+1}\psi^{J_i,K_i,p}(r,R,\theta)$$
$$\times\left\{\frac{(-1)^{-K+1}}{\sqrt{2}}\mu_x\left[\begin{pmatrix}1 & J_i & J'\\ 1 & (K-1) & -K\end{pmatrix}\delta_{K,K_i+1}(1-\delta_{K_i,0})\right.\right.$$
$$\left.+(-1)^{J_i+J'}\sqrt{1+\delta_{0,K}}\begin{pmatrix}1 & J_i & J'\\ 1 & -(K+1) & K\end{pmatrix}\delta_{K,K_i-1}(1-\delta_{K_i,0})\right]$$
$$+\begin{pmatrix}1 & J_i & J'\\ 1 & K & -K\end{pmatrix}\mu_z\delta_{K,K_i}(1-\delta_{K_i,0})$$
$$+\begin{pmatrix}1 & J_i & J'\\ 1 & 0 & -1\end{pmatrix}\mu_x\delta_{K,1}\delta_{K_i,0}\delta_{\lambda,0}+\begin{pmatrix}1 & J_i & J'\\ 0 & 0 & 0\end{pmatrix}$$
$$\left.\times\,\mu_z\delta_{K,0}\delta_{K_i,0}\delta_{\lambda,0}\right\} \tag{A.28}$$

C. Time-Dependent Theory of the Partial Differential Cross Section

The time-independent expression for the partial differential cross section is given in Eq. (4.15):

$$\sigma_{vjm_j}(E;\hat{\mathbf{k}}) = \frac{2\pi^2\nu}{c\,\epsilon_0}\frac{1}{4\pi}\left|\sum_{JM}\sum_{KK'p}(2J+1)^{1/2}D^J_{K,M}(\phi_k,\theta_k,0)D^j_{-K,-m_j}(\phi_k,\theta_k,0)\right.$$
$$\left.\times\,\langle J,K',M,p|\Phi_{K'}^{-JvjKp}(r,R,\theta;E)|\vec{\epsilon}\cdot\vec{\mu}|\psi_i\rangle\right|^2 \tag{A.29}$$

We now expand $\vec{\epsilon}\cdot\vec{\mu}|\psi_i\rangle$ in terms of the initial body-fixed wavepacket [see Ref. 84 and Eq. (4.26):

$$\vec{\epsilon}\cdot\vec{\mu}|\psi_i\rangle = \Phi_i(\mathbf{r},\mathbf{R},t=0)$$
$$=\sum_{J'=J_i-1}^{J_i+1}(-1)^{m+M_i}\begin{pmatrix}1 & J_i & J'\\ m & M_i & -(m+M_i)\end{pmatrix}$$
$$\times\sum_{K''=\lambda'}^{J'}\Phi_i^{J'K''}(r,R,\theta,t=0)|J',K'',M_i+m,p'\rangle \tag{A.30}$$

and obtain

$$\sigma_{vjm_j}(E;\hat{\mathbf{k}}) = \frac{2\pi^2\nu}{c\,\epsilon_0}\frac{1}{4\pi}\Bigg|\sum_{JM}\sum_{KK'p}(2J+1)^{1/2}D^{J}_{K,M}(\phi_k,\theta_k,0)D^{j}_{-K,-m_j}(\phi_k,\theta_k,0)$$
$$\times\sum_{J'=J_i-1}^{J_i+1}(-1)^{m+M_i}\begin{pmatrix}1 & J_i & J'\\ m & M_i & -(m+M_i)\end{pmatrix}\sum_{K''=\lambda'}^{J'}$$
$$\times\langle J,K',M,p|\Phi^{-JvjKp}_{K'}(r,R,\theta;E)|\Phi^{J'K''}_{i}(r,R,\theta,t=0)|$$
$$\times J',K'',M_i+m,p'\rangle\Big|^2 \tag{A.31}$$

Performing the integrations over the Euler angles and using the orthogonality of the $|J',K'',M_i+m,p'\rangle$ functions, we then obtain

$$\sigma_{vjm_j}(E;\hat{\mathbf{k}}) = \frac{2\pi^2\nu}{c\,\epsilon_0}\frac{1}{4\pi}\Bigg|\sum_{JM}\sum_{KK'p}(2J+1)^{1/2}D^{J}_{K,M}(\phi_k,\theta_k,0)D^{j}_{-K,-m_j}(\phi_k,\theta_k,0)$$
$$\times\sum_{J'=J_i-1}^{J_i+1}\sum_{K''=\lambda'}^{J'}\langle\Phi^{-JvjKp}_{K'}(r,R,\theta;E)|\Phi^{J'K''}_{i}(r,R,\theta,t=0)\rangle$$
$$\times(-1)^{m+M_i}\begin{pmatrix}1 & J_i & J'\\ m & M_i & -(m+M_i)\end{pmatrix}\delta_{J,J'}\delta_{K',K''}\delta_{M,M_i+m}\delta_{pp'}\Bigg|^2$$
$$=\frac{2\pi^2\nu}{c\,\epsilon_0}\frac{1}{4\pi}\Bigg|\sum_{J=J_i-1}^{J_i+1}\sum_{K}(2J+1)^{1/2}D^{J}_{K,M_i+m}(\phi_k,\theta_k,0)D^{j}_{-K,-m_j}(\phi_k,\theta_k,0)$$
$$\times\begin{pmatrix}1 & J_i & J\\ m & M_i & -(m+M_i)\end{pmatrix}\Bigg\{\sum_{K'}\langle\Phi^{-JvjKp'}_{K'}(r,R,\theta;E)|\Phi^{JK'}_{i}$$
$$\times(r,R,\theta,t=0)\rangle\Bigg\}\Bigg|^2 \tag{A.32}$$

We may now define the quantities $\left\{\sum_{K'}\langle\Phi^{-JvjKp'}_{K'}(r,R,\theta;E)|\Phi^{JK'}_{i}\ (r,R,\theta,t=0)\rangle\right\}$ as "photofragmentation **T** matrix elements":

$$T^{JKp'}_{vj} = \sum_{K'}\langle\Phi^{-JvjKp'}_{K'}(r,R,\theta;E)|\Phi^{JK'}_{i}(r,R,\theta,t=0)\rangle \tag{A.33}$$

These "photofragmentation **T** matrix elements" contain all the information about the photofragmentation dynamics. We will now discuss how they may be extracted from the time-dependent wavepacket calculations.

Following Ref. 75, we define an analysis line at a large fixed value of the dissociation or scattering coordinate $R = R_\infty$, which should lie in the asymptotic

region where the interaction potential is nearly zero and where Eq. (4.8) is valid. Let us then consider the integral

$$C_{vj}^{JK}(t) = \left\langle \Theta_{jK}(\theta)\chi_{vj}(r) \middle| \left\{ \sum_{K'} \Phi_i^{JK'}(r, R = R_\infty, \theta, t) \right\} \right\rangle \tag{A.34}$$

where the angular brackets $\langle\rangle$ indicate integration over the variables r and θ and it is implied that $\Theta_{jK}(\theta)$ on the left of the integral must be associated only with the same value of K on the right. The sum over all the radial wavepackets corresponding to the various different values of K are kept together in Eq. (A.34) because the wavepackets corresponding to these different values interact and amplitude or flux is exchanged between them as time progresses. We now take the half–Fourier transform of this integral over time to give us an energy dependent quantity:

$$\begin{aligned} A_{vj}^{JK}(E) &= \frac{1}{2\pi}\int_{t=0}^{\infty} \exp\frac{iEt}{\hbar}\, C_{vj}^{JK}(t)dt \\ &= \frac{1}{2\pi}\int_{t=0}^{\infty} \exp\frac{iEt}{\hbar} \left\langle \Theta_{jK}(\theta)\chi_{vj}(r) \middle| \left\{ \sum_{K'} \Phi_i^{JK'}(r, R = R_\infty, \theta, t) \right\} \right\rangle dt \end{aligned} \tag{A.35}$$

We now introduce an integration over R combined with a Dirac delta function [94,95]:

$$A_{vj}^{JK}(E) = \frac{1}{2\pi}\int_{t=0}^{\infty}\int_{R=0}^{\infty} \exp\frac{iEt}{\hbar}\,\delta(R - R_\infty) \left\langle \Theta_{jK}(\theta)\chi_{vj}(r) \middle| \left\{ \sum_{K'} \Phi_i^{JK'}(r, R, \theta, t) \right\} \right\rangle dt\, dR \tag{A.36}$$

We now replace the time-dependent wavepacket $\left\{\sum_{K'} \Phi_i^{JK'}(r, R, \theta, t)\right\}$ by

$$\sum_{K'} \Phi_i^{JK'}(r, R, \theta, t) = \exp\frac{-i\hat{\mathbf{H}}t}{\hbar} \sum_{K'} \Phi_i^{JK'}(r, R, \theta, t = 0) \tag{A.37}$$

to obtain

$$\begin{aligned} A_{vj}^{JK}(E) = \frac{1}{2\pi}&\int_{t=0}^{\infty}\int_{R=0}^{\infty} \exp\frac{iEt}{\hbar}\,\delta(R - R_\infty) \\ &\times \left\langle \Theta_{jK}(\theta)\chi_{vj}(r) \middle| \exp\frac{-i\hat{\mathbf{H}}t}{\hbar} \left\{ \sum_{K'} \Phi_i^{JK'}(r, R, \theta, t = 0) \right\} \right\rangle dt\, dR \end{aligned} \tag{A.38}$$

The identity operator within the space of functions with a fixed value of J and the parity (denoted by p), and that are associated assymptotically with a quantum number $\bar{K}$ of the body-fixed z component of the total angular momentum, is

$$\hat{\mathbf{I}} = \int_{E'=-\infty}^{\infty} \sum_{v'j'} \sum_{\bar{K}} \sum_{K''K'''} |K''\rangle |\Phi_{K''}^{-Jv'j'\bar{K}p}(r,R,\theta;E')\rangle \times \langle \Phi_{K'''}^{-Jv'j'\bar{K}p}(r,R,\theta;E')|\langle K'''|dE' \tag{A.39}$$

where the term $|K''\rangle\langle K'''|$ indicates that the angular functions on either side of the identity operator must be associated with a body-fixed z component of $K = K''$ and with $K = K'''$, respectively.

Inserting this identity operator between $\exp\left(-i\hat{\mathbf{H}}t/\hbar\right)$ and $\Phi_i^{JK'}(r,R,\theta,t=0)$ in Eq. (A.38), we obtain

$$\begin{aligned} A_{vj}^{JK}(E) = \sum_{K'} \sum_{\bar{K}} \frac{1}{2\pi} \int_{t=0}^{\infty} \int_{R=0}^{\infty} \int_{E'=-\infty}^{\infty} \sum_{v'j'} \delta(R-R_\infty) \\ \times \left\langle \Theta_{jK}(\theta)\chi_{vj}(r) \middle| \exp\left[i(E-\hat{\mathbf{H}})t/\hbar\right] |\Phi_K^{-Jv'j'\bar{K}p}(r,R,\theta;E')\right\rangle_{r\theta} \\ \times \langle \Phi_{K'}^{-Jv'j'\bar{K}p}(r,R,\theta;E')|\Phi_i^{JK'}(r,R,\theta,t=0)\rangle_{\text{all}} dt\, dR\, dE' \end{aligned} \tag{A.40}$$

where $\langle\ \rangle_{r\theta}$ indicates integration over the variables r and θ only, while $\langle\ \rangle_{\text{all}}$ indicates integration also over R.

As the continuum functions $\Phi_{K'}^{-JvjKp}(r,R,\theta;E')$ are energy eigenfunctions, we may act on them with the Hamiltonian operator to obtain

$$\begin{aligned} A_{vj}^{JK}(E) = \sum_{K'} \sum_{\bar{K}} \frac{1}{2\pi} \int_{t=0}^{\infty} \int_{R=0}^{\infty} \int_{E'=-\infty}^{\infty} \sum_{v'j'} \delta(R-R_\infty) \exp\frac{i(E-E')t}{\hbar} \\ \times \left\langle \Theta_{jK}(\theta)\chi_{vj}(r) \middle| \Phi_K^{-Jv'j'\bar{K}p}(r,R,\theta;E')\right\rangle_{r\theta} \\ \times \langle \Phi_{K'}^{-Jv'j'\bar{K}p}(r,R,\theta;E')|\Phi_i^{JK'}(r,R,\theta,t=0)\rangle_{\text{all}}\, dt\, dR\, dE' \end{aligned} \tag{A.41}$$

Performing the integaration over R now yields

$$\begin{aligned} A_{vj}^{JK}(E) = \sum_{K'} \sum_{\bar{K}} \frac{1}{2\pi} \int_{t=0}^{\infty} \int_{E'=-\infty}^{\infty} \sum_{v'j'} \exp\frac{i(E-E')t}{\hbar} \\ \times \left\langle \Theta_{jK}(\theta)\chi_{vj}(r) \middle| \middle| \Phi_K^{-Jv'j'\bar{K}p}(r,R=R_\infty,\theta;E')\right\rangle_{r\theta} \\ \times \langle \Phi_{K'}^{-Jv'j'\bar{K}p}(r,R,\theta;E')|\Phi_i^{JK'}(r,R,\theta,t=0)\rangle_{\text{all}}\, dt\, dE' \end{aligned} \tag{A.42}$$

We now utilize the analysis presented in the appendix and in Eqs. 17–23 of Ref. 75. This analysis proves that if we choose R_∞ to be in the asymptotic region, where there is no longer any interaction potential, centrifugal repulsion potential, or centrifigal coupling, then performing the integration over time and energy in Eq. (A.42) permits us to substitute the outgoing radial wave part of the asymptotic form of the radial wavefunction [see Eq. (4.8)] multiplied by $\hbar$ for the radial wavefunction itself. Using Eqs. (4.5) and (4.8) to effect these substitutions, we obtain

$$A_{vj}^{JK}(E) = \left(\frac{\mu}{2\pi k_{vj}}\right)^{1/2} \frac{1}{i} \left\{ \frac{2(-1)^{j-K}}{\sqrt{2(1+\delta_{0,K})}} \right\} e^{ik_{vj}R_\infty} \times \left\{ \sum_{K'} \langle \Phi_{K'}^{-JvjKp}(r, R, \theta; E) | \Phi_i^{JK'}(r, R, \theta, t=0) \rangle_{\text{all}} \right\} \tag{A.43}$$

Comparing this with Eq. (A.33), we see that the photofragmentation T matrix can be related to the energy-dependent $A_{vjK}(E)$ coefficients by

$$A_{vj}^{JK}(E) = \left(\frac{\mu}{2\pi k_{vj}}\right)^{1/2} \frac{1}{i} \left\{ \frac{2(-1)^{j-K}}{\sqrt{2(1+\delta_{0,K})}} \right\} e^{ik_{vj}R_\infty} T_{vj}^{JKp'} \tag{A.44}$$

or

$$T_{vj}^{JKp'} = i(-1)^{K-j} A_{vj}^{JK}(E) \left(\frac{2\pi k_{vj}}{\mu}\right)^{1/2} \left\{ \frac{\sqrt{2(1+\delta_{0,K})}}{2} \right\} e^{-ik_{vj}R_\infty} \tag{A.45}$$

The partial differential photofragmentation cross section is therefore given by (see Eqs. (A.32) and (A.33))

$$\sigma_{vjm_j}(E; \hat{\mathbf{k}}) = \frac{2\pi^2 \nu}{c\,\epsilon_0} \frac{1}{4\pi} \left| \sum_{J=J_i-1}^{J_i+1} \sum_{K} (2J+1)^{1/2} D^J_{K,M_i+m}(\phi_k, \theta_k, 0) D^j_{-K,-m_j}(\phi_k, \theta_k, 0) \times \begin{pmatrix} 1 & J_i & J \\ m & M_i & -(m+M_i) \end{pmatrix} T_{vj}^{JKp'} \right|^2 \tag{A.46}$$

References

1. E. J. Heller, *J. Chem. Phys.* **68**, 2066 (1978).
2. K. C. Kulander and E. J. Heller, *J. Chem. Phys.* **69**, 2439 (1978).
3. E. J. Heller, *Acc. Chem. Res.* **14**, 368 (1981).

4. G. G. Balint-Kurti, in *International Review of Science*, Series II, Vol. 1, A. D. Buckingham and C. A. Coulson, eds. (Butterworths, London, 1975), p. 286.
5. M. Baer, in *Theory of Chemical Reaction Dynamics*, Vol. I, M. Baer, ed., (CRC Press, Boca Raton, FL, 1985), p. 91.
6. W. A. Lester, Jr., in *Dynamics of Molecular Collisions*, Part A, W. H. Miller, ed. (Plenum Press, New York, 1976).
7. D. C. Clary, ed., *The Theory of Chemical Reaction Dynamics* (Reidel, Dordrecht, 1986).
8. R. G. Newton, *Scattering Theory of Waves and Particles* (McGraw-Hill, New York, 1966).
9. M. S. Child, *Molecular Collision Theory* (Academic Press, New York, 1974).
10. J. Z. H. Zhang, *Theory and Application of Quantum Molecular Dynamics* (World Scientific, Singapore, 1999).
11. M. Shapiro and R. Bersohn, *Annu. Rev. Phys. Chem.* **33**, 409 (1982).
12. J. A. Beswick, in *Dynamical Processes in Molecular Physics*, G. Delgado-Barrio, ed. (Institute of Physics Publishing, Bristol, 1993).
13. G. G. Balint-Kurti and M. Shapiro, *Adv. Chem. Phys.* **60**, 403 (1985).
14. R. Schinke, *Photodissociation Dynamics* (Cambridge Univ. Press, Cambridge, U.K., 1993).
15. G. G. Balint-Kurti and M. M. Law, *Photodissociation Dynamics*, Collaborative Computational Project 6 (CCP6) (Darsebury Laboratory, Daresbury, Warrington, WA4 4AD, U.K., 1994).
16. R. Kosloff, *Annu. Rev. Phys. Chem.* **45**, 145 (1994).
17. R. Kosloff and C. Cerjan, *J. Chem. Phys.* **81**, 3722 (1984).
18. C. Leforestier, R. Bisseling, C. Cerjan, M. D. Feit, R. Friesner, A. Guldberg, A. Hammerich, G. Jolicard, W. Karrlein, H.-D. Meyer, N. Lipkin, O. Roncero, and R. Kosloff, *J. Comput. Phys.* **94**, 59 (1991).
19. T. N. Truong, J. J. Tanner, P. Bala, J. A. McCammon, D. J. Kouri, B. Lesyng, and D. K. Hoffman, *J. Chem. Phys.* **96**, 2077 (1992).
20. G. G. Balint-Kurti, R. N. Dixon, and C. C. Marston, *Int. Rev. Phys. Chem.* **11**, 317 (1992).
21. M. Shapiro, *Israel J. Chem.* **11**, 691 (1973).
22. M. Shapiro, *J. Chem. Phys.* **56**, 2582 (1972).
23. O. Atabek and R. Lefebvre, *Chem. Phys.* **23**, 51 (1977).
24. O. Atabek, R. Lefebvre, and M. Jacon, *Chem. Phys. Lett.* **58**, 196 (1978).
25. K. C. Kulander and J. C. Light, *J. Chem. Phys.* **73**, 4337 (1980).
26. Y. B. Band, K. F. Freed, and D. J. Kouri, *J. Chem. Phys.* **74**, 4380 (1981).
27. R. W. Numrich and K. G. Kay, *J. Chem. Phys.* **70**, 4343 (1981).
28. O. Atabek and R. Lefebvre, *Chem. Phys.* **55**, 395 (1981).
29. O. Atabek and R. Lefebvre, *Chem. Phys.* **56**, 195 (1981).
30. S. Chu, *J. Chem. Phys.* **72**, 4772 (1980).
31. J. E. Grabensteller and R. J. LeRoy, *Chem. Phys.* **42**, 41 (1979).
32. K. Kodama and A. D. Bandrauk, *Chem. Phys.* **57**, 461 (1981).
33. M. H. Alexander, B. Pouilly, and T. Duhoo, *J. Chem. Phys.* **99**, 1752 (1993).
34. S. J. Singer, K. F. Freed, and Y. B. Band, *J. Chem. Phys.* **77**, 1942 (1982).
35. Y. B. Band, K. F. Freed, S. J. Singer, and C. J. Williams, *J. Phys. Chem.* **99**, 1752 (1993).
36. E. J. Heller, *J. Chem. Phys.* **68**, 3891 (1978).
37. R. Kosloff, *J. Phys. Chem.* **92**, 2087 (1988).
38. D. Kosloff and R. Kosloff, *J. Comput. Phys.* **52**, 35 (1983).

39. H. Tal-Ezer and R. Kosloff, *J. Chem. Phys.* **81**, 3967 (1984).
40. R. Kosloff and D. Kosloff, *J. Comput. Phys.* **63**, 363 (1986).
41. D. Imre, J. L. Kinsey, A. Sinha, and J. Krenos, *J. Phys. Chem.* **88**, 3956 (1984).
42. A. Untch, K. Weide, and R. Schinke, *J. Chem. Phys.* **95**, 6496 (1985).
43. R. N. Dixon, C. C. Marston, and G. G. Balint-Kurti, *J. Chem. Phys.* **93**, 6520 (1990).
44. F. Le Quere and C. Leforestier, *J. Chem. Phys.* **94**, 1118 (1991).
45. D. Neuhauser, M. Baer, R. S. Judson, and D. J. Kouri, *J. Chem. Phys.* **90**, 5882 (1989).
46. D. Neuhauser, M. Baer, R. S. Judson, and D. J. Kouri, *Chem. Phys. Lett.* **169**, 372 (1990).
47. F. Gögtas, G. G. Balint-Kurti, and A. R. Offer, *J. Chem. Phxys.* **104**, 7927 (1996).
48. S. K. Gray and C. E. Wozny, *J. Chem. Phys.* **94**, 2817 (1991).
49. S. K. Gray, *J. Chem. Phys.* **96**, 6543 (1992).
50. H. Guo, *J. Chem. Phys.* **97**, 2602 (1993).
51. D. G. Xu, D. Q. Xie, and H. Guo, *J. Chem. Phys.* **116**, 10626 (2002).
52. C. Woywod, M. Stengle, W. Domcke, H. Flothmann, and R. Schinke, *J. Chem. Phys.* **107**, 7282 (1997).
53. H. Flothmann, C. Beck, R. Schinke, C. Woywod, and W. Domcke, *J. Chem. Phys.* **107**, 7296 (1997).
54. H. Flothmann, R. Schinke, C. Woywod, and W. Domcke, *J. Chem. Phys.* **109**, 2680 (1998).
55. J. H. Fillion, R. van Harrevelt, J. Ruiz, N. Castillejo, A. H. Zanganeh, J. L. Lemaire, M. C. van Hemert, and F. Rostas, *J. Phys. Chem. A* **105**, 11414 (2001).
56. S. A. Harich, X. F. Yang, X. Yang, R. van Harrevelt, and M. C. van Hemert, *Phys. Rev. Lett.* **8726**, article 263001 (2001).
57. R. van Harrevelt and M. C. van Hemert, *J. Chem. Phys.* **114**, 9453 (2001).
58. R. N. Dixon, D. W. Hwang, X. F. Yang, S. A. Harich, J. J. Lin, and X. M. Yang, *Science* **285**, 1249 (1999).
59. S. A. Harich, D. W. H. Hwang, X. F. Yang, J. J. Lin, X. M. Yang, and R. N. Dixon, *J. Chem. Phys.* **113**, 10073 (2000).
60. S. A. Harich, X. F. Yang, D. W. H. Hwang, J. J. Lin, X. M. Yang, and R. N. Dixon, *J. Chem. Phys.* **114**, 7830 (2001).
61. G. J. Kroes, M. C. van Hemert, G. D. Billing, and D. Neuhausrer, *J. Chem. Phys.* **107**, 5757 (1997).
62. V. A. Mandelshtam and H. S. Taylor, *J. Chem. Phys.* **102**, 7390 (1995).
63. V. A. Mandelshtam and H. S. Taylor, *J. Chem. Phys.* **103**, 2903 (1995).
64. H. W. Jang and J. C. Light, *J. Chem. Phys.* **102**, 3262 (1995).
65. G.-J Kroes and D. Neuhauser, *J. Chem. Phys.* **105**, 8690 (1996).
66. G.-J Kroes, E. J. Baerends, and R. C. Mowrey, *Phys. Rev. Lett.* **78**, 3583 (1997).
67. G.-J Kroes, M. R. Wall, J. W. Peng, and D. Neuhauser, *J. Chem. Phys.* **106**, 1800 (1997).
68. G.-J Kroes, M. C. van Hemert, G. D. Billing, and D. Neuhauser, *Chem. Phys. Lett.* **271**, 311 (1997).
69. R. Chen and H. Guo, *J. Chem. Phys.* **105**, 3569 (1996).
70. R. Chen and H. Guo, *Chem. Phys. Lett.* **261**, 605 (1996).
71. H. Guo, *J. Chem. Phys.* **108**, 2466 (1998).
72. H. Guo and T. Seideman, *Phys. Chem., Chem. Phys.* **1**, 1265 (1999).
73. D. Xie, H. Guo, Y. Amatatsu, and R. Kosloff, *J. Chem. Phys.* **104**, 1009 (2000).
74. H. Guo, *Chem. Phys. Lett.* **289**, 396 (1998).

75. G. G. Balint-Kurti, R. N. Dixon, and C. C. Marston, *J. Chem. Soc. Faraday Trans. 2* **86**, 1741 (1990). [The RHS of Eq. (3) of this reference should be multiplied by $1/(4\pi)$ and Eq. (25), by $1/(16\pi^2)$.]
76. A. Brown and G. G. Balint-Kurti, *J. Chem. Phys.* **113**, 1870 (2000).
77. L. Pauling and E. B. Wilson, *Introduction to Quantum Mechanics* (McGraw-Hill, New York, 1935).
78. G. Herzberg, *Molecular Spectra and Molecular Structure*, Vol. 1, *Spectra of Diatomic Molecules* (Van Nostrand, Princeton, NJ, 1950).
79. L. I. Schiff, *Quantum Mechanics* (McGraw-Hill, New York, 1955).
80. G. G. Balint-Kurti and M. Shapiro, *Chem. Phys.* **61**, 137 (1981).
81. R. D. Levine, *Quantum Mechanics of Molecular Rate Processes* (Clarendon, Oxford, 1969).
82. A. R. Edmonds, *Angular Momentum in Quantum Mechanics* (Princeton Univ. Press, Princeton, NJ, 1960).
83. R. N. Zare, *Angular Momentum: Understanding Spatial Aspects in Chemistry and Physics* (Wiley, New York, 1988).
84. G. G. Balint-Kurti, L. Füsti-Molnár, and A. Brown, *Phys. Chem., Chem. Phys.* **3**, 702 (2001).
85. A. Pe'er, M. Shapiro, and G. G. Balint-Kurti, *J. Chem. Phys.* **110**, 11928 (1999).
86. M. V. Rama Krishna and R. D. Coalson, *Chem. Phys., Phys. Chem., Chem. Phys.* **120**, 327 (1988).
87. A. R. Offer and G. G. Balint-Kurti, *J. Chem. Phys.* **101**, 10416 (1994).
88. Y. Sun and D. J. Kouri, *J. Chem. Phys.* **89**, 2958 (1988).
89. Y. Sun, R. S. Judson, and D. J. Kouri, *J. Chem. Phys.* **90**, 241 (1989).
90. S. K. Gray and C. E. Wozny, *J. Chem. Phys.* **91**, 7671 (1989).
91. K. Weide, K. Kühl, and R. Schinke, *J. Chem. Phys.* **91**, 3999 (1989).
92. J. C. Light, I. P. Hamilton, and V. J. Lill, *J. Chem. Phys.* **82**, 1400 (1985).
93. A. J. H. M. Meijer and E. M. Goldfield, *Phys. Chem., Chem. Phys.* **3**, 2811 (2001).
94. P. A. M. Dirac, *The Principes of Quantum Mechanics*, 4th ed. (Clarendon, Oxford, 1958).
95. C. Cohen-Tanouji, B. Diu, and F. Laloe, *Quantum Mechanics*, 2nd ed. (Wiley, New York, 1977).
96. P. M. Regan, D. Ascenzi, A. Brown, G. G. Balint-Kurti, and A. J. Orr-Ewing, *Phys. Chem., Chem. Phys.* **112**, 10259 (2000).
97. A. Brown and G. G. Balint-Kurti, *J. Chem. Phys.* **113**, 1879 (2000).
98. G. G. Balint-Kurti, A. J. Orr-Ewing, J. A. Beswick, A. Brown, and O. S. Vasyutenskii, *J. Chem. Phys.* **116**, 10760 (2002).
99. E. R. Wouters, M. Ahmed, D. S. Peterska, A. S. Bracker, A. G. Suits, and O. S. Vasyutinskii, in *Imaging in Chemical Dynamics*, A. G. Suits and R. E. Continetti, eds. (American Chemical Society, Washington, DC, 2000), p. 238.
100. M. Karplus and K. T. Tang, *Disc. Faraday Soc.* **44**, 56 (1967).
101. W. H. Miller, *J. Chem. Phys.* **49**, 2373 (1968).
102. G. Wolken, Jr. and M. Karplus, *J. Chem. Phys.* **60**, 351 (1974).
103. G. C. Schatz and A. Kuppermann, *J. Chem. Phys.* **65**, 4642 (1976); ibid. **65**, 4668 (1976).
104. A. Kuppermann, in *Theoretical Chemistry*, Vol. 6, Part A, *Theory of Scattering: Papers in Honour of Henry Eyring*, D. Henderson, ed. (Academic Press, New York, 1981), p. 79.
105. J. C. Light and R. B. Walker, *J. Chem. Phys.* **65**, 4272 (1976).
106. U. Halavee and M. Shapiro, *J. Chem. Phys.* **64**, 2826 (1976).
107. M. Baer, *Chem. Phys.* **15**, 49 (1976).

108. D. J. Kouri, in *Theory of Chemical Reaction Dynamics*, Vol. I, M. Baer, ed. (CRC Press, Boca Raton, FL, 1985), p. 163.
109. M. S. Child, *Mol. Phys.* **12**, 401 (1967).
110. J. N. L. Connor, *Mol. Phys.* **15**, 37 (1968).
111. M. D'Mello, D. E. Manolopoulos, and R. E. Wyatt, *J. Chem. Phys.* **94**, 5985 (1991).
112. J. M. Launay and M. le Dourneuf, *Chem. Phys. Lett.* **163**, 178 (1989).
113. D. C. Clary, *J. Phys. Chem.* **98**, 10678 (1994).
114. R. T Pack and G. A. Parker, *J. Chem. Phys.* **87**, 3888 (1987).
115. D. G. Truhlar, C. A. Mead, and M. A. Brandt, *Adv. Chem. Phys.* **33**, 295 (1975).
116. G. C. Schatz, *Annu. Rev. Phys. Chem.* **39**, 317 (1988).
117. D. E. Manolopoulos and D. C. Clary, *Annu. Rep. C, Roy. Soc. Chem.* **86**, 95 (1989).
118. W. H. Miller, *Annu. Rev. Phys. Chem.* **41**, 245 (1990).
119. J. M. Bowman, ed., *Advances in Molecular Vibrations and Collision Dynamics*, Vols. 2A and 2B (JAI Press, Greenwich, CT, 1994).
120. A. Laganà, R. T. Pack, and G. A. Parker, *Faraday Disc. Chem. Soc.* **84**, 409 (1988).
121. P. Honvault and J. M. Launay, *J. Chem. Phys*. **114**, 1057 (2001).
122. R. Jaquet, in *Lecture Notes in Chemistry 77, Methods in Reaction Dynamics*, W. Jakubetz, ed. (Springer-Verlag, Berlin, 2001).
123. G. Nyman and H. G. Yu, *Rept. Prog. Phys*. **63**, 1001 (2000).
124. J. Mazur and R. J. Rubin, *J. Chem. Phys.* **31**, 1395 (1959).
125. E. A. McCullough and R. E. Wyatt, *J. Chem. Phys.* **54**, 3578, 3592 (1971).
126. Ch. Zuhrt, T. Kamal, and L. Zulicke, *Chem. Phys. Lett.* **36**, 396 (1975).
127. E. Kellerhals, N. Sathyamurthy, and L. M. Raff, *J. Chem. Phys.* **64**, 818 (1976).
128. P. M. Agrawal and L. M. Raff, *J. Chem. Phys.* **74**, 5076 (1981).
129. C. Leforestier, *Chem. Phys.* **87**, 241 (1984).
130. Z. H. Zhang and D. J. Kouri, *Phys. Rev. A* **34**, 2687 (1986).
131. S. Thareja and N. Sathyamurthy, *J. Phys. Chem.* **91**, 1970 (1987).
132. D. Neuhauser and M. Baer, *J. Chem. Phys.* **91**, 4651 (1989); D. Neuhauser, M. Baer, R. S. Judson, and D. J. Kouri, *J. Chem. Phys.* **93**, 312 (1990).
133. S. K. Gray and G. G. Balint-Kurti, *J. Chem. Phys.* **108**, 950 (1998).
134. T. E. Carroll and E. M. Goldfield, *J. Phys. Chem. A* **105**, 2251 (2001).
135. S. M. Kingma, M. F. Somers, E. Pijper, G. J. Kroes, R. A. Olsen, and E. J. Baerends, *J. Chem. Phys.* **118**, 4190 (2003).
136. S. C. Althorpe, *J. Chem. Phys.* **114**, 1601 (2001).
137. E. M. Goldfield and S. K. Gray, *J. Chem. Phys.* **117**, 1604 (2002).
138. S. K. Gray and E. M. Goldfield, *J. Chem. Phys.* **115**, 8331 (2001).
139. V. Mohan and N. Sathyamurthy, *Comput. Phys. Rep*. **7**, 213 (1988).
140. N. Balakrishnan, C. Kalyanaraman, and N. Sathyamurthy, *Phys. Rep*. **280**, 79 (1997).
141. S. C. Althorpe, P. Soldn, and G. G. Balint-Kurti, eds., *Time-Dependent Quantum Dynamics* CCP6; Collaborative Computational Project on Heavy Particle Dynamics (Daresbury Laboratory, Daresbury, Warrington, WA4 4AD, U.K., 2001).
142. J. Tennyson and B. T. Sutcliffe, *J. Chem. Phys.* **77**, 4061 (1982).
143. J. Z. H. Zhang, *J. Chem. Phys.* **92**, 324 (1990).

144. M. Hankel, G. G. Balint-Kurti, and S. K. Gray, *J. Chem. Phys.* **113**, 9658 (2000).
145. Y. C. Zhang, J. F. Zhang, H. Y. Zhang, Q. G. Zhang, and J. Z. H. Zhang, *J. Chem. Phys.* **115**, 8455 (2001).
146. M. Hankel, G. G. Balint-Kurti, and S. K. Gray, *J. Phys. Chem.* **105**, 2330 (2001).
147. M. Hankel, G. G. Balint-Kurti, and S. K. Gray, *Int. J. Quant. Chem.* **92**, 205 (2003).
148. G. G. Balint-Kurti, F. Göğtas, S. P. Mort, A. R. Offer, A. Laganà, and O. Garvasi, *J. Chem. Phys.* **99**, 9567 (1993).
149. S. K. Gray, E. M. Goldfield, G. C. Schatz, and G. G. Balint-Kurti, *Phys. Chem., Chem. Phys.* **1**, 1141 (1999).
150. S. K. Gray, G. G. Balint-Kurti, G. C. Schatz, J. J. Lin, X. Liu, S. Harich, and X. Yang, *J. Chem. Phys.* **113**, 7330 (2000).
151. A. J. H. M. Meijer, E. M. Goldfield, S. K. Gray, and G. G. Balint-Kurti, *Chem. Phys. Lett.* **293**, 270 (1998).
152. I. Miquel, M. Gonzalez, R. Sayos, G. G. Balint-Kurti, S. K. Gray, and E. M. Goldfield, *J. Chem. Phys.* **118**, 3111 (2003).
153. R. T. Pack, *J. Chem. Phys.* **60**, 633 (1974).
154. P. McGuire and D. J. Kouri, *J. Chem. Phys.* **60**, 2488 (1974).
155. J. M. Bowman, *J. Phys. Chem.* **95**, 4960 (1991).
156. M. Bittererova and J. M. Bowman, *J. Chem. Phys.* **113**, 1 (2000).
157. W. H. Miller, *J. Chem. Phys.* **50**, 407 (1969).
158. S. C. Althorpe, *J. Chem. Phys.* **117**, 4623 (2002).
159. S. C. Althorpe, F. Fernandez-Alonso, B. D. Bean, J. D. Ayers, A. E. Pomerantz, R. N. Zare, and E. Wrede, *Nature* **416**, 67 (2002).
160. M. Hankel, Ph. D. thesis, Univ. Bristol, Bristol, U.K., 2001.
161. A. Messiah, *Quantum Mechanics*, Vol. II, (North-Holland, Amsterdam, 1962).
162. The author thanks M. Shapiro for suggesting this method to him.
163. M. D. Feit and J. A. Fleck, Jr., *J. Chem. Phys.* **78**, 301 (1983).
164. M. D. Feit and J. A. Fleck, Jr., *J. Chem. Phys.* **80**, 2578 (1984).
165. C. Leforestier, *J. Chem. Phys.* **94**, 6388 (1991).
166. G. Corey and D. Lemoine, *J. Chem. Phys.* **97**, 4115 (1992).
167. W. H. Press, B. P. Flannery, S. A. Teukolsky, and W. T. Vetterling, *Numerical Recipes* (Cambridge Univ. Press, Cambridge, U.K., 1987).
168. M. Monnerville, P. Halvick, and J. C. Rayez, *Chem. Phys.* **159**, 227 (1992).
169. M. Monnerville, P. Halvick, and J. C. Rayez, *Chem. Soc. Faraday Trans.* **89**, 1579 (1993).
170. N. F. Mott and H. S. W. Massey, *The Theory of Atomic Collisions* (Oxford Univ. Press, Oxford, 1965).
171. C. Leforestier and R. E. Wyatt, *J. Chem. Phys.* **78**, 2334 (1983).
172. D. Neuhauser and M. Baer, *J. Chem. Phys.* **90**, 4351 (1989).
173. D. Neuhauser, M. Baer, R. S. Judson, and D. J. Kouri, *Comput. Phys. Commun.* **63**, 460 (1991).
174. M. S. Child, *Molec. Phys.* **72**, 89 (1991).
175. T. Seideman and W. H. Miller, *J. Chem. Phys.* **96**, 4412 (1992).
176. Á. Vibók and G. G. Balint-Kurti, *J. Chem. Phys.* **96**, 7615 (1992).
177. Á. Vibók and G. G. Balint-Kurti, *J. Phys. Chem.* **96**, 8712 (1992).

178. G. G. Balint-Kurti and Á. Vibók, "Complex absorbing potentials in time dependent quantum dynamics," in *Numerical Grid Methods and Their Application to Schrdinger's Equation*, C. Cerjan, ed., NATO ASI series, Series C: Mathematical and Physical Sciences, Vol. 412 (Kluwer Academic Publishers, 1993), p. 195.
179. S. Mahapatra and N. Sathyamurthy, *Chem. Soc Faraday Trans.* **93**, 773 (1997).
180. D. Macias, S. Brouard, and J. G. Muga, *Chem. Phys. Lett.* **228**, 672 (1994).
181. S. Brouard, D. Macias and J. G. Muga, *J. Phys. A* **27**, L439 (1994).
182. U. V. Riss and H.-D. Meyer, *J. Chem. Phys.* **105**, 1409 (1996).
183. U. V. Riss and H.-D. Meyer, *J. Phys. B* **31**, 2279 (1998).
184. D. E. Manolopoulos, *J. Chem. Phys.* **117**, 9552 (2002).
185. S. K. Gray and J. M. Verosky, *J. Chem. Phys.* **100**, 5011 (1994).
186. S. K. Gray and D. E. Manolopoulos, *J. Chem. Phys.* **104**, 7099 (1996).
187. G. B. Arfken and H. J. Weber, *Mathematical Methods for Physicists* (Academic Press, San Diego, CA, 1970).
188. Y. Huang, D. J. Kouri, and D. K. Hoffman, *J. Chem. Phys.* **101**, 10493 (1994).
189. Y. Huang, S. S. Iyengar, D. J. Kouri, and D. K. Hoffman, *J. Chem. Phys.* **105**, 927 (1996).
190. H.-D. Meyer, U. Manthe, and L. S. Cederbaum, *Chem. Phys. Lett.* **165**, 73 (1990).
191. G. A. Worth, *J. Chem. Phys.* **112**, 8322 (2000).
192. G. A. Worth, H.-D. Meyer, and L. S. Cederbaum, *J. Chem. Phys.* **109**, 3518 (1998).
193. F. Matzkies and U. Manthe, *J. Chem. Phys.* **110**, 88 (1999).
194. G. R. Darling, Z. S. Wang, and S. Holloway, *Chem. Phys. Lett.* **365**, 157 (2002).
195. C. Corriol, G. R. Darling, S. Holloway, W. Brenig, I. Andrianov, T. Klamroth, and P. Saalfrank, *J. Chem. Phys.* **117**, 4489 (2002).
196. A. J. H. M. Meijer, A. J. Farebrother, and D. C. Clary, *J. Phys. Chem.* **106**, 8996 (2002).
197. A. J. H. M. Meijer, A. J. Farebrother, D. C. Clary, and A. J. Fisher, *J. Phys. Chem.* **105**, 2173 (2001).
198. M. Bonn, A. W. Kleyn, and G. J. Kroes, *Surf. Sci.* **500**, 475 (2002).
199. D. H. Zhang and J. C. Light, *J. Chem. Phys.* **105**, 1291 (1996).
200. W. Zhu, J. Dai, J. Z. H. Zhang, and D. H. Zhang, *J. Chem. Phys.* **105**, 4881 (1996).
201. D. H. Zhang, M. A. Collins, and S.-Y. Lee, *Science* **290**, 958 (2000).
202. A. J. H. M. Meijer, *Comput. Phys. Commun.* **141**, 330 (2001).

THE MOMENTUM DENSITY PERSPECTIVE OF THE ELECTRONIC STRUCTURE OF ATOMS AND MOLECULES

AJIT J. THAKKAR

Department of Chemistry, University of New Brunswick, Fredericton, New Brunswick E3B 6E2, Canada

CONTENTS

Advances in Chemical Physics, Volume 128, edited by Stuart A. Rice
ISBN 0-471-44528-2

I. INTRODUCTION

Electronic structure is often visualized with the help of the electron density $\rho(\vec{r})$, which tells us where the electrons are likely to be found. A different perspective of electronic structure is provided by the electron momentum density $\mathbf{\Pi}(\vec{p})$ because $\mathbf{\Pi}(\vec{p})\, d\vec{p}$ is proportional to the probability of finding an electron with linear momentum $\vec{p}$.

Density functional theory purists are apt to argue that the Hohenberg–Kohn theorem [1] ensures that the ground-state electron density $\rho(\vec{r})$ determines all the properties of the ground state. In particular, the electron momentum density $\mathbf{\Pi}(\vec{p})$ is determined by the electron density. Although this is true in principle, there is no known direct route from ρ to $\mathbf{\Pi}$. Thus, in practice, the electron density and momentum density offer complementary approaches to a qualitative understanding of electronic structure.

The possibility that the momentum density viewpoint may bring novel chemical insights was first explored in the 1940s by Coulson and Duncanson [2–8], who recognized that the $\rho(\vec{r})$ and $\mathbf{\Pi}(\vec{p})$ densities are reciprocal in the sense that the valence region corresponds to large distances $r = |\vec{r}|$ and small momenta $p = |\vec{p}|$, whereas the core region corresponds to small r and large p.

Several review articles on the theoretical aspects of electron momentum densities of atoms and molecules were written in the 1970s by Benesch and Smith [9], Epstein [10,11], Mendelsohn and Smith [12], Epstein and Tanner [13], Lindner [14], and Kaijser and Smith [15]. Since that time (e,2e) spectroscopy and the momentum densities of Dyson orbitals have been reviewed very often [16–28]. However, to my knowledge, a review article on molecular electron momentum densities has not been written recently apart from one [29] devoted solely to the zero-momentum critical point. The purpose of this chapter is to survey what is known about the electron momentum density of atoms and molecules, and to provide an extensive, but not exhaustive, bibliography that should be sufficient to give a head start to a nonspecialist who wishes to enter the field.

Since momentum densities are unfamiliar to many, Section II outlines the connection between the position and momentum space representations of wavefunctions and reduced-density matrices, and the connections among one-electron density matrices, densities, and other functions such as the reciprocal form factor. General properties of momentum densities, including symmetry, expansion methods, asymptotic behavior, and moments, are described in

Section III. Methods for obtaining momentum densities, both experimental and computational, are reviewed in Section IV. Only a sample of representative work on the electron momentum densities of atoms and molecules is summarized in Sections V and VI because the topic is now too vast for comprehensive coverage. Electron momentum densities in solids and other condensed phases are not considered at all. The literature on electron momentum spectroscopy and Dyson orbital momentum densities is not surveyed, either. Hartree atomic units are used throughout.

II. QUANTITIES IN *r* AND *p* SPACES

A. Wavefunctions

We restrict ourselves to the clamped-nucleus or Born–Oppenheimer approximation [30,31] because essentially all the work done to date on electron momentum densities has relied on it. Therefore we focus on purely electronic wavefunctions and the electron densities that they lead to.

Suppose that $\Psi(\vec{x}_1, \vec{x}_2, \ldots, \vec{x}_N)$ is the position–space representation of the N-electron wavefunction. It is a function of the space–spin coordinates $\vec{x}_k = (\vec{r}_k, \sigma_k)$ in which $\vec{r}_k$ is the position vector of the kth electron and σ_k is its spin coordinate. The position–space wavefunction Ψ is obtained by solving the usual position- or r-space Schrödinger equation by one of the many well-developed approximate methods [32–34].

The counterpart wavefunction in momentum–space, $\Phi(\vec{y}_1, \vec{y}_2, \ldots, \vec{y}_N)$, is a function of momentum–spin coordinates $\vec{y}_k = (\vec{p}_k, \sigma_k)$ in which $\vec{p}_k$ is the linear momentum of the kth electron. There are three approaches to obtaining the momentum–space wavefunction, two direct and one indirect. The wavefunction Φ can be obtained directly by solving either a differential or an integral equation in momentum– or p space. It can also be obtained indirectly by transformation of the position–space wavefunction.

The differential equation for Φ results from a replacement of each coordinate x in the Hamiltonian operator by $i\partial/\partial p_x$. This approach is not at all simple because of the Coulomb potentials, which involve r^{-1}. Nevertheless, Hylleraas did succeed in solving this equation for the hydrogen atom [35].

The other direct method is to Fourier-transform the Schrödinger equation to obtain an integral equation for Φ. This equation was solved for the hydrogen atom by Fock [36,37]. An iterative method of Svartholm [38,39] for solving the integral equation was first applied to He and H_2^+ by McWeeny and Coulson [40,41], and later to He by Henderson and Scherr [42]. Shibuya and Wulfman [43], Novosadov [44,45], Monkhorst and Jeziorski [46], and Duchon et al. [47] tackled polyatomic one-electron systems. The integral equation approach has been developed and tested by several groups since then, but the amount of effort

devoted to this pales in comparison with the stupendous amount of work done on solving the position–space Schrödinger equation. Although the focus of this review is not the direct solution of the Schrödinger equation in momentum–space, a list of the relatively few references [48–107] is given in hopes of encouraging further work. The momentum–space Schrödinger equation has also been used to derive conditions [108–117] to check and possibly improve the accuracy of approximate wavefunctions obtained by position–space methods.

The technology for solving the Schrödinger equation is so much farther advanced in r space than in p space that it is most practical to obtain the momentum–space Φ from its position–space counterpart Ψ. The transformation theories of Dirac [118,119] and Jordan [120,121] provide the link between these representations:

$$\Phi = (2\pi)^{-3N/2} \int \Psi \ \exp\left[-\mathrm{i} \sum_{k=1}^{N} \vec{p}_k \cdot \vec{r}_k\right] d\vec{r}_1 \, d\vec{r}_2 \cdots d\vec{r}_N \tag{5.1}$$

In short, Ψ and Φ are related by a $3N$-dimensional, norm-preserving, Fourier transform. If the r-space wavefunction is constructed from one-electron functions, then there is an isomorphism [2] between Ψ and Φ. In particular, if the wavefunction Ψ can be written in terms of spin–orbitals $\psi_j(\vec{x})$ as a single Slater determinant

$$\Psi(\vec{x}_1, \vec{x}_2, \ldots, \vec{x}_N) = \frac{1}{\sqrt{N!}} \det|\psi_1(\vec{x}_1)\psi_2(\vec{x}_2) \cdots \psi_N(\vec{x}_N)| \tag{5.2}$$

then the corresponding p-space wavefunction is also a Slater determinant

$$\Phi(\vec{y}_1, \vec{y}_2, \ldots, \vec{y}_N) = \frac{1}{\sqrt{N!}} \det|\phi_1(\vec{y}_1)\phi_2(\vec{y}_2) \cdots \phi_N(\vec{y}_N)| \tag{5.3}$$

in which the spin–*momentals*,[1] or p-space spin–orbitals, $\phi_j(\vec{y})$ are obtained from the r-space spin–orbitals by the one-electron version of Eq. (5.1):

$$\phi_j(\vec{p}, \sigma) = (2\pi)^{-3/2} \int \psi_j(\vec{r}, \sigma) e^{-\mathrm{i}\vec{p}\cdot\vec{r}} \, d\vec{r} \tag{5.4}$$

If the r-space wavefunction is a linear combination of Slater determinants constructed from a set of spin–orbitals $\{\psi_j\}$, then its p-space counterpart is the

[1]In a private letter to me dated August 1, 1986, Robert S. Mulliken suggested the name *momental* for the momentum–space counterpart of an orbital. I have tried to keep this nomenclature alive in his honor.

same linear combination of Slater determinants constructed from the spin–momentals $\{\phi_j\}$ obtained as Fourier transforms (5.4) of the spin–orbitals. The overwhelming majority of contemporary r-space wavefunctions can be expressed as a linear combination of Slater determinants, and hence only three-dimensional Fourier transforms (5.4) of the spin–orbitals are necessary to obtain the corresponding N-electron wavefunction in p space. Use of Eq. (5.1) becomes necessary only for wavefunctions, such as Hylleraas- or Jastrow-type wavefunctions, that are not built from a one-electron basis set.

B. Density Matrices

If we are interested only in properties that can be expressed in terms of q-electron operators, then it is sufficient to work with the qth-order reduced-density matrix rather than the N-electron wavefunction [122–126]. In this section, we consider links between the r- and p-space representations of reduced-density matrices. In particular, we show that if we need the qth-order density matrix in p space, then it can be obtained from its counterpart in r space without reference to the N-electron wavefunction in p space.

The r-space, qth-order, reduced-density matrix [123] is defined by

$$\Gamma^{(q)}(\vec{x}_1,\ldots,\vec{x}_q \mid \vec{x}'_1,\ldots,\vec{x}'_q) = \binom{N}{q} \int d\vec{x}_{q+1}\cdots d\vec{x}_N\, \Psi^*(\vec{x}'_1,\ldots,\vec{x}'_q,\vec{x}_{q+1},\ldots,\vec{x}_N)\Psi(\vec{x}_1,\ldots,\vec{x}_N) \qquad (5.5)$$

where the multiplicative binomial factor leads to the so-called Löwdin normalization. Replacement of this factor by $N!/(N-q)!$ leads to statistical normalization [124] that is appropriate in the limit as $N \to \infty$, whereas omission of the factor leads to unit normalization preferred by mathematicians [125]. If electronic spin is not a focus of attention, then spin can be traced out. The r-space, spin-traced, qth-order, reduced density matrix is

$$\Gamma^{(q)}(\vec{r}_1,\ldots,\vec{r}_q \mid \vec{r}'_1,\ldots,\vec{r}'_q) = \int d\sigma_1\, d\sigma'_1\cdots d\sigma_q\, d\sigma'_q \Gamma^{(q)}(\vec{x}_1,\ldots,\vec{x}_q \mid \vec{x}'_1,\ldots,\vec{x}'_q) \times \delta(\sigma_1-\sigma'_1)\cdots\delta(\sigma_q-\sigma'_q) \qquad (5.6)$$

where δ is Dirac's delta function [118,119]. The reduced-density matrices form a hierarchy as the qth-order density matrix can be obtained from the $(q+1)$st-order density matrix as follows

$$\Gamma^{(q)} = \frac{(q+1)}{(N-q)} \int d\vec{x}_{q+1}\, \Gamma^{(q+1)}(\vec{x}_1,\ldots,\vec{x}_q,\vec{x}_{q+1} \mid \vec{x}'_1,\ldots,\vec{x}'_q,\vec{x}_{q+1}) \qquad (5.7)$$

and an analogous equation can be written for the spin-free case.

In a similar manner, the p-space, qth-order, reduced-density matrix [29,127,128] is defined by

$$\mathbf{\Pi}^{(q)}(\vec{y}_1,\ldots,\vec{y}_q \mid \vec{y}'_1,\ldots,\vec{y}'_q) = \binom{N}{q} \int d\vec{y}_{q+1}\ldots d\vec{y}_N\, \Phi^*(\vec{y}'_1,\ldots,\vec{y}'_q,\vec{y}_{q+1},\ldots,\vec{y}_N)\Phi(\vec{y}_1,\ldots,\vec{y}_N) \tag{5.8}$$

and its spin-traced counterpart by

$$\mathbf{\Pi}^{(q)}(\vec{p}_1,\ldots,\vec{p}_q \mid \vec{p}'_1,\ldots,\vec{p}'_q) = \int d\sigma_1\, d\sigma'_1\cdots d\sigma_q\, d\sigma'_q \times \mathbf{\Pi}^{(q)}(\vec{y}_1,\ldots,\vec{y}_q \mid \vec{y}'_1,\ldots,\vec{y}'_q)\delta(\sigma_1-\sigma'_1)\cdots\delta(\sigma_q-\sigma'_q) \tag{5.9}$$

The p-space density matrices form a hierarchy related through the analog of Eq. (5.7).

The r-space and p-space representations of the qth-order density matrices, whether spin-traced or not, are related [127] by a $6q$-dimensional Fourier transform because the parent wavefunctions are related by a $3N$-dimensional Fourier transform. Substitution of Eq. (5.1) in Eq. (5.8), and integration over the momentum variables, leads to the following explicit spin-traced relationship:

$$\mathbf{\Pi}^{(q)}(\vec{p}_1,\ldots,\vec{p}_q \mid \vec{p}'_1,\ldots,\vec{p}'_q) = (2\pi)^{-3q}\int d\vec{r}_1\cdots d\vec{r}_q\, d\vec{r}'_1\cdots d\vec{r}'_q \times \Gamma^{(q)}(\vec{r}_1,\ldots,\vec{r}_q \mid \vec{r}'_1,\ldots,\vec{r}'_q)\exp\left[-i\sum_{k=1}^{q}(\vec{p}_k\cdot\vec{r}_k - \vec{p}'_k\cdot\vec{r}'_k)\right] \tag{5.10}$$

The corresponding relation including spin is simply Eq. (5.10) with the spin-traced density matrices replaced by their counterparts, including spin.

The relationships of this section are summarized in Figure 5.1, which makes it clear that the reduced density matrices form a hierarchy in each space with

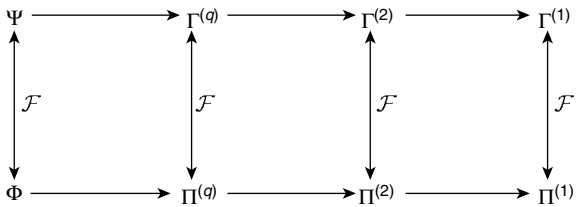

Figure 5.1. The hierarchy of $\vec{r}$- and $\vec{p}$-space wavefunctions (Ψ and Φ) and density matrices ($\Gamma^{(q)}$ and $\mathbf{\Pi}^{(q)}$) and the connections between them. Two-headed arrows with a $\mathscr{F}$ beside them signify reversible Fourier transformations, whereas normal arrows signify irreversible contractions.

increasing removal of undesired information as q is stepped down from N to 1. Moreover, at any step in this reduction process a Fourier transform enables us to move from r to p space or vice versa. Since the usual Hamiltonian contains only one- and two-electron operators, and most other properties of interest can also be expressed in this manner, the most physically interesting density matrices are the one- and two-electron cases with $q = 1$ and $q = 2$.

C. One-Electron Densities

In this chapter, the primary focus is on the one-electron case. Dropping the $q = 1$ labels, we can write the r-space, first-order, density matrix as

$$\Gamma(\vec{x} \mid \vec{x}') = N \int \Psi^*(\vec{x}', \vec{x}_2, \ldots, \vec{x}_N)\Psi(\vec{x}, \vec{x}_2, \ldots, \vec{x}_N)\, d\vec{x}_2 \cdots d\vec{x}_N \tag{5.11}$$

and the p-space, first-order, density matrix as

$$\mathbf{\Pi}(\vec{y} \mid \vec{y}') = N \int \Phi^*(\vec{y}', \vec{y}_2, \ldots, \vec{y}_N)\Phi(\vec{y}, \vec{y}_2, \ldots, \vec{y}_N)\, d\vec{y}_2 \cdots d\vec{y}_N \tag{5.12}$$

If electronic spin is not a focus of attention, then the spin-traced versions of these density matrices can be used. The r-space, spin-traced, first-order, reduced-density matrix is

$$\Gamma(\vec{r} \mid \vec{r}') = \int \Gamma(\vec{x} \mid \vec{x}')\delta(\sigma - \sigma')\, d\sigma\, d\sigma' \tag{5.13}$$

and the p-space, spin-traced, first-order, reduced-density matrix is

$$\mathbf{\Pi}(\vec{p} \mid \vec{p}') = \int \mathbf{\Pi}(\vec{y} \mid \vec{y}')\delta(\sigma - \sigma')\, d\sigma\, d\sigma' \tag{5.14}$$

Setting $q = 1$ in Eq. (5.10) shows that the first-order r- and p-space density matrices (whether spin-traced or not) are related by a six-dimensional Fourier transform [127,129]:

$$\mathbf{\Pi}(\vec{p} \mid \vec{p}') = (2\pi)^{-3} \int \Gamma(\vec{r} \mid \vec{r}') \exp[-i(\vec{p} \cdot \vec{r} - \vec{p}' \cdot \vec{r}')]\, d\vec{r}\, d\vec{r}' \tag{5.15}$$

and its inverse

$$\Gamma(\vec{r} \mid \vec{r}') = (2\pi)^{-3} \int \mathbf{\Pi}(\vec{p} \mid \vec{p}') \exp[+i(\vec{p} \cdot \vec{r} - \vec{p}' \cdot \vec{r}')]\, d\vec{p}\, d\vec{p}' \tag{5.16}$$

The physically meaningful quantities are the densities—the diagonal elements of the density matrices. For $q = 1$, we have the usual one-electron position density

$$\rho(\vec{r}) = \Gamma(\vec{r} \mid \vec{r}) = N \int |\Psi|^2 \delta(\vec{r} - \vec{r}_1)\, d\vec{x}_1\, d\vec{x}_2 \cdots d\vec{x}_N \tag{5.17}$$

and the one-electron momentum density

$$\mathbf{\Pi}(\vec{p}) = \mathbf{\Pi}(\vec{p} \mid \vec{p}) = N \int |\Phi|^2 \delta(\vec{p} - \vec{p}_1)\, d\vec{y}_1\, d\vec{y}_2 \cdots d\vec{y}_N \tag{5.18}$$

Letting $\vec{p}\,' = \vec{p}$ in Eq. (5.15) yields

$$\mathbf{\Pi}(\vec{p}) = (2\pi)^{-3} \int \Gamma(\vec{r} \mid \vec{r}\,') \exp[+i\vec{p} \cdot (\vec{r}\,' - \vec{r})]\, d\vec{r}\, d\vec{r}\,' \tag{5.19}$$

and letting $\vec{r}\,' = \vec{r}$ in Eq. (5.16) gives

$$\rho(\vec{r}) = (2\pi)^{-3} \int \mathbf{\Pi}(\vec{p} \mid \vec{p}\,') \exp[-i\vec{r} \cdot (\vec{p}\,' - \vec{p})]\, d\vec{p}\, d\vec{p}\,' \tag{5.20}$$

If the system is in a pure spin state, that is, $\hat{S}^2\Psi = S(S+1)\Psi$ and $\hat{S}_z\Psi = M_s\Psi$, then the electron density can be decomposed into spin components as follows

$$\rho(\vec{r}) = \rho_\alpha(\vec{r}) + \rho_\beta(\vec{r}) \tag{5.21}$$

and it is then conventional to introduce the spin density defined by

$$\rho_s(\vec{r}) = \frac{\rho_\alpha(\vec{r}) - \rho_\beta(\vec{r})}{2M_s} \tag{5.22}$$

The corresponding decomposition of the momentum density is

$$\mathbf{\Pi}(\vec{p}) = \mathbf{\Pi}_\alpha(\vec{p}) + \mathbf{\Pi}_\beta(\vec{p}) \tag{5.23}$$

and the spin momentum density is

$$\mathbf{\Pi}_s(\vec{p}) = \frac{\mathbf{\Pi}_\alpha(\vec{p}) - \mathbf{\Pi}_\beta(\vec{p})}{2M_s} \tag{5.24}$$

The rest of this section is a brief digression that is too interesting to resist. Equations (5.19) and (5.20) suggest that sum and difference transformations in both $\vec{r}$ space

$$\vec{R} = \frac{\vec{r}' + \vec{r}}{2}, \qquad \vec{s} = \vec{r}' - \vec{r} \tag{5.25}$$

and $\vec{p}$ space

$$\vec{P} = \frac{\vec{p}' + \vec{p}}{2}, \qquad \vec{\mu} = \vec{p}' - \vec{p} \tag{5.26}$$

may prove interesting. This is indeed so. The Jacobians of these transformations are unity, so that

$$d\vec{r}\, d\vec{r}' = d\vec{R}\, d\vec{s}, \qquad d\vec{p}\, d\vec{p}' = d\vec{P}\, d\vec{\mu} \tag{5.27}$$

Then, instead of performing the six-dimensional integral in Eq. (5.19) all at once, we perform successive three-dimensional integrals over $\vec{s}$ and $\vec{R}$. The first step takes us to $W(\vec{R}, \vec{P})$, the Wigner representation [130,131] of the density matrix, and the second step to the p-space density matrix, $\mathbf{\Pi}(\vec{P} - \vec{\mu}/2|\vec{P} + \vec{\mu}/2)$. The reverse transformation of Eq. (5.20) can also be performed stepwise over $\vec{P}$ and $\vec{\mu}$ to obtain $A(\vec{s}, \vec{\mu})$, the Moyal mixed representation [132], and then the r-space representation $\Gamma(\vec{R} - \vec{s}/2|\vec{R} + \vec{s}/2)$. These steps are shown schematically in Figure 5.2.

The electron and momentum densities are just marginal probability functions of the density matrix in the Wigner representation even though the latter, by the Heisenberg uncertainty principle, cannot be and is not a true joint position–momentum probability density. However, it is possible to project the Wigner density matrix onto a set of physically realizable states that optimally fulfill the uncertainty condition. One such representation is the Husimi function [122,133–135]. This seductive line of thought takes us too far away from the focus of this

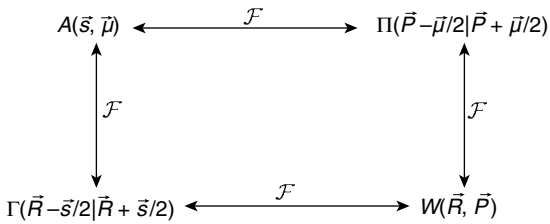

Figure 5.2. The relationships among the r-space density matrix Γ, the p-space density matrix $\mathbf{\Pi}$, the Wigner representation W, and the Moyal representation A. Two-headed arrows with a $\mathcal{F}$ beside them signify reversible, three-dimensional, Fourier transformations.

short chapter, and so we merely refer the reader to the literature [136–144] for applications of the Wigner, Husimi, and Moyal functions to the electronic structure of molecules.

D. Connections with Other Functions

Although the r- and p-space representations of wavefunctions and density matrices are related by Fourier transformation, Eqs. (5.19) and (5.20) show that the densities are not so related. This is easily understood for a one-electron system where the r-space density is just the squared magnitude of the orbital and the p-space density is the squared magnitude of the Fourier transform of the orbital. The operations of Fourier transformation and taking the absolute value squared do not commute, and so the p-space density is not the Fourier transform of its r-space counterpart. In this section, we examine exactly what the Fourier transforms of these densities are.

Since $\mathbf{\Pi}(\vec{p})$ cannot be obtained by Fourier transformation of $\rho(\vec{r})$, we may ask what the function from which $\mathbf{\Pi}(\vec{p})$ can be obtained by Fourier transformation is. Or, to put it the other way around, if Fourier transformation of a density in one space does not yield the density in the other space, what does it give? This question has been considered [127] in some generality and detail. Here we merely summarize the outcome for the one-electron densities.

The substitution $\vec{s} = \vec{r}' - \vec{r}$ allows Eq. (5.19) to be written as

$$\mathbf{\Pi}(\vec{p}) = (2\pi)^{-3} \int e^{i\vec{s}\cdot\vec{p}}\, \Gamma(\vec{r} \mid \vec{r} + \vec{s})\, d\vec{r}\, d\vec{s} \tag{5.28}$$

Performing the $\vec{r}$ integration, we can write

$$\mathbf{\Pi}(\vec{p}) = (2\pi)^{-3} \int e^{i\vec{s}\cdot\vec{p}} B(\vec{s})\, d\vec{s} \tag{5.29}$$

and see that $\mathbf{\Pi}(\vec{p})$ is the Fourier transform of the function $B(\vec{s})$ defined by

$$B(\vec{s}) = \int \Gamma(\vec{r} \mid \vec{r} + \vec{s})\, d\vec{r} \tag{5.30}$$

$B(\vec{s})$ is variously called the *reciprocal form factor*, the *p-space form factor*, and the *internally folded density*. $B(\vec{s})$ is the basis of a method for reconstructing momentum densities from experimental data [145,146], and it is useful for the r-space analysis of Compton profiles [147–151]. The $B(\vec{s})$ function probably first arose in an examination of the connection between form factors and the electron momentum density [129]. The $B(\vec{s})$ function has been rediscovered by Howard et al. [152].

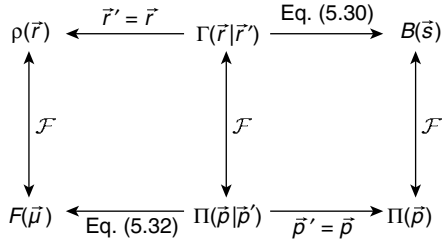

Figure 5.3. Connections among $\vec{r}$- and $\vec{p}$-space densities, density matrices, and form factors. Two-headed arrows signify reversible transformations; single-barbed arrows signify irreversible transformations. A Fourier transform is denoted by $\mathcal{F}$.

We now ask analogous questions about the electron density. The Fourier transform of $\rho(\vec{r})$ is the form factor of X-ray crystallography:

$$F(\vec{\mu}) = \int e^{i\vec{\mu}\cdot\vec{r}}\,\rho(\vec{r})\,d\vec{r} \tag{5.31}$$

How is the form factor related to the p-space density matrix? Substitution of Eq. (5.20) into Eq. (5.31) and integration over $\vec{r}$ and $\vec{p}\,'$ yields [127,129]

$$F(\vec{\mu}) = \int \mathbf{\Pi}(\vec{p}\mid\vec{p}+\vec{\mu})\,d\vec{p} \tag{5.32}$$

Figure 5.3 provides a concise summary of these relationships. A more elaborate figure that combines Figures 5.2 and 5.3 and adds some further detail can be found elsewhere [153].

III. PROPERTIES OF THE MOMENTUM DENSITY

A. Symmetry

The principle of microreversibility [154,155] applies to all bound states corresponding to real Hamiltonian operators. Hence the N-electron momentum density before and after time reversal are related by

$$\mathbf{\Pi}^{(N)}(\vec{p}_1,\ldots,\vec{p}_N,t) = \mathbf{\Pi}^{(N)}(-\vec{p}_1,\ldots,-\vec{p}_N,-t) \tag{5.33}$$

from which it follows that for bound states of atoms and molecules, the exact one-electron momentum density has inversion symmetry:

$$\mathbf{\Pi}(\vec{p}) = \mathbf{\Pi}(-\vec{p}) \tag{5.34}$$

All real-valued wavefunctions and the overwhelming majority of other approximate wavefunctions also produce [156] momentum densities that satisfy

Eq. (5.34). However, it is possible to construct approximate wavefunctions that lead to electron momentum densities that do not have inversion symmetry. Within the Born–Oppenheimer approximation, the total electronic system must be at rest; the at-rest condition

$$\int \vec{p}\,\mathbf{\Pi}(\vec{p})\,d\vec{p} = 0 \tag{5.35}$$

is automatically satisfied because of inversion symmetry [156]. Another immediate consequence of inversion symmetry is that the gradient of $\mathbf{\Pi}(\vec{p})$ vanishes at $\vec{p} = \vec{0}$, and $\vec{p} = \vec{0}$ is always a critical point of $\mathbf{\Pi}(\vec{p})$.

Quite apart from the inversion symmetry described above, within the Born–Oppenheimer approximation, there is symmetry that results from the symmetry of the nuclear configuration. Suppose that the latter has the symmetry described by the point group $\mathscr{G}_n$. In the absence of degeneracies, this ensures that both the exact number density $\rho(\vec{r})$ and the exact momentum density $\mathbf{\Pi}(\vec{p})$ transform as the totally symmetric irreducible representation of $\mathscr{G}_n$. The densities obtained from approximate wavefunctions will also have this symmetry provided that the underlying basis set is closed under the symmetry operations of $\mathscr{G}_n$, and that there are no methodological artifacts that break the symmetry. If there are degeneracies, these arguments remain valid provided that we take averages of the densities over the ensemble of degenerate states.

Taking both the symmetry of the nuclear configuration and the inversion symmetry described above into account, it follows that the symmetry of the momentum density $\mathbf{\Pi}(\vec{p})$ is $\mathscr{G}_n \otimes \mathscr{C}_\mathrm{i}$. If $\mathscr{G}_n$ contains the inversion operation $\hat{i}$, then $\mathscr{G}_n \otimes \mathscr{C}_\mathrm{i} = \mathscr{G}_n$. However, if $\mathscr{G}_n$ does not contain $\hat{i}$, then the symmetry of the momentum density is higher than $\mathscr{G}_n$. For example, a heteronuclear diatomic molecule like HF has $\mathscr{C}_{\infty v}$ symmetry, as does its electron density $\rho(\vec{r})$, but its momentum density $\mathbf{\Pi}(\vec{p})$ has $\mathscr{C}_{\infty v} \otimes \mathscr{C}_\mathrm{i} = \mathscr{D}_{\infty \mathrm{h}}$ symmetry, as seen graphically in the work of Thakkar et al. [157]. Rawlings and Davidson [158] gave other graphical examples: pyrrole for which $\rho(\vec{r})$ has $\mathscr{C}_{2v}$ symmetry but $\mathbf{\Pi}(\vec{p})$ has $\mathscr{D}_{2h}$ symmetry, and the cyclopentadiene anion for which $\rho(\vec{r})$ has $\mathscr{D}_{5h}$ symmetry but $\mathbf{\Pi}(\vec{p})$ has $\mathscr{D}_{10h}$ symmetry. Further discussions of the increased symmetry in p space, including tables of $\mathscr{G}_n \otimes \mathscr{C}_\mathrm{i}$, can be found elsewhere [159–161].

B. Expansions

Within the Born–Oppenheimer approximation, the nuclei are at rest and have zero momentum. So the electron momentum density is an intrinsically one-center function that can be expressed usefully in spherical polar coordinates and expanded as follows [162,163]

$$\mathbf{\Pi}(\vec{p}) = \sum_{\ell=0}^{\infty} \sum_{m=-\ell}^{\ell} \mathbf{\Pi}_{2\ell,m}(p) Y_{2\ell,m}(\theta_p, \varphi_p) \tag{5.36}$$

where the $Y_{2\ell,m}(\theta_p, \varphi_p)$ are the spherical harmonic functions [155,164]. Only terms with even ℓ contribute because of inversion symmetry. This expansion is commonly used in the reconstruction of momentum densities from experimental data [162] and has been used for the analysis of momentum densities [163]. It is often convenient to use real-valued harmonics $S_{2\ell,m}(\theta_p, \varphi_p)$ instead of the complex-valued $Y_{2\ell,m}(\theta_p, \varphi_p)$ in Eq. (5.36).

Molecular symmetry leads to further restrictions on the expansion (5.36). A discussion, with many references, of symmetry-adapted expansions was given by Heuser-Hofmann and Weyrich [165]. A particularly simple case occurs in linear molecules where cylindrical symmetry ensures that there is no φ_p dependence. Hence only the $m = 0$ terms survive, and the expansion (5.36) becomes simply [157]

$$\mathbf{\Pi}(\vec{p}) = \sum_{\ell=0}^{\infty} \mathbf{\Pi}_{2\ell}(p) P_{2\ell}(\cos\theta_p) \tag{5.37}$$

where $\mathbf{\Pi}_{2\ell}(p) = [(4\ell + 1)/(4\pi)]^{1/2} \mathbf{\Pi}_{2\ell,0}(p)$ and $P_{2\ell}(\cos\theta_p)$ is a Legendre polynomial [155,166]. The expansion is rapidly convergent in the chemically important small-p region where it is dominated [157] by the spherical term $\mathbf{\Pi}_0(p)$ and the first three anisotropic terms involving $\mathbf{\Pi}_2(p)$, $\mathbf{\Pi}_4(p)$, and $\mathbf{\Pi}_6(p)$.

Special importance is attached to the leading term

$$\mathbf{\Pi}_0(p) = \frac{\mathbf{\Pi}_{00}(p)}{(4\pi)^{1/2}} \tag{5.38}$$

of the expansions of Eqs. (5.36) and (5.37). This term is simply the spherical average of the electron momentum density:

$$\mathbf{\Pi}_0(p) = (4\pi)^{-1} \int \mathbf{\Pi}(\vec{p})\, d\Omega_{\vec{p}} = (4\pi)^{-1} \int_0^{2\pi} \int_0^{\pi} \mathbf{\Pi}(\vec{p})\, d\theta_p\, d\varphi_p \tag{5.39}$$

For S-state atoms, the momentum density is spherically symmetric and therefore $\mathbf{\Pi}(\vec{p}) = \mathbf{\Pi}_0(p)$. Nonspherical $\mathbf{\Pi}(\vec{p})$ can occur in atomic states of higher angular momentum. However, these states are degenerate, and an ensemble average is required. This is equivalent to a spherical average for any one of the states in the degenerate manifold. The spherically averaged momentum density $\mathbf{\Pi}_0(p)$ is also of interest for molecules because it is a quantity that can be obtained from gas-phase experiments.

C. Asymptotic Behavior

The asymptotic behavior of the spherically averaged momentum density $\mathbf{\Pi}_0(p)$ is well understood. The small-p behavior is most easily treated with the

MacLaurin expansion of $\mathbf{\Pi}_0(p)$ given by [167,168]

$$\mathbf{\Pi}_0(p) = \mathbf{\Pi}_0(0) + \frac{\mathbf{\Pi}_0''(0)p^2}{2!} + \frac{\mathbf{\Pi}_0^{(\mathrm{iv})}(0)p^4}{4!} + \cdots \tag{5.40}$$

in which $\mathbf{\Pi}_0(0) = \mathbf{\Pi}(\vec{0}) = \mathbf{\Pi}(0)$ is the electron momentum density at zero momentum, $\mathbf{\Pi}_0''(0)$ is its curvature at that point, and $\mathbf{\Pi}_0^{(\mathrm{iv})}(0)$ is its fourth derivative at $p = 0$. The coefficients of p^k in Eq. (5.40) have, in some previous work, been denoted by A_k; for example, $A_2 = \mathbf{\Pi}_0''(0)/2$. Only even powers of p appear in the expansion because of inversion symmetry. Combining Eqs. (5.29) and (5.30) and taking the limit as $\vec{p} \to \vec{0}$ leads to the relationships [127]

$$\mathbf{\Pi}_0(0) = \mathbf{\Pi}(\vec{0}) = (2\pi)^{-3} \int B(\vec{s})\, d\vec{s} = (2\pi)^{-3} \int \Gamma(\vec{r} \mid \vec{r} + \vec{s})\, d\vec{r}\, d\vec{s} \tag{5.41}$$

which show the link between the momentum density at zero-momentum and r-space functions.

The asymptotic expansion for large p is given [9,12,168,169] by

$$\mathbf{\Pi}_0(p) = b_8 p^{-8} + b_{10} p^{-10} + b_{12} p^{-12} + \cdots \tag{5.42}$$

In atoms, the coefficient of the leading term in Eq. (5.42) can be expressed in terms of r-space densities as [12,168,169]

$$b_8 = \frac{2}{\pi}\left[-2Z\left(\frac{d\rho_0}{dr}\right)_{r=0} + \left(\frac{dI_0}{du}\right)_{u=0}\right] \tag{5.43}$$

in which

$$\rho_0(r) = (4\pi)^{-1} \int \rho(\vec{r})\, d\Omega_{\vec{r}} \tag{5.44}$$

is the spherical average of the electron density and

$$I_0(u) = (4\pi)^{-1} \int I(\vec{u})\, d\Omega_{\vec{u}} \tag{5.45}$$

is the spherical average of the intracule, or interelectronic vector, density defined [128,170] by

$$I(\vec{u}) = \int \Gamma^{(2)}(\vec{r}_1, \vec{r}_2)\, \delta(\vec{u} - \vec{r}_1 + \vec{r}_2)\, d\vec{r}_1\, d\vec{r}_2 \tag{5.46}$$

If the electron–nucleus cusp condition for the electron density [171,172]

$$\left(\frac{d\rho_0}{dr}\right)_{r=0} = -2Z\rho_0(0) \tag{5.47}$$

and the electron–electron cusp condition for the intracule density [171,173]

$$\left(\frac{dI_0}{du}\right)_{u=0} = I_0(0) \tag{5.48}$$

are satisfied, as they must be for the exact wavefunction, then the leading coefficient of the asymptotic expansion of Eq. (5.42) can be rewritten simply as

$$b_8 = \frac{2}{\pi}\left[4Z^2\rho_0(0) + I_0(0)\right] \tag{5.49}$$

This equation connects the large-p behavior of the momentum density with the small-r behavior of the electron density and small-u behavior of the intracule density. Hence, Eq. (5.49) is a quantitative manifestation of the reciprocal nature of r and p space.

D. Moments

Some simple characteristics of the momentum density are its moments defined by

$$\langle p^k \rangle = \int p^k \mathbf{\Pi}(\vec{p})\, d\vec{p} \tag{5.50}$$

Integration over the spherical polar angles leads to

$$\langle p^k \rangle = 4\pi \int_0^\infty p^{k+2} \mathbf{\Pi}_0(p)\, dp = \int_0^\infty p^k I(p)\, dp \tag{5.51}$$

in which the radial momentum density $I(p)$ is defined by

$$I(p) = 4\pi p^2 \mathbf{\Pi}_0(p) \tag{5.52}$$

In view of the asymptotic behavior of $\mathbf{\Pi}_0(p)$ shown in Eqs. (5.40) and (5.42), it is apparent that the moments $\langle p^k \rangle$ are finite only for $-3 < k < 5$. The $k = 0$ moment is simply the number of electrons because of the normalization condition

$$\langle p^0 \rangle = \int \mathbf{\Pi}(\vec{p})\, d\vec{p} = N \tag{5.53}$$

The second moment $\langle p^2 \rangle$ is twice the electronic kinetic energy, and the fourth moment $\langle p^4 \rangle$ is proportional to the correction to the kinetic energy due to the relativistic "variation of mass with velocity" [174–178].

Since the momentum density is related to the reciprocal form factor or internally folded density by a Fourier transform, Eq. (5.29), there are sum rules that connect moments of momentum with the spherical average of $B(\vec{r})$ defined by

$$B_0(r) = (4\pi)^{-1} \int B(\vec{r})\, d\Omega_{\vec{r}} \tag{5.54}$$

$$= 4\pi \int_0^\infty \mathbf{\Pi}_0(p)\, j_0(pr)\, p^2\, dp \tag{5.55}$$

in which $j_0(x) = x^{-1} \sin x$ is the zeroth-order spherical Bessel function [166]. Specifically [127,179,180], there are the following integral relations

$$\frac{\pi \langle p^3 \rangle}{8} = \int_0^\infty r^{-1} \frac{d^3 B_0}{dr^3}\, dr \tag{5.56}$$

$$\frac{\pi \langle p \rangle}{4} = \int_0^\infty r^{-2} [N - B_0(r)]\, dr \tag{5.57}$$

$$\frac{\pi \langle p^{-1} \rangle}{2} = \int_0^\infty B_0(r)\, dr \tag{5.58}$$

$$\langle p^{-2} \rangle = \int_0^\infty r B_0(r)\, dr \tag{5.59}$$

$$2\pi^2 \mathbf{\Pi}_0(0) = \int_0^\infty r^2 B_0(r)\, dr \tag{5.60}$$

the differential relationships

$$\langle p^2 \rangle = -3 \left(\frac{d^2 B_0}{dr^2} \right)_{r=0} \tag{5.61}$$

$$\langle p^4 \rangle = 5 \left(\frac{d^4 B_0}{dr^4} \right)_{r=0} \tag{5.62}$$

and the normalization condition $B_0(0) = N$.

IV. OBTAINING MOMENTUM DENSITIES

A. Isotropic Compton Profiles

There are well-exploited connections between experimental phenomena and electron momentum densities. Inelastic scattering [167,181–184] of high-energy electrons, X rays, or γ rays by electrons in a molecule allows us to measure the electron momentum density of the molecule. The observable is the intensity of the Compton scattering at wavelengths shifted, by a Doppler broadening–like

mechanism, from the wavelength at which Compton scattering by a motionless electron would be predicted. This intensity yields the probability of an electron having a certain momentum or, in other words, the electron momentum density provided that the experiment can be analyzed within the impulse approximation. The latter assumption is valid only when the energy of the incident photon is much larger than the target electron's binding energy. In that case, the momentum transfer between the photon and the electron can be assumed to take place instantaneously, allowing the target electron to be treated as a free electron with the same momentum. We can imagine that under these circumstances the target electron has been "caught" between collisions with other particles in the system, and the main effect of the other electrons and nuclei in the molecule is to smear out the probability of finding the target electron with a given momentum $\vec{p}$.

Within the impulse approximation, the gas-phase Compton profile $J_0(q)$ is related [185,186] to the isotropic momentum density by

$$J_0(q) = \frac{1}{2}\int_{|q|}^{\infty} p^{-1} I(p)\, dp = 2\pi \int_{|q|}^{\infty} p\, \mathbf{\Pi}_0(p)\, dp \tag{5.63}$$

where q is the momentum transfer. Clearly, Eq. (5.63) can be inverted to give

$$\mathbf{\Pi}_0(p) = \frac{-1}{2\pi p}\left(\frac{dJ_0(q)}{dq}\right)_p \tag{5.64}$$

Since $\mathbf{\Pi}_0(p) > 0$, it follows from Eq. (5.64) that the isotropic Compton profile $J_0(q)$ is a monotonically decreasing function of q. Letting $q = 0$ in Eq. (5.63) and comparing with Eq. (5.51), it is apparent that the peak of the isotropic Compton profile is half of the $k = -1$ moment:

$$J_0(0) = \tfrac{1}{2}\langle p^{-1}\rangle \tag{5.65}$$

The Compton profile satisfies the normalization condition:

$$2\int_0^{\infty} J_0(q)\, dq = N \tag{5.66}$$

Typically the experimental measurements are most accurate at small q. Inserting the MacLaurin expansion, Eq. (5.40), of $\mathbf{\Pi}_0(p)$ into Eq. (5.63) leads to the MacLaurin expansion [167,187] for the isotropic Compton profile:

$$J_0(q) = J_0(0) - [\pi \mathbf{\Pi}_0(0)]q^2 - \frac{\pi \mathbf{\Pi}_0''(0)}{4} q^4 + O(q^6) \tag{5.67}$$

and hence fitting the measured profile at small momentum transfers q to a polynomial in q^2 yields values of $\mathbf{\Pi}_0(0)$ and $\mathbf{\Pi}_0''(0)$. These coefficients have been extracted from experimental Compton profiles for both atoms and molecules [167]. Insertion of the asymptotic expansion of the momentum density, Eq. (5.42), into Eq. (5.63) leads to the large-q expansion [187]

$$J_0(q) = \frac{\pi b_8}{3} q^{-6} + \frac{\pi b_{10}}{4} q^{-8} + \frac{\pi b_{12}}{5} q^{-10} + \cdots \tag{5.68}$$

Other moments of momentum can also be obtained directly from the Compton profile without first going through the numerical differentiation of Eq. (5.64), which is prone to roundoff and truncation errors. In particular, several groups [9,188–191] independently reported one or more of the sum rules

$$\langle p^k \rangle = 2(k+1) \int_0^\infty q^k J_0(q)\, dq, \qquad 0 \le k \le 4 \tag{5.69}$$

which can be derived by integrating by parts, using Eqs. (5.51) and (5.64), and the expansions of Eqs. (5.67) and (5.68) to eliminate the surface terms. The $k = 0$ case of Eq. (5.69) is just the normalization condition, Eq. (5.66). Equations (5.65) and (5.69) provide a direct route from the Compton profile to the moments $\langle p^k \rangle$, $-1 \le k \le 4$. The remaining integral moment $\langle p^{-2} \rangle$ can be obtained from a sum rule [192]

$$\langle p^{-2} \rangle = 2 \int_0^\infty q^{-2} [J_0(0) - J_0(q)]\, dq \tag{5.70}$$

which seems to be less widely known than Eqs. (5.65) and (5.69). Connections between the nuclear geometry dependence of the Compton profile of a polyatomic molecule and its potential energy surface along a uniform scaling path have been derived and explored [193]. A relationship between the Compton profile and the stopping power is also known [194].

B. Directional Compton Profiles

No directional information is obtained from gas-phase experiments because the molecules are freely rotating. In the solid state, the rotational motion can be frozen, and the directional Compton profile can be written as

$$J\left(q, \frac{\vec{q}}{q}\right) = \int_S \mathbf{\Pi}(\vec{p})\, dS \tag{5.71}$$

where S is the plane surface defined by $\vec{p} \cdot \vec{q} = q^2$. In other words, the Compton profile is given by the momentum density integrated over a plane perpendicular

to the scattering vector. An equivalent expression is [15,195]

$$J\left(q, \frac{\vec{q}}{q}\right) = \int \mathbf{\Pi}(\vec{p})\, \delta\left(\frac{\vec{p}\cdot\vec{q}}{q} - q\right) d\vec{p} \tag{5.72}$$

In the special case that the scattering vector is parallel to one of the coordinate axes, these expressions look much simpler. For example, if $\vec{q}$ is parallel to the z axis, the directional Compton profile, expressed in Cartesian coordinates, is simply the marginal momentum density along the p_z axis:

$$J(0, 0, p_z) = \int \mathbf{\Pi}(p_x, p_y, p_z)\, dp_x\, dp_y \tag{5.73}$$

There are two main methods [145] for the reconstruction of $\mathbf{\Pi}(\vec{p})$ from the directional Compton profile. In the Fourier–Hankel method [145,162], the directional Compton profile is expanded as

$$J(\vec{q}) = \sum_{\ell=0}^{\infty} \sum_{m=-\ell}^{\ell} J_{2\ell,m}(q) Y_{2\ell,m}(\theta_q, \varphi_q) \tag{5.74}$$

Then the radial terms of this expansion can be connected to those of the momentum density expansion of Eq. (5.36) by

$$J_{\ell,m}(q) = 2\pi \int_{|q|}^{\infty} \mathbf{\Pi}_{\ell,m}(p)\, P_\ell(q/p) p\, dp \tag{5.75}$$

in which $P_\ell(x)$ is a Legendre polynomial [166]. This allows term-by-term reconstruction of $\mathbf{\Pi}(\vec{p})$ from $J(\vec{q})$. The reciprocal form factor can also be expanded in like manner

$$B(\vec{r}) = \sum_{\ell=0}^{\infty} \sum_{m=-\ell}^{\ell} B_{2\ell,m}(r) Y_{2\ell,m}(\theta, \varphi) \tag{5.76}$$

and related to the expansion of Eq. (5.36) through

$$B_{\ell,m}(r) = 4\pi(-\mathrm{i})^\ell \int_0^{\infty} \mathbf{\Pi}_{\ell,m}(p)\, j_\ell(pr) p^2\, dp \tag{5.77}$$

in which $j_\ell(pr)$ is a spherical Bessel function [166]. Note that the $\ell = 0, m = 0$ terms in Eqs. (5.74) and (5.76) are proportional to the spherically averaged quantities introduced earlier in Eqs. (5.54) and (5.63) as follows:

$$B_0(r) = \frac{B_{0,0}(r)}{(4\pi)^{1/2}} \tag{5.78}$$

and

$$J_0(q) = (4\pi)^{-1} \int J(\vec{q})\, d\Omega_q = \frac{J_{0,0}(q)}{(4\pi)^{1/2}} \tag{5.79}$$

Thus the $\ell = 0, m = 0$ cases of Eqs. (5.75) and (5.77) reduce to Eqs. (5.63) and (5.55), respectively.

The inverse of Eq. (5.29) allows us to write

$$B(0,0,z) = \int e^{-izp_z}\, \mathbf{\Pi}(p_x, p_y, p_z)\, dp_x\, dp_y\, dp_z \tag{5.80}$$

and combine Eq. (5.80) with Eq. (5.73) to find

$$B(0,0,z) = \int_{-\infty}^{\infty} e^{-izp_z}\, J(0,0,p_z)\, dp_z \tag{5.81}$$

Thus Fourier transformation of $J(\vec{q})$ along a single direction yields $B(\vec{r})$ along a single direction. This recognition is the basis of the Fourier reconstruction method [145,146] for $\mathbf{\Pi}(\vec{p})$.

A vast number of directional Compton profiles have been measured for ionic and metallic solids, but none for free molecules. Nevertheless, several calculations of directional Compton profiles for molecules have been performed as another means of analyzing the momentum density.

C. (e,2e) Spectroscopy

In binary (e,2e) or electron momentum spectroscopy, an incoming electron collides with a molecule and two electrons leave the molecule. The measured differential cross section is proportional to the spherically averaged momentum density of the pertinent Dyson orbital within the plane-wave impulse approximation. A Dyson orbital ψ_k is defined by

$$S\psi_k = \int \Psi_{k+}^*(\vec{x}_1, \ldots, \vec{x}_{N-1})\Psi(\vec{x}_1, \ldots, \vec{x}_{N-1}, \vec{x}_N)\, d\vec{x}_1\, d\vec{x}_2 \cdots d\vec{x}_{N-1} \tag{5.82}$$

where S is a normalization constant, Ψ is the ground-state wavefunction of the target molecule, and Ψ_{k+} is the wavefunction for some state of the resulting cation. If the neutral molecule is described within the Hartree–Fock model, then the Dyson orbital is a linear combination of the occupied Hartree–Fock orbitals. If the cation is further approximated using Koopmans' theorem, the Dyson orbital is just a canonical Hartree–Fock orbital of the target molecule. When all these approximations are valid, we may talk about ''looking at orbitals in the laboratory.'' The vast literature on this method and its applications will not be examined here since there are many excellent review articles available [16–28,196].

D. Computational Methods

Given a wavefunction built from a one-particle basis set, it is convenient [9,197,198] to proceed with the computation of the six-dimensional Fourier transform in Eq. (5.15) by inserting the spectral expansion [123,126]

$$\Gamma(\vec{r} \mid \vec{r}') = \sum_k \lambda_k \psi_k^*(\vec{r}')\psi_k(\vec{r}) \tag{5.83}$$

in which the λ_k are the occupation numbers of the natural orbitals $\psi_k(\vec{r})$. Provided that the number of natural orbitals with nonzero occupation number, in other words, the one-rank, is finite, interchanging the order of integration and summation leads to

$$\mathbf{\Pi}(\vec{p} \mid \vec{p}') = \sum_k \lambda_k \phi_k^*(\vec{p}')\phi_k(\vec{p}) \tag{5.84}$$

Here, the p-space natural momentals $\phi_k(\vec{p})$ are Fourier transforms of the r-space natural orbitals:

$$\phi_k(\vec{p}) = (2\pi)^{-3/2} \int \psi_k(\vec{r}) \exp(-i\vec{p} \cdot \vec{r})\, d\vec{r} \tag{5.85}$$

Thus there is an isomorphism between the first-order, r-space density matrix Γ and its p-space counterpart $\mathbf{\Pi}$, just as there is an isomorphism between a r-space wavefunction built from a one-particle basis set and the corresponding p-space wavefunction as described in Section II.

Since the overwhelming majority of wavefunctions are constructed from a one-particle basis set $\{\chi_j(\vec{r}),\ j = 1, \ldots, n\}$, the natural orbitals can be expressed in that basis set as

$$\psi_k(\vec{r}) = \sum_{j=1}^{n} \chi_j(\vec{r}) c_{jk} \tag{5.86}$$

Fourier transformation is a linear operation, and hence the natural momentals have the analogous expansion

$$\phi_k(\vec{p}) = \sum_{j=1}^{n} \omega_j(\vec{p}) c_{jk} \tag{5.87}$$

where $\{\omega_j(\vec{p}),\ j = 1, \ldots, n\}$ is the p-space basis set constructed from the Fourier transforms of the r-space basis functions:

$$\omega_j(\vec{p}) = (2\pi)^{-3/2} \int \chi_j(\vec{r}) \exp(-i\vec{p} \cdot \vec{r})\, d\vec{r} \tag{5.88}$$

Thus the momentum density can be written as

$$\mathbf{\Pi}(\vec{p}) = \sum_{i=1}^{n} \sum_{j=1}^{n} P_{ij} \omega_j^*(\vec{p}) \omega_i(\vec{p}) \tag{5.89}$$

where P_{ij} is an element of the p-space density matrix in the ω basis and of the r-space density matrix in the χ basis:

$$P_{ij} = \sum_{k=1}^{n} \lambda_k c_{ik} c_{jk}^* \tag{5.90}$$

A point that initially surprises some is that many of the off-diagonal terms in Eq. (5.89) are complex-valued, even when the r-space basis functions and expansion coefficients are all real. However, the momentum density is always real because each off-diagonal ij term in Eq. (5.89) is the complex conjugate of the corresponding ji term. The electron density can be written as

$$\rho(\vec{r}) = \sum_{i=1}^{n} \sum_{j=1}^{n} P_{ij} \chi_j^*(\vec{r}) \chi_i(\vec{r}) \tag{5.91}$$

illustrating once again the isomorphism of the densities in r and p space.

The transforms of Eq. (5.88) can be performed in closed form for most basis functions of interest including Gaussian- and Slater-type functions. Moreover, formulas for the computation of the spherically averaged momentum density and isotropic Compton profile have been worked out for most of the commonly used basis sets. The methods and formulas have been summarized in a review article by Kaijser and Smith [15]. Advantages and disadvantages of various types of basis sets, including many unconventional ones, have been analyzed from a momentum–space perspective [199–201]. Most methodological work on integrals relevant to momentum–space properties that is more recent than the review of Kaijser and Smith [15] has focused on basis sets of Gaussian-type functions. Expressions for momentum moments [202,203], spherically averaged Compton profiles and reciprocal form factors [204], spherically averaged momentum densities [202,205] and directional Compton profiles [206] from Gaussian-type functions have been reported more recently. Moreover, formulas for one-center integrals over Slater-type functions were published [207].

V. ATOMS

In atoms, the natural orbitals can be written as products of radial functions and spherical harmonics

$$\psi_{n\ell m}(r, \theta, \varphi) = r^{\ell} f_{n\ell}(r)\, Y_{\ell m}(\theta, \varphi) \tag{5.92}$$

and, as a consequence, so can the natural momentals [9,208]:

$$\phi_{n\ell m}(r, \theta_p, \varphi_p) = u_{n\ell}(p)\, Y_{\ell m}(\theta_p, \varphi_p) \tag{5.93}$$

The radial momental $u_{n\ell}(p)$ is related to the radial orbital $r^{\ell} f_{n\ell}(r)$ by a Hankel

transformation

$$u_{n\ell}(p) = (-\mathrm{i})^{\ell} p^{-1/2} \int_0^{\infty} J_{\ell+1/2}(pr) f_{n\ell}(r)\, r^{\ell+3/2}\, dr \tag{5.94}$$

in which $J_{\ell+1/2}(pr)$ is a Bessel function of half-integer order [166]. The spherically averaged momentum density is then

$$\mathbf{\Pi}_0(p) = (4\pi)^{-1} \sum_{n\ell m} \lambda_{n\ell m} |\mathrm{u}_{n\ell}(p)|^2 \tag{5.95}$$

The momentals for the hydrogen atom were first worked out by Podolsky and Pauling [208]. Results for the hydrogen atom are worth recording since they are a good hook for one's intuition. In the ground state of a hydrogenlike ion with nuclear charge Z, the momentum density is given by

$$\mathbf{\Pi}_0(p) = \frac{8}{\pi^2 Z^3 (1 + p^2/Z^2)^4} \tag{5.96}$$

the isotropic Compton profile by

$$J_0(q) = \frac{8}{3\pi Z (1 + q^2/Z^2)^3} \tag{5.97}$$

the momentum moments by

$$\begin{aligned} \langle p^{-2} \rangle &= \frac{5}{Z^2}, & \langle p^{-1} \rangle &= \frac{16}{3\pi Z} \\ \langle p \rangle &= \frac{8Z}{3\pi}, & \langle p^2 \rangle &= Z^2 \\ \langle p^3 \rangle &= \frac{16Z^3}{3\pi}, & \langle p^4 \rangle &= 5Z^4 \end{aligned} \tag{5.98}$$

and the reciprocal form factor by

$$B_0(r) = e^{-Zr} \left(1 + Zr + \frac{Z^2 r^2}{3} \right) \tag{5.99}$$

Observe from Eq. (5.96) that the momentum density becomes more and more diffuse as the nuclear charge is increased whereas precisely the opposite trend is observed for the electron density

$$\rho_0(r) = Z^3 \pi^{-1} e^{-2Zr} \tag{5.100}$$

This is a manifestation of the reciprocal nature of r- and p-space densities.

A. Momentum Densities

Another vivid illustration of the reciprocity of densities in r and p spaces is provided by Figure 5.4, which shows the radial electron density

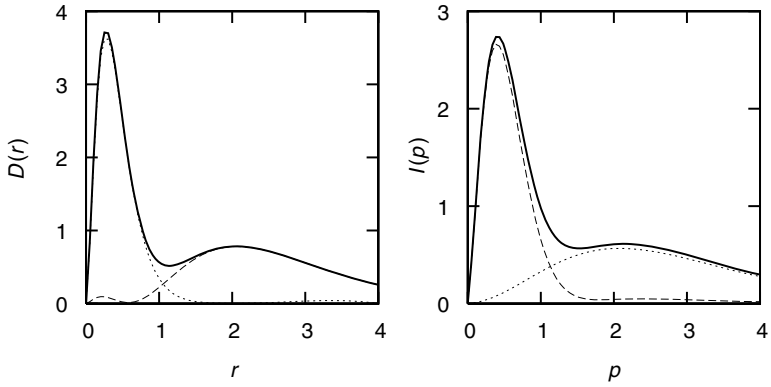

Figure 5.4. The radial electron density $D(r)$ (left) and radial momentum density $I(p)$ (right) for 1^1S Be: $1s$ contribution (dotted), $2s$ contribution (dashed), and total (solid).

$D(r) = 4\pi r^2 \rho_0(r)$ and radial momentum density $I(p) = 4\pi p^2 \mathbf{\Pi}_0(p)$ for the 1^1S ground state of the beryllium atom computed from a high-quality Hartree–Fock–Roothaan wavefunction [209]. Both densities show two peaks, one arising from the K-shell ($1s$) electrons and the other from the L-shell ($2s$) electrons. However, the origin of the peaks is inverted. The $D(r)$ function has a sharp, high K-shell peak at small r and a broad, low L-shell maximum at large r whereas $I(p)$ has a sharp, high L-shell peak at small p and a broad, low K-shell maximum at large p.

A fair amount of effort has been devoted to the manifestations of atomic shell structure in the momentum density and related functions [210–215]. The number of maxima observed in $I(p)$ varies from one to four, with 35 and 48 atoms exhibiting two and three local maxima [215]. No maxima in $I(p)$ corresponding to the most corelike shells are found in heavy atoms. Correlations have been found between $1/p_{\max}$, where $p_{\max}$ is the location of the innermost maximum of $I(p)$, and the relative size of the atom [215].

Computational data suggest that the electron density $\rho_0(r)$ is a monotonically decreasing function of r in all atoms [216–218] and all examined single-charged ions [219]. This is definitely not the case for the momentum density $\mathbf{\Pi}_0(p)$, as was evident from early work [127,151,220]. Smith et al. [221] showed that, within the bare Coulomb approximation [222], $\mathbf{\Pi}_0(p)$ is a monotonically decreasing function of p for an atom with an arbitrary number of closed shells. Since the bare Coulomb model provides the leading term in the Z^{-1} perturbation theory expansion [223] of $\mathbf{\Pi}_0(p)$, the momentum density of highly charged ions must be monotonically decreasing [221,224]. Moreover, the observed nonmonotonic behavior must be due to higher-order terms in the Z^{-1} perturbation theory expansion [223] of $\mathbf{\Pi}_0(p)$.

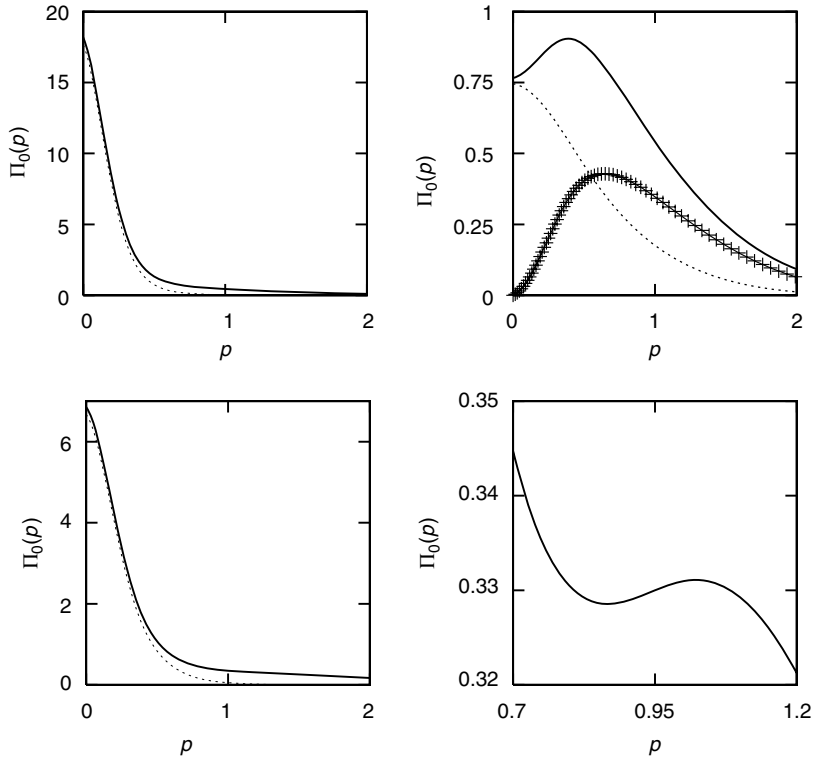

Figure 5.5. Types of electron momentum densities $\mathbf{\Pi}_0(p)$ in atoms. Solid lines are used for the total density, whereas dotted lines and crosses indicate the contribution from the outermost s and p orbitals, respectively. Top left: a type I density for the potassium atom. Top right: a typical type II density for the argon atom. Bottom left: a typical type III density for the silver atom. Bottom right: a closeup of $\mathbf{\Pi}_0(p)$ for the silver atom showing the minimum and secondary maximum. Adapted from Thakkar [29].

Many computations were made to classify the various types of behavior that $\mathbf{\Pi}_0(p)$ can have in atoms and atomic ions [210,211,225–229], but some confusion persisted because different authors obtained different results in a few problematic cases. Purely numerical Hartree–Fock calculations, free from basis set artifacts, were then used to establish that the ground-state momentum densities of all the atoms and their ions can be classified into just three types [230,231] as illustrated in Figure 5.5.

Type I momentum densities, characteristic of He, N, Mn, all atoms from groups 1–6, 13, and 14 except Ge, and the lanthanides and actinides, are unimodal and have a maximum at $p = 0$. A density of this type is shown in Figure 5.5 for the potassium atom. The maximum at $p = 0$ comes mainly from

the outermost s subshell, $4s$ in this case. Type II densities, the norm for nonmetal atoms, are found in Ge, Pd and all atoms from groups 15–18 except He and N. They are unimodal, have a local minimum at $p = 0$ and a global maximum at $p_{\max} > 0$. A representative density of this type is shown in Figure 5.5 for the argon atom. The maximum comes from the outermost p subshell, $3p$ in this case. Type III momentum densities, found for all atoms from groups 7–12 except Mn and Pd, are bimodal with a global maximum at $p = 0$ and a secondary maximum at $p_{\max} > 0$ separated by a local minimum. A typical density of this type is shown in Figure 5.5 for the silver atom. At first glance, $\mathbf{\Pi}_0(p)$ for the silver atom appears to be of type I. However, the closeup view in Figure 5.5 reveals the local minimum and secondary maximum. The global maximum comes from the outermost s subshell ($5s$), whereas the secondary maximum originates from the outermost p and d subshells ($4p$ and $4d$ in this case).

B. Small-p Behavior

At small p, the momentals have the MacLaurin expansion [168]

$$u_{n\ell}(p) = (-\mathrm{i})^{\ell} \sum_{k=0}^{\mu} a_{n\ell k} p^{\ell+2k} + O(p^{\ell+2\mu+1}) \tag{5.101}$$

where

$$a_{n\ell k} = \frac{(2/\pi)^{1/2}(-1)^k F_{n\ell k}}{(2k)!(2k+1)(2k+3)\cdots(2k+2\ell+1)} \tag{5.102}$$

in which

$$F_{n\ell k} = \int_0^{\infty} f_{n\ell}(r)\, r^{2k+2\ell+2}\, dr \tag{5.103}$$

Then the momental densities $\mathbf{\Pi}_{n\ell}(p) = (4\pi)^{-1}|u_{n\ell}(p)|^2$ for various values of the angular momentum quantum number ℓ have the following expansions [187]:

$$\mathbf{\Pi}_{n0}(p) = (360\pi^2)^{-1}\left[180F_{n00}^2 - 60F_{n00}F_{n01}p^2\right] + (360\pi^2)^{-1}(3F_{n00}F_{n02} + 5F_{n01}^2)p^4 + O(p^6) \tag{5.104}$$

$$\mathbf{\Pi}_{n1}(p) = (90\pi^2)^{-1}\left[5F_{n10}^2 p^2 - F_{n10}F_{n11}p^4\right] + O(p^6) \tag{5.105}$$

$$\mathbf{\Pi}_{n2}(p) = \frac{F_{n20}^2}{450\pi^2}p^4 + O(p^6) \tag{5.106}$$

$$\mathbf{\Pi}_{n3}(p) = O(p^6) \tag{5.107}$$

Clearly, only s orbitals contribute to $\mathbf{\Pi}_0(0)$, only s and p orbitals to $\mathbf{\Pi}_0''(0)$, and so on.

Hartree–Fock calculations of the three leading coefficients in the MacLaurin expansion, Eq. (5.40), have been made [187,232] for all atoms in the periodic table. The calculations [187] showed that 93% of $\mathbf{\Pi}_0(0)$ comes from the outermost s orbital, and that $\mathbf{\Pi}_0(0)$ behaves as a measure of atomic size. Similarly, 95% of $\mathbf{\Pi}_0''(0)$ comes from the outermost s and p orbitals. The sign of $\mathbf{\Pi}_0''(0)$ depends on the relative number of electrons in the outermost s and p orbitals, which make negative and positive contributions, respectively. Clearly, the coefficients of the MacLaurin expansion are excellent probes of the valence orbitals. The curvature $\mathbf{\Pi}_0''(0)$ is a surprisingly powerful predictor of the global behavior of $\mathbf{\Pi}_0(p)$. A positive $\mathbf{\Pi}_0''(0)$ indicates a type II momentum density, whereas a negative $\mathbf{\Pi}_0''(0)$ indicates that $\mathbf{\Pi}_0(0)$ is of either type I or III [187,230]. MacDougall has speculated on the connection between $\mathbf{\Pi}_0''(0)$ and superconductivity [233].

Calculations of $\mathbf{\Pi}_0''(0)$ are very sensitive to the basis set. The venerable Clementi–Roetti wavefunctions [234], often considered to be of Hartree–Fock quality, get the sign of $\mathbf{\Pi}_0''(0)$ wrong for the silicon atom. Purely numerical, basis-set-free, calculations [232,235] have been performed to establish Hartree–Fock limits for the MacLaurin expansion coefficients of $\mathbf{\Pi}_0(p)$. The effects of electron correlation on $\mathbf{\Pi}_0(0)$, and in a few cases $\mathbf{\Pi}_0''(0)$, have been examined for the helium atom [236], the hydride anion [236], the isoelectronic series of the lithium [237], beryllium [238], and neon [239] atoms, the second-period atoms from boron to fluorine [127], the atoms from helium to neon [240], and the neon and argon atoms [241]. Electron correlation has only moderate effects on $\mathbf{\Pi}_0(0)$.

C. Compton Profiles and Moments

Duncanson and Coulson [242,243] carried out early work on atoms. Since then, the momentum densities of all the atoms in the periodic table have been studied within the framework of the Hartree–Fock model, and for some smaller atoms with electron-correlated wavefunctions. There have been several tabulations of $J_0(q)$, $\langle p^k \rangle$, and asymptotic expansion coefficients for atoms [187,244–251] with Hartree–Fock-Roothaan wavefunctions. These tables have been superseded by purely numerical Hartree–Fock calculations that do not depend on basis sets [232,235,252,253]. There have also been several reports of electron-correlated calculations of momentum densities, Compton profiles, and momentum moments for He [236,240,254–257], Li [197,237,240,258], Be [238,240,258, 259], B through F [240,258,260], Ne [239,240,258,261], and Na through Ar [258]. Schmider et al. [262] studied the spin momentum density in the lithium atom. A review of Mendelsohn and Smith [12] remains a good source of information on comparison of the Compton profiles of the rare-gas atoms with experiment, and on relativistic effects.

The $\langle p^k \rangle$ moments for all the neutral atoms can be fit to simple functions of the number of electrons [232,263]. These functions are heuristic extensions of expressions [264–266] derived on the basis of the Thomas–Fermi model [267–271], with the Scott-Schwinger correction [272,273] for strongly bound electrons. Thus, the Hartree–Fock $\langle p^k \rangle$ for the neutral atoms from hydrogen ($N = 1$) through lawrencium ($N = 103$) can be fit [232] as follows:

$$\langle p^4 \rangle \approx \frac{5\pi^2 N^4}{3}\left(1 - \frac{1.0574}{N^{1/3}} + \frac{0.496}{N^{2/3}} - \frac{0.134}{N}\right) \tag{5.108}$$

$$\langle p^3 \rangle \approx \frac{32N^3 \log N}{9\pi} + N^3\left(0.492 + \frac{0.97}{N^{1/3}} + \frac{0.26}{N^{2/3}}\right) \tag{5.109}$$

$$\langle p^2 \rangle \approx 1.53749N^{7/3}\left(1 - \frac{0.675}{N^{1/3}} + \frac{0.507}{N^{2/3}} - \frac{0.18}{N}\right) \tag{5.110}$$

$$\langle p \rangle \approx 0.693747N^{5/3}\left(1 + \frac{0.024}{N^{1/3}} + \frac{0.2}{N^{2/3}}\right) \tag{5.111}$$

These fits incur average errors of only 0.3, 0.3, 0.2, and 0.8%, respectively. It is possible [263] to fit the $\langle p^{-1} \rangle$ and $\langle p^{-2} \rangle$ moments by using measures of the numbers of electrons in the various subshells, but the fits are not as accurate, particularly for $\langle p^{-2} \rangle$, because these moments exhibit strongly periodic behavior. The Hartree–Fock values of b_8, the coefficient of the leading term in the large-p asymptotic expansion Eq. (5.42) for the 103 neutral atoms, can be fit with an average error of 0.1% to the simple expression [187,232]

$$b_8 \approx N^5\left(2.0134 - \frac{0.676}{N^{1/3}} - \frac{0.527}{N^{2/3}}\right) \tag{5.112}$$

The fits given above are not meant to replace more accurate tabulations. Instead, they serve to bring out the essential dependence of these complex quantities on the atomic number.

D. Inequalities

Many inequalities involving $\mathbf{\Pi}_0(p)$ and its moments $\langle p^k \rangle$, and sometimes also moments $\langle r^k \rangle$ of the electron density $\rho_0(r)$, have been found. Much work of this type has been done by Gadre and coworkers [274–277]; the Granada group of Dehesa, Gálvez, Porras, Angulo, Antolín, Zarzo, and Romera [278–288]; and Li, Tao, and Wang [289–292]. The list of references given here is representative and not exhaustive. The most interesting of these inequalities are those that interconnect properties of p- and r-space densities. All these inequalities rely on some mathematical constraints on the momentum density. These conditions are

usually verified numerically at the Hartree–Fock level for several, if not all, atoms. However, in most cases, the conditions on $\mathbf{\Pi}_0(p)$ cannot be proved in general. Therefore, a prospective user should bear in mind that it is likely but not guaranteed that the inequalities are satisfied in other cases such as electron-correlated or experimental values for atoms, or for molecules. There are also empirical inequalities that are motivated by semiclassical considerations. They are discussed in the next section because they have been tested for many molecules as well.

A closely related area is the problem of reconstructing the momentum density from a few of its moments and possibly its values at a few points. Representative work along these lines was reported by Gadre [293], Koga [294–297], and Antolín, Angulo, and coworkers [298–301].

VI. MOLECULES

A. Mapping $\mathbf{\Pi}(\vec{p})$ and $J(\vec{q})$

The qualitative study of electronic structure through the electron (number) density $\rho(\vec{r})$ relies heavily on linecut diagrams, contour plots, perspective plots, and other representations of the density and density differences. There is a review article by Smith and coworkers [302] devoted entirely to classifying and explaining the different techniques available for the pictorial representation of electron densities. Beautiful examples of this type of analysis can be seen in the work of Bader, Coppens, and others [303,304].

Obviously, graphical techniques are equally important in the study of electron momentum densities. Coulson [2,4] made the pioneering effort in this direction. Other early work was published by Henneker and Cade [305]; Epstein and Lipscomb [306–308]; Kaijser, Lindner, and coworkers [309–311]; Tanner and Epstein [312]; and Tawil and Langhoff [313,314]. A synthesis of these studies was made by Epstein and Tanner [13], who abstracted some principles that they hoped would be generally applicable to chemical bonding. One of their abstractions pinned down an observation about the anisotropy of $\mathbf{\Pi}(\vec{p})$ that had been made in several of the earlier studies. Epstein and Tanner called it the ''bond directional principle,'' and they stated it as follows [13]:

> The momentum of an electron in a chemical bond is more likely to be directed perpendicular to than along the bond axis. Furthermore, in the chemical bond there is greater density at low momentum along the bond and greater density at high momentum perpendicular to the bond than was the case in the isolated atoms.

Although the principle has turned out to have many exceptions [315], as discussed later, it has served as an inspiration for many researchers interested in uncovering the links between the reorganization of electron momentum densities and chemical bonding.

Subsequent work on graphical analysis of anisotropic momentum densities, directional Compton profiles, and their differences in diatomic molecules was reported by several groups, including Kaijser and Smith [195,316], Ramirez [317–319], Matcha, Pettit, Ramirez, and McIntire [320–328], Leung and Brion [329,330], Simas et al. [331], Rozendaal and Baerends [332,333], Cooper and Allan [334], Anchell and Harriman [138], and Rérat et al. [335,336].

The expansions, Eqs. (5.36) and (5.37), of $\mathbf{\Pi}(\vec{p})$ can be used to reduce dimensionality by focusing on the radial coefficients [157]. Thakkar and coworkers [157] formulated empirical rules to help understand the small-p behavior of $\mathbf{\Pi}(\vec{p})$ for linear molecules using only the first four $\mathbf{\Pi}_{2\ell}(p)$ terms. This technique was subsequently used to analyze bonding in 14-electron diatomics [337], strong hydrogen bonding [338], substituent effects in alkynes and cyanides [339], and bonding in alkaline-earth oxides [340,341].

Koga [342] greatly extended Coulson's analysis [4] of electron momentum densities for planar, conjugated hydrocarbons by providing a definitive analysis of momentum distributions of Hückel π electrons. Momentum densities and directional Compton profiles were studied for benzene and H_2O by Janis et al. [343,344]; cyclopentadiene anion, pyrrole, N_2, C_2H_2, C_2H_4, CH_2O, and H_{49}^+, by Rawlings and Davidson [158]; CH_4, by Kaijser et al. [345]; large polyenes, by Cooper et al. [346]; and C_2H_2 and C_2H_4, by Tripathi et al. [347]. Janis, Kaijser, Smith, and Whangbo [195,343] introduced the $J(0,\vec{q}/q)$ [or $J(\vec{0})$ for short] surface to measure the zero-momentum Compton profile anisotropy. Staroverov and Davidson [206] present Compton maps, two-dimensional contour plots of the directional Compton profile in a selected plane, for H_2^+, water, ammonia, ethylene and singlet methylene.

In view of the many exceptions to the bond directional principle [13] found in the work cited in the last three paragraphs, Tanner carefully reassessed it in a thoughtful paper [315]. He then formulated a new version as follows

> In a chemical bond in a bound molecule at its equilibrium configuration, there are values of $\vec{p}_m$ of momentum which are more probable, i.e., which correspond to local maxima of $\mathbf{\Pi}(\vec{p})$. Those values are determined by both the geometric and electronic symmetries of the molecule. For momenta, $\vec{p} = \vec{p}_m + \delta\vec{p}$, near a maximum it is more likely that $\delta\vec{p}$ is perpendicular rather than parallel to the bond axis.

Tanner pointed out that a few exceptions to the revised bond directional principle were already known. He emphasized that the principle is a qualitative one, and attempts to makes it more precise would defeat the purpose of giving a feel for what $\mathbf{\Pi}(\vec{p})$ is like.

B. Topographic Analysis

The topography of $\rho(\vec{r})$ is often studied [303] in terms of the Hessian of $\rho(\vec{r})$ at its critical points, that is, the set of points $\{\vec{r}_c\}$ for which $\nabla\rho(\vec{r}_c) = \vec{0}$. In an

analogous fashion, the topography of $\mathbf{\Pi}(\vec{p})$ can be discussed [160,212] in terms of the Hessian of $\mathbf{\Pi}(\vec{p})$ at its critical points, that is, the set of points $\{\vec{p}_c\}$ for which $\nabla\mathbf{\Pi}(\vec{p}_c) = \vec{0}$. A critical point is characterized by the rank r and signature s of the Hessian matrix at $\vec{p}_c$. The *rank* is the number of nonzero eigenvalues, and the *signature* is the number of positive eigenvalues minus the number of negative ones. The point $\vec{p} = \vec{0}$ or $p = 0$ is always a critical point of $\mathbf{\Pi}(\vec{p})$ because of the inversion symmetry of the latter.

Topographic studies [160,348] of $\mathbf{\Pi}(\vec{p})$ find that the $p = 0$ critical point is perhaps the most important one because it is a harbinger of the other critical points [349] in the sense that the nature of the other critical points can be predicted from the type of critical point found at $p = 0$. Connections between the zero-momentum critical point and the bond-directional principle [13,315] have been explored [349,350]. Unfortunately, simple rules are hard to find, and all allowed types of topographies are found even in linear molecules [351]. The value of $\mathbf{\Pi}_0(0)$ has been found useful [352,353] as a measure for following a chemical reaction in p space. Schmider and Hô [143] considered molecular networks, defined as a system of local maxima connected by gradient paths, in position, momentum, and phase space for methane, ethane, neopentane, cyclohexane, ethylene, butadiene, cyclopentadiene, benzene, and acetylene. They found that, in momentum–space, complex networks were found only for molecules with high symmetry and bonds only in a few distinct directions. Only a few critical points of $\mathbf{\Pi}(\vec{p})$ were found in molecules with lower symmetry. The high sensitivity of the topography of $\mathbf{\Pi}(\vec{p})$ to computational details has been examined. Even the signature of a critical point can vary with the basis set and amount of electronic correlation included in a calculation [143,241, 350,354].

A taste of topographies [351] of $\mathbf{\Pi}(\vec{p})$ with a maximum at zero momentum is provided by Figure 5.6. N_2 has a $(r = 3, s = -3)$ global maximum at $p = 0$.

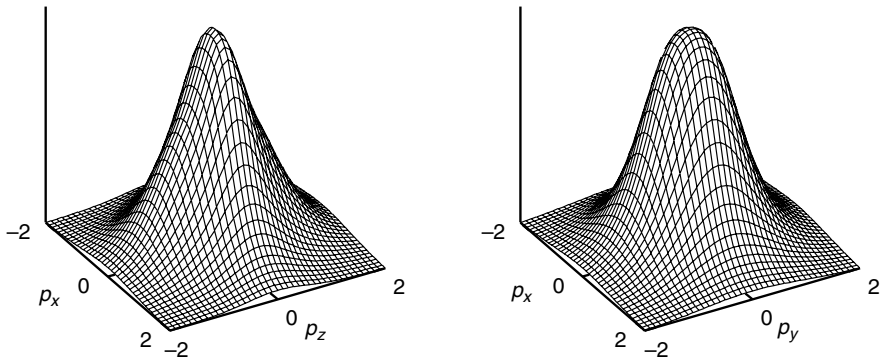

Figure 5.6. Surface plots of the electron momentum density of N_2 illustrating a $(3, -3)$ maximum at $\vec{p} = \vec{0}$. Left: $\mathbf{\Pi}(p_x, 0, p_z)$. Right: $\mathbf{\Pi}(p_x, p_y, 0)$. Adapted from Thakkar [29,351].

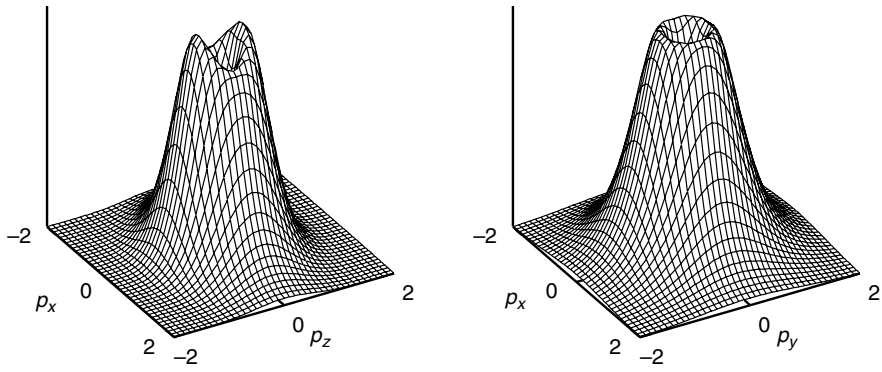

Figure 5.7. Surface plots of the electron momentum density of C_2 illustrating a $(3,3)$ minimum at $\vec{p} = \vec{0}$. Left: $\mathbf{\Pi}(p_x, 0, p_z)$. Right: $\mathbf{\Pi}(p_x, p_y, 0)$. Adapted from Thakkar [29,351].

The surface plot of $\mathbf{\Pi}(\vec{p})$ in the $p_x p_z$ plane is simply a hill. Symmetry ensures that an identical plot would be obtained for all other vertical planes of symmetry. A similar plot is seen for the horizontal $p_x p_y$ plane of symmetry.

C_2 has a $(3,3)$ minimum at $p = 0$. Figure 5.7 shows that the plot in the $p_x p_z$ plane has the structure of a caldera. The local minimum at $p = 0$ is surrounded by a ring of critical points including two local maxima located at ± 0.42 a.u. along the p_z axis. Critical points along the p_x axis must also appear in all other directions perpendicular to the p_z axis. This is seen in the plot for the horizontal $p_x p_y$ plane of symmetry. The plot looks like a volcano. The zero-momentum minimum is surrounded by a ring of critical points in the $p_x p_y$ plane.

Topographies of $\mathbf{\Pi}(\vec{p})$ with a saddle point at zero momentum are illustrated in Figure 5.8, which shows a perspective plot for a typical momentum density

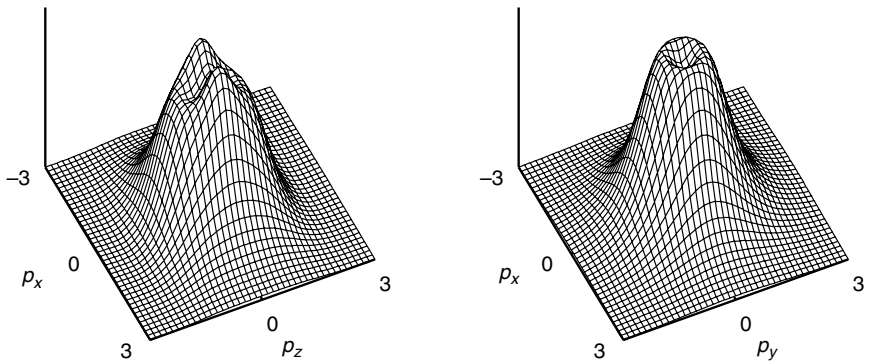

Figure 5.8. Surface plots of the electron momentum density of F_2 illustrating a $(3,1)$ saddle point at $\vec{p} = \vec{0}$. Left: $\mathbf{\Pi}(p_x, 0, p_z)$. Right: $\mathbf{\Pi}(p_x, p_y, 0)$. Adapted from Thakkar [29,351].

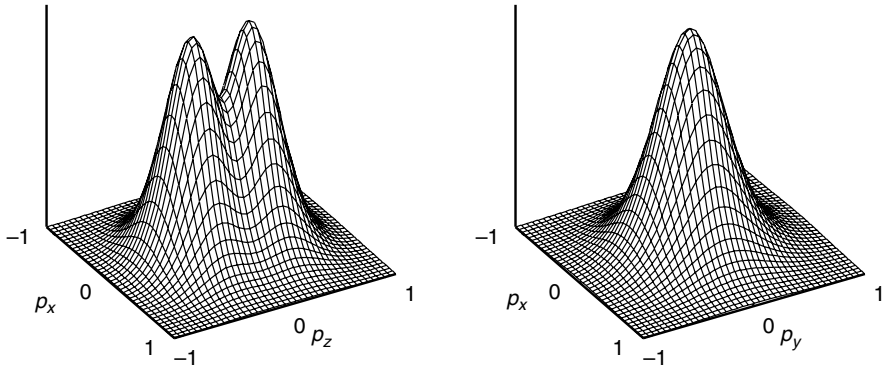

Figure 5.9. Surface plots of the electron momentum density of Be_2 illustrating a $(3,-1)$ saddle point at $\vec{p}=\vec{0}$. Left: $\mathbf{\Pi}(p_x,0,p_z)$. Right: $\mathbf{\Pi}(p_x,p_y,0)$. Adapted from Thakkar [29,351].

with a zero-momentum $(3,+1)$ critical point using the example of F_2. The plot in the (p_xp_z) plane has a complicated structure. The zero-momentum critical point is a pass between two peaks located along the p_x axis at $p_x=\pm 0.52$ a.u., and is a barrier separating two troughs centered along the p_z axis at $p_z=\pm 0.52$ a.u. Critical points along the p_x axis must also appear in all other directions perpendicular to the p_z axis. The plot of $\mathbf{\Pi}(\vec{p})$ in the horizontal p_xp_y plane resembles a volcano.

A $(3,-1)$ critical point indicates a saddle point at $p=0$. A typical momentum density with a zero momentum $(3,-1)$ critical point is shown for Be_2 in Figure 5.9. The surface plot in the vertical plane of symmetry has two local (and global) maxima located symmetrically along the p_z axis at $p_z=\pm 0.26$ a.u. The plot has the structure of two hills separated by a ridge or col. The plot in the horizontal p_xp_y plane has the structure of a hill.

C. Zero-Momentum Behavior

For most molecules, the small momentum expansion of the momentum density requires the full 3×3 Hessian matrix A of $\mathbf{\Pi}(\vec{p})$ at $\vec{p}=\vec{0}$. In Cartesian coordinates, this matrix has elements

$$A_{\alpha\beta}=\mathbf{\Pi}_{\alpha\beta}(0)=\lim_{\vec{p}\to\vec{0}}\frac{\partial^2\mathbf{\Pi}(\vec{p})}{\partial p_\alpha\partial p_\beta}\qquad\text{for }\alpha,\beta\in\{x,y,z\}\tag{5.113}$$

Choosing a coordinate system that diagonalizes the Hessian matrix, the MacLaurin expansion of the three-dimensional momentum density $\mathbf{\Pi}(\vec{p})$ can be written as [241]

$$\mathbf{\Pi}(\vec{p})=\mathbf{\Pi}(\vec{0})+\frac{1}{2}\left[\mathbf{\Pi}_{xx}(0)p_x^2+\mathbf{\Pi}_{yy}(0)p_y^2+\mathbf{\Pi}_{zz}(0)p_z^2\right]+\cdots\tag{5.114}$$

Observe that $\mathbf{\Pi}_0(0) = \mathbf{\Pi}(\vec{0})$ and

$$\mathbf{\Pi}_0''(0) = \frac{1}{3}\lim_{\vec{p}\to\vec{0}} \mathrm{Tr}(\mathsf{A}) \tag{5.115}$$

provide the connections [241] between the coefficients of Eqs. (5.40) and (5.114).

For linear molecules, convention dictates that the high-symmetry axis be the z axis and then the Hessian of $\mathbf{\Pi}(\vec{p})$ is diagonal in this coordinate system. Moreover, the expansion of Eq. (5.114) can be reduced to a two-dimensional one by using spherical polar coordinates to exploit the cylindrical symmetry. The expansion can be written as [355]

$$\begin{aligned}\mathbf{\Pi}(\vec{p}) = A_0 + \left[A_2 + A_{22}P_2(\cos\theta_p)\right]p^2 + \left[A_4 + A_{42}P_2(\cos\theta_p)\right. \\ \left. + A_{44}P_4(\cos\theta_p)\right]p^4 + \cdots\end{aligned} \tag{5.116}$$

in which the $P_{2\ell}(\cos\theta_p)$ are Legendre polynomials, $A_0 = \mathbf{\Pi}_0(0)$, $A_2 = \mathbf{\Pi}_0''(0)/2$, and $A_4 = \mathbf{\Pi}_0^{(\mathrm{iv})}(0)/24$. The connections between the coefficients of Eqs. (5.116) and (5.114) are given [351] by

$$\mathbf{\Pi}_0''(0) = 2A_2 = \frac{\mathbf{\Pi}_{zz}(0) + 2\mathbf{\Pi}_{xx}(0)}{3} \tag{5.117}$$

and

$$A_{22} = \frac{\mathbf{\Pi}_{zz}(0) - \mathbf{\Pi}_{xx}(0)}{3} \tag{5.118}$$

Values of the MacLaurin coefficients computed from good, self-consistent-field wavefunctions have been reported [355] for 125 linear molecules and molecular ions. Only type I and II momentum densities were found for these molecules, and they corresponded to negative and positive values of $\mathbf{\Pi}_0''(0)$, respectively. An analysis in terms of molecular orbital contributions was made, and periodic trends were examined [355]. The qualitative results of that work [355] are correct but recent, purely numerical, Hartree–Fock calculations [356] for 78 diatomic molecules have demonstrated that the highly regarded wavefunctions of Cade, Huo, and Wahl [357–359] are not accurate for $\mathbf{\Pi}_0(0)$ and especially $\mathbf{\Pi}_0''(0)$. These problems can be traced to a lack of sufficiently diffuse functions in their large basis sets of Slater-type functions.

The coefficients of the small-p expansion of $\mathbf{\Pi}_0(p)$, Eq. (5.40), have been extracted by fitting to experimental Compton profiles for both atoms and molecules [167]. Table V.1 gives a flavor of the tense confrontation between

TABLE V.1
Comparison of Theoretical and Experimental Values of $\mathbf{\Pi}_0(0)$ and $\mathbf{\Pi}_0''(0)$ for N_2[a]

Method/Basis	R	$\mathbf{\Pi}_0(0)$	$\mathbf{\Pi}_0''(0)$
SCF/R [361]	2.068	1.2984	−2.073
SCF/L [362]	2.068	1.4075	−2.469
SCF/C [363]	2.068	1.4079	−2.772
SCF/T [363]	2.068	1.4485	−3.765
SCF/aug-cc-pVDZ [241]	2.0743	1.458	−3.70
SCF/aug-cc-pVTZ [241]	2.0743	1.434	−3.22
Numerical HF [356]	2.068	1.436	−3.066
MCSCF-FOCI/R [361]	2.068	1.3206	−2.839
MP2/aug-cc-pVDZ [241]	2.0743	1.640	−6.82
MP2/aug-cc-pVTZ [241]	2.0743	1.584	−5.98
MRCI2E/L [362]	2.068	1.4319	−3.013
MRCI2/T [363]	2.068	1.5237	−5.506
MRCI4/T [363]	2.068	1.5284	−5.600
MRCI4/T+zero point vibration [363]	2.068	1.5277	−5.552
SDQMP4/aug-cc-pVDZ [241]	2.0743	1.597	−6.24
SDQMP4/aug-cc-pVTZ [241]	2.0743	1.534	−5.28
160-keV γ rays [364]		1.39 ± 0.04	-2.9 ± 1.5
160-keV γ rays [365]		1.40 ± 0.09	-2.8 ± 1.0
60-keV γ rays [366]		1.40 ± 0.17	-2.7 ± 1.4
Ag Kα and Mo Kα X rays [364,367]		1.51 ± 0.20	-3.1 ± 1.3
25-keV electron impact [368]		1.56 ± 0.31	-4.0 ± 2.0

[a] The calculations are not all at exactly the same bond length R. The basis set is indicated after the slash in the method. R, L, C, and T are basis sets of Slater-type functions. The aug-cc-pVDZ and aug-cc-pVTZ basis sets [360] are composed of Gaussian functions. SCF stands for self-consistent-field; MC, for multiconfiguration; FO, for first-order; CI, for configuration interaction; MR, for multireference; MPn, for nth-order Møller–Plesset perturbation theory; and SDQ, for singles, doubles, and quadruples.

theory and experiment that can occur over the values of $\mathbf{\Pi}_0(0)$ and $\mathbf{\Pi}_0''(0)$. It lists many measurements and calculations for N_2—the most widely studied molecule in this respect. Notice the rather large error bars on the measured values of $\mathbf{\Pi}_0''(0)$. Agreement between the latest theory and experiment is close but not perfect. The new generation of synchrotrons will provide fresh opportunities for fruitful confrontation between computation and experiment. Calculations of $\mathbf{\Pi}_0''(0)$ will be challenging because it is highly sensitive to both basis set and electron correlation effects as seen above, and in work [241] on 14 small species.

D. Other Work

There has been much quantitative work aimed at achieving agreement between theory and experimental isotropic Compton profiles. Particularly elaborate

efforts have been made for molecular hydrogen [369–373], water [374–376], ammonia [376], methane [345,376], nitrogen [361–363], and ethylene and acetylene [347].

Bond additivity [377] has been studied with localized molecular orbitals by Epstein [308], Smith et al. [378,379], and Measures et al. [380], and with phenomenological analysis of theoretical Compton profiles by Hirst and Liebmann [381–383], Reed et al. [384], and by Cade et al. [385]. Hybridization has been examined from a momentum space viewpoint by Cooper et al. [386] and Clark et al. [387].

Indices of molecular similarity and dissimilarity based on the electron momentum density have been found useful by Allan, Cooper and coworkers [388–393] and Hô et al. [394].

E. Moments

Semiclassical phase space arguments by Burkhardt [395], Kónya [396], and Coulson and March [397,398] have led to the following approximate relationships

$$\langle p^k \rangle \approx I_k, \qquad -1 \leq k \leq 2 \tag{5.119}$$

in which

$$I_k = \frac{(3\pi^2)^{k/3}}{1+k/3} \int [\rho(\vec{r})]^{1+k/3}\, d\vec{r} \tag{5.120}$$

The limits on k are more restrictive in Eq. (5.119) than in Eq. (5.51) because the incorrect asymptotic behavior of the quasiclassical densities leads to divergent moments for $k = -2, 3, 4$. Of course

$$I_0 = \int \rho(\vec{r})\, d\vec{r} = N \tag{5.121}$$

is just the normalization condition, and so the $k = 0$ case of Eq. (5.119) is trivially exact: $\langle p^0 \rangle = I_0$. The relationships in Eq. (5.119) are interesting because they give a direct route from the electron number density to moments of the electron momentum density. The $k = 1$ and $k = 2$ cases are of particular interest in density functional theory [399] because I_1/π is the Dirac approximation to the exchange energy [400], and $I_2/2$ is the venerable approximation for the kinetic energy introduced by Thomas [267] and Fermi [268–270].

Several studies [401–408] found that the approximations of Eq. (5.119) were moderately accurate at the Hartree–Fock level for many atoms and a few diatomic molecules. Pathak et al. [409] suggested extending the same

relationship [Eq. (5.119)] to the remaining allowable values of $k = -2, 3, 4$. They examined the approximation (5.119) for the extended range $-2 \leq k \leq 4$ for 35 diatomic molecules at the Hartree–Fock level. They conjectured the bounds

$$\langle p^k \rangle \leq I_k, \qquad k = -2, -1 \tag{5.122}$$

and

$$\langle p^k \rangle \geq I_k, \qquad k = 1, 2, 3, 4 \tag{5.123}$$

on the basis of their molecular data, and previously published data.

Thakkar and Pedersen [410] continued this study by computing data for 122 linear molecules at the Hartree–Fock level. The bounds of Eqs. (5.122)–(5.123) were satisfied in all cases. Figure 5.10 shows the ratios $R_k = \langle p^k \rangle / I_k$ computed by them [410] for $k = -1, 1, 2$. It shows that Eq. (5.119) is reasonably accurate with median errors of 2.2% in the $k = 1$ case, but less so with median errors of 9.3 and 12% in the $k = 2$ and $k = -1$ cases, respectively. The bounds of Eqs. (5.122) and (5.123) were found to be quite loose for $k = -2, 3, 4$. Thakkar and Pedersen [410] also proposed some simple heuristic models relating $\langle p^k \rangle$ and I_k more closely. The best of these was

$$\langle p^k \rangle \approx I_k \left(1 + \beta_k N^{-1/3} + \gamma_k N^{-2/3} \right) \tag{5.124}$$

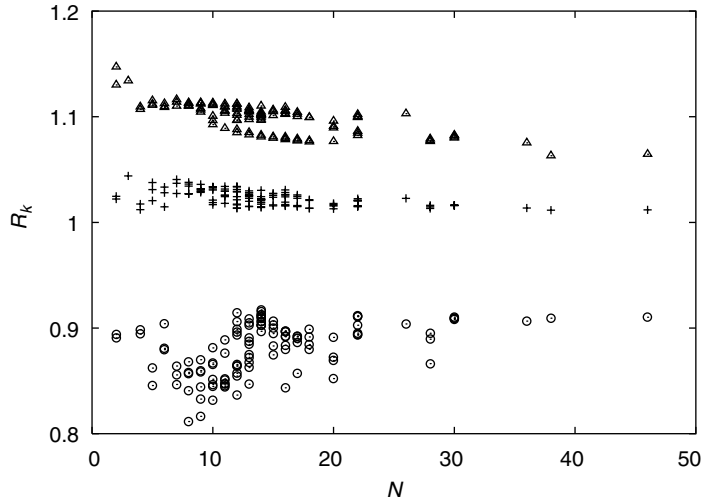

Figure 5.10. Ratios $R_{-1} = \langle p^{-1} \rangle / I_{-1}$ (◯), $R_1 = \langle p^1 \rangle / I_1$ (+), and $R_2 = \langle p^2 \rangle / I_2$ (△) as a function of the number of electrons N for 122 linear molecules. Based on the data of Thakkar and Pedersen [410].

in which the β_k and γ_k are empirical parameters obtained by fitting to their Hartree–Fock data. This model approaches the quasi-classical results for large N. It leads to median errors of 11, 1.8, 0.5, 0.6, 1.3, and 2.6% for the $k = -2, -1, 1, 2, 3, 4$ cases, respectively, for the database of 122 linear molecules to which it was fitted.

F. Concluding Remarks

It is apparent that only a trickle of work has been, and is currently being, done on momentum densities in comparison with the torrent of effort devoted to the position space electron density. Moreover, much of the early work on $\mathbf{\Pi}(\vec{p})$ has suffered from an undue emphasis on linear molecules. Nevertheless, some useful insights into the electronic structure of molecules have been achieved by taking the electron momentum density viewpoint. The most recent phenomenal developments in computer hardware, quantum chemical methods and software for generating wavefunctions, and visualization software suggest that the time is ripe to mount a sustained effort to understand momentum densities from a chemical perspective. Readers of this chapter are urged to take part in this endeavor.

Acknowledgments

This work was supported in part by the Natural Sciences and Engineering Research Council of Canada. My work on momentum densities would have been greatly diminished without those who have worked with me in this field: Richard Brown, Sánchez Dehesa, Abbas Farazdel, Jacob Fisher, Alison Gibbs (formerly Wonfor), Elvira Gutiérrez (formerly Romera), James Hart, William Henneker, Hidenori Inomata, Per Kaijser, Toshikatsu Koga, the late Bowen Liu, Jang Liu, Hisashi Matsuyama, Katsuhisa Ohta, Rajeev Pathak, Ward Pedersen, Philip Regier, Amlan Roy, Robin Sagar, Bhawani Sharma, Alfredo Simas, Vedene Smith, Walter Stevens, Anthony Tanner, Hiroshi Tatewaki, Awadh Tripathi, and William Westgate.

References

1. P. Hohenberg and W. Kohn, *Phys. Rev.* **136B**, 864–871 (1964).
2. C. A. Coulson, *Proc. Camb. Phil. Soc.* **37**, 55–66 (1941).
3. C. A. Coulson and W. E. Duncanson, *Proc. Camb. Phil. Soc.* **37**, 67–73 (1941).
4. C. A. Coulson, *Proc. Camb. Phil. Soc.* **37**, 74–81 (1941).
5. W. E. Duncanson, *Proc. Camb. Phil. Soc.* **37**, 397–405 (1941).
6. W. E. Duncanson and C. A. Coulson, *Proc. Camb. Phil. Soc.* **37**, 406–421 (1941).
7. C. A. Coulson and W. E. Duncanson, *Proc. Camb. Phil. Soc.* **38**, 100–108 (1942).
8. W. E. Duncanson, *Proc. Camb. Phil. Soc.* **39**, 180–188 (1943).
9. R. Benesch and V. H. Smith, Jr., Density matrix methods in X-ray scattering and momentum space calculations, in *Wave Mechanics—the First Fifty Years*, W. C. Price, S. S. Chissick, and T. Ravensdale, eds. (Butterworths, London, 1973), pp. 357–377.
10. I. R. Epstein, *Acc. Chem. Res.* **6**, 145–152 (1973).

11. I. R. Epstein, Electron momentum distributions in atoms, molecules and solids, in *MTP International Review of Science*, Series 2, Theoretical Chemistry, A. D. Buckingham, ed. (Butterworths, London, 1975), Vol. 1, pp. 107–161.
12. L. Mendelsohn and V. H. Smith, Jr., Atoms, in *Compton Scattering: The Investigation of Electron Momentum Distributions*, B. G. Williams, ed. (McGraw-Hill, New York, 1977), pp. 103–138.
13. I. R. Epstein and A. C. Tanner, Chemistry, in *Compton Scattering: The Investigation of Electron Momentum Distributions*, B. G. Williams, ed. (McGraw-Hill, New York, 1977), pp. 209–233.
14. P. Lindner, *Phys. Scr.* **15**, 112–118 (1977).
15. P. Kaijser and V. H. Smith, Jr., *Adv. Quantum Chem.* **10**, 37–76 (1977).
16. J. H. Moore, J. A. Tossell, and M. A. Coplan, *Acc. Chem. Res.* **15**, 192–198 (1982).
17. I. E. McCarthy and E. Weigold, *Contemp. Phys.* **24**, 163–184 (1983).
18. C. E. Brion, *Int. J. Quantum Chem.* **29**, 1397–1428 (1986).
19. I. E. McCarthy and E. Weigold, *Rep. Prog. Phys.* **51**, 299–392 (1988).
20. I. E. McCarthy and E. Weigold, *Rep. Prog. Phys.* **54**, 789–879 (1991).
21. C. E. Brion, Chemical applications of the (e,2e) reaction in electron momentum spectroscopy, in *Correlations and Polarization in Electronic and Atomic Collisions and (e,2e) Reactions*, P. J. O. Turner and E. Weigold, eds. (Institute of Physics, Bristol, 1992), Vol. 122 of Inst. Phys. Conf. Series, pp. 171–179.
22. M. A. Coplan, J. H. Moore, and J. P. Doering, *Rev. Mod. Phys.* **66**, 985–1014 (1994).
23. E. R. Davidson, *Can. J. Phys.* **74**, 757–762 (1996).
24. I. E. McCarthy, *Aust. J. Phys.* **51**, 593–607 (1998).
25. E. Weigold, *Aust. J. Phys.* **51**, 751–761 (1998).
26. E. Weigold and I. E. McCarthy, *Electron Momentum Spectroscopy* (Kluwer Academic, New York, 1999).
27. C. E. Brion, G. Cooper, Y. Zheng, I. V. Litvinyuk, and I. E. McCarthy, *Chem. Phys.* **270**, 13–30 (2001).
28. M. J. Brunger and W. Adcock, *J. Chem. Soc. Perkin Trans. 2*, 1–22 (2002).
29. A. J. Thakkar, Electron momentum distributions at the zero momentum critical point, in *Reviews of Modern Quantum Chemistry—a Celebration of the Contributions of Robert G. Parr*, K. D. Sen, ed. (World Scientific, Singapore, 2002), pp. 85–107.
30. M. Born and J. R. Oppenheimer, *Ann. Phys.* (*Leipzig*) **84**, 457–484 (1927).
31. M. Born and K. Huang, *Dynamical Theory of Crystal Lattices* (Oxford Univ. Press, London, 1954).
32. A. Szabo and N. S. Ostlund, *Modern Quantum Chemistry* (Macmillan, New York, 1982).
33. D. R. Yarkony, ed., *Modern Electronic Structure Theory* (World Scientific, Singapore, 1995).
34. T. Helgaker, P. Jørgensen, and J. Olsen, *Molecular Electronic-Structure Theory* (Wiley, New York, 2000).
35. E. A. Hylleraas, *Z. Phys.* **74**, 216–224 (1932).
36. V. Fock, *Z. Phys.* **98**, 145–154 (1935).
37. M. Levy, *Proc. Roy. Soc. Lond.* **204**, 145–169 (1950).
38. N. Svartholm, *Ark. Mat. Astron. Fys.* **35A**(7), 1–7 (1947).
39. N. Svartholm, *Ark. Mat. Astron. Fys.* **35A**(8), 1–16 (1947).
40. R. McWeeny and C. A. Coulson, *Proc. Phys. Soc. Lond.* **62A**, 509–518 (1949).

41. R. McWeeny, *Proc. Phys. Soc. Lond.* **62A**, 519–528 (1949).
42. M. G. Henderson and C. W. Scherr, *Phys. Rev.* **120**, 150–152 (1960).
43. T. Shibuya and C. E. Wulfman, *Proc. Roy. Soc. Lond. A* **286**, 376–389 (1965).
44. B. K. Novosadov, *Opt. Spectrosc.* **41**, 490–493 (1976).
45. B. K. Novosadov, *J. Mol. Struct.* **52**, 119–133 (1979).
46. H. J. Monkhorst and B. Jeziorski, *J. Chem. Phys.* **71**, 5268–5269 (1979).
47. C. Duchon, M. C. Dumont-Lepage, and J. P. Gazeau, *J. Chem. Phys.* **76**, 445–447 (1982).
48. B. K. Novosadov, *J. Mol. Struct.* **54**, 269–286 (1979).
49. H. J. Monkhorst and K. Szalewicz, *J. Chem. Phys.* **75**, 5782–5784 (1981).
50. J. Navaza and G. Tsoucaris, *Phys. Rev. A* **24**, 683–692 (1981).
51. T. Koga and M. Morita, *Theor. Chim. Acta* **59**, 423–435 (1981).
52. T. Koga, M. Sugawara, and M. Morita, *Theor. Chim. Acta* **61**, 87–101 (1982).
53. J. R. Lombardi, *J. Phys. Chem.* **86**, 3513–3517 (1982).
54. J. R. Lombardi, *J. Chem. Phys.* **78**, 2476–2479 (1983).
55. M. Defranceschi, M. Suard, and G. Berthier, *C. R. Acad. Sci. Ser. II* **296**, 1301–1304 (1983).
56. P. E. Regier and A. J. Thakkar, *Phys. Rev. A* **30**, 30–34 (1984).
57. M. Defranceschi, M. Suard, and G. Berthier, *C. R. Acad. Sci. Ser. II* **299**, 9–12 (1984).
58. M. Defranceschi, M. Suard, and G. Berthier, *Int. J. Quantum Chem.* **25**, 863–867 (1984).
59. G. Berthier, M. Defranceschi, J. Navaza, M. Suard, and G. Tsoucaris, *J. Mol. Struct.* (*THEOCHEM*) **21**, 343–350 (1985).
60. T. Koga, *J. Chem. Phys.* **82**, 2022–2025 (1985).
61. T. Koga, *J. Chem. Phys.* **83**, 2328–2333 (1985).
62. T. Koga, *J. Chem. Phys.* **83**, 6304–6306 (1985).
63. T. Koga and S. Matsumoto, *J. Chem. Phys.* **82**, 5127–5132 (1985).
64. C. Tzara, *Phys. Lett. A* **111**, 343–348 (1985).
65. M. Defranceschi and J. Delhalle, *Phys. Rev. B* **34**, 5862–5873 (1986).
66. T. Koga, *J. Chem. Phys.* **84**, 1636–1639 (1986).
67. T. Koga and R. Kawa-ai, *J. Chem. Phys.* **84**, 5651–5654 (1986).
68. T. Koga and M. Uji-ie, *J. Chem. Phys.* **84**, 335–340 (1986).
69. R. Baretty, Y. Ishikawa, and J. F. Nieves, *Int. J. Quantum Chem. Symp.* **20**, 109–117 (1986).
70. S. A. Alexander and H. J. Monkhorst, *Int. J. Quantum Chem.* **32**, 361–375 (1987).
71. T. Koga and T. Matsuhashi, *J. Chem. Phys.* **87**, 1677–1680 (1987).
72. T. Koga, T. Uchiyama, and M. Uji-ie, *J. Chem. Phys.* **87**, 4025–4030 (1987).
73. T. Koga and M. Uji-ie, *J. Chem. Phys.* **86**, 2854–2858 (1987).
74. T. Koga and M. Uji-ie, *J. Chem. Phys.* **87**, 1137–1141 (1987).
75. Y. Ishikawa, W. Rodriguez, and S. A. Alexander, *Int. J. Quantum Chem. Symp.* **21**, 417–423 (1987).
76. J. Delhalle and M. Defranceschi, *Int. J. Quantum Chem.* **21**, 424–433 (1987).
77. M. Defranceschi, *Chem. Phys.* **115**, 349–358 (1987).
78. J. Avery, *Chem. Phys. Lett.* **138**, 520–524 (1987).

79. P. J. Schreiber, R. P. Hurst, and T. E. Duvall, *Phys. Rev. A* **38**, 3200–3209 (1988).
80. F. Q. Liu and T. K. Lim, *Few-Body Syst.* **5**, 31–43 (1988).
81. W. Rodriguez and Y. Ishikawa, *Chem. Phys. Lett.* **146**, 515–517 (1988).
82. W. Rodriguez and Y. Ishikawa, *Int. J. Quantum Chem. Symp.* **22**, 445–456 (1988).
83. T. Koga, Y. Yamamoto, and T. Matsuhashi, *J. Chem. Phys.* **88**, 6675–6676 (1988).
84. T. Koga and T. Matsuhashi, *J. Chem. Phys.* **89**, 983–986 (1988).
85. J. Avery and P. Sommer-Larsen, *Int. J. Quantum Chem. Symp.* **22**, 437–444 (1988).
86. Y. Ishikawa, W. Rodriguez, S. Torres, and S. A. Alexander, *Chem. Phys. Lett.* **143**, 289–292 (1988).
87. S. A. Alexander, R. L. Coldwell, and H. J. Monkhorst, *J. Comput. Phys.* **76**, 263–280 (1988).
88. T. Koga, *J. Chem. Phys.* **90**, 605–606 (1989).
89. T. Koga and T. Ougihara, *J. Chem. Phys.* **91**, 1092–1095 (1989).
90. T. Koga and M. Uji-ie, *Phys. Rev. A* **39**, 4272–4273 (1989).
91. S. Boukraa and J. L. Basdevant, *J. Math. Phys.* **30**, 1060–1072 (1989).
92. J. Delhalle, J. G. Fripiat, and M. Defranceschi, *Bull. Soc. Chim. Belg.* **99**, 135–145 (1990).
93. J. Avery and F. Antonsen, *Int. J. Quantum Chem.* **42**, 87–101 (1992).
94. M. Defranceschi, L. Dewindt, J. G. Fripiat, and J. Delhalle, *J. Mol. Struct.* (*THEOCHEM*) **90**, 179–196 (1992).
95. L. Dewindt, J. G. Fripiat, J. Delhalle, and M. Defranceschi, *J. Mol. Struct.* (*THEOCHEM*) **86**, 145–159 (1992).
96. P. Fischer, M. Defranceschi, and J. Delhalle, *Numer. Math.* **63**, 67–82 (1992).
97. S. A. V. Katyurin and O. B. Glinkin, *Int. J. Quantum Chem.* **43**, 251–258 (1992).
98. P. Fischer, L. Dewindt, M. Defranceschi, and J. Delhalle, *J. Chem. Phys.* **99**, 7888–7898 (1993).
99. L. Dewindt, M. Defranceschi, and J. Delhalle, *Int. J. Quantum Chem.* **45**, 609–618 (1993).
100. L. Dewindt, M. Defranceschi, and J. Delhalle, *Theor. Chim. Acta* **86**, 487–496 (1993).
101. L. Dewindt, P. Fischer, M. Defranceschi, J. Delhalle, and J. G. Fripiat, *J. Comput. Phys.* **111**, 266–274 (1994).
102. J. Avery, T. B. Hansen, M. C. Wang, and F. Antonsen, *Int. J. Quantum Chem.* **57**, 401–411 (1996).
103. V. Aquilanti, S. Cavalli, C. Coletti, and G. Grossi, *Chem. Phys.* **209**, 405–419 (1996).
104. V. Aquilanti, S. Cavalli, and C. Coletti, *Chem. Phys.* **214**, 1–13 (1997).
105. G. Berthier, M. Defranceschi, J. Navaza, and G. Tsoucaris, *Int. J. Quantum Chem.* **63**, 451–457 (1997).
106. J. Avery and F. Antonsen, *J. Math. Chem.* **24**, 175–185 (1998).
107. D. Andrae, *Mol. Phys.* **99**, 327–334 (2001).
108. B. H. Armstrong, *Bull. Am. Phys. Soc.* **9**, 401 (1964).
109. A. J. Thakkar and V. H. Smith, Jr., *Phys. Rev. A* **18**, 841–844 (1978).
110. T. Koga, K. Ohta, and A. J. Thakkar, *Phys. Rev. A* **37**, 1411–1414 (1988).
111. T. Koga, *J. Chem. Phys.* **89**, 5961–5962 (1988).
112. T. Koga, *J. Chem. Phys.* **90**, 5887–5889 (1989).
113. T. Koga, *J. Chem. Phys.* **91**, 4774–4778 (1989).
114. T. Koga, H. Matsuyama, and A. J. Thakkar, *Phys. Rev. A* **43**, 3299–3304 (1991).
115. T. Koga and A. J. Thakkar, *Can. J. Chem.* **70**, 362–365 (1992).

116. A. J. Thakkar, T. Koga, H. Matsuyama, and E. F. Archibong, *Int. J. Quantum Chem.* **44**, 985–995 (1992).
117. G. Berthier, M. Defranceschi, and G. Tsoucaris, *Int. J. Quantum Chem.* **60**, 195–199 (1996).
118. P. A. M. Dirac, *Proc. Roy. Soc.* **A113**, 621–641 (1927).
119. P. A. M. Dirac, *The Principles of Quantum Mechanics*, 4th ed. (Oxford Univ. Press, London, 1958).
120. P. Jordan, *Z. Phys.* **40**, 809–838 (1927).
121. P. Jordan, *Z. Phys.* **44**, 1–25 (1927).
122. K. Husimi, *Proc. Phys. Math. Soc. Jpn.* **22**, 264–314 (1940).
123. P. O. Löwdin, *Phys. Rev.* **97**, 1474–1489 (1955).
124. R. McWeeny, *Rev. Mod. Phys.* **32**, 335–369 (1960).
125. A. J. Coleman, *Rev. Mod. Phys.* **35**, 668–686 (1963).
126. E. R. Davidson, *Reduced Density Matrices in Quantum Chemistry* (Academic Press, New York, 1976).
127. A. J. Thakkar, A. M. Simas, and V. H. Smith, Jr., *Chem. Phys.* **63**, 175–183 (1981).
128. A. J. Thakkar, Extracules, intracules, correlation holes, potentials, coefficients and all that, in *Density Matrices and Density Functionals*, R. M. Erdahl and V. H. Smith, Jr., eds. (Reidel, Dordrecht, Holland, 1987), pp. 553–581.
129. R. Benesch, S. R. Singh, and V. H. Smith, Jr., *Chem. Phys. Lett.* **10**, 151–153 (1971).
130. E. P. Wigner, *Phys. Rev.* **40**, 749–759 (1932).
131. M. Hillery, R. F. O'Connell, M. O. Scully, and E. P. Wigner, *Phys. Rep.* **106**, 121–167 (1984).
132. J. E. Moyal, *Proc. Camb. Phil. Soc.* **45**, 99–124 (1949).
133. M. E. Casida, J. E. Harriman, and J. L. Anchell, *Int. J. Quantum Chem. Symp.* **21**, 435–456 (1987).
134. J. E. Harriman, *J. Chem. Phys.* **88**, 6399–6408 (1988).
135. J. E. Harriman and M. E. Casida, *Int. J. Quantum Chem.* **45**, 263–294 (1993).
136. M. Springborg, *Theor. Chim. Acta* **63**, 349–356 (1983).
137. J. P. Dahl and M. Springborg, *J. Chem. Phys.* **88**, 4535–4547 (1988).
138. J. L. Anchell and J. E. Harriman, *J. Chem. Phys.* **89**, 6860–6869 (1988).
139. J. L. Anchell and J. E. Harriman, *J. Chem. Phys.* **92**, 2943–2952 (1990).
140. J. E. Harriman, *J. Mol. Struct.* (*THEOCHEM*) **91**, 141–154 (1992).
141. H. Schmider, *J. Chem. Phys.* **105**, 3627–3635 (1996).
142. H. Schmider and J. P. Dahl, *Int. J. Quantum Chem.* **60**, 439–452 (1996).
143. H. Schmider and M. H. Hô, *J. Phys. Chem.* **100**, 17807–17819 (1996).
144. H. Schmider, *Z. Phys. Chem.* **215**, 1289–1302 (2001).
145. P. E. Mijnarends, Reconstruction of three-dimensional distributions, in *Compton Scattering: The Investigation of Electron Momentum Distributions*, B. G. Williams, ed. (McGraw-Hill, New York, 1977), pp. 323–345.
146. F. M. Mueller, *Phys. Rev. B* **15**, 3039–3044 (1977).
147. P. Pattison and B. Williams, *Solid State Commun.* **20**, 585–588 (1976).
148. W. Schülke, *Phys. Stat. Sol.* (*b*) **82**, 229–235 (1977).
149. P. Pattison, W. Weyrich, and B. Williams, *Solid State Commun.* **21**, 967–970 (1977).
150. P. Pattison and W. Weyrich, *J. Phys. Chem. Solids* **40**, 213–222 (1979).

151. W. Weyrich, P. Pattison, and B. G. Williams, *Chem. Phys.* **41**, 271–284 (1979).
152. I. A. Howard, N. H. March, and V. E. van Doren, *Phys. Rev. A* **64**, 042509 (2001).
153. A. J. Thakkar, A. C. Tanner, and V. H. Smith, Jr., Inter-relationships between various representations of one-matrices and related densities: A road map and an example, in *Density Matrices and Density Functionals*, R. M. Erdahl and V. H. Smith, Jr., eds. (Reidel, Dordrecht, Holland, 1987), pp. 327–337.
154. P. O. Löwdin, *Adv. Quantum Chem.* **3**, 323–381 (1967).
155. A. Messiah, *Quantum Mechanics* (North Holland, Amsterdam, 1970).
156. P. Kaijser and V. H. Smith, Jr., On inversion symmetry in momentum space, in *Methods and Structure in Quantum Science*, J. L. Calais, O. Goscinski, J. Linderberg, and Y. Öhrn, eds. (Plenum Press, New York, 1976), pp. 417–426.
157. A. J. Thakkar, A. M. Simas, and V. H. Smith, Jr., *J. Chem. Phys.* **81**, 2953–2961 (1984).
158. D. C. Rawlings and E. R. Davidson, *J. Phys. Chem.* **89**, 969–974 (1985).
159. M. Defranceschi and G. Berthier, *J. Phys.* (*Paris*) **51**, 2791–2800 (1990).
160. S. R. Gadre, A. C. Limaye, and S. A. Kulkarni, *J. Chem. Phys.* **94**, 8040–8046 (1991).
161. J. L. Calais, M. Defranceschi, J. G. Fripiat, and J. Delhalle, *J. Phys. Conden. Matter* **4**, 5675–5691 (1992).
162. P. E. Mijnarends, *Phys. Rev.* **160**, 512–519 (1967).
163. A. Seth and D. E. Ellis, *Phys. Rev. A* **13**, 1083–1090 (1976).
164. A. R. Edmonds, *Angular Momentum in Quantum Mechanics*, 2nd ed. (Princeton Univ. Press, Princeton, NJ, 1960).
165. E. Heuser-Hofmann and W. Weyrich, *Z. Naturfors. Sect. A* **40**, 99–111 (1985).
166. M. Abramowitz and I. Stegun, eds., *Handbook of Mathematical Functions* (Dover, New York, 1968).
167. R. A. Bonham and H. F. Wellenstein, Electron scattering, in *Compton Scattering: The Investigation of Electron Momentum Distributions*, B. G. Williams, ed. (McGraw-Hill, New York, 1977), pp. 234–272.
168. A. J. Thakkar, *J. Chem. Phys.* **86**, 5060–5062 (1987).
169. J. C. Kimball, *J. Phys. A* **8**, 1513–1517 (1975).
170. A. J. Coleman, *Int. J. Quantum Chem. Symp.* **1**, 457–464 (1967).
171. T. Kato, *Commun. Pure Appl. Math.* **10**, 151–177 (1957).
172. E. Steiner, *J. Chem. Phys.* **39**, 2365–2366 (1963).
173. A. J. Thakkar and V. H. Smith, Jr., *Chem. Phys. Lett.* **42**, 476–481 (1976).
174. G. Breit, *Phys. Rev.* **34**, 553–573 (1929).
175. G. Breit, *Phys. Rev.* **36**, 383–397 (1930).
176. G. Breit, *Phys. Rev.* **39**, 616–624 (1932).
177. H. A. Bethe and E. E. Salpeter, *Quantum Mechanics of One- and Two-electron Atoms* (Springer-Verlag, Berlin, 1957).
178. R. McWeeny and B. T. Sutcliffe, *Methods of Molecular Quantum Mechanics* (Academic Press, London, 1969).
179. T. Koga and M. Morita, *J. Chem. Phys.* **77**, 6345–6346 (1982).
180. T. Koga, *J. Chem. Phys.* **79**, 1384–1386 (1983).

181. B. G. Williams, ed., *Compton Scattering: The Investigation of Electron Momentum Distributions* (McGraw-Hill, New York, 1977).
182. M. J. Cooper, *Rep. Prog. Phys.* **48**, 415–481 (1985).
183. M. J. Cooper, *Radiat. Phys. Chem.* **50**, 63–76 (1997).
184. S. Manninen, *J. Phys. Chem. Solids* **61**, 335–340 (2000).
185. J. W. M. DuMond, *Phys. Rev.* **33**, 643–658 (1929).
186. J. W. M. DuMond, *Rev. Mod. Phys.* **5**, 1–33 (1933).
187. A. J. Thakkar, A. L. Wonfor, and W. A. Pedersen, *J. Chem. Phys.* **87**, 1212–1215 (1987).
188. B. L. Hicks, *Phys. Rev.* **57**, 665–666 (1940).
189. I. R. Epstein, *Phys. Rev. A* **8**, 160–168 (1973).
190. H. F. Wellenstein, R. A. Bonham, and R. C. Ulsh, *Phys. Rev. A* **8**, 304–314 (1973).
191. N. H. March, *J. Chem. Phys.* **79**, 3404–3409 (1983).
192. A. J. Thakkar, A. M. Simas, and V. H. Smith, Jr., *Mol. Phys.* **43**, 1153–1162 (1980).
193. A. J. Thakkar, *Int. J. Quantum Chem.* **23**, 227–234 (1983).
194. V. H. Smith, Jr., *Int. J. Quantum Chem. Symp.* **23**, 553–555 (1989).
195. P. Kaijser and V. H. Smith, Jr., *Mol. Phys.* **31**, 1557–1568 (1976).
196. I. E. McCarthy and E. Weigold, *Phys. Rep.* **27**, 275–371 (1976).
197. R. Benesch and V. H. Smith, Jr., *Chem. Phys. Lett.* **5**, 601–604 (1970).
198. R. Benesch and V. H. Smith, Jr., *Int. J. Quantum Chem. Symp.* **4**, 131–138 (1970).
199. A. M. Simas, A. J. Thakkar, and V. H. Smith, Jr., *Int. J. Quantum Chem.* **21**, 419–429 (1982).
200. A. M. Simas, A. J. Thakkar, and V. H. Smith, Jr., *Int. J. Quantum Chem.* **24**, 527–550 (1983).
201. P. E. Regier, J. Fisher, B. S. Sharma, and A. J. Thakkar, *Int. J. Quantum Chem.* **28**, 429–449 (1985).
202. J. Wang and V. H. Smith, Jr., *J. Phys. B* **27**, 5159–5173 (1994).
203. J. M. G. de la Vega, B. Miguel, and G. Ramirez, *J. Math. Chem.* **21**, 211–222 (1997).
204. A. Saenz, T. Asthalter, and W. Weyrich, *Int. J. Quantum Chem.* **65**, 213–223 (1997).
205. A. J. Thakkar and B. S. Sharma, *Int. J. Quantum Chem.* **85**, 258–262 (2001).
206. V. N. Staroverov and E. R. Davidson, *Mol. Phys.* **99**, 175–186 (2001).
207. J. M. G. de la Vega and B. Miguel, *J. Math. Chem.* **14**, 219–229 (1993).
208. B. Podolsky and L. Pauling, *Phys. Rev.* **34**, 109–116 (1929).
209. T. Koga, K. Kanayama, S. Watanabe, and A. J. Thakkar, *Int. J. Quantum Chem.* **71**, 491–497 (1999).
210. S. R. Gadre, S. Chakravorty, and R. K. Pathak, *J. Chem. Phys.* **78**, 4581–4584 (1983).
211. A. M. Simas, W. M. Westgate, and V. H. Smith, Jr., *J. Chem. Phys.* **80**, 2636–2642 (1984).
212. R. P. Sagar, A. C. T. Ku, V. H. Smith, Jr., and A. M. Simas, *J. Chem. Phys.* **90**, 6520–6527 (1989).
213. H. Schmider, R. P. Sagar, and V. H. Smith, Jr., *Can. J. Chem.* **70**, 506–512 (1992).
214. H. Schmider, R. P. Sagar, and V. H. Smith, Jr., *Proc. Indian Acad. Sci.* (*Chem. Sci.*) **106**, 133–142 (1994).
215. T. Koga, *J. Chem. Phys.* **116**, 6910–6913 (2002).
216. G. Sperber, *Int. J. Quantum Chem.* **5**, 189–214 (1971).
217. H. Weinstein, P. Politzer, and S. Srebrenik, *Theor. Chim. Acta* **38**, 159–163 (1975).
218. T. Koga, *Theor. Chim. Acta* **95**, 113–130 (1997).

219. T. Koga and H. Matsuyama, *Theor. Chem. Acc.* **98**, 129–136 (1997).
220. A. J. Thakkar, *J. Chem. Phys.* **76**, 747–748 (1982).
221. V. H. Smith, Jr., D. Robertson, and A. N. Tripathi, *Phys. Rev. A* **42**, 61–62 (1990).
222. N. H. March, *Phys. Rev. A* **33**, 88–89 (1986).
223. S. R. Singh and V. H. Smith, Jr., *Z. Phys.* **255**, 83–92 (1972).
224. R. P. Sagar, R. O. Esquivel, H. Schmider, A. N. Tripathi, and V. H. Smith, Jr., *Phys. Rev. A* **47**, 2625–2627 (1993).
225. A. Harmalkar, A. M. Simas, V. H. Smith, Jr., and W. M. Westgate, *Int. J. Quantum Chem.* **23**, 811–820 (1983).
226. S. R. Gadre and S. Chakravorty, *Chem. Phys. Lett.* **120**, 101–105 (1985).
227. W. M. Westgate, A. M. Simas, and V. H. Smith, Jr., *J. Chem. Phys.* **83**, 4054–4058 (1985).
228. J. C. Angulo, *Phys. Rev. A* **48**, 4768–4770 (1993).
229. E. Romera, T. Koga, and J. S. Dehesa, *Z. Phys. D* **42**, 251–257 (1997).
230. T. Koga, H. Matsuyama, H. Inomata, E. Romera, J. S. Dehesa, and A. J. Thakkar, *J. Chem. Phys.* **109**, 1601–1606 (1998).
231. T. Koga, H. Matsuyama, E. Romera, J. S. Dehesa, and A. J. Thakkar, *Phys. Rev. A* **59**, 4805–4808 (1999).
232. T. Koga and A. J. Thakkar, *J. Phys. B* **29**, 2973–2983 (1996).
233. P. J. MacDougall, *Can. J. Phys.* **69**, 1423–1428 (1991).
234. E. Clementi and C. Roetti, *Atom. Data Nucl. Data Tables* **14**, 177–478 (1974).
235. T. Koga, E. Romera, J. S. Dehesa, H. Matsuyama, and A. J. Thakkar, *Theor. Chem. Acc.* **103**, 70–76 (1999).
236. P. E. Regier and A. J. Thakkar, *J. Phys. B* **18**, 3061–3071 (1985).
237. R. O. Esquivel, A. N. Tripathi, R. P. Sagar, and V. H. Smith, Jr., *J. Phys. B* **25**, 2925–2941 (1992).
238. A. N. Tripathi, R. P. Sagar, R. O. Esquivel, and V. H. Smith, Jr., *Phys. Rev. A* **45**, 4385–4392 (1992).
239. A. N. Tripathi, V. H. Smith, Jr., R. P. Sagar, and R. O. Esquivel, *Phys. Rev. A* **54**, 1877–1884 (1996).
240. A. Sarsa, F. J. Gálvez, and E. Buendía, *J. Phys. B* **32**, 2245–2255 (1999).
241. A. J. Thakkar and B. S. Sharma, *J. Mol. Struct.* (*THEOCHEM*) **527**, 221–227 (2000).
242. W. E. Duncanson and C. A. Coulson, *Proc. Phys. Soc.* **57**, 190–198 (1945).
243. W. E. Duncanson and C. A. Coulson, *Proc. Phys. Soc.* **60**, 175–183 (1948).
244. R. J. Weiss, A. Harvey, and W. C. Phillips, *Phil. Mag.* **17**, 241–249 (1968).
245. M. Naon, M. Cornille, and M. Roux, *J. Phys. B* **4**, 1593–1601 (1971).
246. S. R. Gadre, S. P. Gejji, and S. J. Chakravorty, *Atom. Data Nucl. Data Tables* **28**, 477–491 (1983).
247. W. M. Westgate, R. P. Sagar, A. Farazdel, V. H. Smith, Jr., A. M. Simas, and A. J. Thakkar, *Atom. Data Nucl. Data Tables* **48**, 213–229 (1991).
248. J. M. G. de la Vega and B. Miguel, *Atom. Data Nucl. Data Tables* **54**, 1–51 (1993).
249. J. M. G. de la Vega and B. Miguel, *Atom. Data Nucl. Data Tables* **58**, 307–315 (1994).
250. J. M. G. de la Vega and B. Miguel, *Chem. Phys. Lett.* **236**, 616–620 (1995).
251. J. M. G. de la Vega and B. Miguel, *Atom. Data Nucl. Data Tables* **60**, 321–330 (1995).

252. F. Biggs, L. B. Mendelsohn, and J. B. Mann, *Atom. Data Nucl. Data Tables* **16**, 201–309 (1975).
253. R. Benesch, *Can. J. Phys.* **54**, 2155–2158 (1976).
254. B. Hicks, *Phys. Rev.* **52**, 436–442 (1937).
255. R. Benesch, *J. Phys. B* **9**, 2587–2594 (1976).
256. F. A. de Saavedra, E. Buendía, and F. J. Gálvez, *Z. Phys. D-Atoms Mol. Clusters* **38**, 25–30 (1996).
257. F. A. de Saavedra, E. Buendía, and F. J. Gálvez, *Z. Phys. D-Atoms Mol. Clusters* **39**, 101–107 (1997).
258. H. Meyer, T. Müller, and A. Schweig, *J. Mol. Struct*. (*THEOCHEM*) **360**, 55–65 (1996).
259. R. Benesch and V. H. Smith, Jr., *Phys. Rev. A* **5**, 114–125 (1972).
260. R. E. Brown and V. H. Smith, Jr., *Mol. Phys.* **34**, 713–729 (1977).
261. R. E. Brown and V. H. Smith, Jr., *Chem. Phys. Lett.* **20**, 424–428 (1973).
262. H. Schmider, R. O. Esquivel, R. P. Sagar, and V. H. Smith, Jr., *J. Phys. B* **26**, 2943–2955 (1993).
263. A. J. Thakkar and T. Koga, *Int. J. Quantum Chem. Symp.* **26**, 291–298 (1992).
264. I. K. Dmitrieva and G. I. Plindov, *Z. Phys. A* **305**, 103–106 (1982).
265. I. K. Dmitrieva and G. I. Plindov, *J. Phys.* (*Paris*) **44**, 333–342 (1983).
266. K. Buchwald and B. G. Englert, *Phys. Rev. A* **40**, 2738–2741 (1989).
267. L. H. Thomas, *Proc. Camb. Phil. Soc.* **23**, 542–548 (1927).
268. E. Fermi, *Rend. Accad., Lincei* **6**, 602–607 (1927).
269. E. Fermi, *Rend. Accad., Lincei* **7**, 342–346 (1928).
270. E. Fermi, *Z. Phys.* **48**, 73–79 (1928).
271. N. H. March, *Adv. Phys.* **6**, 1–101 (1957).
272. J. M. C. Scott, *Phil. Mag.* **43**, 859–867 (1952).
273. J. Schwinger, *Phys. Rev. A* **22**, 1827–1832 (1980).
274. S. R. Gadre and S. J. Chakravorty, *Chem. Phys. Lett.* **132**, 535–540 (1986).
275. S. R. Gadre and S. J. Chakravorty, *J. Chem. Phys.* **84**, 7051–7052 (1986).
276. S. R. Gadre and R. D. Bendale, *Phys. Rev. A* **36**, 1932–1935 (1987).
277. S. R. Gadre and R. K. Pathak, *Adv. Quantum Chem.* **22**, 211–300 (1991).
278. J. S. Dehesa and F. J. Gálvez, *Phys. Rev. A* **37**, 3634–3637 (1988).
279. J. S. Dehesa, F. J. Gálvez, and I. Porras, *Phys. Rev. A* **40**, 35–40 (1989).
280. J. S. Dehesa, F. J. Gálvez, and I. Porras, *Phys. Rev. A* **39**, 494–500 (1989).
281. F. J. Gálvez and J. S. Dehesa, *Phys. Rev. A* **37**, 3154–3157 (1988).
282. I. Porras and F. J. Gálvez, *Phys. Rev. A* **41**, 4052–4055 (1990).
283. J. C. Angulo, J. S. Dehesa, and F. J. Gálvez, *Z. Phys. D—Atoms Mol. Clusters* **18**, 127–130 (1991).
284. J. C. Angulo, J. Antolín, and A. Zarzo, *Z. Phys. D—Atoms Mol. Clusters* **28**, 269–273 (1993).
285. J. C. Angulo, *J. Phys. A—Math. Gen.* **26**, 6493–6497 (1993).
286. A. Zarzo, J. C. Angulo, and J. Antolín, *J. Phys. B* **26**, 4663–4669 (1993).
287. I. Porras and F. J. Gálvez, *Int. J. Quantum Chem.* **56**, 763–769 (1995).
288. E. Romera, *J. Phys. B* **34**, 3527–3534 (2001).
289. W. Yue and L. Janmin, *Phys. Scr.* **30**, 414 (1984).
290. J. M. Tao and J. M. Li, *Phys. Scr.* **54**, 335–336 (1996).

291. J. M. Tao and G. B. Li, *Phys. Scr.* **58**, 193–195 (1998).
292. J. Tao, G. Li, and J. Li, *J. Phys. B* **31**, 1897–1909 (1998).
293. S. R. Gadre and S. B. Sears, *J. Chem. Phys.* **71**, 4321–4323 (1979).
294. T. Koga and M. Morita, *J. Chem. Phys.* **79**, 1933–1938 (1983).
295. T. Koga, *Theor. Chim. Acta* **64**, 249–257 (1984).
296. T. Koga, M. Hayashi, and H. Hoshina, *J. Chem. Phys.* **85**, 3128–3130 (1986).
297. E. S. Kryachko and T. Koga, *J. Math. Phys.* **28**, 8–14 (1987).
298. J. C. Angulo, R. J. Yanez, J. Antolín, and A. Zarzo, *Int. J. Quantum Chem.* **56**, 747–752 (1995).
299. J. Antolín, J. C. Cuchí, A. Zarzo, and J. C. Angulo, *J. Phys. B* **29**, 5629–5635 (1996).
300. J. Antolín, A. Zarzo, J. C. Angulo, and J. C. Cuchí, *Int. J. Quantum Chem.* **61**, 77–83 (1997).
301. J. Antolín, J. C. Cuchí, and J. C. Angulo, *Int. J. Quantum Chem.* **87**, 214–219 (2002).
302. P. F. Price, I. Absar, and V. H. Smith, Jr., *Israel J. Chem.* **16**, 187–197 (1977).
303. R. F. W. Bader, *Atoms in Molecules: A Quantum Theory* (Clarendon, Oxford, 1990).
304. P. Coppens, *X-ray Charge Densities and Chemical Bonding* (Oxford Univ. Press, New York, 1997).
305. W. H. Henneker and P. E. Cade, *Chem. Phys. Lett.* **2**, 575–578 (1968).
306. I. R. Epstein, *J. Chem. Phys.* **52**, 3838–3840 (1970).
307. I. R. Epstein and W. N. Lipscomb, *J. Chem. Phys.* **53**, 4418–4424 (1970).
308. I. R. Epstein, *J. Chem. Phys.* **53**, 4425–4436 (1970).
309. P. Kaijser, P. Lindner, A. Andersen, and E. Thulstrup, *Chem. Phys. Lett.* **23**, 409–413 (1973).
310. P. Kaijser and P. Lindner, *Phil. Mag.* **31**, 871–882 (1975).
311. T. Ahlenius and P. Lindner, *J. Phys. B* **8**, 778–795 (1975).
312. A. C. Tanner and I. R. Epstein, *J. Chem. Phys.* **61**, 4251–4257 (1974).
313. R. A. Tawil and S. R. Langhoff, *J. Chem. Phys.* **63**, 1572–1581 (1975).
314. S. R. Langhoff and R. A. Tawil, *J. Chem. Phys.* **63**, 2745–2751 (1975).
315. A. C. Tanner, *Chem. Phys.* **123**, 241–247 (1988).
316. P. Kaijser, V. H. Smith, Jr., and A. J. Thakkar, *Mol. Phys.* **43**, 1143–1151 (1980).
317. B. I. Ramirez, *J. Phys. B* **15**, 4339–4348 (1982).
318. B. I. Ramirez, *Chem. Phys. Lett.* **94**, 180–182 (1983).
319. B. I. Ramirez, *J. Phys. B* **16**, 343–348 (1983).
320. B. I. Ramirez, W. R. McIntire, and R. L. Matcha, *J. Chem. Phys.* **65**, 906–911 (1976).
321. B. I. Ramirez, W. R. McIntire, and R. L. Matcha, *J. Chem. Phys.* **66**, 373–375 (1977).
322. R. L. Matcha, B. M. Pettit, B. I. Ramirez, and W. R. McIntire, *J. Chem. Phys.* **69**, 3025–3033 (1978).
323. R. L. Matcha, B. M. Pettit, B. I. Ramirez, and W. R. McIntire, *J. Chem. Phys.* **70**, 558–564 (1979).
324. R. L. Matcha and B. M. Pettit, *J. Chem. Phys.* **70**, 3130–3132 (1979).
325. R. L. Matcha, B. M. Pettit, B. I. Ramirez, and W. R. McIntire, *J. Chem. Phys.* **71**, 991–996 (1979).
326. R. L. Matcha and B. M. Pettit, *J. Chem. Phys.* **72**, 4588–4590 (1980).
327. B. M. Pettit, S. R. Gadre, and R. L. Matcha, *Int. J. Quantum Chem. Symp.* **14**, 697–706 (1980).
328. B. M. Pettit, R. L. Matcha, and B. I. Ramirez, *J. Chem. Phys.* **79**, 2913–2917 (1983).

329. K. T. Leung and C. E. Brion, *Chem. Phys.* **82**, 113–137 (1983).
330. K. T. Leung and C. E. Brion, *J. Am. Chem. Soc.* **106**, 5859–5864 (1984).
331. A. M. Simas, V. H. Smith, Jr., and P. Kaijser, *Int. J. Quantum Chem.* **25**, 1035–1044 (1984).
332. A. Rozendaal and E. J. Baerends, *Chem. Phys.* **87**, 263–272 (1984).
333. A. Rozendaal and E. J. Baerends, *Chem. Phys.* **95**, 57–91 (1985).
334. D. L. Cooper and N. L. Allan, *J. Chem. Soc. Faraday Trans. II* **83**, 449–460 (1987).
335. M. Rérat and A. Lichanot, *Chem. Phys. Lett.* **263**, 767–774 (1996).
336. M. Merawa, M. Rérat, and A. Lichanot, *Int. J. Quantum Chem.* **71**, 63–74 (1999).
337. A. M. Simas, V. H. Smith, Jr., and A. J. Thakkar, *Int. J. Quantum Chem. Symp.* **18**, 385–392 (1984).
338. A. M. Simas, V. H. Smith, Jr., and A. J. Thakkar, *J. Mol. Struct.* (*THEOCHEM*) **123**, 221–229 (1985).
339. A. M. Simas, V. H. Smith, Jr., and A. J. Thakkar, *Can. J. Chem.* **63**, 1412–1417 (1985).
340. B. S. Sharma, A. N. Tripathi, and A. J. Thakkar, *J. Chem. Phys.* **79**, 3164–3165 (1983).
341. A. Jain, A. N. Tripathi, and V. H. Smith, Jr., *Can. J. Chem.* **67**, 1886–1891 (1989).
342. T. Koga, *Chem. Phys.* **87**, 31–41 (1984).
343. W. J. Janis, P. Kaijser, M. H. Whangbo, and V. H. Smith, Jr., *Mol. Phys.* **35**, 1237–1245 (1978).
344. W. Janis, P. Kaijser, J. Sabin, and V. H. Smith, Jr., *Mol. Phys.* **37**, 463–472 (1978).
345. P. Kaijser, A. N. Tripathi, V. H. Smith, Jr., and G. H. F. Dierksen, *Phys. Rev. A* **35**, 4074–4084 (1987).
346. D. L. Cooper, N. L. Allan, and P. J. Grout, *J. Chem. Soc. Faraday Trans. II* **85**, 1519–1529 (1989).
347. A. N. Tripathi, V. H. Smith, Jr., P. Kaijser, and G. H. F. Diercksen, *Phys. Rev. A* **41**, 2468–2481 (1990).
348. S. A. Kulkarni, S. R. Gadre, and R. K. Pathak, *Phys. Rev. A* **45**, 4399–4406 (1992).
349. S. A. Kulkarni and S. R. Gadre, *Z. Naturforsch. Sect. A* **48**, 145–150 (1993).
350. J. Wang, B. Clark, H. Schmider, and V. H. Smith, Jr., *Can. J. Chem.* **74**, 1187–1191 (1996).
351. A. J. Thakkar, *Z. Phys. Chemie* **215**, 1265–1275 (2001).
352. S. R. Gadre and S. A. Kulkarni, *Proc. Ind. Acad. Sci.* **105**, 149–153 (1993).
353. S. A. Kulkarni and S. R. Gadre, *J. Am. Chem. Soc.* **115**, 7434–7438 (1993).
354. S. A. Kulkarni and S. R. Gadre, *Chem. Phys. Lett.* **274**, 255–263 (1997).
355. A. J. Thakkar and W. A. Pedersen, *Int. J. Quantum Chem. Symp.* **23**, 245–253 (1989).
356. A. K. Roy and A. J. Thakkar, *Chem. Phys. Lett.* **362**, 428–434 (2002).
357. P. E. Cade and W. Huo, *Atom. Data Nucl. Data Tables* **12**, 415–466 (1973).
358. P. E. Cade and A. C. Wahl, *Atom. Data Nucl. Data Tables* **13**, 339–389 (1974).
359. P. E. Cade and W. Huo, *Atom. Data Nucl. Data Tables* **15**, 1–39 (1975).
360. T. H. Dunning, Jr., *J. Chem. Phys.* **90**, 1007–1023 (1989).
361. A. J. Thakkar, J. W. Liu, and W. J. Stevens, *Phys. Rev. A* **34**, 4695–4703 (1986).
362. A. J. Thakkar, J. W. Liu, and G. C. Lie, *Phys. Rev. A* **36**, 5111–5117 (1987).
363. A. J. Thakkar and H. Tatewaki, *Phys. Rev. A* **42**, 1336–1345 (1990).
364. P. Eisenberger and W. A. Reed, *Phys. Rev. A* **5**, 2085–2094 (1972).
365. P. Eisenberger and W. A. Reed, *Phys. Rev. B* **9**, 3237–3241 (1974).
366. T. Paakkari and M. Merisalo, *Chem. Phys. Lett.* **33**, 432–435 (1975).

367. P. Eisenberger, *Phys. Rev. A* **5**, 628–635 (1972).
368. T. C. Wong, J. S. Lee, H. F. Wellenstein, and R. A. Bonham, *Phys. Rev. A* **12**, 1846–1858 (1975).
369. R. E. Brown and V. H. Smith, Jr., *Phys. Rev. A* **5**, 140–143 (1972).
370. V. H. Smith, Jr., A. J. Thakkar, W. H. Henneker, J. W. Liu, B. Liu, and R. E. Brown, *J. Chem. Phys.* **67**, 3676–3682 (1977). Erratum: **73**, 4150 (1980).
371. J. W. Liu and V. H. Smith, Jr., *Mol. Phys.* **35**, 145–154 (1978).
372. B. Jeziorski and K. Szalewicz, *Phys. Rev. A* **19**, 2360–2365 (1979).
373. J. N. Migdall, M. A. Coplan, D. S. Hench, J. H. Moore, J. A. Tossell, V. H. Smith, Jr., and J.-W. Liu, *Chem. Phys.* **57**, 141–146 (1981).
374. M. H. Whangbo, E. Clementi, G. H. Diercksen, W. von Niessen, and V. H. Smith, Jr., *J. Phys. B* (*Atom. Mol. Phys.*) **7**, L427–430 (1974).
375. G. H. F. Diercksen, W. Kraemer, and V. H. Smith, Jr., *Phys. Lett.* **54A**, 319–320 (1975).
376. T. Ahlenius and P. Lindner, *Chem. Phys. Lett.* **34**, 123–127 (1975).
377. C. A. Coulson, *Mol. Phys.* **26**, 507–508 (1973).
378. V. H. Smith, Jr. and M. H. Whangbo, *Chem. Phys.* **5**, 234–243 (1974).
379. M. H. Whangbo, W. von Niessen, and V. H. Smith, Jr., *Chem. Phys.* **6**, 282–290 (1974).
380. P. T. Measures, N. L. Allan, and D. L. Cooper, *Int. J. Quantum Chem.* **60**, 579–592 (1996).
381. D. M. Hirst and S. P. Liebmann, *Mol. Phys.* **30**, 597–607 (1975).
382. D. M. Hirst and S. P. Liebmann, *Mol. Phys.* **30**, 1693–1699 (1975).
383. D. M. Hirst and S. P. Liebmann, *Chem. Phys. Lett.* **42**, 403–406 (1976).
384. W. A. Reed, L. C. Snyder, P. Eisenberger, X. J. Pinder, T. Weber, and Z. Wasserman, *J. Chem. Phys.* **67**, 143–146 (1977).
385. P. E. Cade, W. H. Henneker, and A. Kostyla, *J. Chem. Phys.* **70**, 3715–3725 (1979).
386. D. L. Cooper, S. D. Loades, and N. L. Allan, *J. Mol. Struct.* (*THEOCHEM*) **75**, 189–196 (1991).
387. B. J. Clark, H. L. Schmider, and V. H. Smith, Jr., On hybrid orbitals in momentum space, in *Pauling's Legacy: Modern Modelling of the Chemical Bond*, Z. B. Maksic and W. J. Orville-Thomas, eds. (Elsevier, Amsterdam, 1999), pp. 213–229.
388. D. L. Cooper and N. L. Allan, *J. Am. Chem. Soc.* **114**, 4773–4776 (1992).
389. N. L. Allan and D. L. Cooper, *J. Chem. Inform. Comput. Sci.* **32**, 587–590 (1992).
390. N. L. Allan and D. L. Cooper, *Top. Curr. Chem.* **173**, 85–111 (1995).
391. P. T. Measures, K. A. Mort, N. L. Allan, and D. L. Cooper, *J. Comput.-Aided Mol. Design* **9**, 331–340 (1995).
392. N. L. Allan and D. L. Cooper, *J. Math. Chem.* **23**, 51–60 (1998).
393. L. Amat, R. Carbo-Dorca, D. L. Cooper, and N. L. Allan, *Chem. Phys. Lett.* **367**, 207–213 (2003).
394. M. Hô, R. P. Sagar, H. Schmider, D. F. Weaver, and V. H. Smith, Jr., *Int. J. Quantum Chem.* **53**, 627–633 (1995).
395. G. Burkhardt, *Ann. Phys.* (*Leipzig*) **26**, 567–584 (1936).
396. A. Kónya, *Hung. Acta Phys.* **1**, 12–24 (1949).
397. C. A. Coulson and N. H. March, *Proc. Phys. Soc.* (*Lond.*) **A63**, 367–374 (1950).
398. N. H. March, *Theor. Chem. Spec. Per. Rep.* **4**, 92–174 (1981).
399. R. G. Parr and W. Yang, *Density Functional Theory of Atoms and Molecules* (Oxford Univ. Press, New York, 1989).

400. P. A. M. Dirac, *Proc. Camb. Phil. Soc.* **26**, 376–385 (1930).
401. R. K. Pathak and S. R. Gadre, *J. Chem. Phys.* **74**, 5925–5926 (1981).
402. R. K. Pathak and S. R. Gadre, *J. Chem. Phys.* **77**, 1073 (1982).
403. N. L. Allan and N. H. March, *Int. J. Quantum Chem. Symp.* **17**, 227–240 (1983).
404. R. K. Pathak, S. P. Gejji, and S. R. Gadre, *Phys. Rev. A* **29**, 3402–3405 (1984).
405. N. L. Allan, D. L. Cooper, C. G. West, P. J. Grout, and N. H. March, *J. Chem. Phys.* **83**, 239–240 (1985).
406. N. L. Allan and D. L. Cooper, *J. Chem. Phys.* **84**, 5594–5605 (1986).
407. N. H. March, *Int. J. Quant. Chem. Symp.* **20**, 367–376 (1986).
408. N. L. Allan and D. L. Cooper, *J. Chem. Soc. Faraday Trans. II* **83**, 1675–1687 (1987).
409. R. K. Pathak, B. S. Sharma, and A. J. Thakkar, *J. Chem. Phys.* **85**, 958–962 (1986).
410. A. J. Thakkar and W. A. Pedersen, *Int. J. Quantum Chem. Symp.* **24**, 327–338 (1990).

AUTHOR INDEX

Numbers in parentheses are reference numbers and indicate that the author's work is referred to although his name is not mentioned in the text. Numbers in *italic* show the pages on which the complete references are listed.

Advances in Chemical Physics, Volume 128, edited by Stuart A. Rice
ISBN 0-471-44528-2

SUBJECT INDEX

Advances in Chemical Physics, Volume 128, edited by Stuart A. Rice
ISBN 0-471-44528-2